ORNL/4741

PROCEEDINGS OF THE TWENTIETH ANNUAL CONFERENCE ON FOSSIL ENERGY MATERIALS

June 12-14, 2006

Prepared by
R. R. Judkins

OAK RIDGE NATIONAL LABORATORY
MANAGED BY
UT-BATTELLE, LLC
FOR THE
U.S. DEPARTMENT OF ENERGY
UNDER CONTRACT DE-AC05-00OR22725

ORNL/4741

PROCEEDINGS OF THE TWENTIETH ANNUAL CONFERENCE ON FOSSIL ENERGY MATERIALS

June 12-14, 2006
Knoxville, Tennessee

Compiled by
R. R. Judkins and L.S. Mack

Date Published: January 2007

Prepared by
OAK RIDGE NATIONAL LABORATORY
P.O. Box 2008
Oak Ridge, Tennessee 37831-6285
Managed by
UT-Battelle, LLC
for the
U.S. DEPARTMENT OF ENERGY
Under contract DE-AC05-00OR22725

CONTENTS

4c. Inorganic Membranes & Structures

DISCLAIMER

PREFACE

The 20th Annual conference on Fossil Energy Materials was held in Knoxville, Tennessee, on June 12 through June 14, 2006. The meeting was sponsored by the U.S. Department of Energy's (DOE) Office of Fossil Energy through the Advanced Research Materials Program (ARM).
The objective of the ARM Program is to conduct research and development on materials for longer-term fossil energy applications, as well as for generic needs of various fossil fuel technologies. The management of the program has been decentralized to the DOE Oak Ridge Operations Office and Oak Ridge National Laboratory (ORNL). The research is performed by staff members at ORNL and by researchers at other national laboratories, universities, and in private industry. The work is divided into the following categories: (1) New Alloys, (2) Breakthrough Concepts, (3) Coatings and Protection of Materials, and (4) Functional Materials.

These proceedings were produced primarily from electronic files provided by the authors. They have been neither refereed nor extensively edited. However, most of the papers have already undergone technical review within the individual organizations before submission to the Program Office. The proceedings are available on the Fossil Energy home page at http://www.ornl.gov/fossil.

The successful completion of the conference and publication of the proceedings has required help from several people. The organizers wish to thank Angela Beach of the ORNL Conference Office for her help in the many arrangements and the numerous staff and support personnel associated with the conference. Finally we express our sincere appreciation to the authors whose efforts are the very basis of the conference.

Conference Chairmen

ORNL
Roddie R. Judkins
Ian G. Wright

DOE
Robert R. Romanosky Jr.

Conference Coordinators
LaRonda Mack/ORNL
Pam Stanley/NETL
Regina Pride/NETL

SESSION 1

NEW ALLOYS

ADVANCED PRESSURE BOUNDARY MATERIALS

Michael Santella
Oak Ridge National Laboratory, 1 Bethel Valley Road, Oak Ridge, TN 37931-6096
Email: santellaml@ornl.gov; Telephone: 865-574-4805

John Shingledecker
Oak Ridge National Laboratory, 1 Bethel Valley Road, Oak Ridge, TN 37931-6155
Email: shingledecjp@ornl.gov; Telephone: 865-574-4929

ABSTRACT

Increasing the operating temperatures of fossil power plants is fundamental to improving thermal efficiencies and reducing undesirable emissions such as CO_2. One group of alloys with the potential to satisfy the conditions required of higher operating temperatures is the advanced ferritic steels such as ASTM Grade 91, 9Cr-2W, and 12Cr-2W. These are Cr-Mo steels containing 9-12 wt% Cr that have martensitic microstructures. Research aimed at increasing the operating temperature limits of the 9-12 wt% Cr steels and optimizing them for specific power plant applications has been actively pursued since the 1970's. As with all of the high strength martensitic steels, specifying upper temperature limits for tempering the alloys and heat treating weldments is a critical issue. To support this aspect of development, thermodynamic analysis was used to estimate how this critical temperature, the A_1 in steel terminology, varies with alloy composition. The results from the thermodynamic analysis were presented to the Strength of Weldments subgroup of the ASME Boiler & Pressure Vessel Code and are being considered in establishing maximum postweld heat treatment temperatures. Experiments are also being planned to verify predictions. This is part of a CRADA project being done with Alstom Power, Inc.

INTRODUCTION

Postweld heat treatment (PWHT) is the process of annealing welds after welding operations are completed for the purpose of improving their properties or mitigating potential problems.[1] It can produce both metallurgical and mechanical effects that depend on the chemical composition of the alloy being treated, its processing history prior to and including welding, and the specific details of the PWHT including heating and cooling rates, annealing temperatures, and holding times.[1-3] For carbon and alloy steels, PWHT may be used for a variety of reasons including reducing or redistributing residual stresses, controlling distortion in subsequent fabrication operations, tempering hardened microstructures, restoring toughness, removing hydrogen, and minimizing stress corrosion cracking.[2,3]

Temperature control in PWHT is critical from both a metallurgical and a practical perspective. Metallurgically, maximum temperatures will largely govern the kinetics of annealing phenomena and the thermodynamic stability of microstructures.[4-6] In practice, it is generally desirable to use the highest PWHT temperature possible to minimize processing time, labor, and energy resources. Of course, temperature control is a key element of all heat treating operations so knowing important transformation temperatures and how microstructures vary with temperature is critical for effective processing. For convenience when heat treating carbon and alloy steels, critical temperatures and temperature ranges are customarily based on terms associated with the iron-carbon binary phase diagram. For example, under equilibrium condi-

tions, the lowest temperature where the austenite phase is stable is designated as A_1, and the lowest temperature where a hypo-eutectoid steel (C concentration < ~ 0.8 wt%) is 100% austenite is referred to A_3.[1]

Of the various transformation temperatures associated with the Fe-C binary system, the most important one for PWHT of carbon and alloy steel weldments is A_1. One of the more common features of weldments in these steels is the formation of hard microstructures, typically martensite, in either the weld deposits, the heat affected zones of the base metal, or both. Postweld heat treatment is then used to temper the microstructure with the intent of restoring some toughness.[2,3] Implicit expectations of PWHT are that all existing martensite is tempered and no new martensite is formed. The only way new, untempered martensite can form during PWHT is by exceeding the A_1. This condition would cause austenite to form. The austenite could then transform to untempered martensite during cooling depending on the chemical composition of the steel in question and the details of its transformation behavior.

The Cr-Mo steels containing 9-12% Cr are among the highest strength ferritic alloys that are suitable for construction of large power generation components such as piping and manifolds for boilers and heat exchangers, turbine parts, and pressure vessels that operate at elevated temperatures.[7] These are martensitic alloys that generally contain strengthening precipitates of $M_{23}C_6$, various M(C,N) phases, and possibly intermetallic phases. They are typically used in a heat treated condition referred to as normalized and tempered. They are frequently welded, and PWHT is almost always required for components built to ASME Boiler & Pressure Vessel Code requirements.[8]

An important item in the ASME Code rules is specification of PWHT requirements. When it is required, welds in the 9-12% Cr steels must be postweld heat treated at a minimum of 704°C. The rules for construction of power boilers and pressure vessels also specify that maximum temperatures exceeding the 704°C minimum are permissible.[8] However, the intention of the ASME Code requirements is that higher PWHT temperatures, if used, do not exceed the A_1 of the alloy being heat treated. It is recognized that there are limited data from experimental measurements of A_1's, and that the base metal specifications for both 9 and 12 Cr steels span ranges that may result in large variations of A_1's. Because of these uncertainties, this study was undertaken to evaluate the variations of A_1's in several of these steels using commercially available (Thermo-Calc) computational thermodynamics analysis. This information would then be factored into possible future limitations on maximum permissible PWHT temperatures for the 9-12 Cr steels. Also, some data are presented to illustrate the effect of heating rate on the measured A_1 of a 9 Cr steel using a high temperature extensometer on a Gleeble® machine.

EXPERIMENTAL

The steel compositions subjected to thermodynamic analysis for estimation of the variations of A_1's are shown in Table 1. The composition ranges specified in ASTM A387 for product analysis were used for those of Grade 91 and Grade 911. The composition ranges of the 9Cr-2W and the 12Cr-2W alloys were taken respectively from Case 2179-3 and Case 2180-2 of the ASME Boiler and Pressure Vessel Code. The composition range for the SAVE12 alloy was taken from Sumitomo product certification information. The minor elements Al, B, P and S were ignored in the analyses because their effects on the A_1's was expected to be slight. The elements Nd and Hf were also omitted from the SAVE12 composition[9] because they are not treated in the available thermochemical databases for steels, but their effects on A_1's are also expected to be very small.

The analyses for estimating the variations of A_1 with composition were done using Thermo-Calc software with the Fe-DATA version 6 thermochemical database.[10] To produce groups of alloys that spanned

Table 1. Alloy composition ranges

	Composition range, wt%				
Element	**Grade 91**	**Grade 911**	**9Cr-2W**	**SAVE12**	**12Cr-2W**
Carbon	0.06-0.15	0.08-0.14	0.07-0.13	0.08-0.13	0.07-0.14
Manganese	0.25-0.66	0.25-0.66	0.30-0.60	0.10-0.80	0.70
Silicon	0.18-0.56	0.08-0.56	0.50	0.50	0.50
Chromium	7.90-9.60	8.40-10.70	8.50-9.50	8.80-12.00	10.00-12.50
Molybdenum	0.80-1.10	0.85-1.15	0.30-0.60	---	0.25-0.60
Tungsten	---	0.85-1.15	1.50-2.00	2.50-3.50	1.50-2.50
Nickel	0.43	0.43	0.40	---	0.50
Cobalt	---	---	---	2.50-6.00	---
Copper	---	---	---	---	0.30-1.70
Vanadium	0.16-0.27	0.16-0.27	0.15-0.25	0.20-0.40	0.15-0.30
Niobium	0.05-0.11	0.05-0.11	0.04-0.09	0.20-0.10	0.04-0.10
Tantalum	---	---	---	0.20	---
Nitrogen	0.025-0.080	0.035-0.095	0.030-0.070	0.050	0.040-0.100
Conditions	1812	2012	2004	1305	1740

each specification range, five reference compositions were selected for each alloy. Then each element was varied from its minimum to its maximum while all other elements were maintained at their reference values. The 5 reference compositions were:

1. Each element set to the mid-point of its specified range
2. Austenite stabilizers[5] (C, Co, Cu, Mn, Ni, N) set to their specified maximums; ferrite stabilizers[5] (Cr, Mo, Nb, Si, Ta, V, W) set to their specified minimums
3. Ferrite stabilizers set to their specified maximums; austenite stabilizers set to their specified minimums
4. Each element set to the maximum specified for its range
5. Each element set to the minimum specified for its range

Default conditions in Thermo-Calc divided each individual composition range into 40 equally spaced intervals. While this approach did not produce totally random sets of chemical compositions, it did encompass the upper and lower chemistry limits of each alloy. The total number of unique chemical compositions generated by this approach for each alloy specification are indicated as *Conditions* in Table 1. The basic procedure for calculating the A_1's involved verifying that temperature was within the lower austenite + ferrite phase field, and then releasing constraints on temperature and calculating the equilibrium conditions where the austenite phase disappeared. The phases included in the equilibrium calculations were austenite (fcc iron), ferrite (bcc iron), M_6C, $M_{23}C_6$, M(C,N), sigma phase, and laves phase. For the 12Cr-2W steel the possibility of Cu phase formation was also considered in the analysis.

A specimen of SAVE12 alloy was used to evaluate the effect of heating rate on measured A_1. The analyzed chemical composition of this specimen was Fe-0.099C-0.68Mn-0.25Si-9.89Cr-3.08W-3.21Co-0.31Ni-0.05Nb-0.31V-0.013N, wt%. A Gleeble® machine was used for the experiments which were conducted in vacuum by heating a 10-mm-diameter rod to 1100°C at rates of 2, 20, 200, and 2000°C/min. A single specimen was used for all the measurements which were done in the order of highest to lowest heating rate. The rod was given a solution treatment of 1100°C for 15 min prior to the heating rate experiments. A high temperature diametral extensometer (Model 3580, Epsilon Technology Corp.) was

used to record instantaneous changes of specimen diameter during the heating/cooling cycles. The extensometer was attached to the specimen rod at the position of a thermocouple that was used for closed-loop feedback control of temperature. This is a fairly common arrangement for Gleeble® experiments.

RESULTS

The predictions for ranges of A_1's for the 9 Cr steels are shown in Figure 1 and for the 12Cr-2W steel in Figure 2. The results were plotted as histograms mainly to enable a graphical display, but the histograms show some noteworthy features. Each histogram in Figure 1 contains 5 prominent peaks that are centered on the 5 reference chemical compositions. The peaks at the low temperature extrema correspond to the reference no. 2 compositions in each alloy where the austenite formers were maximized and the ferrite formers were minimized. The order of the peaks from lowest to highest predicted A_1's was reference nos. 2, 4, 1, 5, and 3. One reason the peaks at each reference composition are so prominent relates to the choice of accepting default conditions for varying individual elements within their specified ranges. For example, elements such as the carbide formers Nb, Ta, and V occur in relatively small composition ranges and they have relatively small effects on A_1. This is the main reason there are relatively large frequencies of compositions centered about the 5 reference conditions.

Figure 1 shows that the minimum predicted A_1's increased with the sophistication of the alloying used to maximize creep strengths.[7] It is likely that the expanded ranges of A_1's for Grade 911 and SAVE12 are the result of having larger specified ranges for Cr additions compared to Grade 91 and 9Cr-2W.

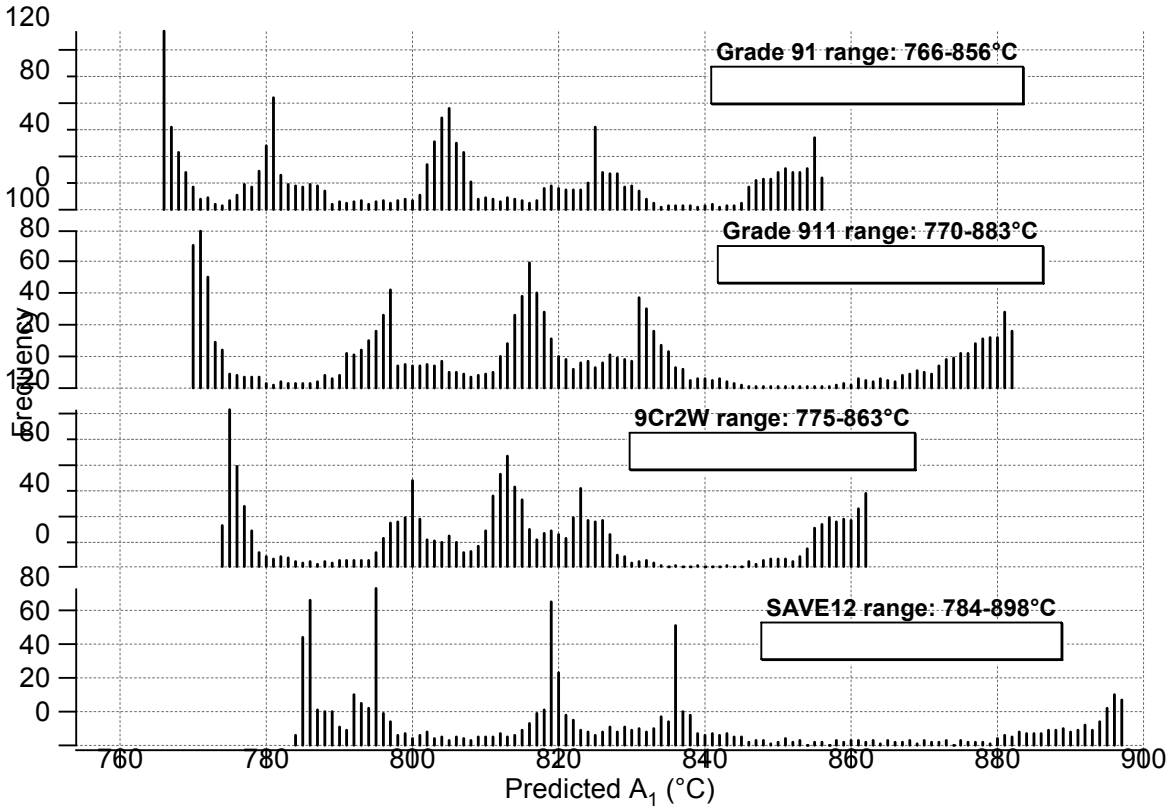

Figure 1. Histogram frequency plots of predicted A_1's for 9 Cr steels.

There are only 4 major peaks for the 12Cr-2W steel predictions shown in Figure 2 because the analysis of this alloy is incomplete. The only condition not yet done is reference composition no. 5 that has all elements set to their minimum specified ranges. However, the extrema conditions of reference composition nos. 2 and 3 are shown so the predicted A_1 range for this alloy is accurately represented in Figure 2.

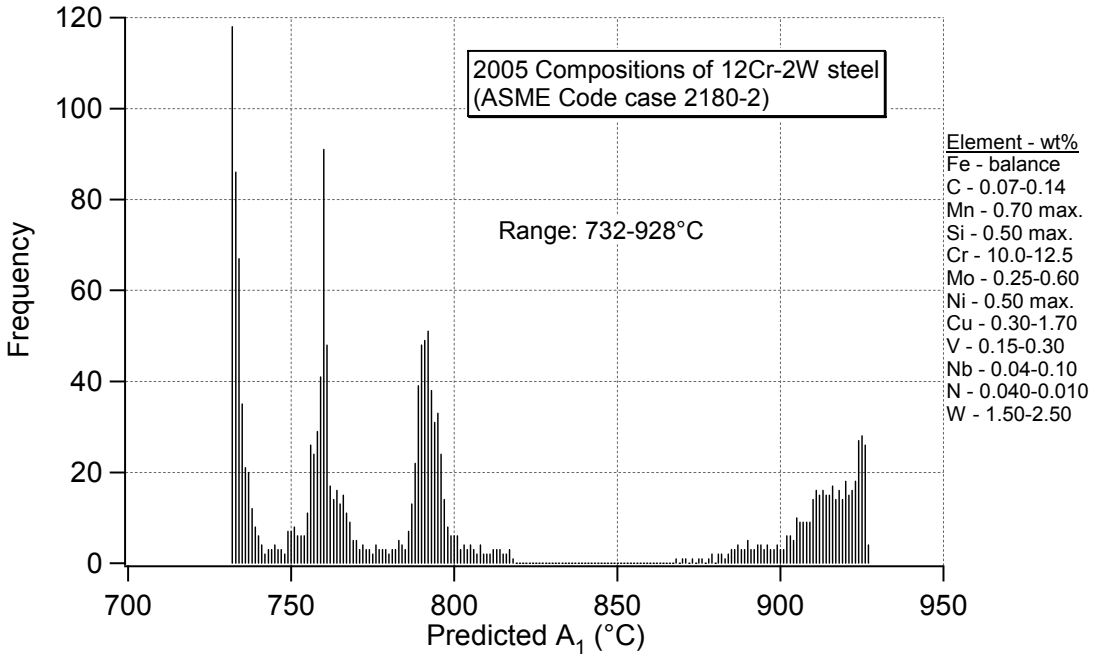

Figure 2. Histogram frequency plot of predicted A_1 for 12Cr-2W steel.

The results from measurements of the effects of heating rate on the details of austenite formation and growth in the SAVE12 alloy are presented in Figure 3. Austenite fractions were determined from thermal arrests that occurred during heating using the procedure described by Eldis.[11] The measurements show that the detected start temperature for austenite formation systematically increased with heating rate. Experimentally measured austenite transformation start temperatures are designated by A_{C1} to distinguish them from true equilibrium temperatures, A_1.[1] Figure 3 shows that increasing the heating rate from 2°C/min to 2000°C/min increased A_{C1} about 70°C. At the 2°C/min heating rate austenite formation was detected around 810°C, about 35°C higher than the A_1 predicted by equilibrium thermodynamics.

DISCUSSION

Except for SAVE 12, the other four steels analyzed conform to the material designation of P5B Group 2 that is used by the ASME Code to classify materials for PWHT requirements.[8] In other words, according to ASME Code requirements Grade 91, Grade 911, 9Cr-2W steel, and 12Cr-2W steel must all be post-weld heat treated using the same rules. These rules require a minimum PWHT temperature of 704°C with higher temperatures permitted but not specified. If one rule was used to limit the PWHT temperature for the steels then the results presented in Figures 1 & 2 indicate that the maximum limiting temperature should be 732°C. This is the lowest predicted temperature where austenite is stable in the 12Cr-2W steel. Limiting PWHT of the P5B Group 2 steels to less than 732°C should prevent the formation of unwanted austenite and subsequent untempered martensite in all of these alloys including SAVE12. The SAVE12

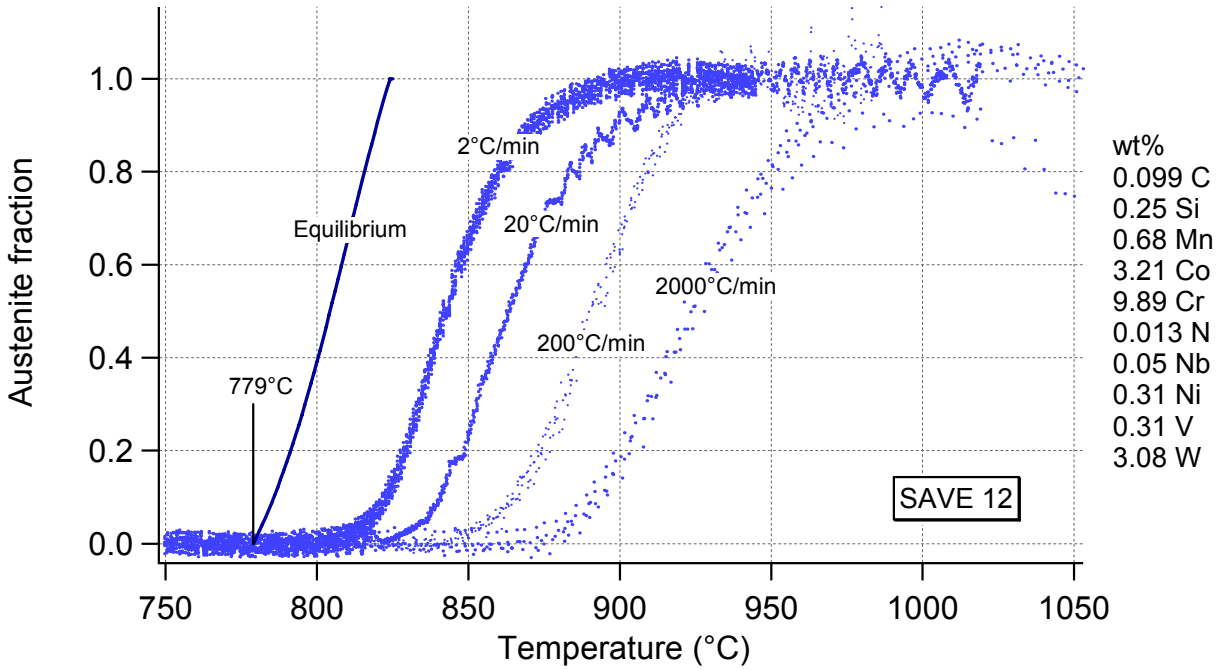

Figure 3. Variation with temperature of measured austenite fraction in SAVE12 alloy for 4 heating rates. The variation of the equilibrium austenite amount was calculated.

steel is not approved for ASME Code constructions but judging by the similarity of its chemical composition to those of the P5B Group 2 alloys it would likely be assigned to this designation if it were approved.

This study also suggests information derived from computational thermodynamics analysis could be a reasonable alternative to specifying PWHT temperature limits rather than by rules that cover wide ranges of alloy behavior. Of course, this would require access to the computational thermodynamics tools like Thermo-Calc and the appropriate databases. In addition, it would also be prudent to supplement thermodynamic information with some experimental measurements of A_1 to build confidence in the accuracy of the predictions.

The data presented in Figure 3 graphically illustrate the effects heating rate has on measuring the starting temperature and progress of austenite formation. The increase with heat rate of A_{C1} relative to A_1 is basically due to austenite formation occurring by diffusion controlled nucleation and growth. Nucleation events typically involve an initial incubation period. Subsequent growth of newly formed austenite grains will occur by diffusional processes. Consequently, increases in heating rate reduce the time available for formation at the equilibrium temperature and they produce the appearance of higher than equilibrium transformation temperatures. The calculated A_1 is about 35°C below the A_{C1} measured at 2°C/min heating. This is a very slow heating rate, about as slow as is practical for the Gleeble®, suggesting that Thermo-Calc may be underestimating A_1 in the SAVE12 alloy system.

CONCLUSION

Analysis by computational thermodynamics was used to predict the temperature range and the absolute minimum equilibrium temperature, i.e., A_1, where austenite is stable for the specified composition range for each of 5 Cr-Mo steels. The steels and the predicted values are:

A387 Grade 91, minimum A_1 = 766°C, A_1 range = 766-856°C
A387 Grade 911, minimum A_1 = 770°C, A_1 range = 770-883°C
9Cr-2W, minimum A_1 = 775°C, A_1 range = 775-863°C
12Cr-2W, minimum A_1 = 732°C, A_1 range = 732-928°C
SAVE12, minimum A_1 = 784°C, A_1 range = 784-898°C

Measurements showed that the start of austenite transformation, A_{C1}, of SAVE12 increased from about 810°C for heating at 2°C/min to about 880°C for heating at 2000°C/min. Equilibrium calculation, representing infinitely slow heating rate, estimated a transformation temperature of A_1 = 779°C.

ACKNOWLEDGEMENT

The support and encouragement of certain colleagues cannot be overstated. These include Jeff Henry of Alstom Power, Inc., Bob Swindeman retired from the Oak Ridge National Laboratory, and the members of the ASME Boiler & Pressure Vessel Committee Subgroup on Strength of Weldments.

REFERENCES

1. *ASM Handbook*, Volume 4, *Heat Treating* (online), Third Printing (1995), ASM International
2. R. D. Stout, "Postweld Heat Treatment of Pressure Vessels," *Welding Research Council Bulletin 302*, February, 1985, pp. 1-14
3. C. E. Spaeder, Jr. and W. D. Doty, "ASME Post-weld Heat Treating Practices: An Interpretive Report," *Welding Research Council Bulletin 407*, December, 1995, pp. 50-65
4. *Steels: Microstructures and properties*, *Second edition*, R. W. K. Honeycombe and H. K. D. H. Bhadeshia, 1995, Edward Arnold, London
5. *Phase Transformations in Metals and Alloys, Second edition,* D. A. Porter and K. E. Easterling, 2001 reprint, Nelson Thornes Ltd, Cheltenham, United Kingdom
6. *Transformations in Metals,* P. G. Shewmon, 1969, McGraw-Hill, New York
7. R. L. Klueh, "Elevated temperature ferritic and martensitic steels and their application to future nuclear reactors," *International Materials Reviews*, vol. 50 (5), 2005, pp. 287-310
8. *ASME Boiler and Pressure Vessel Code*, "Rules for Construction of Power Boilers," Section I; "Rules for Construction of Nuclear Facility Components," Section III; and, "Rules for Construction of Pressure Vessels," Section VIII, The American Society of Mechanical Engineers, New York
9. M. Igarashi and Y. Sawaragi, "Development of 0.1C-11Cr-3W-3Co-V-Nb-Ta-Nd-N Ferritic Steel for USC Boilers, pp. 107-112 in *Proceedings of International Conference on Power Engineering-97, Volume 2*, The American Society of Mechanical Engineers, New York
10. N. Saunders, "Fe-DATA, a database for thermodynamic calculations for Fe alloys,"
Thermotech Ltd., Surrey Technology Centre, The Surrey Research Park,
Guilford, Surrey GU2 7YG, U.K.
11. G. T. Eldis, "A Critical Review of Data Sources for Isothermal and Continuous Cooling Transformation Diagrams," pp. 126-148 in *Hardenability Concepts with Applications to Steels,* The Metallurgical Society of AIME, Warrendale, Pennsylvania, 1978

FIRESIDE CORROSION OF ALLOYS FOR USC PLANTS

K. Natesan and J. -H. Park
Argonne National Laboratory, 9700 South Cass Avenue, Argonne, IL 60439
E-mail: natesan@anl.gov; Telephone: (630) 252-5103; Fax: (630) 252-8681

ABSTRACT

A program on fireside and steamside corrosion, in support of ultra supercritical (USC) plants, was conducted to evaluate the performance of several structural alloys in the presence of mixtures of synthetic coal ash, alkali sulfates, and alkali chlorides and in a steam environment. Experiments address the effects of deposit chemistry, temperature, and alloy chemistry on the corrosion response of alloys at temperatures in the range of 650-800°C. Materials selected for the study included intermediate-Cr ferritic steels, high-Cr austenitic alloys, and Ni-base alloys. Data were obtained on weight change, scale thickness, internal penetration, microstructural characteristics of corrosion products, mechanical integrity of the scales, and cracking of scales.

The intermediate-Cr ferritic steels were found to corrode significantly even with a low concentration of 25 ppm NaCl in the exposure environment. Based on acquired corrosion information, we have proposed a mechanism for accelerated corrosion in the presence of a NaCl-containing oxidizing environment. We have developed a relatively low temperature process to develop (Al,Si) coating on intermediate-chromium steels. The coated alloys have been tested at 650°C in simulated combustion environments with and without NaCl in a concentration range of 25-300 ppm. Results showed superior corrosion performance for the coated specimens.

BACKGROUND

Conceptual designs of advanced combustion systems that utilize coal as a feedstock must include improved thermal efficiency and significant reduction in release of sulfur oxides, nitrogen oxides, and carbon dioxide. Such systems require materials and components that can operate at much higher temperatures than those found in current coal-fired power plants. Component reliability and long-term, trouble-free performance of structural materials for these systems necessitate development/evaluation of materials in simulated coal-combustion environments. Apart from the environmental aspects of the effluent from coal combustion, one concern from the systems standpoint is the aggressiveness of the combustion environment toward boiler structural components, such as steam superheaters and reheaters.

Recently, the U.S. Department of Energy has started to reevaluate coal-fired steam generation plants and, in particular, the designs based on supercritical and ultra supercritical steam conditions. The ultimate goal of the staged development of power systems is to change steam pressure and temperature from the current values of 16.5-24 MPa (2400-3500 psig) and 540°C (1000°F), respectively, to 34.5 MPa (5000 psig) and 650°C (1200°F) in the near term to 34.5 MPa (5000 psig) and 760°C (1400°F) [1]. The higher steam temperature is expected to lead to another 2-3% increase in efficiency over a 700°C design, thus improving fuel usage and diminishing CO_2 emissions [2].

Fireside metal wastage in conventional coal-fired boilers can occur by gas-phase oxidation or deposit-induced liquid-phase corrosion. The former can be minimized by using materials which are resistant to oxidation at the service temperatures of interest. The latter is an accelerated type of attack, influenced by the vaporization and condensation of small amounts of impurities such as sodium, potassium, sulfur, chlorine, and vanadium (or their compounds) that are present in the coal feedstock. At the temperatures of interest in advanced combustion systems, mixtures of alkali sulfates, and alkali chlorides, dominate fireside deposit, and viable structural alloys must be resistant to attack by such deposits.

In advanced combustion systems, alkali sulfate and coal ash will be the predominant deposit because the metals in the superheater regions will be subjected to a much higher steam temperature. Several factors (including sulfur, alkali, and chlorine in coal feedstock; excess air level during the combustion process; and metal temperature dictated by the steam temperature) determine the extent of corrosion of superheater materials in coal-fired boilers. The objective of the present work is to evaluate the corrosion performance of state-of-the-art candidate materials in coal ash, alkali sulfate, and alkali chloride environments at temperatures in the range of 650-800°C. The goal of the experimental program is to develop a scientific understanding of corrosion mechanisms as a function of alloy composition and deposit chemistry, and to quantitatively determining the scaling and internal penetration of the alloys. In this paper, we present our study on the corrosion performance of intermediate-chromium ferritic steels that are being considered for superheater application up to a steam temperature of 650°C.

Corrosion In Cl-Containing Environments

From the materials-corrosion standpoint, the major important gas species are oxygen, sulfur, and chlorine. Any solid compound that contains alkali sulfates and alkali chlorides can also affect the corrosion performance of structural materials due to chemical reactions or by creating an environment in which the vaporization (from the solid deposits) of S and Cl containing phases can occur. Thermodynamic calculations have been made to evaluate the gas and condensed-phase chemistries during combustion of coal under excess-air and air-deficient conditions. The calculations showed that at temperatures <1200K, HCl is the dominant chlorine-containing phase in the gaseous environment during coal combustion under USC plant conditions [3].

In an earlier study [4], laboratory experiments were conducted at 650°C under simulated combustion gas chemistries that included SO_2 and HCl. Results indicated that in the presence of HCl, the scale is more prone to cracking and spallation, and eventually, accelerated metal wastage, especially in Fe-based alloys such as austenitic stainless steels and Alloy 800. The results also indicated that high-Ni alloys are more resistant to corrosion in Cl-containing combustion atmospheres, primarily because of the formation of solid $NiCl_2$ corrosion product. However, pull-test results indicated that scales developed on high-Ni alloys were more susceptible to spallation or erosion-induced loss when exposed in combustion environments without Cl_2 or HCl.

In another study [5], experiments were conducted to evaluate the effect of preformed oxide layers on the corrosion of alloys that were subsequently exposed to mixed-gas atmospheres. Several conclusions can be drawn from the study. The presence of Cl in the environment can lead to metal chlorides of the alloy constituents, which generally exhibit high vapor pressures.

Reaction of Fe, Cr, and Al with Cl_2 or HCl leads to volatile chlorides, whereas the reaction of oxides of Fe and Al can lead to chloride phases with low partial pressures. Therefore, to be corrosion-resistant to Cl, the alloys must develop oxides of Fe and Al. Reaction of chromia with Cl_2 can lead to significant corrosion, whereas chromia can offer protection against HCl corrosion. Reaction of Ni and NiO with Cl_2 or HCl will lead to solid $NiCl_2$ at 650°C; the vapor pressure of $NiCl_2$ is $\approx 5 \times 10^{-4}$ atm, which indicates a lower corrosion rate for alloys with a higher Ni content. Elemental depth profiles generated by Auger electron spectroscopy clearly showed that elements such as Fe, Cr, and Al can react with Cl to form volatile chlorides and thus lead to catastrophic corrosion.

Subsequently, additional experiments were conducted to develop an understanding of the mechanism and morphology of corrosion of materials used in waterwall and superheater, assess the extent of corrosion, and propose and validate potential remedial measures for mitigating the combined effects of S, Cl, and deposits on corrosion [6]. In recent studies of corrosion of Fe-based austenitic alloys in simulated fireside environments, the presence of low concentrations (≈1 wt.%) of NaCl in the ash deposit led to significant acceleration of the corrosion process and high metal wastage [7-9]. In most these studies, Fe-based intermediate-chromium advanced ferritic steels were not included, primarily because of the lack of availability of the materials. During the past two years, we have made a concerted effort to evaluate the corrosion performance of several advanced ferritic alloys in environments that are pertinent to USC plants and also to establish the role of oxygen, sulfur, and alkali chlorides in the corrosion process. Results from such a study on the ferritic and austenitic Fe-based alloys are presented in this paper.

EXPERIMENTAL PROCEDURE

Materials

Numerous alloys, both ASME coded and uncoded, were selected for corrosion evaluation. The advanced ferritic alloys included modified 9Cr, E 911, HCM 12A, and NF 616. These alloys contain varying amounts of W, Nb, M, and V, and are designed to improve the creep strength for service at temperatures up to 650°C. The compositions of the Fe-base alloys selected for the study are listed in Table 1. The included austenitic alloys were broadly based on 18-20Cr and 20-25Cr steels. Super 304H, 347HFG, and NF709 fall into 18-20Cr steels, with improved creep strength achieved by addition of Nb and/or Ti. HR3C, 310TaN, and SAVE 25 fall into 20-25Cr steels, with improved creep strength achieved by addition of Nb, Ti, Ta, and N. Modified 800 contains the base constituents of Alloy 800, with additions of the strengthening elements Nb, V, N, and B. HR120 is a Fe-Ni-Cr alloy with additions of Co, W, N, and Nb. Specimens of 800H clad with Alloy 671 and Fe aluminide clad super 304 stainless steel were included in the study.

Corrosion Experiments

To examine the role of NaCl vapor (arising from combustion of coal) during the corrosion process, several corrosion experiments were conducted at 650°C with the Fe-base austenitic alloys and four intermediate-chromium ferritic steels (see Table 1) in air-1 vol% SO_2, argon-300 ppm NaCl, and air-1 vol% SO_2- 300 ppm NaCl environments. The specimens were exposed for

Table 1. Nominal composition (in wt.%) of Fe-base alloys selected for corrosion study

Material	C	Cr	Ni	Mn	Si	Mo	Fe	Other
Modified 9Cr	0.10	9	0.8	0.5	0.4	1.0	Bal	Nb 0.08, V 0.20, N 0.06
E 911	0.12	9	0.3	0.5	0.2	0.9	Bal	W 0.9, V 0.2, Nb 0.06, N 0.06
NF 616	0.10	9	0.1	0.5	0.1	0.5	Bal	W 1.8, V 0.20
HCM12A	0.10	12	0.3	0.5	0.3	0.4	Bal	W 2.0, V 0.2, Nb 0.05, Cu 0.9, N 0.05
Super 304H	0.10	18	9	1.0	0.3	-	Bal	Nb 0.45, Cu 3.0, N 0.09
347HFG	0.08	18	11	2.0	1.0	-	Bal	Nb + Ta = 10 x C minimum
HR3C	0.06	25	20	1.2	0.4	-	Bal	Nb 0.45, N 0.2
310TaN	0.05	25	20	1.0	0.2	-	Bal	Ta 1.5, N 0.2
NF709	0.07	20	25	1.0	0.6	1.5	Bal	Ti 0.6, Nb 0.2, N 0.18, B 0.004
SAVE 25	0.10	23	18	1.0	0.4	-	Bal	Nb 0.45, W 1.5, Cu 3.0, N 0.2
Modified 800H	0.10	20	30	1.5	0.2	1.5	Bal	Ti 0.25, Nb 0.25, V 0.05, N 0.03, B 0.004
HR120	0.05	25	37	0.7	0.6	2.5	Bal	Co 3, W 2.5, N 0.2, Cu, Al 0.1, Nb 0.7
MA956	-	20	-	-	-	-	Bal	Al 4.5, Ti 0.5, Y_2O_3 0.6
671-clad 800H								
671	0.05	48	Bal	0.02	0.2	-	0.2	Ti 0.4
800H	0.05	21	32	0.5	0.2	-	Bal	Ti 0.4, Al 0.4
Fe_3Al-clad/Super 304								
Fe_3Al	-	2	-	-	-	-	Bal	Al 16
Super 304	0.1	18	9	1	0.3	1	Bal	Nb 0.45, Cu 3

100 h at 650°C. The experimental setup (see Fig. 1) consisted of a resistance-wound furnace in which an alumina tube was inserted as the reaction chamber. A small boat containing NaCl, ahead of the specimens, was used as the source of NaCl. The temperature of the NaCl-containing boat was independently controlled to obtain the desired concentration of NaCl in the gas phase. Calculations, based on the temperature dependence of vaporization of NaCl, were made to ensure that sufficient amount of NaCl was present in the source boat for the duration of the experiment. Figure 2 shows the vaporization curves and the amount of NaCl required for experiments of different durations. Specimens of various austenitic and ferritic alloys and cladded materials were suspended from quartz hangers at 650°C for 100 h in the three environments mentioned above. Subsequently, several of the intermediate chromium ferritic alloys were tested in environments containing lower concentrations (150 and 25 ppm) of NaCl in the gas phase. Upon completion of the exposures, the specimen surfaces were analyzed using a scanning electron microscope equipped with an energy dispersive X-ray analyzer.

Coating Development

The coating approach was to tailor the surface of the material to prevent and/or minimize transport of chlorine containing species so as to enable development of protective Cr-rich oxide scale. The Fe-Cr ferritic steels were contacted with a solution of Si and Al dissolved in lithium at temperatures in the range of 600-650°C and for times in the range of 1-2 h, sufficient for the dissolved Si and Al to react with the surface transition metals such as Fe and Cr to form a silicide and/or aluminide coating. The coating process is done under a vacuum or inert atmosphere. Specifically, 4 g of Li together with 1-2 wt% Si (in powder form) and 0.1-0.5 wt.% Al (in powder form) was sealed in a gas tight SS capsule together with a number of Fe-based alloy

specimens. After heating to appropriate temperature to melt the Li and dissolve the Si and Al powder in the molten Li, the specimens were coated with the liquid metal mixture. After coating was complete, the capsule was opened and the liquid metal mixture was drained. A small amount of methanol was used to dissolve any residual Li from the specimen surfaces. Subsequent testing of the coated specimens was performed in an environment containing low concentrations (0-300 ppm) of NaCl in air containing 1 vol.% SO_2 at 650°C.

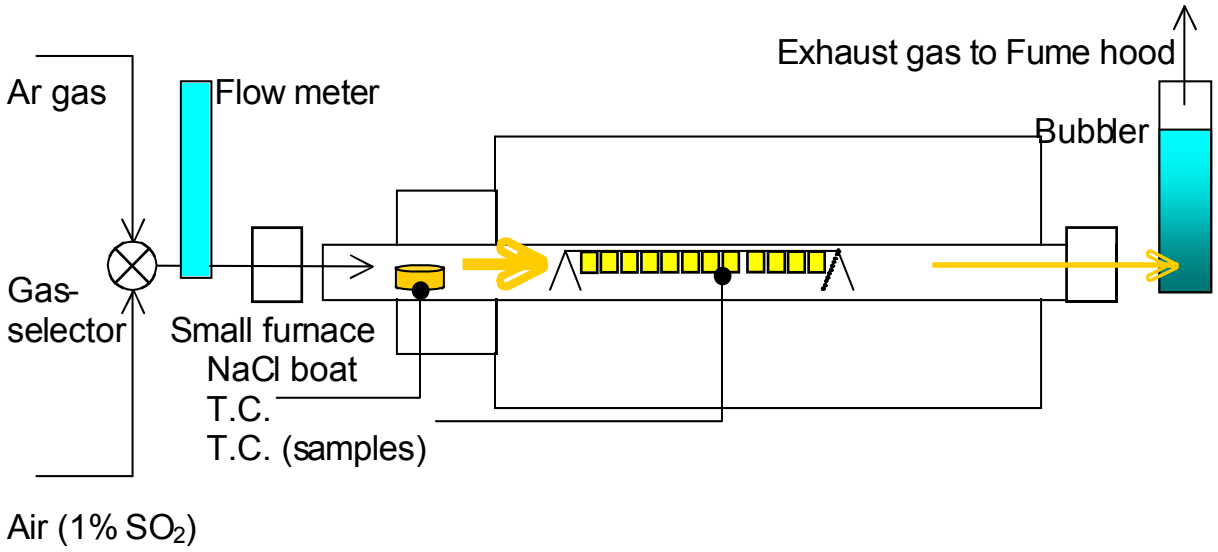

Figure 1. Schematic representation of setup for corrosion experiments.

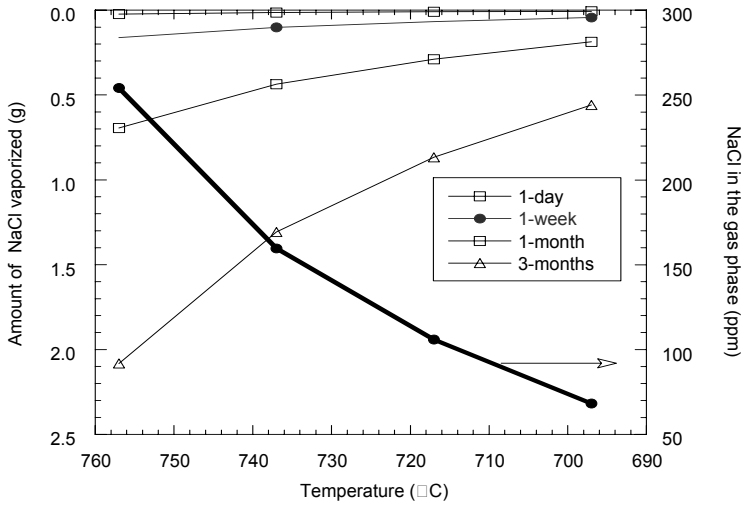

Figure 2. NaCl vaporization curves.

Results and Discussion

Specimens exposed for 100 h at 650°C to air-1%SO_2 environment exhibited little weight change, as expected since the oxygen partial pressure is high and the sulfur partial pressure is low and all the alloys developed very thin oxide scales. Specimens exposed to Argon-300 ppm NaCl also showed negligible weight change. The oxygen content in Argon was of the order of 20-50 ppm and a combination such a low oxygen environment and 300 ppm NaCl didn't seem to accelerate corrosion of the alloys.

Figure 3 shows the weight change data for the alloys after 100–h exposure to Argon-300 ppm NaCl at 650°C. Figure 4 shows the weight change data for the same alloys after 100-h exposure at 650°C to air-1%SO_2-300 ppm NaCl environment. Figure 5 shows a compilation of the data generated for all the alloys in the three environments. It should be noted that the ordinate in this figure is in log scale and the weight changes are substantially greater in the air-SO_2-NaCl environment than in others.

Figure 5 also shows similar data for duplicate specimens of HCM12A that were used in the experiments. Among the austenitic alloys HR3C exhibited superior performance in these 100-h tests and all the intermediate–chromium ferritic steels performed poorly, as evidenced by excessive weight loss in the presence of 300 ppm NaCl.

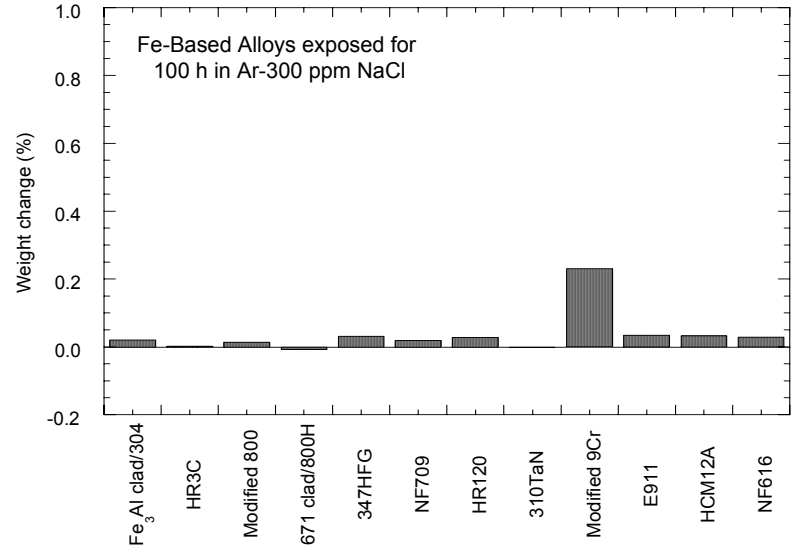

Figure 3. Weight change data for the Fe-base alloys after 100-h exposure at 650°C to Argon-300 ppm NaCl gas mixture.

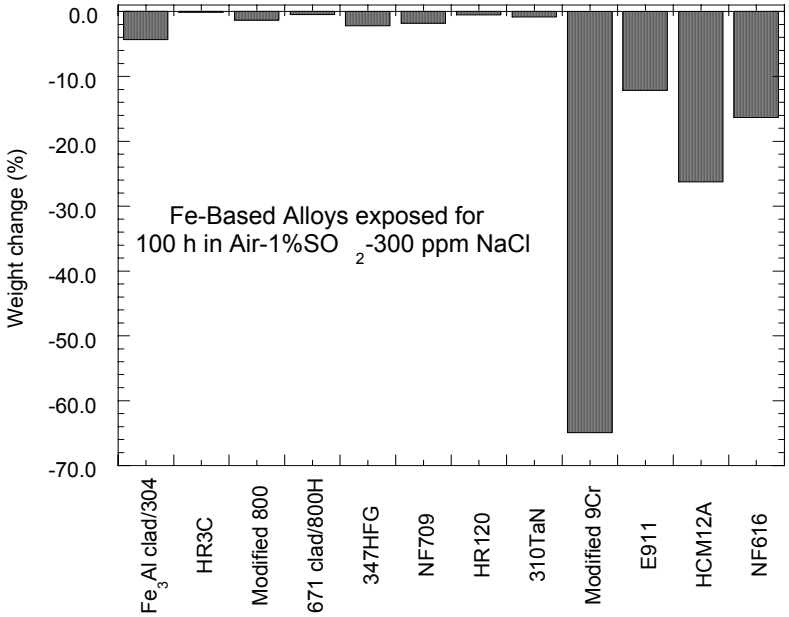

Figure 4. Weight change data for the Fe-base alloys after 100-h exposure at 650°C to air-1% SO_2-300 ppm NaCl gas mixture.

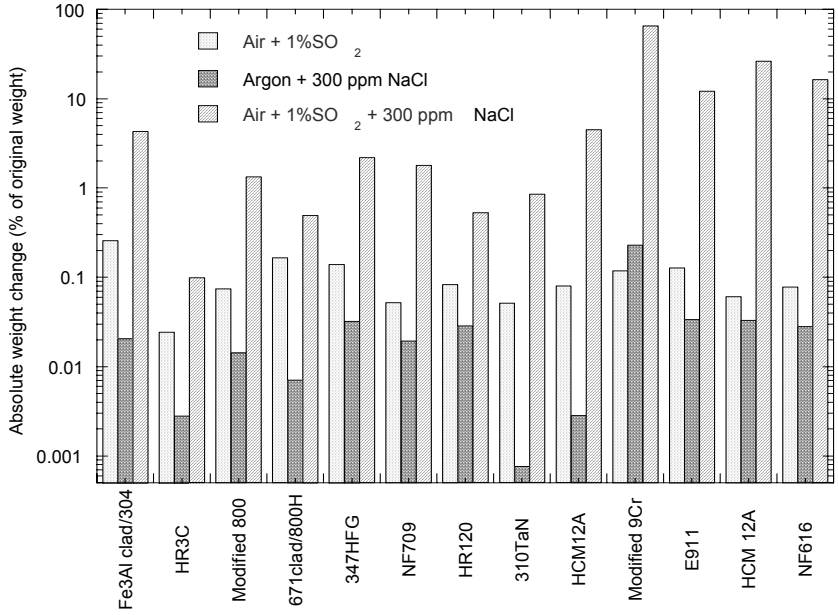

Figure 5. Absolute weight change data for the Fe-base alloys after 100-h exposure at 650°C to three environments.

Figure 6 shows a macrophotograph of duplicate specimens of intermediate-chromium steels after 100-h exposure at 650°C to air-1%SO_2-300 ppm NaCl environment. Since the alloys exhibited catastrophic attack in this test, additional experiments were conducted on these alloys with lower concentration of NaCl in the exposure environment. Also, coatings were developed to resist the chlorine-induced attack in these steels and were tested along with uncoated steel specimens.

Figure 7 shows a comparison of the weight change data for the uncoated and coated intermediate-chromium ferritic alloys after 100-h exposure at 650°C to air-1% SO_2-150 or 300 ppm NaCl gas mixture. Results showed substantial reduction in corrosion induced weight loss for the (Al,Si) coated specimens in an environment containing 150 ppm NaCl. In uncoated alloys, a detailed analysis of the physical characteristics of the scales developed in the presence of NaCl showed that the scales were dense, with almost no porosity. Furthermore, the scales were concave shaped indicating that the scale was pushed away from the substrate, probably by a volatile species at the scale/metal interface.

The cause of the accelerated corrosion in the heat-resistant alloys in the presence of NaCl is twofold: the NaCl in the vapor phase establishes a Cl activity, which can attack the carbides that are present in the alloy as strengtheners; and the Cl activity in the deposit near the alloy can be high enough to form volatile chlorides of Fe, Cr, and Al (if present in the alloy). The volatile chlorides can lead to a microstructure conducive to continued transport of Cl from the gas phase to the alloy substrate.

Based on our experiments, the corrosion rates for the intermediate-chromium ferritic steels are accelerated by the simultaneous presence of compounds that contained Cl and gas phase oxygen. Even though these alloys develop iron oxide scales, the NaCl from the vapor phase deposits on the oxide surface and thereby incorporates the sodium ions on the iron sites and the chlorine ions

Figure 6. Photograph of duplicate specimens of intermediate-chromium ferritic alloys, that were exposed for 100 h at 650°C to air-1% SO_2 environment containing 300 ppm NaCl.

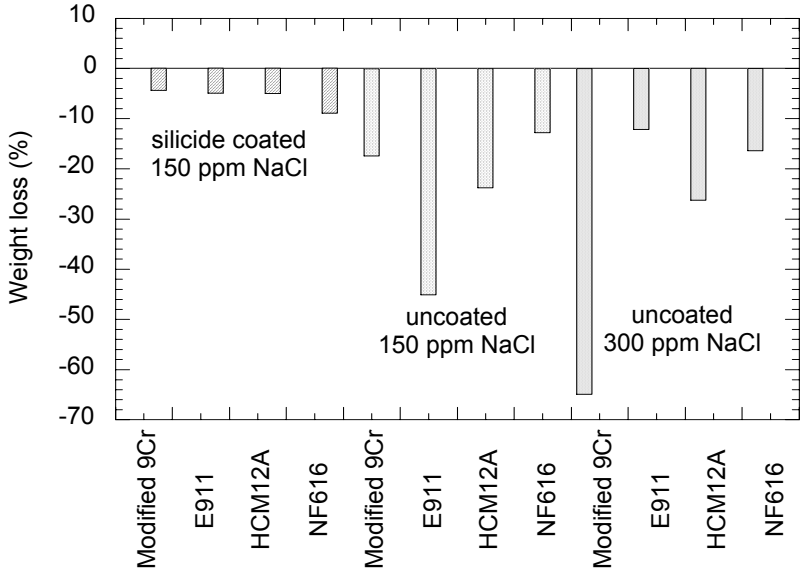

Figure 7. Weight change data for the uncoated and coated intermediate-chromium ferritic alloys after 100-h exposure at 650°C to air-1% SO_2-150 or 300 ppm NaCl gas mixture.

on the oxygen sublattice. We have discussed the possible corrosion mechanism in an earlier paper [10].

To establish the threshold level, if any, of NaCl in the gas phase below which Cl may not accelerate the corrosion process in intermediate-chromium ferritic steels, additional experiments were conducted with the four alloys (both in uncoated and coated conditions) at 650°C in air-1% SO_2-25 ppm NaCl . As expected, the exposure time of 100 h was not sufficient to see the effect of Cl at the low concentration of NaCl used. Figure 8 shows the weight change for the uncoated and coated alloys after 100, 400, and 600-h exposure at 650°C. The data show that up to 400 h, the uncoated alloys exhibit adherent scaling as evidenced by the weight gain. However, after 600-h exposure the uncoated alloys exhibited significant weight loss and the scaled were completely spalled. The results indicate that at a given temperature, the scale spallation and associated corrosion are dependent on the NaCl content in the gas phase (100 and 600 h at 300 and 25 ppm NaCl respectively, at 650°C). On the contrary, the coated alloys exhibited protective scaling during the 600-h exposure and the weight change was relatively small. Figure 9 shows a macrophotograph of various specimens after 600-h exposure at 650°C in air-1% SO2-25 ppm NaCl environment. The top row of uncoated specimens clearly shows bare metal surface,

indicating complete spallation of the oxide scale. The coated specimens in the bottom row exhibit oxide scales that seem adherent to the substrate.

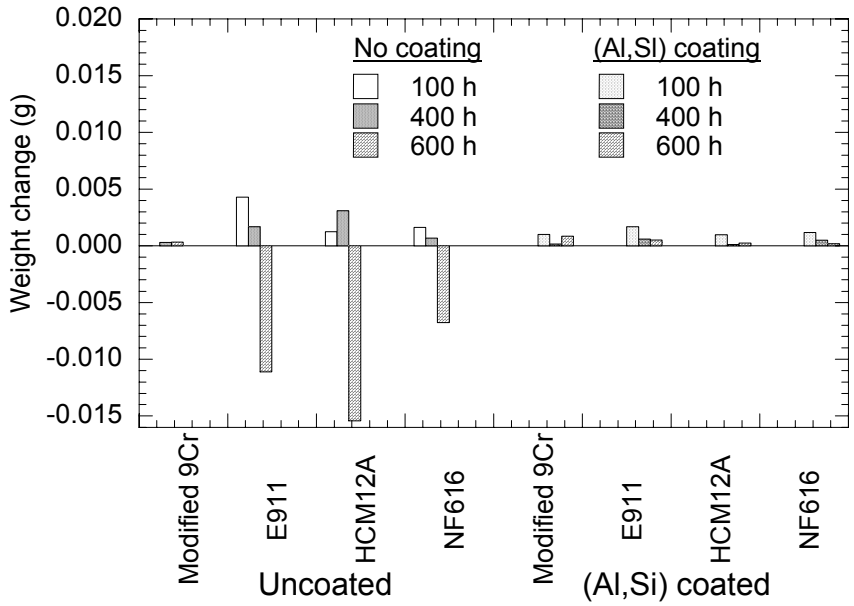

Figure 8. Weight change data for the uncoated and coated intermediate-chromium ferritic alloys after 100-h exposure at 650°C to air-1% SO_2-25 ppm NaCl gas mixture. Weight change for the uncoated modified-9Cr specimen after 600-h exposure was not measured.

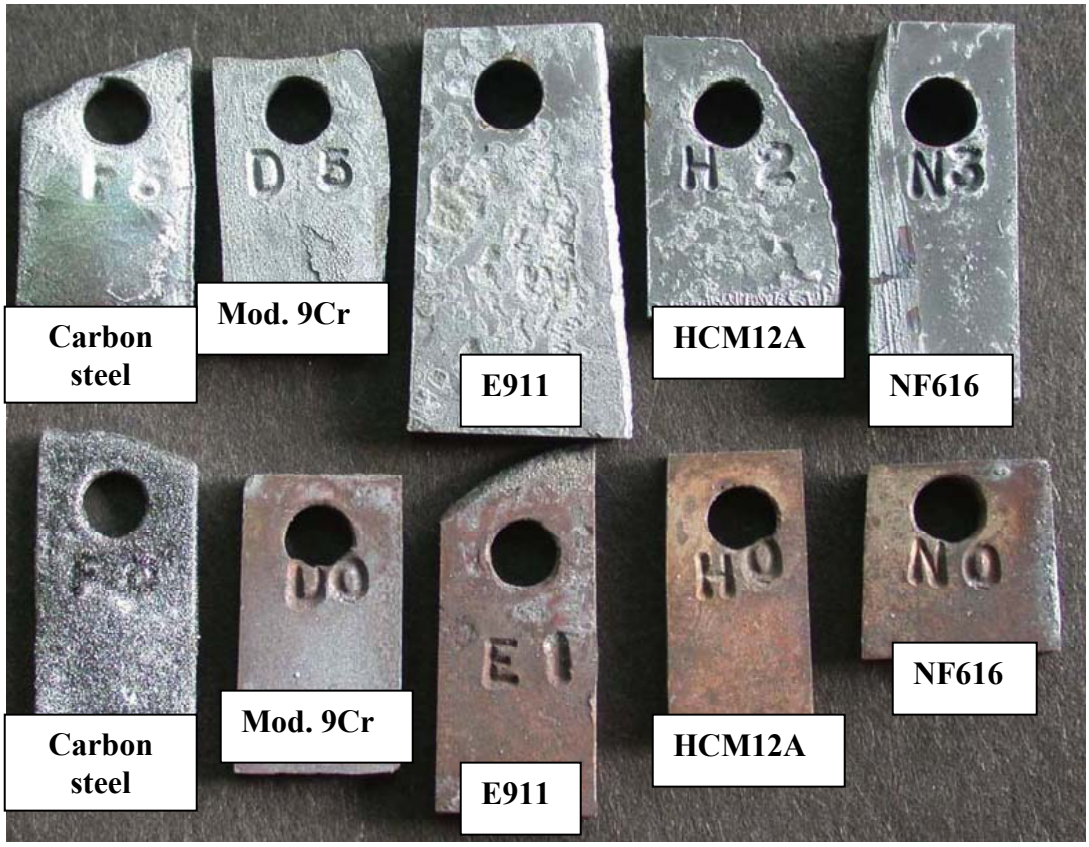

Figure 9. Macrophotograph of uncoated and (Al,Si) coated specimens after 600-h exposure at 650°C in an air-1% SO_2-25 ppm NaCl environment. Top Row: Uncoated; Bottom Row: Coated.

SUMMARY

Fireside and steam-side corrosion are major issues when selecting materials for advanced steam-cycle systems. At Argonne National Laboratory, we have continued studies to evaluate the corrosion performance of candidate Fe- and Ni-base alloys in coal-ash and in steam environments. The laboratory tests simulate the combustion atmosphere of advanced steam-cycle systems and three deposit chemistries that included ash constituents, alkali sulfates, and NaCl. In this paper, results are presented on the corrosion performance of several Fe-base alloys, claddings, and coated alloys in simulate environments that contained NaCl vapor.

Intermediate-Cr ferritic steels showed accelerated corrosion in the presence of oxidizing environments that contained 25-300 ppm NaCl. Based on the obtained test data and an understanding of the mechanism for Cl-induced corrosion in these steels, we developed a relatively low-temperature approach to modify the surface of these alloys to minimize chlorine transport through the oxide scale and thereby decrease the corrosion rate. Test data obtained after 600-h exposures showed substantial decrease in corrosion rate for the surface-modified alloys at NaCl concentration of 25 ppm. Additional tests are in progress to evaluate the long-term performance and the effect, if any, of NaCl in the corrosion resistance of Ni-base alloys in similar environments.

REFERENCES

[1]. Viswanathan R, Henry JF, Tanzosh J, Stanko G, Shingledecker J, and Vitalis B, U. S. Program on Materials Technology for USC Power Plants, Proc. 4th Intl. Conf. on Advances in Materials Technology for Fossil Power Plants, Hilton Head Island, SC, October 25-28, 2004, eds. R. Viswanathan, D. Gandy, and K. Coleman, ASM International.

[2]. Global Climate Committee of the International Energy Agency's Coal Industry Advisory Board Report, published by International Energy Agency, France, 1998.

[3]. S. N. Sinha, K. Natesan, and M. Blander, Chemistry of Gaseous and Condensed Products in Coal Combustion and Conversion Systems, Argonne National Laboratory Report ANL-89/25, August 1989.

[4]. K. Natesan and C. Reignier, Corrosion Performance of Structural alloys in Oxygen/Sulfur/Chlorine-Containing Environments, Proc. 12th Annual Conference on Fossil Energy Materials, Knoxville, TN, May 12-14, 1998.

[5]. K. Natesan, Corrosion Performance of Structural Alloys, Proc. 13th Annual Conference on Fossil Energy Materials, Knoxville, TN, May 11-13, 1999.

[6]. K. Natesan and C. Kraus, Corrosion Performance of Structural alloys and Coatings in the Presence of Depoits, Proc. 15th Annual Conference on Fossil Energy Materials, Knoxville, TN, April 30-May2, 2001.

[7]. K. Natesan, A. Purohit, and D. L. Rink, Fireside Corrosion of Alloys for Combustion Power Plants, Proc. 16th Annual Conference on Fossil Energy Materials, Baltimore, MD, April 22-24, 2002.

[8]. K. Natesan, A. Purohit, and D. L. Rink, Coal-ash Corrosion of Alloys for Combustion Power Plants, Proc. 17th Annual Conference on Fossil Energy Materials, Baltimore, MD, April 22-24, 2003.

[9]. K. Natesan and D. L. Rink, Fireside and Steamside Corrosion of Advanced Steam-Cycle Materials, Proc. 18th Annual Conference on Fossil Energy Materials, Knoxville, TN, June 2-4, 2004.
[10]. K. Natesan, J. –H. Park, and D. L. Rink, Fireside Corrosion of Alloys for USC Plants, Proc. 19th Annual Conference on Fossil Energy Materials, Knoxville, TN, May 9-11, 2005.

ACKNOWLEDGMENT

This work was supported by the U.S. Department of Energy, Office of Fossil Energy, Advanced Research Materials Program, Work Breakdown Structure Element ANL–4, under Contract W–31–109–Eng–38.

MULTI-PHASE HIGH TEMPERATURE ALLOYS: EXPLORATION OF LAVES-STRENGTHENED STEELS

Yukinori Yamamoto
Oak Ridge National Laboratory, Oak Ridge, TN 37831-6115
yamamotoy@ornl.gov; Tel: (865) 576-7095; FAX (865) 574-7659

Michael P. Brady
Oak Ridge National Laboratory, Oak Ridge, TN 37831-6115
bradymp@ornl.gov; Tel: (865) 574-5153; FAX (865) 241-0215

Zhao Ping Lu
Oak Ridge National Laboratory, Oak Ridge, TN 37831-6115
luzp@ornl.gov; Tel: (865) 576-7196; FAX (865) 574-7659

C.T. Liu
Oak Ridge National Laboratory, Oak Ridge, TN 37831-6115
liuct@ornl.gov; Tel: (865) 574-4459; FAX (865) 574-7659

ABSTRACT

Exploratory effort was initiated for the development of Fe-base alloys strengthened by intermetallic Laves phase combined with MC (M: metals) carbide for improved elevated-temperature strength in fossil energy system components such as super-heater tubes and industrial gas turbines. Work in FY 2006 was focused on strengthening of Fe-Cr-Ni base austenitic stainless alloys by Fe_2Nb Laves-phase precipitates with/without MC carbides, in combination with the improvement of oxidation resistance via Al-modification to promote alumina scale formation. A series of Fe-Cr-Ni-Nb base austenitic alloys with additions of Mo, Al, Si, C, B, etc. were cast and thermomechanically processed, and then tensile creep-rupture tested at the conditions of 750-850^{o}C/70-170 MPa. The Al-modified alloys strengthened by Laves + MC show superior creep strength to that of conventional type 347 stainless steels, and their creep life-limit reaches up to 500 h at 750 ^{o}C/100 MPa. These alloys also show an excellent oxidation resistance from 650-800^{o}C in air and air + 10% water vapor environments due to formation of a protective Al_2O_3 scale. Microstructural analysis of alloys strengthened by only Laves phase revealed that the Laves phase was effective to pin dislocations when the particle size is less than 0.5 μm, but the resultant creep rupture lives were relatively short. The Al-modification was also applied to an advanced carbide-strengthened austenitic stainless steel, and it yielded creep resistance comparable to state-of-the-art austenitic alloys such as NF709, together with protective alumina scale formation. Modification of this alloy composition for its creep strength and oxidation resistance will be pursued in FY2007. Preliminary results suggest that the developed alloys with Al-modification combined with MC carbide strengthening are promising as a new class of high-temperature austenitic stainless steels.

INTRODUCTION

The efficiency of boiler/steam turbine power plants is a strong function of steam temperature and pressure [1]. Consequently, it is attractive to operate at higher temperatures and pressures to increase energy efficiency. However, under such conditions, high-temperature creep strength is a major issue for hot components in advanced fossil energy conversion and combustion systems. For example, current goals for advanced fossil energy power plants call for ferritic steels capable of operation above 600°C, and austenitic steels capable of operation at greater than 700°C. Components of interest range from superheater tubes to industrial gas turbine components. A key need is the concurrent development of strength and oxidation resistance, especially in oxidizing environments also involving exposure to sulfidation, hot corrosion, or water vapor species.

State-of-the-art ferritic and austenitic steels currently use solid solution strengthening in combination with carbide and/or nitride precipitate strengthening. Significant gains in creep strength have recently been achieved via control of these dispersions at nanoscale [e.g. 2-4], in some cases achieving strength likely beyond the upper-temperature limit for the alloys set by oxidation in environments containing aggressive species such as water vapor. The current effort is based on multi-phase microstructures utilizing intermetallic phases for high-temperature strengthening and, depending upon the specific alloy system, as a reservoir for protective scale-forming elements. This approach offers a possible path to achieve a balance of properties in Fe-base alloys sufficient to enable increased operating temperatures for applications in aggressive environments encountered in advanced fossil energy power plants.

DISCUSSION OF CURRENT ACTIVITIES

Efforts in FY 2006 were focused on the strengthening of Fe-Cr-Ni base austenitic stainless alloys by solid solutes, carbide precipitates (MC), and Laves as well as other intermetallic phase precipitates, in combination with the improvement of oxidation resistance via Al-modification to promote alumina scale formation. The selection of Laves phases for intermetallic strengthening leverages previous work under the Fossil Energy ARM program on Laves-strengthened Cr and Cr(Fe) alloys [5,6], and recent phase equilibria studies by Takeyama et al. [7], which showed that precipitation of Fe_2Nb-base Laves phase could be controlled in austenitic Fe via manipulation of the Ni content of the alloy. Alumina-based scales are of interest due to their superior resistance to water vapor-containing environments, compared to chromia-based scales, which are susceptible to accelerated oxidation due to volatilization-related effects [8]. More details of the effect of Al-modification on the oxidation behavior were described in the report in FY2005 [9].

There were three key goals in FY2006. The first goal was to screen high-temperature creep strength as well as oxidation behavior of the Al-modified austenitic stainless alloys strengthened by Laves phase and MC carbide proposed in this project. In FY2005, the authors reported that local regions of BCC phase, stabilized by the addition of Al, degraded the creep resistance of the initially developed alloys. The microstructure of the alloys was successfully controlled to an austenitic single matrix, and the creep properties and the oxidation behavior were elucidated. The

second one was to identify the strengthening mechanism of austenitic stainless alloys by only Laves phase during creep testing at elevated temperatures. Although a microstructure of fine Fe_2Nb Laves dispersion within an austenitic matrix was obtained by Takeyama [7] using Fe-Cr-Ni-Nb alloys with the potential for high temperature strength, there was no report of the mechanical properties so far. The third one is to apply the Al-modification to an advanced carbide-strengthened austenitic stainless steel. From the effort in FY2005, protective alumina-scale formation may also be achieved in conventional austenitic stainless steels by proper Al-modification. Compositional control of the steels has been explored and correlated with creep rupture lives.

Baseline compositions selected for study were in the range of Fe-(15-20)Cr-(15-30)Ni, atomic percent (at.%), with minor additions of elements such as Al, B, C, Mo, Nb, Si, Ti, V, W, etc. The alloys were cast and thermomechanically processed, and then tensile creep-rupture tested at 750-850°C/70-170 MPa. Oxidation behavior of the samples was also screened from 650 to 800°C in air and air + 10% water vapor environments. Full compositional and processing details are considered proprietary at this time.

1. Al-modified austenitic alloys strengthened by Laves + MC

High-temperature creep properties were screened for the Al-modified austenitic alloys strengthened by Laves phase with/without MC carbide. Thermo-mechanical processing was conducted in order to obtain homogeneous materials with grain sizes in the range of 30 - 80 μm. Sheet creep specimens with a thickness of 0.4 - 0.6 mm, a gage length of 12.7 mm and a width of 3.2 mm were cut by electro-discharged machine and polished using SiC paper to a 600 grit

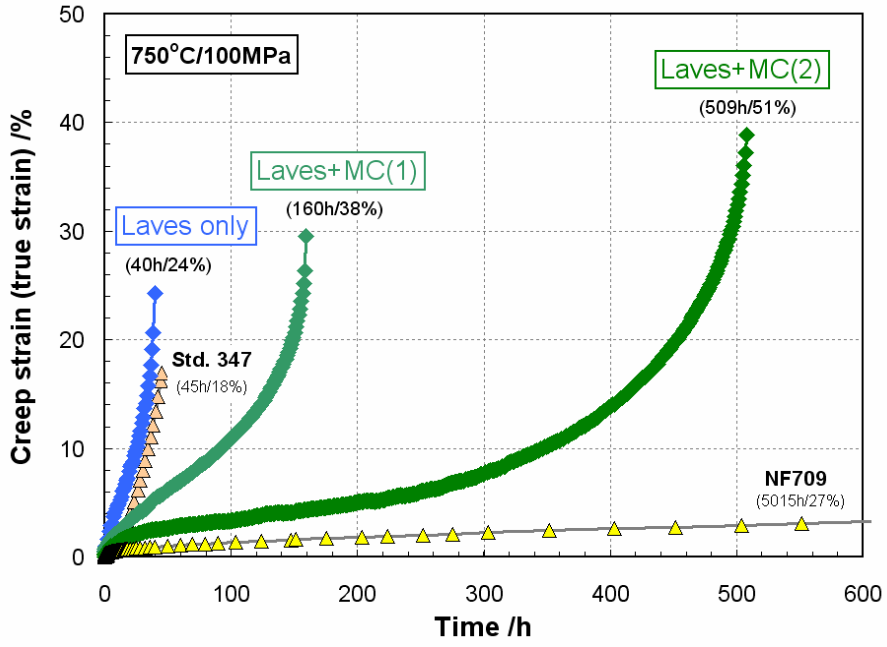

Figure 1: Creep curves of the developed alloys in the current study and commercial heat-resistant austenitic stainless steels (type 347 and NF709) tested at 750°C/100 MPa.

surface finish. Tensile creep-rupture testing was conducted without a strain gage directly on the specimens, and should therefore be considered semi-quantitative. Oxidation behavior of the samples was also screened. All the specimens were solution heat-treated, but their microstructures contained some un-dissolved Fe_2Nb and/or NbC particles with the size of 5-10 μm, mainly on the grain boundaries.

The Al modified alloys strengthened by Lave + MC showed moderate creep strength. Figure 1 shows the creep curves of the alloys tested at 750°C/100 MPa. The curves of commercial heat-resistant austenitic stainless steels, type 347 (18Cr-12Ni-Nb-C) and NF709 (20Cr-25Ni-Nb-C, N), are also plotted for comparison. The first screenings of the alloys strengthened by Laves with and without MC shows comparable creep life-limit to that of type 347, although the alloy with MC carbides shows 4 times longer life-limit than that without MC ["Laves + MC (1)" and "Laves only" in Fig. 1, respectively]. The second series of the alloy containing higher amount of Laves and MC than the first series shows about a 500 h life-limit. However, this creep rupture life is still well short of the best commercially available austenitics, such as NF709, which is estimated to exhibit a creep rupture life on the order of 5000 h under these conditions.

Figure 2 shows a macro view of a creep-ruptured specimen strengthened by Laves + MC carbides (the second series, a), together with a TEM bright field image obtained from gage portion (b). The surface showed little external oxide scale formation, consistent with the formation of a protective alumina-scale. At the gage portion of the specimen, dense Fe_2Nb/NiAl particles on the order of 300 nm and 10 nm NbC were observed. These dispersions pinned dislocations to resist creep deformation effectively. The microstructural analysis combined with the creep results suggest that the creep strength could be improved by increasing the amounts of

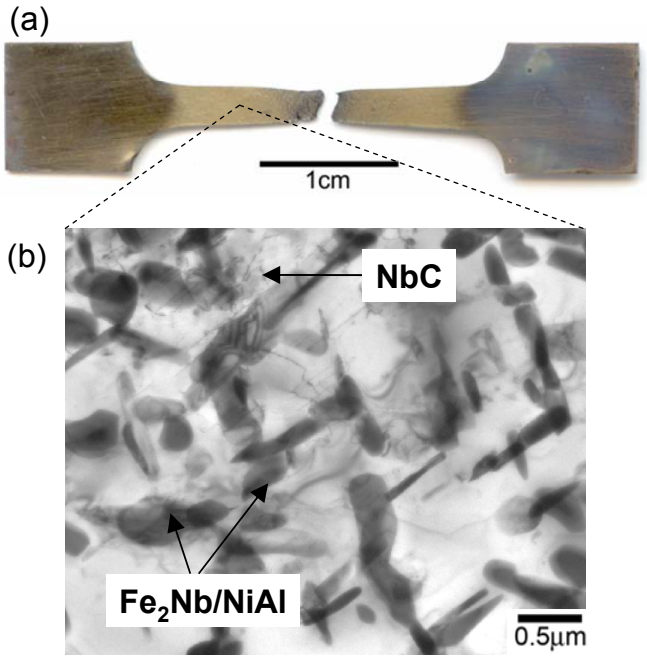

Figure 2: (a) A whole view of creep-ruptured specimen strengthened by Laves + MC carbides (second series), and (b) a TEM bright field image obtained from gage portion of the specimen.

the intermetallic phases and MC carbides. Figure 3 shows specific weight changes of the proposed alloy and commercial heat resistance stainless steels, NF709 and HR120 (25Cr-37Ni-Nb-C, N), plotted as a function of exposure time at 800°C in air + 10% water vapor. The Al-modification resulted in superior oxidation resistance to the high Ni/high Cr NF709 and HR120 alloys shown for comparison.

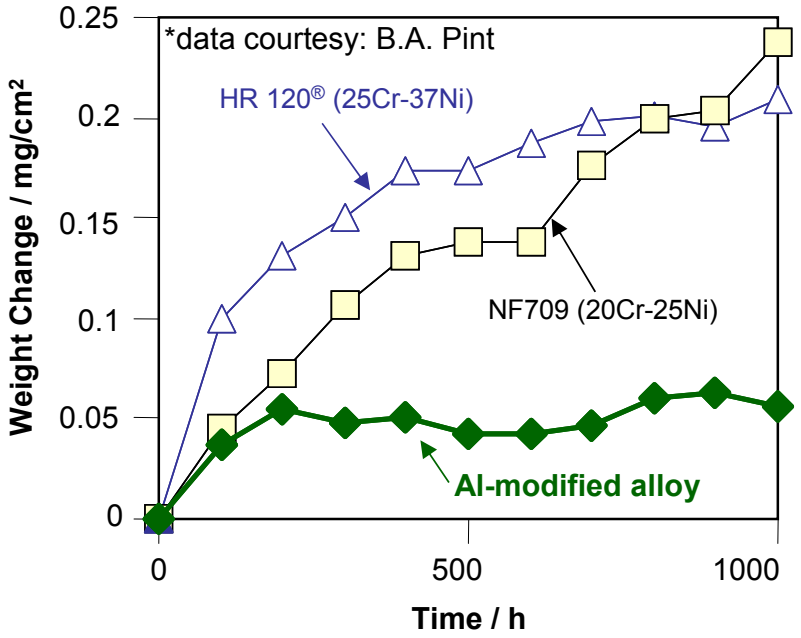

Figure 3: Weight change of the developed alloy and commercial heat resistance stainless steels (NF709 and HR120, foil samples) plotted as a function of exposure time at 800°C in air + 10% water vapor.

2. Strengthening mechanism by Fe_2Nb Laves phase

In order to identify the strengthening effect of Laves phase itself on the austenitic stainless alloys, tensile creep testing was performed by using Fe-20Cr-30Ni-2Nb base model alloys originally reported by Takeyama [7]. The alloys show complete solid solution (γ single phase) at around 1200°C and fine Fe_2Nb Laves phase dispersion by aging at around 800°C. The size of the Fe_2Nb particles increase with increasing aging temperature, c.f. 750°C:0.2-0.3 μm, 800°C: 0.5 μm. The creep specimens were prepared for both solution-treated and aged conditions, and tested at 750°C/100M Pa.

The creep properties strongly depended on the Fe_2Nb particle size. Figure 4 shows the creep curves of Fe-20Cr-30Ni-2Nb alloys with and without aging at 800°C, together with that of the type 347 stainless steel. The aged specimen contained 0.5 μm size Fe_2Nb particle dispersions within the austenitic matrix before creep testing. It shows poor creep properties with a higher creep rate and a similar life-limit to those of the type 347. On the other hand, the non-aged specimen, which has 0.2 μm size Fe_2Nb particles appeared during creep testing, showed

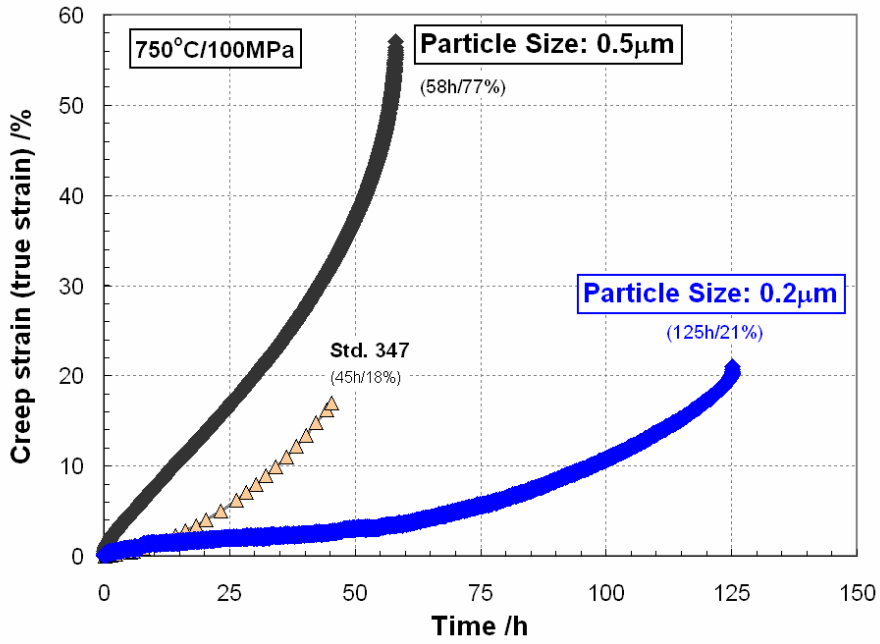

Figure 4: Creep curves of Fe-20Cr-30Ni-2Nb base alloys strengthened by only Fe_2Nb-Laves phase and type 347 tested at 750°C/100 MPa.

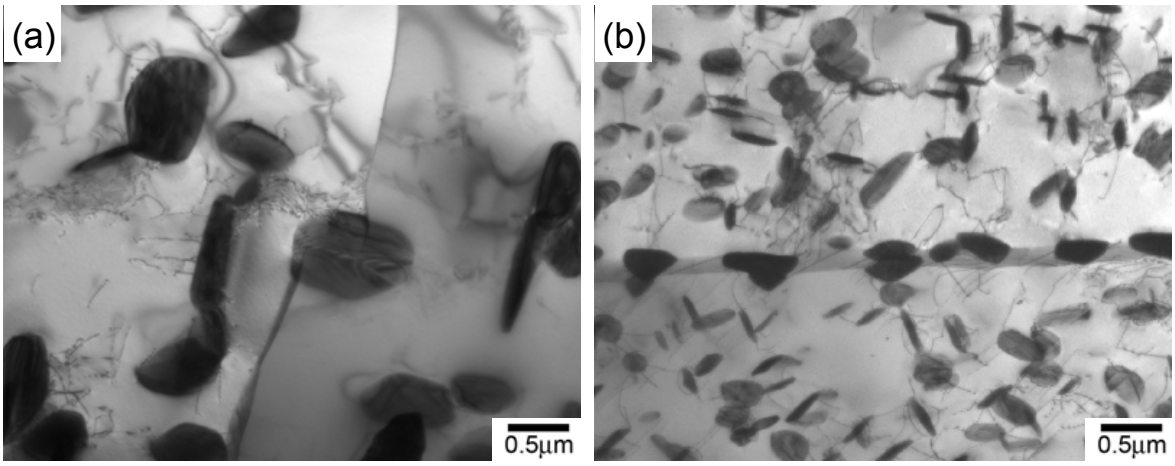

Figure 5: TEM bright field images of creep-ruptured Fe-20Cr-30Ni-2Nb alloys tested at 750°C/100 MPa, which show uniform dispersions of Fe_2Nb-Laves phase with the size of (a) 0.5 mm and (b) 0.2 mm, respectively.

moderately improved creep properties to those of the aged specimen (note that an alloying addition was made to this alloy to help refine the Fe_2Nb particle size). Figure 5 shows TEM bright field images obtained from gage portions of the creep ruptured specimens with (a) and without (b) aging, which correspond to the 0.5 and 0.2 μm particle sizes, respectively. The former shows very few dislocations within the matrix but sub-boundaries as seen in the center of

the image. However, the latter shows fine and dense Fe_2Nb dispersions which pin dislocations effectively. From the results, it is concluded that the size of Fe_2Nb particles has to be controlled at least less than 0.5 μm, and controlling the particle size with less than 0.2 μm would significantly improve the creep properties. However, overall, the creep rupture lives obtained thus far by Laves-strengthening were unimpressive.

3. Al-modification of a carbide-strengthened austenitic stainless steel

The Al-modification approach was also applied to an advanced carbide-strengthened austenitic stainless steel. The HTUPS (high-temperature ultrafine-precipitation-strengthened steel) family of alloys (Fe-14Cr-16Ni-Mo, Nb, C, etc., wt%) were chosen for study because it exhibits excellent creep resistance, with a 6173 h creep life-limit at 700°C/170 MPa. However, these alloys were developed for environments where oxidation was not a significant concern, and oxidation resistance is poor. [10]. The Al-modification was performed by compositional control, in an attempt to achieve alumina-scale formation without otherwise degrading the microstructure or creep resistance of the alloy. The specimens were prepared as solution-treated condition with the grain size of about 100 μm by thermo-mechanical processing, and then pre-strained before creep testing.

Modified HTUPS optimized for alumina-scale formation showed comparable creep properties to state-of-the-art austenitic alloys such as NF709, and also exhibited excellent oxidation resistance at elevated temperatures. Figure 6 shows a creep curve of the Al-modified HTUPS together with those of the type 347 and NF709 tested at 750°C/100 MPa. The Al-modified HTUPS shows more than 2000h creep life-limit and less than a half of the minimum creep rate of NF709. (It should be noted the comparative NF709 data was obtained from commercially produced foil

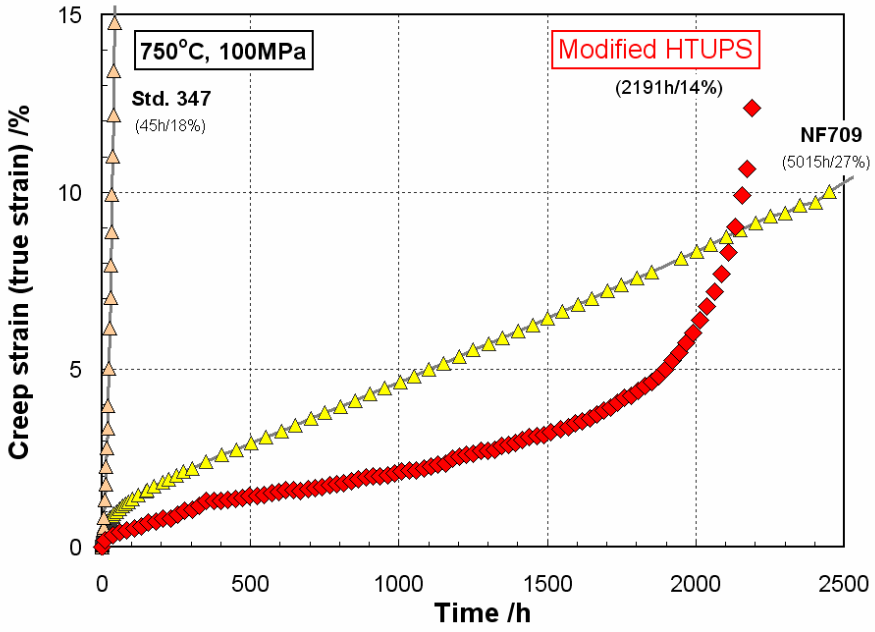

Figure 6: Creep curve of modified HTUPS optimized for Al_2O_3 continuous scale formation tested at 750°C/100 MPa, together with those of commercial heat-resistant stainless steels (type 347 and NF709).

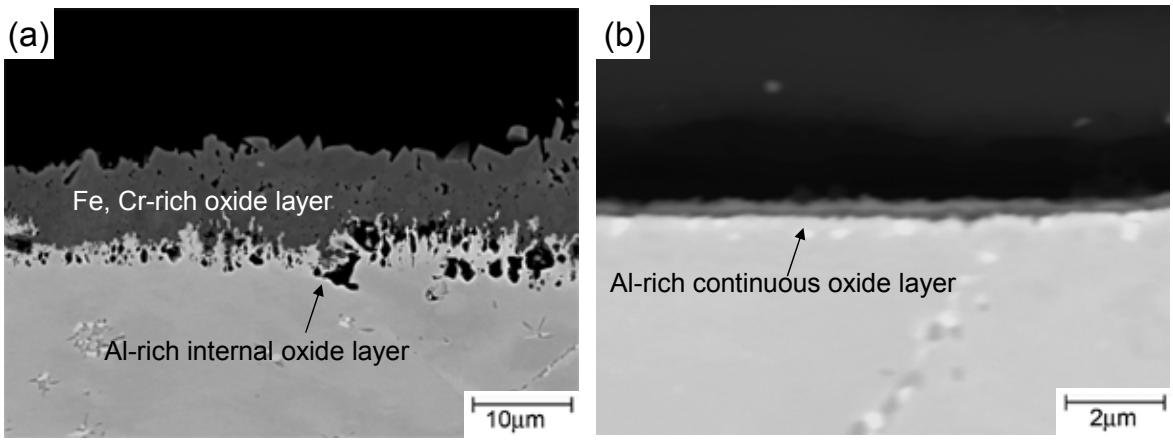

Figure 7: SEM-BSE images showing cross sectional views at the surface of HTUPS series after oxidation for 72 h at 800°C in air; (a) initial Al-modified HTUPS (b) optimized for Al_2O_3 scale formation.

samples; however, it correlates well with data extrapolated from other NF709 data sets). Figure 7 shows SEM back-scattered electron images of cross sectional views at the surface of HTUPS series modified with Al after aging for 72 h at 800°C in air. With proper alloy modification, alumina scale formation was achieved. Preliminary, in-progress studies indicate that alumina scale formation on this alloy is achieved at 650°C and 800°C in air + 10% water vapor environments.

Figure 8 summarizes the efforts in FY2006 showing Larson-Millar-Parameters of all the

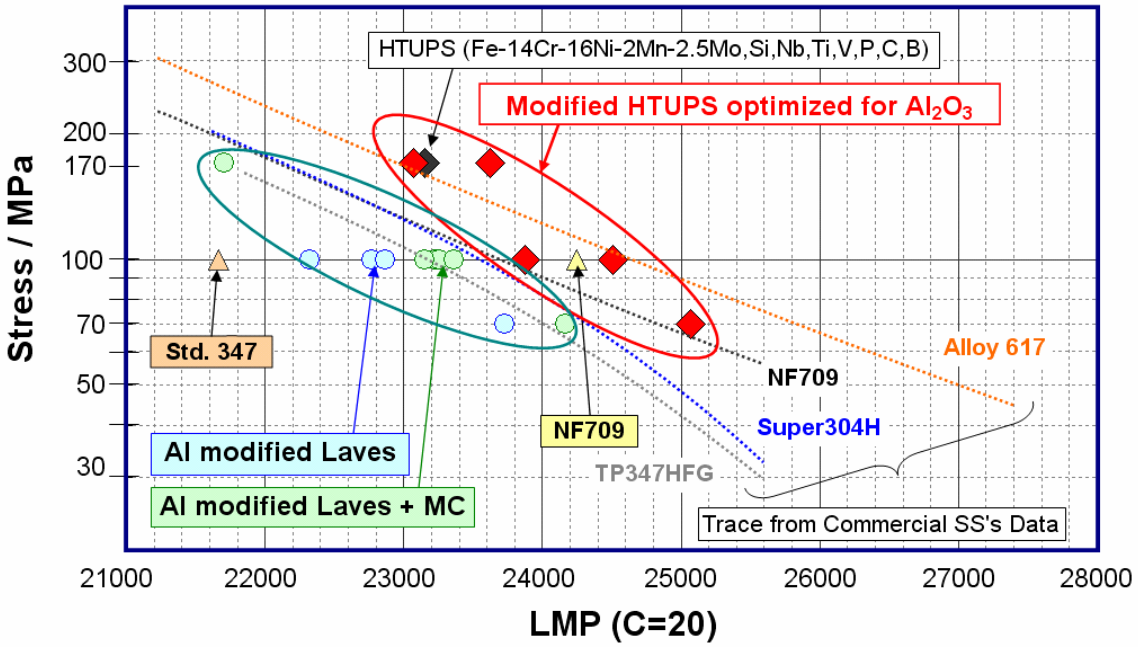

Figure 8: Comparison of Larson Miller Parameter of the developed alloys in the present study with several commercial heat-resistant austenitic stainless steels and alloys.

developed alloys and steels, together with those of the type 347, NF709, and some other commercial austenitic stainless steels including a Ni base super-alloy. Modified HTUPS optimized for alumina-scale formation shows comparable creep properties with those of Alloy 617 (Ni-22Cr-9Mo, Co, Fe, etc.) to relatively high stresses. It should be noted that these results were obtained from creep testing at 750-850^{o}C which are very severe conditions for conventional austenitic stainless steels. At those temperatures the oxidation behavior can easily degrade the mechanical properties by degrading the materials from the surface. This indicates that Al-modification to promote the protective alumina-scale formation can lead to the development of a new class of austenitic stainless steels for high temperature use with excellent oxidation resistance. These alloys are also potentially far less expensive than the high-Ni austenitics and Ni-base alloys currently available.

FUTURE WORK

To improve the creep properties of the Al-modified alloys strengthened by Laves + MC, the amounts of Fe_2Nb and MC will be optimized by controlling the levels of Nb, V, Ti and C. The effect of solid solutes on the strengthening will also be evaluated by additions of Mo and W. Composition optimization of the Al-modified carbide-strengthened austenitic stainless steels will be pursued in order to further improve their creep strength. Fundamental mechanistic studies will explore alumina formation on these alloys, and long-term oxidation resistance will be evaluated. Studies in FY 2007 will also evaluate the weldability of this new class of alloys (preliminary results are promising). An invention disclosure on these alloys was submitted in FY2006 [11].

REFERENCES

1. R. Viswanathan and W. Bakker, *J. Mat. Eng. Perf.*, 10 (1), 81 (2001).

2. R.L. Klueh, N. Hashimoto and P.J. Maziasz, *Scripta Mater.*, 53 (3), 275 (2005).

3. P.J. Maziasz, J.P Shingledecker, R.W. Swindeman, R.L. Klueh and N.D. Evans, *18th Annual Conf on Fossil Energy Mtls, Knoxville, TN USA, Fossil, Oak Ridge National Laboratort, Oak Ridge, TN USA, 06/02/2004-06/04/2004*.

4. T. Sourmail, *Mater. Sci Tech.*, 17 (1), 1 (2001).

5. M.P. Brady, J.H. Zhu, C.T. Liu, P.F. Tortorelli, L.R. Walker, C.G. McKamey, J.L. Wright, C.A. Carmichael, D.J. Larson, M.K. Miller, and W.D. Porter, *Mater. High Temp.*, 16(4), 189 (1999).

6. M.P. Brady, C.T. Liu, J.H. Zhu, P.F. Tortorelli, and L.R. Walker, *Scripta Mater.*, 52, 9, 815 (2005).

7. M. Takeyama, S. Morita, A. Yamauchi, M. Yamanaka, and T. Matsuo, in Superalloys 718, 625, 706 and Various Derivatives, E.A. Loria, Ed., TMS 2001 p. 333.

8. E.J. Opila, *Mater. Sci. For.*, 461-464, 765 (2004).

9. M. P. Brady, C. T. Liu, Y. Yamamoto, Z. P. Lu, and H. Meyer, Annual review of Fossil ARM project (2005).

10. P. J. Maziasz et al., "Developing an Austenitic Stainless Steels for Improved Performance in Fossil Power Facilities" in *Journal of Metals,* vol.41, pp. 14-20 (1989)

11. M. P. Brady, Y. Yamamoto, Z. P. Lu, C. T. Liu, P. J. Maziasz, and B. A. Pint, Invention disclosure entitled "Oxidation Resistant, High Creep Strength Austenitic Stainless Steels", submitted in 2006.

ACKNOWLEDGEMENTS

This research was sponsored by the U.S. Department of Energy, Fossil Energy Advanced Research Materials (ARM) Program. Oak Ridge National Laboratory is managed by U.T.-Battelle, LLC for the U.S. Department of Energy. The authors thank Mike Santella and Joe Horton for reviewing this manuscript. Extensive discussions and technical input from Masao Takeyama, Phil Maziasz, Bruce Pint, John Shingledecker, and Ian Wright are also gratefully acknowledged.

ENABLING THE PRACTICAL APPLICATION OF OXIDE DISPERSION-STRENGTHENED FERRITIC STEELS

I.G. Wright
Oak Ridge National Laboratory, 1 Bethel Valley Road, MS 6156, Oak Ridge, TN 37831
E-mail: wrightig@ornl.gov; telephone: 865-574-4451; Fax: 865-241-0215

N.S. Bornstein
Consultant, 43 Richmond Lane, W. Hartford, CT 06117
E-mail: normanbornstein@sbcglobal.net; telephone: 860-233-0472

E. Dyadko
MER Corporation, 7960 S. Kolb Rd., Tucson, AZ 85706
E-mail: edyadko@mercorp.com; telephone: 520-574-1980 x142; Fax: 520-574-1983

S. Dryepondt
Oak Ridge National Laboratory, 1 Bethel Valley Road, MS 6156, Oak Ridge, TN 37831
E-mail: dryepondtsn@ornl.gov; telephone: 865-241-5158; Fax: 865-241-0215

ABSTRACT

Two major shortcomings to the practical application of oxide dispersion-strengthened (ODS) alloys are the lack of techniques for producing reliable joints with strength commensurate with the parent material, and significant anisotropy in creep strength in extruded tubing. The focus of the research reported has been (i) on evaluating the joining techniques of plasma-assisted pulsed diffusion bonding, and transient liquid phase (TLP) bonding, and (ii) modification to the post-consolidation processing of the alloy to influence the secondary recrystallization behavior (hence grain size and shape), to reduce creep strength anisotropy. Progress is reported in both areas.

INTRODUCTION

This project is part of a cluster of projects that is addressing specific, perceived barriers to the practical application of oxide dispersion-strengthened (ODS) ferritic steels. Although these alloys exhibit creep strength at temperatures well in excess of those attainable by conventional alloys, and also possess exceptional environmental resistance, they are not widely used because they are (1) difficult to join; (2) have unusual mechanical behavior (anisotropic properties); and (3) are very expensive. The overall goal of this project is to facilitate the exploitation of ODS alloys by addressing these perceived technical barriers, as well as to develop a mathematical model of the oxidation behavior to allow lifetime prediction; cost is considered to be an issue that will be resolved when these alloys are more widely used. In the areas of joining and mechanical properties, the achievement of the project goals depends on developing the desired alloy microstructure after processing. In particular, it is considered essential that there is minimal disruption in the distribution or alignment of the yttria dispersion, since such changes would be expected to strongly influence the alloy microstructure upon secondary recrystallization.

In the joining studies, where reliance is placed on the temporary presence of a molten phase at the joint (TLP), or on the local creation of a plasma (pulsed plasma-assisted diffusion bonding), particular attention has been focused on understanding the influence of any changes in the details of the alloy microstructure resulting from the processing involved.

The current approach under evaluation for modifying the alloy grain size and shape, with the aim of increasing the hoop strength of ODS-FeCrAl tubes, is torsional deformation. The goal is to develop a spiral alignment of the oxide dispersion (and associated oxide stringers) in the alloy in the fine-grained condition as a way of influencing the direction taken by the large grains grown during the subsequent secondary recrystallization process.

The major criterion for assessing the success of the approaches being used is the creep strength of the final microstructures, as judged against that of the parent alloy. Baseline creep measurements are in progress for future comparisons.

RESULTS AND DISCUSSION

JOINING

Transient Liquid-Phase (TLP) Bonding

Joints made using non-recrystallized and secondary-recrystallized versions of ODS-FeCrAl alloy PM2000 (supplies of MA956 were exhausted) were examined by transmission-electron microscopy (TEM) to provide insight into microstructural changes in the vicinity of the joints. Images from electron-probe microanalysis (EPMA) shown in Figs. 1 and 2 illustrate the region around such joints in which microstructural changes were observed. Overall, the joints appeared to be clean, with relatively few optically-visible features along the bond line; some features that appeared to be voids were observed parallel to the bond line, as can be seen in the backscattered image (BSE) in Figs. 1 and 2. Note that the bond line runs horizontally across the center of the microstructure shown in Fig. 1, and along the top of

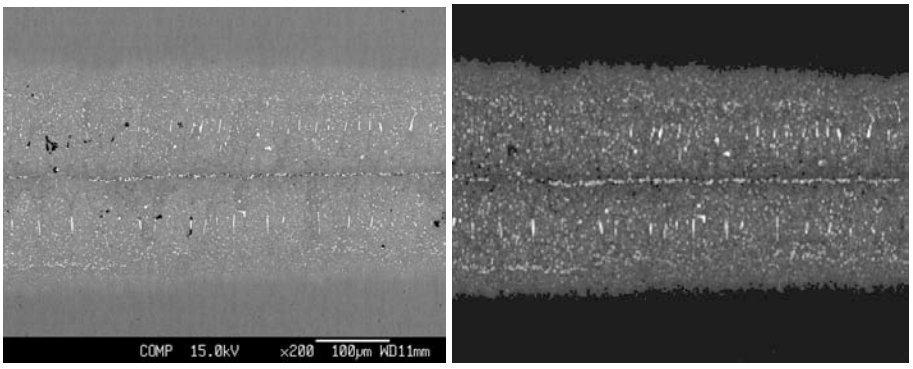

BSE ‘X’

Figure 1. EPMA images of a section of as-joined (unrecrystallized) alloy PM2000 showing back-scattered electron image and corresponding elemental X-ray map for element ‘X’.

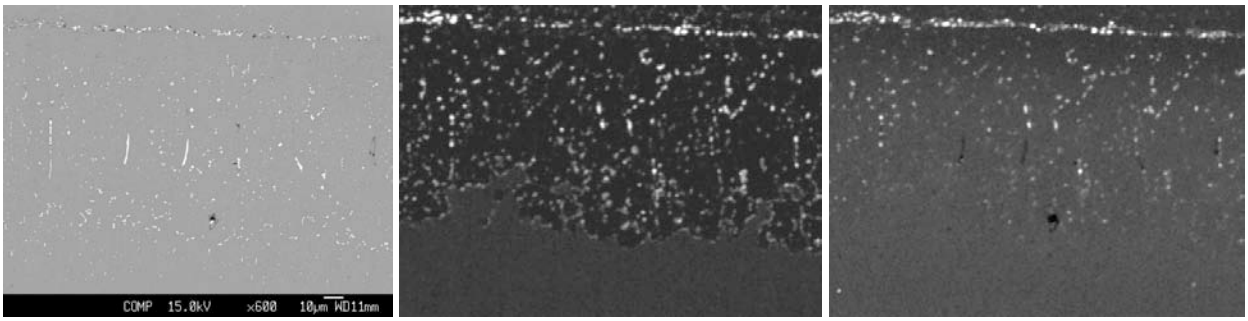

BSE Y Al

Figure 2. EPMA images of a section of (unrecrystallized) alloy PM2000 joined + annealed for 5h at 1000°C, showing back-scattered electron image and corresponding elemental X-ray maps for Y and Al.

Fig. 2. Also, there was some concentration of particles rich in Y, Al and 'X' (from the TLP alloy 'X-Z') along the bond line (the actual composition of the TLP alloy is withheld pending resolution of IP issues).

The most notable feature was, however, the zone (which ranged in thickness, being thinnest at the specimen centerline) either side of the joint that was affected by element 'X,' in which it appeared that the Y from the dispersed oxide phase in the alloy (nominally yttria, Y_2O_3) had been agglomerated. In Fig. 2 there is the suggestion that the agglomerated areas of Y are associated with Al. Such agglomeration is of concern, since redistribution of the Y-containing oxides may significantly influence the alloy recrystallization behavior. The desired result from such joining is that the alloy can be recrystallized to form the large grain structure needed for high-temperature creep strength, with no major difference in the final microstructure around the joint.

Examination by transmission electron microscopy (TEM) of samples removed from the area of Y-agglomeration shown in Fig. 2 revealed that the Y-containing particles were typically variants of YAG (yttrium-aluminum garnet), and that most remained as discrete, small particles (Fig. 3a). Essentially all of the discrete YAG particles were associated with crystallites that were essentially element 'X' (black-appearing features in Fig. 3a) containing low levels of Al and Ti. The larger particles observed by EPMA

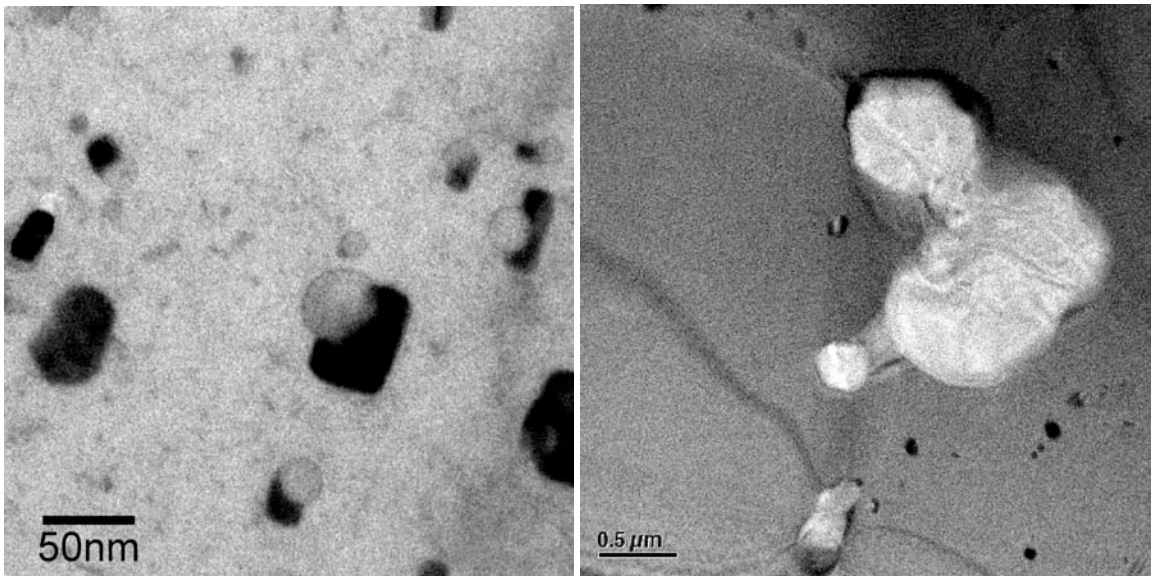

(a) (b)

Figure 3. TEM images of a section of (unrecrystallized) alloy PM2000 joined + annealed for 5h at 1000°C, showing: (a) discrete YAG particles (grey-appearing spherical particles) and associated, 'X'-rich crystallites (black-appearing); and (b) agglomeration of several YAG particles.

appeared to be agglomerations of these YAG particles (Fig. 3b). Detailed examination of several agglomerations, such as that shown in Fig. 3b, revealed that these also were associated with element 'X' (plus Al and Ti), though these associations usually involved significantly more YAG than element 'X'.

A possible explanation of these structures is that they resulted from the penetration of the molten TPL phase along preferential paths in the alloy (such as grain boundaries and dislocation bands), which brought it into contact with the dispersed oxide particles (nominally yttria; possibly YAG). Where there was sufficient molten TLP phase present for sufficient time, the oxide particles apparently were able to migrate and possibly rotate, and occasionally meet and join together. The 'X'-rich crystallites (Fig. 3a) probably were simply the result of precipitation on cooling due to the sharply-reduced solubility of 'X' in the alloy matrix.

The implications of these observations are that the joining conditions used resulted in the presence of too much molten phase for too long. The practical explanation for this involves the fact that the composition of the 'X-Z' TLP actually in place at the joint was sufficiently removed from that intended that its melting point was much higher than expected, and the layer of TLP used was too thick. Thus, a significant amount of molten phase was present during the annealing part of the joining cycle, which was intended to diffuse the TLP constituents away from the joint.

Subsequent heat treatment to induce secondary recrystallization of the joined samples (1h at 1380°C) resulted, as expected, in full dispersion of the 'X-Z' constituents throughout the specimens; the resulting structure and distribution of the YAG particles in the agglomerated zone around the joint is not exactly known, but appeared to be relatively fine. However, recrystallization was only accomplished in the immediate region of the joint; it appeared that the heat treatments associated with the joining process were sufficient to remove any driving force for recrystallization for the bulk of the alloy. The introduction of some level of cold work into the alloy by rolling will be explored as a way of promoting secondary recrystallization. It is necessary to develop a large grain structure if specimens from this phase of joining are to be subjected to creep testing. In addition, further processing of the TLP alloy has produced 10 μm-thick foil that should allow better control of the amount and composition of the TLP applied to the joint.

Pulsed Plasma-Assisted Bonding

This process is being developed, using funding from an Office of Fossil Energy Small Business Innovative Research grant, by MER Corp. of Tucson, Arizona, with whom the Oak Ridge National Laboratory (ORNL) is collaborating to evaluate the influences of iterations of the processing parameters. Prior progress [1] resulted in butt-welds that exhibited very promising strength in a creep-screening test. As shown in Fig. 4, in which the solid lines represent values for monolithic specimens cut from tubes, the joints gave strength values at 900°C that were up to 64% of the axial strength of the base alloy (and 188%

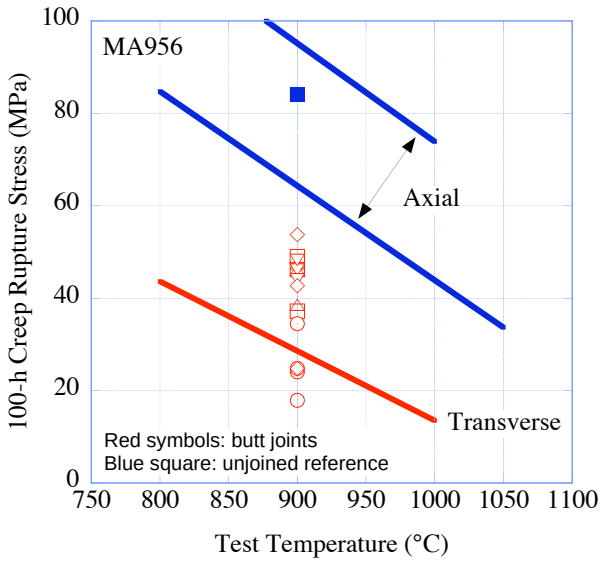

Figure 4. Comparison of strength of butt joints with that of the monolithic ODS FeCrAl alloy (Incoloy MA 956) in a creep-screening test at 900°C.

the transverse strength). Analysis of the processing conditions that resulted in the joints having the highest strength shown in Fig. 4 led to further iterations, in which attention also was given to combining joining and secondary recrystallization of the ODS alloy in one step. The joints were butt joints, made in 19 mm diameter rods of unrecrystallized ODS-FeCrAl alloy PM2000. In the envelope of processing adjustments made, fifty percent of the specimens exhibited at least partial recrystallization through the

joints during the bonding process, while this number rose to more than eighty percent after a post-bonding recrystallization anneal of 1 hr at 1380°C.

Figure 5 shows cross sections of two of the joints in which some degree of secondary recrystallization occurred in the ODS alloy during the joining process. In the joint shown in Fig. 5a, the grain in the center

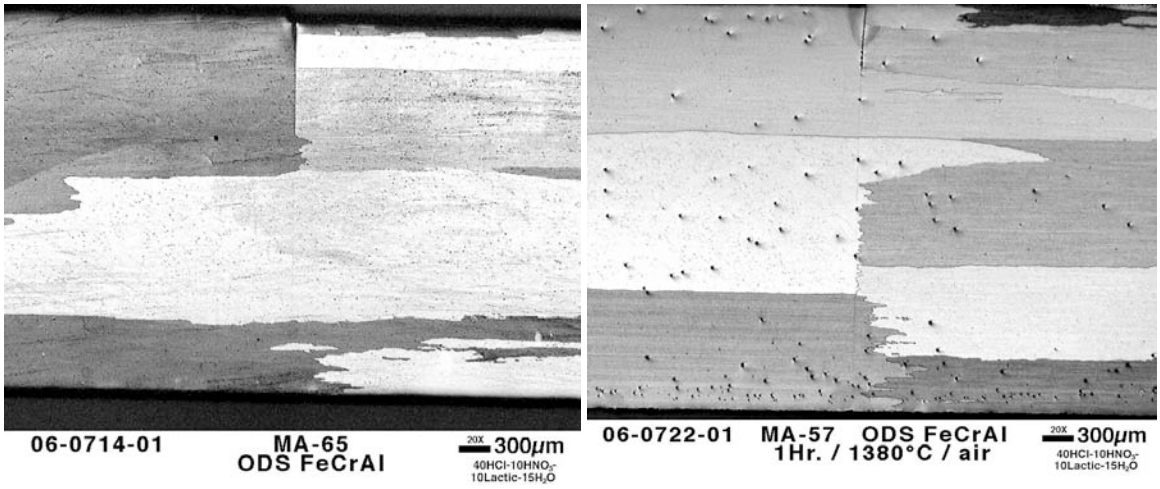

(a) (b)

Figure 5. Etched cross sections of butt joints in alloy PM2000 (a) MA-65, as-joined (recrystallized), and (b) MA-57, as-joined and recrystallized by a separate heat treatment.

of the micrograph grew across the bond unimpeded. In contrast, grain growth in the region shown at the top of the micrograph was stopped at the bond line; this apparently was due to the fact that the bonding in that location was incomplete. This condition is shown more clearly in Fig. 5b (top of micrograph) where, immediately below the incomplete part of the joint, grain growth has proceeded through the bond line. Of interest are the finger-like features, seen in the center of the micrograph in Fig. 5b, where part of a given grain grew through the bond line, whereas another part of the same grain stopped (or started) in the vicinity of, or at, the bond line. This behavior appears to be linked to the presence of small particles or voids in the bond line, as illustrated in Fig. 6. As shown in the top region of Fig. 6a, growth of the recrystallized grain stopped where the particles/voids along the bond line were spaced less than

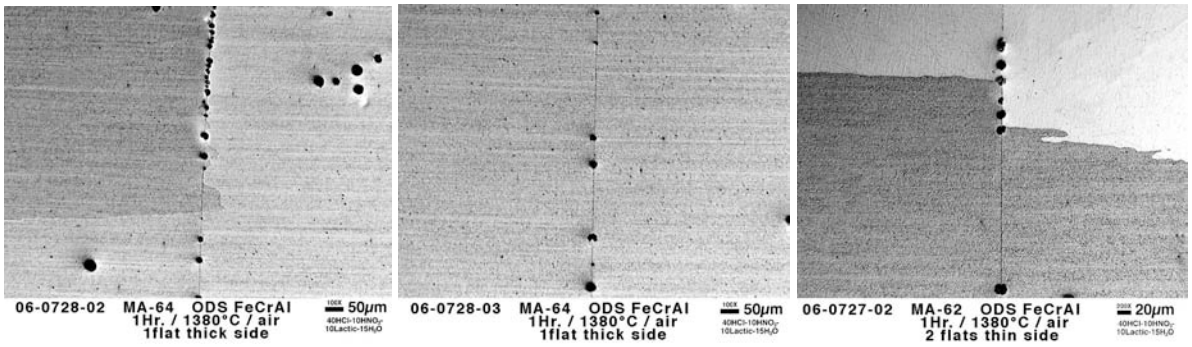

(a) (b) (c)

Figure 6. Cross sections of butt joints in alloy PM2000 showing the presence of particles or voids in the bond line: (a) a dense population of particles/voids inhibiting recrystallization across the bond line in MA-64 (b) a lower density of particles/voids in MA-64, with no effect on recrystallization, and (c) local inhibition of recrystallization in MA-62.

approximately 20 μm apart, but continued through the bond when the particles/voids were more than approximately 50 μm apart. Figures 6b and c show further examples of this behavior.

A further phenomenon that requires explanation is the fact that, even where grain growth was unimpeded through the bond with no indication of any change in grain structure (for example, as shown in Fig, 6b), the bond line remained visible in optical microscopy, suggesting the possibility of some structural change. TEM examination of earlier joints indicated the presence of Al_2O_3/YAG/TiN particles along the bond lines [1], presumably formed during the bonding process; these issues are to be addressed by further TEM examination.

STRENGTH ANISOTROPY

Although ODS alloys exhibit exceptional high-temperature creep strength, the very large length-to-diameter (l/d) ratio of the grain structure of typically extruded tubes after secondary recrystallization results in anisotropic properties, with the creep strength in the transverse (hoop) direction being less than 50% of that in the axial direction. Based on results from a European Brite program [2], exploration has been made of the application of torsional deformation of 25 mm diam. tubes of PM2000 in the unrecrystallized condition, with the aim using the realignment of the oxide dispersion (and associated impurity oxide particles) to 'steer' the direction taken by grain growth during secondary recrystallization. The tubes were subjected to various degrees of well-controlled hot torsion, as summarized in Table I. The strain rate used in all cases was 10^{-3} s^{-1}, which corresponded to a torsion rate of 0.12 °s^{-1}. Following torsion testing, the tubes were given a secondary recrystallization heat treatment of 1 hour at 1380°C in air. Figure 7a is an overview of the nine tubes tested, with the hot zone visible in the center of the tube length, and Fig. 7b shows the macro grain structure after recrystallization, and the transition from axially-

Table I. Summary of Torsion Testing Parameters

Tube	Total Torsion	Increments	T°C	Comments
I	83°	43°+ 40°	750	No collapse
II	122.5°	5 °(with pause)	750	4 runs of 27.5°, 40°, 40° and 15°
III	119°	5° (with pause)	750	3 runs of 40°, 40° and 39°
IV	160°	5° (with pause)	750	4 runs of 40°; collapsed during 4th run
V	80°	66°+ 14°	750	2 runs of continuous twist
VI	80°	continuous	750	
VII	80°	continuous	675	
VIII	160°	80°+ 80°	750	collapsed between 100 and 120°
IX	95°	continuous	750	No collapse

oriented grains (with a large l/d ratio) in the unaffected tube ends, to spirally-oriented grains (with an apparently smaller l/d ratio) in the tube center regions. After flattening, creep specimens were made from the areas of the tubes where the microstructure had been modified by torsion, to allow comparative measurement of changes in strength as a function of degree of twist. Miniature 'dog-bone specimens (25 mm long) were used, and specimens were cut from both axial and transverse orientations. Specimens from the ends of the flattened tubing furthest from the zone subjected to hot torsion were used to obtain baseline data.

The range of grain structures in tubes with nominal degrees of maximum twist of 99, 119, and 123° are illustrated in Fig. 8, which shows longitudinal and transverse cross sections, and the transition in grain orientation from the end of a tube to the twisted section.

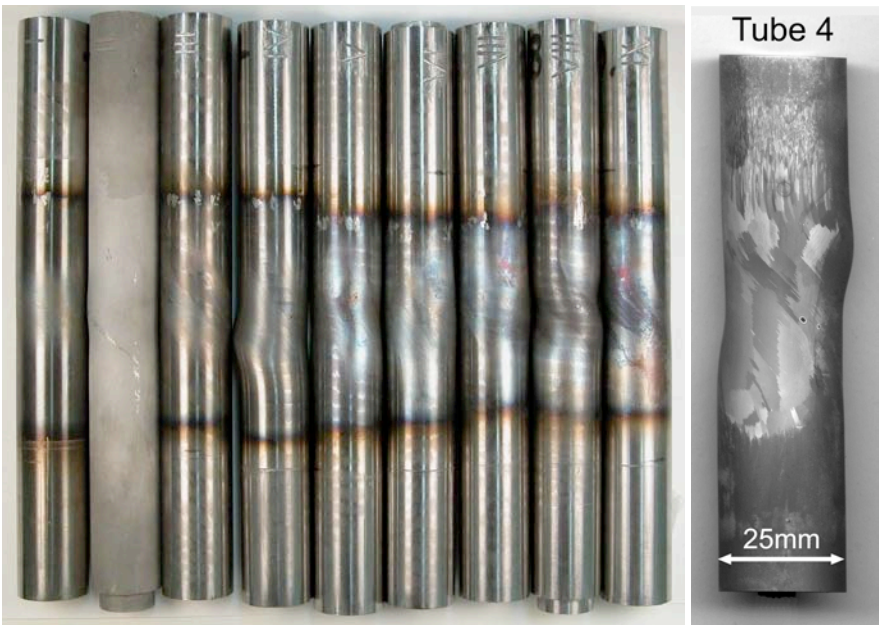

(a) (b)

Figure 7. Macro views of tubes after hot torsion (a) as tested (Tube No. II had been cleaned and etched); and (b) Tube No. IV after etching to reveal the grain structure.

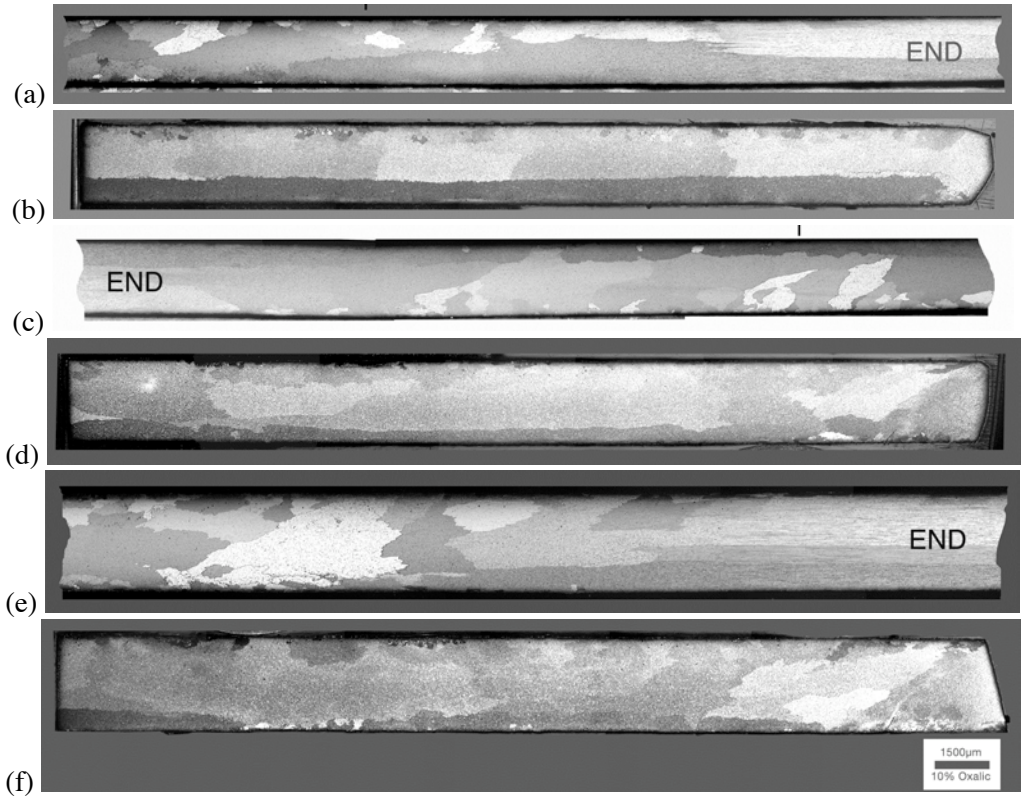

Figure 8. Etched cross sections of tubes after hot torsion, secondary recrystallization, and flattening: cross sections (a) from one end (longitudinal section), and (b) center (transverse cross section) from Tube No. II (max. degree of twist 123°); (c) and (d) similar cross sections from Tube No. III (119°); (e) and (f) Tube No. IX (99°).

The ‘accelerated’ creep test procedure employed starts with a load substantially below the expected strength and, when sufficient data have been gathered to conclude that there is no indication that creep is occurring, an increment in load is made (typically of 3 to 5 MPa). When creep is detected, data are gathered to allow calculation of the creep rate, before the load is further increased; these iterations are continued until rupture occurs.

Examples of creep curves obtained on the parent alloy (for establishing a baseline for comparison) are shown in Fig. 9, in which the test in the longitudinal direction involved several loading increments, and lasted for 582 hours, with failure occurring with minimal strain. For the transverse test, the initial loading chosen was sufficient to cause rupture in 34 hours, demonstrating the expected anisotropy. The resulting rupture strengths are seen to be somewhat higher than measured for alloy MA956 (Fig. 4), but are in line with the values reported by the alloy manufacturer [3]. Similar testing of the microstructures modified by hot torsion is in progress.

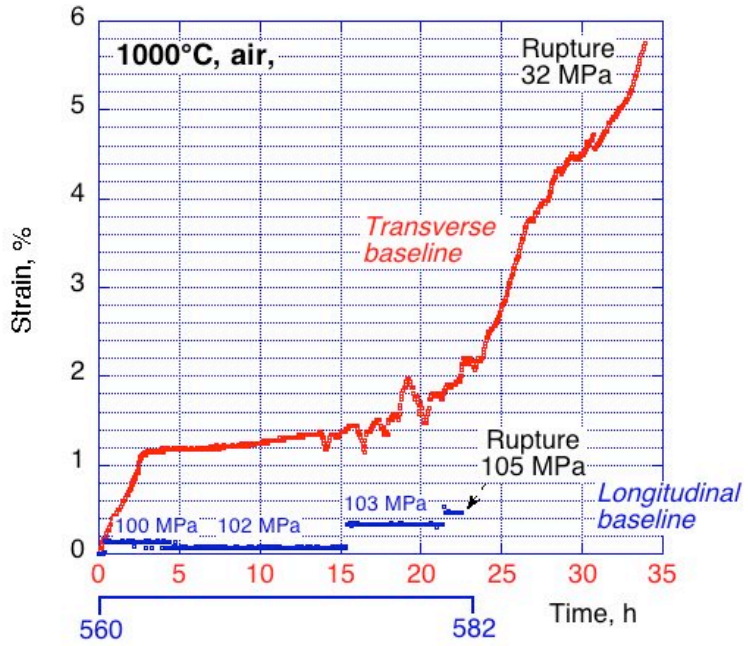

Figure 9. Baseline creep curves for recrystallized ODS FeCrAl alloy PM2000 made using specimens from the ends of the tubes used for hot torsion testing.

SUMMARY

Two techniques have shown good potential for joining ODS-FeCrAl alloys, in that clean-appearing joints can be made with what appears to be manageable disruption of the yttria dispersion in the alloy. In particular, upon secondary recrystallization of the ODS alloy, it has been possible for grain growth to proceed unimpeded through joints made by pulsed plasma-assisted bonding. Such joined structures promise to retain a high fraction of the strength of the parent alloy; specimens have been prepared for determination of the creep strength of these joints. Hot torsion (up to a total twist angle of 160°) of tubes of a fine-grained ODS-FeCrAl alloy, followed by secondary recrystallization, resulted in the formation of a spiral grain structure in which the l/d ratio of the grains was significantly reduced, compared to the parent alloy. Buckling of the tubes was not observed below a twist angle of 122.5°. The modified specimen grain size and shape were considered to be promising (in the absence of creep data) in terms of

improving the creep strength of the tubes in the hoop direction, and creep testing of specimens from these tubes is in progress.

ACKNOWLEDGMENTS

This research was sponsored by the Fossil Energy Advanced Research Materials (ARM) Program, U.S. Department of Energy, under contract DE-AC05-96OR22464 with UT-Battelle LLC. The authors thank the director of the ARM program, Robert Romanosky, of the National Energy Technology Laboratory, and Roddie Judkins, Director of the Fossil Energy program at ORNL, for their continued enthusiasm and support. The authors would like to acknowledge the contributions of John Hurley of the North Dakota Energy and Environmental Research Center in the development of the TLP processing parameters, and Johannes Schröder of Metallwerk Plansee for accommodating our requests for specific alloy samples. Special recognition is due to Justin Ritherdon, of the University of Liverpool, who conducted the hot torsion testing at ORNL, and to Gordon Tatlock, also of the University of Liverpool who, while on sabbatical at ORNL, provided the TEM expertise needed to understand the microstructures resulting from TLP bonding. We are also most grateful to Hu Longmire for developing metallographic preparation skills for ODS-FeCrAl alloys; to Larry Walker for electron microprobe analysis expertise; and to Dorothy Coffey for her skill with focused ion-beam milling to produce the TEM samples.

REFERENCES

1. I.G. Wright, B.A. Pint, and Z.P. Lu, "ODS Alloy Development," Proc. 18th Annual Conference on Fossil Energy Materials, Knoxville, Tennessee (2004).
2. Y.L. Chen, A.R. Jones, R.C. Pond, U. Miller, "The microstructure and recrystallization of flow-formed oxide-dispersion-strengthened ferritic alloy: Part II. Recrystallization behavior," Met. Mat. Trans. A-Phys. Met. & Matls. Sci., 33 (12), 3787-3794 (2002).
3. Data Sheets: "Material Data PM2000," Plansee Holding AG, 6600 Reutte, Austria (2004).

CONTROL OF DEFECTS AND MICROSTRUCTURE IN ODS ALLOYS

Andy R. Jones
University of Liverpool, 3 Brownlow St., Liverpool L69 3GL, UK, E-mail: andy.jones@liv.ac.uk;
Telephone: + 44 151 794 8026; Fax: +44 151 794 8370

Özgur Selsil
University of Liverpool, Department of Mathematical Sciences, Liverpool L69 7ZL, UK, E-mail: oselsil@liv.ac.uk;
Telephone: + 44 151 794 3779; Fax: +44 151 794 4754

Sara E. Burns
University of Liverpool, Department of Engineering, Brownlow Hill, Liverpool L69 3GH, UK, E-mail:
s.e.burns@liv.ac.uk; Telephone: + 44 151 794 6801; Fax: +44 151 794 4930

ABSTRACT

Oxide Dispersion Strengthened (ODS) FeCrAl alloys; such as PM2000, have the potential for improved high temperature creep life in applications in high temperature high pressure environments. This is partly due to the fine yttria dispersion in the alloy which provides improved high temperature strength compared with numbers of other high temperature alloys. However, developing a coarse-grained microstructure during secondary recrystallisation can significantly enhance high temperature creep life in these alloys. But achieving such microstructures is highly sensitive to the thermomechanical processing history of the alloy. For example, in extruded tubes a columnar grain structure elongated parallel to the extrusion direction is usual and has been shown to give enhanced creep performance in applications where the principal stress aligns parallel to the columnar grains. On the other hand, when the maximum principal stress is a hoop stress and acts perpendicular to the major axis of the columnar grains, as in tubes subject to internal pressurisation, such microstructures demonstrate reduced creep life. Optimally, a coarse, helically wound grain structure, which could resist creep both in the hoop and axial directions would seem to be a more appropriate microstructure for pressurised tubes. A simple industrial technique involving torsional deformation of tube prior to final recrystallisation has been proposed and appears to produce promising microstructures, examined in the current study. Modelling work using shell theory has commenced, in order to study the onset of buckling in torsionally deformed tubes.

INTRODUCTION

In an era where energy prices have increased dramatically, improved energy conversion efficiency is highly desirable, especially in the power generation industry[1]. Power generation plant designed to operate at higher temperatures will have an intrinsic capacity for higher energy conversion efficiencies. However, to develop such plant alloys for key components, such as tubing for high temperature heat exchangers, need to be custom developed to deliver acceptable service performance and duration at higher temperatures. Mechanically Alloyed (MA) Oxide Dispersion Strengthened (ODS) alumina-forming FeCrAl steels, such as alloy PM2000, offer promise for service as tubing for such high temperature heat exchanger markets. Alloys of this type exhibit reasonable strength at high temperatures (e.g. the yield strength of PM2000 is about 80MPa compared to about 25MPa in Haynes 214 at 1000ºC (ref.2)) due to two main factors: a dispersion of fine (20-50nm diameter) Y_2O_3-Al_2O_3 particles, which is stable against significant Ostwald ripening; and a coarse, anisotropic, recrystallised grain structure that provides enhanced creep resistance[3,4]. It is the latter which is of particular interest in this study.
Evidence has shown that careful thermo-mechanical processing and high temperature heat treatment of such ODS alloys can produce a very coarse and highly textured microstructure as a result of recrystallisation[5,6]. However, grain morphology and microstructure are sensitive to the specifics of thermomechanical processing history[6,7]. For instance, coarse columnar grains with a Grain Aspect Ratio (GAR) as high as 30:1 are often found in extruded tube subject to secondary recrystallisation. For applications where the principal creep stress is parallel to the major axis of the grain structure (see Fig. 1), tube with these high GAR microstructures provides excellent creep resistance at elevated temperatures. However, when these ODS alloy tube microstructures are subject to biaxial stresses under

internal pressurisation at high temperatures, resultant creep life is unsatisfactory. This arises because the maximum principal stress (hoop stress) is orthogonal to the major axis of the columnar grain structure (see Fig 1). As a result, the creep life in the hoop direction is significantly reduced compared to that in the longitudinal direction. It has been reported that ODS tubes with microstructures similar to Fig. 1 may have a biaxial creep life of only ~15% (~14,500h/1100^{o}C/5.9MPa) of that required to operate successfully (100,000h life) as heat exchanger tubing for power generation applications[8].

Techniques such as cold and warm flow forming have been explored to develop ODS alloy tubing with improved GAR and creep performance in the hoop direction; and some success has been achieved[5,9]. However, the pattern of deformation in flow forming can lead to development of significant variation in recrystallised grain size and GAR across the wall of processed tube, which outcome is not optimal. In fact, the type of microstructure produced by flow forming and heat treatment of ODS alloy tube was difficult to control. Although some interesting microstructures arose following high levels of deformation, the control of flow forming to reproducibly generate through-wall coarse grain structures 'on demand' across a range of different tube sizes is likely to be difficult.

Recently, Ritherdon and Jones[4] have proposed a simpler, yet commercially practical technique that seems to offer a potential solution to the problem. Using a machine such as that shown in Fig. 2, which is used commercially to introduce torsionally spiralled cooling channels in tool steel drill bits, a torsionally deformed tube can be produced which can be subject to subsequent recrystallisation. Results so far have been found to be encouraging, since helical striations that represent deformation traces can clearly be seen to spiral around the surface of PM2000 tube deformed in this manner (see below, Fig. 3). There is a suggestion that the yttria oxide particles in the alloy will be aligned along these deformation traces, and it is this alignment that influences grain growth direction during recrystallisation[10]. Hence, when the tube undergoes a secondary recrystallisation, it would be anticipated that a helically oriented, coarse grain structure would develop. During tube plastic deformation, a tube buckling effect was encountered (see Fig. 3). However, two methods have been suggested as means to counter the problem[4]: firstly, to superimpose a degree of axial tension during torsional processing; secondly, to insert a loose-fitting, internal mandrel in the tube. Either or both of these methods may be attempted in further trials.

The main objective of the current paper is to report the microstructural changes that occur in torsionally deformed PM2000 tube before and after secondary recrystallisation. The results will also be compared with microstructures seen after flow-forming and recrystallisation. In addition, some initial modelling work has been undertaken to investigate likely buckling behaviour in tubes subject to torsional loading.

EXPERIMENTAL

An ODS PM2000 tube of dimensions 25mmOD, 20mmID and over 1m in length in the primary recrystallised condition was subjected to a torsion testing trial on a commercial unit operated by Forécreu SA, France. The

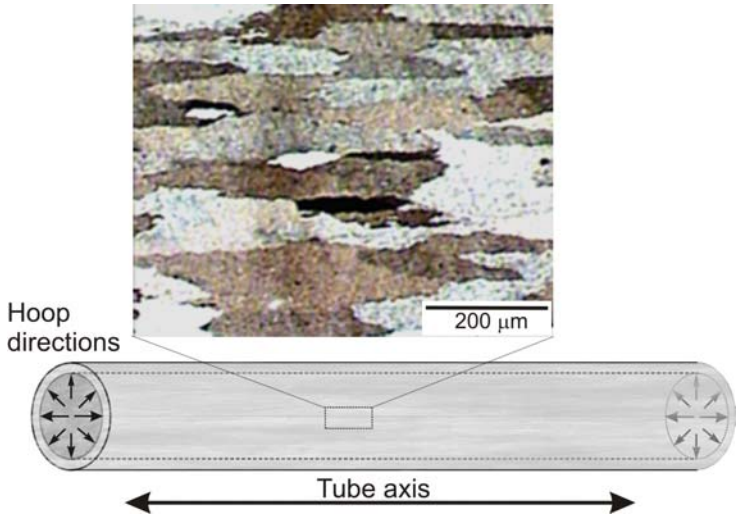

Figure 1. Schematic diagram showing the hoop and tube axial directions in PM 2000 tube. The micrograph shows a coarse, high GAR columnar recrystallised (1380ºC/ 1h) grain structure aligned parallel to the tube axis..

production machine used (shown in Fig. 2) was equipped with an induction heater with a ~50mm hot zone that was used to localise deformation during tube torsion. During the torsion test, the tube was gripped between two chucks, one fixed, the other rotating at ~2rpm, while the hot zone (720^0C) was traversed along the tube at a rate of ~7mm.s^{-1}. Due to the occurrence of a slight axial contraction during tube torsion, the finished PM2000 tube exhibited an overall macroscopic spiral, as shown in Fig. 3, as well as torsion within the tube walls; the latter is seen as striations that are clearly visible on the external surface of the tube. Despite tube distortion, there was no sign of buckling of the tube cross-section along its length. In order to investigate the development of grain structure in these torsionally deformed materials during subsequent secondary recrystallisation, cut samples of tube were first given an anneal of 1 hour at 1380ºC[4]. Subsequently, metallographic samples were polished to a 0.5µm finish using OPS silica suspension solution then etched in Kallings Reagent[4].

RESULTS AND DISCUSSIONS

TORSIONAL DEFORMATION TRIALS ON A PRODUCTION FACILITY

As noted previously, entrained oxide particle stringers, which become aligned with the directions of macroscopic shape change during alloy processing, tend to define the grain morphology, alignment and grain aspect ratio which evolves during subsequent secondary recrystallisation in these alloys[9,10]. Such behaviour also appears to occur in the current work. This view is supported by the evidence of Figs. 4(a) and (b) below, which show the plan section microstructure of the twisted PM2000 tube before and after the secondary recrystallisation process, respectively. The figures reveal

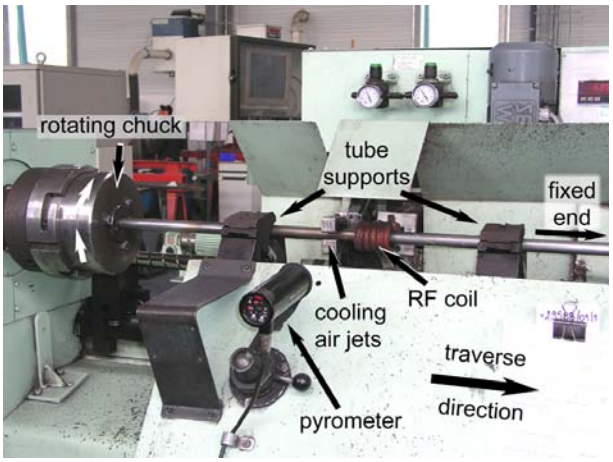

Figure 2. The production facility used in the torsional deformation trial (after ref.4).

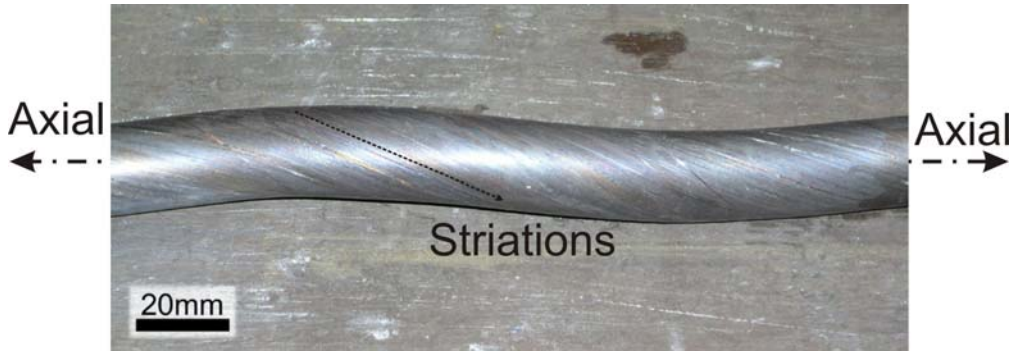

Figure 3. The trace of striations (indicated by arrows) on the ODS PM2000 tube after torsional deformation [4].

that the path of the deformation traces, inclined at about 20º (± 5º) to the tube axis (see Fig 4(a)), has been replaced by an equally inclined helical array of anisotropic, coarse grains (see Fig 4(b)). The size of these grains is estimated to range from ~200-1000µm in length and ~50-100µm in width. This leads to a GAR estimated to vary between 4:1 and 20:1.

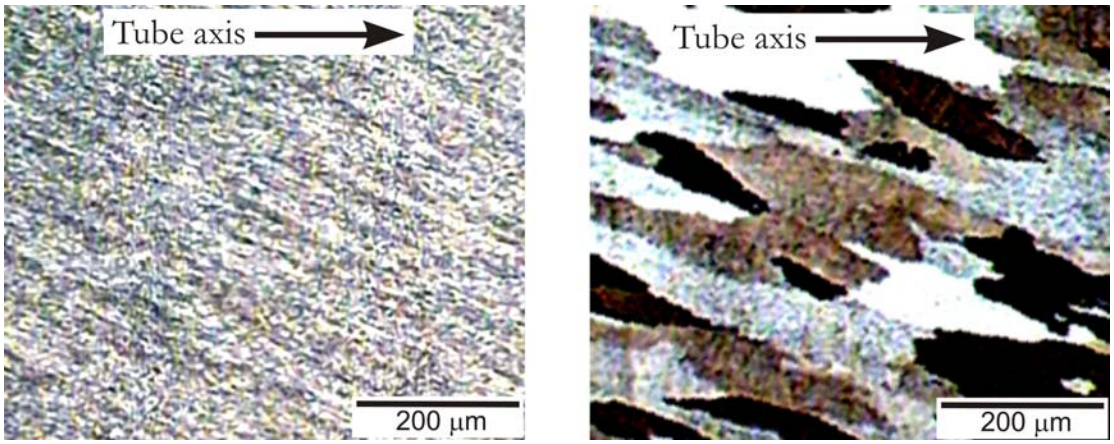

(a) (b)

Figure 4. (a) Plan section showing inclined deformation traces on the PM2000 tube axis after torsional deformation. (b) Coarse, columnar recrystallised microstructure along the prior deformation path following annealing 1380ºC/1h.

The microstructure of a typical cross-section from a hot flow formed PM2000 tube is shown in Fig. 5(a) and demonstrates the substantial variation in secondary recrystallised grain size that can develop across the wall of tube that has undergone hot flow forming[4,5,9]. Such microstructures are unlikely to be ideal for sustained creep life in these alloys, as noted by Ritherdon et al[4]. In comparison, the cross-section of a secondary recrystallised sample of torsionally deformed tube is shown in Figure 5(b), where a much more homogeneous, coarse grain structure can be seen to have evolved through the entire tube wall. Thus, it seems that torsional deformation of ODS FeCrAl alloy tube combined with subsequent secondary recrystallisation may produce the type of grain structures that are likely to have potential for extended high temperature creep performance in high pressure service applications. However, tube processing control needs further adaptation and refinement in order to achieve straight torsionally deformed product and higher total levels of torsional strain.

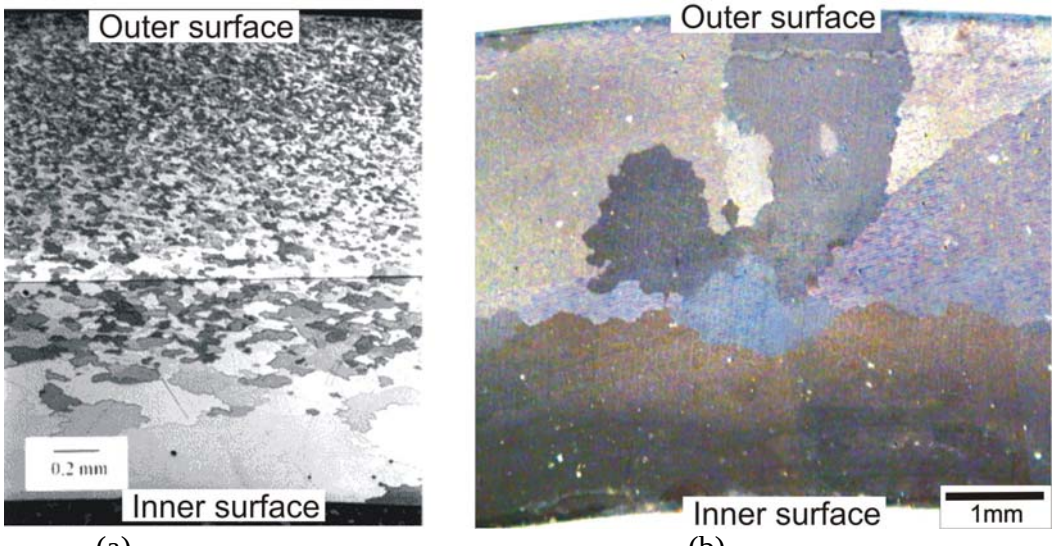

(a) (b)

Figure 5. The microstructure of transverse sections of PM2000 tube after recrystallisation at 1380C for 1 hour after (a) flow forming [9] (b) torsional deformation.

SCANNING ELECTRON MICROSCOPY AND ELECTRON BACK-SCATTERED DIFFRACTION

Scanning Electron Microscopy (SEM) combined with Electron Back-Scattered Diffraction (EBSD) has been performed on torsionally deformed and secondary recrystallised samples in order to determine grain orientations and microstructural texture in the PM2000 tube. Results are shown in Fig. 6(a) where the orientations of the coarse columnar grains are represented by different colours, where each colour represents a particular orientation that is also represented by the same colour in the pole figure shown in Fig. 6(b). For clarity, the X- and Y axes in the figure are parallel to tube axis and the hoop direction, respectively. Also, the normal to the image is the normal to the surface of the tube. From Fig. 6(b) it can be seen that a complicated picture of the texture emerges. However, the texture represented by the individual crystal orientations is summarised in the pole figures shown in Fig. 6(c). From this figure, it is deduced that the columnar grains exhibit <100> texture aligned at an angle to the tube axis. Also, the tube direction is close to <112>. The plan section shows weak {111} clustering. These results differ from the finding by Wasilkowska et al[11], who found a <111> crystallographic texture in MA956 aligned close to the extrusion direction. However, the torsional deformation of the current PM2000 tube has resulted in a different and more complex columnar grain texture after recrystallisation. Nevertheless, further work is required to elaborate on these texture results and to determine the influence of these textures on subsequent creep performance.

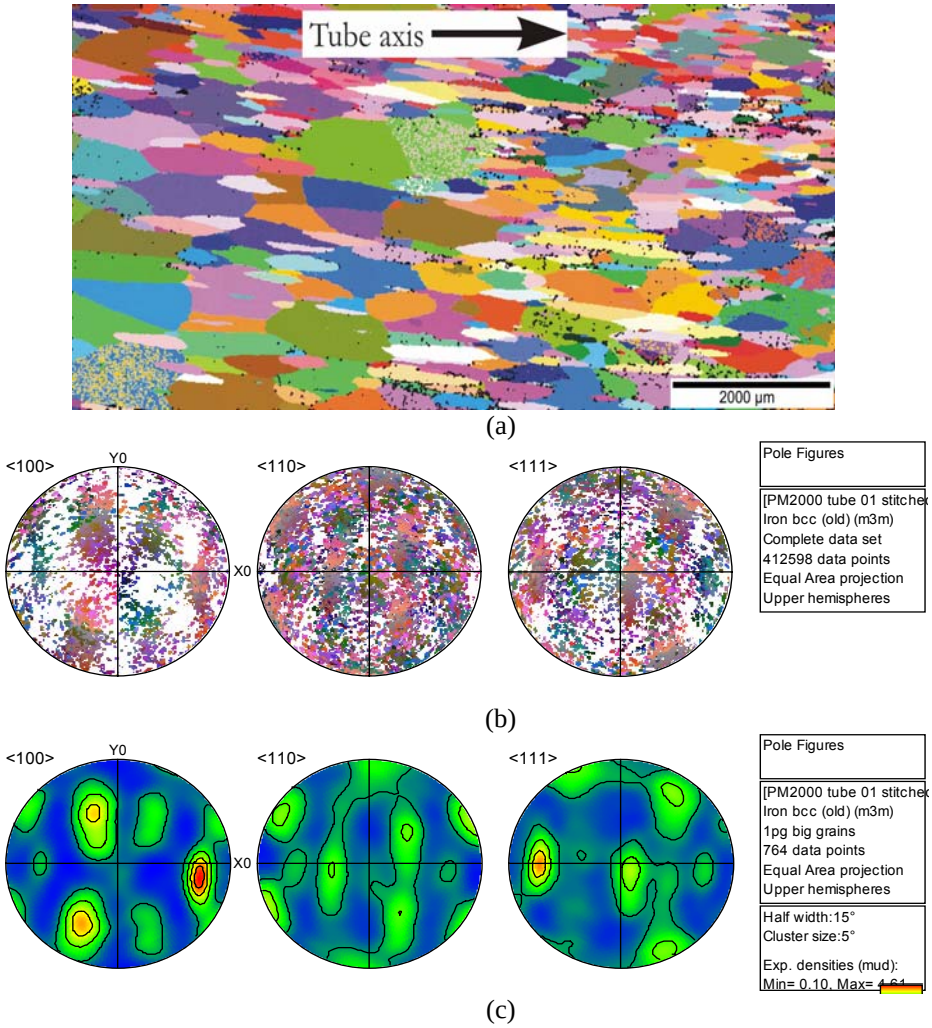

Figure 6. (a) SEM micrograph showing an orientation map of the columnar microstructure of the helical twisted tube, and (b) is the corresponding orientation of the grains from Figure 6(a). (c) shows the orientation contour of the columnar grains.

A representation of the distribution of high and low angle boundaries in the plan section is shown in Fig. 7 and indicates that most of the grain boundaries in the torsionally deformed, secondary recrystallised PM2000 are high

angle (>10º) in nature. This suggests that the optically visible grain size is a reliable indication of the likely grain size of importance for determining creep performance.

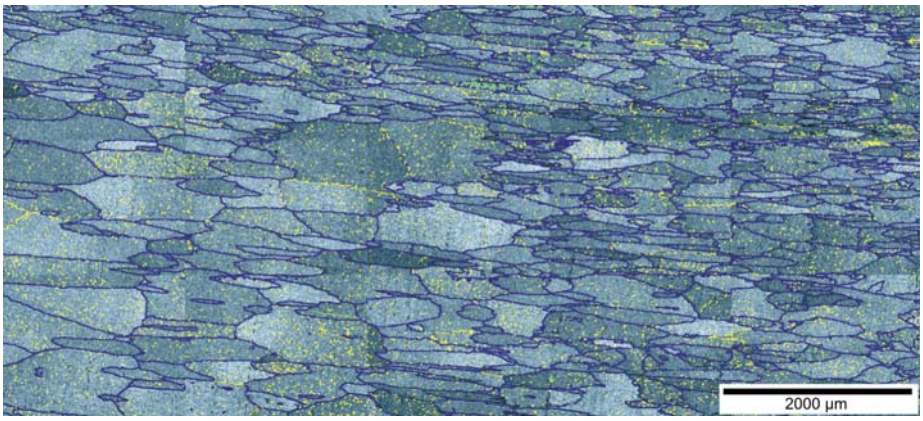

Figure 7. Shows the angular grain boundary mapping corresponding to Fig. 6(a). Blue and yellow lines represent high angle (>10º) and low angle (<10º) grain boundaries, respectively.

MODELLING BUCKLING OF SHELLS: INITIAL APPROACHES

In the approach taken in the current work, the buckling behaviour of tube has been studied as a particular case within the family of buckling behaviour of thin walled cylindrical shells. The governing differential equations used in the study follow from Flügge[12]. The current results are part of a wider study that, without any a priori assumptions, established a mathematical model for an inhomogeneous shell under thermal loading (a tube with a hot zone) using the equilibrium equations for linear elasticity[13]. In studying the example of a cylindrical shell with a circular cross-section subject to torsional loading only, solutions to the governing differential equations (Flügge[12]) exist for buckling of a shell provided that it is sufficiently long. Following this approach and making reasonable assumptions, it has been possible to establish a formula for the value of critical torque, M_{cr}, at the onset of buckling collapse of such a shell (tube):

$$M_{cr} = \frac{\pi\sqrt{2}}{3\,(1-\nu^2)^{3/4}}\,E\,\sqrt{h^5\,r_0}. \qquad - \ 1.$$

where ν is Poisson's ratio, E is Young's modulus, h is tube wall thickness and r_0 is the tube radius (to mid-wall thickness). An illustrative plot of equation 1 is presented in Fig. 8 for torsion of PM2000 alloy tube performed at 750^0C and suggests that at tube wall thicknesses of 2-2.5mm and below, the critical torque for buckling, M_{cr}, is

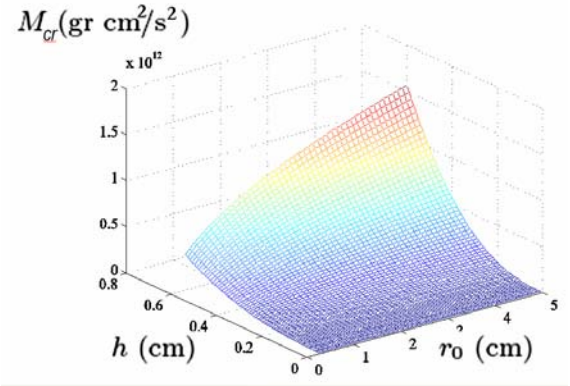

Figure 8. A plot of critical torque, M_{cr}, for buckling collapse vs. h and r_0 in long PM2000 tube.

relatively insensitive to variations in tube radius: to achieve higher torque before onset of buckling requires thicker walled tube, preferably combined with larger tube diameters. The work was extended, again using the approach of Flügge[12], to deal with two cases of simultaneous shear load and axial extension in a cylindrical shell of finite length. The background to this part of the study was an interest in determining whether an axial tensile load superimposed during torsional deformation could limit the tendency towards buckling behaviour or the kind of spiralling seen in the tube deformed in the current study (Fig.3). Initially, the material properties (Young's modulus E and Poisson's ratio) were considered to be constant. Subsequently the study went on to consider the case where Young's modulus is dependent upon position along the axis of the tube (shell), while Poisson's ratio remains constant; this example would cover the case of a moving hot zone during torsional loading of tube, see Fig.9.

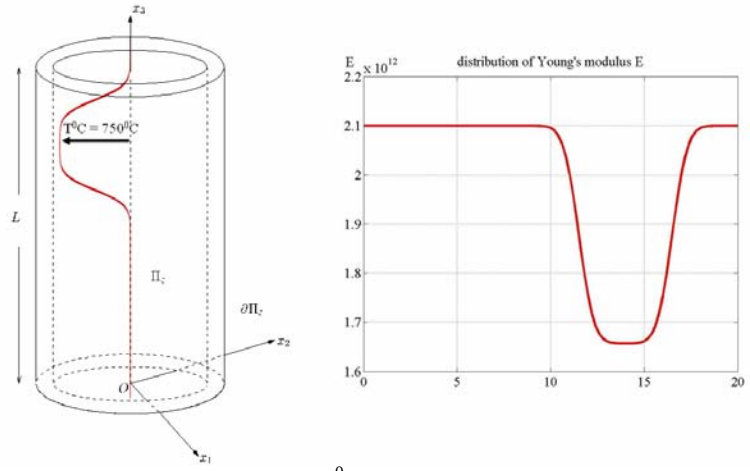

Figure 9. Schematic illustrating a moving hot zone (750^0C) treated as a dip in Young's modulus (E).

For the latter case, as this introduced inhomogeneity along the axis of the cylindrical shell, it was necessary to reformulate the governing differential equations for the buckling problem. This was possible by the modification of the normal forces and moments representing the elastic law for the cylindrical shell stated in Flügge[12]. The ultimate aim is to model the critical values for torsional and tensile loads before the shell begins to buckle. Currently, the necessary spectral problem has been set and the results have been presented[13]. The construction of the solution to these problems was found to be fairly complex. A set of six coupled ordinary differential equations needs to be solved, either numerically or asymptotically, and this will require additional study. Further extension to this research would be to explore the buckling problem for shear load and axial extension of a cylindrical shell, taking into consideration the effect of temperature.

CONCLUSIONS

Studies of the microstructure that evolves in PM2000 alloy tube on secondary recrystallisation following commercially implemented torsional deformation have continued, extending earlier studies. The key conclusions of this work, as well as of some initial modelling of tube buckling behaviour are:

- After secondary recrystallisation, a coarse, helical grain structure can be obtained in PM2000 tube following commercial processing in torsional deformation.

- The secondary recrystallised grain size, in particular, is more uniform across the tube wall thickness than is found in tube deformed to similar levels using flow forming techniques.

- At a torsional deformation level leading to a ~20º inclination of the secondary recrystallised grain structure to the tube axis, the grains tend to align along <100>. Also, the tube axis was found to be close to <112>

- The modelling of buckling of tubes (thin walled cylindrical shells) under torsional loading has been initiated. In general, these problems are complex and will require either numerical or asymptotic solutions to the coupled differential equations derived.

ACKNOWLEDGMENTS

The authors are grateful for funding from the Advanced Research Materials (ARM) Programme, U.S. Department of Energy, Office of Fossil Energy under contract DE-AC05-96OR22464 managed by U.T.–Battelle, LLC. The authors also acknowledge Plansee GmbH, Germany and Forécreu SA, France who, respectively, supplied the

PM2000 tube and carried out the torsional deformation trials referred to in this study. The authors also appreciate the access to facilities and support of Professor D.J.Prior and Mr D Atkinson in the SEM-EBSD studies.

REFERENCES

1. China View, www.chinaview.cn 2005-09-17.
2. Brochure of PLANSEE, *'High Temperature Materials'*, Materials properties and applications, p 7.
3. A.Czyrska-Filemonowicz and B.Dubiel, *J. of Mat Processing Technology*, **64**, (1997), pp 53-64.
4. J. Ritherdon and A.R. Jones: *Proc. 19th Annual Conf. on Fossil Energy Materials*, Knoxville, Tennessee, May 9-11, 2005, Eds. Judkins et al., (ORNL, 2005).
5. J. Ritherdon and A.R. Jones: *Proc. 18th Annual Conf. on Fossil Energy Materials*, Knoxville, Tennessee, June 2-4, 2004, Eds. Judkins et al., (ORNL, 2004).
6. K.H Matucha and M Ruhle, *Metal Powder Reports*, 1993, November, 24.
7. I.C. Elliott and G A J Hack, *'Structural Applications of Mechanical Alloying'* in ASM International Conference, Myrtle Beach, March 1990, Eds. Froes and deBarbadillo, 15.
8. F. Starr, A R White and B Kazimierzak, *Proc. Conf. 'Materials for Advanced Power Engineering'*, 1994, Liege, Eds Coutsouradis et al., Kluwer Academic Pub., 1393.
9. C.Capdevilla, U.Miller, H.Helenak, H.K.D.H.Bhadeshia, *Mat.Sci.and Eng.A* **316**, (2001), p 161-165
10. C.Capdevilla Montes and H.K.D.H.Bhadeshia, *Advanced Eng. Mat*, **5**(2003), No.4, p232-237.
11. A.Wasilkowska, W.Ratuszek,R.Toporowski,A.Czyrska Filemonowicz, *Proc. of the XVII Conf. on Applied Crystalography*, Katowice-Wisla, Poland, to be published.
12. W. Flügge 'Stresses in Shells', Springer-Verlag, 1973
13. S.E.Burns 'Mathematical Modelling of inhomogeneous Cylindrical Shells Under Thermal Loading and an Investigation of their Buckling', MSc dissertation, University of Liverpool, 2005.

SOLID STATE JOINING OF OXIDE DISPERSION STRENGTHENED ALLOY TUBES

Bimal K. Kad[1], Phuoc-Hai Nguyen[1], Ian Wright[2], and Rod Judkins[2]
[1]University of California - San Diego, La Jolla, CA 92093
[2]Oak Ridge National Laboratory, Oak Ridge, TN 37830

ABSTRACT

Oxide dispersion strengthened (ODS) Fe_3Al and Fe-Cr-Al based (MA956) alloys are currently being developed for heat-exchanger tubes for eventual use at operating temperatures of up to 1100^{o}C in the power generation industry. The development challenge is to produce thin walled tubes, employing powder extrusion methodologies, with a) adequate increased strength for service at operating temperatures to b) mitigate creep failures by enhancing the as-processed grain size via secondary recrystallization. While these mechanical property challenges are being steadily achieved, there is now a forward looking effort to explore joining methods essential to fabricating component systems and assemblies. The challenge is to preserve the dispersion microstructure, responsible for the high temperature strength, during subsequent joining operations which precludes all melting driven welding techniques. We report here on efforts at non-fusion based inertia welding of MA956 tubes in butt-joint configurations. Detailed examinations of the weld microstructure, observations of the grain size, micro-hardness and the nature of the solid state interface between the mating surfaces suggest that high quality welds are feasible for a variety of welding conditions. Mechanical properties are explored using tensile and creep testing. The results obtained are discussed in terms of the process variables employed, the resulting heat affected zone (HAZ) width and the joint microstructures obtained.

Research Sponsored by the U.S. Department of Energy, Office of Fossil Energy, Advanced Research Materials Program, under contract DE-ACOR-96OR22464 with UT-Batelle subcontract to the University of California-San Diego.

INTRODUCTION

Oxide dispersion strengthened (ODS) ferritic FeCrAl (MA956, PM2000, ODM751) and the intermetallic Fe_3Al-based alloys are promising materials for high temperature, high pressure, tubing applications, due to their superior corrosion resistance in oxidizing, oxidizing/ sulphidizing, sulphidizing, and oxidizing/chlorinating environments[1-4]. Such high temperature corroding environments are nominally present in the coal or gas fired boilers and turbines in use in the power generation industry. The target applications for ODS alloys in the power generation industry are thin walled (0.1" thick) tubes, about 1 to 3 inches in diameter, intended to sustain internal pressures (P) of up to 1000psi at temperatures of 1000-1100^{o}C. Within the framework of this intended target application, the candidate dispersion strengthened alloys must strive to deliver a combination of high mechanical strength at temperature, as well as prolonged creep-life (hoop creep in particular) in service.

This material migration to ODS alloys for high temperature service poses significant fabrication challenges. These materials are not readily welded via conventional means or the welds perform poorly. Early work on Fe_3Al, FeCrAl family of ODS alloys provides the outlook that they cannot be subjected to a fusion based joining process. The density disparity between the matrix and the dispersoid precludes any melt based joining, as the lighter oxide dispersion so critical to the high temperature creep performance will simply float away. Thus, solid-state joining methodologies that preserve the dispersion microstructure are inherently more suitable and attractive. Thus, process design and validation of appropriate solid-state joining methodologies represent a critical developmental and design challenge that must be overcome in order to exploit and deploy ODS alloys. Solid-state welding procedures like a) Inertia welding, b) Flash welding and c) Magnetic Pulse welding and d) Braze/Diffusion welding are the norm in this developmental regime. Recent work has addressed inertia and friction welding of ODS Fe_3Al & MA956 alloys[5-9] with significant promise of developing meaningful joining solutions for component fabrication.

EXPERIMENTAL DETAILS

Materials: All materials for this study were provided by Special Metals Corporation in the form of nominal 2-1’2”OD, ¼” wall thick MA956 tubing in the un-recrystallized fine-grained state. Short sections were cut for inertia welding trials ensuring that the mating surfaces are orthogonal to the rotational axis for full contact. The joint sections were recrystallized for 1-hour at 1375^{o}C to produce the coarse grained microstructure necessary for maximum creep performance.

Figure 1. Sequence of inertia welding operations to produce robust joints in MA956 tubes.

Welding Equipment: Figure 1 shows the sequence of welding operation to produce robust joints in MA956 tubing. All joints were fabricated using either the Caterpillar model 150B, 180B inertia welding machines. Initial trials were attempted on model 150B followed by a production style configuration adopted for the 180B model which provide for better joint concentricity. The intended mating pieces are suitably clamped in the head chuck (spinning piece) and the tailstock (stationery) piece. The head stock moves to the starting position (separated by 1/8" from the tail stock piece) and rotates to the desired RPM. Upon achieving the prescribed flywheel RPM (fixed kinetic energy), the drive mechanism disengages and a fixed weld force is applied which brings the parts in contact. Frictional heat causes mating surfaces to soften and plastically deform to form a full circumferential through wall-thickness joint. When rotation stops, the parts are held for a few seconds during which the weld cools while still held firmly in the collets. The entire weld process takes up to 60 seconds. Process variables such as friction force, rotational speed and upset displacement are monitored for evaluation of overall joint performance.

Mechanical Testing: Test coupons were directly spark machined and turned from the tubes. Tensile tests coupons are of large round cross section (1/8" diameter) spanning the bulk of the joint wall thickness. Creep tests coupons are flat dog-bone shaped samples 0.125" wide and 0.040" nominal thickness where the width and the thickness correspond respectively to the tube circumference ad the wall thickness.

MATERIALS CHARACTERIZATION

Figure 2(b) shows the optical micrograph of polished and etched longitudinal section microstructure of a typical inertia welded joint. The initial tubes have their grains elongation along the tube axis. However in the as-welded configuration the macroscopic grain flow rotates the grain elongation from being parallel to the tube axis to perpendicular near the bond line, Figure 2(c). Heat localization at the mating surfaces results in dynamic recrystallization in a narrow region of the bond line where the grains can be resolved at the resolution of an optical microscope, Figure 2(a). The joints were

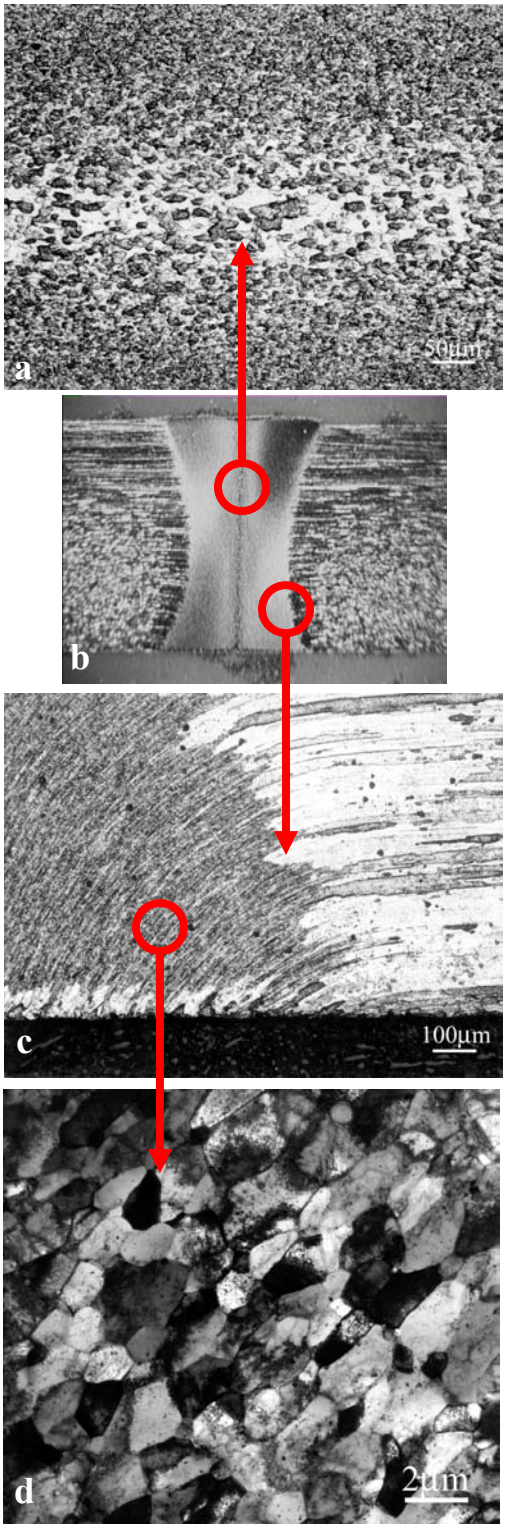

Figure 2. Weld HAZ microstructure (b) with coarse grains at the bond centerline (a). Macroscopic flow in welding causes grain rotation parallel to bond centerline (c) with (d) grain fragmenting upon recrystallization.

subsequently recrytsallized as this is the default treatment for high creep performance. TEM micrographs of recrytsallized grains present a slightly different picture, Figure 2(d). The most significant difference is that the bent grains are fragmented and reorganized into small grains with only a slight aspect ratio parallel to the bond line. Any grain shape anisotropy is mitigated and the microstructure can be treated as isotropic.

MECHANICAL PROPERTIES

Microhardness Measurements

A microhardness trace across the weld region for the as-welded (red curve) and the recrystallized (blue curve) joint section is presented in Figure 3. The spatial positioning of the curves is consistent with the scale of the underlying microstructure. The mean diamond pyramid hardness (DPH) in the unrecrystallized (red curve) base material is 340Kg/mm^2 which gradually dips down to 220Kg/mm^2 in the joint heat affected zone (HAZ). The hardness minima at the bond centerline stems from the maximum thermal excursion at the mating surfaces resulting in dynamic recyrstallization. As noted previously the grains at the bond centerline are rather coarse, Figure 2(a), and can be viewed using an optical microscope.

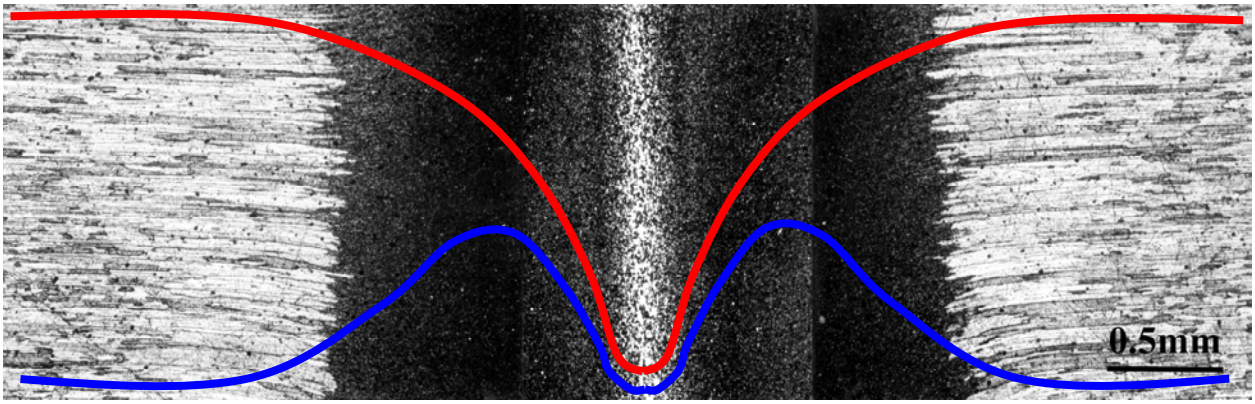

Figure 3. Microhardness profiles of as-welded (red curve) and recrystallized (blue curve) joint superimposed on the underlying recrystallized HAZ microstructure revealing a maxima symmetrically adjacent to bond centerline.

The hardness profile across the recrystallized joint (blue curve) shows that the base microstructure softens to about 220Kg/mm^2 and the hardness value at the bond line is relatively stable dropping to about 210-215Kg/mm^2. However, local maxima are observed in the HAZ region located symmetrically across the bond centerline. It is likely that some agglomeration of particles occurs in this vicinity which precludes grain coarsening in this region. Subsequent serial cross-sectional TEM examination, Figure 4, does indeed reveal the presence of unrecrystallized regions of submicron grain size within the bulk of the HAZ region.

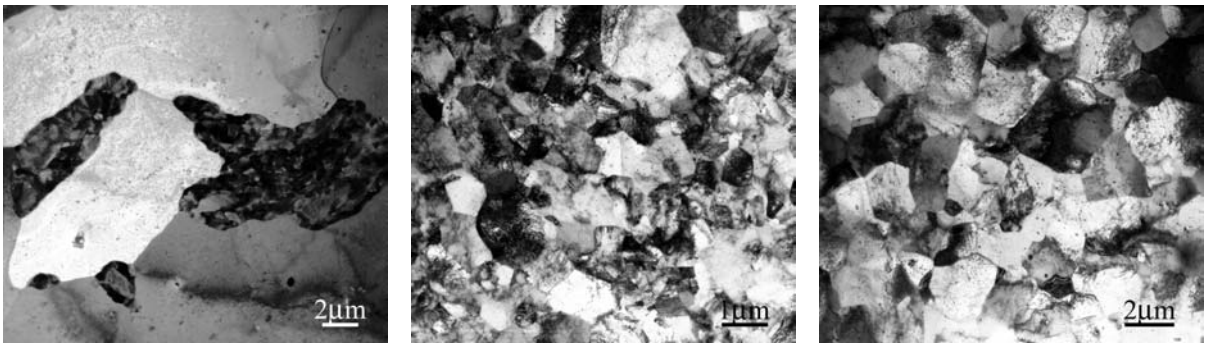

Figure 4. Sequence of cross-sectional TEM views (left to right) from the edge of the HAZ to the bondline indicating presence of fine stringers and agglomerates of fine grains dispersed in the HAZ region.

Considerable effort has been expended to control the HAZ width and the grain microstructure in the joints produced. As a consequence joints have been produced with HAZ widths in the rage of 0.1mm – 3.0mm. The testing of this entire array continues till date. Looking ahead at the creep performance we note that the general trend of reducing the HAZ width produces impressive gains in the over all creep performance

Tensile Properties

Room temperature mechanical properties are recorded for both the as-welded and the recrystallized joints as shown in Figure 5(a). The as-welded joint fails at about 140Ksi that is approximately the base material fracture stress for unrecrystallized MA956 as measured in the longitudinal direction. Hence, we surmise that the as-welded structure confers no weakness to the overall tube section. The recrystallized joints fail not at the joint but in the base material away from the joint. This is consistent with the microhardness results, see Figure 3, indicative of the relatively fine grained structure preserved in the joint-section despite the recrystallization treatments.

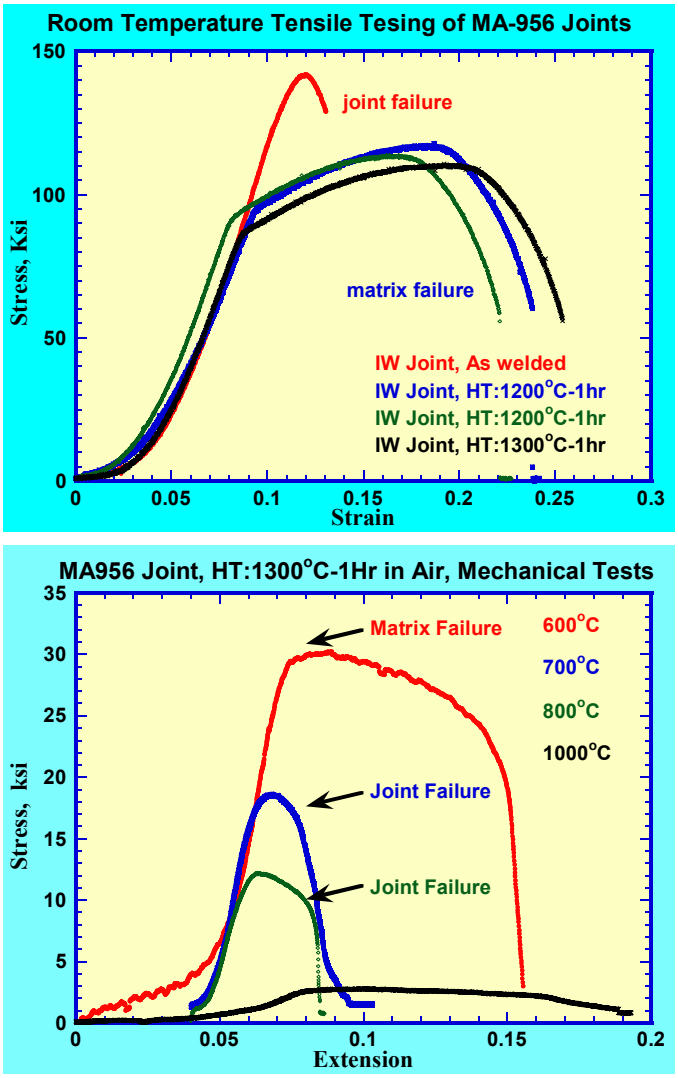

Figure 5. a) Room temperature tensile properties of inertia as-welded and recrystallized joints. b) High temperature tensile property of recrystallized joints.

We note that while the joints are produced with unrecrystallized MA956 tubes, the preferred microstructure is intended to be a well recrystallized coarse grain structure. Thus further high temperature test were attempted only on fully recrystallized coupons. Figure 5(b) shows the tensile and failure response of the recrystallized joint at successively increasing temperatures indicating that failure eventually transitions from the matrix to the joint region at about 700°C. All tests are performed at about 10^{-3}sec^{-1} strain rate where diffusion based creep events coupled with the fine grain size in the joint region play an increasingly important role in the joint failure. Looking ahead to the section on creep testing we note that this failure transition temperature is an important threshold for eventual creep performance in the joint segments.

Creep Properties

The geometrical considerations for creep testing of joints are an important issue as illustrated here. The baseline hoop creep data is extracted from 2-1/2”OD tubes that were subsequently

flattened and samples cut in the transverse orientation. However, for the joint sections, transverse samples are not feasible as the processed joint width is considerably narrower than the 0.125" specimen width and any sample cross-section will contain the base material as well. The issue is further exacerbated as the tube joint will need to be flattened to extract the transverse specimen. Thus an alternate strategy of extracting longitudinal specimens ensures the joint section comprises the entire gage cross-section. We like to point out that sample orientation is a particular issue in MA956 tubes on account of the grain shape anisotropy where grains are extended along the longitudinal direction. However, the joint microstructure reveals that the recrystallized grain microstructure in the joint is fairly isotropic, see Figure 2(d), and the particular orientation of the volume of material comprising the joint region during testing is not critical. Thus the joint creep performance can be evaluated in the longitudinal sample geometry where the base material in the gage length is loaded elastically and the bulk of the creep, as surmised from the tensile tests in Figure 5(b) will occur in the small volume of the joint region in the gage length.

Test	Forge upset	HAZ width	Temp	Stress	Creep rate/day	strain	LMP
IW#8	**8.71mm**	**2.5–3.0mm**	**800°C**	**2Ksi**	**4.6×10^{-3}**	**4%**	**42.72**
IW#7	**4.95mm**	**1.0–1.5mm**	**850°C**	**2Ksi**	**4.0×10^{-4}**	**<1%**	**44.50**

Table 1 lists the creep test results for two series (IW#7, IW#8) of inertia welds produced using variations in energy input and forge upset conditions. The corresponding creep performance profile is shown in Figure 6 color coded (red and blue) for the two series of joints. At the outset the results seem to indicate the importance of processing parameters in dictating overall creep response as indicated by observed creep rate and overall Larsen-miller parameter (LMP). Sample IW#8 yielded the best LMP performance at 800°C whereas in sample IW#7 this performance temperature was nudged higher to 850°C. The performance curves indicate a tendency to achieve a threshold temperature where test life can be extended to several thousand hours when though the data presented here is only projected to 1500 hours of test life.

In keeping with the general trend of reducing the joint HAZ width subsequent batches of joints have been produced, via a combination of energy input and forge upset process parameter variables. Results of one such processing strategy are elucidated in Figure 6 (see brown curve) with performance superior to both the IW#7 and IW#8 joints with a peak LMP of 47.71 as measured for a 900°C creep test. The threshold performance has been systematically improved from 700°C (test IW#8) to 775°C (test IW#7) to 850°C. Thus the notion of improving joint creep performance via manipulating the factors that dictate HAZ width has significant merit and has been demonstrated here.

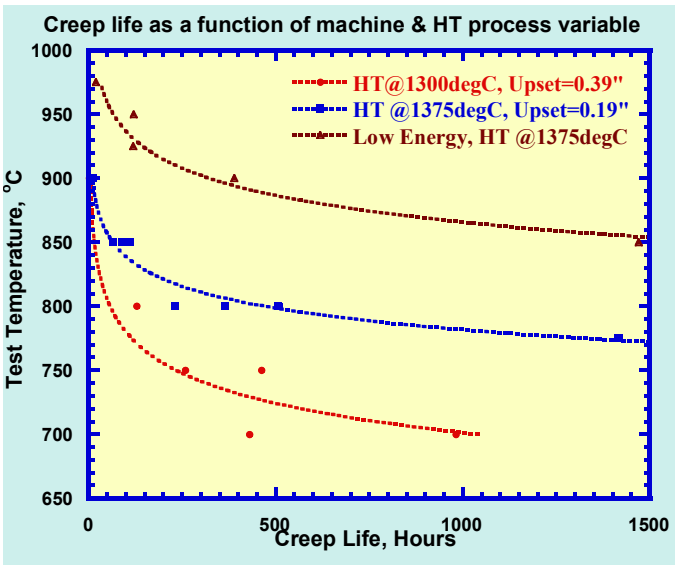

Figure 6. Creep response of inertia-welded MA956 joints.

Summary and Conclusions

Inertia welding of ODS MA956 tubes has been successfully attempted. The butt joint configuration is a viable joint intended for heat exchanger fabrication employing MA956 tubes. Results show that robust joints can be produced over a wide range of processing parameters. However, the process needs to be optimized specifically to improve the overall creep performance of the joint and consequently the fabricated component. Signifcant improvements have been demonstrated via manipulating the process parameters of energy input, forge upset that dictate the thermal excursion in the heat affected zone as well as the overall deformation history in the vicinity of the bonding interface. Our results till date suggest that the scale of the HAZ region has an effect on the ensuing creep performance and efforts to manipulate process parameters to mitigate HAZ width have significant merit for overall creep enhancement of the fabricated joint.

ACKNOWLEDGEMENTS

Electron microscopy studies are conducted in part at the DOE-BES funded SHaRE facility at the Oak Ridge National Laboratory with the assistance of Dr. Ed Kenik and Dr. Neal Evans.

REFERENCES

1 C. Capdevila and H.K. Bhadeshia, 'Manufacturing and Microstructural Evolution of Mechanically Alloyed Oxide Dispersion Strengthened Superalloys', *Advanced Engineering Materials*, 2001, **3**(9), 647.

2. R.F. Singer and E. Arzt, *High Temperature Alloys for Gas Turbine and Other Applications*, D. Reidel Publishing Co., Liege, 1986.

3. F. Starr, 'Emerging Power Technologies and Oxide Scale Spallation', *Mater. High. Temp*., 1995, **13**(4), 185-192.

4 B.A. Pint and I.G. Wright, 'Long Term High Temperature Oxidation Behavior of ODS Ferritics', *Journal of Nuclear Materials*, 2002, **307-311**, 763-768.

5. I.A. Bucklow, S.B. Dunkerton, P.L. Threadgill, 'Investigation into the Joining of Creep Resistant Oxide Dispersion Strengthened Alloys', TWI Members Report 570/1996.

6. C.Y. Kang, T.H. North, D.D. Perovic, 'Microstructural Features of Friction Welded MA956 Material' *Met. Mater. Trans A*, 1996, **27A** (12) 4019–4029.

7. K. Shinozaki, C.Y. Kang, Y.C. Kim, M. Aritoshi, T.H. North, Y. Nakao, 'The Metallurgical and Mechanical Properties of ODS Alloy MA956 Friction Welds' *Welding J. Res. Suppl*. August 1997, 289–299.

8. B.J. Inkson and P.L. Threadgill, 'Friction Welding of FeAl40 Grade 3 ODS Alloy' *Mater. Sci. Eng*. 1998, **A258**, 313–318.

9. T.H. North, Friction Joining of Particle Reinforced Composites. *Proc. 6th Int. Symp*., JWS, Nagoya, 1996, 673-682.

SESSION 2

POSTERS

DEVELOPMENT OF ULTRA-HIGH TEMPERATURE MOLYBDENUM BOROSILICIDES

Joachim H. Schneibel
Oak Ridge National Laboratory, P.O. Box 2008, Oak Ridge, TN 37831-6115
E-mail: schneibeljh@ornl.gov; Telephone: (865) 576-4644; Fax: (865) 574-7659

Jamie J. Kruzic
Oregon State University, 204 Rogers Hall, Corvallis, OR 97331
Email: kruzicj@engr.orst.edu; Telephone: (541) 737-7027; Fax: (541) 737-2600

Robert O. Ritchie
Lawrence Berkeley National Laboratory, 1 Cyclotron Road, Berkeley, CA 94720
Email: roritchie@lbl.gov; Telephone: (510) 486-5798; Fax: (510) 486-4881

ABSTRACT

Mo-Si-B silicides consisting of the phases Mo_ss (Mo solid solution), Mo_3Si, and Mo_5SiB_2 ("T2 phase") exhibit melting points on the order of 2000°C. Because these alloys can exhibit high creep strength, fracture toughness, or oxidation resistance, they have potential as ultra-high temperature structural materials. However, achieving all these properties at the same time is difficult. If the ductility of the Mo_ss can be improved, a smaller volume fraction of the Mo_ss phase is required to achieve the required fracture toughness. Less Mo_ss translates also into improved creep and oxidation resistance. We show that the room temperature fracture toughness of Mo-Si-B alloys is improved by adding small amounts of Zr. Experiments designed to show that this improvement is due to a beneficial effect of Zr on the Mo_ss were so far inconclusive. The room temperature ductility of Mo may also be improved by adding spinel ($MgAl_2O_4$) particles. In a series of Mo-$MgAl_2O_4$ alloys, which all fractured intergranularly, we found that although the $MgAl_2O_4$ did not improve the fracture toughness, it improved the ductility. The ductility increase was attributed to grain refinement. Processing with improved interstitial control changed the fracture behavior to a transgranular mode. At the same time, grain growth occurred much more readily. It remains to be seen whether spinel particles improve the ductility of Mo, if the fracture mode is transgranular. In addition to this basic research, an effort is underway to test a Mo-Si-B alloy in a coal gasifier.

INTRODUCTION

In order to increase the thermodynamic efficiency of Fossil Energy systems, strong, tough and oxidation resistant materials capable of service temperatures well beyond 1000°C are needed. Berczik[1,2] has pioneered alloys consisting of the phases Mo_3Si, Mo_5SiB_2 ("T2-phase"), and a toughening Mo solid solution (Mo_ss). Figure 1 shows the ternary Mo-Si-B phase diagram[3]. The oxidation resistance, creep strength, or room temperature fracture toughness of such Mo-Si-B intermetallic alloys can reach the corresponding values for nickel-base superalloys.[4,5] In particular, the fracture toughness can be significantly improved by using a novel processing technique which makes the Mo_ss phase continuous.[6,7] However, so far these properties have not been achieved in one and the same alloy. Further optimization of the Mo-Si-B system may be possible if the ductility and fracture toughness of the Mo_ss phase is improved. If this can be achieved, less Mo_ss will be needed to reach acceptable values of the fracture toughness. Less Mo_ss also translates into improved oxidation and creep resistance of Mo-Si-B alloys.

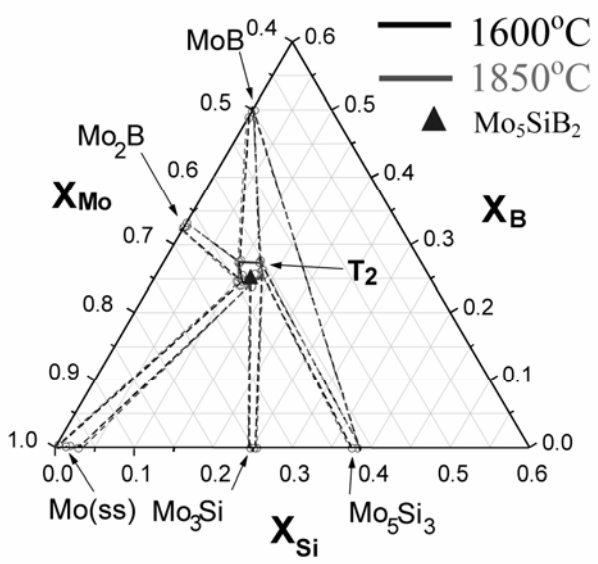

Fig. 1. Ternary Mo-Si-B phase diagram

In this paper, experiments designed to better understand the improvement of the fracture toughness of Mo-Si-B by microalloying with Zr will be described. The room temperature ductility of Mo can also be improved by adding $MgAl_2O_4$ spinel particles. This effect was first demonstrated in 1967 by Scruggs,[8] but has never been independently verified. We show that the ductility increase due to the spinel particles is due to grain refinement. More recent experiments show that improved control of interstitials changes the fracture mode in Mo-$MgAl_2O_4$ from intergranular to transgranular. However, the question whether $MgAl_2O_4$ improves the ductility in the case of transgranular fracture still remains to be answered.

EXPERIMENTAL PROCEDURE

Alloys were prepared by arc-melting elemental starting materials in a partial pressure of argon (70 kPa) on a water-cooled copper hearth. The purity of the starting materials Mo, Si, Zr and B was 99.95, 99.99, 99.5, and 99.5 weight % (wt%), respectively. Alloy compositions are stated in atomic % (at%) unless otherwise noted. The alloys were re-melted several times in order to improve their homogeneity and drop-cast into 12.5 mm or 25 mm diameter rods, or 12.5×6.3 mm rectangular bars. The cast alloys were homogenized by vacuum-annealing for 24 hrs at 1600ºC.

Room temperature fracture toughness values (K_q) were estimated from the controlled fracture of chevron-notched specimens in three-point bending as:

$$K_q = \sqrt{\frac{(W/A)E}{1-\nu^2}}, \qquad (1)$$

where W is the energy required to break the specimen, A is the area traversed by the crack, E is Young´s modulus (329 GPa), and ν is Poisson´s ratio (0.288). The span for the three-point bend testing was 40 mm, and the cross-head speed was 10 μm/s. It should be pointed out that the K_q measurements are not precise fracture toughness measurements; they are used here only to determine trends in the fracture toughness as a function of alloy composition and processing.

Mo-$MgAl_2O_4$ specimens were fabricated from molybdenum (purity 99.95%, particle size 3-7 μm) and $MgAl_2O_4$ spinel powder (-635 mesh size; ≤ 20 μm). Zr was added as Mo_2Zr powder (-325 mesh size; ≤ 45

μm) to strengthen the grain boundaries.[9] Batches of 300 g each of Mo-$MgAl_2O_4$ materials with $MgAl_2O_4$ volume fractions of 0.1, 2.5, and 5% (0.035, 0.89, and 1.81 wt%), and Mo_2Zr and MoB additions resulting in a nominal Mo matrix composition of Mo-0.16Zr-0.09B (at%) were blended for 8 hrs in argon in rotating bottles containing ZrO_2 media. Consolidation was carried out in a graphite hot-press in vacuum (mechanical pump) for 1 hr at 1800°C and 21 MPa. The carbon content of the consolidated Mg-5 vol% $MgAl_2O_4$ material was determined by combustion analysis to be 0.024 at% (0.003 wt%). The oxygen concentration was not measured because it was governed almost exclusively by the volume fraction of the $MgAl_2O_4$ particles.

In a second set of experiments, two 200 g batches of Mo, $MgAl_2O_4$ and Mo_2Zr powders were blended for 8 hrs in argon in rotating bottles containing ZrO_2 media. The nominal compositions were Mo-0.16 at% Zr-0.1 vol% $MgAl_2O_4$ and Mo-0.16 at% Zr-2.5 vol% $MgAl_2O_4$. The powders were filled into Nb cans, which were evacuated and sealed in an electron beam welder. The sealed cans were hot isostatically pressed (HIPed) for 1 h at 1800°C and 210 MPa. Since the can with 2.5 vol.% $MgAl_2O_4$ leaked, only the material containing 0.1 vol.% Mo could be examined.

Metallographic sections and fracture surfaces were examined using optical and scanning electron microscopes. Etching was carried out with Murakami's reagent. Compositions were measured via energy dispersive spectroscopy (EDS) in a scanning electron microscope (SEM), as well as by wave length dispersive spectroscopy (WDS) in a microprobe.

RESULTS AND DISCUSSION

MICROALLOYING WITH Zr

Figure 2 shows that the room temperature fracture toughness K_q of Mo-12Si-8.5B-xZr increases initially with increasing Zr concentration, and then decreases.[10] The microstructure of the alloy with the highest fracture toughness, Mo-12Si-8.5B-1.5Zr is very similar to that without any added Zr (Fig. 3). The Mo solid solution phase images as the brightest constituent, the T2 phase is the darkest and most deeply etched phase, and the Mo_3Si phase tends to be intermediate in its etching behavior and its contrast. The Mo_ss volume fraction is approximately 40 vol%[11] and is expected to be approximately constant regardless of the Zr concentration. In previous EDS measurements[12] the Si concentration of the Mo_ss was determined to be 4.0±0.6 for the alloy without Zr, and 3.1±0.1 at% for the alloy with 1.5 at% Zr. Table 1 shows the results of a more precise WDS determination. It is concluded that Zr reduces the equilibrium concentration of Si only slightly, if any. While the Zr concentration in the Mo_ss of Mo-12Si-8.5B-1.5Zr is 0.4 at%, the Mo_3Si and T2 phases contain larger amounts of Zr, namely, 0.6 and 1.0 at%, respectively. EDS analysis of the fracture surface also showed occasional Mo_2Zr particles.

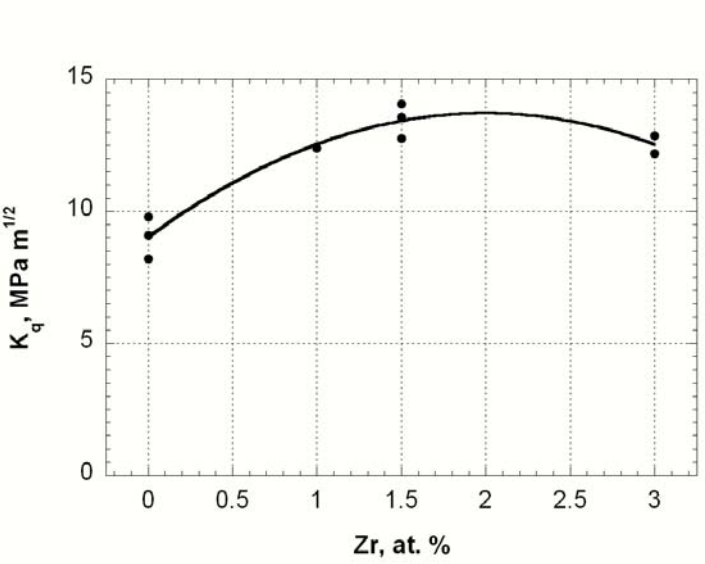

Fig. 2. Room temperature fracture toughness of cast and annealed Mo-12Si-8.5B-xZr.

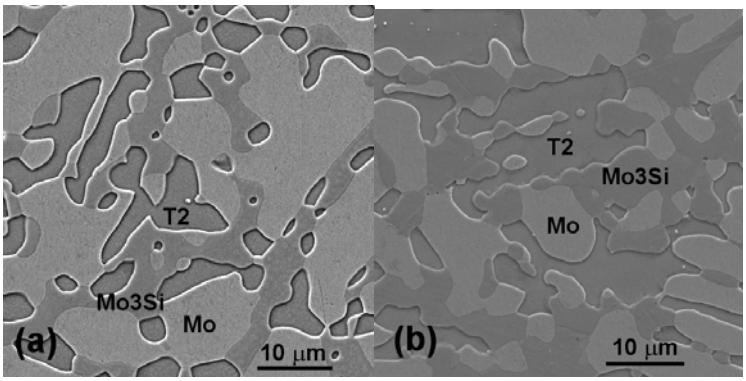

Fig. 3. SEM micrographs of polished and etched (a) Mo-12Si-8.5B and (b) Mo-12Si-8.5B-1.5Zr (at%).

	Mo	Zr	Si
Mo-12Si-8.5B, at%	bal	0	3.03±0.02
Mo-12Si-8.5B-1.5Zr, at%	bal	0.39±0.01	2.86±0.02

Table 1. WDS compositions (at%) of the Mo solid solution phase in Mo-Si-B and Mo-Si-B-Zr. The standard deviations for the Si concentrations were obtained from 5 measurements each.

The Mo_ss in Mo-Si-B contains silicon, and silicon is a potent strengthener of molybdenum. Bruckart *et al.*[13] report that an addition of 1.7 at% Si to Mo increases the room temperature 0.2% yield stress from 509 to 840 MPa. At the same time, the total elongation decreases from 24 to 3%, i.e., Si embrittles Mo. Since it is unlikely that Zr additions improve the fracture toughness of the brittle intermetallics Mo_3Si and Mo_5SiB_2, it is anticipated that the Zr, in some way, improves the ductility or fracture toughness of the Mo_ss in Mo-Si-B. This would also be expected from the work of Miller et al.[9], in which Zr was found to be segregated at the grain boundaries in ductile molybdenum weldments. Unfortunately, the results shown in Fig. 4 do not suggest an improvement of the fracture toughness of Mo-2.5Si by Zr additions.

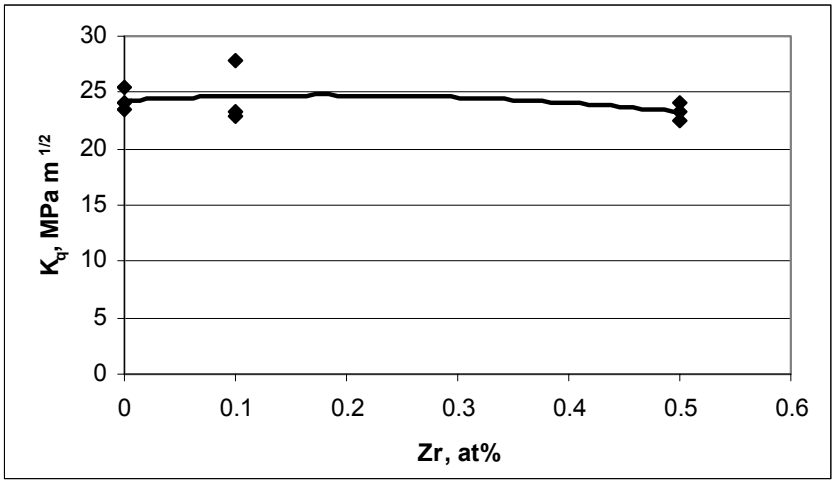

Fig. 4. Fracture toughness of Mo-2.5 at% Si doped with different concentrations of Zr.

The fracture modes in Mo-2.5 at% Si and Mo-2.5 at% Si-0.1 at% Zr were primarily transgranular whereas Mo-2.5Si-0.5Zr showed a mixed fracture mode (Fig. 5). Submicron particles of a second phase were found in the Mo-2.5Si-0.5 at% Zr alloy. Inspection of the ternary Mo-Si-Zr phase diagram[14] coupled with chemical composition measurements in a scanning electron microscope (SEM) showed this phase to be the ternary MoSiZr phase.

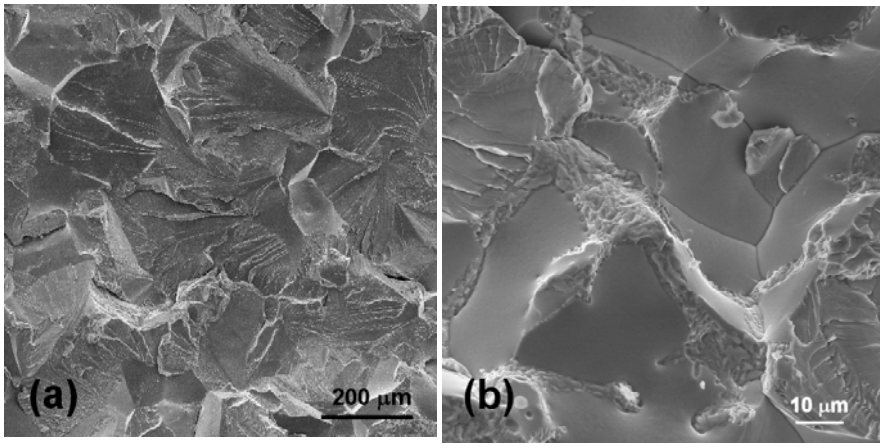

Fig. 5. SEM micrographs of room temperature fracture surfaces of (a) Mo-2.5Si and (b) Mo-2.5Si-0.5Zr (at%). Note the different magnifications of the two micrographs.

It should be pointed out that the relationship between processing, microalloying additions or residual impurities, and the mechanical properties of Mo-Si solid solutions remains a difficult topic. In recent work on powder-metallurgy processed Mo-Si solid solutions, a pronounced drop in the fracture toughness accompanied by a transition to an intergranular fracture mode was reported, as the Si concentration was increased.[15] Because of the transition to intergranular fracture, the measured fracture toughness values in that work are a lower limit to that fracture toughness which would be expected for transgranular fracture. In order to determine the "transgranular" fracture toughness, experiments on Mo-Si alloys with stronger grain boundaries (i.e., by micro-alloying with Zr) would be needed.

DUCTILIZATION WITH SPINEL PARTICLES

In 1967, Scruggs suggested that the room temperature ductility of Mo is improved when $MgAl_2O_4$ spinel particles are added.[8] He suggested that this effect was due to the gettering of detrimental impurities by the $MgAl_2O_4$. Using hot-pressed Mo-$MgAl_2O_4$, we have recently verified Scrugg's ductility enhancement experiments, although our interpretation is different (Fig. 6).[16]

In previous work we estimated the critical local stress intensity factor required to catastrophically propagate an intergranular microcrack forming on the specimen surface.[16] With the assumption that the size of the microcracks scales with the grain size we found that the local stress intensity factor, ~7 MPa $m^{1/2}$, did not depend on the $MgAl_2O_4$ volume fraction. As the $MgAl_2O_4$ volume fraction increased, the grain size decreased and higher stresses were required to unstably propagate a crack. This resulted in higher elongations to fracture. At even higher volume fractions the inherent brittleness of the $MgAl_2O_4$ caused a reduction in the elongation to fracture.

In more recent work, we determined the macroscopic room temperature fracture toughness of Mo-$MgAl_2O_4$.[17] Compact tension specimens were pre-cracked in fatigue and their fracture toughness was subsequently evaluated by loading them to fracture. The fracture toughness was independent of the spinel volume fraction (Table 4). As in our previous work[16] the fracture mode was primarily intergranular, with only 20-30 % of the fracture surface showing transgranular fracture.

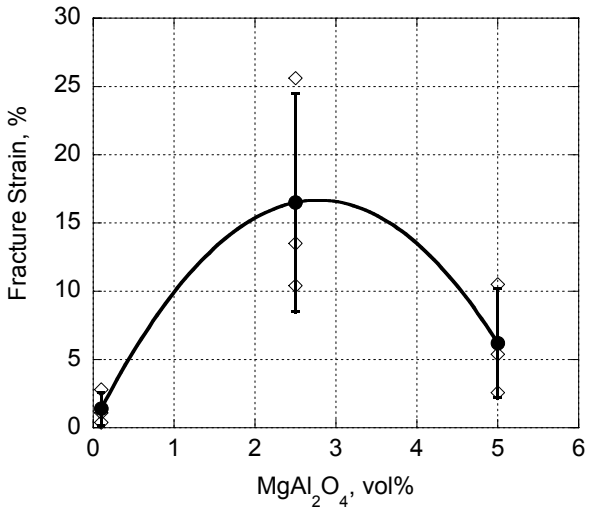

Fig. 6. Room temperature ductility of Mo-$MgAl_2O_4$ as a function of the $MgAl_2O_4$ volume fraction, for a strain rate of 10^{-2} s^{-1}. In addition to the individual data points, average values including error bars with the standard deviation have been plotted.

Table 4. Average fracture toughness values and standard deviations.

Material	Average Fracture Toughness, MPa $m^{1/2}$	Standard Deviation, MPa $m^{1/2}$	σ_{UTS}, M Pa	Grain size, μm
Mo-0.1 vol.% $MgAl_2O_4$	11.5	1.5	523	21.9
Mo-2.5 vol.% $MgAl_2O_4$	11.6	0.8	641	16.9
Mo-5.0 vol.% $MgAl_2O_4$	11.5	0.4	630	13.5

It should be noted that these fracture toughness values are significantly higher than those inferred from the crack lengths and fracture loads in our previous work, which were only on the order of 7 $MPa*m^{1/2}$. Assuming semi-elliptical surface cracks, the critical crack lengths required for catastrophic fracture are estimated from eqn. (2) below, in which σ_{UTS} is the ultimate tensile stress (see Table 4), *a* the crack size on the specimen surface (major axis of ellipsis), *c* the minor axis of the elliptical crack, and F a geometrical factor.[18]

$$K_{Ic} = \sigma_{UTS} \sqrt{\frac{\pi a}{1+1.464(\frac{a}{c})^{1.65}}} F \qquad (2)$$

From eqn. (2) the critical crack sizes were estimated to be between a value of ~200 μm for circular cracks with an aspect ratio equal to 1 to a value of ~800 μm for shallow elliptical cracks with an aspect ratio of 0.1, see Fig. 7. These values are much larger than the grain sizes which range from 13.5 to 21.9 μm. Consistent with this, a detailed examination of the specimen surfaces indicated significant coalescence of surface cracks resulting in cracks much larger than the grain size. It is therefore suggested that during tensile testing sub-critical crack growth initially occurs along many grain boundary facets until the critical crack size necessary for failure is reached. The grain size is important for the ductility in various ways. First, for smaller grain sizes it is believed that the crack initiation process is suppressed until higher loads are reached, allowing larger strains to failure. Second, for a given stress level, the small facet cracks corresponding to small grain sizes experience a relatively low stress intensity factor. Third, a small grain size means that a sub-critically growing crack encounters many more crack deflection sites as compared to a material with a large grain size.

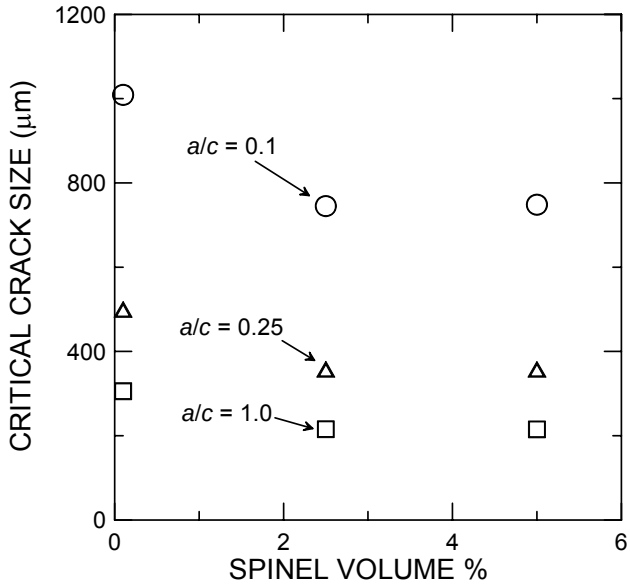

Fig. 7. Calculated critical crack sizes leading to catastrophic fracture of Mo-$MgAl_2O_4$ specimens assuming a crack depth to half surface length ratio (*a*/*c*) between 0.1 and 1 using the semi-elliptical surface crack solution in eqn. (2).

The hot-pressed Mo-$MgAl_2O_4$ material fractures intergranularly, and we interpret the ductility enhancement due to spinel additions as a grain size effect. The question immediately comes to mind whether the ductility is also enhanced if the fracture mode is fully transgranular. Experiments were carried out with Zr-doped Mo-$MgAl_2O_4$ material which was processed by vacuum-encapsulation of powders followed by hot isostatic pressing. The purpose of the encapsulation was to minimize oxidation of the Zr-providing Mo_2Zr powder

(which did oxidize severely in the hot-pressed materials, which contained substantial amounts of ZrO_2). Two alloys containing 0.1 and 2.5 vol.% $MgAl_2O_4$ were processed by HIPing, but the 2.5 vol.% batch did not consolidate due to a leak. Although the Mo-0.1 vol.% $MgAl_2O_4$ alloy contained also ZrO_2 particles, its microstructure was very different from that of the hot-pressed Mo-0.1 vol.% $MgAl_2O_4$. First, its grain size was much larger, see Fig. 8. Second, its fracture mode was transgranular, see Fig. 9. In order to conclusively assess the effect of spinel particles on ductility in the presence of transgranular fracture, the mechanical properties for different $MgAl_2O_4$ volume fractions would have to be compared for similar grain sizes. This means that a verification of the Scruggs effect for the case of transgranular fracture will require additional processing designed to control the grain size.

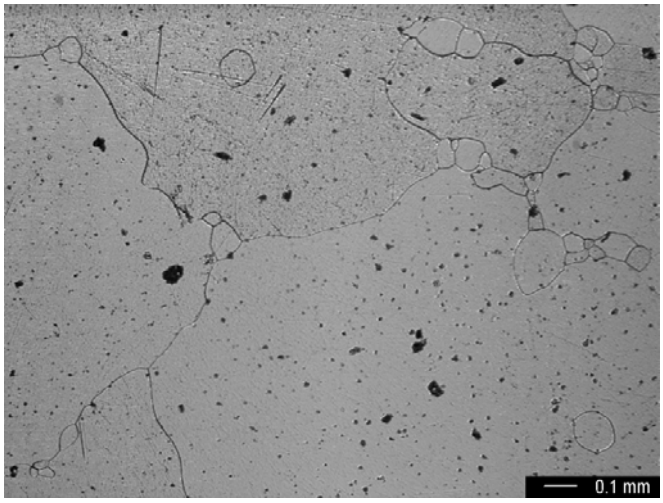

Fig. 8. Optical micrograph of HIPed Mo-0.1 vol.% $MgAl_2O_4$

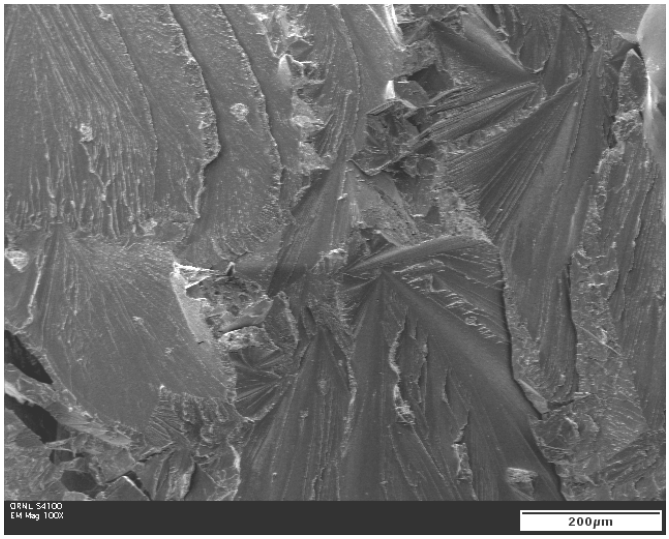

Fig. 9. SEM micrograph of room temperature fracture surface of HIPed Mo-0.1 vol.% $MgAl_2O_4$.

TESTING IN A COAL GASIFICATION REACTOR

D. M. Berczik from Pratt&Whitney kindly provided sintered Mo-Si-B rods with the nominal composition Mo-3 wt% Si-1 wt% B (Mo-8.9Si-7.7B, at%). These rods could be conventionally machined on a lathe. One rod with a diameter of 1" and a length of 6", and one with a diameter of 1.5" and a length of 9.8", were machined. The rods were pre-oxidized by annealing for 1h at 1100°C in air. Figure 10 depicts the pre-oxidized rods.

Fig. 10. Pre-oxidized Mo-3 wt% Si-1 wt% B rods scheduled for testing in the Wilsonville, Alabama, coal gasifier.

Stephen O. Kimble from the Power Systems Development Facility (PSDF) in Wilsonville, Alabama, is planning to test these Mo-Si-B rods in a thermal well application in a coal gasification reactor. Initially, this reactor will be heated to approximately 1000°F (538°C) in an oxygen-rich environment. At this point, coal is injected, and the temperature rises quickly to the operating temperature of 1700-1850°F (927-1010°C). The flux will be approximately 1400 lbs/(ft^2 min) of coal particles traveling at a speed of 50 ft/s. Presently, only one proprietary ceramic thermal well material can withstand these conditions.

As a caveat, it should be pointed out that the Mo-Si-B rods were sintered without any further consolidation and therefore contain porosity. Also, it is not clear whether the volume fraction of intermetallics is large enough to provide adequate erosion resistance. If substantial erosion is encountered, the erosion resistance can be improved substantially by increasing the Si and B concentration, i.e., by increasing the volume fraction of the hard and erosion resistant Mo_3Si and Mo_5SiB_2 intermetallics. Therefore, even if these particular rods do not perform adequately, this does not preclude the Mo-Si-B system for this type of application.

SUMMARY AND CONCLUSIONS

The room temperature fracture toughness of Mo-Si-B is improved by micro-alloying with Zr. Experiments attempting to show that Zr acts by improving the fracture toughness of the Mo_ss in Mo-Si-B have been inconclusive to date. The Scruggs approach for improving the room temperature ductility of Mo by adding $MgAl_2O_4$ spinel particles has been verified. Mo-$MgAl_2O_4$ processed by hot-pressing fractures intergranularly with a fracture toughness which is independent of the $MgAl_2O_4$ volume fraction. The enhanced ductility is interpreted in terms of grain refinement. By controlling interstitial impurities, the fracture mode changed from intergranular to transgranular, but at the same time the grain size increased substantially. A significant processing effort would be required to fabricate a series of Mo-$MgAl_2O_4$ alloys which fracture transgranularly

and have similar grain sizes. An exploratory experiment to assess the performance of a Mo-Si-B alloy in a coal gasifier is underway.

ACKNOWLEDGEMENTS

This work was sponsored by the Office of Fossil Energy, Advanced Research Materials (ARM) Program, U.S. Department of Energy, under contract DE-AC05-00OR22725 with Oak Ridge National Laboratory managed by UT-Battelle, LLC and under contract DE-AC02-05CH11231 with the Lawrence Berkeley National Laboratory. The efforts of D. M. Berczik and S. O. Kimble concerning the assessment of Mo-Si-B in coal gasifier environments is greatly appreciated.

REFERENCES

1. D. M. Berczik, United States Patent 5,595,616 (1997), "Method for enhancing the oxidation resistance of a molybdenum alloy, and a method of making a molybdenum alloy."
2. D. M. Berczik, United States Patent 5,693,156 (1997), "Oxidation resistant molybdenum alloys."
3. C. A. Nunes, R. Sakidja, and J. H. Perepezko, "Structural Intermetallics," 1997, M. V. Nathal et al., eds., TMS, Warrendale, PA, 1997, pp. 831-839.
4. J. H. Schneibel, R. O. Ritchie, J. J. Kruzic, and P. F. Tortorelli, "Optimization of Mo-Si-B intermetallic alloys," Metall. Mater. Trans. A, 36A (2005) 525-531.
5. J. H. Schneibel, "Beyond nickel-base superalloys," Proceedings of "Processing and Fabrication of Advanced Materials XIII (PFAM XIII), M. Gupta, T. S. Srivatsan, C. Y. H. Lin, R. A. Varin, eds., Stallion Press, Singapore, 2005, pp. 563-576.
6. J.H. Schneibel, M.J. Kramer, D.S. Easton, "A Mo-Si-B intermetallic alloy with a continuous α-Mo matrix," Scripta Materialia 46 (2002) pp. 217-221.
7. J. J. Kruzic, J. H. Schneibel, and R. O. Ritchie, "Ambient- to elevated-temperature fracture and fatigue properties of Mo-Si-B alloys: role of microstructure," Metall. Mater. Trans. A, 36A (2005) 2393.
8. D. M. Scruggs, "Ductile molybdenum composition containing a spinel dispersion," United States Patent 3,320,036, Patented May 16, 1967.
9. M. K. Miller and A. J. Bryhan, "Effect of Zr, B and C additions on the ductility of molybdenum," Mater. Sci. Eng. A327 (2002) 80-83.
10. J. H. Schneibel, J. J. Kruzic, and R. O. Ritchie, "Mo-Si-B alloy development," Proceedings 18th Annual Conference on Fossil Energy Materials, R. R. Judkins, I. G. Wright, T. R. Armstrong, and R. R. Romanosky, eds., 2004, url http://www.ornl.gov/sci/fossil/pdf/Proceedings18Fossil04.
11. J. H. Schneibel, M. J. Kramer, Ö. Ünal, and R. N. Wright, "Processing and mechanical properties of a molybdenum silicide with the composition Mo-12Si-8.5B (at.%)," Intermetallics 9 (2001) 25-31.
12. J. H. Schneibel, M. P. Brady, H. M. Meyer III, J. A. Horton, J. J. Kruzic, and R. O. Ritchie, "Mo-Si alloy development," Proceedings 19th Annual Conference on Fossil Energy Materials, R. R. Judkins, I. G. Wright, and R. R. Romanosky, eds., 2005, url http://www.ornl.gov/sci/fossil.
13. W. L. Bruckart, M. H. LaChance, C. M. Craighead, and R. I. Jaffee, "Properties of some hydrogen-sintered, binary molybdenum alloys," Trans. Am. Soc. Metals 45 (1953) 286.
14. P. Villars, A. Prince, and H. Okamoto, Handbook of ternary alloy phase diagrams, ASM International, Materials Park, OH, 1997, vol. 10.
15. D. Sturm, M. Heilmaier, J. H. Schneibel, P. Jehanno, B. Skrotzki, and H. Saage, "The influenceof silicon on the strength and fracture toughness of molybdenum," accepted for publication in Mater. Sci. Eng. A.
16. J. H. Schneibel, M. P. Brady, J. J. Kruzic, and R. O. Ritchie, "On the improvement of the ductility of molybdenum by spinel ($MgAl_2O_4$) particles," Z. Metallkd. 96 (2005) 632-637.
17. I. M. Gunter, J. H. Schneibel, and J. J. Kruzic, "Ductility and fracture toughness of molybdenum with $MgAl_2O_4$ additions," submitted to Metall. Mater. Trans. A.
18. J. C. Newman Jr. and I. S. Raju, in : S. N. Atluri (ed.), "Computational methods in the mechanics of fracture," Elsevier Science, Amsterdam, 1986, pp. 312-334.

DEVELOPMENT OF SILICIDE DIFFUSION COATING ON MULTIPHASE Mo-Si-B ALLOY BY HALIDE-ACTIVATED PACK CEMENTATION

Matthew J. Kramer
225 Wilhelm Hall, Ames Laboratory and Department of Materials Science and Engineering,
Iowa State University, Ames, IA 50011 USA
Email: mjkramer@ameslab.gov; Telephone: (515) 294-0726; Fax: (515) 294-4291

Zhihong Tang and Mufit Akinc
2220 Hoover Hall, Ames Laboratory and Department of Materials Science and Engineering,
Iowa State University, Ames, IA 50011
Email: makinc@iastate.edu; Telephone: (515) 294-0738; Fax: (515) 294-5444

ABSTRACT

Ongoing research into Mo-Si-B alloys has shown that multiphase composites that incorporate the $Mo_5Si_3B_x$ (T1) phase possess excellent oxidation resistance and have a strong likelihood of meeting the oxidation requirement of Vision 21. However, the alloy is inherently brittle since its constitution includes only brittle phases. Moving towards the Mo-rich portion of the Mo-Si-B diagram leads to multiphase composites based on the bcc-Mo phase. These alloys possess dramatically improved fracture toughness, but they degrade rapidly in an oxidizing environment above about 1400°C. Alloy coating strategies are currently being pursued for graded microstructures that take advantage of the superior oxidation resistance of the higher Si-B rich phases combined with the superior mechanical properties of the Mo rich alloys. Two coating techniques are currently being developed. First, thermal spraying has been demonstrated as a viable technique for producing fine-grained, homogeneous samples from complex intermetallics. Secondly, pack cementation is a type of chemical-vapor deposition process carried out under isothermal conditions and typically in a thermodynamically closed system. Oxidation tests at 1600ºC in air for 2 hrs and 100 hrs, respectively, were conducted, and excellent oxidation resistance was observed until the $MoSi_2$ is completely changed into Mo_5Si_3 by inter-diffusion. After the disappearance of $MoSi_2$ layer, the coating can not prevent the oxidation. The coating lifetime was limited by the depletion of silicon into substrate.

INTRODUCTION

Molybdenum borosilicides have been investigated as a candidate material capable of service temperatures much higher than 1100ºC. As shown in the schematic Mo-Si-B phase diagram[1], two alloy systems have been examined to date. Alloys based on the T1 phase ($Mo_5Si_3B_x$), which was pioneered by Dr. Akinc and collaborators[2-6], have excellent oxidation resistance and creep strength. The boron additions are crucible for providing the observed oxidation resistance. However, these alloys also have low fracture toughness, and the thermal expansion anisotropy of the T1 phase make these alloys susceptible to thermal stress induced microcracking[7]. These deficiencies in mechanical behavior can be improved by moving towards the Mo-rich portion of the system. Alloys[8-10] which incorporate the bcc-Mo phase have dramatically improved fracture toughness, but they present a challenge in achieving as oxidation resistance as $Mo_5Si_3B_x$–based alloys. The oxidation resistant phase of these alloys is the T2 phase (Mo_5SiB_2), and its high boron content renders a borosilicate glass with a viscosity much lower than that formed on the T1 phase. This enables excessive volatility of MoO_3 through the scale, contributing to unacceptable metal recession rates above about 1300°C [11, 12]. Other recent works have explored microstructurally designing a bcc-Mo containing composite to balance both oxidation resistance and adequate mechanical behavior[13].

An emerging consensus is to protect the bcc-Mo-based alloys with an oxidation resistant coating such as the T1-based alloy. One technique to produce such a coated component is to plasma spray the T1-based coating onto a bcc-Mo-based substrate. Spraying of the T1-based composition has been investigated recently, and those results indicated that reasonable coating densities can be achieved without excessive loss of Si and B due to evaporation during spray transit time[14, 15]. Another technique for developing an oxidation resistant coating is to deposit a silicon-rich coating onto the surface of the component. The halide activated pack cementation (HAPC) process is a technique which has been successfully deposit $MoSi_2$ onto a two-phase T2/Mo(ss) alloy [16-18]. Although the steady-state oxidation rate of the coated alloy was nearly equal to $MoSi_2$ for up to 50 hours at 1300°-1500°C, the $MoSi_2$ layer partially transformed to the T1 phase, and the long term effect of this microstructural change on oxidation resistance of the coating was not investigated. The present work investigates feasibility of using the HAPC process to form oxidation resistant coatings on the bcc-Mo-based alloys.

EXPERIMENTAL

Alloy preparation

Ternary intermetallic alloys consisting of the phases Mo_3Si, Mo_5SiB_2 (T2) and α-Mo (Mo solid solution) were fabricated by either drop-casting or powder metallurgy (PM). The starting alloys for drop-casted alloys was 99.7 % molybdenum pellets (Alfa AESAR, Ward Hill, MA), 99.99 % silicon lump (Alpha Chemicals, Danvers, MA) and 99.5 % Boron pieces (Alfa AESAR, Ward Hill, MA). The Mo-Si-B alloy was prepared by arc-melting the starting materials on a copper hearth with a tungsten electrode, each sample was typically melted five times to achieve homogeneity.

The powder used in this study was obtained from Exotherm Corp (Camden NJ). An Mo-4.3 wt.%Si-1.1 wt.% B powder was milled and sieved through a 635 mesh screen with a nominal opening of 20μm, and uniaxially dry pressed into a 0.95 diameter pellet using stearic acid as a lubricant. The pellets were heated in Ar in a tube furnace to 1000ºC to remove the stearic acid, and then sintered at 1900ºC for 2 hrs in Ar.

Coating development

The drop-casted and sintered alloys were cut into small coupons and polished with 600-grit SiC paper, then ultrasonically cleaned in acetone and ethanol. The edges were made round in order to minimize the crack formation at these sites. The halide-activated pack cementation process was employed to deposit silicon and/or boron onto the substrate samples. Pack cementation is an *in-situ* chemical vapor deposition (CVD) batch process that has been used to produce corrosion- and wear-resistance coating on inexpensive or otherwise inadequate substrate for over 85 years. These measured and weighed coupons were loaded into Al_2O_3 crucible with powder pack listed in Table 1. The crucible was sealed with an Al_2O_3 lid using an Al_2O_3-based cement. The sealed crucibles were then inserted into a mullite tube in a horizontal tube furnace, and ultra-high purity (UHP) argon was introduced at a flow rate of approximately 80 ml/min. after the inert atmosphere had been established, the packs were heated to either 900ºC or 1000ºC for various time. After pack cementation, the furnace was cooled at 1ºC/min in UHP Ar, and the coupons removed from the pack, washed in hot water and ultrasonically cleaned in acetone to remove any salt condensate or loosely embedded pack powder. Pack-cemented samples were annealed in Ar atmosphere at 1600ºC for 24hrs to examine the thermal stability of the coating.

Characterization

HAPC coated substrates were examined by X-ray diffraction (XRD, Scintag XDS 2000, Cupertino, CA) to identify the phases formed, and both the surface and cross-section were examined by scanning electron microscopy using backscattered electron imaging (SEM/BSE, JEOL, JSM 6100, Peabody, MA) with energy dispersive spectroscopy (EDS, Oxford Instruments, Valley, CA).

Table 1. Composition of powder mixture (wt.%) and processing conditions

No.	Pack mixture			Temperature	Time
	Master alloy	Activator	Filler		
1	10% Si	2% NaF	Al_2O_3	900-1000ºC	16-100hrs
2	10% B	2% NaF	Al_2O_3	900-1000ºC	24-100hrs
3	9%Si, 1%B	2% NaF	Al_2O_3	900-1000ºC	48-100hrs
4	10%Si, 2%B	2% NaF	Al_2O_3	900-1000ºC	48-100hrs
5	5%Si, 5%B	2% NaF	Al_2O_3	900-1000ºC	48-100hrs
6	10%Si, 0.5%B	2% NaF	Al_2O_3	900-1000ºC	48-100hrs

RESULTS AND DISCUSSION

Characterization of siliconzing coating

Fig.1.a shows the cross-section of the coating on alloy 1 (Mo-4.3wt%Si-1.1wt.%B) coupon formed by pack cemented in a Si pack (#1). A uniform coating layer with a thickness of about 40 μm formed on the substrate. EDS and XRD analysis confirmed that the coating was $MoSi_2$ with $C11_b$ structure. Neither Mo_5Si_3 nor Mo_3Si, T2 (Mo_5SiB_2) phases were detected between the $MoSi_2$ layer and the substrate. This observation is well agreement with the studies of Mo/Si diffusion couple [19]: the apparent growth rate of Mo_5Si_3 and Mo_3Si are slower than that of $MoSi_2$ by about two or three orders of magnitude at 1000ºC.

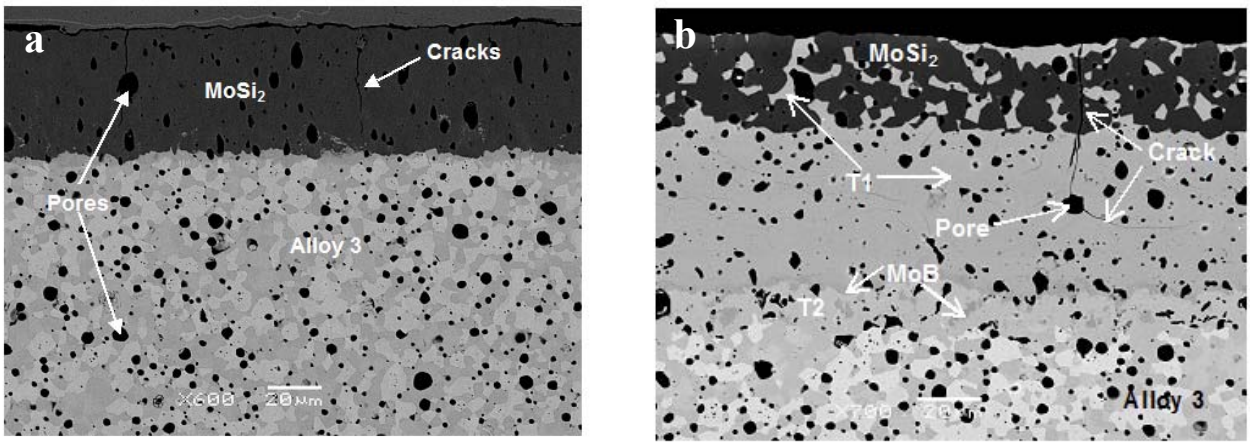

Figure 1. Cross-sectional micrographs of sintered Mo-4.3Si-1.1B alloy pack cemented in Si pack: a). as-packed; b). after oxidized at 1600ºC for 2 hours in air

The thickness of $MoSi_2$ was measured with SEM observation. At least 10 measurements were taken for $MoSi_2$ layer and the average thickness was determined for the data analysis. It was found that the growth of $MoSi_2$ layer was parabolic with deposition time. The rate constant was determined to be $8\times10^{-11}cm^2/s$ at 1000ºC, which is comparable with intrinsic parabolic growth rate constant of $MoSi_2$ layer using Si/Mo diffusion couple (3.91×10^{-10} cm^2/s)[19]. According to studies by Salamon etc.[20], the self-diffusion of molybdenum in $MoSi_2$ is slower than silicon by several orders of magnitude. This suggests that inward-diffusion of silicon is the rate controlling step.

Microcracks perpendicular to the substrate was observed in the $MoSi_2$ layer due to due to thermal expansion coefficients mismatch between $MoSi_2$ and substrate phases such as Mo, Mo_3Si and Mo_5SiB_2 during cooling from the deposition temperature to room temperature. $MoSi_2$ is essentially brittle below

its ductile-to-brittle transition temperature of approximately 1000ºC. The stresses caused by CTE mismatch can produce micrcracks in the coating if they exceed the strength of the $MoSi_2$. Since the tensile strength of $MoSi_2$ is much lower than its compressive strength (275 Mpa vs. more than 1378 Mpa)[21], tensile stresses are particularly damaging and will promote transverse microcracking in the coating, which is the case of current pack siliconizing coating.

After pack siliconizing on Mo-4.3Si-1.1B, metastable equilibrium is established at the $MoSi_2$/substrate. However, the interdiffusion between coating and substrate results in silicon depletion from the coating by the formation of Mo_5Si_3 layer upon exposure to high temperature. Fig.1.b shows the microstructure of pack siliconzing coating oxidized at 1600ºC for 2 hours in air. The $MoSi_2$ layer was partially transformed into Mo_5Si_3 phase. And two intermediate layers were observed between the $MoSi_2$ layer and the Mo-4.3Si-1.1B substrate. The first is a 50μm thick layer of Mo_5Si_3 single phase, in which parallel microcracks were observed due to the anisotropy in the thermal expansion coefficient of tetragonal Mo_5Si_3 phase. The second layer with 10μm thickness consists of mostly T2 with dispersed MoB particles. The borides (T2 and MoB) have formed by segregation of B atoms, which were expelled from newly formed T1 phase, to Mo(ss) and Mo_3Si in the three-phases matrix.

Co-deposition of silicon and boron

Fig.2.a shows the cross-sectional micrograph of the B-modified silicide coating on sintered Mo-4.3Si-1.1B formed by a pack mixture with Si/B=9 (#3). The deposited coating consists of three layers: an 20μm thick outer $MoSi_2$ layer; an 30μm thick intermediate $MoSi_2$ layer with MoB particles; and a 10μm thick inner T2/MoB mixed layer. The MoB phases was confirmed by XRD analysis on the coating after carefully gradually grinding to remove 30μm thick $MoSi_2$ layer. Therefore, MoB phase was successfully added into $MoSi_2$ layer by partial substituting Si with B in the pack mixture. And also a T2/MoB mixed boride layer can be formed underneath the silicide coating. In contrast, with only the Si-pack (#1), no any boride phase in the $MoSi_2$ coating or T2/MoB interlayer was detected.

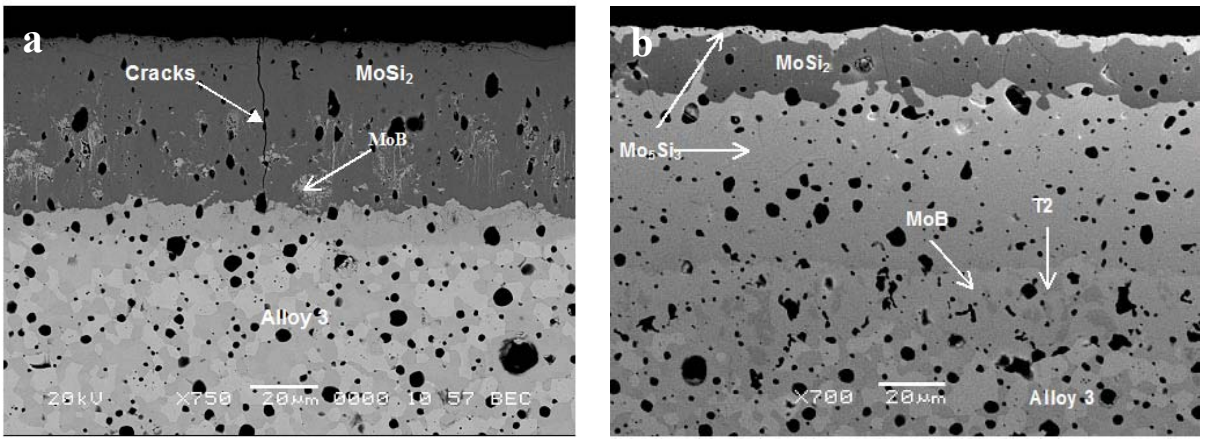

Figure 2. Cross-sectional micrographs of sintered Mo-4.3Si-1.1B alloy pack cemented in a pack mixture of Si:B:NaF:Al_2O_3=9:1:2:88 : a) as-packed; b) oxidized at 1600ºC for 2 hours in air

Fig.3 shows that boronsilicozing coating on drop-casted Mo-4.3Si-1.1B by pack cementation in the pack mixture with various B/Si ratios (#3-5). With the increased B/Si ratio in the pack mixture, the concentration of MoB phase in the $MoSi_2$ layer increases and T2/MoB mixed layer expanded to the coating surface. B-rich phase such as Mo_2B_5 begins to appear, for example the coupon buried in pack #5, the XRD analysis of coating confirmed the existence Mo_2B_5 phase. It should be noted that pores was

formed in the in the boride phases in the coating and the porosity increases with the increasing B/Si ratio in the pack.

Comparing the boronsiliconizing coating on both sintered and drop-casted Mo-4.3Si-1.1B alloy by pack cementation (Fig. 2a and Fig. 3a), the coating on the sintered alloy possesses a better surface quality and fewer microcracking in the coating due to fine and uniform structure. In drop-casted sample, more microcracks was induced because of dendrite structure of Mo, which is not completely broken even annealed at 1600ºC for 24 hours.

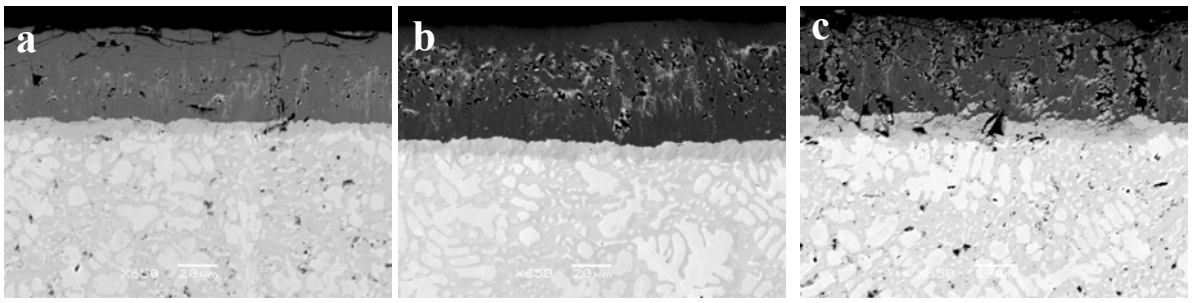

Figure 3 Cross-sectional micrographs of casted Mo-4.3Si-1.1B alloy pack cemented in pack mixture with Si/B ratio of: a). 9/1; b). 5/1; c). 1/1

Although MoB phase can be thermodynamically stable with $MoSi_2$ and Mo_5Si_3 phases as indicated in phase diagram, the MoB phase do not stabilize with $MoSi_2$ in the $MoSi_2$ layer after high temperature exposure. Figure 2.b shows back-scattered electron (BSE) images of co-deposited alloy after oxidized at 1600ºC for 2 hours in air. Two layers are formed in the diffusion zone between $MoSi_2$ and substrate: a 40µm thick layer of the single Mo_5Si_3 phase and a 20µm thick two-phase layer consisting of MoB and T2 phase. The boride phases was no longer exists with $MoSi_2$ layer, and no boride phase was identified in Mo_5Si_3 single-phase layer. This suggested that boride phase (MoB and/or Mo_2B_5) in the coating was transformed into Mo_5Si_3 as Si diffuses inward and expelled surplus B. The expelled B must have segregated to the three-phase substrate to form boride at the expense of Mo and Mo_3Si since B has a limited solubility in Mo_5Si_3 and $MoSi_2$ phase.

Two-step boronizing and siliconizing coating

Fig.4 shows the cross-sectional micrographs of drop-casted Mo-4.3Si-1.1B alloy pack boronizing in a B pack. Comparing with siliconizing, the growth rate of boride layer is a little faster than that of $MoSi_2$ in pack siliconzing. A complex two-layer diffusion microstructure was developed: a ~10µm thick outer Mo_2B_5 layer with dispersed MoB particles, which are identified by XRD and EDS analysis; an ~30µm thick inner T2 and MoB mixed layer, in which T2 and MoB formed a network structure. Fine T2 particles were found in Mo_3Si_3 phase adjacent to the interface between T2/MoB layer and substrate. Some dark phases was found in the T2 phase in the T2 and MoB mixed layer and identified as $MoSi_2$ by EDS analysis. The formation of $MoSi_2$ could occur that silicide must have been formed to balance the silicon if B reacts with Mo_3Si to form Mo_5SiB_2.

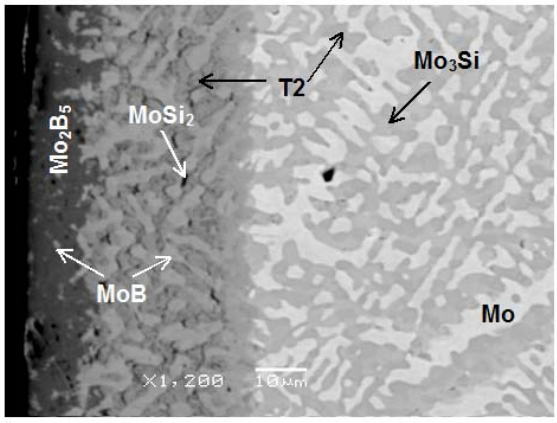

Figure 4. Cross-sectional micrographs of casted Mo-4.3Si-1.1B alloy pack cemented in a B pack (#2)

Fig.5.a shows the cross-sectional microstructure of as-prepared and annealed two-step coating (B+Si). After two step pack cementation (boronizing and siliconizing), Mo_2B_5 top layer formed by boronizing is totally converted into $MoSi_2$ and a ~12μm thick $MoSi_2$ layer was formed on the top. A 40μm thick borides (T2/MoB) intermediate layer was formed between $MoSi_2$ and substrate. The thickness of boride layer is similar with that of B-packed alloy 3 (Fig. 4). This suggested that B atom expelled when Mo_2B_5/MoB transformed into $MoSi_2$ phases diffuse inward to the interface between coating and substrate since solubility of boron in $MoSi_2$ is negligible.

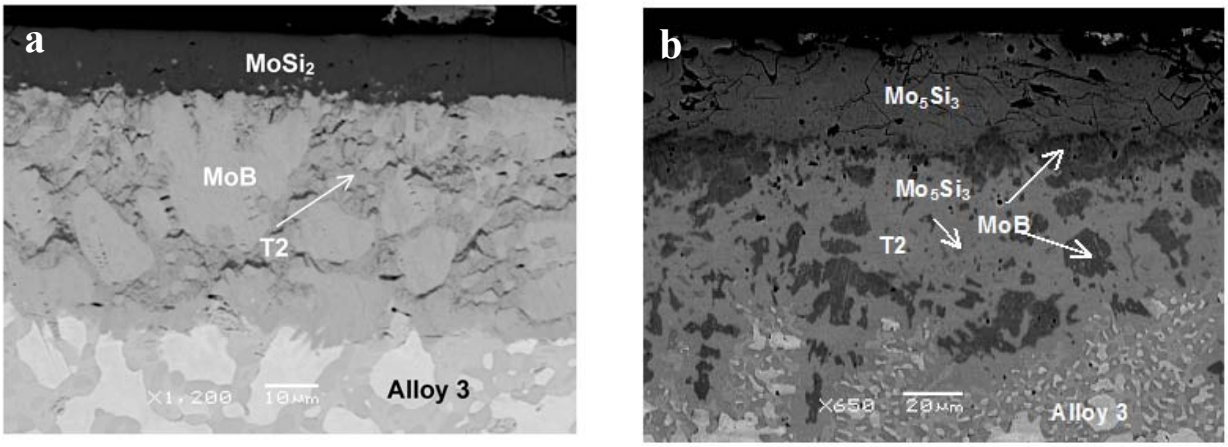

Figure 5. Cross-sectional micrographs of casted Mo-4.3Si-1.1B alloy by boronizing in a B pack and followed by siliconizing in a Si pack: a). as packed coating; b). annealed at 1400ºC for 24 hours

After 1400ºC annealing for 24 hours, the $MoSi_2$ phase is completely transformed into Mo_5Si_3, and a T2/MoB interlayer is underneath the Mo_5Si_3. Unlike the as-packed coating in which the T2/MoB interlayer consists of MoB matrix with interconnected T2 phase, the interlayer in the annealed coating consists of T2 matrix with isolated MoB agglomerates. Since the sluggish diffusion rate of Si in the T2 phases, the growth of T2 phase is much slow comparing with the growth rate of Mo_5Si_3 layer. Some Mo_5Si_3 particles were observed in the T2 phases, and they may result from the silicon-rich phase in the T2 phases in the as-packed coating.

Evalution of siliconizing and boron-siliconizing coating by pack cementation

The excellent high temperature strength and oxidation resistance of $MoSi_2$ qualify it for such application as protective coating for bcc-Mo-based alloys. The $MoSi_2$ coating was successfully deposited on Mo-4.3%Si-1.1%B (wt.) alloy with three phases (Mo+Mo_5SiB_2+Mo_3Si) by pack cementation as shown above, and boride phase can be added into the coating by partially substituting B with Si in pack mixture. Similar works were done by Ito etc. on Mo-9Si-18B (at.%) alloy and Sakidja etc. on Mo-14.2Si-9.6B at.%. However, two problems limited the application of silicide coating on Mo-based alloy by pack cementation: 1). thermal stresses generated by CTE mismatch at the coating-substrate or coating-oxide interface, also by the large CTE anisotropy of Mo_5Si_3 along the c-axis and a-axis, as shown in table 2; 2). the rapid coating/substrate inter-diffusion through the growth of a B containing Mo_5Si_3 interlayer.

Table 2 CTE of various phases in Mo-Si-B system

Materials	α_a (10^{-6} /K)	α_c (10^{-6} /K)	α_c/α_a
Mo_5SiB_2	7.72	7.20	0.93
Mo_3Si	7.17	-	-
Mo	6.5	-	-
$MoSi_2$	7.99	9.69	1.24
MoB	8.38	6.38	1.21

Thermal stress

$MoSi_2$ is essentially below its ductile-to-brittle transition temperature of approximately 1000ºC. Stress caused by the CTE mismatch between $MoSi_2$ coating and the substrate can produce cracks in the coating if they exceed the strength of $MoSi_2$ as shown Fig. 1a and Fig. 2a, in which the perpendicular microcracking was formed in as-packed $MoSi_2$ coating. In addition, the large CTE anisotropy of Mo_5Si_3 along the c-axis and a-axis can induce microcracking, as shown in Fig. 1b and Fig. 2b, in which the parallel microcracking was developed in Mo_5Si_3 single layer after 2hrs oxidation at 1600ºC. The microcracks can lead to accelerated coating degradation during oxidation. Theoretically, the thermal stress caused by CTE mismatch can be reduced by incorporating either low expansion second phases into the coating or alloying element to strengthen $MoSi_2$ coating. For example, tungsten-alloyed coating exhibited 30% lower crack density relative to coating without tungsten. However, in practice, the selection and processing of incorporating elements will be critical in order to be compatible with the Mo-Si-B system. Another method is to introduce an interlayer with a value of CTE between the $MoSi_2$ coating and substrate. In present study, the cracks density obviously decreased by introducing a T2/MoB interlayer between $MoSi_2$ and substrate (Fig. 5a).

Thermodynamic stability

Thermodynamic stability between coating and substrate is a major concern at high temperature application. As shown above, inter-diffusion results in silicon depletion from the coating by the formation of Mo_5Si_3 interlayer. Although the growth rate of Mo_5Si_3 interlayer was not determined experimentally, it was pretty rapid at 1600ºC since a 40μm $MoSi_2$ layer was completely transformed into Mo_5Si_3 phase after 10 hours exposure in air. As noted above, surplus B atoms must have been produced when multi-phase alloy ($Mo+Mo_5SiB_2+Mo_3Si$) transformed into Mo_5Si_3 phase, in which B solubility is only about 2 at.% at 1800ºC. Boron atoms was segregated to interface between coating and substrate to form boride at the expense of Mo and Mo_3Si. As a result $MoSi_2$/ Mo_5Si_3-B/T2+MoB/substrate layered structure was observed following the diffusion path as indicated in Fig. 2. Thus coating lifetime depends on the oxidation resistance properties of Mo_5Si_3-B after $MoSi_2$ disappear.

The oxidation behavior of Mo_5Si_3-based mateirals is strongly dependant on the amount of boron. Meyer etc. [6] studied the isothermal oxidation behavior of several B-Mo_5Si_3 alloys around Mo_5Si_3 phase field at 1450ºC and concluded that a minimum boron content somewhere between 0.85 at.% and 5.45 at.% required in order for a passivating scale form on Mo_5Si_3-based materials. It is difficult techniquely to determine that how much boron was dissolved in the T1 phase layer since the B solubility in T1 phase is about 2 at.% at 1800ºC, and the microcracks in the coating make it difficult to determine which factor is responsible for the high temperature degradation of the coating oxidized at 1600ºC for 100 hours in air: either microcracks or poor oxidation resistance of B- Mo_5Si_3 phase layer. However, it is obvious that the coating lifetime can be prolonged if some boride phase, either MoB or Mo_5SiB_2 phase, can be stabilized in the Mo_5Si_3 phase somehow. Another method is to add another silica glass former, for example Ge, into $MoSi_2$ coating. Coating lifetime can be increased since Ge have a large solubility in both $MoSi_2$ and Mo_5Si_3 phase unlike B.

SUMMARY

In the pack siliconizing coating, a $MoSi_2$ layer was developed on the three phases substrate ($Mo+Mo_3Si+Mo_5SiB_2$). After annealing or exposure to air at high temperature, $MoSi_2$ was transformed to silicon-deplete silicide, a diffusion microstructure with $MoSi_2$/Mo_5Si_3/T2+MoB particles/($Mo+Mo_3Si+Mo_5SiB_2$) substrate. And this microstructure does not provide any oxidation resistance after $MoSi_2$ top layer is disappeared.

In the pack boronsiliconizing coating (co-deposition of Si and B by pack cementation), boride phases (MoB and/or Mo_2B_5) was successfully added into $MoSi_2$ coating and the concentrations of borides phase

can be controlled by changing the Si/B ratio in the pack mixture. However, those boride phases can not be stabilized with $MoSi_2$ or Mo_5Si_3 after exposure to high temperature. MoB phase was consumed by the formation of Mo_5Si_3 as silicon diffuses downward and the released boron diffuse downward into substrate to form new borides because of the limited solubility of boron atom in Mo_5Si_3. As a result, a diffusion microstructure with $MoSi_2/Mo_5Si_3$/T2+MoB partiles/($Mo+Mo_3Si+Mo_5SiB_2$) substrate, which is similar with that for siliconizing coating, was developed.

ACKNOWLEDGEMENTS

This report was prepared with the support of the U.S. Department of Energy (DOE) National Energy Technology Laboratory under Field Work Proposal number AL-00-360-011. Ames Laboratory is operated for the U.S. Department of Energy by Iowa State University under contract number W-7405-ENG-82.

REFERENCES

1. H. Nowotny, E. Dimakopoulou, H. Kudielka, Monatshefte fuer Chemie 88 (1957) 180-192.
2. M. K. Meyer, M. Akinc, United States 5865909 (1999), "Boron-modified molybdenum silicide for sintered articles resistant to creep and oxidation".
3. M. K. Meyer, M. Akinc, M. J. Kramer, Advanced Ceramics for Structural and Tribological Applications, Proceedings of the International Symposium on Advanced Ceramics for Structural and Tribological Applications, Vancouver, B. C., Aug. 20-24, 1995 (1995) 637-645.
4. M. Meyer, M. Kramer, M. Akinc, Advanced Materials (Weinheim, Germany) 8 (1996) 85-88.
5. M. Akinc, M. K. Meyer, M. J. Kramer, A. J. Thom, J. J. Huebsch, B. Cook, Materials Science & Engineering, A: Structural Materials: Properties, Microstructure and Processing A261 (1999) 16-23.
6. M. K. Meyer, M. Akinc, Journal of the American Ceramic Society 79 (1996) 2763-2766.
7. H. L. Zhao, M. J. Kramer, M. Akinc, Intermetallics 12 (2004) 493-498.
8. D. M. Berczik, United States 9622402 (1996), "Oxidation-resistant molybdenum alloys and composites with boron and silicon for dispersed phases".
9. D. M. Berczik, United States 5693156 (1997), "Molybdenum alloys with silicon and boron for oxidation resistance".
10. J. H. Schneibel, Intermetallics 11 (2003) 625-632.
11. M. G. Mendiratta, T. A. Parthasarathy, D. M. Dimiduk, Intermetallics 10 (2002) 225-232.
12. T. A. Parthasarathy, M. G. Mendiratta, D. M. Dimiduk, Acta Materialia 50 (2002) 1857-1868.
13. J. H. Schneibel, J. J. Kruzic, R. O. Ritchie, in: Proceeding of the 17th Annual Conference on Fossil Energy Materials, "http://www.netl.doe.gov/publications/proceddings/03/materials/", 2003.
14. M. J. Kramer, S. C. Okumus, M. F. Besser, O. Unal, M. Akinc, Journal of Thermal Spray Technology 9 (2000) 90-94.
15. T. C. Totemeier, R. N. Wright, W. D. Swank, Intermetallics 12 (2004) 1335-1344.
16. K. Ito, T. Murakami, K. Adachi, M. Yamaguchi, Intermetallics 11 (2003) 763-772.
17. K. Ito, T. Hayashi, M. Yokobayashi, H. Numakura, Intermetallics 12 (2004) 407-415.
18. K. Ito, T. Hayashi, M. Yokobayashi, T. Murakami, H. Numakura, Metallurgical and Materials Transactions A: Physical Metallurgy and Materials Science 36A (2005) 627-636.
19. J.-K. Yoon, J.-Y. Byun, G.-H. Kim, J.-S. Kim, C.-S. Choi, Thin solid films 405 (2002) 170-178.
20. M. Salamon, A. Strohm, T. Voss, W. Frank, J. Raisanen, H. Mehere, Philosphical Magazine 84 (2004) 737-756.
21. T. A. Kircher, E. L. Courtright, Materials Science & Engineering, A: Structural Materials: Properties, Microstructure and Processing 155 (1992) 67-74.

EFFECTS OF TUNGSTEN ON THE MICROSTRUCTURES OF TiAl-BASED INTERMETALLICS

L. Huang, P. K. Liaw, and C. T. Liu
Dept. of Materials Science & Engineering,
University of Tennessee, Knoxville, TN, 37996

ABSTRACT

The effects of tungsten on the microstructure of the TiAl-based alloys, including the colony size and lamellar spacing, were studied in this investigation. A small additional amount of W can refine the grain size of the Ti-Al-Nb-W-B alloys. The lamellar spacing decreases with increasing the W concentration. But as the amount of W exceeds 0.4 atomic percent (at.%), its beneficial effect becomes small. When the amount of W is greater than 0.4 at.%, the β phase is stabilized and remains at room temperature. A refined grain-sized TiAl-based alloy can be obtained through merely the alloy design. Mechanical testing, such as hardness experiments, has been conducted on the alloys. The addition of the alloying element, tungsten, increases the hardness of TiAl alloys by the solution strengthening and refinement of grain sizes. The present research is sponsored by the Fossil Energy Materials Program, with Dr. R. Judkins and Dr. J. Zollar as program managers, under the contact number of 11X-SP173V, and the National Science Foundation Combined Research-Curriculum Development (CRCD) Program, with Ms. Mary Poats as the contract monitor, under the contract number of EEC-0203415.

Keywords: TiAl intermetallics; microalloying; microstructures

INTRODUCTION

The mechanical properties of the TiAl-based alloys with lamellar structures depend on three factors: the colony size, interlamellar spacing, and alloying addition. The tensile elongation at room temperature is strongly dependent on the lamellar colony size, showing the increased ductility with decreasing the colony size. The strength at room and elevated temperatures is sensitive to the interlamellar spacing, exhibiting the increased strength with decreasing the interlamellar spacing [1,2].

The as-cast TiAl-based alloys are usually coarse in the grain size. A refinement in the microstructures is necessary to meet the desirable applications. Additional elements, such as W and B, added into the base alloy can help refine the grain size [3-8]. Related heat treatments can facilitate the development of the desirable microstructures. In general, the duplex structure (DP) tends to have a good room-temperature tensile ductility, but its fracture toughness is low. The fully lamellar (FL) structure has a better overall property than the other microstructures. But it has a low tensile ductility at room temperature. However, by both refining the colony size and the lamellar spacing through the cyclic heat treatment [9],

thermo-mechanical treatment [10], and alloying [11], the fine fully lamellar (FFL) microstructure can have both good ductilities and fracture strengths.

In this study, a refinement in the colony size of the TiAl-based alloy has been obtained by alloying and heat treatments, without additional thermomechanical processes and cyclic heat treatments. Note that thermal mechanical processes are expensive to be conducted. An investigation regarding the effects of the tungsten addition on the phase formation, the microstructural features, and the stability of both lamellar structure and β phase has been performed. Mechanical testing, such as the hardness tests, has been conducted. The relationship among the tungsten addition, microstructure, and the hardness of the material, has been studied.

EXPERIMENTAL PRODEDURES

In this investigation, the compositions of the TiAl-based samples fabricated at the Oak Ridge National Laboratory (ORNL) are as follows:
Ti-45at.% (atomic percent, at.%) Al-7at.%Nb-0.15at.%B
Ti-45at.%Al-7at.%Nb-0.2at.%W-0.15at.%B
Ti-45at.%Al-7at.%Nb-0.4at.%W-0.15at.%B
Ti-45at.%Al-7at.%Nb-0.7at.%W-0.15at.%B
All alloys were prepared by arc melting and drop casting, using pure Ti, Al, W, and Nb metal lumps together with the semiconductor-grade boron. Alloy buttons were melted at least 5 times, and, then, drop cast into a water-cooled copper mold with an ingot size of 12.7 × 12.7 × 76.2 mm^3. The TiAl-based alloys were hot-isostatic pressed (HIPed) at 1,250^{0}C, for 4 h at a pressure of 150 MPa.

Specimens were prepared for the optical microscopy by conventional grinding and polishing, using a 0.5 μm diamond paste, followed by etching with the Kroll solution, 1%HNO_3 + 1%HF + 98%H_2O (volume percent, vol.%). The scanning-electron microscopy (SEM) is used for more detailed analyses of the microstructures. For the backscattered-electron detection, specimens do not need any etching. For more detailed structure and composition analyses, a field-emission-scanning microscope, Sirion200 (20 KV), was used. In order to study the lamellar structure of the TiAl alloys, transmission-electron microscopy (TEM) analyses were performed. Specimens are spark eroded into slices with a diameter of 3 mm, and a thickness of 0.3 mm, then mechanically thinned into 35 - 45 μm. Foils for TEM are prepared with a twin jet electropolishing, using a solution of a 30% nitric acid plus 70% methanol (volume percent), operating at -20^{0}C, 100 mA, and 30 V. Hitachi H-800 TEM (200 KV) is used for the TEM analyses.

RESULTS

1. As-cast microstructures

Figure 1 shows the as-cast microstructures of TiAl alloys. The microstructures mainly consist of dendrites. As it is in backscattered electron mode, the bright phases indicate an enrichment in large-numbered atoms, such as Nb and W. It is clearly seen that W and Nb are enriched at the cellular boundaries and the peripheries of the dendrites. Comparing the Figs. 1(a), (b), (c), and (d), as the amount of W differs, the microstructure of the as-cast alloys varies. In Fig. 1(a), where no W was added, the cellular interfaces of the alloy are bright, indicating that there is a strong segregation of Nb at the grain boundaries. After the addition of W, the interface of the cellular structures became even brighter. Since the composition of Nb is kept constant, it indicates that W tends to segregate in the interface of the dendrites.

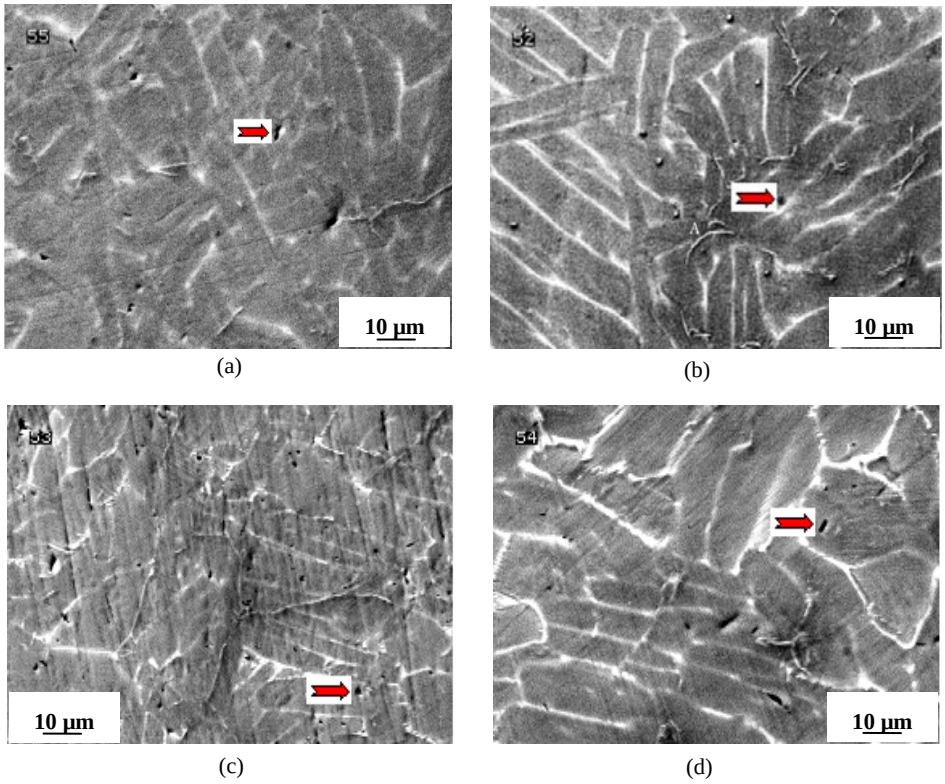

(a) (b) (c) (d)

Figure 1 Backscattered images of the as-cast Ti-Al-Nb-W-B alloys (The arrows show the porosities. Point A in (b) indicates the ribbon-shaped Ti-B boride phase.) (a) Ti-45Al-7Nb-0.15B, (b) Ti-45Al-7Nb-0.15B-0.2W, (c) Ti-45Al-7Nb -0.15B-0.4W, and (d) Ti-45Al-7Nb-0.15B-0.7W

2. Microstructures after HIPing and homogenization

After the Ti-Al-Nb-W-B alloys were HIPed, porosities in the as-cast material were eliminated. Furthermore, the alloy composition can be homogenized through the atomic diffusion. Comparing Figs. 1 and 2, before and after the HIPing and homogenization, respectively, the microstructures of the Ti-Al-Nb-W-B alloys have changed greatly. The lamellar structure after the treatments is more continuous, and the colony size of the lamellae refines.

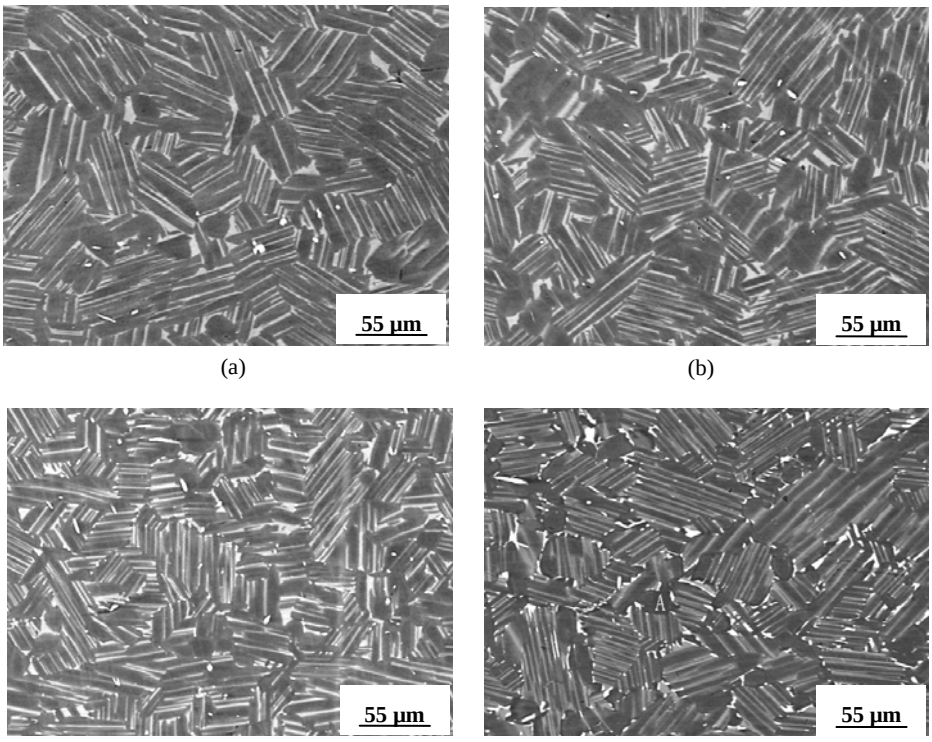

Figure 2 Backscattered images of the Ti-Al-Nb-W-B alloys after the HIPing and homogenization (Point A in (d) shows the γ phase), (a) Ti-45Al-7Nb-0.15B, (b) Ti-45Al-7Nb-0.15B-0.2W, (c) Ti-45Al-7Nb-0.15B-0.4W, and (d) Ti-45Al-7Nb-0.15B-0.7W

More accurate analyses in the structure have been conducted. Figure 3 shows the microstructure of the TiAl alloy containing 0.7 at.% W. Electron-microprobe analyses (EMPA) were conducted. The bright needle-shaped phase with compositions of Ti-1.0 at.% Al-9.6 at.% Nb-3.6 at.% W-51.9 at.% B can be determined as borides. The other bright blocky phases, which distribute in the grain boundaries, composed of Ti-35.7 at.% Al-8.5 at.% Nb-1.7 at.% W, can be determined as the β phase. No β phases with these characteristics are found in the samples containing 0.4 at.% W. Thus, the β phase tends to form at a W amount above 0.4 at.%. Further detailed microstructural observations were conducted, using the field-emission SEM. In Fig. 4(a), the needle-shaped boride has a hexagonal cross-section. The gray phase in Fig. 4(b) containing 49.54 at.% of Al is determined as γ twins. It seems that the γ twin phases can form in regions beside the borides. This trend might be caused through the capture of Ti by B, which can lead to a fast decrease of Ti in the boride-surrounding region, and trigger the formation of the high-Al, low-Ti γ twins.

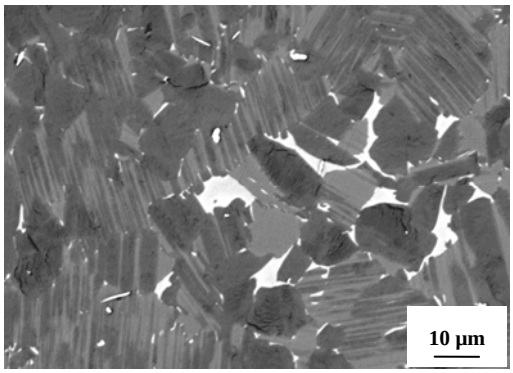

Figure 3 Microstructure of the Ti-45Al-7Nb-0.15B-0.7W alloy after HIPing and homogenization, electron microprobe image

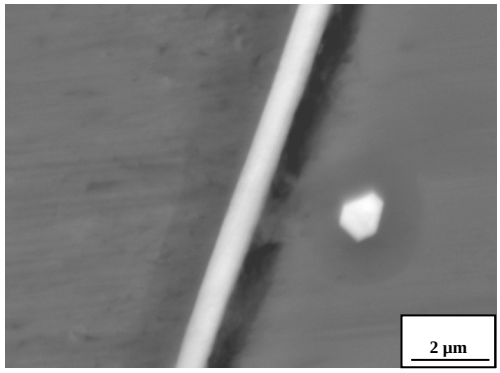

(a)

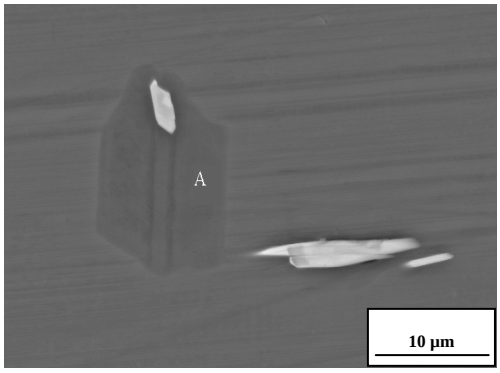

(b)

Figure 4 Backscattered images of the Ti-45Al-7Nb-0.15B-0.7W alloy after HIPing and homogenization, (a) TiB_2 needles, and (b) formation of γ-twin caused by TiB_2 (shown in area A)

As shown in Fig. 2, with the content of W increases, the equilibrium microstructures of the TiAl-based alloys vary. By measuring the microstructures in Fig. 2, it indicates that with the content of W increasing from 0 at.% to 0.2 at.%, 0.4 at.%, and 0.7 at.%, the lamellar colony sizes are 70 μm, 50 μm, 32 μm, and 25 μm, respectively; and the interlamellar spacings are 2.46 μm, 2.35 μm , 2.28 μm, and 2.08 μm, respectively, shown in Fig. 5. The TEM observations of Ti-Al-Nb-W-B alloys after the HIPing and homogenization shown in Fig. 6 also indicate that the content of W has a great effect on the lamellar structure. As W increases, the interlamellar spacing decreases.

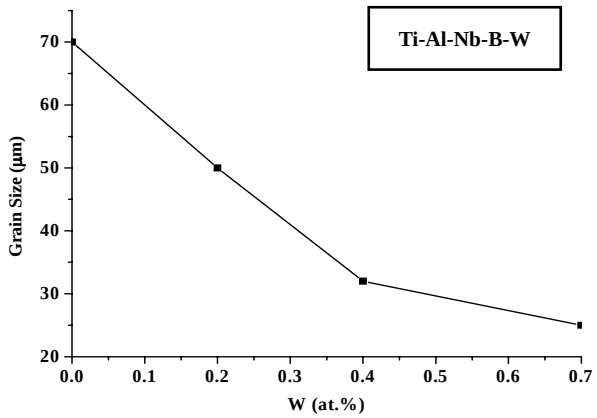

(a)

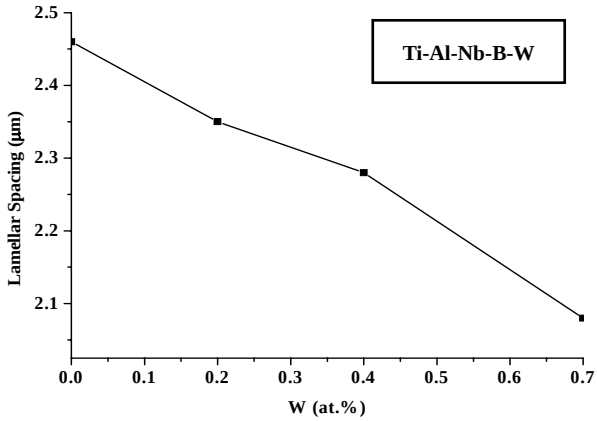

(b)

Figure 5 Effect of W on the (a) grain size, and (b) lamellar spacing of the Ti-Al-Nb-W-B alloys after the HIPing and homogenization

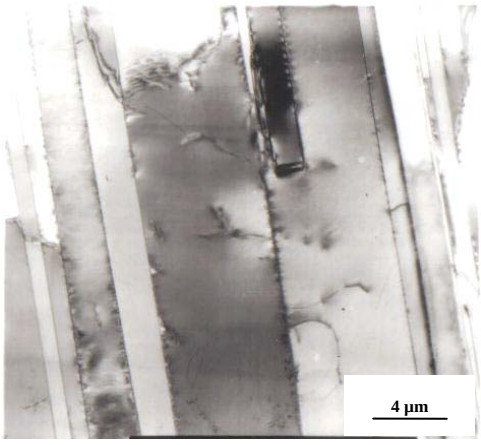

(a)

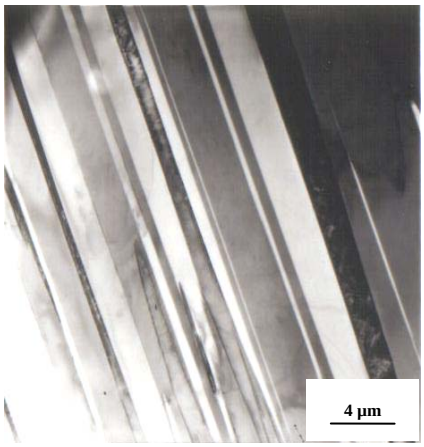

(b)

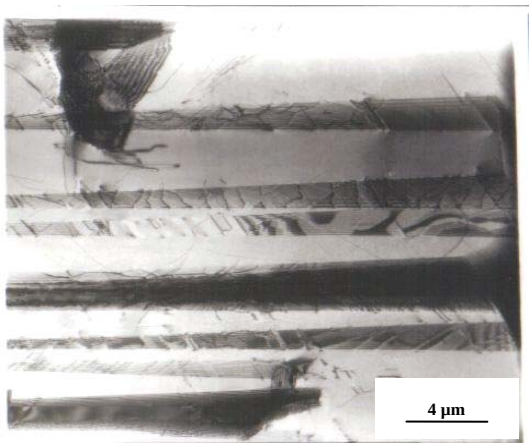

(c)

Figure 6 TEM analyses of the Ti-Al-Nb-W-B alloys after HIPing and homogenization, (a) Ti-45Al-7Nb-0.15B-0.2W, (b) Ti-45Al-7Nb-0.15B-0.4W, and (c) Ti-45Al-7Nb-0.15B-0.7W

3. Hardness of the TiAl-based alloy

Exhibited in Fig. 7(a), the hardnesses of the TiAl-based alloys are very sensitive to the changes in the interlamellar spacing. As the interlamellar spacing of the alloys slightly decreases, the hardness of the alloys increases. Alloy additions, such as W, in the TiAl-based alloys can increase the hardness of the alloy, shown in Fig. 7(b). W can effectively refine the microstructure of the alloys. As the amount of W increases, the colony size of the alloy decreases, leading to an increase in the hardness of the alloy.

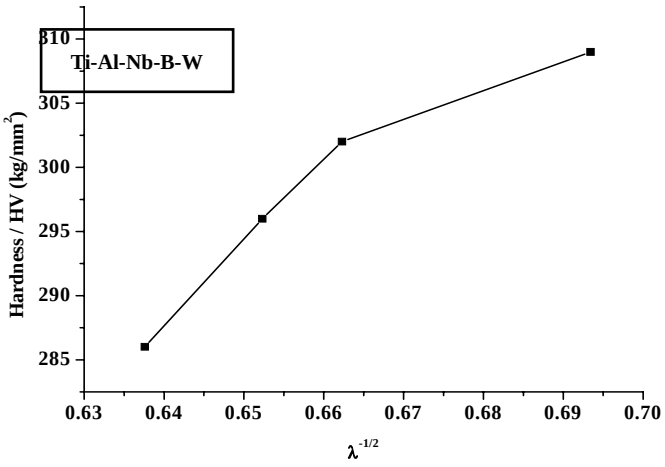

(a)

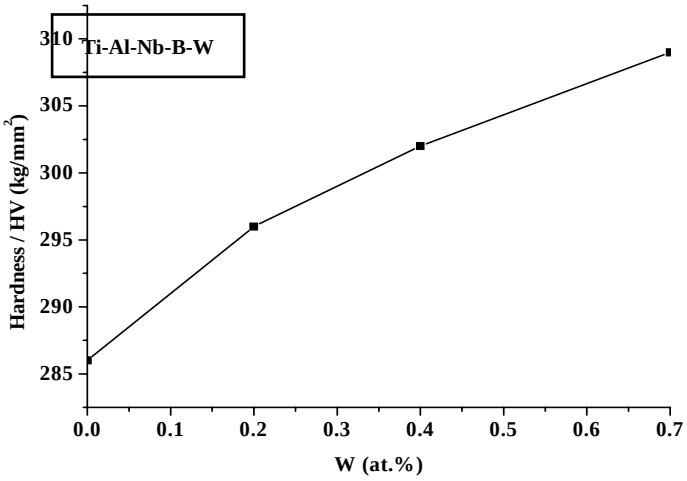

(b)

Figure 7 Effects of (a) interlamellar spacing, and (b) W content on the hardness of the Ti-Al-Nb-W-B alloys after heat treatment at 1,280^{0}C / 4 h

DISCUSSIONS

1. Effect of W and alloying elements on the microstructure of TiAl alloys

From the Ti-Al binary phase diagram, the equilibrium condition of the TiAl-based alloy containing 45 at.% Al mainly consists of two phases, the α_2 and γ phases, resulting in the formation of the lamellar structure. In the as-cast condition, the TiAl-based alloy is composed of typical non-equilibrium structures. The addition of B in the TiAl-based alloy can cause the *in-situ* formation of TiB_2 in the melt. Since the melting temperature of TiB_2 is high (3,253^{0}C), it is surrounded by the TiAl melt during casting and can induce the heterogeneity nucleation during cooling. Under the condition of drop casting, the cooling rate of the Ti-Al-Nb-W-B alloy is very fast, and a peritectoid reaction is involved, as the TiAl alloy cools down. This trend made the compositions within the colony and between the colonies not uniform. Thus, non-uniform as-cast structures, such as the cellular structures and dendrites, are formed.

Figure 3 indicates the formation of the β phase at a higher content of W in the TiAl-based alloys. W is a beta-phase stabilizer, which is rich in the β phase at a high temperature. The β phase is a high-temperature residual phase, which exists as the β_2 phase at room temperature. The orientation relationships among the α_2 phase, γ phase and β phase are: $(0001)\alpha_2$ // $\{111\}\gamma$ // $\{110\}\beta_2$, and $\langle 1120\rangle\alpha_2$ //$\langle 110\rangle\gamma$ //$\langle 111\rangle\beta_2$. With the increase of the W content, the amount of W in the β solute increases, more β_2 phases can be stabilized at a lower temperature. The β_2 phase can precipitate either in the grain, or at the boundaries of the equiaxed γ crystals [11]. W also segregates at the interface of the γ/γ and α_2/γ phase, and it stabilizes the α_2 lamellae from dissolving during aging [12]. Thus, with the addition of W, the microstructure of the

Ti-Al-Nb-W-B alloy refines. As the amount of W exceeds 0.4 at.%, the trend of the refinement slows down.

W has little influence on the precipitation and growth of the γ phase, because it has very small solubility in the γ phase. Therefore, W does not affect the size of the equiaxed γ crystal.

2. Effect of W on the hardness of the alloy

The hardness of the TiAl-based alloys is related to three factors: the interlamellar spacing, the colony size, and the alloy addition [2]. The essential factor lies in the interlamellar spacing of the microstructure. As shown in the Hall-Petch equation,

$$\sigma_{0.2} = \sigma_0 + k_\lambda \lambda^{-1/2},$$

where $\sigma_{0.2}$ is the 0.2% offset yield strength, σ_0 and k_λ are material constants, and λ is the lamellar spacing. The yield strength of the alloy increases, as the interlamellar spacing decreases. The addition of W can refine the lamellar colony size and reduce the interlamellar spacing of the alloy. In the meantime, W dissolved in the lamellar colony will also increase the strength of TiAl alloy. Thus, W strengthens the alloy by the microstructural refinement and solution strengthening.

CONCLUSIONS

1. A small additional amount of W can refine the grain size of the Ti-Al-Nb-W-B alloys. The lamellar spacing also decreases with increasing the W concentration. But as the amount of W exceeds 0.4 at.%, its beneficial effect becomes small.
2. The addition of W promotes the formation of the β phase. When the amount of W exceeds 0.4 at.%, the β phase precipitates.
3. Borides in the TiAl-based alloys tend to capture Ti from the base alloy, resulting in a decreased amount of Ti in the surrounding area and triggering the γ-twin formation around the borides.
4. A beta-phase-free and fine-grain-sized (< 50 μm) microstructure can be obtained from the Ti-45Al-7Nb-0.15B-0.4W alloy directly after the casting and homogenization treatment.
5. The hardness of the alloy increases with increasing the W concentration. This trend indicates that W strengthens the TiAl-based alloys by the grain-size refinement and solution strengthening.

ACKNOWLEDGEMENTS

The present research is sponsored by the Fossil Energy Materials Program, with Dr. R. Judkins and Dr. J. Zollar as program managers, under the contact number of 11X-SP173V, and the National Science Foundation Combined Research-Curriculum Development (CRCD) Program, with Ms. Mary Poats as the contract monitor, under the contract number of EEC-0203415.

REFERENCES

[1] V. Recina and B. Karlsson, “Tensile Properties and Microstructure of Ti-48Al-2W-0.5Si γ-titanium Aluminide at Temperature between Room Temperature and 800°C,” Mater. Sci. Techno., 1999, 15(1), 57-66.

[2] C. T. Liu, J. H. Schneibel, P. J. Maziasz, J. L. Wright, and D. S. Easton, “Tensile Properties and Fracture Toughness of TiAl Alloys with Controlled Microstructures,” Intermetallics, 1996, 4, 429-440.

[3] R. Yu, L. L. He, Z. Y. Cheng, J. Zhu, and H. Q. Ye, “B_2 Precipitates and Distribution of W in a Ti-47Al-2W-0.5Si Alloy,” Intermetallics, 2002, 7, 661-665.

[4] Z. C. Liu, J. P. Lin, S. J. Li, and G. L. Chen, “Effects of Nb and Al on the Microstructures and Mechanical Properties of High Nb Containing TiAl Base Alloys,” Intermetallics, 2002, 10, 653-659.

[5] P. J. Maziasz, R. V. Ramanujan, C. T. Liu, and J. L. Wright, “Effects of B and W Alloying Additions on the Formation and Stability of Lamellar Structures in Two-Phase γ-TiAl,” Intermetallics, 1997, 2, 83-95.

[6] D. J. Larson, C. T. Liu, and M. K. Miller, “Tungsten Segregation in α_2 + γ Titanium Aluminides,” Intermetallics, 1997, 7, 497-500.

[7] D. Hu, “Effect of Boron Addition on Tensile Ductility in Lamellar TiAl Alloys,” Intermetallics, 2002, 10, 851-858.

[8] D. L. Guan, C. R. Brooks, and P. K. Liaw, “Microstructure and Mechanical Properties of As-cast and Aged Nb-15 at.% Al-10 at.% Ti, -25 at.% Ti and -40 at.% Ti alloys,” Intermetallics, 2002, 10(5), 441-458.

[9] C. Q. Peng, “Effects of Cyclic Heat Treatment on the Microstructure and Mechanical Properties of TiAl Base Alloy,” Ph.D. Dissertation, Central South University, 2001.

[10] Y. W. Kim, “Effects of Microstructure on the Deformation and Fracture of γ-TiAl Alloys,” Materials Science & Engineering A, 1995, 192-193(2), 519-533.

[11] C. T. Liu, P. J. Maziasz, and D. J. Larson, “Effect of B and W Addition on Microstructures and Mechanical Properties of Dual Phase Lamellar TiAl Alloys,” In: Interstitial and Substitutional Solute Effects in Intermetallics, Eds, I. Baker, P. D. Noebe, and E. P. George, TMS Publication, Warrendale, PA, 1998, 179-188.

[12] Y. Shida and H. Anada, “Role of W, Mo, Nb and Si on Oxidation of TiAl in Air at High Temperature,” Mater Trans, JIM, 1994, 35(9), 623-631.

IN-SITU MECHANICAL PROPERTY MEASUREMENT AND STUDY OF IMPURITY EMBRITTLEMENT AND METAL OXIDES DUCTILITY ENHANCEMENT MECHANISM IN CHROMIUM ALLOYS BASED ON ELECTRONIC STRUCTURE ANALYSIS

B. S.-J. Kang[1], N. Ma[2], C.-Y. Feng[1], and B. R Cooper[2]
[1]Mechanical and Aerospace Engineering Department
[2]Physics Department
West Virginia University
Morgantown, WV 26506

ABSTRACT

This research contains two research tasks: (i) to conduct atomistic computational modeling and simulations on the study of impurity embrittlement and metal oxides ductility enhancement mechanism in Cr alloys, and (ii) to apply and further develop of a transparent indenter measurement (TIM) method for in-situ material mechanical property measurement of selected metallic alloys relevant to the Fossil Energy Materials Program**.**

Impurity elements segregated near the grain boundaries such as O, N and S can weaken the mechanical properties of hosting structural materials. To minimize the detrimental effect, dispersions (e.g. MgO for Cr) are included to alter the microstructures for ductility enhancement. In this research, we performed *ab-initio* electronic structure analysis for selected Cr-based material systems to understand the fundamental mechanisms behind the nitrogen embrittlement and ductility enhancement of Cr by MgO dispersions, as recently studied by Brady, *et.al*.[1] We identified several microscopic features, alterable by the inclusion of impurities, which are correlated to the material's mechanical properties. Based on these results, we proposed new microscopic mechanisms to understand the observed impurity embrittlement and ductility enhancement. These understandings are useful for optimization of the dispersion materials for improved ductility enhancement. The techniques developed in this project may be extended to solve problems in other transition metal systems, such as the hydrogen embrittlement of steel.

For the second research task, we have developed a simplified TIM technique coupled with a multiple partial unloading procedure for material Young's modulus measurement. Experimental results of several metallic alloys and related discussions are presented.

TASK 1: STUDY OF IMPURITY EMBRITTLEMENT AND METAL OXIDES DUCTILITY ENHANCEMENT MECHANISM IN CHROMIUM ALLOYS

INTRODUCTION

Tiny amount of impurities, such as nitrogen (N), are known to cause dramatic changes in the mechanic properties of chromium (Cr) and Cr-rich alloys. For example, the ductile-to-brittle transition temperature (DBTT) of pure Cr (with less than 0.0001 atomic pct of N) is within the ambient temperature range, while that of unalloyed recrystallized Cr with commercial purity is approximately 150^{o}C in tension [2]. Below the DBTT, Cr has virtually no ductility, which

places severe limitations on its potential applications in the high temperature gas turbine engine components for increased efficiency.

There have been numerous studies concerning improving the ductility of Cr and Cr-based alloys at ambient temperature. In order to stabilize or remove the interstitial impurities, scavenging elements, such as tungsten, molybdenum, and rhenium were alloyed with Cr [3] resulting in increased ductility. Another route was demonstrated by Brady *et.al*.[1] that suitable amount of MgO dispersion can improve the room temperature tensile ductility of Cr by 10-20%. From TEM microstructural analysis, they found the oxide dispersions attracted the detrimental agents (notably N and S) to precipitate near the oxide-metal interface. Therefore, detrimental impurity management mechanism (i.e., by preventing the detrimental impurities from segregating to the Cr grain boundaries) has been invoked to explain the ductility enhancement. Interestingly, similar microstructures were discovered in their later experiments using La_2O_3, TiO_2 and Y_2O_3 as dispersions, but none displayed any ductility enhancement. This indicates that other factors, perhaps hiding at deeper levels below the microstructures, are contributing to the ductility enhancement of Cr alloys.

On the theoretical side, the classic theory of Griffith [4] demonstrates that brittle fracture will occur when the hosting material can stably sustain an atomically sharp crack in the lattice without breakdown by dislocation generation. Therefore, the characteristic failure mode of a material depends on the relative easiness of creating new surfaces compared with forming and emitting dislocations. Based on this theory, Rice [5] proposed a criterion to quantitatively measure the tendency of a material to be brittle or ductile in terms of the ratio of the energies for surface and dislocation formation. The actual applications of these theories to realistic problems was not carried out due to the lack of *ab-initio* knowledge of the rich variety of interactions among the imperfections within the system, including impurities, dislocations, cracks, and grain boundaries at quite different length scales. At the basic fundamental level, the mechanisms responsible for the impurity and addictive effects are still largely unknown.

In this research task, we investigate the electronic structures of Cr, with or without N impurity and/or MgO, based on *ab-initio* techniques. Our purpose is to identify the changes in electronic structure due to the presence of impurity elements that are connected to the observed mechanical properties. The electronic structures dictate the properties of the valence electrons that participate in forming various types of chemical bonds among the atoms within the solids. Therefore, they are relevant to the material's mechanical properties. In the following sections, we first describe our modeling schemes and techniques in Section 1.2. We then present the detailed results and discussions in Section 1.3, with a brief conclusion and future study plan in Section 1.4

MODELS AND METHODOLOGY

To study the mechanisms of the impurity and addictives effect, we considered the following three model Cr systems, as shown in Figure 1. These models contain limited number of independent atoms due to the extensive computing resource requirements imposed by typical *ab-initio* calculations. Nevertheless, we found that the supercell size is sufficiently large to

yield both distinguished and converged electronic structures for Cr with impurity effect (see Section 1.*3.2 L-DOS*).

Full potential linear muffin-tin orbital (FP-LMTO) techniques [6], which accurately treat the muffin-tin's interstitial region, have been used to calculate the electronic structures for the above systems. To achieve maximum accuracy, a three-kappa linked base is used to expand the muffin-tin tail functions. The energies for these bases are set to be -0.9, 0.3, and 1.2, respectively. Iterations are repeated until a convergence of 10^{-5} rydberg is achieved, after which the electronic structures are analyzed. No atomic relaxations within the cell are performed as their effect on electronic properties is negligible. The valence electrons under investigation include Cr's 4s and 3d bands, N and O's 2s and 2p bands, and Mg's 3s bands.

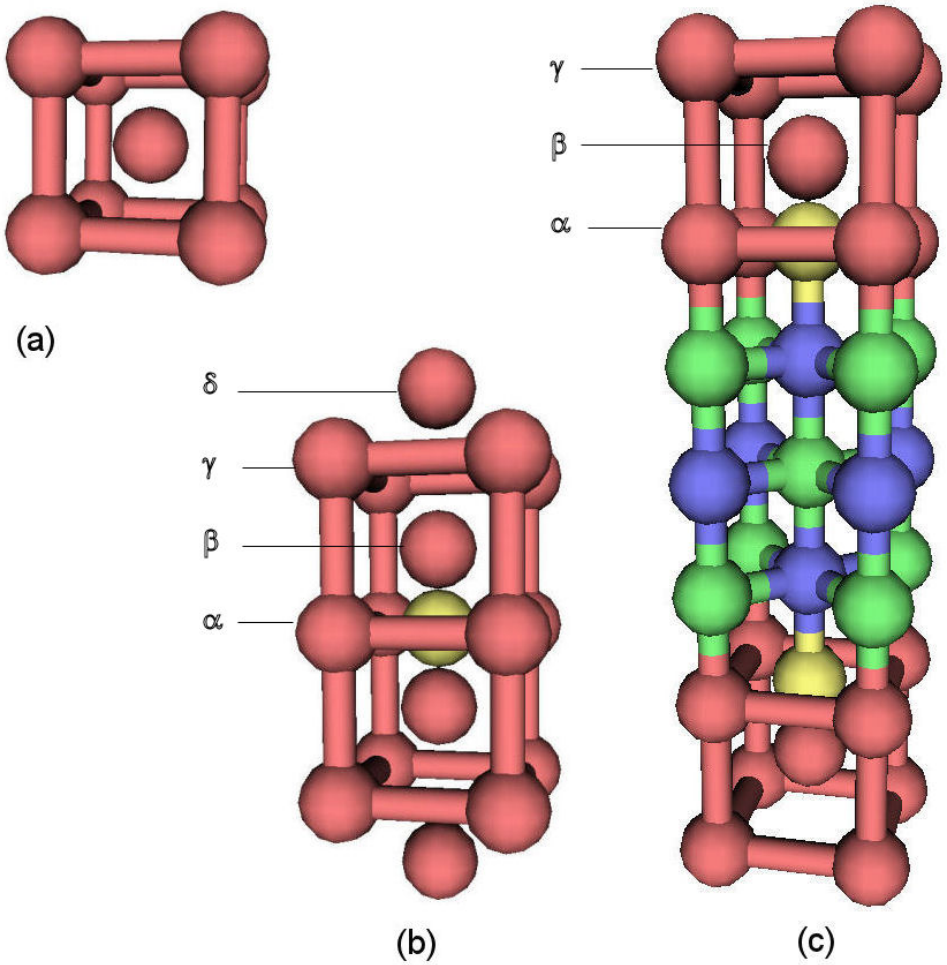

Figure 1. The supercells of the model Cr/N/MgO systems. The red, yellow, green, and blue sphere respectively represents a chromium, nitrogen, oxygen, and magnesium atom.

(a) Pure b.c.c. Cr system
(b) Nitrogen embrittled Cr: A 6-atom b.c.c. Cr supercell containing one nitrogen impurity
(c) MgO ductilized Cr: A supercell containing 6-atom b.c.c. Cr interfaced with 6-atom MgO, with two additional nitrogen impurities placed at Cr-MgO boundary

Note: the inequivalent Cr atoms in system (b) and (c) are labeled by Greek letters according to their distances from the impurity atom for convenience.

The electronic structures being analyzed include the electron energy levels (the band structure) and the density of states (DOS). The full band structure of a supercell, however, is over crowded and often obscure the features caused by impurity effects. It turns out to be more convenient to study the electron energy level and the DOS that is associated with a specific angular orbital on a specific atom, in order to compare and identify the changes due to an impurity. We call the latter as atomic, angular-projected energy level (L-EL) and L-DOS. In particular, we define the L-EL to be the energy parameter used to create the basis muffin-tin orbital within the specified atom at convergence. In our modeling for Cr's 4s state, this parameter is determined by the condition that the muffin-tin orbital so created be orthogonal to the core states. For Cr's 3d states, the energy is obtained through occupied L-DOS weighted average [7].

RESULTS AND DISCUSSIONS

L-EL

The L-EL for 4s and 3d states of each individual Cr atoms were determined and the results are tabulated in Table I. In system (a) of pure Cr, the 3d state has a higher L-EL than the 4s state by 0.09 rydberg. However this order is reversed in system (b), the N-embrittled Cr, where the 4s state has higher L-EL than 3d by 0.20-0.23 rydberg. This happens because the N impurities effectively raise the 2s and 3s core levels for nearby Cr, which results in a corresponding raise in 4s L-EL (The 4s state has to be orthogonal to the core states). In the ductility enhanced system (c), the difference between 4s and 3d L-ELs becomes smaller. Evidentially, the introduction of MgO stabilizes (lowers down) nearby Cr's core levels, and (partially) restore their original L-EL order between the 3d and 4s states. We thus see that the electronic structures of Cr can be influenced in different ways by forming bonds with different species of atoms, and there exists a correlation between the L-EL ordering and the material's brittle ductile properties.

Table I. Calculated L-ELs (in rydberg) for Cr's 4s (2nd row) and 3d (3rd row) valence states. The third row shows the difference.

system	(a)	(b)				(c)		
atom	Cr	α-Cr	β-Cr	γ-Cr	δ-Cr	α-Cr	β-Cr	γ-Cr
4s	0.583	1.004	0.954	1.078	1.077	0.837	0.940	1.058
3d	0.672	0.808	0.730	0.854	0.849	0.868	0.934	1.047
difference d-s	0.09	-0.20	-0.22	-0.22	-0.23	0.03	-0.01	-0.01

L-DOS

The computed L-DOS for system (a), (b), and (c) are plotted in Figures 2 to 4. Comparing Figures 2 and 3, we find that L-DOS plots for γ- and δ-Cr in system (b) are converging to that of a pure Cr, indicating that impurity effect diminishes as the distance increases. For α-Cr and β-Cr, the plots are quite distinct in that additional peaks emerge from the low end of the spectrum at roughly 0.7 and 0.65 rydberg below the Fermi level. These peaks correlate very well with N's p states, representing states forming strong ionic N-Cr bonds. Similar peaks occur for α-Cr and β-Cr in system (c) (Figure 4), however, at slight shorter distances (0.6 and 0.45 rydberg) away from the Fermi level. In the case of β-Cr, the additional peak starts to overlap with the main peaks stretching across the Fermi level, suggesting that the chemical bonding between N and Cr might somehow hybridize with Cr-Cr bonds to have some characteristics of metallic feature. In addition, an extra high peak at around 0.1 rydberg below the Fermi surface can be identified in α-Cr and β-Cr, indicating a stronger Cr-Cr bond.

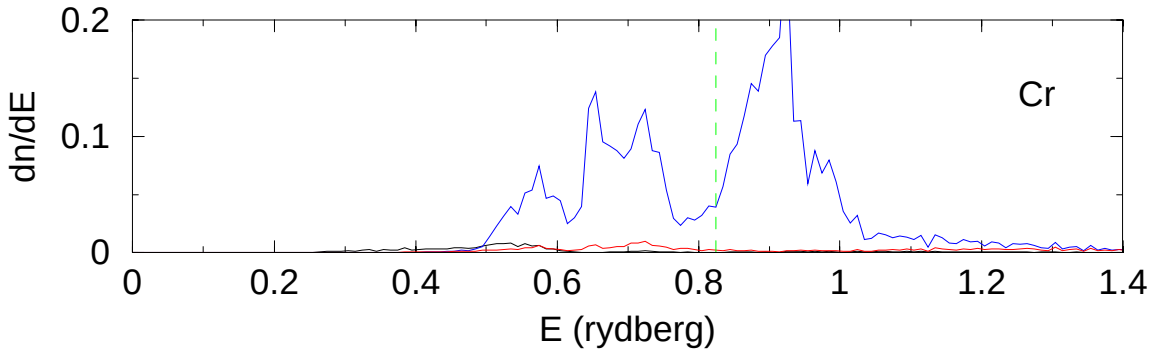

Figure 2. The computed L-DOS for system (a). The black and blue line represents s- and d-component of the L-DOS, and the vertical line is the Fermi energy.

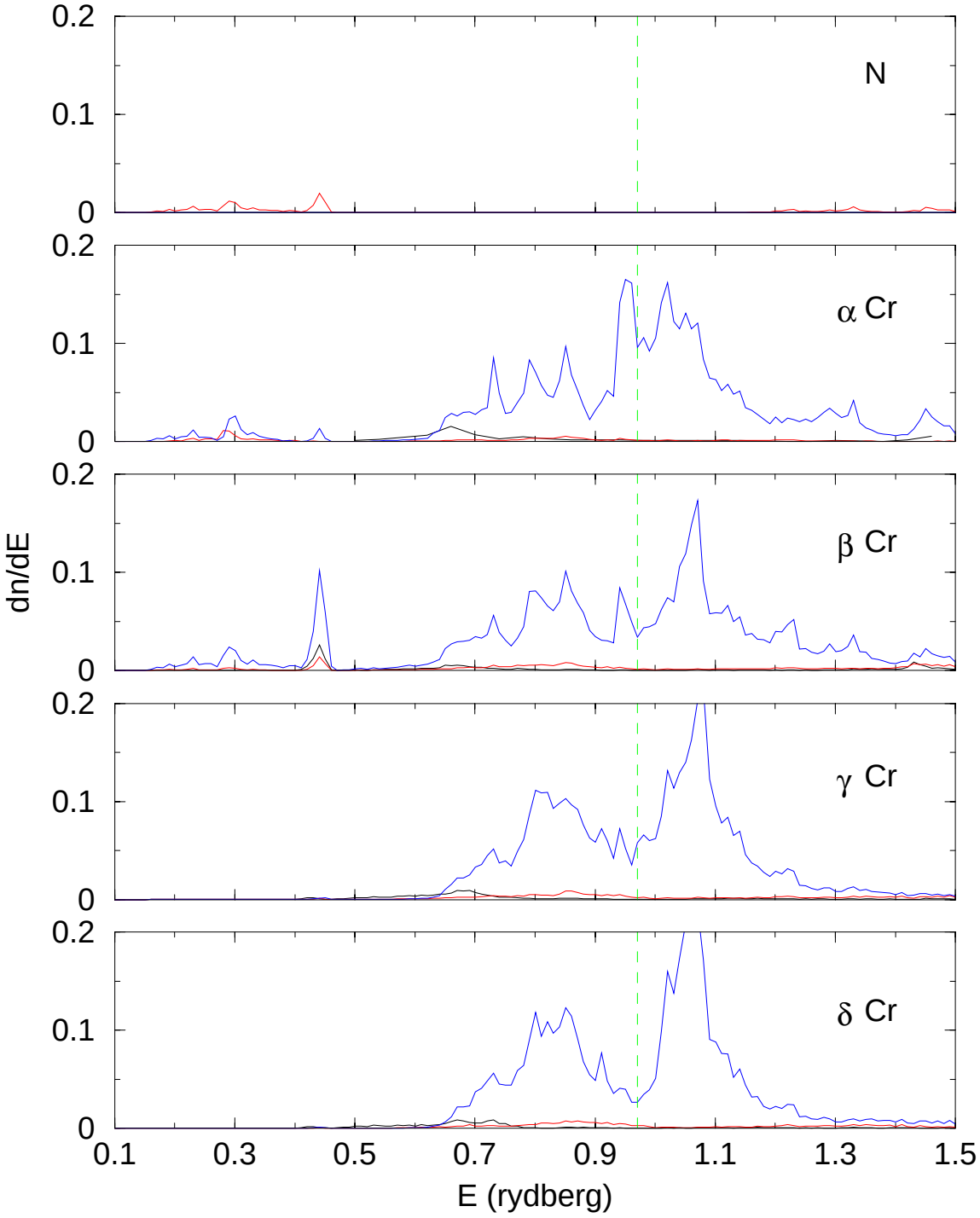

Figure 3. The computed L-DOS for system (b). The black, red, and blue line represents s-, p-, and d-component of the L-DOS, and the vertical line is the Fermi energy. From the top to bottom are the plots for N, α-Cr, β-Cr, γ-Cr, and δ-Cr, respectively.

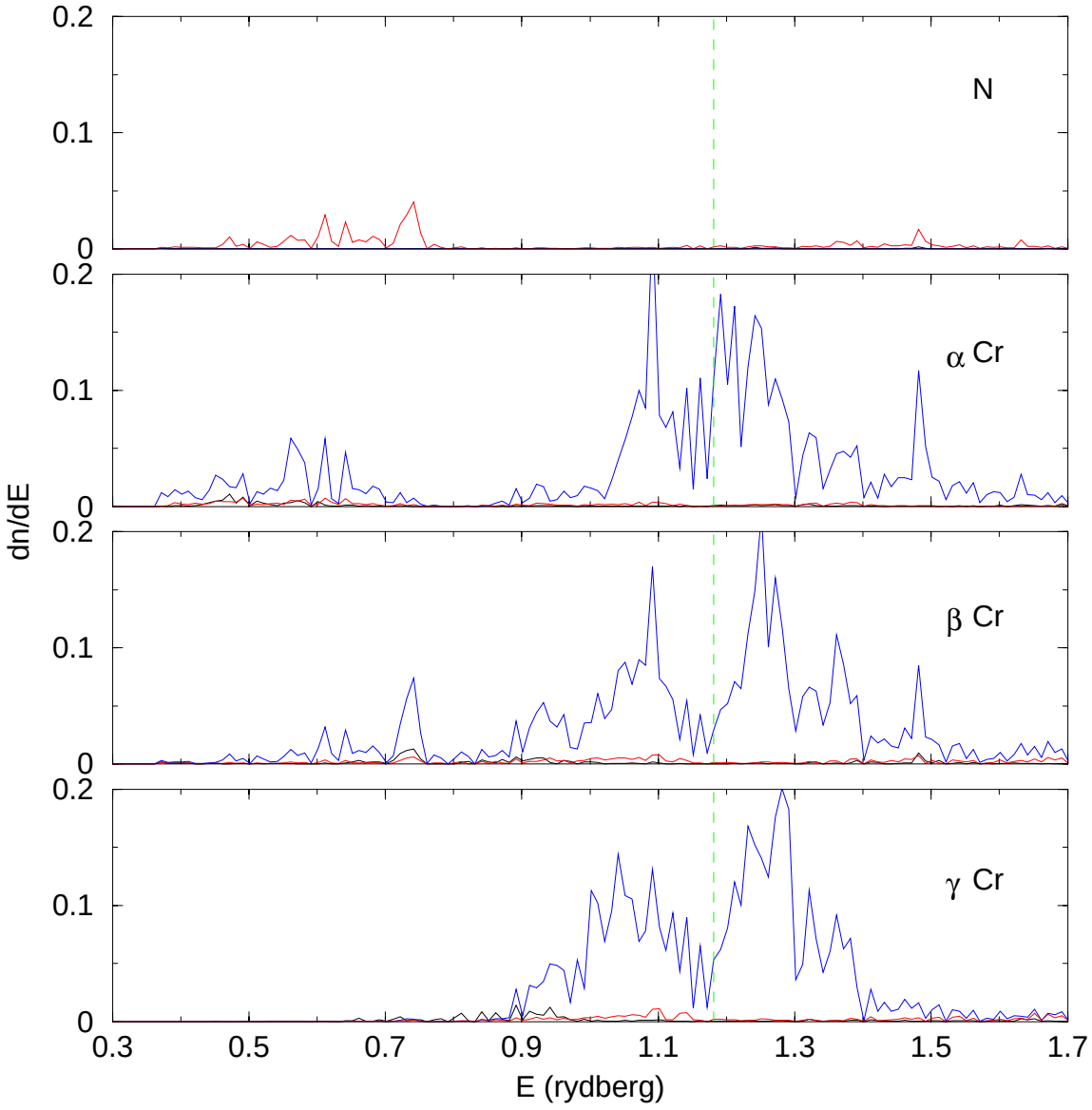

Figure 4. The computed L-DOS for system (c). The black, red, and blue line represents s-, p-, and d-component of the L-DOS, and the vertical line is the Fermi energy. From the top to bottom are the plots for N, α-Cr, β-Cr, and γ-Cr, respectively.

To differentiate between s- and d- components of the L-DOS, we integrate the respective curves up to the Fermi level, and the resulting values for the L-projected valence charge are presented in Table II. In consistency with the observation in L-EL, we find that the ratio of s- and d-projected charge is higher in ductile systems (a) and (c) than in the brittle system (b).

Table II. L-projected valence charge for Cr. The third row is the ratio of the s- partial charge to the d- partial charge.

system	(a)	(b)				(c)		
atom	Cr	α-Cr	β-Cr	γ-Cr	δ-Cr	α-Cr	β-Cr	γ-Cr
s-component	0.286	0.172	0.260	0.204	0.206	0.256	0.297	0.245
d-component	3.846	3.772	3.970	3.603	3.585	4.137	3.998	3.734
ratio s/d (%)	7.4	4.6	6.5	5.7	5.7	6.2	7.5	6.6

DISCUSSIONS

It is known that an electron in s-orbit is isotropic distributed in space. Correspondingly, bonds formed by s-electrons behave more like metallic bonds. On the other hand, bonds formed by d-electrons have strong directional preferences, which behave more like covalent bonds. The fact that metallic bonds render ductility and covalent bonds cause brittleness can be understood through Rice's criterion which states that in systems where metallic bonds dominant, the uniformly shared electrons are more tolerant with stacking faults; whereas in covalent materials, dislocation flow usually means breaking and reconnecting bonds with significant higher energy barrier. Assuming an equal energy cost to create new surfaces by cleavage, the Rice ratio, $\gamma_{us}/\gamma_{0,}$ is then higher in metallic systems than in covalent systems. Therefore, the ratio of occupied s- and d- valence charge is an indicator of whether the material shall display brittle or ductile behavior. The detrimental impurity nitrogen raises nearby Cr's 4s levels, resulting in a decreased proportion of s- electrons and a brittle system. The introduction of MgO restores the L-EL levels and s/d- charge ratio, making the system ductile.

TASK 1 CONCLUSION

Through atomistic modeling using FP-LMTO technique, we obtained and compared the electronic structures of selected Cr systems containing N and/or MgO. We found that the brittle/ductile behavior of a transition metal system can be correlated with certain features in the material system's electronic structures. These include the L-EL ordering, the additional peaks in L-DOS, and the relative ratio between s- and d- projected charge. It becomes evident that the inclusion of impurities or foreign precipitated phases significantly alters the electronic structures, which in turn induces changes in the mechanical properties of the hosting material. We have demonstrated possible mechanisms and criteria to explain and predict the impurity and addictives effects on the mechanical behavior, which are in consistent with Rice's criterion.

Our future work will include performing electronic structure analysis for a much larger, more realistic systems, possibly at the nano-scale, as well as other metal oxide ductilized Mo- and Cr-based alloys systems. The larger systems will be simulated using tight-binding (TB) method. We have developed a unique scheme to extend the capabilities of our existing FP-LMTO package, to extract the TB parameters directly from *ab-initio* calculations [8]. Contrary to the conventional approach which involves numerical fittings to band structures, this scheme inverts the Hamiltonian matrix elements to directly obtain the original TB parameters. Without numerical fitting procedures, this scheme is particularly useful for multi-element structure modeling, for example the study of impurity effect. The TB method can be used to simulate systems consisting up to 10^5 independent atoms, providing accurate electronic structure information that may be difficult to obtain with other empirical classical-potential based techniques. Through these simulations, we will understand how various controlling factors, such as dispersion material's composition, size and morphology, can interplay and affect the ductility enhancement mechanism. For example, we can change the diameter of the MgO in the simulations and see the resulting change of electronic structures near the Mo and O interface, and hence the corresponding mechanical properties. The results of the numerical simulations will provide useful guidance for experimentalists in searching for optimal size to improve the mechanical properties.

TASK 2: A MULTIPLE PARTIAL UNLOADING INDENTATION TECHNIQUE FOR YOUNG'S MODULUS MEASUREMENT

INTRODUCTION

In material nano- and micro-indentation research, among all the indentation parameters, load-depth relation and unloading characteristics have been studied extensively either experimentally or numerically to elucidate the relevant mechanical behavior or properties. For example, it is well accepted to use the initial unloading stiffness of the load-depth curve to determine the material Young's modulus [9-11]. This approach can be traced to Sneddon's [9] classical elastic indentation solutions which describe the general relationship among the load, displacement and contact area for any punch that can be treated as a solid of revolution of a smooth function. In the 1970s, Bulychev and co-workers [10] defined the initial unloading slope and reduced modulus, thus provided a theoretically sound methodology for determining the Young's modulus, this method is applicable to both spherical and pyramidal indenters. In 1992, Pharr and Oliver [11] showed Bulychev's technique can be applied to any indenter that can be described as a body of revolution of a smooth function. In indentation research for Young's modulus measurement, the contact area and initial unloading stiffness are the key parameters to be determined. However, in most cases, measurement of the contact area is not applicable or not possible. Typically, the unloading stiffness is used to estimate the contact area through some iterative algorithm [14,15]. Furthermore, high precision displacement sensors are needed to calibrate the loading system compliance in order to obtain load-depth curve and the unloading stiffness data, accurately [10].

Recently, we have developed a Transparent Indenter Measurement (TIM) method [12,13] which is capable of direct in-situ contact area measurement. In this research task, we present a new simplified TIM technique coupled with a multiple partial unloading procedure for material Young's modulus measurement. The new simplified TIM method requires only small-size test pieces and can also be used to access the degree of brittleness or ductility of the test alloy. Continued development of the TIM technique is ongoing to extend its applications including indentation fatigue test and indentation test at elevated temperatures (up to 1200 ^{o}C).

THEORY

As shown in Equation (1) [10,11], for material Young's modulus measurement using indentation method, the initial unloading stiffness (dp/d*h*) of a load-depth curve and the contact area (*A*) need to be determined. Usually, the contact area, A, is estimated indirectly from the measured unloading stiffness coupled with some iterative scheme [14,15].

$$\frac{dp}{dh} = \frac{2}{\sqrt{\pi}} E_r \sqrt{A} \qquad (1)$$

Where $\frac{1}{E_r} = \frac{1-\nu^2}{E} + \frac{1-\nu_0{}^2}{E_0}$,

and subscript $_0$ denotes the indenter's mechanical properties.

With the optical TIM technique, the contact area, A, is measured directly by using a transparent indenter, as shown schematically in Figure 7. As for the initial unloading stiffness, dp/d*h*, measurement, in the following, we show a simpler approach to obtain (dp/d*h*) using TIM method. A close-loop PZT actuator is implemented in the TIM apparatus as the loading device to conduct the indentation tests. The PZT actuator provides high resolution displacement control (+/- 1 nm). However, the measured PZT tip displacement includes both the system displacement and the indention depth. In terms of compliance, it can be written as

$$\frac{dh_{PZT}}{dp} = \frac{dh_s}{dp} + \frac{dh}{dp} \qquad (2)$$

Where h_{PZT} is the PZT tip displacement,

h_s is the system displacement and h is the indentation depth.

Substitute Equation (1) into Equation (2),

$$\frac{dh_{PZT}}{dp} = \frac{dh_s}{dp} + \frac{\sqrt{\pi}}{2}\frac{1}{\sqrt{A}}\frac{1}{E_r} \qquad (3)$$

During TIM indentation test, the TIM system compliance (S_s) is assumed to remain constant as long as the applied loads do not introduce any plastic deformation to the loading apparatus.

$$\frac{dh_{PZT}}{dp} = S_s + \frac{\sqrt{\pi}}{2}\frac{1}{\sqrt{A}}\frac{1}{E_r} \tag{4}$$

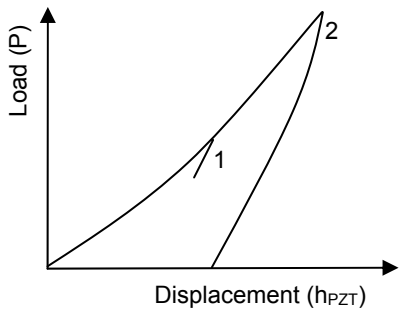

Figure 5. Typical indentation load-displacement curve of a TIM test.

As shown in Figure 5, for a TIM indentation test with two unloading steps, Equation (4) can be written as

$$\left.\frac{dh_{PZT}}{dp}\right|_1 = S_s + \frac{\sqrt{\pi}}{2}\frac{1}{\sqrt{A_1}}\frac{1}{E_r} \tag{5}$$

$$\left.\frac{dh_{PZT}}{dp}\right|_2 = S_s + \frac{\sqrt{\pi}}{2}\frac{1}{\sqrt{A_2}}\frac{1}{E_r} \tag{6}$$

Subtracting Equation (5) from Equation (6), the system compliance is cancelled out. The difference of unloading compliance thus becomes,

$$\left.\frac{dh_{PZT}}{dp}\right|_2 - \left.\frac{dh_{PZT}}{dp}\right|_1 = \frac{\sqrt{\pi}}{2}\frac{1}{E_r}\left(\frac{1}{\sqrt{A_2}} - \frac{1}{\sqrt{A_1}}\right) \tag{7}$$

And the reduced modulus can be calculated from Equation (7)

$$E_r = \frac{\frac{\sqrt{\pi}}{2}\left(\frac{1}{\sqrt{A_2}} - \frac{1}{\sqrt{A_1}}\right)}{\left.\frac{dh_{PZT}}{dp}\right|_2 - \left.\frac{dh_{PZT}}{dp}\right|_1} \tag{8}$$

Equation (8) shows that the reduced modulus can be obtained experimentally from two partial unloading steps during a TIM indentation test. Young's modulus of the tested material can thus be calculated.

$$E = \frac{1-v^2}{\frac{1}{E_r} - \frac{1-v_0^{\,2}}{E_0}} \tag{9}$$

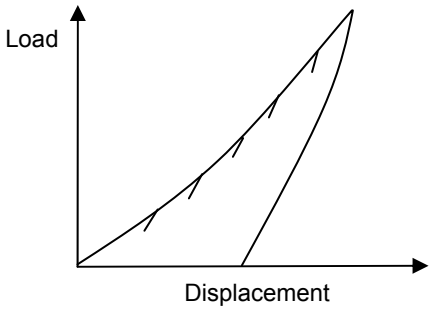

Figure 6. Multiple partial unloading steps during one TIM indentation test.

Using the TIM method, multiple partial unloading steps and the corresponding contact area measurement (as shown in Figure 6) are easy to obtain. To further improve measurement accuracy of the Young's modulus and system compliance, let's re-write Equation (4) as Equation (10) such that both ***a*** (reciprocal of reduced modulus) and ***b*** (system compliance) can be obtained using linear regression method.

$$\left(\frac{dh_{PZT}}{dp}\right) = \left(\frac{1}{E_r}\right)\left(\frac{\sqrt{\pi}}{2}\frac{1}{\sqrt{A}}\right) + S_s \tag{10}$$

Or $y = ax + b$

Where $y = \frac{dh_{PZT}}{dp}$, $a = \frac{1}{E_r}$, $x = \frac{\sqrt{\pi}}{2}\frac{1}{\sqrt{A}}$, $b = S_s$

EXPERIMENTAL SETUP

As shown in Figure 7, a sapphire half-spherical indenter (1.5 mm diameter in this research) is attached to a hollow stainless steel supporting block, which is then attached to a load cell and PZT actuator. A mirror is mounted inside the hollow stainless steel supporting block. An exchangeable long working distance microscope is attached to the indentation apparatus to capture the surface indentation images (i.e. the indented area, A). In this test, a 10x objective lens was used.

In order to run the indentation test and record related load-displacement data and indented area automatically, two LabVIEW™ programs were developed. One controls the initial position of the indenter, and the other controls the indentation test as well as data and image recording.

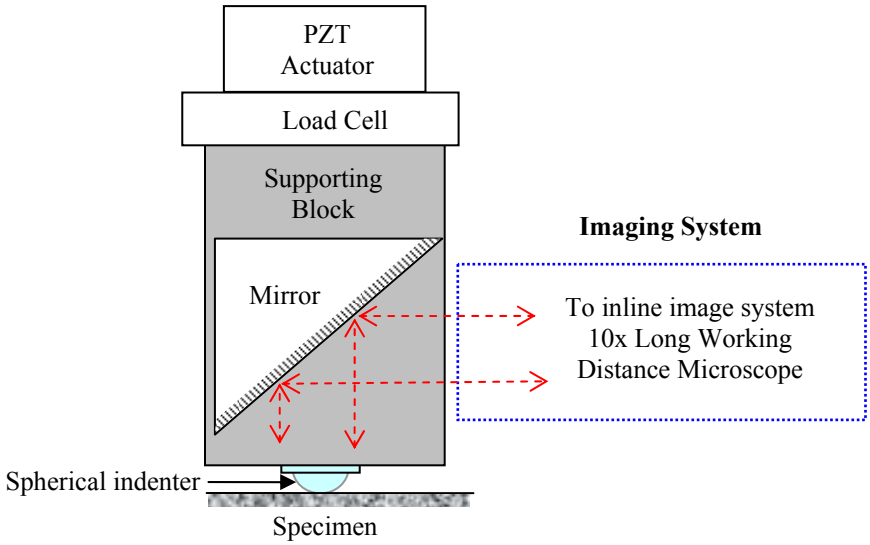

Figure 7. Transparent Indenter Measurement System with in-line imaging system.

TESTING PROCEDURES

A typical TIM test involves two steps. The first step is the initial adjustment. After the specimen is firmly attached to the specimen holder, the initial contact between the indenter and the specimen surface is established by running the initial adjustment program. This LabVIEW™ program automatically searches the position until it identifies the initial contact. In our case, the initial contact criterion is set to a certain small threshold load (less than 0.1 newton). When the applied load approaches the threshold load, the indenter will stop moving and record the current

position. The program can also retract the indenter to a certain distance if initial contact is to be avoided. After the initial contact is established, a second LabVIEW™ program is used to conduct the indentation test automatically. For the results shown in this paper, all tests have nine partial unloadings and one full unloading.

TESTED MATERIALS

Al 7075-T6 and IN783 alloys were selected for the verification tests. The published Young's modulus values are 71.7GPa and 177.3GPa, respectively [16,17]. The IN783 superalloy had standard heat treatment (1120°C/1hr/AC + 845°C/8hrs/AC + 720°C/8hrs 50°C/hr 620°C/8hrs/AC). The Young's modulus of the sapphire indenter is 340GPa and Poisson's ratio is 0.29. Preliminary test results of cast Re-(26-30 wt%)Cr alloy are also presented.

RESULTS

Al 7075-T6

Figure 8 shows the indentation images (1 to10) at each partial unloading step. Those images are then processed to obtain the contact area at corresponding loading/unloading stage. For all the tests, the nominal unloading is one micron meter. The indentation load and PZT tip displacement data are shown in Figure 9(a). The inserted circle in Figure 9(a) shows one magnified unloading part. Using the unloading data, compliances at different unloading steps are then calculated. The processed data are shown in Figure 9(b), which shows linear relation at lower loads. However, the data start to deviate from the linear relation at higher indentation loads. The demarcation point may be related to onset of surface failure strength of the material, Using the linear part, Young's modulus is calculated using Equation (10) by assuming a Poisson ratio of 0.3. Table III summarizes the results.

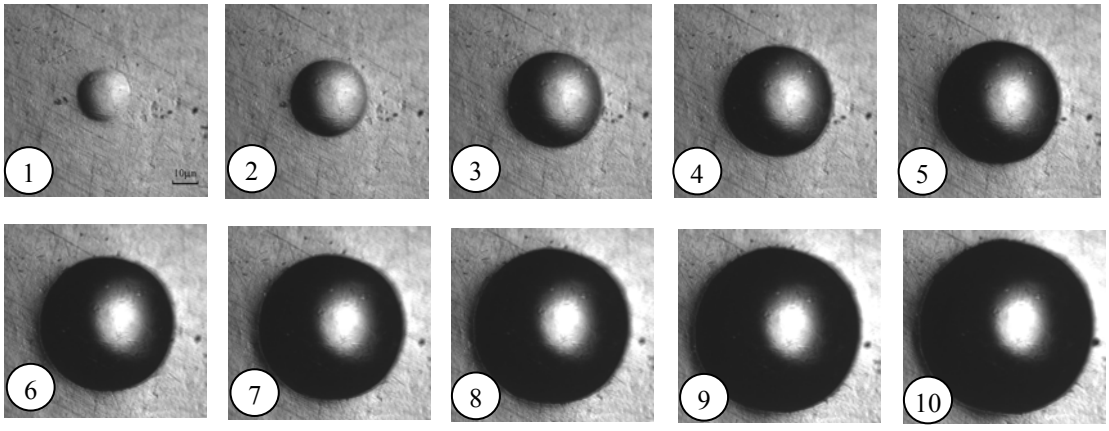

Figure 8. Al 7075-T6 indentation contact zone images at specified partial unloading steps during an indentation test.

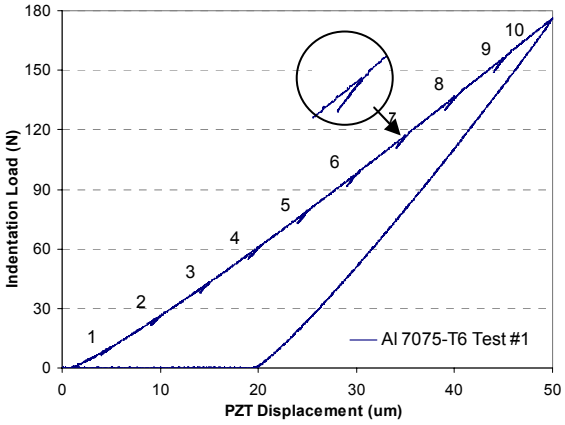

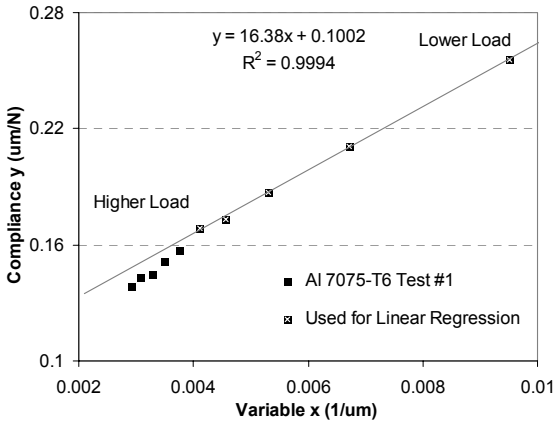

(a) Load displacement curve with partial unloading. (b) Compliance $y = \frac{dh_{PZT}}{dp}$ vs. variable $x = \frac{\sqrt{\pi}}{2}\frac{1}{\sqrt{A}}$.

Figure 9. Results of Al 7075-T6 indentation test.

Table III. Measured Young's modulus of Al 7075-T6

Test	Young's modulus (GPa)	Error (%)
#1	66.5	-7.3%
#2	68.2	-4.9%

(Book value: E=71.7GPa)

INCONEL 783

Figure 10 shows the indentation images (1 to 10) at each partial unloading step. The images are then processed to obtain the contact area at corresponding loading/unloading stage. With the indentation load and PZT tip displacement data (as shown in Figure 11(a)), compliances at different unloading steps are calculated. The processed data are shown in Figure 11(b). Similar to the Al 7075-T6 test, linear relation is observed at lower loads and the data starts to deviate after a certain applied load. Correlation of the demarcation point to the materials failure strength will be investigated. Again, using the linear part and based on Equation (10), Young's modulus is calculated. Table IV shows the results for IN783 superalloy. Less than 3% error is noted.

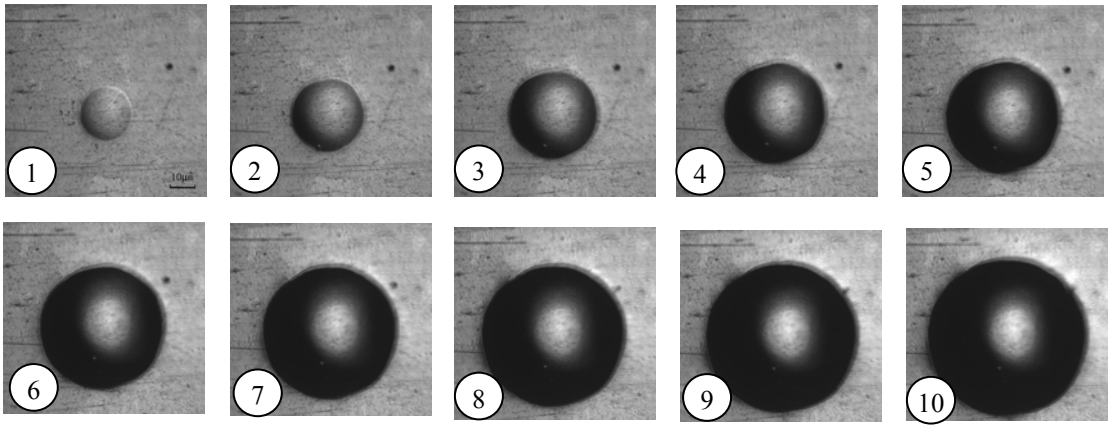

Figure 9. IN783 indentation contact zone images at specified partial unloading steps during an indentation test.

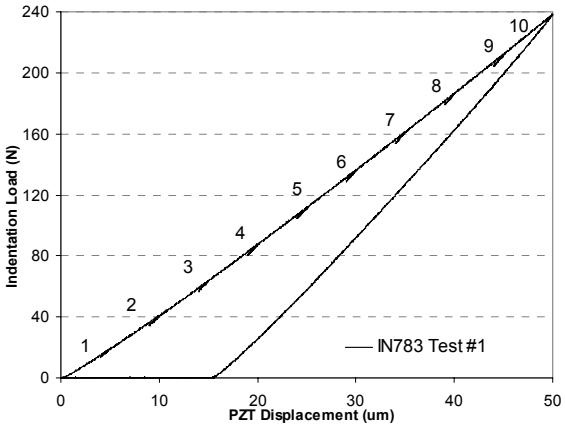

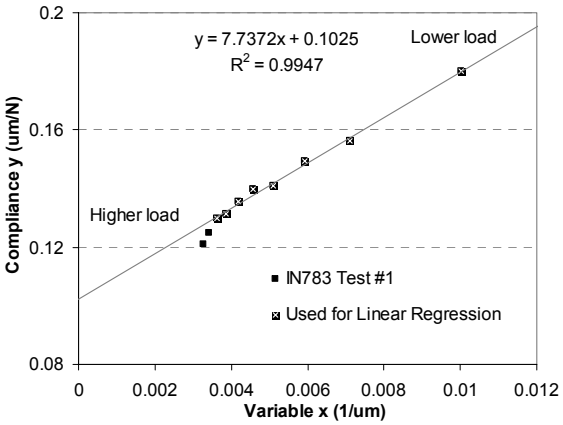

(a) Load displacement curve with partial unloading. (b) Compliance $y = \frac{dh_{PZT}}{dp}$ vs. Variable $x = \frac{\sqrt{\pi}}{2}\frac{1}{\sqrt{A}}$.

Figure 10. Results of IN783 indentation test.

Table IV. Measured Young's modulus of IN783

Test	Young's modulus (GPa)	Error
#1	180.4	+1.7%
#2	181.6	+2.4%

(Book value: E=177.3GPa)

CAST RE-CR ALLOY

Test results for Al7075-T6 and IN783 alloys confirmed the validity of using TIM with multiple partial unloading procedure to determine material Young's modulus. Following the same procedure, a series of TIM indentation tests on Cr alloys were conducted. The Cr alloys were from ORNL as reported in [1,8]. Figures 12 and 13 show preliminary results of a cast Re-(26-30)Cr wt% alloy. As shown, the load-depth curve shows a suddenly drop of load between marks 7 and 8, which occurred at the onset of slip lines formation at the surface high tensile stress region while under indentation loading. Using data before mark 7, Young's modulus from this test was determined to be 234GPa. By analyzing those slip lines, ductility and/or brittleness of the material can be further characterized and failure/fracture properties may be estimated thereafter.

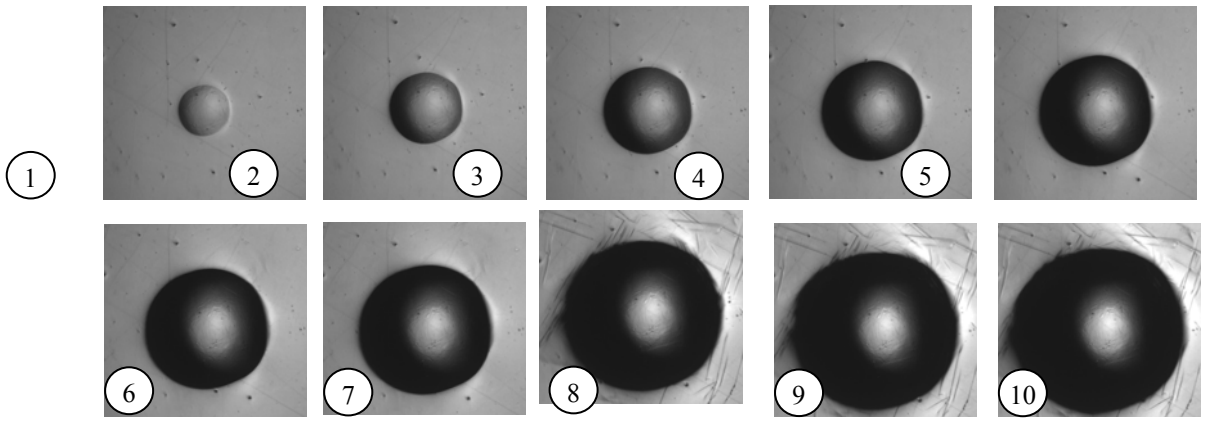

Figure 11. Indentation contact zone images at specified unloading steps, cast Re-(26-30)Cr wt% alloy.

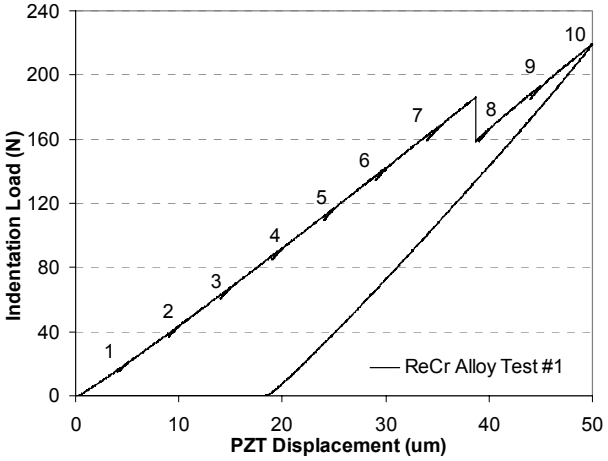

(a) Load displacement curve with partial unloading.

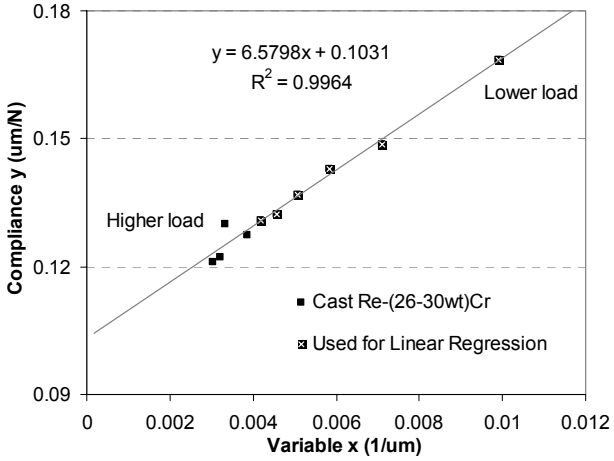

(b) Compliance $y = \frac{dh_{PZT}}{dp}$ vs. Variable $x = \frac{\sqrt{\pi}}{2}\frac{1}{\sqrt{A}}$.

Figure 12. Results of cast Re-(26-30)Cr wt% indentation test.

TASK 2 CONCLUSION

Based on a recently developed simplified TIM indentation technique and coupled with a multiple partial unloading procedure, we present a method for material Young's modulus measurement. Verification tests of Al 7075-T6 and IN 783 were conducted and the results agree well with the book values. Preliminary test results of cast Re-(26-30 wt%)Cr alloy was also conducted. The method presented is easy to use and works well with small-size test pieces. Further development of the TIM technique is planned to extend it's applications including indentation fatigue test and indentation test at elevated temperatures (up to 1200 ^{o}C).

ACKNOWLEDGEMENT

The work is sponsored by the Office of Fossil Energy, Advanced Research Materials (ARM) Program, U.S. Department of Energy, under contract DE-AC05-00OR22725 managed by UT-Battelle, LLC.

REFERENCE

1. M.P. Brady, I.M. Anderson, M.L. Weaver, H.M. Meyer, L.R. Walker, M.K. Miller, D.J. Larson, I.G. Wright, V.K. Sikka, A. Rar, G.M. Pharr, J.R. Keiser, C.A. Walls, Mater. Sci. & Eng. A358, 243-254 (2003)
2. W.D. Klopp, NASA TM X-1867, September 1969.

3. Y.F. Gu, H. Harada, Y.Ro, and T. Kobayashi, Metal. & Mater. Trans. A 36A, 577-582 (2005)
4. A.A. Griffith, Trans. First Intl. Cong. Appl. Mech. Delft, 55-63 (1924)
5. J.R. Rice, J. of the Mech. & Phys. of Sol. (UK), 40, 239-271 (1992)
6. D.L. Price and B.R. Cooper, Phys. Rev. B 39, 4945-4957 (1989); D.L. Price, J.M. Wills and B.R. Cooper, ibid. 46, 11368-11375 (1992).
7. J.M. Wills, O. Eriksson, M. Alouani, and D.L. Price, in "Electronic Structure and Physical Properties of Solids, The Uses of the LMTO Method", Springer, Berlin, 148-167 (2000)
8. N. Ma, B.R. Cooper, and B.S. Kang, J. App. Phys. 99, 053514 (2006)
9. Ian N. Sneddon, 'The Relation between Load and Penetration in the Axisymmetric Boussinesq Problem for a Punch of Arbitrary Profile', Int. J. Engng Sci, Vol. 3, pp. 47-57, 1965.
10. S.I. Bulychev, V. P. Alekhin, M. Kh. Shorshorov, A. P. Ternovskii and G. D. Shnyrev, Determining Young's modulus from the indentor penetration diagram, Industrial laboratory, Vol.41, No.9, pp 1409-1412, Sep 1975.
11. W. C. Oliver; G. M. Pharr, An improved technique for determining hardness and elastic modulus using load and displacement sensing indentation experiments, JOURNAL OF MATERIALS RESEARCH, 7 (6):1564-1583 June 1992.
12. Chuanyu Feng, Development of a Transparent Indenter Measurement system and Indentation Analysis for Material Mechanical Properties Evaluation, Dissertation, West Virginia University, 2005.
13. Chuanyu Feng, Bruce S. Kang, A Transparent Indenter Measurement Method for Mechanical Property Evaluation, accepted by the Journal of Experimental Mechanics on Oct 13, 2005.
14. B. Taljat, T. Zacharia, New analytical procedure to determine stress-strain curve from spherical indentation data, Int. J. Solids structures, Vol. 35, No. 33, pp. 4411-4426, 1998.
15. F. M. Haggag, Field Indentation Microprobe for structural integraity evaluation, U.S. Patent No. 4,852,397, August 1, 1989.
16. IN783 Mechanical properties, Special Metals Corporation, http://www.specialmetals.com

MICROSTRUCTURE AND PROPERTIES OF HVOF-SPRAYED Ni-50Cr COATINGS

Terry C. Totemeier
Idaho National Laboratory
P.O. Box 1625, MS 2218, Idaho Falls, ID 83415
Email: terry.totemeier@inl.gov; Telephone: 208-526-3074; Fax: 208-526-4822

Joel A. Simpson
Idaho National Laboratory
P.O. Box 1625, MS 2218, Idaho Falls, ID 83415
Email: joel.simpson@inl.gov; Telephone: 208-526-9797; Fax: 208-526-4822

Richard N. Wright
Idaho National Laboratory
P.O. Box 1625, MS 2218, Idaho Falls, ID 83415
Email: richard.wright@inl.gov; Telephone: 208-526-6127; Fax: 208-526-4822

ABSTRACT

Chromia-forming Ni-50%Cr coatings were prepared by a HVOF thermal spray process and characterized. The microstructure and physical and mechanical characteristics are similar to other metallic HVOF coatings recently studied: low fractions of porosity and oxide are observed combined with compressive residual stresses. The performance of Ni-50%Cr coatings in corrosion tests in simulated coal combustion gas and gas-slag environments was slightly worse than FeAl and Fe_3Al coatings prepared by similar processes. The corrosion behavior of the iron aluminide coatings was only slightly worse than a wrought Fe_3Al-based alloy.

INTRODUCTION

Advanced fossil energy systems, such as FutureGen and Vision 21, are being designed for high efficiency and low or zero emissions. Increased efficiency requires increased operating temperatures, whether steam temperatures for steam raising plants and combustion gas temperatures for gas turbines. Advanced fossil-fired steam plants also use higher steam pressures with final steam conditions into the ultrasupercritical regime of 30 MPa pressure and 600°C temperature[1]. These conditions require greater high-temperature strength from structural materials, e.g., tubing and piping, and have led to consideration of new alloy systems for these components, such as Fe-Al intermetallics and Ni-base alloys, instead of the more traditional ferritic steels.[2]

Higher operating temperatures also increase the kinetics of high-temperature corrosion processes, both fireside and steamside, a problem which is further exacerbated by altered operating conditions to produce lowered emissions (low NO_x burning).[3] For a given component corrosion conditions may range from oxidizing to reducing to sulfidizing to carburizing depending on the local environment, and erosion frequently contributes to the corrosive attack.[4] Existing and advanced materials which have been designed primarily with creep strength in mind may not possess adequate resistance to such aggressive environments.[3]

A solution to this problem is the use of coatings to provide or enhance the corrosion resistance of high-strength alloys. For example, high-temperature corrosion-resistant coatings are essential to the operation of advanced aerospace gas turbine engines. Materials used for coatings typically form very stable alumina, chromia, or silica layers and are applied in a variety of ways, including solid-state diffusion, chemical and physical vapor deposition, and thermal spraying. Of these, thermal spray techniques hold the most promise for large fossil energy systems due to their lower expense and potential for field application. Thermal spray coatings of many types currently find wide use in a number of industries for corrosion and wear protection.

The overall goal of Idaho National Laboratory research on thermal-spray coatings for high-temperature environmental resistance has been to better understand the relationships between coating processes, coating characteristics, and coating performance. Towards these ends, the effects of coating process variables (primarily thermal spray particle temperature and velocity) on the characteristics of alumina- and silica-forming coating materials have been studied. These include iron aluminides formed by high-velocity oxy-fuel (HVOF) spraying and Mo-Si-B coatings formed by air plasma spraying (APS).[5-7] This paper describes the preparation and characterization of chromia-forming Ni-50%Cr thermal spray coatings by the HVOF process. The Ni-50%Cr alloy composition is similar to that of the INCOCLAD 671 cladding which has shown excellent performance in the Niles service plant tests.[8] The corrosion resistance of iron aluminide and Ni-50Cr coatings was compared in simulated coal combustion gas and gas-slag environments at test temperatures ranging from 500 to 800°C. In both environments the iron aluminide coatings show superior corrosion resistance not markedly different than Fe_3Al in wrought form.

EXPERIMENTAL METHODS

PREPARATION AND CHARACTERISTICS OF Ni-50%Cr COATINGS

Ni-50wt.%Cr coatings 250 μm to 1500 μm thick were prepared from gas-atomized powder by HVOF thermal spraying in air onto Grade 91 steel and 316 stainless steel substrates. Coatings were produced at two different torch chamber pressures, 340 and 620 kPa, which resulted in varied mean spray particle velocities and temperatures. Coating microstructures were examined using standard techniques; residual stresses as a function of coating thickness were characterized by curvature measurements of coating-substrate couples using the Stoney approximation as described in Ref. [9]. Mean coefficients of thermal expansion (CTE) were measured on free-standing coatings using a vertical dilatometer. Tensile adhesion tests (ASTM C 633) were performed on coatings sprayed onto Grade 91 steel and 316 stainless steel substrates. Typical coating microstructures are shown in Figure 1; spray conditions and coating characteristics are listed in Tables 1 and 2. The microstructure and characteristics of the Ni-50%Cr coatings are similar to other metallic coatings prepared by HVOF thermal spray—porosity is low and residual stresses are compressive and increase with spray particle velocity.

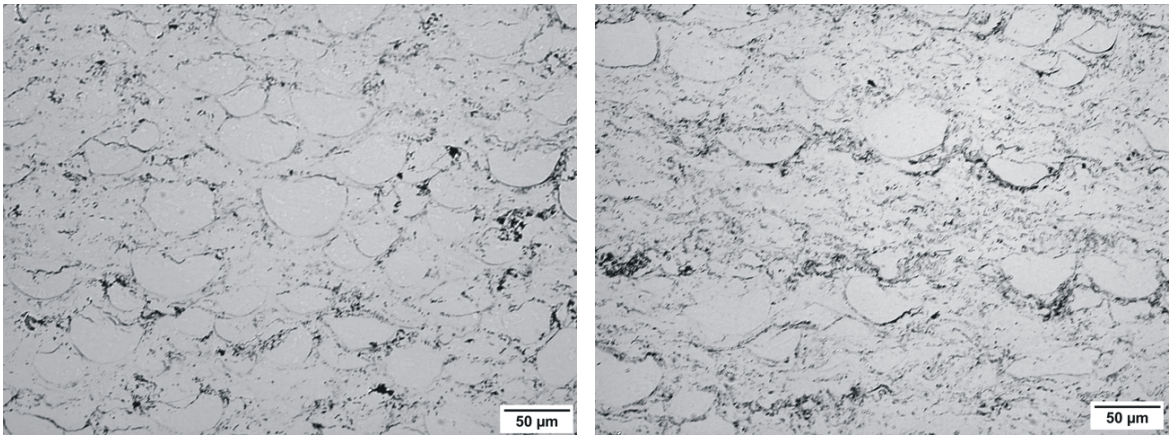

(a) (b)

Figure 1: Microstructures of Ni-50%Cr coatings sprayed at (a) 490 m/s and (b) 540 m/s particle velocities.

Table 1: Ni-50%Cr coating spray conditions and microstructural characteristics

Spray conditions			Microstructural characteristics		
HVOF chamber pressure (kPa)	Mean spray particle velocity (m/s)	Mean spray particle temperature (°C)	Porosity (%)	Oxide (%)	Unmelted particles (%)
340	490	1480	0.05	5	28
620	540	1680	0.05	5	16

Table 2: Ni-50%Cr coating physical characteristics

Particle velocity (m/s)	Residual stress (MPa)	Microhardness (VHN)	Mean CTE @ 700°C (ppm/°C)	Tensile adhesion strength	
				Grade 91 substrate (MPa)	316 SS substrate (MPa)
490	– 100	440	15.3	6.2-7.0	4.8-6.2
540	– 400	500	14.6	7.4-9.0	4.8-5.9

TGA CORROSION TESTING

Corrosion tests were performed on free-standing iron aluminide and Ni-50%Cr coatings and a wrought Fe_3Al-based alloy. Fe_3Al and FeAl coatings were prepared by HVOF spraying onto stainless steel substrates at spray particle velocities of 560 and 620 m/s for Fe_3Al and 540 and 700 m/s for FeAl.[6, 7] Ni-50%Cr coatings were prepared at spray particle velocities of 490 and 540 m/s as described above. Coatings roughly 1.5 mm thick were created from which free-standing rectangular coating TGA specimens $4 \times 4 \times 0.5$ mm^3 were machined. Similar-sized specimens were machined from wrought Fe_3Al sheet (alloy FAS with 2% Cr). Isothermal TGA tests were performed at 500, 600, 700, and 800°C for 25 hr and 100 hr durations in an environment of flowing (~200 ml/min) N_2-9%CO-4.5%CO_2-1.8%H_2O-0.12%H_2S. This is the mixed oxidizing-reducing environment used by Lehigh University[10] and Albany Research Center.[11] For this gas mixture the equilibrium oxygen and sulfur activities are reported as 10^{-19} and 10^{-8}, respectively. For all materials reaction rates typically decreased at the beginning of the tests, sometimes becoming linear at longer times. Consistent linear, parabolic, or paralinear behavior was not observed. For the purpose of material and temperature comparison the corrosion rates were characterized by a linear fit to the weight gain versus time curve near the end of the test.

GAS-SLAG CORROSION TESTING

A variety of free-standing thermal spray coatings were corrosion tested in a simulated coal combustion environment: the gas mixture given above and contact with iron sulfide powder to simulate furnace coal ash. The iron sulfide powder was contained on top of each specimen in a quartz ring. Grade 91 steel substrate material was tested for comparison. Specimens were isothermally exposed to the gas-slag environment for 100 hours at 700°C in a tube furnace and also to thermal cycling conditions which consisted of heating to 700°C, a 1 hour hold at 700°C, and furnace cooling to 100°C. This cycle was repeated 75 times such that the time specimens were held between 600 and 700°C was equal to 100 hours. The depth of corrosion was measured after exposure by metallographic evaluation: the tested specimens were potted in epoxy along with the iron sulfide powder and quartz ring, sectioned in half, and prepared for metallography.

RESULTS AND DISCUSSION

TGA CORROSION TESTING

Results of TGA tests of Ni-50%Cr coatings in simulated coal combustion gas are shown in Figure 2 in the form of weight gain versus time for individual tests at all temperatures. No consistent trends in rates of magnitudes of weight gain with temperature or spray particle velocity are present. Figure 3 further illustrates this point and compares data obtained on Ni-50%Cr coatings with those from iron aluminide coatings and wrought Fe_3Al reported previously.[12] The lack of consistent trends in data between the different coating materials is clear, but wrought Fe_3Al does appear to show slightly better performance than the coatings. The reason for the lack of trends is currently unclear; it is suspected that the environment is not sufficiently aggressive to clearly differentiate the materials, since the low weight gains observed correspond to little observable corrosion (about one micron of attack)., and variable initial weight gains may be overwhelming the true behavior.

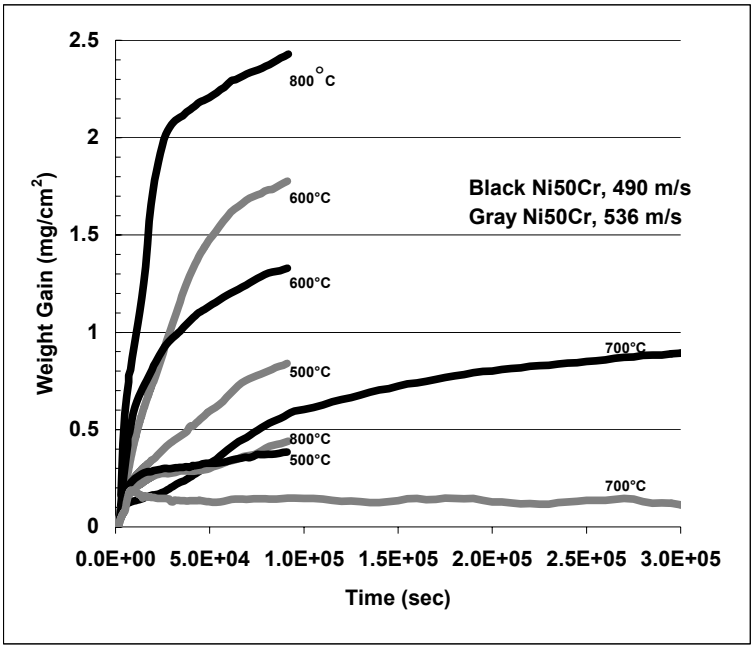

Figure 2: Weight gain versus time for free-standing Ni-50%Cr coatings in a simulated coal combustion gas environment.

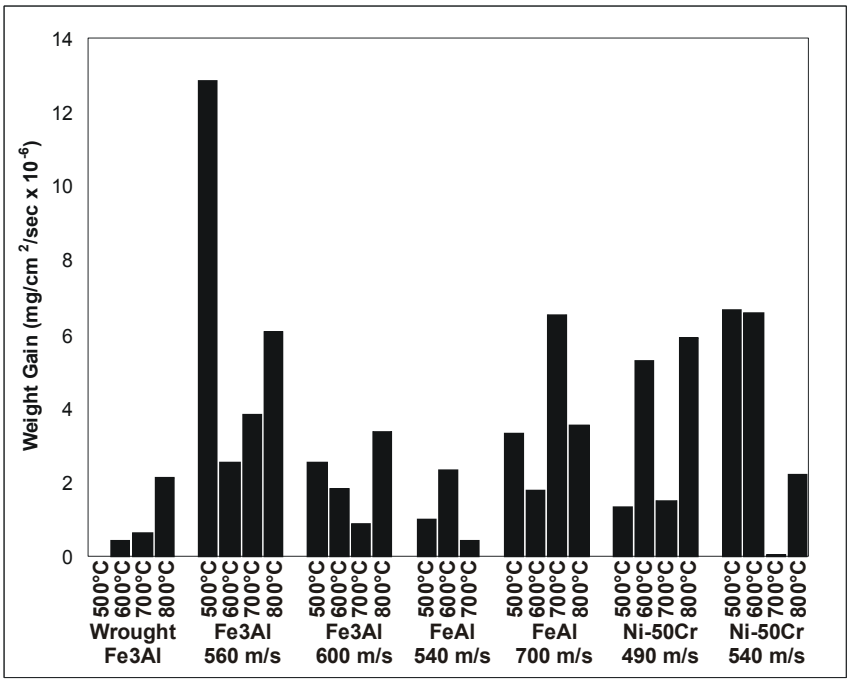

Figure 3: Comparison of linear weight gain rates in simulated coal combustion gas environment for different coating materials and temperatures.

GAS-SLAG CORROSION TESTING

SEM micrographs of typical corrosion layers for the different materials tested in the gas-slag environment are shown in Figures 4 through 7; Table 3 lists approximate average depths of attack. The iron aluminides were the most resistant; the behavior of wrought Fe_3Al and FeAl coatings was comparable. Fe_3Al and Ni-50%Cr coatings showed more attack. The Grade 91 steel was severely attacked in the isothermal test, much less so in the cyclic test; the reason for this is unknown. Corrosion depths were generally greater in the isothermal exposure, contrary to the expected accelerating effect of thermal cycling. A possible explanation for this effect is that the exposure duration in the cyclic tests was not equivalent to 100 hours. Only 75 one-hour hold periods were performed, and the additional time at temperatures near 700°C during heatup and cooldown may not have significantly contributed to the corrosion process, contrary to expectations. There was no significant effect of spray particle velocity in the FeAl and Ni-50%Cr coatings, but greater corrosion was observed for the Fe_3Al coating sprayed at the higher velocity.

Given the generally good corrosion resistance shown by the coatings in this series of tests, future work will focus on mechanical aspects of coating failure, i.e. adhesion and cracking resistance.

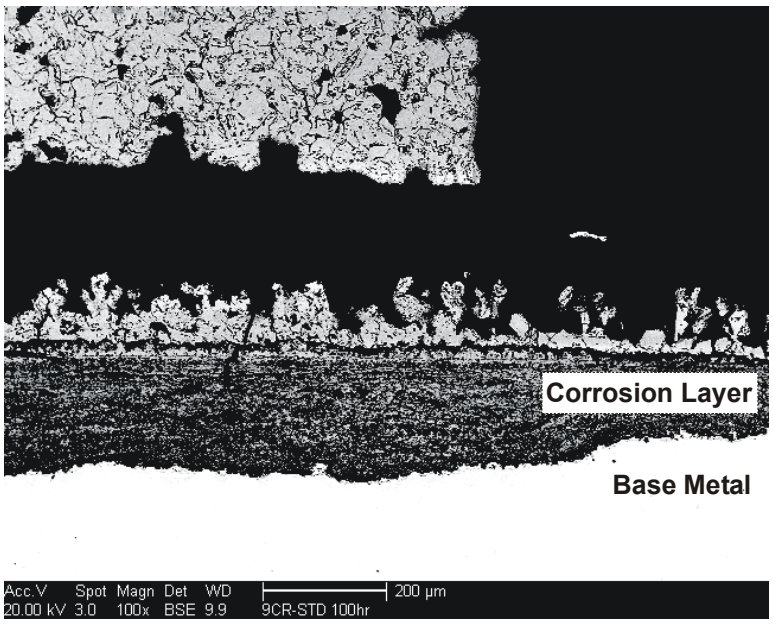

Figure 4: Typical corrosion layer observed in Grade 91 steel exposed to iron sulfide and simulated coal combustion gas at 700°C for 100 h (100X).

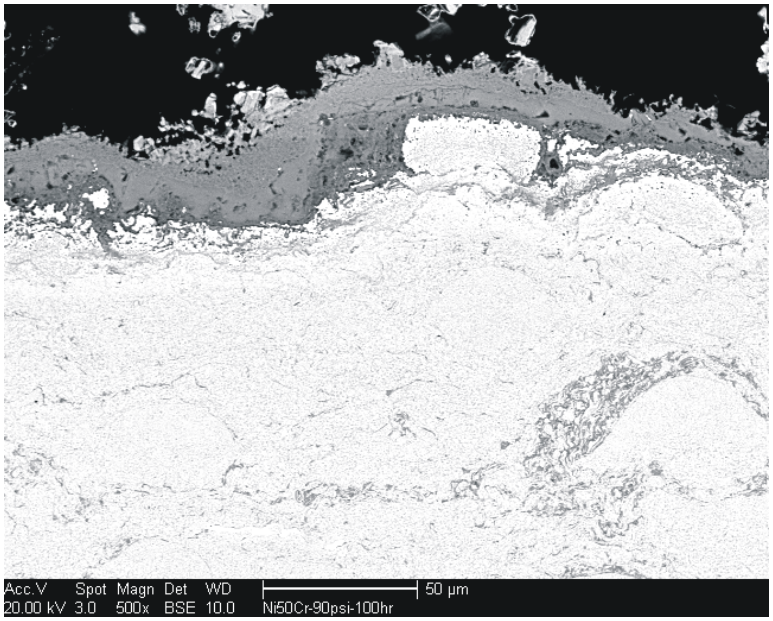

Figure 5: Typical corrosion layer observed in Ni-50%Cr coating sprayed at 540 m/s, exposed to iron sulfide and simulated coal combustion gas at 700°C for 100 h (500X).

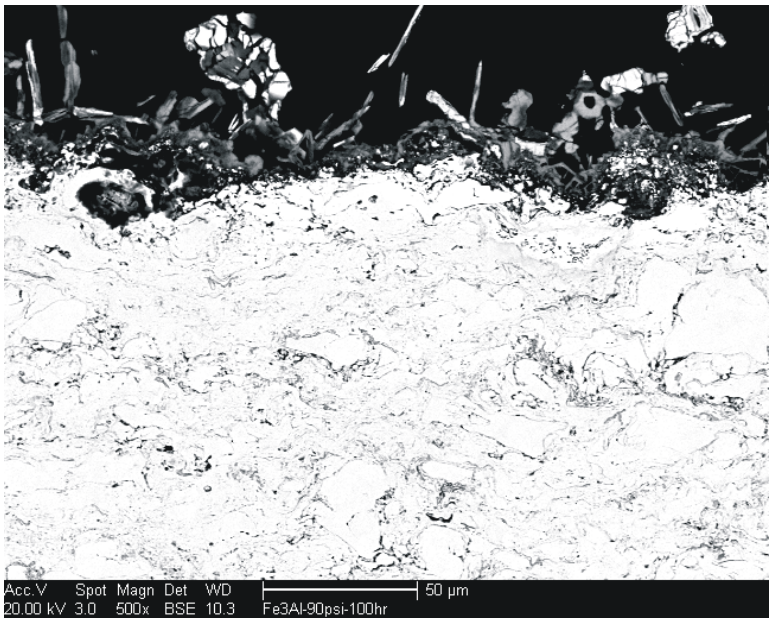

Figure 6: Typical corrosion layer observed in Fe_3Al coating sprayed at 620 m/s, exposed to iron sulfide and simulated coal combustion gas at 700°C for 100 h (500X).

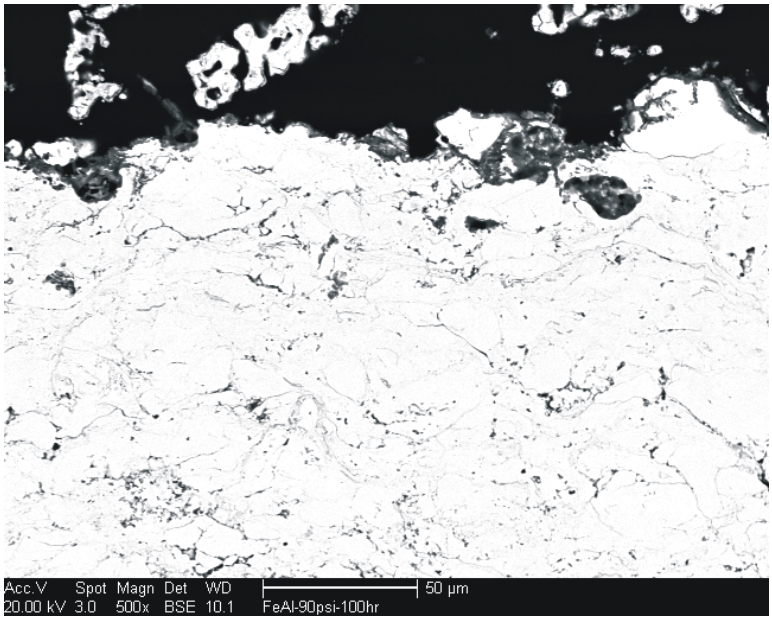

Figure 7: Typical corrosion layer observed in FeAl coating sprayed at 700 m/s, exposed to iron sulfide and simulated coal combustion gas at 700°C for 100 h (500X).

Table 3: Average corrosion depths observed in gas-slag corrosion tests

Material	Isothermal corrosion depth (µm)	Cyclic corrosion depth (µm)
Ni-50%Cr coating, 490 m/s	24	26
Ni-50%Cr coating, 540 m/s	27	20
FeAl coating, 540 m/s	3	3
FeAl coating, 700 m/s	4	1
Fe_3Al coating, 560 m/s	8	6
Fe_3Al coating, 620 m/s	20	11
Wrought Fe_3Al	5	1
Grade 91 steel	210	24

CONCLUSIONS

Chromia-forming Ni-50%Cr coatings were prepared by a HVOF thermal spray process and characterized. The microstructure and physical and mechanical characteristics are similar to other metallic HVOF coatings recently studied: low fractions of porosity and oxide are observed combined with compressive residual stresses. The performance of Ni-50%Cr coatings in corrosion tests in simulated coal combustion gas and gas-slag environments was slightly worse than FeAl and Fe_3Al coatings prepared by similar processes. The corrosion behavior of the iron aluminide coatings was only slightly worse than a wrought Fe_3Al-based alloy.

ACKNOWLEDGEMENTS

The authors wish to acknowledge the help of W.D. Swank and D.C. Haggard with coating preparation and T.C. Morris with metallography. This work was supported by the U.S. Department of Energy, Office of Fossil Energy, under contract DE-AC07-05ID14517.

REFERENCES

1. F. Masuyama: *ISIJ Int.*, 2001, vol. 41, pp. 612-25.
2. R. Viswanathan and W. Bakker: *Materials for Boilers in Ultra Supercritical Power Plants*. in *2000 International Joint Power Generation Conference IJPG2000*. 2000. Miami Beach, FL: ASME.
3. J.C. Nava and J. Henry: *Materials at High Temperatures*, 2003, vol. 20, pp. 55-60.
4. R.A. Rapp, J.H. DeVan, D.L. Douglass, P.C. Nordine, F.S. Pettit, and D.P. Whittle: *Materials Science and Engineering*, 1910, vol. 50, pp. 1-17.
5. T.C. Totemeier, R.N. Wright, and W.D. Swank: *J. Therm. Spray. Technol.*, 2002, vol. 11, pp. 400-08.
6. T.C. Totemeier, R.N. Wright, and W.D. Swank: *Metall. Mater. Trans. A*, 2003, vol. 34A, pp. 2223-31.
7. T.C. Totemeier, R.N. Wright, and W.D. Swank: *Intermetallics*, 2004, vol. 12, pp. 1335-44.
8. D.K. McDonald and E.S. Robitz: *Coal Ash Corrosion Resistant Materials Testing Program - Evaluation of the Second Section Removed in August 2003*. in *4th International Conference on Advances in Materials Technology for Fossil Power Plants*. 2004. Hilton Head, SC.
9. T.C. Totemeier and J.K. Wright: *Surf. Coat. Technol.*, 2006, vol. 200, pp. 3955-62.
10. J.R. Regina, J.N. DuPont, and A.R. Marder: *Corrosion*, 2004, vol. 60, pp. 501-09.
11. B.S. Covino, S.J. Bullard, S.D. Cramer, M. Ziomek-Moroz, S. Shrestha, and D. Harvey: *Corrosion Behavior of an HVOF-Sprayed Fe3Al Coating in a High-Temperature Oxidizing/Sulfidizing Environment*. in *4th International Conference on Advanced Materials Technology for Fossil Power Plants*. 2004. Hilton Head, SC: EPRI.
12. T.C. Totemeier and R.N. Wright: in *19th Annual Conference on Fossil Energy Materials*, National Energy Technology Laboratory, Pittsburgh, PA, 2005, available at www.netl.doe.gov.

NEW PROCESSING DEVELOPMENTS IN METALLIC POWDERS FOR FOSSIL ENERGY APPLICATIONS

Robert L. Terpstra
109 Metals Development, Ames Lab. (USDOE), Iowa State University, Ames, IA 50011
E-mail: terpstra@ameslab.gov; Telephone: (515) 294-5747; Fax: (515) 294-8727

Iver E. Anderson
222 Metals Development, Ames Lab. (USDOE), Iowa State University, Ames, IA 50011
E-mail: andersoni@ameslab.gov; Telephone: (515) 294-9719; Fax: (515) 294-8727

ABSTRACT

To promote the implementation of several emerging Fossil Energy technologies that utilize metal powders of specific size ranges and types, which are not currently efficiently produced by industrial powder makers, further advancements are needed in the fundamental understanding and design of high efficiency gas atomization nozzles to maximize powder yields in specific size ranges with reduced standard deviation. Part I of the report describes a continued effort to advance powder production goals, where an atomization nozzle capable of delivering a high volumetric gas flow rate was designed, fabricated, and tested. Coupled with a ceramic (ZrO_2) version of our slotted trumpet bell pour tube, the latest trial on Fe-16Al-2Cr (wt.%) demonstrated the ability to initiate pre-filming of the liquid metal stream and to promote spray uniformity at a nozzle manifold pressure of 2.0 MPA (290 psi). Part II of this report includes a study that probes the feasibility of a new process to address the high production cost of mechanically alloyed (MA) oxide dispersion strengthened (ODS) alloy materials. To illustrate the innovative procedure, Fe-Cr-Y was gas atomized using the GARS technique after which the powder particles were consolidated to intentionally alter the initial powder particle microstructure and composition. The microstructure evolution was verified using SEM micrographs, and mapping techniques, as well as micro-hardness tests.

INTRODUCTION

Part I: This portion of this report builds on previous results of high velocity shear (open-wake) atomization with helium that provided high yields of high-purity, ultrafine (dia. < 20μm) Fe-16Al-2Cr (wt.%) powder for hydrogen membrane development. It should be noted, however, that the experiments that explored this control capability utilized a nozzle configuration that was designed to maximize the simplest atomization mechanism, i.e., "shearing" of melt surface waves by a high velocity gas flow traveling in a substantially parallel path. Since common industrial atomizers typically lack He gas supply and recycling systems due to their increased costs, a two-stage (shear/shock disruption) gas atomization mechanism was selected as an alternative to the single-stage shear mechanism of He atomization for this task. Closed-wake atomization gas flows in gases of higher density (Ar, N_2) are known to produce this two-stage effect.

One major stumbling block to the industrial implementation of two-stage or closed wake atomization has been the high atomization gas manifold pressures needed to establish the desired "Mach disk" flow feature in the atomization zone of a close-couples nozzle[1], which is typically beyond the capacity of common atomization gas supply systems. Therefore, one major aspect of this work was to investigate the potential for reduction of the manifold pressure needed for wake closure by augmenting the volumetric flow within the atomization zone of a discrete jet nozzle with a high (45˚) apex angle that is generally preferred for wake closure intensity[2,3]. Such a discrete jet close-coupled atomization nozzle with high gas flow was intended to force the onset of wake closure to a lower manifold pressure, since an increased gas momentum would be involved in the concentrated flow region that surrounds the wake recirculation (atomization) zone[1].

Part II: Structural ODS alloys, typically Fe or Ni based alloys, offer high temperature creep strength and excellent corrosion/oxidation resistance up to temperatures of 1000˚ C and above and are well suited for FE applications[4]. As with almost any processes, MA, conventionally used to produce ODS materials, has inherent processing challenges that must be overcome to consistently produce a high quality, cost-effective product. First, the process is subject to contamination that can be traced several sources. The second hurtle is the high cost associated with the production of ODS materials due to the extended milling times required produce the desired microstructure of the composite

ODS powder particles[5]. Compared to the current ODS production process, the proposed technique can supply an uncontaminated atomized powder feedstock consisting of the desired alloy composition, particle size, as well as dispersion size and yield[6]. Such atomized powder may offer a cleaner more uniform feedstock, without the high cost of MA.

Figure 1 illustrates a simplified process to produce ODS metallic particles. The proposedprocess design involves a combination of metal alloy design and gas atomizing parameters. The process design considers four alloying components: 1) a base metal, 2) alloying metal(s), 3) a dispersoid forming metal, and 4) a reactive gas. The base metal and alloying metal(s) are selected to achieve the fundamental material properties required for the final product application. The disperoid forming metal, added at a concentration level to generate a supersaturated liquid alloy, is typically selected such that when in the presence of a reactive gas, it forms a metal oxide dispersoid within the metal matrix of the powder particle. During the atomization process, the reactive gas, which can be supplied via a carrier atomization gas, provides the catalyst to trigger the dispersion forming reaction in-situ during the atomization process.

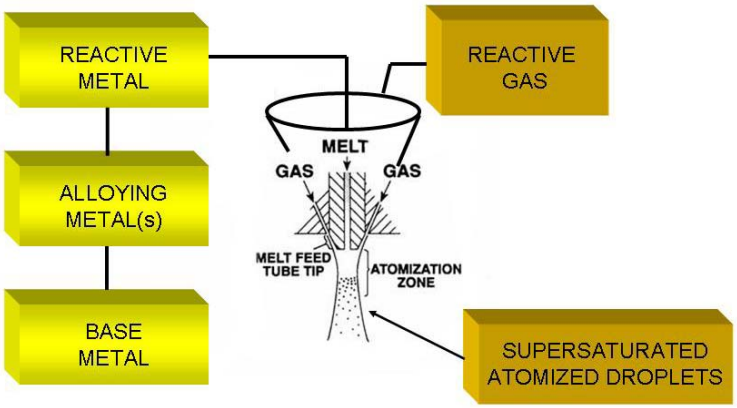

Figure 1: A series of alloy design steps to be considered to produce an atomized ODS alloy.

I. EXPERIEMENTAL PROCEDURE

The effect of a highly concentrated atomization gas flow on the wake closure pressure was studied with two versions of a cylindrical discrete jet nozzle that shared the same apex angle and central bore diameter (10.4 mm). For this test, the augmented volumetric flow rate was accomplished by increasing the diameter for each jet in the circular discrete jet array, while maintaining a the same 45˚ jet apex angle and nozzle throat diameter of 10.4 mm (0.904 in.). Figure 2 schematically illustrates that increasing the jet diameter from 0.737 mm (0.029 in.) to 1.274 mm (0.052 in.) reduces the number of jet from 30 to 22 jets while maintaining the same jet spacing and nozzle throat diameter while increasing the total jet exit area and relative gas flow capacity by a factor of 2.4.

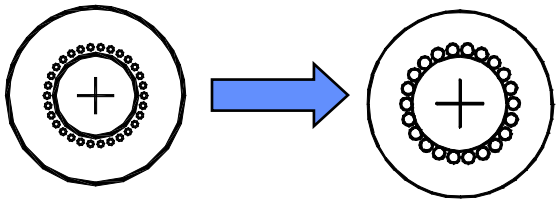

Figure 2: Schematic bottom-view of the enlargement of the jet diameters from 0.737 mm to 1.274 mm.

For this study, gas-only flow studies (schlieren imaging and orifice pressure measurements) were performed on a nozzle bench test apparatus with both Ar and N_2 atomization gases to investigate any differences that could arise, although Ar has been pre-selected to perform an experimental atomization test due to its complete lack of reactivity with the Fe-16Al-2Cr melt. The objective is to compare the powder size distribution resulting from a closed wake two-stage atomization process with that resulting from the previous He atomization trials.

Compared to the previous He gas atomization trials for the Fe-16Al-2Cr alloy that used an HPGA I (45-30-029) nozzle with flat base pour tube, the Ar atomization experiment used an HPGA I (45-22-052) atomization nozzle with a trumpet bell slotted pour tube[7]. Both nozzles were described in detail above and are shown schematically in Figure 2. Based on the results of the high flow nozzle study, a manifold pressure of only 2.0 MPa was selected to conduct an atomization experiment of Fe-12.5Al-2.0Cr using the HPGA I (45-22-052) nozzle using argon as the atomization gas. The size distribution of the powder produced was analyzed with a set of ASTM standard screens < 140 mesh (106 µm) and compared to the average of the 3 He atomization experiments previously reported[6].

I. RESULTS and DISCUSSION

Comparison of the gas flow field behavior of the new high flow nozzle, HPGA I (45-22-052), to the more conventional HPGA I (45-30-029) nozzle revealed that a major orifice aspiration pressure minimum, which typically represents the onset of wake closure, occurred in the high flow nozzle at roughly half of the manifold pressure of that feature with the conventional nozzle, as shown in Figure 3. To confirm this finding, schlieren gas flow images were collected in parallel with the orifice aspiration measurements, shown in Figure 4. Analysis of these images reveals the development of a Mach disk (indicated by the arrows) is realized at a manifold pressure of approximately 2.0 MPa. The appearance of a Mach disk feature indicates the onset of wake closure in the atomization gas flow field that correlates exactly with the minimum point in the orifice aspiration pressure measurements.

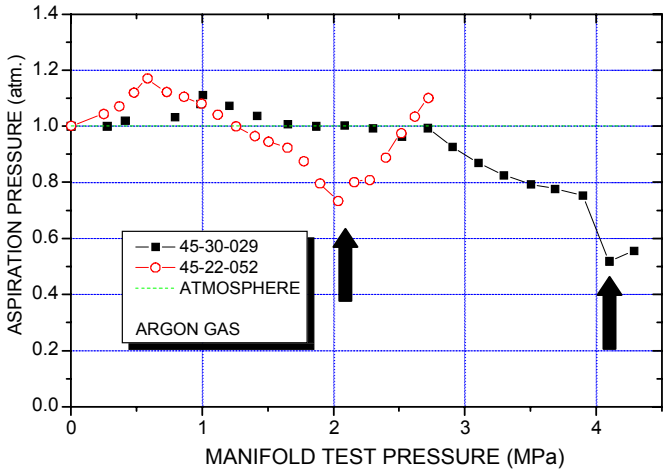

Figure 3: Comparison of the orifice aspiration pressure for 45-30-029 and 45-22-052 nozzles.

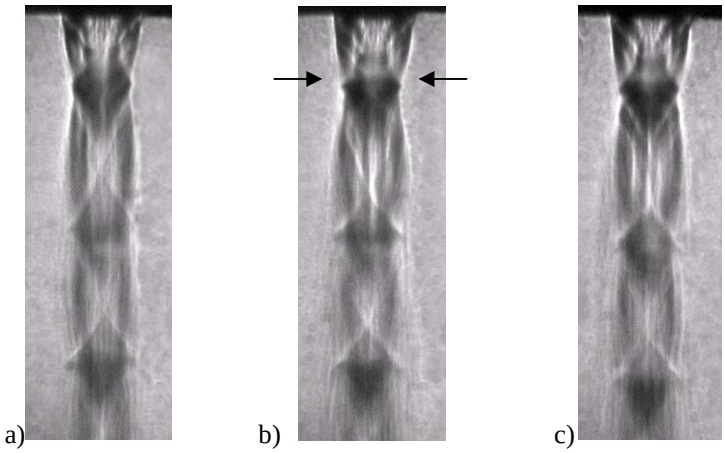

Figure 4: Schlieren gas flow images of Ar gas at pressures of a) 1.9 MPa, b) 2.0 MPa, and c) 2.1 MPa.

Sieve size distribution analysis of the resulting powder, as shown in Figure 5, revealed that the d_{50} or average particle dia. is 35 µm. The standard deviation of the powder size distribution is 1.7, as calculated by d_{84}/d_{50}. The cumulative particle size distribution results are compared in Figure 5 with data from the average of the other He atomization experiments for Fe-16Al-2Cr. All 3 of the He atomization experiments used open wake gas flow conditions, but the current Ar experiment operated with closed wake gas flow, as mentioned above. Another difference between the parameters is the choice of the interior profile of the melt pour tube, i.e., the current experiment used the trumpet bell slotted pour tube[7] and the other previous runs used the cylindrical flat base tube. It should be noted that the average particle diameter (APD) of the average of the three He runs was only slightly smaller than the APD of the Ar run. However, the G/M of the Ar run was unusually high, which would have contributed to enhanced particle size refinement. However, the average standard deviation of the He atomization runs was greater than that of the Ar atomization run, consistent with typical He atomization results, although the 1.7 value for the Ar run is more narrow than conventional results, consistent with the results for nitrogen atomization of pure Fe that used the same type of slotted trumpet bell pour tube[8].

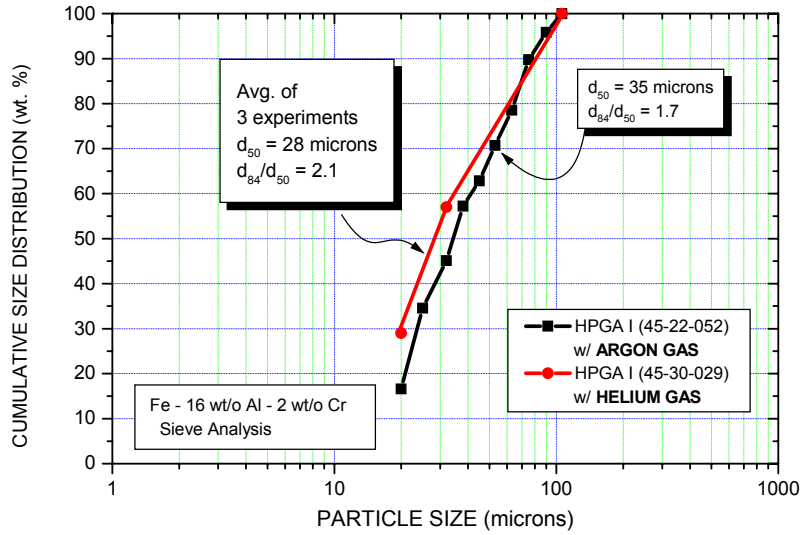

Figure 5: Comparison of cumulative size distribution results from ASTM sieve analysis.

Probably the most important technological result to arise from the current study is the discovery that the high flow nozzle, HPGA I (45-22-052) is capable of closed wake operation at a manifold pressure of only 2.0 MPa (290 psi) for argon gas. Thus, with an atomization gas supply system that is sized adequately (with minimal pressure drops), it may be possible to perform an effective two-stage atomization process with either a low pressure compressor or from cryogenic boil-off from a standard liquid gas storage vessel[9]. While this low-pressure wake closure was established for Ar gas, which was preferred for the current experiment on generation of Fe-16Al-2Cr powder because of its inert nature, it was also decided to investigate nitrogen gas behavior in the same nozzle. By the same criteria as the Ar results, the critical manifold pressure for wake closure with nitrogen appears to be only 1.8 MPa. Again, this aspiration result was verified by analysis of schlieren images, which shows the appearance of a sharp Mach disk at a pressure of 1.8 MPa, in exact agreement with the orifice aspiration result[8].

Although the relatively low pour rate for the molten Fe-16Al-2Cr may have helped to reduce the mean diameter of the resulting powder[8], the intense two-stage atomization mechanism of the closed wake atomization gas flow probably also contributed to highly effective production of these ultrafine powders. Also, the use of the slotted trumpet bell pour tube seems to have been useful again for promoting a narrow standard deviation of only 1.7. Clearly, the potential for use of the combined high flow nozzle and slotted trumpet bell pour tube for closed wake atomization appears great, especially for production of high yields of ultrafine powders. Also, the possibility of using closed wake nitrogen gas (where permitted by melt reactivity considerations) at an even lower pressure would provide further economy for the atomization gas that is consumed during this type of ultrafine powder production process.

I. SUMMARY

Gas-only flow was studied by schlieren imaging and orifice pressure measurements on a set of atomization nozzles designed for closed-wake operation. The results showed that a new high flow nozzle produced a low onset pressure of 2.0 MPa (290 psi) for wake closure, measured at the nozzle manifold, when operated with Ar gas. Subsequently, Fe-16Al-2Cr was atomized with closed wake Ar flow from the high-flow nozzle under comparable melt parameters to the He gas runs and the powder size yield proved to be very similar to previous He atomization results.

II. EXPERIMENTAL PROCEDURE

Incoloy MA956 was selected as a benchmark alloy for comparative purposes. Incoloy MA 956 is an iron based ODS superalloy steel having a nominal composition of Fe-20 Cr-4.5 Al-0.5Ti-0.5Y_2O_3 (in wt. %) that has demonstrated excellent mechanical strength and oxidation resistance to temperatures up to 1300° C for extended periods of time[4]. In an effort to develop a similar iron based alloy, ANSI 410 stainless steel containing 10.5 – 13.5 Cr, 0.15C,1.0 Mn, 1.0Si, 0.04P, and 0.03S (in wt. %) was selected as a test alloy to be modified by this novel ODS approach.

Atomization experiments were carried out using the Ames Lab high pressure gas atomizer operated by the Materials Preparation Center of Ames Laboratory. Two unique alloys were designed and atomized using identical atomization parameters. The experimental alloys in wt.% were: 1) Fe-12.5Cr-1Y and 2) Fe-13.5Cr-2Y. Both alloys were atomized at an atomization pour temperature of 1750° C using high purity argon mixed with 5 vol. % oxygen.

The powder produced during the atomization experiments was collected and sieved to generate size distributions having particle diameters less than 20μm and particle diameters between 20 - 53 μm. The powders sized 20 - 53 μm from both alloys were consolidated using hot isostatic pressing (HIP) for 2 hrs. at 1300° C under 303 MPa pressure. After the HIP process, a portion of each alloy sample was heat treated for 2 hrs. at 1300° C in a 10^{-6} Torr vacuum furnace. Portions of the HIP samples were evaluated using transmission electron microscopy (TEM) and scanning electron microscopy (SEM) techniques, as well as hardness testing.

II. RESULTS and DISCUSSION

The first task of this study was to determine if it was possible to form dispersions of Y_2O_3 within the metal matrix of the atomized powder particles. Figure 6 contains SEM micrographs of the as atomized powder surface morphology and a cross sectional view. The cross sectional view reveals the presence of a surface shell, approximately 1 – 3 μm thick. The composition of the shell, analyzed using energy dispersive spectroscopy (EDS), appears to be a chrome oxide that formed as the liquid metal droplet cooled.

Unfortunately, efforts to prepare TEM foils of the as-atomized powders of both alloys have not yet been successful, preventing direct evidence of in-situ dispersoid formation from being observed. However, the partial consolidation of the spray deposit sample was more conducive to TEM foil preparation and the results were described in a recent report[10].

a) 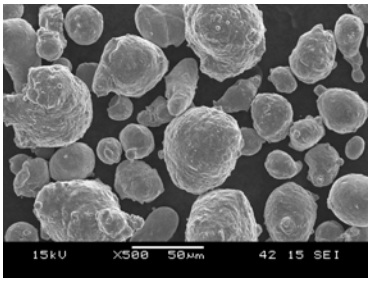

b) 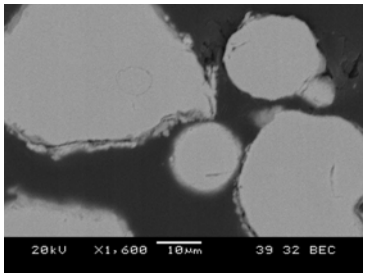

Figure 6: SEM micrographs of: a) atomized powder b) cross section of atomized powder.

Figure 7 is an EDS map of Fe-12.5Cr-1Y powder, 20 < dia.<53µm, after full consolidation by HIP. The map reveals the relative concentration of the alloy constituents in this un-etched metallographic cross-section. As can be seen in the map, the concentration of the Fe, Cr, and O_2 are closely correlated with the prior particle grain boundaries. Whereas the Y appears to be more generally distributed throughout the metal matrix and adjacent to the prior particle boundaries.

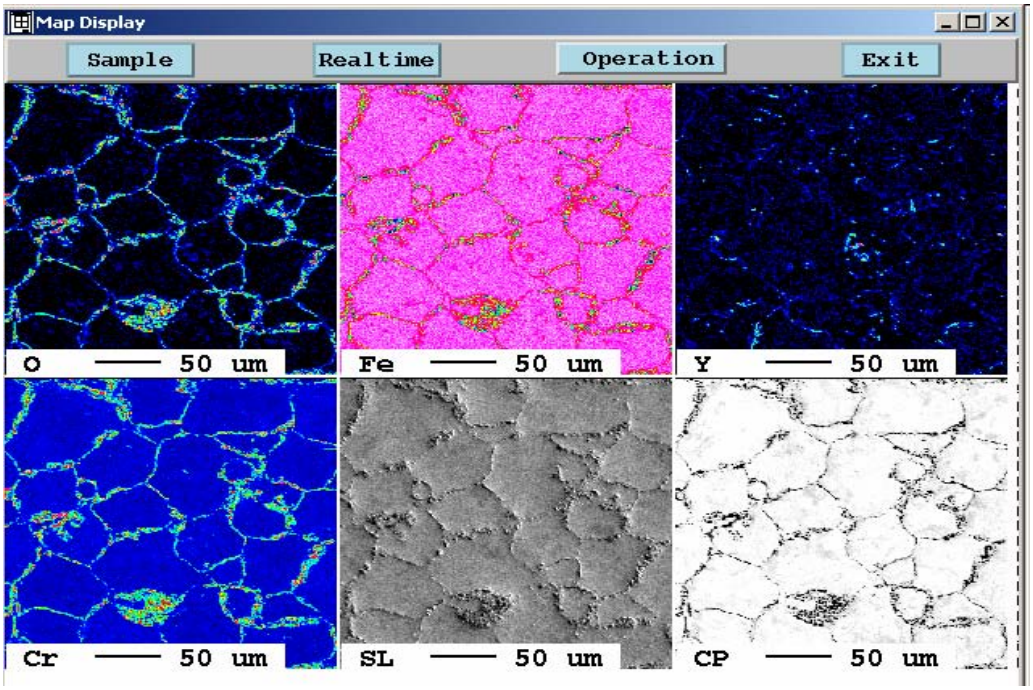

Figure 7: EDS map of as-HIP Fe-12.5Cr-1Y.

TEM foils were prepared form the as-HIP samples. The TEM images shown in Figure 8 and EDS analysis indicate that dispersions of reacted yttrium ($Y_2O_{3)}$ and un-reacted yttrium (Y) were formed within the powder particle during the atomization process for both alloys. As can be seen in Figure 6a and b, the dispersoid size and spacing are comparable to the size and spacing cited for MA ODS materials[4]. Also shown in the TEM images are examples of dislocation pinning due to the presence of the dispersoids, potentially enhancing the mechanical strength of the alloy at elevated temperatures.

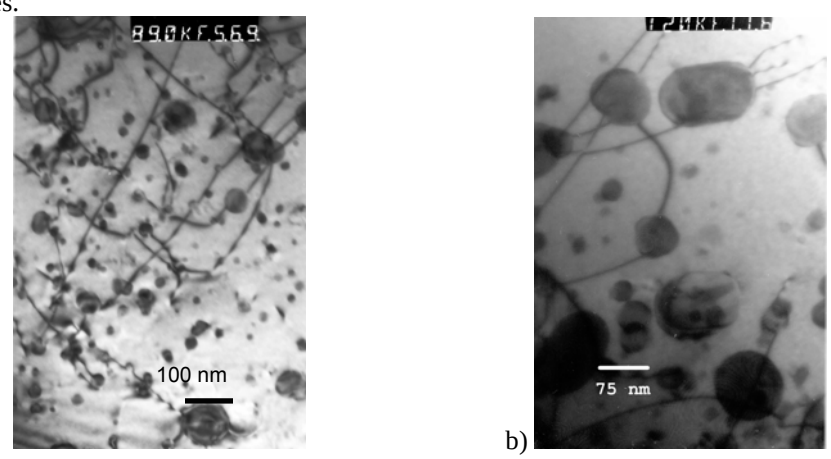

a) b)

Figure 8: TEM Images of a) Fe-12.5Cr-1Y and b) Fe-13.5-2Y.

Hardness measurements were conducted on the as-HIP samples of each alloy and then compared to the hardness of MA 956 and the ANSI 410 stainless steel. The results of the hardness test are shown in Table 1. This data indicates that the as-HIP sample of the Fe-Cr-1wt%Y has a hardness that is comparable to the commercially available MA

956 alloy and nearly twice the hardness of the 410 stainless steel alloy. The hardness of the Fe-13.5Cr-2Y alloy appears to be significantly lower than the hardness of the MA 956 alloy. More testing is on-going to identify the primary factors that influence the hardness of these alloys and to design more optimum heat treatments.

ALLOY	MA 956	410 SS	Fe-12.5Cr-1Y	Fe-13.5Cr-2Y
HV	383	172	374	278

Table 1: Hardness test results.

As stated earlier, conventional MA fabrication requires and relies on extrusion, hot working, and heat treatment to promote the secondary recrystallization required to produce the desired ODS microstructure and resulting material properties. However, given that the hardness (Table 1) along with the size and distribution of the Y_2O_3 (Figure 8a) of the as HIP Fe-12.5-1Y are comparable to the properties reported for the commercially produced MA 956 alloy, there appears to be the potential to produce ODS material with controlled grain size without relying on the secondary recrystallization. Producing the desired grain size containing a Y_2O_3 dispersoid laden microstructure without relying on secondary recrystrallization would contribute to improving the quality/uniformity of the ODS material while reducing processing cost. Figure 9 schematically illustrates a conceptual process that incorporates gas atomized ODS powder followed by an appropriate consolidation cycle (HIP/hot extrusion) followed by heat treatment.

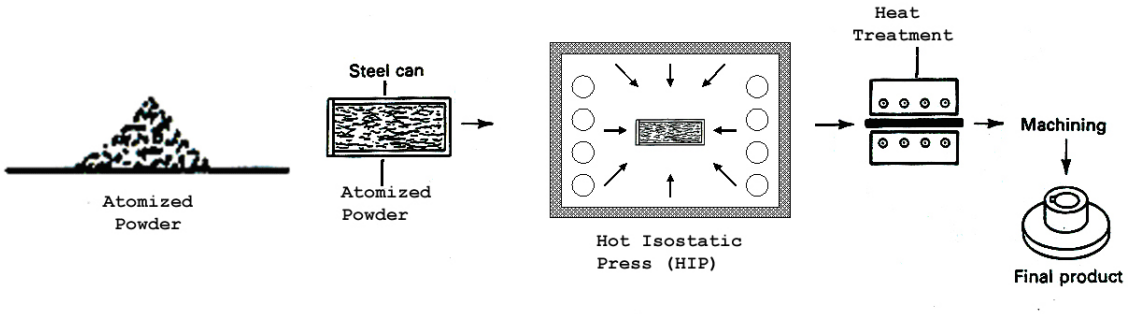

Figure 9: A schematic illustrating a potential ODS production process with reduced processing steps.

II. SUMMARY

The purpose of this study was to investigate the feasibility of producing ODS powder using a combination of alloy design and gas atomization procedures. This study included two Fe-based alloys containing small amounts of yttrium that were reacted with an argon atomization gas containing 5 vol.% oxygen. TEM micrographs verified the formation of reacted and un-reacted yttrium dispersoids located within the metal matrix of the powder particles, as well as along the prior particle boundaries. The TEM micrographs also illustrated that the size and spacing of the dispersoids were similar to that seen in commercial ODS alloy materials. Based on the size and distribution of the dispersoids within the particle matrix and the comparable hardness test data, there appears to be the potential to produce ODS material with controlled grain size without relying on the secondary recrystallization process.

ACKNOWLEDGEMENTS

The authors would like to acknowledge the Ames Laboratory Materials Preparation Center and staff for their efforts in supporting this study. Support from DOE-FE (ARM program) through Ames lab contract no. 7405-Eng-82 is gratefully acknowledged.

REFERENCES

1. J. Ting and I.E. Anderson, "A computational fluid dynamics (CFD) investigation of the wake closure phenomenon," *Materials Science and Engineering*, **A379**, (2004), pp. 264-276.

2. I. E. Anderson, R. S. Figliola, and H. Morton, "Flow Mechanisms in High Pressure Gas Atomization", *Materials Science and Engineering* **A148**, 1991, pp.101-114.
3. I. E. Anderson, R. S. Figliola, R. L. Terpstra, S. Rau and B. Rauscher, "Progress in Experimental Analysis of Gas Atomization Process Physics", *Advances in Powder Metallurgy and Particulate Materials*, compiled by V. Arnhold, C.-L. Chu, W.F. Jandeska, and H. I. Sanderow, Metal Powder Industries Federation, Princeton, NJ, 2002, part 3, pp. 150-162.

4. C. Suryanarayana, "Oxide-Dispersion Strengthened alloys", ASM Handbook Online, Powder Metals Technologies and Applications, 2002, vol. 7, www.asminternational.org/hbk/index.jsp.

5. C. Suryanarayana, "Powder Contamination", ASM Handbook Online, Powder Metals Technologies and Applications, 2002, vol. 7, www.asminternational.org/hbk/index.jsp

6. I.E. Anderson, R.L. Terpstra, "Dispersoid Reinforced Alloy Powder and Method of Making, U.S. Patent application filed May 8, 2006.

7. I.E. Anderson and R. L. Terpstra, "Progress Toward Gas Atomization Processing with Increased Uniformity and Control," *Materials Science and Engineering*, **A326**, (2002), p. 101.

8. I.E. Anderson, R. L. Terpstra, J.A. Cronin, and R.S. Figliola, "Verification of Melt Property and Closed Wake Effects on Controlled Closed-Coupled Gas Atomization Processes", *Advances in Powder Metallurgy and Particulate Materials-2006*, compiled by W. R. Gasbarre and J.W. von Arx, Metal Powder Industries Federation, Princeton, NJ, 2006, (accepted for publication).

9. J. T. Strauss, "Low pressure Close-Coupled Gas Atomization" *Advances in Powder Metallurgy and Particulate Materials,* Vol. 3. compiled by J. J. Oakes and J. H. Reinshagen, MPIF-AMPI, Princeton, NJ, (1998), pp. 10-3 to 10-11.

10. R. L. Terpstra, I.E. Anderson, F. A. Laabs, J. R. Rieken, "Simplified Powder of Oxygen Dispersion Stainless Steel", *Advances in Powder Metallurgy and Particulate Materials-2006*, compiled by W. R. Gasbarre and J.W. von Arx, Metal Powder Industries Federation, Princeton, NJ, 2006, (accepted for publication).

STEAM TURBINE MATERIALS AND CORROSION

Gordon R. Holcomb
NETL-Albany, 1450 Queen Ave SW, Albany, OR 97321
Email: holcomb@alrc.doe.gov; Telephone: (541) 967-5874; Fax: (541)-967-5914

Malgorzata Ziomek-Moroz
NETL-Albany, 1450 Queen Ave SW, Albany, OR 97321
Email: moroz@alrc.doe.gov; Telephone: (541) 967-5943; Fax: (541)-967-5914

ABSTRACT

Ultra supercritical (USC) power plants offer the promise of higher efficiencies and lower emissions. Current goals of the U.S. Department of Energy's Advanced Power Systems Initiatives include coal generation at 60% efficiency, which would require steam temperatures of up to 760°C. This research examines the steamside oxidation of alloys for use in USC systems, with emphasis placed on applications in high- and intermediate-pressure turbines.

The list of alloys being examined is discussed, including the addition of new alloys to the study. These include alloy 625, selected because of its use as one of the two alloys used for turbine rotors, valves, casings, blading and bolts in the European AD700 full-scale demonstration plant (Scholven Unit F). The other alloy, alloy 617, is already one of the alloys currently being examined by this project. Other new alloys to the study are the three round robin alloys in the UK-US collaboration: alloys 740, TP347HFG, and T92.

Progress on the project is presented on cyclic oxidation in 50% air – 50% water vapor, furnace exposures in moist air, and thermogravimetric analysis in argon with oxygen saturated steam. An update on the progress towards obtaining an apparatus for high pressure exposures is given.

INTRODUCTION

For many years the temperatures and pressures of steam boilers and turbines were intentionally increased. These increases allowed for greater efficiencies in steam and power production, and were enabled by improvements in materials properties such as high temperature strength, creep resistance, and oxidation resistance. From 1910 to 1960, there was an average increase in steam temperature of 10°C per year, with a corresponding increase in plant thermal efficiency from less than 10% to 40%.[1] The first commercial boiler with a steam pressure above the critical value of 22.1 MPa (3208 psi) was the 125 MW Babcock & Wilcox (B&W) Universal Pressure steam generator in 1957—located at the Ohio Power Company's Philo 6 plant.[2] Since 1960 in the United States, the overall trend of increasing temperatures and pressures has stopped and stabilized at about 538°C and 24.1 MPa.[3] In Europe and Japan, where fuel costs are a higher fraction of the cost of electricity, temperatures and pressures continued to rise. An example of a state of the art power plant in Europe is the Westfalen (2004) plant, with steam conditions of 31.0 MPa/593°C/621°C.[4] It has a net plant efficiency of 43.5%, compared to 37% for a typical subcritical 16.5 MPa/538°C/ 538°C plant.[4] Today there is again interest in the United States for advanced supercritical power plants. Large increases in the cost of natural gas have led to the re-examination of coal power plants, and advanced supercritical plants offer advantages in lower fuel costs and lower emissions of SO_X, NO_X, and CO_2.[5]

Current U.S. Department of Energy research programs are aimed at 60% efficiency from coal generation, which would require increasing the operating conditions to as high as 760°C and 37.9 MPa. In general terms, plants operating above 24 MPa/593°C are regarded as ultra supercritical (USC), those operating below 24 MPa as subcritical, and those at or above 24 MPa as supercritical (SC).[3]

OBJECTIVES

The research aims to bridge the gap in information between various steam conditions to study the resistance of target alloys and the role of pressure in the corrosion mechanisms. The objectives of this project are to:

- Determine the steam oxidation behavior of target alloys to identify viable materials for use in ultra-supercritical steam (USC) turbines.
- Determine the role of pressure on oxidation mechanisms.
- Examine curvature effects on spallation.

TECHNICAL PROGRESS

ALLOYS

Six alloys were investigated at the start of this research effort: Save12 (9.5Cr and 10.5Cr versions), HR6W, Haynes 230, Inconel 617 and Inconel 740. The compositions of these alloys are shown in Table 1. All are high strength alloys that were part of the Advanced Power System Initiative on USC boilers.[6] Then two superalloys identified[7-8] by EPRI as candidates for blade materials for USC conditions were added: Nimonic 90 and Inconel 718. Two NETL developed alloys, J1 and J5, were produced for alloy development into low coefficient of thermal expansion (CTE) alloys.[9] J1 has an equivalent composition to Mitsubishi alloy LTES700, a low CTE nickel-base alloy developed for use as fasteners and blades in both current and USC steam turbines.[10] Alloy J5 is a modified version of J1 for solid oxide fuel cell applications (Al was removed to prevent insulating alumina formation and was Mn added to promote Cr-Mn spinel formation for reduced Cr-oxide evaporation).

Table 1

Alloy compositions. Analysis types: XRF is x-ray fluorescence, Cert is a manufacturer's certificate for the specific heat, and Nom is a nominal composition.

Alloy	Analysis	Fe	Cr	Ni	Co	Mo	Nb	Mn	Si	Ti	Al	Other
SAVE12-9.5Cr	XRF	83.0	9.5	0.4	2.6	0.04	0.05	0.5	0.4	0.02		2.9 W 0.3 V
SAVE12-10.5Cr	XRF	82.9	10.3	0.2	3.0		0.06	0.5	0.8	0.01		2.9 W 0.3 V
HR6W	XRF	24.2	23.6	43.4	0.4	0.2	0.2	1.0	0.3	0.2	0.04	6.1 W 0.1 Cu
Inconel 230	XRF	1.3	22.6	58.8	<0.05	1.3		0.5	0.3		0.4	14.3 W
Inconel 617	XRF	0.6	21.9	54.0	11.8	9.5		0.7	0.1	0.5	1.0	0.01 V
Inconel 740	Cert	0.5	24.4	Bal	20.0	0.5	2.0	0.3	0.5	1.8	1.0	
Nimonic 90	XRF	1.5	19.2	59.7	15.6	0.12	0.04	0.02	0.3	2.3	1.2	0.06 Cu
Haynes 718	Cert	18.1	18.0	53.8	0.2	3.0	5.3	0.2	0.08	1.0	1.6	0.04 Cu
J1	Nom		12.1	Bal		18				1	0.8	
J5	Nom		12.5	Bal		22		0.5		1		0.04 Y
Inconel 625	Nom	<5	21.5	Bal	<1	9	*	<0.5	<0.5	<0.4	<0.4	Nb+Ta = 3.6
T92	Nom		9	<0.4		0.5		0.5	<0.5		<0.04	1.75 W 0.2 V 0.07 Cb
TP347HFG	Nom	Bal	18	11			*	2.0	1.0			Nb+Ta≥10xC

Recently, additional alloys were added to the research program. Inconel 625 is one of two alloys used for turbine rotors, valves, casings, blading and bolts in the European AD700 full-scale demonstration plant (Scholven Unit F).[11] (The other alloy, Inconel 617, was already one of the alloys currently being examined by this project). The US/UK

Collaboration on Energy R&D: Clean Coal Technology Advanced Materials Program has led to the inclusion of three round-robin testing alloys: Inconel 740, T92, and TP347HFG. Thus there are two versions of Inconel 740 in the study. At this time there are no results for Inconel 625 or the US/UK alloys.

All surfaces on each sample (except where noted) were polished to 600 grit. Curvature effects were examined on Save12 (10.5Cr) and HR6W by machining samples from thick walled pipe. Each of the curvature samples had one curved surface, representing either the inside (concave) or outside (convex) surface of a pipe, Fig. 1. The curved surfaces were machined from as-received pipe (to remove mill-scale) and not subsequently polished to 600 grit.

Fig. 1. Section of Save12 10.5Cr pipe (2-in O.D.) and curvature samples cut from pipe. All but one side of the curvature samples are flat. Samples: concave (left) and convex (right).

SUPERCRITICAL STEAM

A test loop in supercritical steam with temperatures and pressures up to 760°C (1400°F) and 37.9 MPa (5500 psi) was designed. The material of construction for the autoclave was to be Rene 41. The autoclave was due for delivery on 12/31/2004. After much delay, the contract for the autoclave was cancelled. After consultation with autoclave manufactures, a new solicitation (DE-RQ26-06NT00425) was posted on 5/4/2006 for a system with temperatures and pressures up to 746°C (1375°F) and 34.5 MPa (5000 psi), Fig. 2. The new material of construction is to be Haynes 230. The feed water system, shown in Fig. 3, will allow for measurement and some control of water chemistry (pH, dissolved oxygen (DO), and conductivity). Tests would be done to represent an oxygenated system with 150-200 ppb DO and a pH of 9.2 to 9.6.

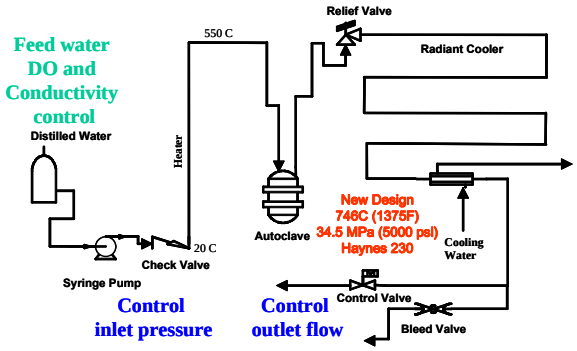

Fig. 2. Supercritical test loop for exposures in supercritical steam with temperatures and pressures up to 746°C (1375°F) and 34.5 MPa (5000 psi). Autoclave size of 1 liter.

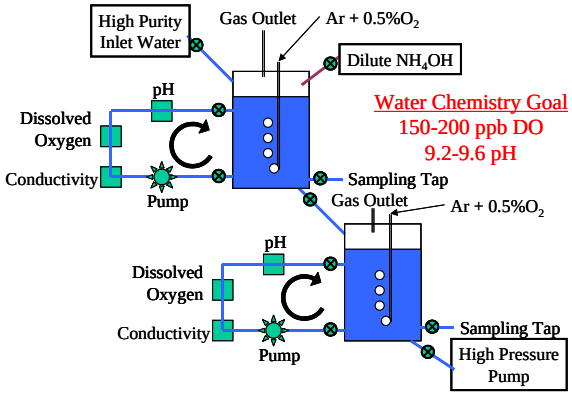

Fig. 3. Feed water system for supercritical steam exposures.

CYCLIC OXIDATION

Cyclic oxidation experiments were conducted in air in the presence of steam at atmospheric pressure. This was designed to examine the adhesion and spallation behavior of the protective oxides that form. The tests consisted of 1-hour cycles of heating and cooling (55 minutes in the furnace and 5 minutes out of the furnace) in a tube furnace equipped with a programmable slide to raise and lower the samples. Water was metered into the bottom of the furnace along with compressed air (50% water vapor-50% air, by volume). The exposure temperature for these initial tests was 760°C. Both flat and curvature samples were examined.

Results are shown in Figs. 4-9. Overall, all of the nickel-base alloys have relatively thin oxide scales and also have internal oxidation. Of these, Inconel 740 and Haynes 230 have scales with the least amount of metal damage. Both of these also have slowly declining masses with test duration, which is probably due to Cr-oxide evaporation. No spalling was observed in the collection cups used to hold the samples during removal from the apparatus for mass measurement. While not definitive (spalling could have occurred within the furnace), other alloy systems examined with this apparatus have shown spalling in the collection cups.

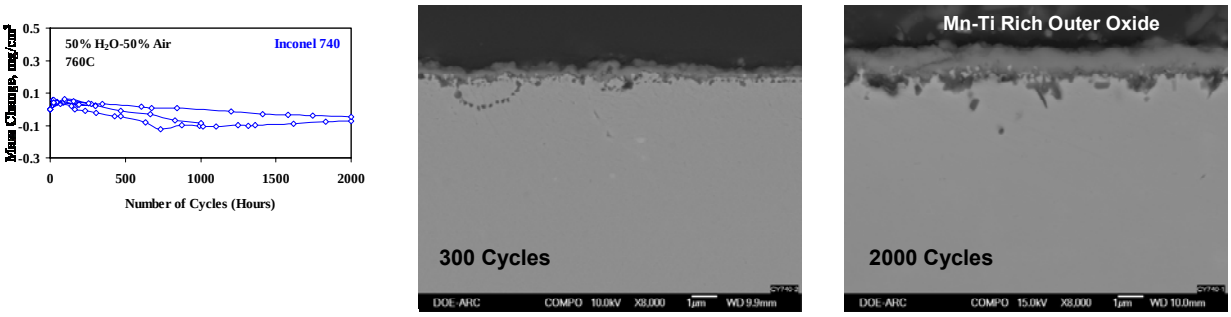

Fig. 4. Cyclic test results for Inconel 740 in 50%H_2O-50% air at 760°C.

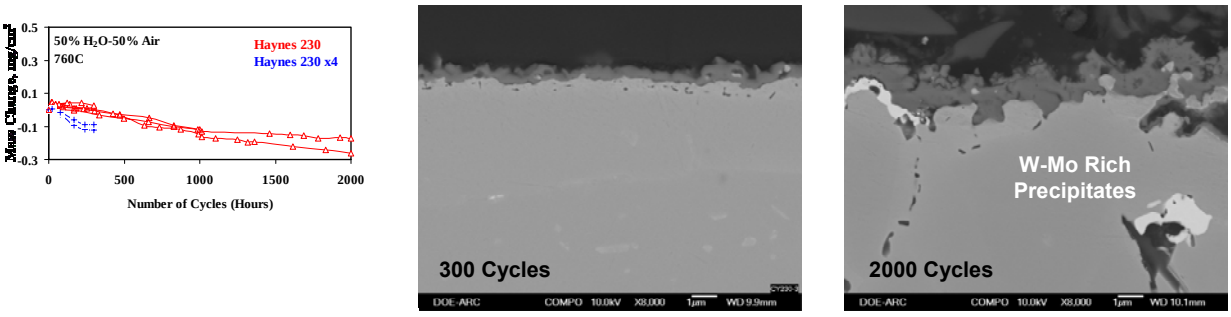

Fig. 5. Cyclic test results for Haynes 230 in 50%H_2O-50% air at 760°C.

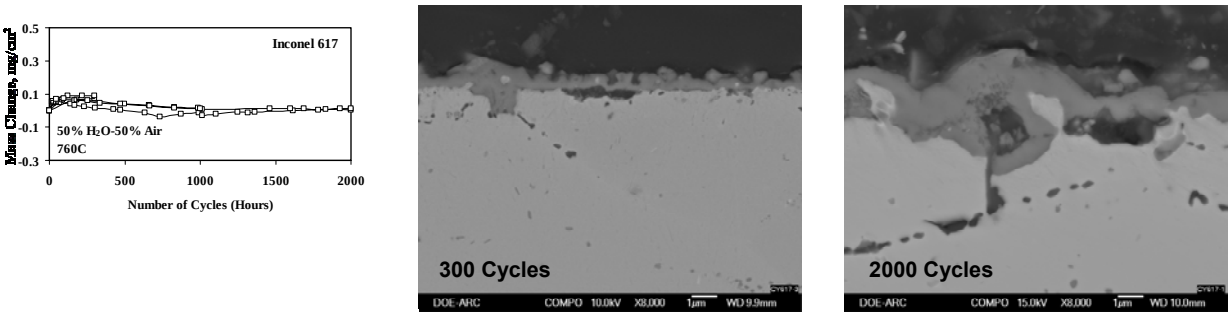

Fig. 6. Cyclic test results for Inconel 617 in 50%H_2O-50% air at 760°C.

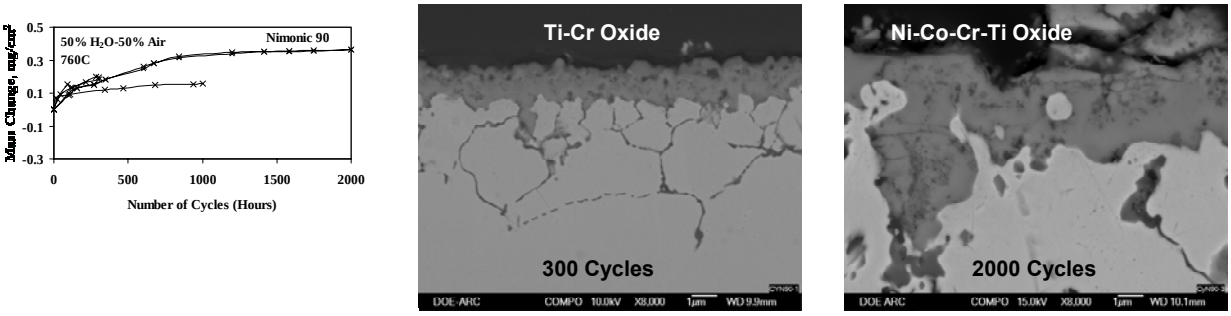

Fig. 7. Cyclic test results for Nimonic 90 in 50%H_2O-50% air at 760°C.

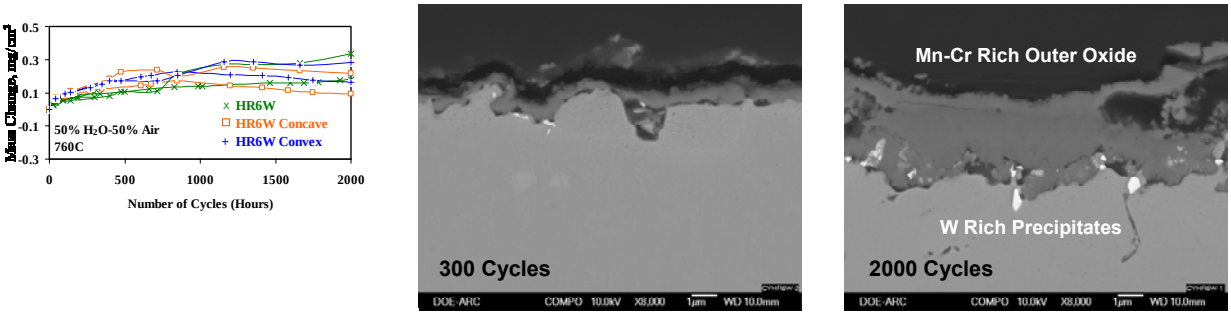

Fig. 8. Cyclic test results for HR6W in 50%H_2O-50% air at 760°C.

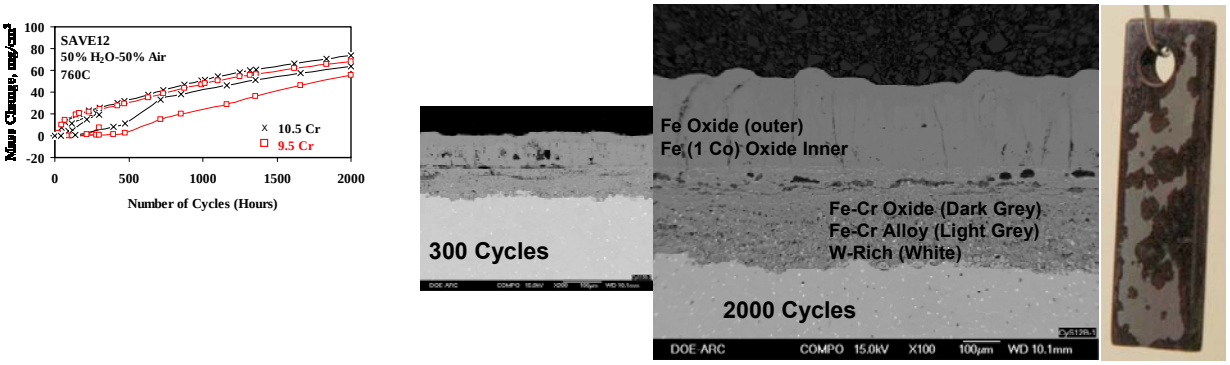

Fig. 9. Cyclic test results for Save12 in 50%H_2O-50% air at 760°C.

The figure for HR6W includes results for curvature samples. However, the curvature results closely match the results for the planar samples.

Save12 results in very thick oxides. Initial oxidation of Save12 also varies by quite a bit. A photo of an exposed sample (included in Fig. 9) shows a mottled surface with heavily oxidized regions next to relatively intact regions. So the variation in initial oxidation is attributed to relative percentages of each type of surface. As with the HR6W results, the Save12 curvature samples showed no significant difference from the planar samples.

THERMOGRAVIMETRIC ANALYSIS (TGA)

Experiments were conducted using thermogravimetric analysis (TGA) with steam at atmospheric pressure. This was designed to obtain information on oxidation kinetics using relatively short (300 hr) test durations. The TGA tests

consist of suspending a sample from a Cahn D-101 microbalance in flowing steam for 300 hours at a constant elevated temperature (650-800°C). Steam is generated by injecting a metered amount of O_2-saturated water into heated tubing to supply a minimum flow rate of 2 mm/s of steam in the reaction chamber. Initial experiments used pure steam. More recent tests used a carrier gas of 60% Ar along with the steam. Table 2 summarizes the results of the 300 hr TGA tests in O_2-saturated steam plus 60%Ar at 800°C.

The reaction order and parabolic R^2 are measures of how well the data fit parabolic kinetics of:

$$\text{Mass change} = k_p t^{1/n} \qquad (1)$$

where k_p is the parabolic rate constant, t is time, and n is the reaction order (n = 1 for linear kinetics and n = 2 for parabolic kinetics). The parabolic R^2 measures how well the data correlate with parabolic behavior using the calculated k_p (with 1 being exact correlation and 0 being no correlation). The parabolic R^2 values for Save12, J1, J5, and one of the Alloy 617 tests were quite close to 1, showing excellent correlation with parabolic kinetics and with relatively little noise in the data. The oxidation rates of Alloy 230, HR6W, Alloy 740, and one of the Alloy 617 tests were lower, and with more noise in the mass change data, which resulted in lower parabolic R^2 values. As discussed last year, further TGA tests of the highly resistance nickel-base alloys has been curtailed.

Table 2

Thermogravimetric analysis (TGA) for 300 hr tests in O_2-saturated steam plus 60%Ar at 800°C

Alloy	%Cr	Reaction Order, n	Parabolic R^2	Parabolic Rate Constant, k_p $mg^2cm^{-4}s^{-1}$
12 (9.5Cr)	9.5	1.78	1.000	1.2×10^{-3}
12 (9.5Cr)	9.5	1.90	1.000	1.4×10^{-3}
12 (10.5Cr)	10.5	1.70	1.000	1.6×10^{-3}
12 (10.5Cr)	10.5	1.76	0.995	1.7×10^{-3}
J1	12.1	1.73	0.990	3.5×10^{-7}
J5	12.5	1.91	0.990	1.5×10^{-7}
617	22	1.62	0.960	1.4×10^{-7}
617	22	2.63	0.585	3.9×10^{-8}
230	22	1.78	0.878	6.9×10^{-8}
230	22	1.79	0.645	3.7×10^{-8}
6W	23	1.87	0.524	3.3×10^{-8}
740	24	2.20	0.527	7.2×10^{-7}

FURNACE EXPOSURES

Experiments were added that exposed samples to moist air at atmospheric pressure. These tests consisted of exposing the samples to air that was bubbled through water, resulting in up to 3% water vapor in the atmosphere. Samples were periodically removed from the furnace for mass measurements, and then replaced in the furnace for further exposure. More recent tests have attempted to improve the procedures by ensuring that the input air is water saturated and that the temperature cycles are more tightly controlled (100 hr cycles with 200 °C/hr ramp rates). The results for furnace exposures in moist (3% H_2O) air are shown in Fig. 10.

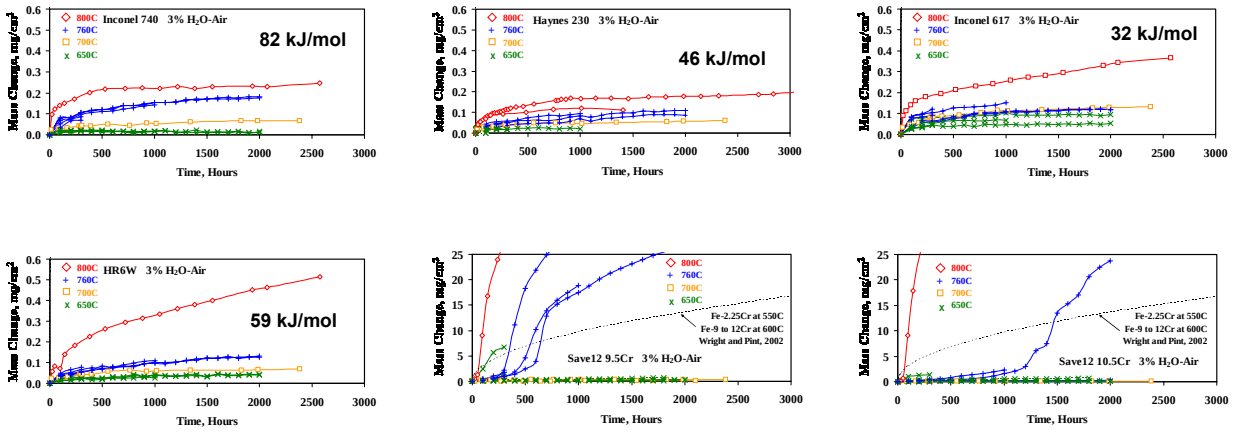

Fig. 10. Furnace exposure results for superalloys and Save12.

Included in the furnace exposure plots is a dotted line showing the average oxidation behavior of 2.25Cr steels at 550°C and 9-12Cr steels at 600°C. The parabolic rate constants used to generate these curves are from the compilation by Wright and Pint[12] for the corrosion of steels in water vapor and steam. This gives a comparison for the experimental results with acceptable oxidation rates of currently used alloys. Many of the Ni-base alloys have oxidation rates too low for the oxidation behavior of 2.25Cr steels at 550°C and 9-12Cr steels at 600°C to be visible in the same data range.

All of the nickel base alloys had modest mass gains at 650 and 700°C. Nimonic 90 (at 760°C) and HR6W (at 800°C) had higher mass gains than the other nickel alloys. To a lesser extent, Alloy 617 (at 800°C) also had higher mass gains and trends than Alloy 740 or Alloy 230. Overall, the best alloys in this test were Alloys 230 and 740. The oxidation rates for Save12 were quite high, and showed breakaway oxidation in some cases. The 10.5Cr version of Save12 looked acceptable at 650°C with low oxidation rates and no observed cases of breakaway oxidation.

PROGRESS COMPARED TO ORIGINAL PLAN

The original key milestones were as follows:

- Completion of facility for high-temperature and high-pressure steam exposures.
- Analysis of steam oxidation data of candidate USC turbine materials as a function of temperature and pressure, and in selected materials, sample curvature.
- Application of steam oxidation data to advance the knowledge of oxidation and spallation mechanisms in USC steam.

The first milestone has not been met. The delivery of the Rene 41 autoclave was postponed, delayed, and then finally cancelled. The original delivery date was 12/31/2004. A new solicitation for an autoclave made from Haynes 230 was posted in May of 2006.

The delay in the autoclave will postpone the pressure component on the second milestone listed above.

The cyclic, furnace exposure and TGA tests are proceeding as planned. Findings are listed below in Summary/Conclusions. A second and third cyclic rig may be added later this year.

The TGA tests have shown a limitation in the TGA system at low oxidation rates (that the nickel base alloys have even at 800°C). Future tests at lower temperatures will primarily be restricted to alloys that oxidize faster, such as the Save12 alloys.

Efforts to examine the effects of specimen geometry with simple curvature samples, Fig. 1, have not shown any conclusive differences.

OBJECTIVES FOR NEXT PERIOD

The objectives for the next year include:

- Obtain, setup, and operate a high temperature and pressure autoclave system.
- Continuing TGA, cyclic, and furnace tests.
- Examine other methods to quantify the effects of curvature and geometry on steam oxidation. These include selective oxidation studies on wire samples of various diameters, and possibly the use of hardness indents to show spallation and adhesion properties.

SUMMARY/CONCLUSIONS

The status of research to examine the steamside oxidation of advanced alloys for use in supercritical systems was presented. The alloys of interest were mainly nickel-base superalloys. The initial results from cyclic oxidation in moist air at 760°C, TGA in steam plus 60% Ar at 800°C, and furnace exposures in moist air at 700°C and 800°C were described:

- From a simplistic mass change standpoint, all of the Ni-base alloys look acceptable at up to 800°C.
- Save12 9.5-Cr shows breakaway oxidation ≥ 650°C.
- Save 12 10.5-Cr appears acceptable (from steam oxidation standpoint) at 650°C.
- All the Ni-base alloys show internal oxidation below the oxide scale. Of the alloys examined, Inconel 740 and Haynes 230 show the least damage from internal oxidation
- No evidence of curvature effects.

REFERENCES

1. B.B. Seth, "US Developments in Advanced Steam Turbine Materials," Advanced Heat Resistance Steels for Power Generation, Electric Power Research Institute, 1999, pp. 519-542.
2. Steam, 40th ed., Eds. S.C. Stultz and J.B. Kitto, Babcock & Wilcox, 1992, p. 9.
3. R. Viswanathan, A.F. Armor, and G. Booras, "Supercritical Steam Power Plants—An Overview," Best Practices and Future Technologies, October 2003, Proceedings (New Delhi, India), National Thermal Power Corporation's Center for Power Efficiency and Environmental Protection and the US Agency for International Development (USAID), 2003.
4. R. Swanekamp, Power, 146 (4), 2002, pp. 32-40.
5. R. Viswanathan, A.F. Armor, and G. Booras, Power, 148 (4), 2004, pp. 42-49.
6. J. M. Sarver and J. M. Tanzosh, "Steamside Oxidation Behavior of Candidate USC Materials at 650°C and 800°C," presented at the 8th Ultra-Steel Workshop, Tsukuba, Japan (July 2004).
7. Y. Tamada, A. M. Beltran, and G. P. Wozney, EPRI Report TR-100979, Electric Power Research Institute, Palo Alto, CA, 1992.
8. R. Viswanathan and W. Bakker, *J. of Materials Eng. and Performance*, 10, 2001, pp. 96-101.
9. D.E. Alman and P.D. Jablonski, "Low Coefficient of Thermal Expansion (CTE) Nickel-Base Superalloys for Interconnect Applications in Intermediate Temperature Solid Oxide Fuel Cells (SOFC)," Superalloys 2004, TMS, 2004, pp. 617-622.
10. R. Yamamoto, Y. Kadoya, H. Kawai, R. Magoshi, T. Noda, S. Hamano, S. Ueta, and S. Isobe, "New Wrought Ni-Based Superalloys with Low Thermal Expansion for 700C Steam Turbines," Materials of Advanced Power Engineering—2002, Proc. 7th Liege Conf., Sept 30-Oct 3, 2002, Energy and Technology Vol. 21, Forschungszentium Julich Gmbh Inst. Fur Wekstoffe und Verfahren der Energietechnik.
11. Materials Development in the European AD700 Program, Materials & Components in Fossil Energy Applications, No. 162, Spring/Summer 2005, U.S. Department of Energy.
12. I. G. Wright and B. A. Pint, "An Assessment of the High-Temperature Oxidation Behavior of Fe-Cr Steels in Water Vapor and Steam," Corrosion/2002, paper 02377, NACE International, Houston, TX, 2002.

FIRESIDE CORROSION PROBES – AN UPDATE

Bernard, S. Covino, Jr., Sophie J. Bullard, Gordon R. Holcomb,
Małgorzata Ziomek-Moroz, and Steven A. Matthes
National Energy Technology Laboratory
(Formerly Albany Research Center)
1450 Queen Ave., SW
Albany, OR 97321

ABSTRACT

The ability to monitor the corrosion degradation of key metallic components in fossil fuel power plants will become increasingly important for FutureGen and ultra-supercritical power plants. A number of factors (ash deposition, coal composition changes, thermal gradients, and low NO_x conditions, among others) which occur in the high temperature sections of energy production facilities, will contribute to fireside corrosion. Several years of research have shown that high temperature corrosion rate probes need to be better understood before corrosion rate can be used as a process variable by power plant operators. Our recent research has shown that electrochemical corrosion probes typically measure lower corrosion rates than those measured by standard mass loss techniques. While still useful for monitoring changes in corrosion rates, absolute probe corrosion rates will need a calibration factor to be useful. Continuing research is targeted to help resolve these issues.

INTRODUCTION

Corrosion of metals and alloys is a natural occurrence in high temperature energy conversion systems. Thermodynamic calculations predict that elements such as Fe, Ni, and Cr (which make up the majority of alloys used in this industry) will always seek their lowest energy state, that of an oxide, sulfide, or chloride. It is then the stability of this compound that will determine the long term corrosion rate. Successful coatings or alloying additions can help slow down or in some cases eliminate the corrosion process. When this is not possible, it is necessary to observe corrosion damage after the fact during plant shutdowns or to seek ways to monitor the corrosion of key components during operation.

Monitoring of corrosion during power plant operation has, up to the present, consisted primarily of inserting and removing metal coupons on a periodic basis. While this can give plant operators an early warning of accumulated corrosion damage, it usually has a minimum time period of months and can not give an instantaneous measure of corrosion that can sometimes be correlated to changes in process. If instantaneous reading corrosion rate probes were available, power plant operators would then have the ability to make changes in their processes to reduce the corrosion of their assets.

There have been a number of research efforts aimed at developing high temperature corrosion probes for various industries, such as Pulverized Coal-Fired (PC) plants using lower quality fuel and in Waste-to-Energy (WTE) plants[1]. The majority of this research has been based on the use of electrochemical noise (EN)[2-7] techniques. Others have considered the use of electrochemical

impedance spectroscopy (EIS)[4-6] and linear polarization resistance (LPR)[7], zero resistance ammetry (ZRA)[5], and electrical resistance (ER)[5]. There has been, however, only a limited effort reported to quantify[3] the operation of corrosion rate probes.

This paper will discuss some of the results and problems encountered in research to develop electrochemical corrosion rate probes for high temperature ash-covered conditions common to waterwalls and superheaters. Previous research[8-11] has addressed the issues of response and zero baseline as well as the quantitative nature of the corrosion probes in these environments. The state of this research as well as questions to be answered and suggestions for future research will be presented.

EXPERIMENTAL DETAILS

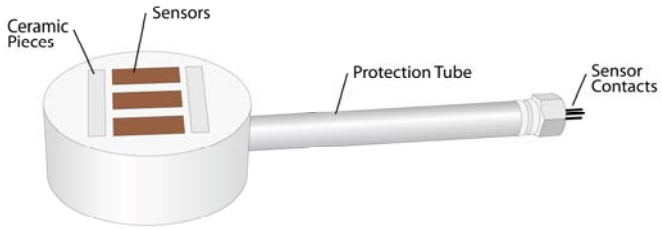

Figure 1: Schematic representation of a typical ECR probe

A single three-sensor isothermal electrochemical corrosion rate (ECR) probe, shown schematically in Figure 1, was designed and constructed for laboratory experiments using either mild carbon steel (CS), 304L stainless steel (SS), or 316L SS sensors (sensors are the same as electrodes used in a typical electrochemical cell). Wires were welded to each sensor and a protection tube allowed the wires to exit the furnace and not be corroded. The two outer sensors in Figure 1 are the working and counter electrodes and the inner sensor is the reference electrode. Sensors were embedded within a plastic removable form using Ceramcast 586, a zirconia/magnesia potting compound. The ceramic pieces shown in Figure 1 were used as reference surfaces for optical profilometry measurements (not discussed in this paper). After curing the potting compound, the probes were covered with ash and then exposed to high temperature gaseous conditions, along with ash-covered mass loss coupons made from the same material as the sensors.

Table 1
Composition (wt %) of major corrosion-causing elements in 2 combustion ashes used in ECR probe research.

Ash	Al	K	Pb	Na	Cl	Fe	S
Waste	3.6	3.7	2.7	3.5	6.7	5	6.5
Coal	4.0	Trace	0	trace	0	4.5	6

Two different types of ash were used in this research. The first was an ash from the Lee #1 Municipal Incinerator supplied by Covanta Energy, Inc. The second was a coal ash described as AEP TIDD (American Electric Power TIDD Coal Plant in Brilliant, OH) ash derived from Illinois #8 coal, and supplied by EERC, the University of North Dakota Energy and

Environmental Research Center. Table 1 compares the composition of the two types of ash. Waste ash was used for the majority of the experiments discussed in this report because it provided a more corrosive environment. This ash shows high concentrations of corrosion-causing elements such as S, Cl, Pb, and K, all of which are able to form low melting point compounds and eutectic mixtures. The gas mixture consisted of 68 vol% N_2, 15 vol% H_2O, 9 vol% O_2, and 8 vol% CO_2. The temperature used was 500ºC and typical test periods were 100 to 500 hours. Coal ash was used for several experiments. In these experiments, the gas mixture consisted of 69 vol% N_2, 15 vol% CO_2, 10 vol% H_2O, 5 vol% O_2, and 1 vol% SO_2.

Figure 2 – Data displayed during an ECR probe test.

The hardware used to measure the majority of the corrosion rates from the ECR probes was the SmartCET® Real-Time Corrosion Monitoring System*. This system used three separate electrochemical techniques: linear polarization resistance, electrochemical noise (EN), and harmonic distortion analysis (HDA). All three techniques measure a corrosion rate; EN also measures a localized (pitting) corrosion factor that varies from 0 to 1; and HDA measures the Tafel (βa, βc) constants used to calculate the Stern-Geary (B) factor. Corrosion rates and other variables are reported every seven minutes and stored to computer using FieldCET® software*. A typical output is shown in Figure 2. Most of the corrosion rates in this report were taken from the LPR measurements modified using the measured B values from each experiment. The default ECR probe corrosion rates were determined by integrating the LPR corrosion rates to calculate the mass loss, which was then converted to a penetration rate with units of millimeters per year (mm/y).

All experiments were conducted in a three-zone tube furnace containing a 2 in diameter alumina tube. Each zone was controlled with a separate temperature controller. Set temperatures for each zone were determined for each test temperature using an external calibration thermocouple and taking measurements at 1 cm intervals. For example, settings of 490, 510, and 400ºC for zones 1, 2, and 3, respectively, gave an internal temperature of 500ºC with a flat profile over 12 in (30.5 cm) of the 24 in (61 cm) heated zone. An alumina D-tube was inserted in the furnace tube to provide a platform for mass loss coupons. Measurement and control thermocouples were inserted in a 316 SS sheath that was then inserted in the D-tube.

Gas flows, and thus gas mixture compositions, were controlled using digital mass flow controllers that were controlled using Lab-view programs. Water vapor was added through an air-powered metering pump that pumped a specific quantity of water into a heated chamber where the water vapor was picked up by the test gas mixture.

*Honeywell InterCorr, Houston, TX USA

RESULTS AND DISCUSSION

The goal of this research was to show that electrochemical corrosion rate probes can be used to monitor corrosion in high temperature environments where ash is deposited on metallic surfaces. The optimal result of this research would be that probes are able to quantitatively measure corrosion rates (that is, electrochemical corrosion rates = mass loss corrosion rates). In the case where the probes are not quantitative, but semi-quantitative, it is necessary to determine if a calibration factor can be established to make the probes appear to act quantitatively. In order for a semi-quantitative probe to work for the many different environments (ash compositions, temperature, gas compositions, etc.) encountered in energy production, it will also be necessary to understand the operation of the probes.

Semiquantitative Probe Nature

Electrochemical corrosion rate probes based on either LPR or EN measurements have been reported to be semi-quantitative for measurements made on mild and stainless steels in high temperature gaseous ash-depositing environments[11]. This conclusion is based on a comparison of mass loss measurements to electrochemical measurements which has shown that for a large number of measurements in waste ash, the corrosion rates are under-reported (that is, the sensors measure less of the corrosion than actually occurs). For a smaller number of tests in coal ash, the measurements are over-reported (that is, the sensors measure more of the corrosion reaction than actually occurs). In the former case, the electrochemical sensors "see" only a part of the corrosion process. In the latter case, the electrochemical sensors apparently measure other electrochemical reactions. Some of these data are shown in Table 2 along with a comparison of the mass loss (ML) to the electrochemical corrosion rates based on LPR and EN.

Table 2
Real-Time Corrosion Monitoring Corrosion rate ratios with ML corrosion rates for select experiments.

Alloy	Ash	ML/LPR	ML/EN
CS	Waste	9.6	19.9
304 SS	Waste	4.2	9.7
304 SS	Waste	6.5	8.5
316 SS	Waste	1.4	3.2
316 SS	Waste	12.9	7.6
304 SS	Coal	0.35	0.31
316 SS	Coal + FeS	0.05	0.08
ML = mass loss corrosion rates, LPR = LPR probe corrosion rates, and EN = electrochemical noise probe corrosion rates			

Probe Sensitivity

Tables 3-5 show the response of the electrochemical corrosion rate probes based on LPR measurements. In general, the data show that LPR measurements are sensitive to changes in alloy composition, ash composition, and temperature and water vapor content of the environment, despite the fact that the measurements are not quantitative. Table 3 shows that for carbon steel and 316 SS in the same environment, higher temperatures result in higher corrosion rates. Secondly, at the same temperature, the corrosion rate is higher for carbon steel.

Table 3
Effect of alloy and temperature on Real-Time Corrosion Monitoring corrosion rate measurements

Alloy	Temp, ºC	ECR, mm/y
Carbon Steel	450	0.89
Carbon Steel	500	2.74
316 SS	500	0.28
316 SS	600	3.73

Table 4 shows that the waste ash causes higher corrosion rates than the coal ash. As seen in Table 1, the waste ash has a higher concentration of elements, such as chlorine, lead, sodium, and potassium, elements that are known to accelerate corrosion. Also, the addition of iron sulfide, as shown in Table 4, increased the corrosion rate in the coal ash. Table 5 shows that increased water vapor content in the environment leads also to higher corrosion rates. It has also been reported[11] that these measurements are sensitive to changes in gas phase composition, such as O_2 and CO_2 content.

Table 4
Effect of ash type on Real-Time Corrosion Monitoring corrosion rate measurements

Alloy	Ash	ECR, mm/y
316 SS	Waste	0.28
316 SS	Coal	0.005
316 SS	Coal + FeS	1.44

Field Use of Corrosion Rate Probe

The probe sensitivity measurements reported above suggest that, at the very least, electrochemical corrosion rate probes can be used as qualitative indicators of the corrosivity of the environment (a function of ash, gas, and alloy composition). Research indicates that the corrosion rate probe can be successfully used in energy conversion power plants, if information about the corrosivity of the operating environment is desired. However, the probe will give indications of levels of corrosion that may not equal the actual corrosion rate. If corrosion rate measurements are made in a WTE facility, they could be multiplied by 7 (the approximate average of the ML/LPR values for waste ash in Table 2), which should give a fair approximation of the corrosion rate. The probe will also indicate changes (increases and decreases) in corrosion rate that plant operators may chose to try to link to changes or upsets in the energy conversion process.

Table 5
Effect of water content on Real-Time Corrosion Monitoring corrosion rate measurements

Alloy	% H_2O	ECR, mm/y
304 SS	0	0.563
304 SS	14	1.1

On this basis, a six-month field test in a commercial WTE boiler has been scheduled to begin during October 2006. This test will include four probes at distinctly different positions in the WTE power plant boiler. The data to be collected will include corrosion rates from LPR, HDA, and EN measurements, localized corrosion factors, Stern-Geary factors, and temperature. Attempts will be made to adjust the probe temperature to that of the waterwall tubes using an air-cooling technique. Ultrasonic transducer (UT) measurements will be made in the areas of the probes both before and after the field trial to provide a secondary measurement of corrosion, and for comparison to the ECR probe corrosion rates.

Questions that Need to Be Answered

Because the nature of the current probe system appears to be qualitative to semi-quantitative, and because the ML/LPR ratio is as varied as shown in Table 2, there is a need to find a means to make the probe act more quantitatively if it is to develop wide-spread industrial acceptance. To do that, it is important that the complexity of the system be better understood. The corrosion system involves at least three solid phases (the metal, the corrosion product, and the ash) and a multi-component mixed gas phase. As a further complication, the ash is heterogeneous, consisting not only of many chemical compounds, but multiple physical forms of these compounds (powder, rock, slag). Also these compounds can react with each other, with different

components of the alloy, and/or with different components of the gaseous phase to form other compounds, some of which could have melting points below the process temperature. In addition, all of these components can behave differently, depending on ash and gas composition, both of which can vary from location to location within the same power plant, and from plant to plant.

Listed below are several thoughts or questions that, if explored, may provide a path toward more quantitative operation of the ECR probe:

1. How does the ash contribute to the electrochemical corrosion reactions? Do low melting eutectic mixtures form and cause molten salt chemical attack?
2. Does corrosion in the presence of ash occur in the same manner as in high temperature oxidation?
3. How important is a physically stable probe in making accurate corrosion rate measurements?
4. Is there significant intergranular corrosion (IGC) that can account for the higher ML corrosion rate?
5. Are the electrochemical corrosion reactions limited by the cathodic reaction, as occurs frequently in aqueous environments?
6. What role does the ash resistivity play in the electrochemical measurements?
7. Can unburned carbon in the ash short-circuit the electrochemical measurements?

Insight into Question 2

Past research[11] has verified that there is an electrochemical nature to the corrosion reaction on stainless steel in ash-covered high temperature gaseous environments. Often the electrochemical nature of these high temperature reactions is ignored, because the reaction rate is controlled by diffusion and not electrochemistry. It has also been verified that measurements made using standard laboratory potentiostats produce the same values of corrosion rate as produced by the SmartCET® Realtime Corrosion Monitoring System. Keeping in mind from Table 2 that these same electrochemical techniques measure only a small part of the actual corrosion reaction, begs the question of WHY? What part of the corrosion reaction is not being measured? As discussed below, it may not be a question of which reactions occur, but rather where these reactions occur.

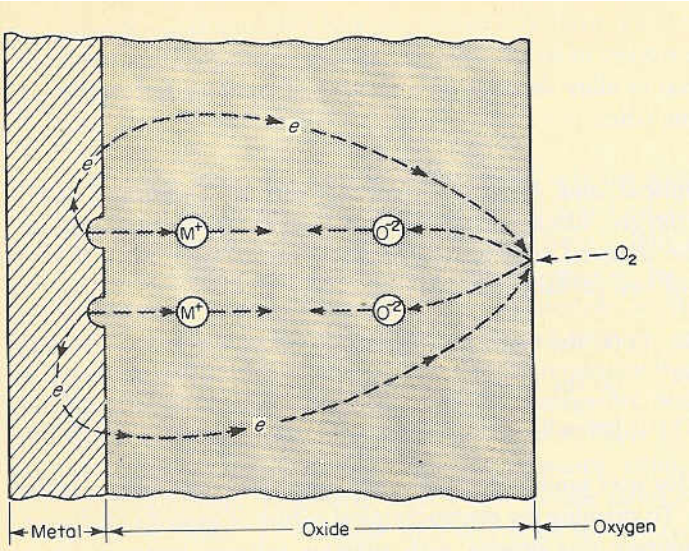

Figure 3 – Schematic illustration of electrochemical processes occurring during gaseous oxidation[12]

Figure 3 is a schematic[12] of the electrochemical processes that occur in the high temperature oxidation of a metal. Note that even though metal ions are generated at the metal-oxide interface, and electrons travel through the metal, the cathodic reaction does not occur at the metal surface, as happens in lower temperature gaseous and aqueous corrosion. The reduction of oxygen occurs at the oxide-oxygen interface, partly because of the enhanced electron conductivity of the oxide at high temperatures.

For ash-covered metals, the ash is on the outer surface of the oxide and it is likely that this reduction reaction may occur at the ash-oxygen interface. The problem this presents for the electrochemical measurement of corrosion rate is considerable, because the probe's sensors are at the physical level of the metal in Figure 3, and not at the oxide- or ash-oxygen interface where the cathodic reaction is occurring. It may be that the electrochemical probe will measure a corrosion reaction based only on whatever part of the oxygen is able to diffuse to the metal (sensor) surface. It is known that scales on Fe, Ni, Cu, Cr, Co, and others do grow principally at the scale-gas interface[12]. It has also been suggested[12] that some of the oxide in the middle of the scale dissociates, sending cations outward and oxygen molecules inward (towards the sensors). If this occurs, it could account for the observation that a smaller part of the corrosion reaction is detected by the electrochemical corrosion rate probe, especially in the WTE environment.

SUMMARY AND CONCLUSIONS

- Electrochemical corrosion rate probes have been shown to be sensitive to changes in the alloy (composition) and in the environment (temperature, gas phase composition, and ash composition).
- Standard electrochemical techniques have measured electrochemical polarization diagrams that are typical of actively corroding metals.
- Electrochemical corrosion rate probes appear at this time to be either qualitative or semi-quantitative in nature. Electrochemical corrosion rate probes measure less of the corrosion reaction than measured by the mass loss technique.
- Corrosion in high temperature gaseous environments is different than at lower temperatures because of the increased electron conductivity of oxides at high temperatures. The reduction reaction generally occurs at the oxide-gas interface rather than at the metal surface where electrons are generated from the oxidation of metal atoms.
- Several questions were posed to help stimulate discussion/research to gain insight about electrochemical corrosion rate measurements in high temperature ash covered gaseous environments.

REFERENCES

1. H. Thielsch and F. M. Cone, "Remedies for WTE's Most Vexing O&M Problem: Tube Failure," Solid Waste Technologies, January-February, pp 32-39, 1994.
2. T.M. Linjeville, K.A. Davis, G.C. Green, W.M. Cox, R.N. Carr, N.S. Harding, and D. Overacker, "On-Line Technique for Corrosion Characterization in Utility Boilers, Proceedings of Power Production in the 21st Century: Impacts of Fuel Quality and Operations," United Engineering Foundation, Snowbird, UT, October 28-November 2, 2001.
3. T.M. Linjeville, J. Valentine, K.A. Davis, N.S. Harding, and W.M. Cox, "Prediction and Real-time Monitoring techniques for Corrosion Characterization in Furnaces," Materials at High Temperatures, Vol. 20, No. 2, pp. 175-184, 2003.
4. D.M. Farrell, W.Y. Mok, and L.W. Pinder, "On-line Monitoring of Furnace-Wall Corrosion in a 125 MW Power Generation Boiler," Materials Science and Engineering, Vol. A121, pp. 651-659, 1989.
5. D. M. Farrell, "On-line Monitoring of Fireside Corrosion in Power Plant," 12th International Corrosion Congress, Vol. 12, pp. 4131-4140, 1993.
6. G. Gao, F.H. Stott, J.L. Dawson, and D.M. Farrell, "Electrochemical Monitoring of High-Temperature Molten Salt Corrosion," Oxidation of Metals, Vol. 33, Nos. 1/2, pp. 79-94, 1990.
7. G.J. Bignold and G.P. Quirk, "Electrochemical Noise Measurements in a 500 MW Steam Turbine to Maximize Lifetime Under Changing Operational Demands," Paper no, 02333, CORROSION/2002, NACE International, Houston, TX, 20 pp, 2002.
8. B. S. Covino, Jr., S. J. Bullard, S. D. Cramer, G. R. Holcomb, M. Ziomek-Moroz, D. A. Eden, R. D. Kane, and D. C. Eden, "High Temperature Electrochemical Noise Corrosion Sensors For Fossil Fuel Combustion," Paper No. 04528, Corrosion/2004 (New Orleans, LA, March 28-April 1, 2004), NACE International, Houston TX, 2004, 9 pp.
9. B. S. Covino, Jr., S. J. Bullard, S. D. Cramer, G. R. Holcomb, M. Ziomek-Moroz, D. A. Eden, and M. S. Cayard, "Electrochemical Corrosion Rate Probes for High Temperature Energy Applications," Proceedings of the Fourth International Conference on Advances in Materials Technology in Fossil Power Plants, Hilton Head Island, South Carolina, October 25-28, 2004.
10. B. S. Covino, Jr., S. J. Bullard, S. D. Cramer, G. R. Holcomb, M. Ziomek-Moroz, R. D. Kane, and D. C. Eden, "Monitoring Power Plant Fireside Corrosion Using Corrosion Probes," Proceedings of the 30th International Technical Conference on Coal Utilization & Fuel Systems, Coal Technology Association, Clearwater, FL, April 17-21, 2005.
11. B. S. Covino, Jr., S. J. Bullard, M. Ziomek-Moroz, G. R. Holcomb, and D. A. Eden, "Fireside Corrosion Probes For Fossil Fuel Combustion," Paper No. 06472, Corrosion/2006 (San Diego, CA, March 12-17, 2006), NACE International, Houston TX, 2006, 11 pp.
12. M. G. Fontana and N. D. Greene, "Corrosion Engineering," 2nd edition, McGraw-Hill Book Company, New York, NY, 1978, p.350.

JOINING OF ODS FeCrAl ALLOYS FOR VERY HIGH-TEMPERATURE HEAT EXCHANGERS

John P. Hurley
University of North Dakota, Energy & Environmental Research Center, 15 North 23rd Street, Stop 9018, Grand Forks, ND 58202-9018
E-Mail: jhurley@undeerc.org; Telephone: (701) 777-5159; Fax: (701) 777-5181

Norman S. Bornstein, Senior Metallurgical Consultant
43 Richmond Lane, West Hartford, CT 06117
E-Mail: normanbornstein@sbcglobal.net; Telephone: (860) 233-0472; Fax: (860) 232-6007

Ian G. Wright
Oak Ridge National Laboratory, 1 Bethel Valley Road, MS 6156, Oak Ridge, TN 37831-6156
E-Mail: wrightig@ornl.gov; Telephone: (865) 574-4451; Fax: (865) 241-0215

ABSTRACT

Laboratory- and pilot-scale tests of a very high-temperature heat exchanger (HTHX) that could be used to produce pressurized air at up to 1090°C for an indirectly fired combined-cycle (IFCC) power plant have been performed at the University of North Dakota Energy & Environmental Research Center (EERC). An IFCC using this type of heat exchanger has the potential to reach efficiencies of 45% when firing coal and over 50% when a natural gas-fired duct burner is used to additionally heat the gas entering the turbine. Because of its high efficiency, an IFCC system is the most appropriate power concept for employing oxygen-enriched combustion in order to make carbon dioxide removal more economical. By staging combustion of the coal in such an oxygen-blown system, the need for flue gas recirculation to manage the flame temperature is reduced, and the maximum amount of energy can be channeled to the gas turbine, raising overall plant efficiency. In addition, reducing the volume of flue gas would substantially reduce the required size of the baghouse or electrostatic precipitator, the flue gas desulfurization system, and induced- and forced-draft fans, thereby reducing both capital and operating costs. After water condensation, only carbon dioxide is left in the gas stream, which can then be used industrially or sequestered, leaving near-zero emissions. If the system is cofired with coal and biomass, sequestration of the carbon dioxide would create a net reduction of its concentration in the atmosphere.

Two oxide dispersion-strengthened (ODS) alloys have been tested for construction of the HTHX: one composed primarily of nickel and chromium, the other of iron, chromium, and aluminum. Although both performed well, the iron-based material has shown exceptional corrosion resistance because it forms an alumina scale when oxidized. As the name suggests, ODS alloys contain a small quantity of very fine particulate metal oxide particles distributed throughout the structure to increase creep resistance at high temperatures. This prevents fusion welding of the material because melting would permit the oxide particles to agglomerate and lose their effectiveness in reducing creep. In this paper, we summarize the initial generalized results of a

transient liquid-phase bonding method for joining Plansee PM2000, a FeCrAl ODS alloy. The tests show that different elements in the bonding alloys separate during diffusion into the PM2000, in some cases forming large pores or precipitates, which weaken the joint. However, it is expected that the size of the pores and precipitates are strongly affected by the times and temperatures used in bonding, as well as by the alloy type.

INTRODUCTION AND BACKGROUND

Directly fired combined-cycle power systems employ a gas turbine followed by a steam turbine to make one of the most efficient thermal energy cycles possible. These systems are fired with natural gas which has increased severalfold in price over the last several years. The price is also very volatile. In contrast, coal costs less per energy unit, and because of its limited market, is much more stable in price. However, coal cannot be fired directly into a turbine because it produces ash during combustion, which would foul and erode the turbine blades. Instead, coal firing can be used to heat the process air entering a gas-fired combined cycle turbine by passing it through a high-temperature heat exchanger (HTHX) heated with a coal flame. These indirectly fired combined-cycle (IFCC) plants are capable of reaching efficiencies of 45% when firing coal and over 50% when the process air entering the turbine is further heated with a gas-fired duct burner,[1, 2] much higher than the 35% efficiency of current coal-fired power plants. Incorporating an HTHX into integrated gasification combined-cycle (IGCC) plants is also expected to produce marked improvements in plant efficiency.

The maximum temperature and, hence, the maximum efficiency of both IFCC and IGCC systems is often limited by materials issues. Heat exchanger materials are required that retain appreciable strength and have good creep resistance at high temperatures, resist corrosion by the products of coal combustion or gasification, can withstand both oxidizing and reducing environments, and resist fracture because of rapid thermal cycling.[3] Previous work has identified iron-based oxide dispersion-strengthened (ODS) alloys as excellent candidates for this type of environment.[1, 4-6] The presence of small stable oxides (often yttria [Y_2O_3]) helps to prevent dislocation motion and preserve the high-temperature strength of these materials. Grain boundary sliding and Herring–Nabarro diffusional creep are both retarded by the elongated grain structure typical of ODS alloys.[1] Iron-based ODS alloys such as PM2000 can exhibit excellent corrosion resistance at high temperatures if they contain approximately 4.5% aluminum or more. The aluminum forms a protective oxide layer that can resist even direct contact with flowing slag,[4, 5] as long as the surface is cooled below the solidus temperature of the slag.

Identifying candidate materials with desirable properties is not enough to make commercially viable HTHXs. Production of the final heat exchanger requires joining several sections of the material either to each other or to other materials.[7] These joints must perform as well at elevated temperatures as the sections of bulk material do. Joining ODS alloys is not trivial. The excellent high-temperature properties of the bulk material can only be obtained with strict control of the processing parameters because of the strong dependence of the strength and creep behavior on the microstructure. Joining techniques which alter the microstructure, chemical composition, or

oxide dispersion in the joint region can impair the behavior of the joint and cause the overall structure to fail prematurely.

One technique that has been shown to be successful at joining ODS alloys is transient liquid-phase (TLP) bonding.[3, 7] This method involves sandwiching a thin foil of low-melting-temperature material between the sections to be joined. When the foil is then heated above its melting temperature, diffusion into the surrounding ODS sections forms a continuous joint. The mechanical and chemical properties of the joint are a function not only of the bulk ODS material, but also of the foil joining material. Under several past programs, the Energy & Environmental Research Center (EERC), in collaboration with Oak Ridge National Laboratory (ORNL), has tested TLP bonding as a method for joining ODS FeCrAl alloys. Joints made using the TLP bonding are shown in Figure 1. In both cases, excess levels of the joining alloy remain near the joints. Based on those results, the current extension program was set up under Advanced Research Materials (ARM) funding to test a specific method of applying the joining material to the pieces to be joined. Once coated, the surfaces are placed in contact and heated to effect the joint. Cross sections of the joints are then prepared, analyzed by scanning electron microscopy (SEM) at the EERC, then sent to ORNL for strength testing and further SEM analyses. This paper describes some of the initial results of that testing. The details of the coating and joining procedures are currently proprietary.

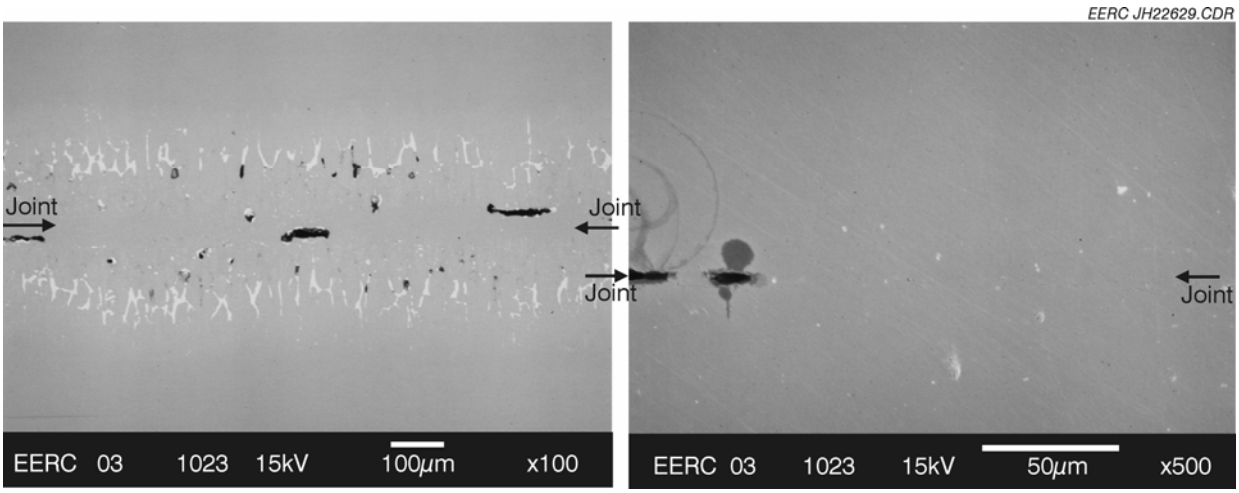

Figure 1. Scanning electron microscopy pictures of the trial TLP joints made between pieces of ODS alloy using two different joining alloys.

RESULTS AND DISCUSSION

Two different forms of the PM2000 were tested in the joining work. Both are available commercially from Plansee, and both are prepared using powder metallurgy techniques. The overall manufacturing process involves blending powders of iron, chromium, aluminum, yttrium oxide, and trace metals and mechanically alloying them in a ball mill. The granular material is then densified by hot isostatic pressing and hot extrusion. The material is further treated by hot

and cold rolling. The product Kornklasse 4 (KKL4) is the alloy after the cold working and contains fine crystals. Kornklasse 6 (KKL6) has been further heat treated to recrystallize the material, leaving very large and long crystals oriented in the direction of extrusion.
Figure 2 shows three SEM photographs, taken at higher magnifications moving from left to right, of a cross section of a joint prepared between two pieces of the KKL4 material. This and all following SEM images were prepared at ORNL. The pictures show significant porosity remaining near the joint, especially approximately 10 to 20 μm from the joint. Relatively little porosity is left at the joint itself. It is expected that the porosity will be substantially reduced if higher temperatures and longer times are used in preparing the joints.

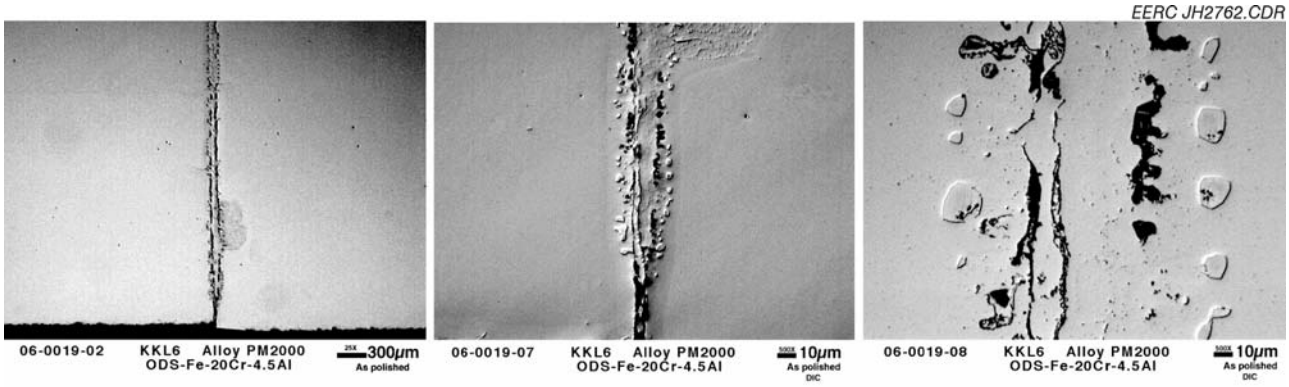

Figure 2. Joint prepared from KKL4 material, not etched.

Figure 3 shows the same joint at a different location, but in this case the material has been etched to bring out the zones into which the joining alloy has penetrated. The figure shows that the joining alloy has penetrated approximately 200 μm away from the joint. The inner gray zone contains residual joining alloy. It is not clear at this time what caused the outer dark band.

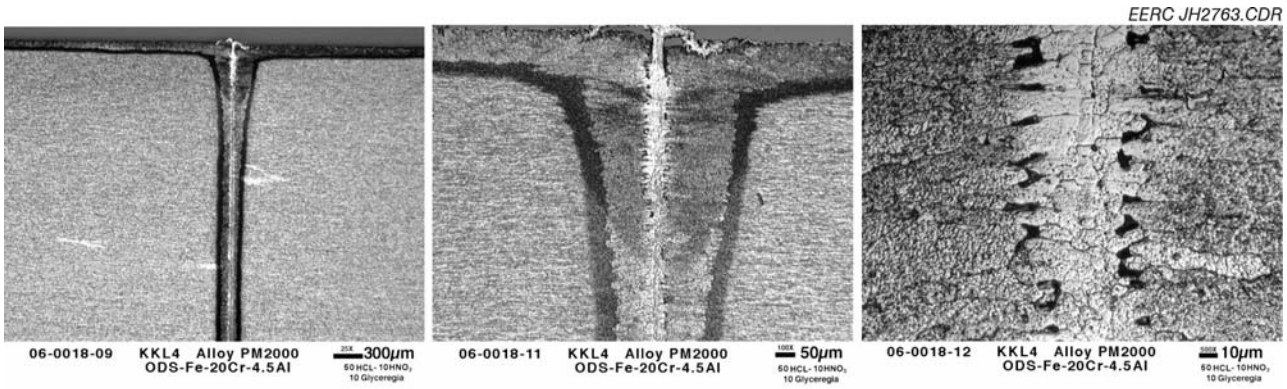

Figure 3. Joint prepared from KKL4 material, etched.

Figure 4 shows a joint prepared between pieces of KKL6. It shows much less large porosity than the joints made with the KKL4 material, but some larger precipitates of the joining material.

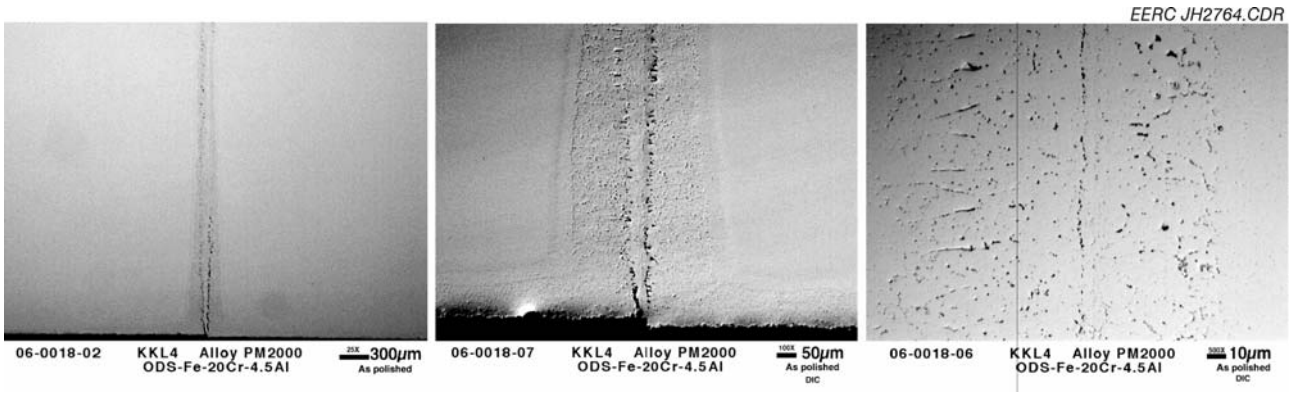

Figure 4. Joint prepared from KKL6 material, not etched.

Figure 5 shows the same joint in the KKL6 material, but at a different position and etched to bring out the grain structure. The large high aspect ratio grains can be seen in this figure. It shows that the joining material penetrated from 50 to 150 μm into the KKL6, and that the penetration distance was dependent on the grain orientation. Grain growth across the joint was not observed.

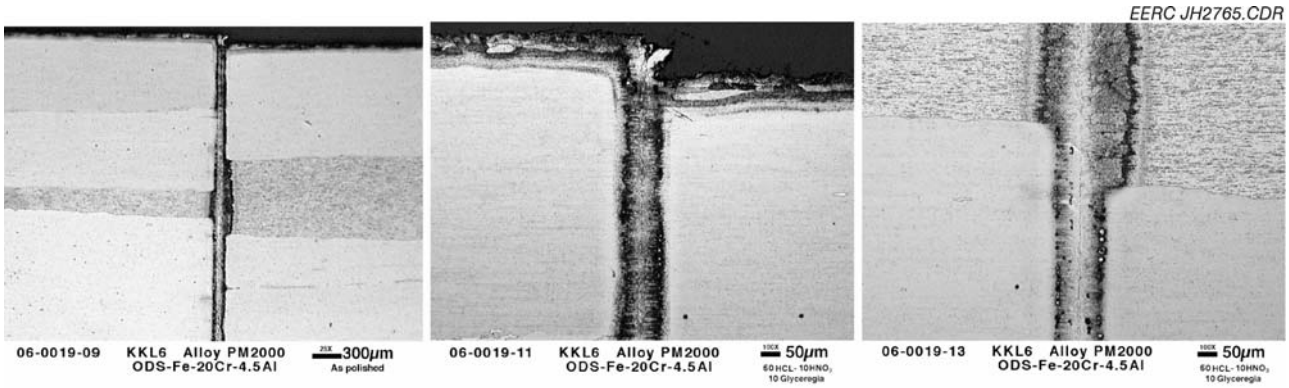

Figure 5. Joint prepared from KKL6 material, etched.

CONCLUSIONS

The transient liquid phase joining work of PM2000 FeCrAl ODS alloy is in its early stages at the EERC. The initial tests show that joints made in the KKL4 material show more porosity than when made in the KKL6 material, although it is expected that it will be reduced as processing conditions are refined. The joining material diffused approximately 200 μm into the KKL4 material and was well distributed. In the KKL6 joints, the joining material diffused between

50 and 150 μm from the joints depending on the grain orientation and formed larger precipitates than in the KKL4 joints. No grain growth was observed across the joints for either the KKL4 or KKL6 materials. It is expected that the size of the pores and precipitates are strongly affected by the times and temperatures used in bonding, as well as by the alloy type, and will likely be reduced by refining the processing procedures.

REFERENCES

1. United Technologies Research Center. *Combustion 2000 Phase II Final Technical Report*; DE-AC22-95PC95144, 2001.

2. Robson, F.L.; Ruby, J.D.; Nawaz, M.; Seery, D.J.; Jones, M.L.; Hurley, J.P. Application of High-Performance Power Systems (HiPPS) in Vision 21 Power Plants. In *Proceedings of the 2002 American Power Conference*; Chicago, IL, 2002.

3. Wright, I.G.; Stringer, J. Materials Issues for High-Temperature Components in Indirectly Fired Cycles. In *Proceedings of the International Gas Turbine and Aeroengine Congress and Exhibition*; Orlando, FL, 1997.

4. Hurley, J.P.; Weber, G.F.; Jones, M.L. Tests of High-Temperature Heat Exchangers for Indirectly Fired Combined Cycles. In *Proceedings of the 20th Annual International Pittsburgh Coal Conference*; Pittsburgh, PA, 2003.

5. Turker, M.; Hughes, T.A. Oxidation Behavior of Three Commercial ODS Alloys at 1200°C. *Oxidation of Metals* **1995**, *44*, 505–525.

6. Whittenberger, J.D. Elevated Temperature Mechanical Properties of the Iron Base Oxide Dispersion-Strengthened MA956 Bar. *Metallurgical Transactions A* **1981**, *12A*, 845–851.

7. McKimpson, M.G.; O'Donnell, D. Joining ODS Materials for High-Temperature Applications. *JOM* **1994**, *46*, 49–51.

SESSION 3

COATINGS AND PROTECTION OF MATERIALS

ALUMINIDE COATINGS FOR POWER GENERATION APPLICATIONS

Y. Zhang, D.A. Ballard and J.P. Stacy
Department of Mechanical Engineering, TTU Box 5014, Tennessee Technological University, Cookeville, TN 38505-0001
E-mail: yzhang@tntech.edu; Telephone: (931) 372-3265; Fax: (931) 372-6340

B.A. Pint
Materials Science and Technology Division, Oak Ridge National Laboratory, MS 6156, Oak Ridge, TN 37831-6156
E-mail: pintba@ornl.gov; Telephone: (865) 576-2897; Fax: (865) 241-0215

ABSTRACT

Simple Pt-enriched γ+γ' coatings were synthesized on René 142 and N5 Ni-based superalloys by electroplating a thin layer of Pt followed by a diffusion treatment at 1150-1175°C. The Al content in the resulting γ+γ' coating was in the range of 16-19 at.% for superalloys with 13-14 at.% Al. After oxidation testing, alumina scale adherence to these γ+γ' coatings was not as uniform as to the β-(Ni,Pt)Al coatings on the same superalloy substrates. To better understand the effect of Al, Pt and Hf concentrations on coating oxidation resistance, a number of Ni-Pt-Al cast alloys with γ+γ' or β phase were cyclically oxidized at 1100°C. The Hf-containing γ+γ' alloys with 22 at.% Al and 10-30 at.% Pt exhibited similar oxidation resistance to the β alloys with 50 at.% Al. An initial effort was made to increase the Al content in the Pt-enriched γ+γ' coatings by introducing a short-term aluminizing process via pack cementation. However, too much Al was deposited, leading to the formation of β phase on the coating surface.

INTRODUCTION

The constant demand for increased operating temperatures in gas turbine engines has been the driving force for development of more reliable thermal barrier coating (TBC) systems to protect Ni-based superalloys.[1] Single-phase β-(Ni,Pt)Al coatings have been one accepted industrial standard as the bond coat for TBCs deposited by electron beam-physical vapor deposition (EB-PVD).[2] Failure of EB-PVD TBCs is often associated with spallation of the Al_2O_3 scale along the scale-bond coat interface.[1] In service, due to formation of Al_2O_3 scales and interdiffusion with superalloy substrates, depletion of Al leads to phase transformations from the as-deposited β phase to more Ni-rich phases such as martensite and γ'-Ni_3Al.[3,4] The formation of these new phases compromises the ability of the bond coat to maintain an adherent Al_2O_3 scale and contributes to rumpling at the bond coat surface.[5-7]

Recent studies by Gleeson et al. [8] indicate that the Ni-22Al-30Pt+Hf (at.%) cast alloys with a γ+γ' microstructure could form adherent α-Al_2O_3 scales with significantly reduced rumpling during thermal cycling. A simple γ+γ' coating can be synthesized by electroplating a superalloy substrate with ~7 μm of Pt followed by a diffusion treatment.[9-12] Studies in the laboratory have shown improved oxidation performance for the γ+γ' coatings on directionally-solidified (DS) René 142 alloys as compared to bare substrates. However, the scale spallation resistance was inferior to the β coatings on these DS substrates.[9] The present work indicates that substrate sulfur content alone cannot explain the inferior performance of γ+γ' coatings on the DS alloys. The oxidation results for model γ+γ' alloys suggest that higher Al and Hf levels may be beneficial. Therefore, additional processing steps are investigated to increase the Al content in the γ+γ' coatings.

EXPERIMENTAL PROCEDURES

Two versions of DS alloy René 142 and two versions of single-crystal René N5 were used as substrates. Table I shows the compositions of the substrate alloys determined by induction coupled plasma analysis and combustion analysis. As compared to the 142-C alloy, which had shown the best oxidation resistance among the three René 142 alloys previously studied,[9] the D alloy contained lower S (11 vs. 38 ppma) and slightly higher Hf (0.52 vs. 0.45 at.%). The low-S and high-S René N5 alloys contained 1 and 7 ppma S, respectively.[13] Test coupons of the superalloys, 16 mm diameter x 1.5 mm thick, were polished to 600-grit SiC paper and grit blasted using 220-grit alumina prior to Pt electroplating. The "simple" Pt-enriched γ+γ' coating was synthesized by electroplating the substrate with ~7 μm of Pt in a laboratory plating setup using commercial "Q" salt,[14] followed by a diffusion treatment in vacuum (~10^{-5} Pa) for 2 h at 1150-1175°C.[9]

Table I. Chemical Compositions of the Superalloy Substrates Determined by Induction Coupled Plasma Analysis and Combustion Analysis

	142-C		142-D		Low-S N5		High-S N5	
	wt.%	at.%	wt.%	at.%	wt.%	at.%	wt.%	at.%
Ni	58.9	60.4	58.2	59.5	63.2	64.7	64.3	64.8
Al	6.0	13.4	6.2	13.9	6.1	13.5	6.3	13.8
Cr	6.6	7.7	6.8	7.8	7.0	8.1	7.1	8.1
Co	11.7	11.9	11.7	11.9	7.4	7.5	7.4	7.4
Ta	6.3	2.1	6.3	2.1	6.3	2.1	6.1	2.0
W	4.7	1.6	4.7	1.5	5.2	1.7	4.4	1.4
Mo	1.5	0.9	1.5	0.9	1.4	0.9	1.3	0.8
Re	2.8	0.9	2.7	0.9	3.1	1.0	2.8	0.9
Ti	<0.01	—	0.03	0.04	0.008	0.01	—	—
Hf	1.32	**0.45**	1.54	**0.52**	0.20	0.067	0.17	0.057
Y (ppm)	—	—	—	—	4	3	5	3
C (ppm)	1100	5513	1200	5997	985	4930	984	4846
S (ppm)	20	**38**	6	**11**	0.5	**1.0**	4	**7.0**

The phase constitution and chemical compositions of the model Ni-Pt-Al alloys tested are given in Table II (all compositions in at.%). All of these alloys were vacuum-induction melted and cast in a water-chilled copper mold.[7,15] The castings were annealed for 4 h at 1300°C in ~10^{-4} Pa vacuum to homogenize the compositions and stabilize the grain size. Oxidation samples with dimensions similar to the superalloy specimens were polished to a 0.3 μm finish and ultrasonically cleaned prior to testing. Cyclic oxidation tests with cycles of 1 h at temperature and 10 min out of the furnace were performed on both the coatings and cast specimens at 1100°C in dry O_2.

Table II. Phase Constitution and Chemical Compositions of the Cast Alloys (at.%)

	Phase (s)	Ni	Al	Pt	Hf	C (ppma)	S (ppma)
Ni-22Al-10Pt	γ+γ'	67.8	22.2	9.9	0	271	0
Ni-22Al-10Pt+0.4Hf	γ+γ'	68.1	21.7	9.7	0.39	115	0
Ni-22Al-30Pt+0.02Hf	γ+γ'	48.0	22.1	29.5	0.02	77	0
Ni-50Al-5Pt	β	45.1	49.6	5.2	0	400	9
Ni-50Al-2Pt+0.05Hf	β	47.8	49.7	2.4	0.05	400	4

Secondary processing steps were carried out to explore the possibility of increasing the Al content in the Pt-enriched γ+γ' coatings. A short-term aluminizing process was performed after Pt plating via laboratory pack cementation, Table III. The pack aluminization was conducted in a tube furnace with flowing Ar at 1050°C. The coating time in Table III refers to the holding time at the coating temperature 1050°C. The packs consisted of 2-6% NH_4Cl activator, 10-25% (Cr-15Al) master alloy, balance inert Al_2O_3 filler powder (all in wt.%). The substrates were wrapped in a porous Al_2O_3 paper to avoid direct contact with the powders.[16]

Table III. Conditions of the Pack Cementation Experiments

Process	No.	Conditions
Pack Cementation (composition in wt.%)	#1	$2NH_4Cl$-25(Cr-15Al)-$73Al_2O_3$, 2 h
		$6NH_4Cl$-25(Cr-15Al)-$69Al_2O_3$, 2 h
	#2	$2NH_4Cl$-10(Cr-15Al)-$88Al_2O_3$, 0 h
	#3	$2NH_4Cl$-10(Cr-15Al)-$2HfO_2$-$86Al_2O_3$, 0 h

Selected specimens were characterized by field emission gun-scanning electron microscopy (FEG-SEM) equipped with energy dispersive spectroscopy (EDS). The coating composition profiles were measured by electron probe microanalysis (EPMA) using pure metal standards.

RESULTS AND DISCUSSION

3.1. OXIDATION PERFORMANCE OF SIMPLE γ+γ' COATINGS

Figure 1 shows the specific specimen mass changes during 1100°C cyclic oxidation testing of the simple Pt-enriched γ+γ' coatings on superalloys René 142 and N5. The CVD β-(Ni,Pt)Al coatings on 142-D and low-S N5 were included for comparison. The mass gains of the γ+γ' coatings on 142-D and C alloys (11 vs. 38 ppma S) were comparable after 800 cycles, whereas slight mass loss was found for the coated D alloy after 560 cycles. The β coating on 142-D exhibited substantially lower mass gain for 600 cycles. No significant difference in mass change was found for γ+γ'-coated N5 (high-S or low-S) and β-coated low-S N5, though all of them experienced lower mass gains than γ+γ'-coated 142 alloys.

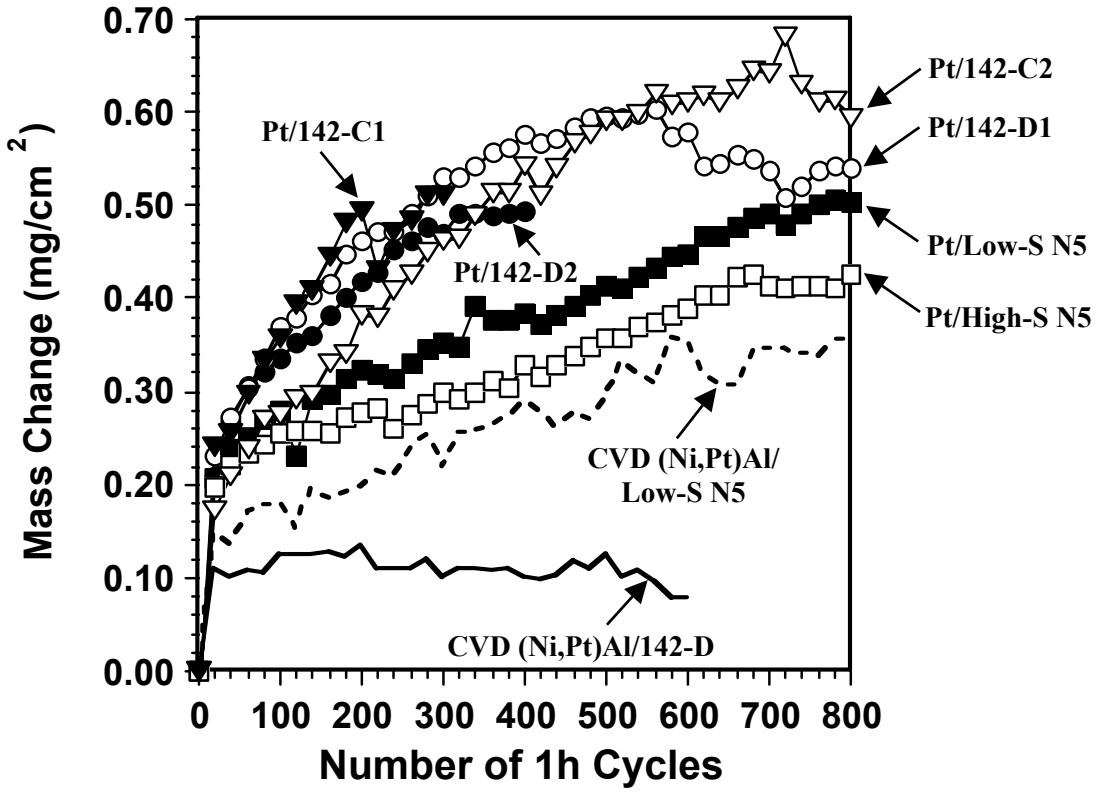

Figure 1. Specific specimen mass change for several Ni-based superalloys coated with simple Pt-enriched γ+γ' coatings during 1h cyclic oxidation tests at 1100°C. René 142-D and low-S N5 specimens with CVD β-(Ni,Pt)Al coatings were included for comparison.

Analysis of the oxidized surfaces by SEM revealed a uniform and adherent oxide scale on β-coated 142-D alloy after 500 cycles, Fig. 2(a). By comparison, some scale spallation occurred on γ+γ'-coated 142-D after 700 cycles, Fig. 2(b), particularly near the specimen center, similar to what was previously reported on the γ+γ'-coated 142-C alloy.[9] Though the γ+γ' coating surface after oxidation was slightly rougher on high-S N5, very adherent scales were observed on the γ+γ'-coated N5 after 700 cycles, Figs. 2(c)-(d), regardless of the different S contents in the substrate. The similarity could be due to the S introduced during the Pt electroplating process, which overshadowed the effect of S from the substrate.[17] Also, the overall oxidation performance of the γ+γ' coating on N5 was similar to the β coating on N5 at 1100°C. These results suggest that the oxidation behavior of the γ+γ' coatings was more substrate-dependent (although insensitive to substrate S), whereas the coating on single-crystal N5 clearly demonstrated better scale adhesion than on DS 142 alloys.

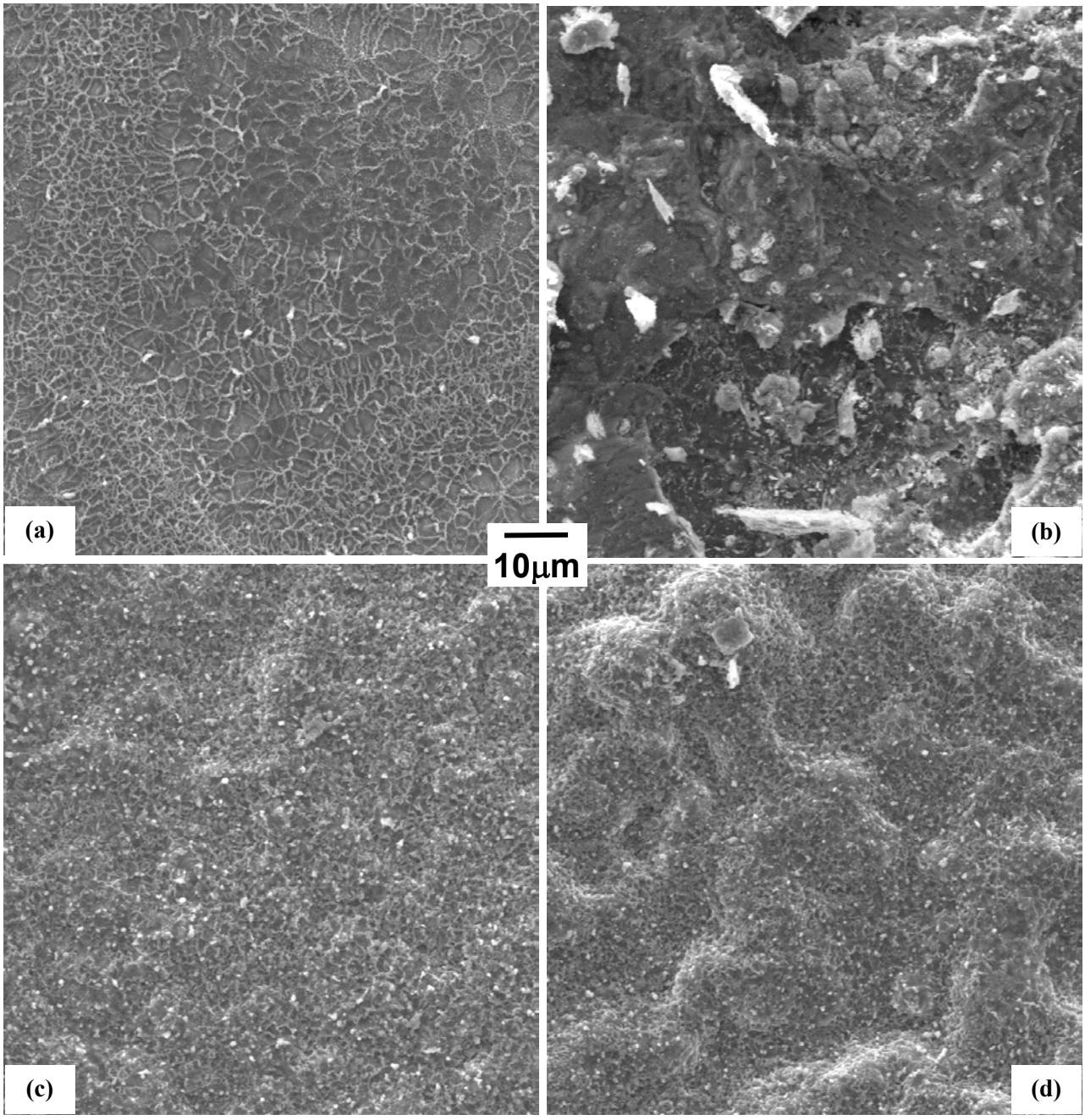

Figure 2. Secondary-electron images of the coating surfaces after cyclic oxidation testing at 1100°C: (a) β-(Ni,Pt)Al coating on 142-D after 500 cycles, (b) γ+γ' coating on 142-D after 700 cycles, (c) γ+γ' coating on low-S N5 after 700 cycles, and (d) γ+γ' coating on high-S N5 after 700 cycles.

3.2. OXIDATION PERFORMANCE OF MODEL γ+γ' ALLOYS

The cyclic oxidation behavior at 1100°C of five Ni-Pt-Al cast alloys is shown in Fig. 3. Lower Pt contents were investigated, as interdiffusion would likely reduce the Pt content during service.[9] The specimen of Ni-22Al-10Pt registered nearly the same mass gain as Ni-50Al-5Pt after 2000 cycles, indicating that with Pt incorporation, 22% Al was sufficient to form a protective Al_2O_3 scale. The Hf

additions significantly reduced the scale growth rate, as revealed by the lower mass gains for the alloys with 0.02-0.4% Hf, where ≤0.05% Hf appeared to be more beneficial than 0.4% Hf.[18] Higher Hf levels were included because the solubility of Hf in the γ+γ' two-phase field is higher than that in the β phase.[19] This result was consistent the previous findings by Gleeson et al. after 1150°C oxidation.[8] The optimum level of Hf in the Pt-containing γ+γ' alloys for the best oxidation resistance must be determined, and is needed to serve as a guideline for the target Hf level in the γ+γ' coatings.

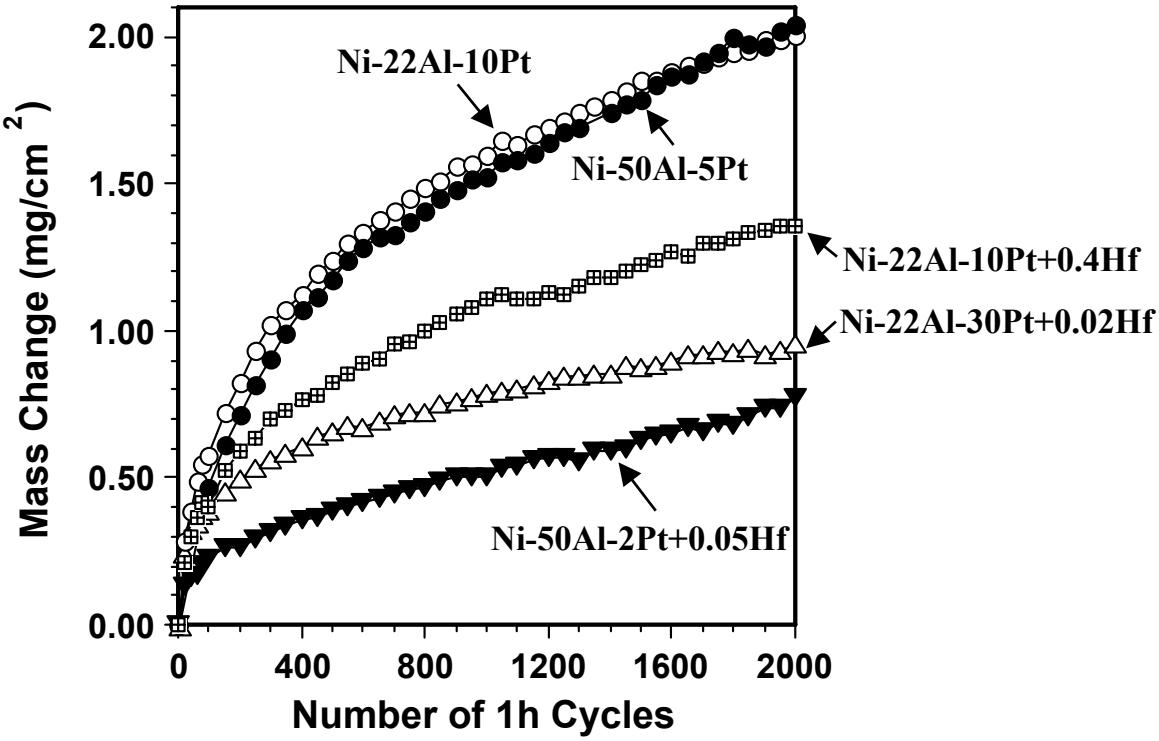

Figure 3. Specific specimen mass change for a group of Ni-Pt-Al cast alloys with and without Hf additions during 1h cyclic oxidation testing at 1100°C.

3.3. SECONDARY γ+γ' PROCESSING

In order to improve the oxidation resistance of the simple γ+γ' coatings, it was considered necessary to increase the Al content from 16-19% to ~22%, and to optimize the Hf contents. Initial attempts to increase the Al content were made by short-term aluminization via pack cementation, Table III.

In the first experiment (Pack #1), the coating exhibited a single β-(Ni,Pt)Al phase (~25 μm thick), and no effect of the amount of activator (2 vs. 6 wt.%) was noticed. The quantity of the master alloy was then reduced from 25 to 10 wt.%, and only 2 wt.% of activator was used. In addition, the aluminizing time was shortened from 2h to 0h, i.e., once the temperature reached 1050°C the furnace was turned off (Pack #2). The Al deposition actually occurred during heating and cooling, and the time above 800°C was estimated as 35 min. The coating consisted of a thin layer of β phase (~4 μm) with 50 at.% Al near the surface, and a Pt-enriched γ+γ' layer underneath, Fig. 5. Compared to the simple γ+γ' coating, the Al level was only marginally increased in the γ+γ' layer.[9] In Pack #3, Hf was incorporated by replacing 2

wt.% of Al_2O_3 with HfO_2. However, the Hf content in the coating was too low to be detected by EDS or EPMA. Oxidation testing may determine whether sufficient Hf is present in the coating.

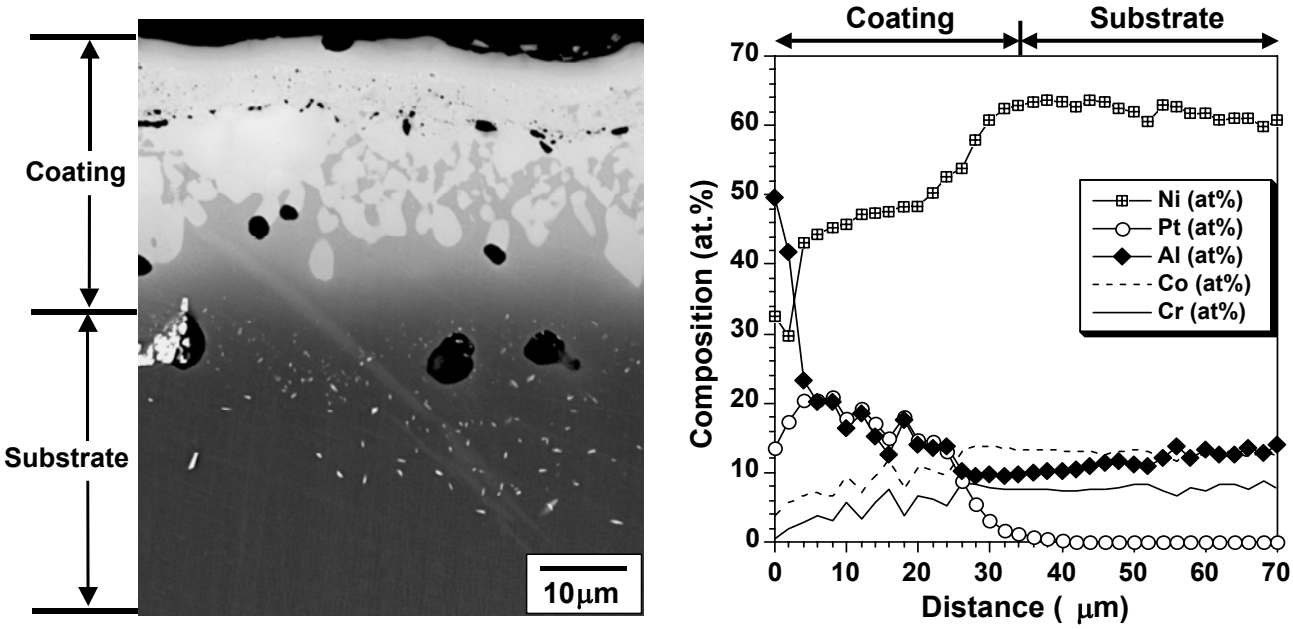

(a) (b)

Figure 4. (a) Back-scattered electron image of cross section of the modified γ+γ' coating synthesized by pack cementation, and (b) composition profiles of the major alloying elements measured by EPMA.

These preliminary results of coating development suggest that the Al activity in the pack aluminizing process was too high, and resulted in the formation of β phase at the coating surface. More attention will be given to reduce the Al deposition. For the pack process, since the surface Al concentration is practically time invariant,[20] the Al activity may be decreased by using Cr-Al or Ni-Al binary master alloys with lower Al content. However, if Cr-Al alloys are used as the master alloy, the Al cannot be reduced to below 10 wt.% where Cr co-deposition might occur.[16] Utilization of more stable activators than NH_4Cl, such as NaCl or NaBr [21] may also be able to reduce the Al deposition. Moreover, by increasing the distance between the specimen and pack powders using an "above-pack" arrangement, the Al content in the coating could be further reduced.[16]

CONCLUSIONS

Simple Pt-enriched γ+γ' coatings with 16-19 at.% Al on single-crystal René N5 superalloy showed comparable scale adhesion to the β-(Ni,Pt)Al coating during cyclic oxidation at 1100°C, which was superior to the γ+γ' coatings on DS alloy René 142. A beneficial effect of reduced S impurities in superalloy substrates on the oxidation performance of γ+γ' coatings was not noticeable during the 800 cycles at 1100°C, at least for the present S levels (up to 38 ppma in starting alloy). The cyclic oxidation testing of Ni-Pt-Al cast alloys with γ+γ' or β phase structure confirmed the excellent oxidation resistance for Hf-doped Ni-22Al alloys with 10-30% Pt. Initial experiments were conducted to increase the Al content in the Pt-containing γ+γ' coatings by a secondary aluminizing process such as short-term pack cementation. However, the formation of β phase near the coating surface suggests that the Al deposition in the aluminizing process was too high.

ACKNOWLEDGEMENTS

The authors acknowledge K.M. Cooley, J.L. Moser, and L.R. Walker at Oak Ridge National Laboratory (ORNL) and S.J. Geng at Tennessee Technological University (TTU) for assisting with the experimental work, and P.F. Tortorelli and J.A. Haynes at ORNL for reviewing the manuscript. This research is sponsored by the U.S. Department of Energy, Fossil Energy Advanced Materials Research Program, under contract DE-AC05-00OR22725 with UT-Battelle LLC and subcontract 4000032193 with TTU. Some of this material is based upon recent work supported by the National Science Foundation-GOALI Program under Grant No. 0504566.

REFERENCES

1. G.W. Goward, Surf. Coat. Technol., 108-109 (1998) 73
2. B.M. Warnes and D.C. Punola, Surf. Coat. Technol., 94-95 (1997) 1
3. Y. Zhang, J.A. Haynes, B.A. Pint, I.G. Wright, and W.Y. Lee, Surf. Coat. Technol., 163-164 (2003) 19
4. M.W. Chen, R.T. Ott, T.C. Hufnagel, P.K. Wright, and K.J. Hemker, Surf. Coat. Technol., 163-164 (2003) 25
5. V.K. Tolpygo and D.R. Clarke, Acta Mater., 48 (2000) 3283
6. D.R. Mumm, A.G. Evans, and I.T. Spitsberg, Acta Mater., 49 (2001) 2329
7. B.A. Pint, S.A. Speakman, C.J. Rawn, and Y. Zhang, JOM, Jan. (2006) 47
8. B. Gleeson, W. Wang, S. Hayashi, and D. Sordelet, Mater. Sci. Forum, 461-464 (2004) 213
9. Y. Zhang, B.A. Pint, J.A. Haynes, and I.G. Wright, Surf. Coat. Technol., 200 (2005) 1259
10. B. A. Nagaraj, W. B. Connor, R. W. Jendrix, D. J. Wortman, and L. W. Plemmons, US Patent No. 5,427,866, 1995
11. D. S. Rickerby, S. R. Bell, and R. G. Wing, US Patent No. 5,667,663, 1997
12. O. A. Adesanya, K. Bouhanek, F. H. Stott, P. Skeldon, D. G. Lees, and G. C. Wood, Mater. Sci. Forum, 369-372 (2001) 639
13. J.A. Haynes, B.A. Pint, K.L. More, Y. Zhang, and I.G. Wright, Oxid. Met., 58 (2002) 513
14. J.M. Albon, W.J. Davis, P.E. Skinner, and S.G. Warren, *US Patent* 5,102,509, 1992
15. B.A. Pint, Surf. Coat. Technol., 188-189 (2004) 71
16. R. Bianco and R.A. Rapp, J. Electrochem. Soc., 140 (1993) 1181
17. Y. Zhang, W.Y. Lee, J.A. Haynes, I.G. Wright, B.A. Pint, K.M. Cooley, and P.K. Liaw, Metall. Mater. Trans., 30A (1999) 2679
18. B.A. Pint, K.L. More, and I.G. Wright, personal communication, Oak Ridge National Laboratory, 2006
19. Al-Hf-Ni Phase Diagram, in G. Petzow and G. Effenberg (eds.) Ternary Alloys: A Comprehensive Compendium of Evaluated Constitutional Data and Phase Diagrams, Vol. 6, VCH Publishers, New York, NY, 1993, p. 176
20. S. Shankar and L.L. Seigle, Metall. Trans., 9A (1978) 1467
21. S.R. Levien and R.M. Caves, J. Electrochem. Soc., 121 (1974) 105

HIGH – TEMPERATURE CORROSION RESISTANCE OF CANDIDATE FeAlCr COATINGS IN LOW NOx ENVIRONMENTS

J.T. Murphy, A.R. Marder, and J.N. DuPont
Materials Science and Engineering
Lehigh University
5 E. Packer Ave.
Bethlehem, PA 18015

ABSTRACT

FeAlCr alloys are being evaluated for implementation as corrosion resistant overlay coatings for structural components in ultra supercritical coal fired boilers. Previous work has shown these alloys exhibit excellent corrosion resistance in current low NOx conditions. This behavior makes them prime candidate for the next generation of PC boilers. Conceptual USC boilers show a change to ASTM 213 T-92 and T-23 as the candidate alloys for the actual construction of waterwall tubes. In addition there are plans to extend the use of T-92 into the superheater section. Within the superheater there is a shift from the sulfidizing environment of the waterwalls to an oxidizing environment that will promote coal-ash corrosion. This type of corrosion occurs when both alkali salts and oxidizing gas environments react to form low melting temperature phases that aggressively attack metal surfaces. Therefore aside from the sulfidizing environment of the waterwalls, the FeAlCr alloys need to be evaluated in the coal ash condition. A weldability study of FeAlCr alloys was performed on the candidate structural alloys using a single pass gas tungsten arc weld. Weld compositions were measured using electron probe microanalysis. From the regime of weldable compositions, candidate alloys were selected for corrosion study. A testing of three coal-ash procedure setups was conducted to determine the style that would best promote the reaction. Synthetic coal ash of 0.5g, 1.0g, and 1.5g was deposited on bare T-92 material and exposed at 625°C for times of 50, 100, and 150 hours in a simulated low NO_x oxidizing gas. The setups were evaluated with change in weight and depth of attack measurements.

INTRODUCTION

In order to cope with ever increasing energy demands, power companies have undertaken efforts to increase the efficiency of pulverized coal (PC) boilers. The efforts are geared towards constructing plants that operate in what has been termed the ultra-supercritical (USC) burning condition. USC boilers will operate at higher combustion temperatures and pressures than current PC boilers. As has been previously reported, the atmospheric conditions present in the combustion area of the boilers lead to accelerated metal wastage of the boiler waterwall tubes, mainly through a sulfidation attack from both the gaseous environment and slag that is deposited on the metal surface [1]. The elevated temperatures associated with USC can only help to accelerate this corrosion problem.

Aside from the sulfidation attacks associated with the combustion stage of the boiler, a second corrosion mechanism, coal-ash corrosion, becomes a concern in the superheater regions of the boilers. Within the superheater section, there is a shift from a sulfidizing to an oxidizing environment. Along with the atmospheric changes there is a further increase in temperature. The temperatures seen here coupled with the oxidizing environment produces conditions that promote the formation of liquid alkaline-iron trisulfates (AIT's) which aggressively attack the tube metal surface through a fluxing process[2-13].

Candidate alloys have been selected for the structural component of USC boilers that show good high temperature fatigue strength. The candidate alloys for the waterwall sections are T-23 and T-92[14-17]. Conceptual designs for USC boilers have both alloys in use in the waterwall sections, with T-23 in the

lower sections. The T-92 will be implemented in the higher sections of the waterwalls along with the initial portions of the superheaters[14]. Although both alloys show strong high temperature fatigue strength they are severely limited by their corrosion resistance under the aforementioned conditions. Therefore, coatings of some type are required to protect the water bearing tubes under the various corrosive environments associated with a USC boiler. Previous work with weld overlay coatings have shown that iron-aluminum-chromium alloys demonstrated excellent corrosion resistance against the sulfidizing environment for current low NOx boiler waterwalls[1]. This corrosion resistance makes FeAlCr alloys prime candidates for overlay coatings in the next generation of coal fired boilers. The objectives of this study are two-fold. First it will be necessary to determine the weldablity of these FeAlCr alloys on the candidate alloys selected for use in the USC waterwalls and superheaters. Secondly, the corrosion resistance of candidate FeAlCr weld alloys must be characterized in both the sulfidizing waterwall environment and coal ash conditions seen in the superheater section.

EXPERIMENTAL PROCEDURE

WELDABILITY INVESTIGATION OF T-92 AND T-23 SUBSTRATES

Single pass Gas Tungsten Arc Welding (GTAW) was performed on alloys ASTM 213/213M T-23 and T-92. The T-23 substrates were plates in dimensions of 2" x 12" x ¼". T-92 welds were performed on tube substrate with 3/16" wall thickness. Aluminum and chromium additions were made by simultaneously depositing two filler metal wires on to the substrates. Single pass welds were made by depositing pure aluminum (1100) wire and a ferritic stainless steel (430SS). Weld compositions were varied by independently altering the feed rates of the two filler metal wires from 0 – 200 ipm (inches per minute). The metal substrates were prepared by grinding the surface with SiC to remove any scale and to expose bare metal.

When welding on plates, a constant current of 220A was used. The electrode was kept at a constant distance above the substrate to maintain an arc gap of 0.045". This kept a contolled voltage of around 11V. Approximately 9" long weld beads were made with a travel speed of 4.5ipm. For the T-92 tubes, all welding parameters were kept except for welding current. Due to the decreased thickness the welding current was varied between 150 – 200A, until an acceptable looking weld was made. Weld compositions were obtained through electron probe microanalysis (EPMA). Multiple point measurements were taken from three different areas within a sample fusion zone in order to get a representative value of composition.
The cracking behavior of the welds for both substrates was determined using a non-destructive dye-penetration method. After laying the weld, the substrates were allowed to cool for at least 48 hours. This was done to allow sufficient time for cracking to occur.

COAL ASH PROCEDURE TESTING

Two main methods have been used in the literature for testing in the simulated coal ash condition. The first, referred to as the slurry method, involves combining the comprised ash with either water or ethanol to form a paste that is then coated onto the samples. The samples are then suspended and placed into the furnace. The second setup, referred to as the crucible style, centers around placing the sample in a crucible, covering in dry ash, and then exposing the samples in that condition. A third style existed which has been used at Lehigh University for testing solid slag of FeS in the simulated waterwall environment. This style is very similar to the crucible testing, however the ash is concentrated over one local spot on the sample and contained within a quartz ring. In order to determine which setup would allow for the

most aggressive condition and also greatest reproducibility, a testing matrix was performed with the three testing styles.

For the testing of the various coal ash procedures, samples were taken from the T-92 substrates used in the welding study. For both the slurry and crucibles, samples were ground into square coupons, roughly 10x10cm, up to 600 grit using SiC paper. The sides and corners were rounded in order to minimize edge effects. Each sample was then cleaned in acetone, dried and weighed. For the solid state test it was only necessary to ground one surface down to 600 grit. The synthetic ash was made in 0.5g, 1.0g, and 1.5g deposits, composed of Fe_2O_3-Na_2SO_4-K_2SO_4 in a ration of 25wt%-37.5wt%-37.5wt% respectively. The components were measured out on an electronic scale in an aluminum crucible and then ground together using a pestle for rough 7-10 minutes in order to ensure good mixing. For the slurry test, small amounts of ethanol were added to the mixed ash and the mixture was applied to the sample with a small brush. After application the sample was allowed to dry for 1 hour and then weighed to calculate the amount of ash applied. The fully coated specimens were suspended with alumina rods in perforated aluminum crucibles and depicted in Figure 4. For the crucible test, the specimen was placed within the same type of aluminum crucible used in the slurry test. The dry ash was the deposited on top and then entire setup was placed within the furnace. Figure 5 depicts this set. Finally for the solid state test, the surface was wiped clean with acetone. A quartz ring was attached to the surface using Crazy Glue. The dry ash was then deposited within the confines of the quartz ring. A schematic of the setup is shown in Figure 6.

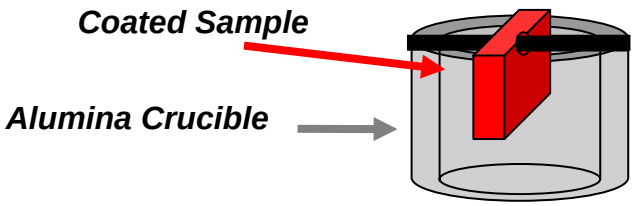

Figure 4 – Schematic picture of slurry testing setup

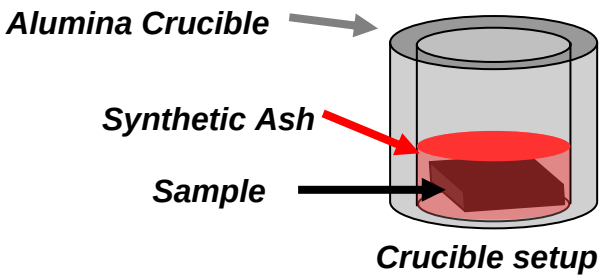

Figure 5 – Schematic image of crucible testing setup

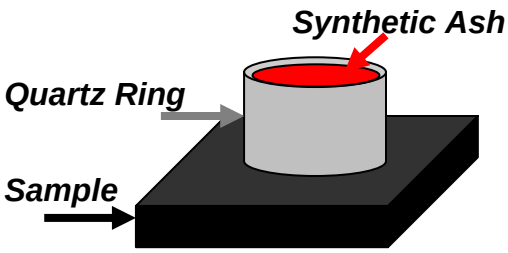

Figure 6 – Schematic drawing of solid state test

With each setup, every deposit amount was exposed to an oxidizing gas environment (2vol%O_2–15vol%CO_2–6vol%H_2O–0.12vol% SO_2–Bal. N_2) for time intervals of 50, 100, and 150 hrs at 625C. Testing was performed in a Lindberg/Blue Horizontal Tube Furnace with water vapor inserted in the furnace at a controlled rate, via a capillary tube connected to a programmable syringe pump. With the crucible and slurry samples, the samples were then mounted in clear low viscosity epoxy, under vacuum. The mounts were then prepared up to 1um diamond. For the solid state samples, they were first mounted in clear low viscosity epoxy, left to cure, then sectioned in half and re-mounted. The solid state samples were prepared in the same manner as the other two tests. The corrosion behavior was characterized by depth of attack measurements. In order to firmly establish the ash/metal interface for each of the testing styles, a platinum marker was tack welded to the sample surfaces. The platinum markers were only used on the samples in which the largest amount of ash was deposited and exposed for the longest exposure time. For taking the depth of attack measurements, the samples were taken on a Nikkon LOM with the Leco 3001 software program. For each sample, three measurements were taken in three different fields for a total of nine depth measurements that were then averaged.

RESULTS AND DISCUSSION

WELDABILITY INVESTIGATION OF T-92 AND T-23 SUBSTRATES

Figure 1 is a plot compositions and their weldability on the T-23 substrate. The 'Previous Weldability" line labeled in the figure comes from the previous welding study that was performed using FeAlCr alloys on a plain carbon steel substrate, A285C. Despite the change in substrates, the cut-off of weldable compositions remains the same. The T-23 overlays will only be subjugated to the sulfidizing environment associated with the initial stages of the coal combustion process. For this reason, the only composition of interest in the critical Fe-10wt%Al-5wt%Cr, which provided the best corrosion resistance up to 2000 hours of exposure in the previous study.[1] For the scope of this project it is only important to be able to hit this composition and then test it in the simulated USC low NOx waterwall environments.

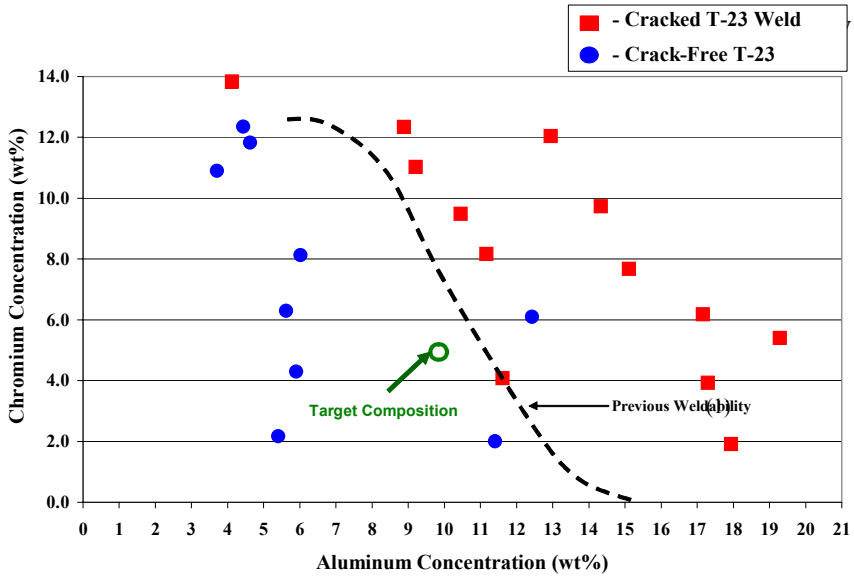

Figure 1 – Weldability plot of chromium versus aluminum concentration (wt%) for the T-23 substrate

Figure 2 displays the weldability of alloys deposited on the T-92 substrate. Again the 'Previous Weldability' line is referring to the cracking boundary determined through the FeAlCr welding study performed on a A285C steel substrate. It can be seen that the range of weldable compositions for this alloy differs greatly from what was seen with the T-23 and A285C.

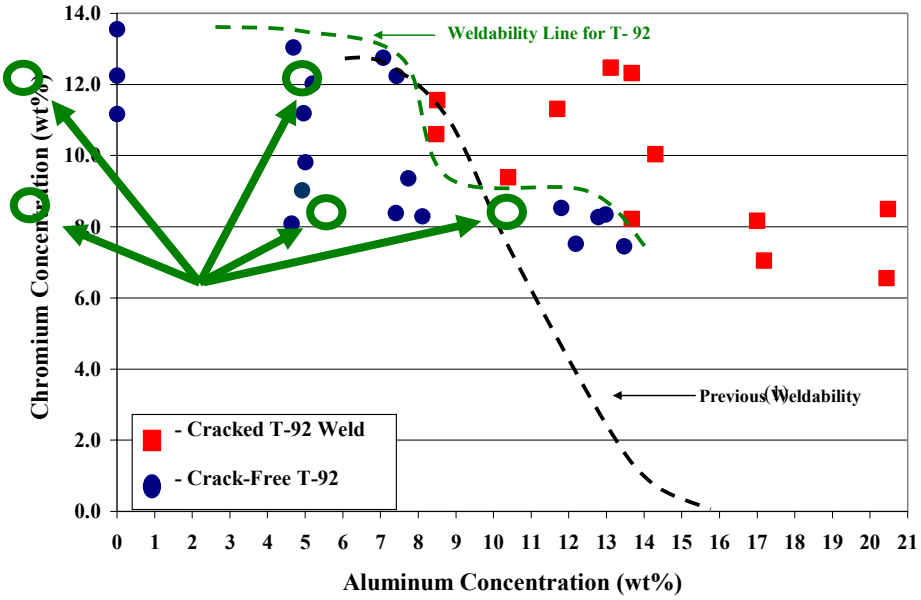

Figure 2 – Compositional plot of chromium versus aluminum (in wt%) for the T-92 substrate.

First, it is possible to achieve higher concentrations of chromium in a binary Fe-Cr overlay alloy with the T-92 substrate. In fact the cracking boundary for the binary Fe-Cr weld could not be reached. The highest concentration displayed, ~14wt%Cr, represents a FeCr wire feed speed of 200 ipm. This is the maximum allowable wire feed rate allowed with the GTAW setup used in this study. Therefore, it was not possible to reach a chromium concentration that was susceptible to hydrogen cracking. The boundary established in the figure is therefore established as a process limitation and not an actual welding boundary. Second, at a chromium composition of 8wt% it can be seen that the weldability boundary shifts out from 10wt%Al (seen in the T-23 and A285C substrates) and is extended up to 14wt%Al. Initially, it was not clear whether the welds at these compositions were truly crack free or simply one time anomalies. Further testing was performed, in which a composition at near the nose boundary and a composition at the previously determined boundary was obtained. The dye penetrant showed neither weld to posses any cracks. Thus it was determined that they were in fact truly weldable compositions and that the extension of the weldable regime did exist. Finally, it can be seen that for the T-92 substrate, there are no compositions below 8wt% Cr. This is due to the base composition of the base plate. T-92 has a Cr composition of about 9wt%. Thus even when using only the pure aluminum wire, it is not possible to reach any compositions below 8wt%Cr.

The T-92 alloy will be implemented as the structural material for not only the upper sections of the waterwall tubes, but also for sections of the superheater as well. Therefore, T-92 will be exposed to both the sulfidizing environment as well as the coal ash condition. For the simulated waterwall section, only one candidate composition will be tested. With the extended region of weldable composition at the lower chromium concentration, it is possible to obtain alloys that have compositions beyond the critical 10wt%Al-5wt%Cr determined in the previous study. Therefore, for protection against the sulfidizing environment, a composition of Fe-13wt%Al-8.5wt%Cr will be selected for testing from the T-92 substrate.

For the coal-ash condition, the literature has shown that chromium is the critical alloying element for corrosion resistance. It has also been established that an alumina scale forming from intermetallic iron-

aluminides catastrophically fail under a fluxing attack from AIT's[18-23]. In the case of these FeAlCr alloys it is unclear as to what makes up the bulk of the oxide passive layer. Also any alumina forming agents will be in solid solution with the chromium. Therefore, it would be improper to base the behavior of these alloys off of Fe-Al intermetallic results. For this reason, a matrix of compositions will be selected from the T-92 substrate. These are the highlighted compositions in Figure 2. The reasoning behind the selection is the desire to individually test the effect of chromium and aluminum additions to the overall weld composition. The alloy selected for the waterwall section will also be included to see the effect of large aluminum additions.

COAL ASH PROCEDURE TESTING

Solid State Test

Of all the test methods examined in this study, the solid state provided the weakest reaction of the synthetic ash. As demonstrated in the plot of depth of attack in Figure 7, this setup saw little corrosion up to 100 hrs. and then saw an acceleration of attack as the time changed from 100 to 150hrs. However, even at this time the depth of attack was still less than then other two methods at the same time of exposure. At the final testing time, the all three ash deposits should no sign of exhaustion. This might be considered good as it could mean that this set up requires little refreshing of the ash, however, visual inspection of the samples that a large amount of the synthetic ash was not being consumed during the testing exposure.

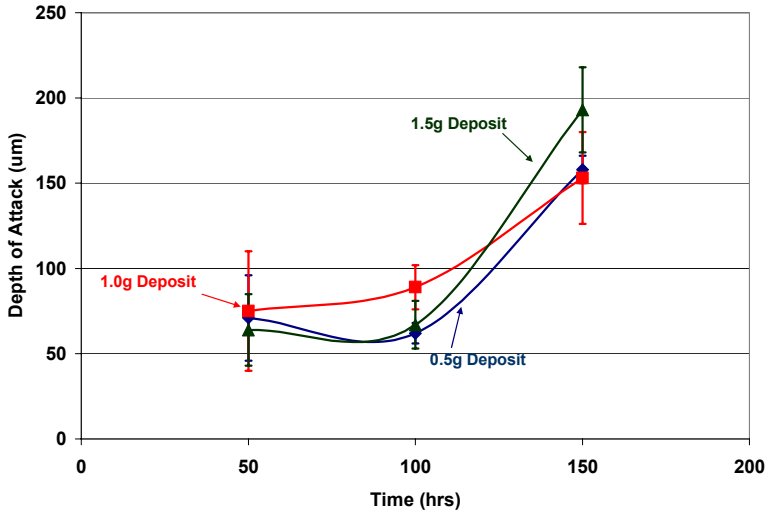

Figure 7 – Plot of average depth of AIT attack on a T-92 substrate with various deposit sizes for times up to 150hrs using the solid state test style.

When the ash is first deposited on the samples it is a strong brick red color. After testing a change to a darkish grey color was an easily discernable characteristic to show if there was an actual reaction between the ash and the metal. In the case of the solid state test, the majority of ash did not change color. From the LOM images, it was deduced that there was an initial reaction that lead to the formation of small amount of corrosion product present. However, something then prevents the majority of the ash deposit to react. There are two possible explanations to the behavior. One scenario is that the AIT that actually does react with the metal forms a scale surface above the metal that prevents the higher ash from interacting with the metal surface. It is also possible, that the way the ash is arranged it hinders diffusion of gas to the metal interface and thus limits the reaction. The amount of attack for each of the deposits is relatively the same at all three time intervals. Therefore this method is showing no difference in corrosion with change in amount of ash present. From this behavior it can be deduced that a particular amount of ash is reacting to

for the liquid AIT (a small portion directly at the metal surface) and preventing further reaction. Even the smallest deposit is seeing this effect, otherwise it should be showing high corrosion rates with the lower deposit amounts. This is reiterated again through the LOM images shown in Figure 11. The solid state sample clearly shows a visibly lower amount of corrosion attack compared to the other two methods.

As mentioned earlier the quartz ring used to contain the ash is adhered to the sample by simple crazy glue. At higher temperatures, however, this adhesive will disintegrate and allow the ring to disconnect from the sample surface. This results in an open path for the liquid AIT to escape from the quartz enclosure and attack areas of the sample outside the area of interest. There was evidence of this by similar corrosion scale both outside and inside the area enclosed by the quartz ring. The ability of the liquid AIT to leak to other areas posses a problem as it could reach other areas of the furnace and react. The combination of the aforementioned factors prevents the solid state setup from being a feasible style to use as the testing setup.

Slurry Test

From the date presented in the plot of Figure 8 there does not seem to be any discernable trend between with either change over time or alterations in deposit amount. The largest visible discrepancy is seen at the 100hr mark. Here there are two ash deposits, 0.5g and 1.5g, which show a decrease in depth of attack from the 50hr test. The 1.0g deposit, however, has a spike in attack at the 100hr mark. This irregularity points to the main problem with the slurry method, namely its reproducibility. For this method the ash is made into a paste and applied to the sample. However, there is no way to guarantee an even distribution of the ash over the sample. Because of the need to apply the ash as a coat, there will be variability in the total amount of ash place on the sample. However, visual inspection did show this method did encourage better reaction of the synthetic ash.

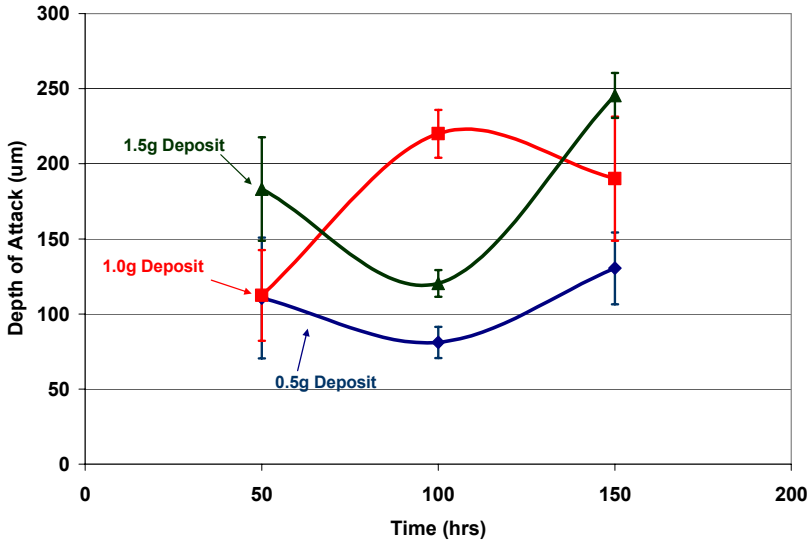

Figure 8 – Plot of average depth of attack on T-92 substrate with various deposit sizes for times up to 150hrs, using the slurry test style.

Crucible Test

As compared to the plots for the slurry and solid state test, the plot for the crucible test, shows discernable trends for both changes deposit size and time. One point of interest in Figure 9 is that in the initial 50hr test the 0.5g deposit actually shows a greater attack than the other two deposit size. However, as time increases the other two weights eventually surpass the 0.5g deposit in depth of attack. A possible explanation for this behavior is similar to the behavior seen in the solid state testing. For the 50hr test, the greater deposit amounts hinder a good reaction occurring between the ash and metal. Thus more of the

ash in the 0.5g deposit is able to take part in the corrosion process. This idea is also supported by the fact that at 50hrs, the larges deposit, 1.5g, shows the least amount of attack followed the second largest deposit.

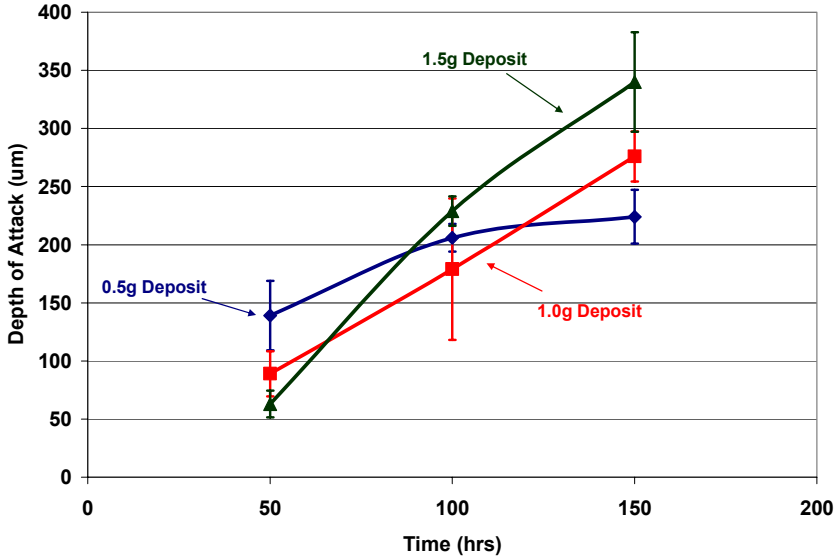

Figure 9 – Plot of average depth of attack on T-92 substrate with various deposit sizes for times up to 150hrs, using the crucible test style.

By the shape of the curve for the 0.5g deposit, it can be estimated that the deposit is actually being exhausted by and the depth of attack bottoming out by 150hrs. The other two deposits, 1.0g and 1.5g, catch up to the smaller deposit in regards to aggressiveness of attack by 100hrs. This hints at a sort of incubation time for these level of deposits, where it take time for all the agents involved with the reaction to properly mix and actively attack the metal surface. It may be noticed that the depth of attack associated with this style is much greater than either of the other two, especially at 150hrs. This can be attributed to the orientation of the sample and how the ash is dispersed. The sample is place with a planar face oriented down, as demonstrated in Figure 5. The synthetic ash is then poured over the sample. Thus, in regards to ash dispersion, the main difference between this method and the slurry is that all the ash is set to attack only one surface, where with the slurry setup the ash is spread to attack the entire surface area of the sample.

All of these results for the crucible test point to the ability of this setup to promote a reaction that does see discrete changes over time and also detect effects related to change in deposit size. Finally in the terms of actually set up, this method is the easiest of the three. The entire reaction is contained within the crucible so there is no fear of leaks reaching other parts of the furnace and as evidenced by the 0.5g deposit this setup can allow a deposit to go to complete exhaustion unlike the solid state setup. Compared to the slurry style, the crucible method provides a much more even distribution of ash over the area of contact, but most importantly, because the dry ash is poured into the crucible directly after measure the crucible method has a much higher degree of confident reproducibility.

CONCLUSIONS

A weldability test using a single GTAW weld pass was performed on candidate USC boiler structural alloys. Along with the weldability examination, high temperature coal ash corrosion tests were performed on T-92 samples using three various testing setups. The following conclusions were drawn from the two aforementioned investigations:

1. The weldability behavior of the T-23 makes it possible to obtain the critical composition necessary for good corrosion resistance in low NOx boilers.
2. The weldability behavior of T-92 allows for elevated chromium and aluminum concentrations then previously seen in T-23 and A285C
3. The crucible style of testing coal ash corrosion allows for easy reproducibility and shows good sensitivity with changes in deposit size and exposure time
4. The solid state style of testing hinders good reaction of the synthetic ash and results in very limited formation of AIT
5. The slurry style of testing allows for good reaction between synthetic ash and metal, however application process introduces large source of error and prevents good reproducibility

REFERENCES

1. J. R. Regina, J. N. DuPont, and A. R. Marder, "High-temperature corrosion behavior of Fe-Al weld overlay coatings for the protection of boiler tubes in low NOx environments". *Proceedings of the International Technical Conference on Coal Utilization & Fuel Systems* **29th**, 397-408 (2004).

2. J. L. Blough, G. J. Stanko, and W. T. Bakker. "Coal ash corrosion in a reheater of an ultra-supercritical power plant". 2001. Advances in Materials Technology for Fossil Power Plants, Proceedings of the Conference, 3rd, Swansea, United Kingdom, Apr. 5-6, 2001.

3. J. L. Blough and W. W. Seitz, "Fireside corrosion testing of candidate superheater tube alloys, coatings, and claddings - phase II". *Chemical Engineering World* **34**, 65-68, 71 (1999).

4. S. Van Weele and J. L. Blough. "Attack of superheater tube alloys, coatings, and claddings by coal-ash corrosion". 367-374. 1992. Oak Ridge Natl. Lab., [Rep.] ORNL/FMP (U. S.).

5. J. Blough and W. T. Bakker. "Measurement of superheater corrosion by molten alkali sulfates". 1991. Heat-Resist. Mater., Proc. Int. Conf., 1st.

6. S. Van Weele and J. L. Blough. Literature search update: fireside corrosion testing of candidate superheater tube alloys, coatings, and claddings . Foster Wheeler Report. 1990.

7. P. Castello, V. Guttmann, N. Farr, and G. Smith, "Simulated coal ash corrosion of Ni-based alloys". *Materials at High Temperatures* **19**, 29-40 (2002).

8. S. Kihara, K. Nakagawa, W. Wolowodiuk, J. L. Blough, and W. T. Bakker. "Corrosion resistance of advanced tube materials in coal-fired boilers". 1992. High Temp. Corros. Adv. Mater. Prot. Coat., Proc. Workshop.

9. S. Kihara, K. Nakagawa, A. Ohtomo, H. Aoki, and S. Ando. "Simulating test results for fireside corrosion of superheater and reheater tubes operated at advanced steam condition in coal-fired boilers". 1985. High Temp. Corros. Energy Syst., Proc. Symp.

10. B. A. Baker and G. D. Smith. “Corrosion Resistance of Alloy 740 as Superheater Tubing in Coal-Fired Ultra-Supercritical Boilers”. 2004. Corrosion 2004.

11. K. Natesan, A. Purohit, and D. L. Rink. “Fireside Corrosion of Alloys for Combustion Power Plants”. 2003. 17th Annual Conference on Fossil Energy Materials.

12. J. L. Blough, G. Stanko, W. T. Bakker, and J. B. Brooks. “Superheater Corrosion in Ultra-Supercritical Power Plants”. 2000. Corrosion 2000.

13. W. T. Bakker, J. L. Blough, and W. W. Seitz. “Low NOx Combustion Systems and Superheater Corrosion”. 2001. Corrosion 2001.

14. S. L. Goodstine and J. C. Nava. “Use of surface modification of alloys for ultrasupercritical coal-fired boilers”. 2005. Advances in Materials Technology for Fossil Power Plants, Proceedings from the International Conference, 4th, Hilton Head Island, SC, United States, Oct. 25-28, 2004.

15. J. F. Henry, J. D. Fishburn, I. J. Perrin, B. Scarlin, G. N. Stamatelopoulos, and R. W. Vanstone. “Advanced Supercritical Technology: A Vital Component of Future Power Generation”. 2004. 29th International Tech Conference on Coal Utilization and Fuel Systems.

16. R. Viswanathan and W. Bakker, “Materials for ultra-supercritical coal power plants-boiler materials: part 1”. *Journal of Materials Engineering and Performance* **10**, 81-95 (2001).

17. R. Viswanathan, J. F. Henry, J. Tanzosh, G. Stanko, J. Shingledecker, and B. Vitalis, “Materials for ultrasupercritical coal-fired power plant boilers”. *Proceedings of the International Technical Conference on Coal Utilization & Fuel Systems* **29th**, 1051-1067 (2004).

18. D. Das, R. Balasubramaniam, and M. N. Mungole, “Hot corrosion of Fe3Al”. *Journal of Materials Science* **37**, 1135-1142 (2002).

19. M. A. Espinosa-Medina, M. Casales, A. Martinez-Villafane, J. Porcayo-Calderon, L. Martinez, and J. G. Gonzalez-Rodriguez, “Hot corrosion of atomized iron aluminides doped with boron and reinforced with alumina”. *Materials Science & Engineering, A: Structural Materials: Properties, Microstructure and Processing* **A300**, 183-189 (2001).

20. F. Gesmundo, Y. Niu, F. Viani, L. C. Li, and O. Tassa. “Hot Corrosion of Iron Aluminides for Automotive Components”. 1992. Materials Development in Rail, Tire, Wing, Hull Transportation.

21. W. H. Lee and R. Y. Lin. “Molten salt-induced hot corrosion of iron aluminides”. 1990. Proc. Annu. Conf. Fossil Energy Mater., 4th.

22. W. H. Lee and R. Y. Lin, “Oxidation, sulfidation and hot corrosion of intermetallic compound Fe3Al at 605°C and 800 °C”. *Materials Chemistry and Physics* **58**, 231-242 (1999).

23. P. F. Tortorelli and K. Natesan, “Critical factors affecting the high-temperature corrosion performance of iron aluminides”. *Materials Science & Engineering, A: Structural Materials: Properties, Microstructure and Processing* **A258**, 115-125 (1998).

CONCEPTS FOR SMART PROTECTIVE HIGH-TEMPERATURE COATINGS

P.F. Tortorelli
Oak Ridge National Laboratory, Oak Ridge, TN 37831-6156
tortorellipf@ornl.gov ; Tel: (865) 574-5119; FAX (865) 241-0215

M.P. Brady
Oak Ridge National Laboratory, Oak Ridge, TN 37831-6115
bradymp@ornl.gov; Tel: (865) 574-5153; FAX (865) 241-0215

I.G. Wright
Oak Ridge National Laboratory, Oak Ridge, TN 37831-6156
wrightig@ornl.gov; Tel: (865) 574-4451; FAX (865) 241-0215

ABSTRACT

Smart protective coatings may provide one avenue to overcoming materials barriers imposed by the requirements of advanced fossil energy systems. To this end, the high-temperature oxidation-sulfidation of TiAlCr-(Nb,Ta) compositions was qualitatively evaluated as part of efforts to develop schemes for using alloy coatings for corrosion protection under aggressive high-temperature environments. The TiAlCr system shows initial promise as a candidate protective coating for sulfidation resistance when a continuous Al_2O_3 surface layer can form, even at the low oxygen partial pressure of the sulfidizing environment.

INTRODUCTION

Environmental resistance is a critical material barrier to the operation of fossil energy systems with improved energy efficiencies, economies, and environmental benefits. All fossil fuel-derived processes contain reactive species such as sulfur, chlorine, hydrogen, carbon, water vapor, and oxygen and high-temperature degradation arising from reactions of solids with gases and condensible products often limits performance or materials lifetimes such that efficiency, emission, and/or economic targets or requirements of advanced systems are not realized. High-temperature corrosion resistance is predicated on the formation of stable, protective (slowly reacting, mechanically sound, adherent) surface products. Factors affecting the establishment and stability of such layers have been studied for many years, yet the selection or development of materials to withstand the harsh operating conditions of advanced fossil-fuel-based technologies is still an imposing technical challenge in terms of acceptable lifetimes and associated costs when faced with multiple reactive species, high temperatures and pressures, and variations in operating conditions. Consequently, to seek solutions that have the most far-ranging impact on this

difficult, wide-ranging problem, this work seeks advances in materials and materials protection that require new research, development, synthesis and/or performance approaches for candidate coating compositions and structures that are corrosion resistant in multiple or changing high-temperature environments (such as the smart corrosion-resistant coatings proposed by Nicholls[1]). The focus is on coating concepts as coatings offer possibilities for corrosion protection under aggressive (and changing) environmental conditions while the substrate provides strength or other desired properties.

The purpose of this work is to assess the feasibility of different material and design approaches to smart protective coatings by exploring new alloying and microstructural routes to improved high-temperature environmental resistance of metallic materials. As such, this work supports the overarching goal of the Department of Energy's Fossil Energy Advanced Research (AR) Materials Program to provide a materials technology base to assure the success of coal fuels and advanced power generation systems. This specific project is motivated by need for materials with improved high-temperature environmental resistance that could be used as protective coatings under the harsh conditions encountered in advanced fossil systems. Historically, the development of materials for fossil-fuel combustion and conversion systems has been closely linked to corrosion studies of alloys and ceramics in appropriate environments so as to identify reaction or degradation mechanisms and develop and/or select materials that offer improved performance. This work, however, differs from these others in that it evaluates the feasibility of new routes to controlling the critical chemical and mechanical phenomena that collectively form the basis for corrosion resistance in relevant fossil environments by exploring compositional and microstructural manipulations and cooperative phenomena that have not necessarily been examined in any detail to date. Its goal is not to develop coatings per se. Rather, it is to examine concepts that can then be translated into coatings by further developmental efforts if promising high-temperature corrosion results are found for a particular composition/microstructure combination (and possible synthesis routes can be identified). This approach can hopefully lead to concepts for "smart" coatings or materials that have the ability to sense and respond appropriately to a particular set or series of environmental conditions in order to provide high-temperature corrosion protection.

The current effort is a modest one, focused on concept definition and exploratory experimentation aimed at proof-of-principle. The most successful concepts can transition to a more comprehensive project within the AR Materials Program or graduate to a technology development project. The strategies being explored in this work involve cooperative or in-place oxidation or sulfidation reactions of multiphase alloys.[2,3] The first material system evaluated involved the multiphase Mo-Si-B system. More recently,

the oxidation and sulfidation of TiAlCr and TiAlCr-X compositions (X = Nb, Ta, or both) have been investigated.

RESULTS AND DISCUSSION

The oxidation behavior of ternary, multi-phase γ-TiAl + $Ti(Al,Cr)_2$ Laves Phase alloys has been extensively studied.[4-6] The presence of Cr promotes the exclusive formation of alumina by modifying subsurface depletion and stabilizing and sustaining the $Ti(Cr,Al)_2$ Laves phase at the alloy/scale interface rather than deleterious, less oxidation-resistant phases such as α_2-Ti_3Al. Accordingly, the present work sought to conduct a preliminary assessment of similar compositions of TiAlCr in terms of their behavior under sulfidizing conditions as good resistance would be anticipated if alumina layers can still form. The addition of X = Nb,Ta was made in an attempt to enhance their resistance to sulfidation, as Nb and Ta sulfides should be slow growing.[7] There is also some limited prior evidence that titanium aluminides have good sulfidation resistance (under less aggressive conditions than the present work).[8] Because of this, and the ability to form protective alumina over a range of oxygen partial pressures, the TiAlCr system could have potential as a basis for smart coatings that perform well in multiple or varying high-temperature environments.

Four TiAlCr-based alloys in the as-cast condition were included in this study: Ti-51Al-12Cr, Ti-45Al-15Cr-15Ta, Ti-45Al-15Cr-15Nb, and Ti-48Al-13Cr-10Nb-5Ta (at.%, nominal). All have multi-phase microstructures.[9] Coupons were ground and then screened for oxidation and sulfidation resistance using 800ºC exposures in air for 100 h and in H_2S-H_2-H_2O-Ar for 50 h, respectively. The composition of the H_2S-H_2-H_2O-Ar gas was set to yield partial pressures of 10^{-6} atm of S_2 and 10^{-22} atm of O_2. This environment represents severe sulfidation conditions, but has been used previously to evaluate the corrosion of the most sulfidation-resistant alloys.[10,11] Under this exposure condition, the Ti-51Al-12Cr composition falls within the calculated stability of Al_2O_3 based on equilibrium thermodynamics. This is the desired protective product, but, as shown in Fig. 1, the relative sulfidizing and oxidizing potential of the reference environment lie close to the phase boundary of Cr and Ti sulfides. It is therefore important to conduct experimental screening as described to determine whether kinetic considerations can result in the formation of fast growing sulfides.[11,12]

Preliminary results on of the TiAlCr-(Nb,Ta) compositions showed that the TiAlCr ternary composition showed very good sulfidation resistance after isothermal exposure to H_2S-H_2-H_2O-Ar at 800ºC because a protective Al-rich oxide layer formed at the low oxygen partial pressure associated with this simulated

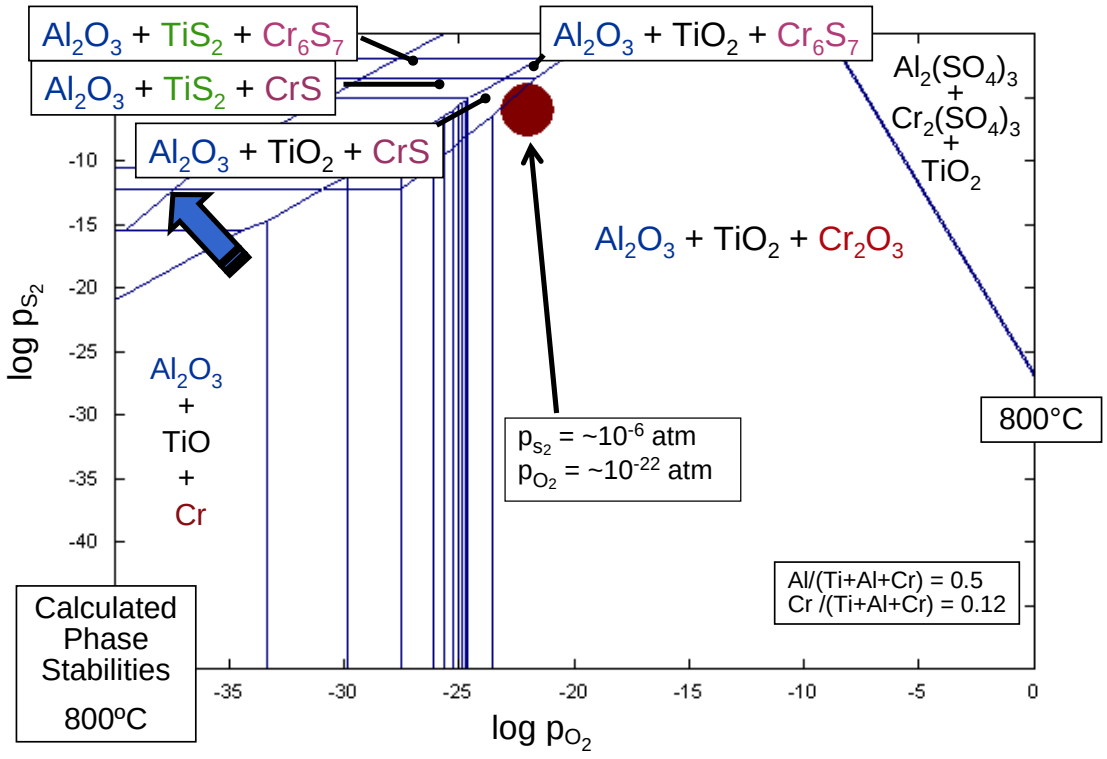

Fig.1. Calculated phase stability diagram for the Ti-Al-Cr system at 800°C. Filled circle represents gas environment used in experimental exposures.

syngas. This was attributed to the fact that, under the sulfidizing conditions, a protective Al_2O_3 must have formed, consistent with the thermodynamic prediction (Fig. 1) and initial, qualitative analysis.[9] In contrast, an alloy based on TiAlCr-15%Nb showed substantially greater sulfidation under the same exposure conditions as it appeared that a continuous alumina layer did not form. Because the Ti-Al-Cr-15%Nb alloy also showed a significantly greater mass gain after the 100 h exposure in air,[9] it appeared this particular composition/microstructure did not promote a fundamentally protective Al_2O_3 scale even in the absence of sulfur in the environment and that the addition of Nb at this concentration did not improve sulfidation resistance.

The base Ti-Al-Cr alloy system seems to hold some promise in terms of high-temperature sulfidation resistance. Furthermore, application of such compositions as (thermal spray) coatings has already been demonstrated.[13] As shown by the mass change results in Fig. 2, this system appears to have short-term sulfidation behavior comparable to the most resistant alloy systems examined to date (certain Fe-Al and Mo-Si-B alloys[10-12,14]). However, as observed with the Ti-Al-Cr-Nb results,[10] the addition of other alloying elements may lead to decreased sulfidation resistance if the ability to form a continuous surface layer of Al_2O_3 is compromised. Therefore, efforts to achieve sulfidation resistance must focus on

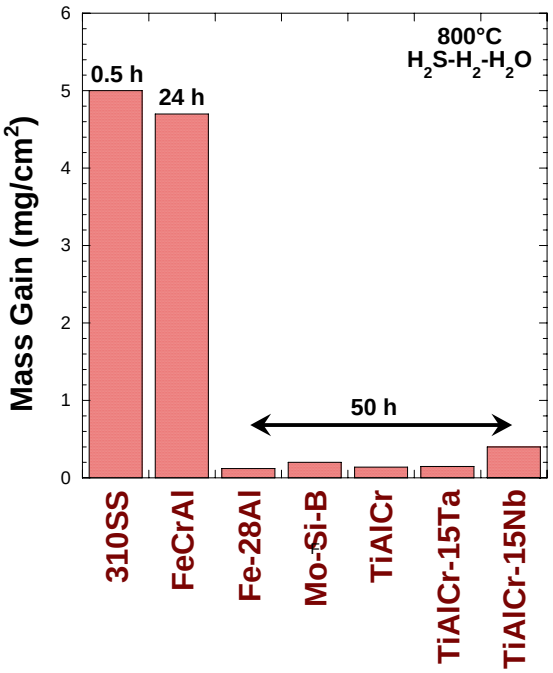

Fig.2. Mass gains after indicated time periods for exposures to the H_2S-H_2-H_2O gas at 800°C

developing the compositions and microstructures that promote protective alumina formation, even at the low partial pressures found in coal gasification environments.

Future work will include exposures of selected TiAlCr alloys to H_2S-H_2-H_2O-Ar at lower, more realistic temperatures and extended exposure times, and under isothermal and thermal cycling conditions, to quantitatively gauge sulfidation resistance. The knowledge gained from such will be used to help explore phase-size and composition manipulations in the Ti-Al-Cr system in order to evaluate the possibilities of developing these compositions as protective coatings in sulfidizing environments.

SUMMARY

The high-temperature sulfidation of TiAlCr compositions was qualitatively evaluated as part of efforts to develop schemes for using multiphase alloy coatings for corrosion protection under aggressive high-temperature environments. The TiAlCr system shows potentially good sulfidation resistance when compositions and microstructures yield protective alumina at low oxygen partial pressures associated with gasification processes.

ACKNOWLEDGEMENTS

Research sponsored by the Office of Fossil Energy Advanced Research Materials Program, U. S. Department of Energy, under contract DE-AC05-00OR22725 with UT-Battelle, LLC.

REFERENCES

1. J.R. Nicholls, *JOM* 52 (2000)

2. F. Gesmundo and B. Gleeson, *Oxid. Met.* 44 (1995) 211.

3. M. P. Brady, B. Gleeson and I. G. Wright, *JOM* 52 (2000) 16.

4. M.P. Brady, J.L. Smialek, J.W. Smith, and D.L. Humphrey, *Acta Mater*. 45 (1997) 2357.

5. M.P. Brady, J.L. Smialek, D.L. Humphrey, and J.W. Smith, *Acta Mater*. 45 (1997) 2371.

6. N.S. Jacobson, M.P. Brady, and G.M. Mehrotra, "Thermodynamics of Selected Ti-Al and Ti-Al-Cr Alloys", *Oxid. Met.* 52 (1999) 537.

7. S. Mrowec, *Oxid. Met.* 44 (1995) 177.

8. J.J. Soler, J.F. Norton, M. Noth, and M. Schütze, *Mater. and Corros.* 50 (1999) 394.

9. P.F. Tortorelli, M.P. Brady, and I.G. Wright, *Proc 19th Annual Conf. Fossil Energy Materials.*, R.R. Judkins and L.S. Mack (compilers), U.S. Department of Energy, 2005; http://www.ms.ornl.gov/FEM/pdf/Proceedings19Fossil05.pdf

10. J.H. DeVan and P.F. Tortorelli, *Mater. at High Temp.* 11 (1993) 30.

11. K. Natesan and P.F. Tortorelli, pp. 265-80 in Nickel and Iron Aluminides: Processing, Properties, and Applications, S. C. Deevi, V. K. Sikka, P. J. Maziasz and R. W. Cahn (eds.), ASM International, Materials Park, OH, 1997.

12. J. H. DeVan, pp. 107-15 in Oxidation of Intermetallics, T. Grobstein and J. Doychak (eds.), TMS, Warrendale, PA, 1989.

13. M.P. Brady, W.J. Brindley, J.L. Smialek, and I.E. Locci,, *JO*, 48 (1996) 46.

14. P.F. Tortorelli, J.H. Schneibel, K.L. More, and B.A. Pint, *Mater. Sci. Forum* 461-464 (2004) 1063.

EXTENDED ALLOY LIFETIMES THROUGH IMPROVED COATING PERFORMANCE AND REACTIVE ELEMENT OPTIMIZATION

Bruce A. Pint
Oak Ridge National Laboratory, P.O. Box 2008, Oak Ridge, TN 37831-6156
E-mail: pintba@ornl.gov; Telephone: (865) 576-2897; Fax: (865) 241-0215

Ying Zhang
Dept. of Mech. Eng., Tennessee Tech. Univ., P.O.Box 5014, Cookeville, TN 38505-0001
E-mail: yzhang@tntech.edu; Telephone: (931) 372-3265; Fax: (931) 372-6340

J. Allen Haynes
Oak Ridge National Laboratory, P.O. Box 2008, Oak Ridge, TN 37831-6063
E-mail: haynesa@ornl.gov; Telephone: (865) 576-2894; Fax: (865) 574-6918

Sebastien Dryepondt
Oak Ridge National Laboratory, P.O. Box 2008, Oak Ridge, TN 37831-6156
E-mail: dryepondtsn@ornl.gov; Telephone: (865) 576-2894; Fax: (865) 241-0215

Ian G. Wright
Oak Ridge National Laboratory, P.O. Box 2008, Oak Ridge, TN 37831-6156
E-mail: wrightig@ornl.gov; Telephone: (865) 574-4451; Fax: (865) 241-0215

ABSTRACT

Factors that influence the oxidation-limited lifetime of alumina-forming alloys and coatings are being investigated in order to improve performance and predictive capabilities. The behavior of aluminide coatings on representative ferritic (Fe-9Cr-1Mo) and austenitic (type 304L stainless steel) is being studied at elevated temperatures, 650°-800°C, in order to verify and/or improve a proposed model based on degradation due, mainly, to Al interdiffusion with the substrate. At present, coatings have not failed after 9,000h at 800°C or 14,000h at 700°C in air+10%H_2O, an environment that readily attacks uncoated specimens of these alloys. For alumina-forming alloys, work is continuing on ferritic Fe(Al) and intermetallic FeAl compositions. The role of alloy thermal expansion on spallation resistance is being quantified and it appears that a significant loss in lifetime is associated with a minor increase in thermal expansion when Fe-Al alloys move from disordered to ordered compositions. An optimized minor alloying addition with Hf or Ti has overcome an unusual accelerated oxidation problem for Y-doped Fe(Al) alloys at 1200-1250°C. This modification allows higher temperature tests to be conducted, thereby reducing the extended exposure times typically required to quantify the effect of various experimental variables. Other accelerated testing procedures are being investigated.

INTRODUCTION

Alloys and coatings that form a dense, adherent external Al_2O_3 layer or scale have significant advantages over Cr_2O_3 or SiO_2 scales because of the slow growth rate and higher chemical stability of Al_2O_3.[1-12] This includes environments containing water vapor,[5-9] sulfur[1,3,10] and carbon,[2,11,12] where degradation rates can be orders of magnitude slower than conventional alloys. However, Al additions can be detrimental to mechanical properties, including room temperature ductility and high temperature creep strength,[6] and can make fabrication and joining more difficult. Thus, Al-rich coatings are one option for

improving the environmental resistance of lower cost or higher strength alloys.

In order to understand the potential benefits and limitations of alumina-forming coatings, model aluminide coatings made by chemical vapor deposition (CVD) are being tested on representative ferritic (Fe-9Cr-1Mo) and austenitic (type 304L stainless steel) substrates in humid air at 700° and 800°C. This environment causes rapid oxidation (formation of FeO_x) of the substrate if the coating is breached, resulting in a large mass gain.[8] The current testing at 700°-800°C was initiated in order to determine the critical Al content at coating failure, C_b, i.e. the minimum amount of Al needed to form a protective alumina scale. In this temperature range, the Al content primarily decreases with exposure time due to interdiffusion with the substrate, and not due to alumina formation. The test temperatures are higher than anticipated service conditions in order to accelerate interdiffusion. Obtaining more information about the failure criteria will assist in the development of predictive lifetime models.[13,14] However, no failures have been observed and the tests are continuing.

Unlike aluminide coatings, alumina-forming alloys are tested at much higher temperatures (1100°-1300°C) and are depleted in Al due to the formation, and re-growth after spallation, of the alumina scale. Testing has focused on Fe-Al alloys. After optimizing the reactive element[15] (RE) additions in Fe-base alloys,[16-20] the work is now focusing on other factors that increase spallation resistance, such as alloy thermal expansion, or that may decrease C_b in Fe(Al) alloys, thereby increasing the Al reservoir and increasing lifetime. An improved understanding of the oxidation performance of alumina-forming alloys may assist in the development of improved alloys or coatings.

EXPERIMENTAL PROCEDURE

Substrates used in the coating study included commercial Fe-9Cr-1Mo (Fe-9.26Cr-0.96Mo-0.47Mn-0.23V-0.19Si-0.16Ni) and commercial type 304L stainless steel (Fe-18.29Cr-8.75Ni-1.84Mn-0.24Mo-0.18Co-0.29Cu-0.47Si). The laboratory-scale CVD reactor and coating process for low-activity (thin coatings) and high-activity (thick coatings) have been described elsewhere.[8,21-23] Coatings made by CVD have been used in this work in order to have a well-controlled, high purity coating for long-term testing. Similar aluminide coatings are being made for testing by a commercial-like pack cementation process.[13] Characterization of the as-deposited coatings also has been described elsewhere.[8,21,23] Cast Fe-Al alloys were fabricated using vacuum-induction melting, and were annealed for 4h at 1300°C. Chemical compositions (all in at.%) are provided in Table I. Coated specimens were tested with the as-coated surface finish, while cast specimens were polished to a 0.3μm surface finish. All were ultrasonically cleaned in acetone and methanol prior to exposure.

Cyclic oxidation tests with cycle times of 1h, 100h and 500h at temperature were used with details provided elsewhere.[24] In all tests, the specimen mass changes were measured before and after oxidation using a Mettler model AG245 balance. For the coating tests in humid air at 700° and 800°C, the addition of water vapor to the carrier gas was controlled by a water injection system described elsewhere.[25] Selected specimens were examined by light microscopy, field emission gun, scanning electron microscopy (SEM) equipped with energy dispersive x-ray analysis (EDXA) and electron probe microanalysis (EPMA) using wavelength dispersive x-ray analysis. For cross-sections, the surface reaction product was protected by Cu-plating the specimen, prior to mounting in epoxy.

Table I. Alloy chemical compositions (atomic% or ppma) determined by inductively coupled plasma analysis, including the ratio of Hf or Zr to the C content.

Material	Al	Mo	Cr	Si	Hf	Other	C	S	O	[RE]/[C]
Fe-40Al	40.1	<	<	0.02	<		100	18	90	n.a.
Fe-40Al+Zr,0.4C	39.3	0.17	<	<	<	490 Zr	3920	22	140	0.12
Fe-40Al+Zr,0.2C	40.1	0.17	<	<	<	490 Zr	1890	<14	110	0.26
Fe-40Al+Zr	40.3	0.17	<	0.02	<	390 Zr	<40	<14	50	11
Fe-40Al+Hf	39.5	<	<	<	470		70	21	100	6.7
Fe-40Al+Hf,0.2C	40.3	0.18	0.01	0.03	520		2120	30	140	0.25
Fe-40Al+Hf,Mo	40.2	0.19	0.01	0.03	520		520	19	190	1.0
Fe-40Al+hi Hf	39.3	<	0.02	0.05	2990	50 Zr	130	20	150	23
Fe-17Al+Hf	16.7	<	<	0.05	570		50	67	80	12
Fe-18Al+Y	18.0	<	0.02	0.02	<	570 Y	130	<15	90	n.a.
Fe-22Al+Y	21.6	<	0.01	0.02	<	670 Y	80	<15	100	n.a
Fe-17Al+Y,Ti	16.9	<	<	<	<	0.4Ti, 690 Y	120	<5	70	n.a.
Fe-17Al+Y,Hf	17.1	<	<	0.02	230	100 Y	90	8	50	2.7
Fe-17Al-1Mn	17.0	<	<	0.02	260	0.9Mn, 130Y	120	11	60	2.8
Fe-19Al-5Cr	17.9	<	4.73	0.04	<		40	32	40	n.a.

< indicates below the detectability limit of <0.01% or <0.001% for interstitials

RESULTS AND DISCUSSION

DETERMINATION OF THE CRITICAL Al CONTENT FOR COATING FAILURE

Mass gain results for CVD aluminide coatings being exposed in 100h cycles to air + 10%water vapor are shown in Figure 1. Prior work suggested that the coefficient of thermal expansion (CTE) mismatch between the aluminide coating and substrate can lead to coating degradation.[8] Therefore, coatings of different thickness are being tested. The thinner coatings (~5 µm Al-rich outer layer, ~50µm total thickness) have a lower Al reservoir than the thicker coatings (~40 µm outer layer, ~200µm total thickness)

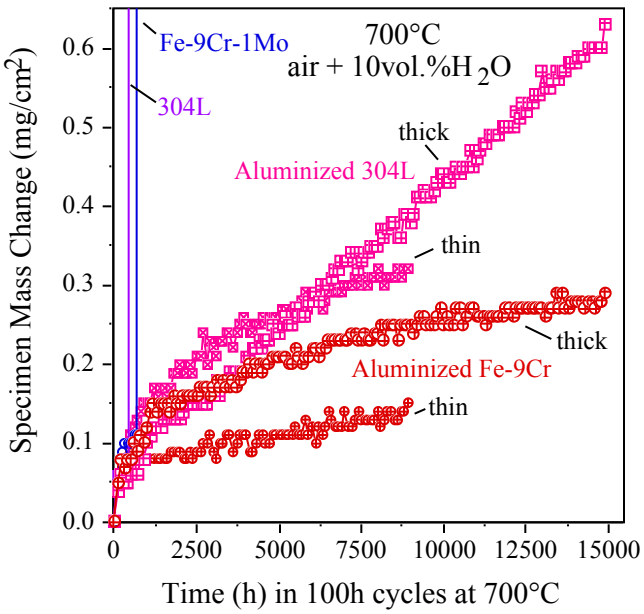

Figure 1. Specimen mass changes during 100h cycles at 700°C in air+10%H_2O. Results are shown for uncoated and coated specimens with different coating thicknesses.

but also develop less strain during heating and cooling that might lead to cracking in the coating. Without a coating, the type 304L stainless steel and Fe-9Cr-1Mo specimens showed high mass gains after short times, Figure 1. In contrast, the thicker coatings have passed 14,000h, while the thinner coatings have reached 9,000h, with relatively low mass gains. The mass gain was higher for both coatings on the 304L substrate. The coatings were examined by SEM every 2,000h. This difference in performance is attributed to higher coating degradation on the 304L substrate, especially at the coating edges, Figure 2. In this case, the Al-stabilized ferritic interdiffusion zone creates an additional layer with a CTE mismatch between the austenitic substrate and the intermetallic, $(Fe,Ni)_3Al$, outer layer. Some cracking in the faces were observed in both thick coatings after 140, 100h cycles. Lower mass gains were observed for both thinner coatings, with the difference being more dramatic on the ferritic substrate, Figure 1. For the Fe-9Cr-1Mo substrate, the interdiffusion layer has a similar CTE as the substrate, and only the thin (~5μm) outer layer has a different CTE.

Attempting to accelerate coating failure, coated specimens also were tested at 800°C in humid air. Diffusion tests showed that the surface Al content dropped to 12at.% after only 2,000h at 800°C.[14] Therefore, a coating failure was expected in a much shorter time than at 700°C. The longest running Fe-9Cr-1Mo coated specimen has reached almost 10,000h, in 100h cycles, Figure 3, with no indication of rapid oxidation such as that observed for the uncoated Fe-9Cr-1Mo specimen. This coated specimen also is being examined every 2,000h and some scale spallation has been observed. This may have reduced the mass gain to some degree, but clearly no FeO_x has formed. This specimen will continue to be cycled. A second specimen was recently stopped at 5,000h to characterize the Al interdiffusion. Heckel's diffusion model[14,26] suggested that the Al content should have dropped to 9% at the surface, and the Al diffusion tail should be near the center of the specimen. A coated 304L specimen was recently stopped after 6,000h because of the high mass gain (Figure 3) and severe edge cracking. This specimen will be sectioned to characterize the degradation.

Nitrogen is used to strengthen both of these substrate alloys, but high N contents have been shown to adversely affect the as-deposited coating adhesion and defect content.[13,27] Laboratory-scale heats of 304L and Fe-9Cr-1Mo were made with lower N contents. Coatings formed on these substrates had fewer

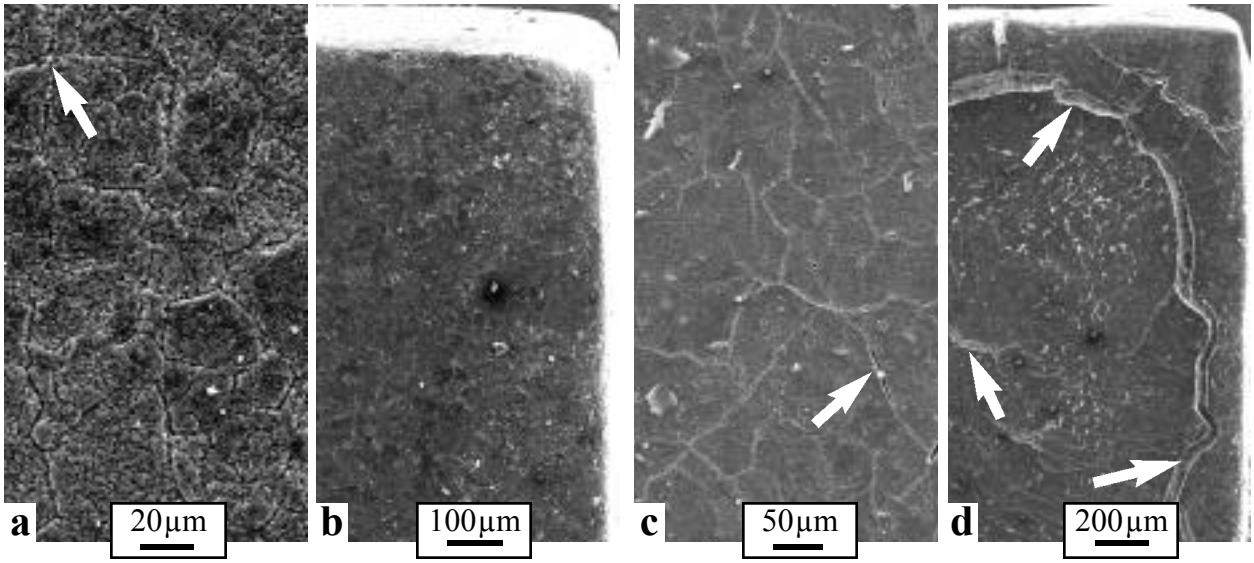

Figure 2. SEM secondary electron plan-view images of coated specimens exposed for 140, 100h cycles at 700°C in humid air; (a - b) Fe-9Cr-1Mo and (c - d) 304L. Arrows point to cracks in the coating.

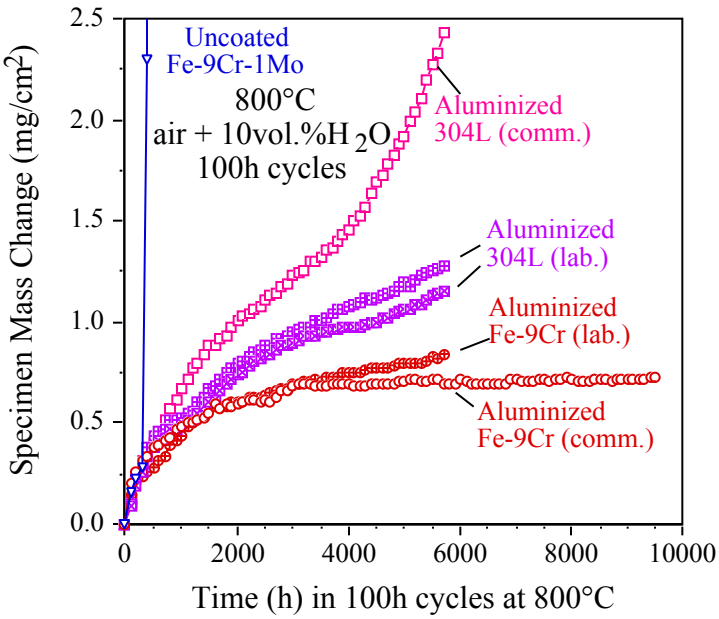

Figure 3. Specimen mass changes during 100h cycles at 800°C in air+10%H_2O for uncoated Fe-9Cr-1Mo and for coated commercial and laboratory (low N) Fe-9Cr-1Mo and 304L specimens.

coating defects. However, coating performance has not consistently improved. For example, coatings on laboratory 304L showed lower mass gains at 800°C, Figure 3. The coating on laboratory Fe-9Cr-1Mo showed similar mass change as the commercial substrate.

INCREASED OXIDATION LIFETIME OF ALUMINA-FORMING ALLOYS

Lifetime modeling of alumina-forming alloys generally starts with a simple model developed by Quadakkers et al.[28] which assumes uniform consumption of Al because of its rapid diffusion rate. The model calculates time to failure, t_b when the Al content drops to a critical level, C_b. The supply vs. consumption balance for a specimen of thickness, d, density ρ and starting Al content C_o is given by:

$$(C_o - C_b) \bullet \rho \bullet d = A \bullet k \bullet t_b^n \qquad [1]$$

where A is a constant, k is a rate constant, n=0.5 for parabolic kinetics and n=1 for linear kinetics. Thus, comparing alloy specimens with similar Al content and thickness, those with better scale adhesion (i.e. lower k and n) should consume Al more slowly and have a longer lifetime, t_b.

One of the most well known methods for increasing the lifetime of alumina-forming alloys is the addition of RE dopants.[15] Almost all commercial alloys have some RE dopants, but optimization is usually empirically based. However, recent focus on RE-interstitial ratios has led to an improved understanding of optimization.[17,29] Prior work on this program used Fe-40Al alloys as a case study to show the importance of the RE/C ratio and the benefit of switching from Zr to Hf doping.[19,20] To further confirm this hypothesis, a new series of Hf-doped Fe-40Al alloys was fabricated, Table I. The previous study showed the importance of Zr/C > 1. Figure 4a shows the prior results for t_b at 1200°C in 1h cycles (normalized to a 1.5mm thickness) and includes the current results for the new alloys. When C was added to a Hf-doped alloy (Hf/C=0.25), the lifetime dropped in a similar fashion as for Zr-doped FeAl, confirming the importance of a higher Hf/C ratio. The addition of Mo to Hf-doped FeAl was made as a more direct comparison to the Zr-doped alloys, which all contained Mo, and a higher Hf content was tested

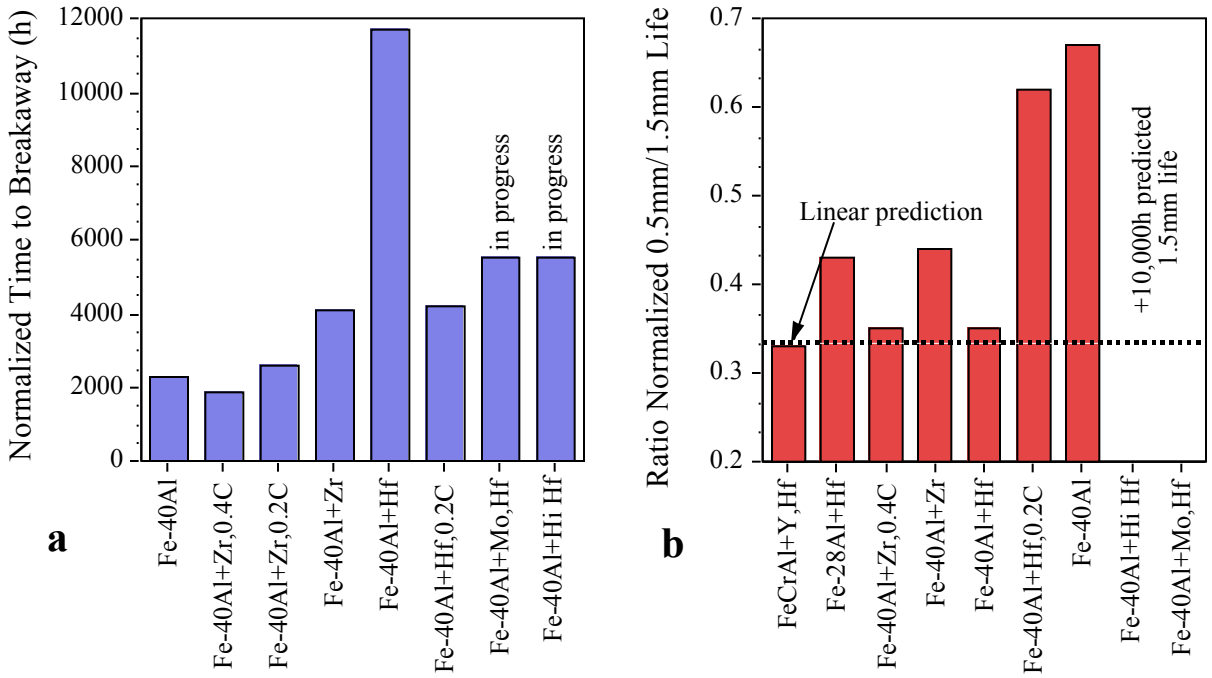

Figure 4. (a) Time to breakaway values for various Fe-40Al alloys tested in dry O_2 at 1200°C in 1h cycles normalized to 1.5mm thickness. (b) Ratio of normalized 0.5mm lifetime and 1.5mm lifetime for a similar set of alloys. Thinner specimens were tested as a method to reduce the experiment time.

to assess its effect on high temperature strength. The last two alloys have not failed after almost 6,000h of testing.

Table II shows a compilation of the oxidation data obtained at 1200°C and the 1000°C compressive yield stress.[19,30] The 6X longer lifetime of Fe-40Al+Hf could be partially attributed to its lower strength, which would be better able to accommodate stress from the scale than a stronger substrate.[31] The ~3X increase in lifetime compared to the best Zr-doped FeAl could not be attributed to a higher Al reservoir (C_o-C_b), or slower scale growth rate, Table II.

Table II. Summary of 1h cyclic tests run at 1200°C, showing the starting specimen thickness, the Al reservoir, the normalized time to breakaway for a 1.5mm thick specimen and the ratio of the normalized times for various FeAl modifications. The isothermal parabolic rate constant at 1200°C and the compressive yield stress measured at 1000°C also are included.

Material	Thickness (mm)	Al reservoir C_o-C_b (at.%)	Normalized Life (h)	Ratio	Rate Constant (g^2/cm^4s)	1000°C Yield Stress (MPa)
Fe-40Al+Zr,0.4C	1.46	20.9	1,910	base	8.6-13.7 x10^{-12}	17.4
Fe-40Al+Zr,0.2C	1.58	~ 27.8	2,610	1.4	11.2-12.3	17.2
Fe-40Al+Zr	1.44	~ 28.0	4,110	2.2	4.7-6.3	17.6
Fe-40Al+Hf	1.32	27.2	11,750	6.2	5.9-7.6	14.3
Fe-40Al+Hf,0.2C	1.56	~ 28.0	4,230	2.2	21	16.1
Fe-40Al+Hf,Mo	1.55	~ 27.9	<5500	n.d.	4.5	17.8
Fe-40Al+hi Hf	1.55	~ 27.0	<5500	n.d.	3.3	18.5,22.5
Fe-40Al	1.53	n.d.	2,300	1.2	23	14.5

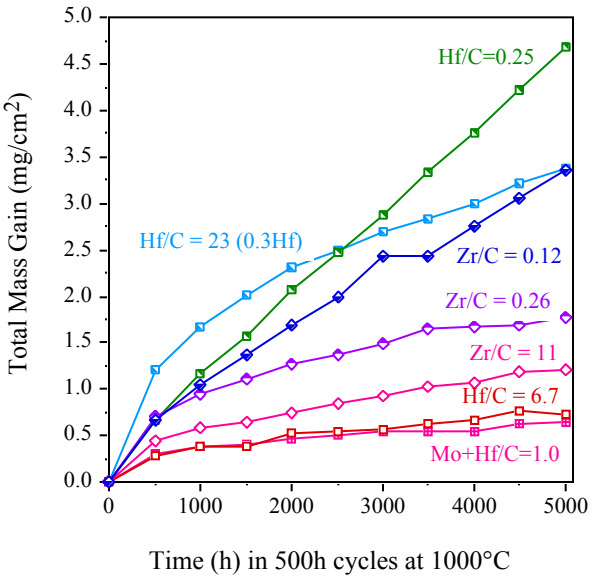

Figure 5. Specimen mass changes during 500h cycles at 1000°C in laboratory air for various dopant levels in Fe-40Al.

Using the 1000°C compressive yield stress to assess the 1200°C oxidation lifetime was a first assessment, based on available information. Tensile creep data would be preferred, and initial tests are being conducted on Fe_3Al compositions.[30] Higher temperature mechanical tests require more expensive equipment, whereas lower temperature oxidation tests would require orders of magnitude longer exposures to obtain failures. However, testing has been conducted for 5,000h at 1000°C to assess the oxidation behavior of this group of alloys at the lower temperature, Figure 5. As reported previously,[19] increasing the Zr/C ratio reduced the spallation and decreased the total mass gain during 10, 500h cycles. The spallation observed on the alloy with Zr/C=0.12 resulted in a very convoluted metal-scale interface, Figure 6c. The thinnest scale was observed on Hf-doped FeAl, Figure 6d. Among the new alloys, the addition of Mo had almost no effect on the mass change (Figure 5) and scale thickness. Increasing the C content resulted in a much higher mass gain due to repeated spallation (Figure 5)and a significant increase in scale thickness, Figure 6e, these effects were somewhat similar to those observed among the Zr-doped alloys when the RE/C ratio was < 1. Finally, increasing the Hf addition resulted in a higher mass gain due, to significant internal oxidation, Figures 5 and 6f.

Because of the scale spallation problems associated with the high CTE of Fe-Al intermetallic compositions,[16,32,33] recent work has focused on ferritic Fe(Al) compositions.[18] Previous work showed promising results for Y-doped Fe-18Al.[20] However, as summarized using t_b results at 1200°C, Figure 7a, higher Al contents did not yield increased lifetimes. Even for the Hf-doped materials, the lifetime data did not increase for Fe-24Al, as predicted by the lifetime model (Eqn. 1).[18] In order to better understand the behavior of alloys in this composition range, the thermal expansion of alloys in the 18-24% Al range as well as Fe-40Al+Hf was measured to complement earlier data. The results in Figure 7b correlate well with the oxidation results in Figure 7a. No increase in CTE was observed up to 18at.%Al. At 20at%Al, the same composition where cracking begins to occur in Fe-Al weld overlay coatings,[10] an increase in CTE was observed near 400°C, likely associated with some fraction of intermetallic phase in this composition. At 22% and 24%Al, the volume fraction increased and the CTE also increased, resulting in a higher stress in the scale on cooling and more scale spallation. Increasing Al content should increase the Al reservoir;

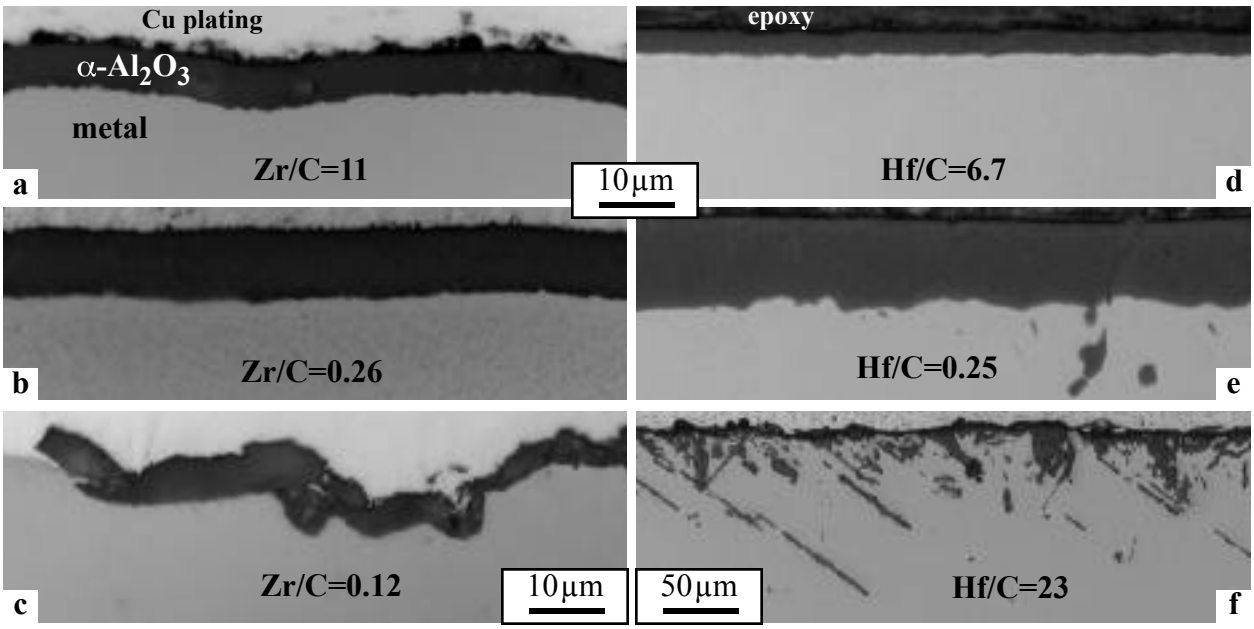

Figure 6. Light microscopy of polished cross-sections after 10, 500h cycles at 1000°C in laboratory air of (a) Fe-40Al+Zr (b) Fe-40Al+Zr,0.2C, (c) Fe-40Al+Zr,0.4C, (d) Fe-40Al+Hf, (e) Fe-40Al+Hf,0.2C and (f) Fe-40Al+0.3Hf.

however, the increase in CTE results in faster Al consumption, because of alumina re-growth after spallation caused by the CTE mismatch between the substrate and alumina.

Because of the long experiment times required to obtain the data shown in Figures 4a and 7a, several strategies have been explored for decreasing the experiment time but still obtaining the same type of time to breakaway information. According to Eqn. 1, one possibility is to reduce the specimen thickness. A series of ~0.5mm thick specimens were tested to failure in 1h cycles at 1200°C. Figure 4b presents the

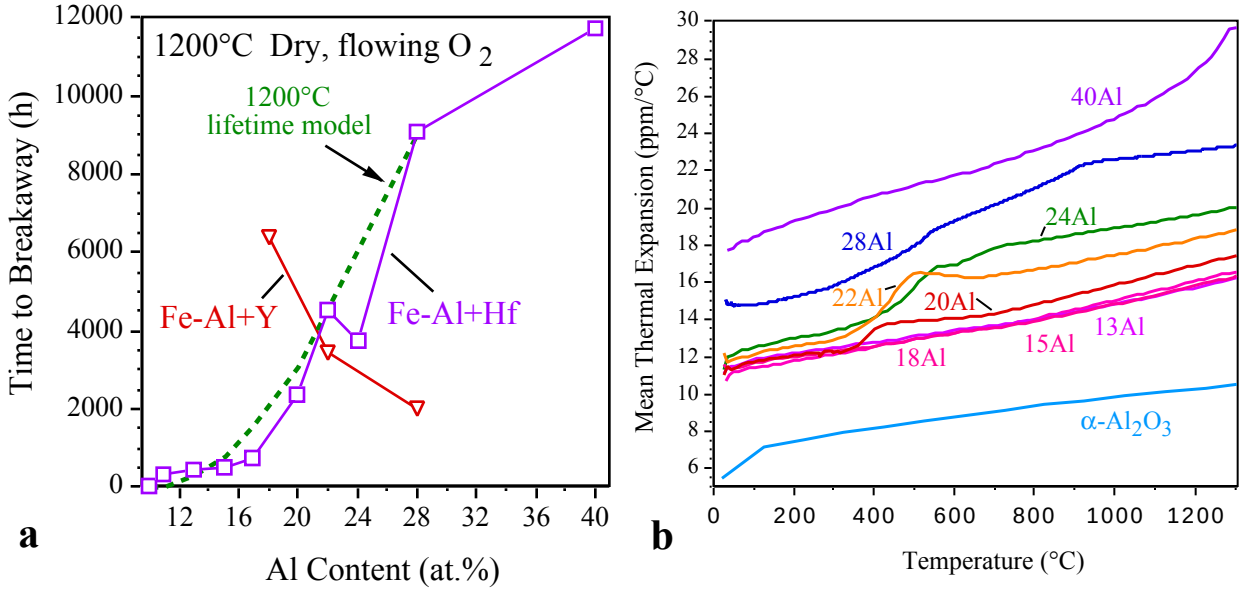

Figure 7. (a) Normalized time to breakaway as a function of Al content for Hf- and Y-doped Fe-Al alloys and (b) mean thermal expansion coefficient for various Al contents.

ratio of the normalized 0.5mm lifetime to the normalized 1.5mm lifetime. For n=1, an approximation for a number of alloys,[18,20] this ratio should be 1:3. Several specimens fit the prediction well, typically those with long lifetimes. However, several ratios were significantly higher. The most likely explanation for higher ratios, i.e. longer life than expected for the thinner specimen, is the formation of Al gradients in thicker specimens which resulted in early failures for the thicker specimens.[34] Thinner specimens are less likely to form large Al concentration gradients. It appears that results from thinner specimens will tend to overpredict the lifetime of thicker specimens, a critical problem for accurate lifetime predictions.

Another well-used method to accelerate oxidation testing is to increase the temperature. Testing of these alloys has been on-going at 1250°C. However, as reported previously,[20] there can be alternative failure mechanisms at higher temperatures, such as the "broccoli" attack associated with accelerated oxidation of grain boundary carbides.[35] This problem has been observed for Y-doped Fe(Al) compositions at 1200°-1300°C[20,36] and likely contributed to the reduced lifetime of Fe-22Al+Y and Fe-28Al+Y, Figure 7a. The suggested solution to this problem is co-doping with Y and a strong carbide former such as Ti, Hf or Zr.[35] Figure 8 provides an update on the testing of Fe-17Al+Y,Ti and Fe-17Al+Y,Hf. Both compositions have prevented the accelerated attack observed for Fe-18Al+Y and Fe-18Al-10Cr+Y, and the specimen with Y and Ti has equaled the lifetime of Fe-17Al+Hf which did not suffer from this problem. However, Ti co-doping was not successful[20] in preventing rapid oxidation in Fe-22Al, so that the most recent series of Fe(Al) alloys was produced with Y and Hf co-doping. In FeCrAl, this optimized composition has produced the longest lifetimes.[17] Experiments now are being conducted to assess if Cr or Mn additions to Fe-17Al can increase lifetime by lowering C_b. Figure 8 shows results for a specimen of Fe-17Al-1Mn+Y,Hf. While the test is still in progress, the higher mass gain for this alloy compared to Fe-17Al+Y,Hf is not a positive indication for Mn additions.

To follow up on previous work,[20,37] a second type of unusual attack was encountered for undoped Fe(Al) and Fe(Al)-Cr specimens at 900° and 1000°C in laboratory air. Higher mass gains were observed for these alloys due to internal oxidation/nitridation, which has previously been reported for undoped Fe_3Al and FeAl alloys.[38,39] The internal attack is a combination of Al oxide and AlN, with AlN at the deepest part of the penetration. In order to further quantify this attack, the depth and volume of internal precipitates were measured as a function of time. Figure 9 presents results on the maximum penetration depth as a

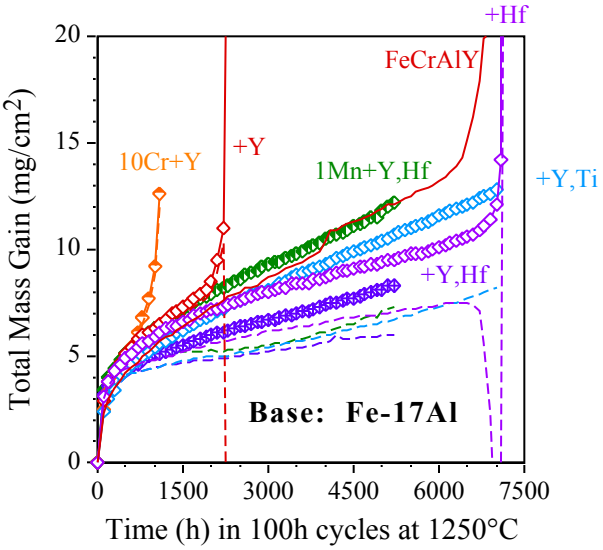

Figure 8. Total mass gain during 100h cycles at 1250°C in laboratory air for base Fe-17Al alloys.

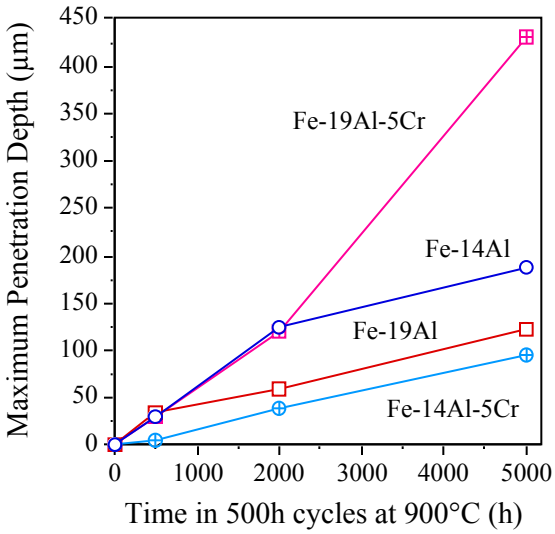

Figure 9. Maximum penetration depth for various Fe-Al alloys in 500h cycles in laboratory air at 900°C.

function of time for several of the alloys. The behavior is unusual in that higher Al and Cr contents normally decrease the amount of oxidation but did not in the case of Fe-19Al-5Cr. The internal nitridation was not observed when Ti, Hf, Zr or Y was present and was not observed at 700° and 800°C.[20] It appears that this mechanism is confined to higher temperatures (900°-1000°C) than the intended aluminide coating operating temperatures.

SUMMARY

Long-term testing of CVD aluminide coatings on one ferritic (Fe-9Cr-1Mo) and one austenitic (304L) Fe-base substrate is being conducted in air+10%H_2O. The program is now primarily focused on determining the coating failure criteria in low cycle frequency testing in order to improve the lifetime model that has been developed.[14] Improvements in high-temperature oxidation resistance are being investigated by optimizing the base alloy composition and by gaining a better understanding of coating lifetime limits. The lifetime of alumina-forming alloys often can be extended by increasing the Al reservoir and/or by slowing the Al consumption rate. Examples have shown how minor alloying additions can greatly influence lifetime. Ferritic Fe-Al alloys up to 18at%Al are more spallation resistant than Fe-Al intermetallics because of their lower CTE; however, other failure mechanisms have been encountered at high temperature (1200-1250°C) and lower temperature (900°-1000°C).

ACKNOWLEDGMENTS

The authors would like to thank K. Cooley, G. Garner, J. L. Moser and H. Longmire at ORNL for assistance with the experimental work and M. P. Brady and P. F. Tortorelli at ORNL for manuscript comments. This research was sponsored by the U.S. Department of Energy, Fossil Energy Advanced Materials Research Program under contract DE-AC05-00OR22725 with UT-Battelle, LLC.

REFERENCES

1. P. F. Tortorelli and J. H. DeVan, *Mat. Sci. and Eng.*, A153 (1992) 573.
2. B. Jönsson and C. Svedberg, *Mater. Sci. Forum*, 251-4 (1997) 551.

3. P. F. Tortorelli and K. Natesan, *Mater. Sci. Eng.*, A258 (1998) 115.
4. M. Zheng and R. A. Rapp, *Oxid. Met.*, 49 (1998) 19.
5. E. J. Opila, *Mater. Sci. Forum*, 461-4 (2004) 765.
6. B. A. Pint, R. Peraldi and P. J. Maziasz, *Mater. Sci. Forum*, 461-4 (2004) 799.
7. I. G. Wright, B. A. Pint, Y. Zhang, R. A. Bishop, J. C. Farmer, A. Jankowski, and R. B. Rebak, NACE Paper 04-531, Houston, TX, presented at NACE Corrosion 2004, New Orleans, LA, March 2004.
8. Y. Zhang, B. A. Pint, G. W. Garner, K. M. Cooley and J. A. Haynes, *Surf. Coat. Tech.*, 188-189 (2004) 35.
9. J. R. Regina, J. N. DuPont and A. R. Marder, *Oxid. Met.*, 61 (2004) 69-90.
10. S. W. Banovic, J. N. Du Pont and A. R. Marder, *Mater. High Temp.*, 16 (1999) 195.
11. R. R. Kirchheiner, P. Becker, D. J. Young and R. Durham, NACE Paper 05-428, Houston, TX, presented at NACE Corrosion 2005, Houston, TX, April 2005.
12. H. E. McCoy, *Corr.*, 21 (1965) 84.
13. Y. Zhang, B. A. Pint, J. A. Haynes, K. M. Cooley and I. G. Wright, in: *Proc. Eighteenth Annual Conf. Fossil Energy Materials*, R. R. Judkins (comp.), U. S. Department of Energy, 2004.
14. Y. Zhang, A. Liu, B. A. Pint, J. A. Haynes, I. G. Wright, submitted to *Acta Mater*.
15. B. A. Pint, *Oxid. Met.*, 45 (1996) 1.
16. B. A. Pint, K. L. More, P. F. Tortorelli, W. D. Porter and I. G. Wright, *Mater. Sci. Forum*, 369-372 (2001) 411.
17. B. A. Pint, *J. Am. Ceram. Soc.*, 86 (2003) 686.
18. B. A. Pint and I. G. Wright, *Mater. Sci. Forum*, 461-464 (2004) 799.
19. B. A. Pint and J. H. Schneibel, *Scripta Mater.*, 52 (2005) 1199.
20. B. A. Pint, Y. Zhang, J. A. Haynes and I. G. Wright, in: *Proc. Nineteenth Annual Conf. Fossil Energy Materials*, R. R. Judkins (comp.) U. S. Department of Energy, 2005.
21. Y. Zhang and B. A. Pint in: *Proc. Sixteenth Annual Conf. Fossil Energy Materials*, R. R. Judkins (comp.), U. S. Department of Energy, 2002.
22. W. Y. Lee, Y. Zhang, I. G. Wright, B. A. Pint and P. K. Liaw, *Met. Trans.*, 29A (1998) 833.
23. Y. Zhang, B. A. Pint, K. M. Cooley and J. A. Haynes, for submission to *Surf. Coat. Tech.*
24. B. A. Pint, P. F. Tortorelli and I. G. Wright, *Oxid. Met.*, 58 (2002) 73.
25. B. A. Pint and J. M. Rakowski, NACE Paper 00-259, Houston, TX, presented at NACE Corrosion 2000, Orlando, FL, March 2000.
26. J. A. Nesbitt and R. W. Heckel, *Oxid. Met.*, 29 (1988) 75.
27. Y. Zhang, B. A. Pint, K. M. Cooley and J. A. Haynes, *Surf. Coat. Tech.*, 200 (2005) 1231.
28. W. J. Quadakkers and M. J. Bennett, *Mater. Sci. Tech.*, 10 (1994) 126.
29. J. L. Smialek and B. A. Pint, *Mater. Sci. Forum*, 369-372 (2001) 459.
30. S. Dryepondt and B. A. Pint, unpublished work in progress, ORNL (2006).
31. H. E. Evans, J. R. Nicholls and S. R. J. Saunders, *Solid State Phenom.*, 41 (1995) 137-56.
32. J. L. Smialek, J. Doychak and D. J. Gaydosh, *Oxid. Met.*, 34 (1990) 259.
33. I. G. Wright, B. A. Pint and P. F. Tortorelli, *Oxid. Met*., 55 (2001) 333.
34. B. A. Pint, L. R. Walker and I. G. Wright, *Mater. High Temp.*, 21 (2005) 175.
35. V. Kochubey, D. Naumenko, E. Wessel, J. Le Coze, L. Singheiser, H. Al-Baidary, G. J. Tatlock and W. J. Quadakkers, *Mater. Lett.*, 60 (2006) 1564.
36. B. A. Pint, P. F. Tortorelli and I .G. Wright, *Mater. High Temp*., 16 (1999) 1.
37. B. A. Pint and R. M. Deacon, unpublished work in progress, ORNL (2006).
38. B. A. Pint, J. R. Regina, K. Prüßner, L. D. Chitwood, K. B. Alexander and P. F. Tortorelli, *Intermetallics*, 9 (2001) 735.
39. C.-H. Xu, W. Gao and Y.-D. He, *Scripta Mater*., 42 (2000) 975-80.

YSZ THERMAL BARRIER COATINGS BY MOCVD

T. M. Besmann, S. Mandowara, and J. J. Henry, Jr.
Oak Ridge National Laboratory, Oak Ridge, TN 37831
E-mail: besmanntm@onrl.gov; Telephone: (865) 574-6852; Fax: (865) 574-6918

T. L. Starr
Chemical Engineering Department, University of Louisville, Louisville, KY 40292
E-mail: thomas.starr@louisville.edu; Telephone: (502) 852-1073; Fax: (502) 852-6355

ABSTRACT

An MOCVD system has been scaled up to deposit coatings on prototypical turbine blade width sections, with samples 5 cm x 12 cm. The system is a hot-walled reactor, with a stainless steel susceptor heated by an radio-frequency (RF) field, which is positioned around the substrate. Liquid precursor is directly injected into the system through an atomizer, and evaporates rapidly to provide a vapor source for deposition. The system is operated at reduced pressure to improve uniformity of the coating and prevent homogeneous nucleation. The sample substrate material being used is Ni-41.9Al+0.05Hf (designation N2AH). Efforts have been successful in demonstrating the coating of the entire sample surface. Interactions with Pratt & Whitney have resulted in an informal agreement on testing prototype YSZ coatings. Pratt & Whitney has supplied standard burner rig test substrates for coating at ORNL. These will be then provided to Pratt & Whitney for burner rig testing. Samples will be shared for evaluation.

INTRODUCTION

Yttria-stabilized zirconia (YSZ) is used as a thermal barrier coating (TBC) to protect super-alloy blades such as Mar-M247 or Rene-N5 during engine operation. The current method for YSZ fabrication for TBC applications is by air-plasma spraying (APS) or electron beam-physical vapor deposition (EB-PVD).[1-5] APS gives reasonable deposition rates, but has a more limited life with aging effects due to its porous and lamellar structure. EB-PVD coatings are more stable and can accommodate larger thermomechanical stresses due to their characteristic strain-tolerant, columnar microstructure. EB-PVD and APS are, however, line-of-sight deposition processes, which often leave "hidden areas" uncoated. EB-PVD in particular has only modest throughput, and high capital cost. The process of metal-organic chemical vapor deposition (MOCVD) has been investigated as an economical alternative to EB-PVD and APS, with the potential for better overall coverage as well as the ability to produce thick (>250 μm), strain-tolerant, columnar coatings.

MOCVD of YSZ involves the use of zirconium and yttrium metalorganic precursors reacting with an oxygen source. Previous researchers have used a variety of metalorganic and chloride precursors.[6-9] These precursors have low transport rates due to their low carrier solvent solubility.[10] Solvated zirconium propoxide and yttrium butoxide precursors were investigated here due to their higher vapor pressures and high solvent solubility. This work uses previously performed predictive equilibrium modeling and experiments involving butoxide precursors for tetragonal YSZ fabrication.[11] Recent efforts have focused on scaling up the process to coat prototypical turbine blade surfaces.

MODELING

The design of the sub-scale system is based on coating a prototypical blade specimen shown in Figure 1. The geometry of this specimen is close to an actual turbine blade geometry and is a 12 cm x 5 cm x 1.5 mm rectangle, representing a cross-section of an airfoil along the width direction.

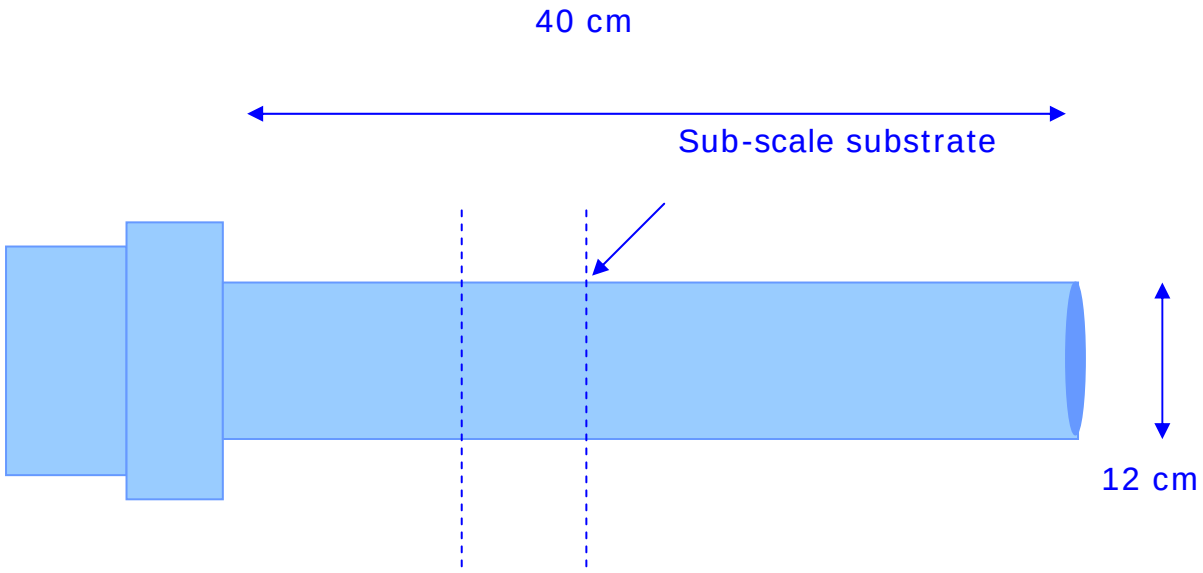

Fig. 1. Sub-scale substrate will demonstrate two-sided deposition over a length comparable to the width of a full-scale gas turbine blade.

For the finite volume modeling effort, the 8 cm x 20 cm reactor area is divided into 9200 quadrilateral elements of variable size, with a finer grid near the substrate surface. The substrate is 12 cm long and 0.2 cm thick and is centered in the reactor area. Boundary conditions for the model are set to match selected operating conditions for the reactor. Substrate temperature is assumed uniform along the length and is set from 1000 to 1300 K for various model runs. The outer walls are set to 500 K.

PARALLEL FLOW DESIGN

In the parallel flow design, precursor vapor enters the reactor from one end, travels along the length of the substrate and leaves the reactor at the opposite end. With this arrangement the average deposition rate remains high (~ 25 μm/hr) and uniformity is good through the central part of the airfoil substrate. As the vapor travels parallel to the substrate, precursor is depleted near the surface. As this concentration boundary layer gradually increases in thickness, the deposition rate decreases. The deposition rate also increases sharply at each airfoil edge, particularly the upstream edge near the inlet.

Coating uniformity is improved greatly with three modifications to the basic parallel flow design (Fig. 2). Reducing the width of the reactor near the outlet restrains the boundary layer development and produces uniform deposition through the central part of the substrate. The sharp increases at the edges are greatly reduced by splitting the inlet flow and by adding "baffles" to the reactor at the inlet and outlet ends. With these changes the coating rate varies gradually over the full length of the airfoil with about 15% total variation. Further improvement can be achieved by further reducing the reactor width near the outlet, by adjusting the inlet positions, and by changing inlet flow rates.

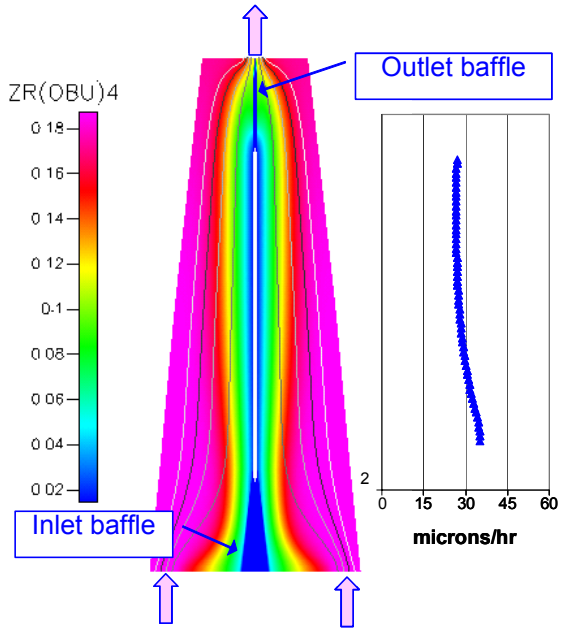

Fig. 2. Modification to the parallel flow reactor controls the concentration boundary layer and produces uniform deposition along the entire substrate.

Overall, this reactor design shows great promise for achieving uniform coating thickness over the full length of an airfoil substrate. In addition, this parallel flow design can be expanded to create a full-scale, multi-blade coating system. A conceptual design for such a reactor consists of a series of single-blade chambers connected so that the outlet of one feeds the inlet of another, with a number of these series organized in parallel.

EXPERIMENTAL

Based on the modeling efforts and the exigencies of existing facilities, a scale-up system for demonstrating YSZ MOCVD over a large area was developed. Figure 3 shows a schematic of the system. The design-basis sample substrate had dimensions 120 x 50 x 1.525 mm with composition Ni-41.9Al+0.05Hf (designation N2AH). The sample was fixtured vertically within the reactor, with an ultrasonic injector positioned centrally in the upper flange of the reactor (Fig. 4). The precursor used was proportional mixture of zirconium n-propoxide and yttrium-III butoxide carried in n-propanol. As in the earlier bench-scale system, a liquid gear pump was used to supply the ultrasonic injector with precursor at a controlled rate of 1-4 of liquid. Oxygen heated to 200°C was allowed

to flow at 1000 cm^3/min in a concentric injector and aided in the vaporization of the precursor. The sample was heated radiatively by a stainless steel susceptor positioned between the sample and the inner wall of the reactor. The susceptor coupled to the radio frequency field produced by a coil positioned outside of the fused silica reactor tube wall. The susceptor was relatively uniformly heated by the field and efficiently transferred heat to the substrate. Temperatures in excess of 1000°C were obtained, with deposition occurring at 600-1000°C. The reactor was exhausted at the bottom flanged to a vacuum pump at a nomial pressure of 1 kPa. A butterfly control valve on the exit side coupled to a pressure sensor allowed automatic pressure control. Temperature was measured using an optical pyrometer viewing the sample through the fused silica reactor wall and down the bore of the susceptor.

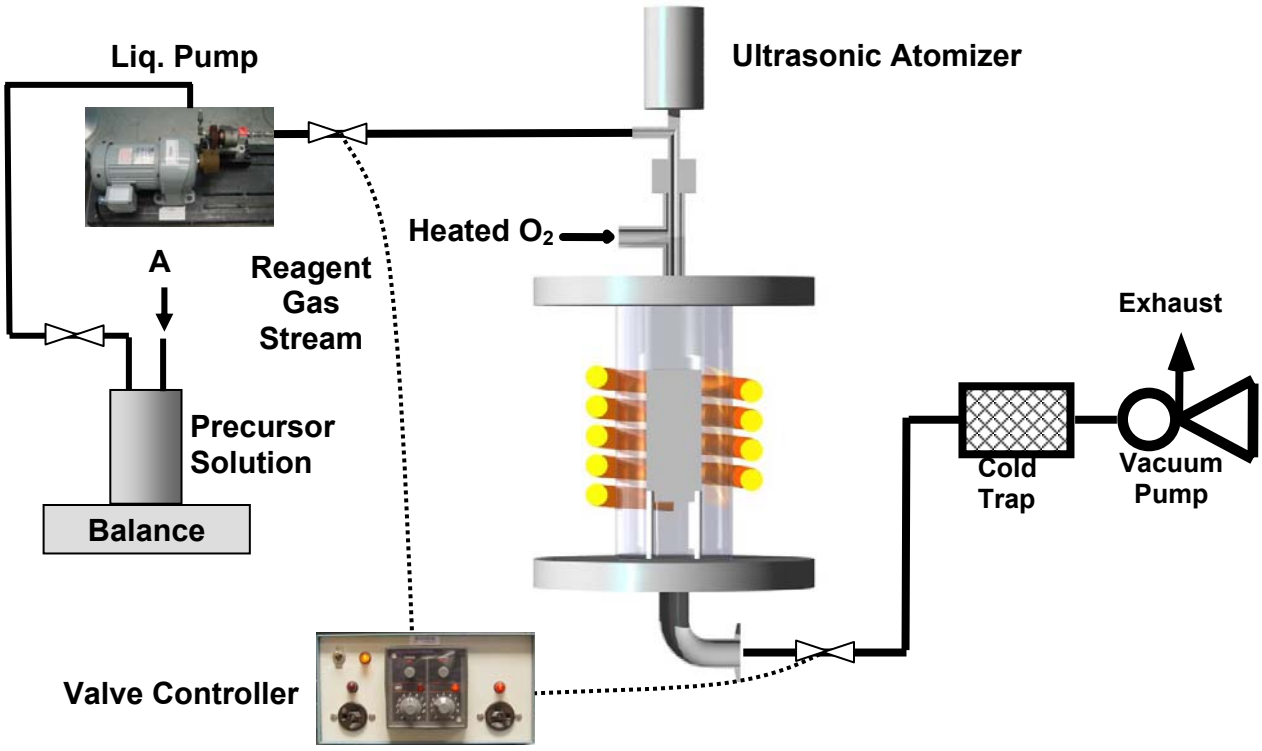

Fig. 3. Schematic of the MOCVD scale-up system for coating prototypical turbine blade sections.

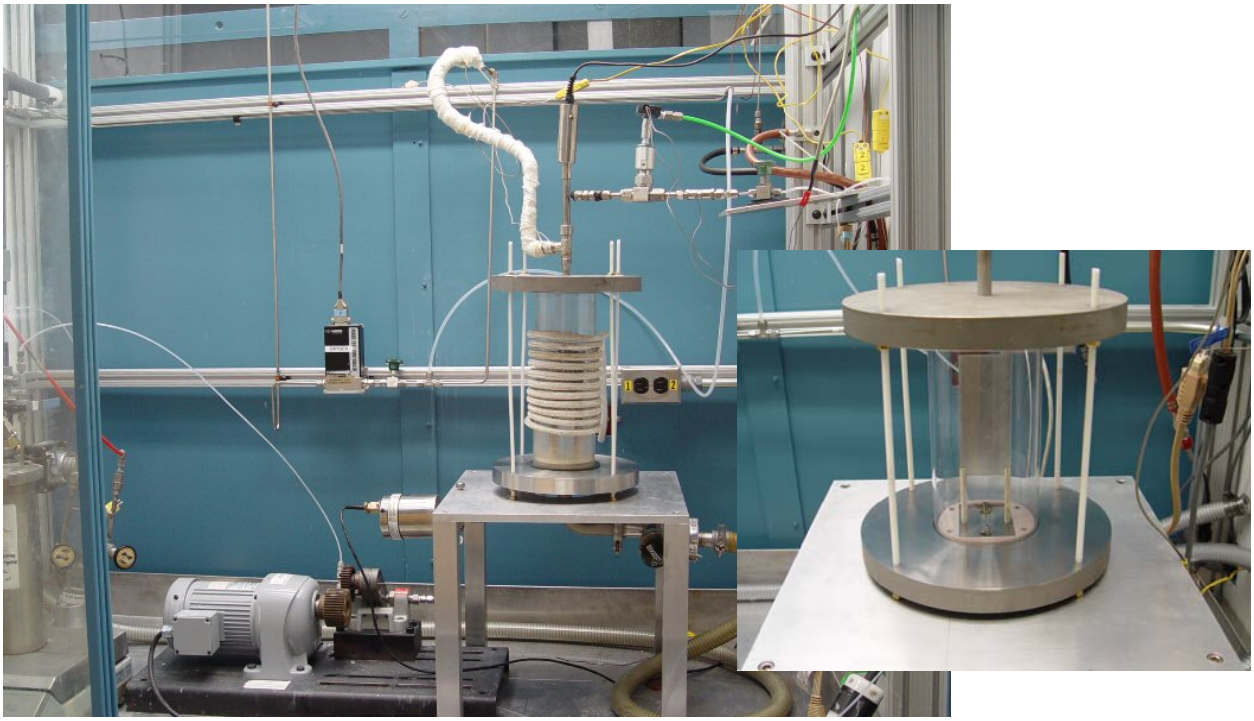

Fig. 4. Photograph of MOCVD scale-up facility for coating prototypical turbine blade sections.

RESULTS

The modeling efforts were used to guide experimental work in coating the larger-scale substrate. A variety of sets of conditions and geometrical configurations were explored, although all the options available from the modeling could not be explored.[12] The two most interesting were baffling the flow to so that reactant streams would efficiently encounter the substrate surface. The second approach attempted was using the system in pulse mode, alternating opening and closing inlet and exhaust valves.

The most successful approach was found in baffling the reactor. Figure 4a illustrates a typical coating on a substrate, and Fig. 4b shows the columnar microstructure the process can produce. The pulse mode was attempted several times, however, a pressure pulse generated by the rapid closure of the exhaust valve appeared to dampen the ultrasonic vibration in the injector, causing it to fail to atomize the precursor. This approach was therefore abandoned until a system redesign can eliminate that problem.

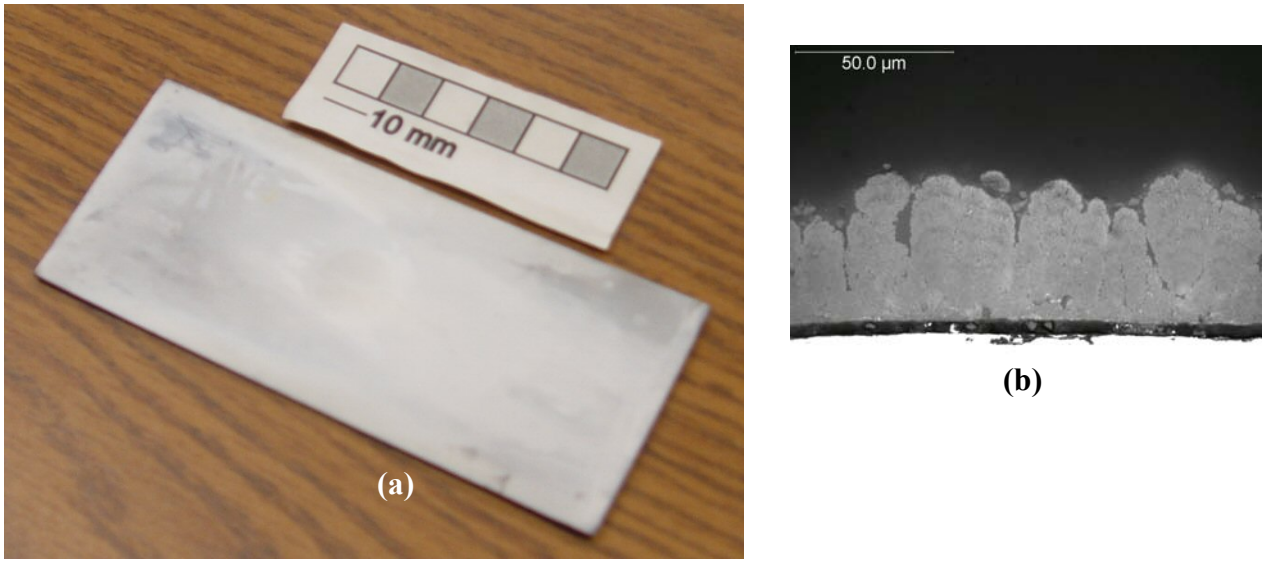

Fig. 4. MOCVD coating on (a) a prototypical turbine blade section and (b) an optical micrograph of the columnar cross-section of the deposited YSZ.

DISCUSSION

The scale-up design for the MOCVD reactor has been developed based on computational fluid dynamics modeling coupled with chemical kinetic information. The coating of large surfaces using MOCVD, however, is challenging and even the current design has exhibited difficulties. One of the major issues remains the formation of powder, i.e., homogeneous nucleation.

Interactions with Pratt & Whitney have resulted in an informal agreement on testing prototype YSZ coatings. Pratt & Whitney has supplied standard burner rig test substrates for coating at ORNL. These will be then provided to Pratt & Whitney for burner rig testing. Samples will be shared for evaluation.

CONCLUSIONS

The relatively thick columnar YSZ thermal barrier coatings have been deposited by MOCVD in a scale-up system on prototypical diameter samples. A variety of conditions and configurations were explored in modeling, and direct deposition using low pressure and furnace baffling produced reasonably good results. A pulse MOCVD system was tested, however the ultrasonic atomizer suffered from damping of the ultrasonic signal and resulting lack of atomization. Burner rig testing of samples at Pratt & Whitney will be used to evaluate future coatings.

ACKNOWLEDGMENTS

The authors wish to thank B. Pint for sample substrates. Research was sponsored by the Office of Fossil Energy, National Energy Technology Laboratory, U.S. Department of Energy, under contract number DE-AC05-00OR22725 with UT-Battelle, LLC.

REFERENCES

1. J. R. Nicholls, "Advances in Coating Design for High-Performance Gas Turbines," *MRS Bull.*, **28** 659-670 (2003).
2. D. R. Clarke and C. G. Levi, "Materials Design for the Next Generation Thermal Barrier Coatings," *Annu. Rev. Mater. Res.*, **33** 383-417 (2003).
3. A. G. Evans, D. R.Mumm, J. W. Hutchinson, G. H. Meier and F. S. Pettit, "Mechanisms Controlling the Durability of Thermal Barrier Coatings", *Progr. Mat. Sci.*, **46** 505-553 (2001).
4. N. P. Padture, M. Gell and E. H. Jordan, "Thermal Barrier Coatings for Gas-Turbine Engine Applications", *Science*, **296** 280-284 (2002).
5. P. K. Wright and A. G. Evans, "Mechanisms Governing the Performance of Thermal Barrier Coatings" *Curr. Opin. Sol. State Phys.*, **4** 255-65 (1999).
6. G. W. Wahl, W. Nemetz, M. Giannozzi, S. Rushworth, D. Baxter, N. Archer, F. Cernuschi, and N. Boyle "Chemical Vapor Depostion of TBC: An Alternative Process for Gas Turbine Components," *Transactions of the ASME*, **123** 520-4 (2001).
7. G. Wahl, Ch. Metz, and S. Samoilenkov "Thermal Barrier Coatings," in Proceedings: Thirteenth European Conference on Chemical Vapor Deposition, EDP Sciences, Les Ulis, France, 2001, pp. Pr3-835-46.
8. H.Yamane and T. Hirai, "Yttria Stabilized Zirconia Transparent Films Prepared by Chemical Vapor Deposition." *Journal of Crystal Growth*, **94** 880-4 (1989).
9. S. P. Krumdieck, O. Sbaizero, A. Bullert, R. Raj, "YSZ Layers by Pulsed-MOCVD on Solid Oxide Fuel Cell Electrodes." *Surf. Coat Tech.*, **167** 226-33 (2003).
10. V. G. Varanasi and T. M. Besmann, "Parametric Study of the Chemical Vapor Deposition of Yttria-Stabilized Zirconia From Organometallic Precursors," in Proceedings of the Electrochemical Society: Chemical Vapor Deposition XVI and EuroCVD 14, Vol. 2, The Electrochemical Society, Pennington, NJ, 2003, pp. 783-9.
11. V. G. Varanasi, T. M. Besmann, J. J. Henry, Jr., T. L. Starr, W. Xu, T. J. Anderson, "Yttria-Stabilized Zirconia Thermal Barrier Coatings By Metal-Organic Chemical Vapor Deposition," pp. 595-601, in *Proc. 5th Int. Conf. On High Temp. Ceramic Matrix Composites*, eds. M . Singh, R. J. Kerans, E. Lara-Curzio, R. Naslain, American Ceramic Society, Westerville, OH, 2004.
12. T. L. Starr, *Modeling Of Chemical Vapor Deposited Zirconia For Thermal Barrier And Environmental Barrier Coatings,* Draft Final Report, Fossil Energy Advanced Materials Program, 2006.

PROTECTION SYSTEMS: CORROSION RESISTANT COATINGS

Beth L. Armstrong
Oak Ridge National Laboratory
1 Bethel Valley Road, P.O. Box 2008, Oak Ridge, TN 37831-6063
Email: armstrongbl@ornl.gov; Telephone: (865) 241-5862; Fax: (865) 574-6918

Kevin M. Cooley
Oak Ridge National Laboratory
1 Bethel Valley Road, P.O. Box 2008, Oak Ridge, TN 37831-6063
Email: cooleykm@ornl.gov; Telephone: (865) 574-4559; Fax: (865) 574-6918

ABSTRACT

Material loss caused by exposure to the severe operating environments in gasifiers (slagging and non-slagging), industrial waste incinerators, and other advanced fossil or biomass-fueled power systems results in reduced service life, reduced reliability and increased operating costs. This project aims to improve material performance by combining intelligent materials design with colloid science and coating technology to develop cost-effective materials and processes engineered for optimum performance and maximum service life in their specific fossil environment. There are two basic material systems which comprise "fossil power systems", ceramics and metallics. Previously, this work was focused on providing protection systems for ceramic based materials. The issues of protecting ceramics for uses at very high temperatures (> 1400°C) have not been solved, but recent work in this project and in collaboration with NETL-Albany Research Laboratory have proven the feasibility of utilizing low cost processing methods to apply dense coatings to porous ceramic refractories for improved molten slag resistance. Now, lower cost methods and novel approaches of applying coatings to metals are being explored to meet more near term goals. Thus, the development of novel coatings utilizing low-cost aqueous processing methods such as dip coating is being pursued. Colloidal processing of metallic particles in aqueous suspension offers an economic route for forming uniform, metallic coatings on complex-shaped components via a simple process. A review of the application of the ORNL dip coating process for the past work on ceramic systems, mullite coatings on sintered alpha silicon carbide substrates and the ARC developed chromia system on chromia refractory bricks, will be presented. The transition of this process into the application of coatings onto ferritic martensitic alloys will be discussed as well.

INTRODUCTION

Advanced fossil energy processes have hostile environments with temperatures as high as 1550°C and atmospheres that contain water vapor, sulfur, nitrogen, trace heavy metals, molten slag and alkali salts. Ceramic and metallic material systems can potentially play important roles in the harsh fossil environments. There are two classes each of metals and ceramics that are of interest to this project. The ceramic systems that were examined were silicon-based, nonoxide ceramics (e.g. SiC and SiC/SiC composites) and non silicon-based oxide ceramics for refractory applications. The metal systems of interest are ferritic martensitic steels to address corrosion issues in superheaters, boilers, heat exchangers, turbines, etc… and Ni-based super alloys to address corrosion issues in ultrasupercritical systems.

Silicon-based ceramics such as SiC or SiC/SiC composites are attractive for use in fossil environments for applications such as hot-gas filters, heat exchangers, and other devices for advanced energy producing systems. They are candidates due to their higher temperature capability relative to metals, high thermal conductivity, retention of mechanical properties at operating temperatures, and excellent thermal shock resistance. A slow growing silica scale is the typical protection mechanism for the SiC material. This scale limits oxygen diffusion and thus prevents further attack of the substrate. A major drawback of SiC ceramics, however, is the susceptibility of the silica scale to volatilization and corrosion by water vapor and alkali salts such as Na_2SO_4 at high temperatures.

This factor limits the applicability of SiC ceramics for extended service in many fossil energy conversion and combustion system environments.[1-3] Thus, the use of protective coatings (e.g. mullite) or the development of material with improved stability in these harsh environments is necessary.

Chromia-based (non silicon-based) refractory materials play an important role in thermal management for slagging and non-slagging gasifiers and are currently, the only feasible option for reaction containment in slagging gasifiers,[4-9] which are predicted to be at the heart of many of the Advanced Fossil Fuel Power Systems planned for the future. Although coal gasification has proven to be an efficient and relatively clean way to produce electricity, liquid fuels, and chemicals, it has not yet reached the level of reliability, availability, and maintainability that will lead to widespread market acceptance. Rapid refractory material loss caused by exposure to the severe operating environments present in gasifiers (i.e., elevated temperatures, pressures, corrosive slag and gas concentration) results in reduced refractory service life and directly impacts the on-line availability of the gasifier island to produce synthesis gas. Because the entire system must be shutdown to reline these materials, refractory service life has a direct impact on gasifier on-line availability. Attempts to enhance gasifier output and economics by operating at higher temperatures, with higher throughputs, and/or with variable feedstocks, put additional stress on the materials exposed to the operating environment, and typically result in a corresponding decrease in their useful service life. As a result, the reliability and economics of gasification as a means to generate electricity and other products are adversely impacted. For example, current generation high chromium-oxide refractories typically last between three and 18 months inside a gasifier, depending on the operating conditions and locations of the specific system.

To address the need for improved performance in gasifier lining materials, the Albany Research Center (ARC) has developed a modified chromia refractory brick that is designed specifically for longer life in the slagging gasifier environment.[9] Further improvements in refractory performance may also be gained through the addition of a coating, particularly if it is both slag resistant and economical to apply. The Oak Ridge National Laboratory (ORNL) slurry coating technology (described below) offers the opportunity to apply a dense, slag resistant ceramic layer to the modified refractory without significantly increasing production costs. Coatings for both ceramic and metallic systems have been well and long utilized for protection purposes in many industries. Some applications include paint (architectural, automotive, marine), environmental barriers for micro turbines and other distributed energy systems, and thermal barriers for fossil and distributed energy systems. There are many techniques available to fabricate layers (coatings) of varying thicknesses. Some of these include plasma vapor deposition (PVD), electron beam – plasma vapor deposition (EB-PVD), chemical vapor deposition (CVD), pack cementation, and slurry or dip coating (1-5, 14-15). With the exception of pack cementation and slurry coating, the above mentioned processes are typically costly, line of sight techniques which would not lend themselves well to the coating of large, three dimensional parts. Pack cementation is very effective for non-complex stoichiometric coating material systems while slurry coating can handle a wider variety of material systems.

Colloidal processing of ceramic slurries offers a low cost alternative approach for producing uniform, thick ceramic coatings on complex-shaped components via a simple dip coating process (i.e., the ORNL slurry coating process). This approach has been demonstrated in many multi-disciplinary areas such as coatings (paints, glazes), fabrication of monolithic components (casting, deposition), and emulsions (gels, food additives, cosmetics). Control of the suspension rheological behavior is paramount to produce quality coatings and can be accomplished by tailoring interparticle (or surface) forces. In aqueous-based suspensions, long-range attractive van der Waals forces are ubiquitous and must be balanced by repulsive forces to tailor the desired degree of suspension stability. For example, ionizable polymeric dispersants, or polyelectrolytes, are commonly used to modify the surface of particles to impart repulsive electrosteric forces.[10, 11]

This year, the work on the development of concentrated, aqueous suspensions comprised of mullite and chromia particles for use in a dip-coating process was tested and work brought to a close. Mullite and chromia were chosen to demonstrate the feasibility of these processes as their behavior is well-characterized in their respective fossil environments. The approach consists of zeta potential measurements as a function of pH to understand the electrochemistry of the ceramic material surface in aqueous suspension, rheological characterization of concentrated suspensions to understand how to control its flow behavior using polyelectrolyte-based dispersants, and characterization of mullite and chromia dip coatings on SiC substrates and chromia-based refractory brick, respectively. A summary of the past work will be presented here as well as an introduction to the proposed new research path.

EXPERIMENTAL PROCEDURE

Mullite, i.e., $3Al_2O_3$-$2SiO_2$, (MULCR®, Baikowski International Corporation, Charlotte, NC), three (3) commercial chromia refractory brick (CB) materials, and an ARC modified chromia based system were used as the ceramic powders in this study. The mullite powder was attritor milled to an average particle size of ~ 0.5 μm and surface area of 26.0 m^2/g, determined using dynamic light scattering (Zetasizer 3000HS, Malvern Instruments Ltd., Worcestershire, UK) and BET (Autosorb-1, Quantachrome Instruments, Boynton Beach, FL), respectively. ARC provided ORNL all four (4) chromia based systems, and the materials were used in as-received form. Polyethylenimine (PEI), a cationic polyelectrolyte with a weight average molecular weight of 10,000 g/mole and one protonizable amine group (NH) per monomer unit was used as a rheological modifier for the mullite system. Due to reactivity of the chromia system in water, the dispersant, a poly(acrylic acid)-poly(ethylene oxide) (PAA-PEO) copolymer (Advaflow®, Grace Construction Products, Cambridge MA) was used, which has been demonstrated to be effective for fine ceramic powders that react with water.[12] (Note, the average molecular weight was 5000 g/mole and 2000 g/mole for the PAA and PEO, respectively).

Zeta potential measurements were carried out on the chromia particles in dilute aqueous suspension using capillary electrophoresis (Zetasizer 3000HS, Malvern Instruments Ltd., Worcestershire, UK). Dilute suspensions (10^{-3} vol% solids) were prepared by adding the appropriate amount of powder to aqueous, KNO_3 solutions (0.01 *M*) of varying pH ranging from 2 – 11. The solutions were adjusted to the appropriate pH using stock solutions of nitric acid or ammonium hydroxide. The suspensions were ultrasonically treated for 120 s to break up soft agglomerates prior to measurement.

Rheological measurements were carried out on concentrated mullite and chromia suspensions using a controlled-stress rheometer (Rheometric Scientific SR5, TA Instruments, New Castle, DE) fitted with concentric cylinder geometry. Concentrated mullite suspensions (45 vol% solids) were formulated by mixing an appropriate amount of mullite powder into aqueous solutions (pH 7) of varying PEI concentration. Chromia suspensions of varying solids loading were prepared by combining an appropriate amount of ceramic powder to aqueous solutions (pH 9) and varying PAA-PEO concentration. The suspensions were ultrasonically treated for 300 s to break up soft agglomerates, and then stirred for 24 hours to achieve equilibrium. Prior to measurement, the suspensions were presheared at a stress of 200 Pa for 300 s and then allowed to equilibrate for 900 s. Furthermore, a solvent trap was used to minimize the evaporation of water. In this way, variations in sample handling were minimized to ensure reproducibility of the data. Stress viscometry measurements were carried out by ramping an applied shear stress (logarithmically) from 0.025 to 200 Pa. A delay time (i.e., the time between two consecutive data acquisition events) of 60 s was used in this study.

Silicon carbide substrates (Hexaloy, Carborundum Co., Niagara Falls, NY) that were 20 mm x 6.5 mm x 6.5 mm in size were dipped into the concentrated mullite suspensions (45 vol%) of varying PEI concentration. The chromia refractory brick compositions (CB1, CB2, CB3 and ARC1) were cut into cubes of approximately 1 cm^3 in size. The cubes were subsequently inserted into concentrated chromia-based suspensions of comparable composition, e.g., the CB1 bricks were dipped into the CB1 slurries. All of the coated substrates were dried under ambient conditions, heat treated at 600°C to burn out any organic additions, and sintered at varying temperature and atmosphere (e.g., air, argon, and nitrogen)

RESULTS AND DISCUSSION

ZETA POTENTIAL

Zeta potential measurements were carried out on dilute chromia suspensions (10^{-3} vol% solids) of varying pH and the results are shown in Fig. 1. The isoelectric point (IEP) was observed at pH 4.6. In addition, at pH 9, the Cr_2O_3 particle surface underwent charge reversal and a sharp increased in zeta potential to 40 mV. This phenomenon may indicate the formation of a passive hydroxide layer on the surface of the Cr_2O_3 particles. The net positive surface potential at pH 9 indicates that an anionic polyelectrolyte (e.g., the PAA-PEO copolymer) that is fully (negatively) charged at these pH conditions will strongly adsorb to the surface of the particles. The adsorbed PAA-PEO, in turn, promotes dispersion of the particles. (Note, prior zeta potential measurements identified the cationic polyelectrolyte, PEI, as a good dispersant for the mullite system).[13]

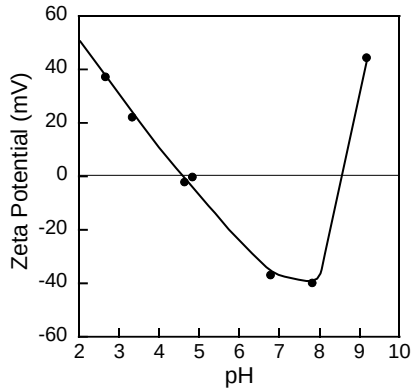

Fig. 1. Zeta potential as a function of pH for dilute chromia suspensions (10^{-3} vol% solids).

RHEOLOGICAL BEHAVIOR

Previously, mullite gels with slightly shear-thinning flow behavior were identified as the optimum rheological conditions for coating dense, silicon carbide substrates with mullite suspension. Porous refractory brick, on the other hand, is a much different surface and may not require the same conditions. Capillary forces that emerge from solvent wicking out of the coating layer into the porous brick aid to retain a uniform coating on the surface. In addition, the high surface roughness of the brick improves wetting. Thus, the particle gel network that serves to retain mullite slurries onto a nonporous substrate may not be necessary for chromia-based slurries on porous brick. For the latter, Newtonian flow behavior, indicative of a fully stabilized colloidal fluid may promote uniform coating, and perhaps, promote infiltration of the slurry into the porous brick.

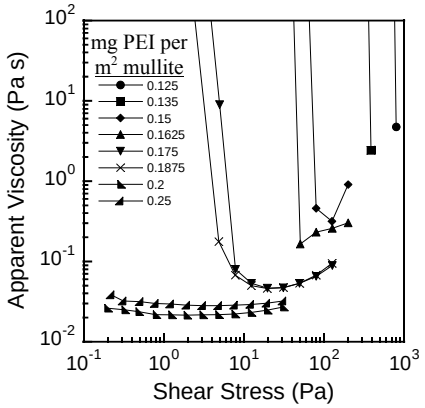

Fig. 2. Apparent viscosity as a function of shear stress for concentrated mullite suspensions (45 vol% solids) of varying PEI concentration.

Rheological measurements were carried out on concentrated mullite suspensions of varying PEI concentration as shown by the plot of apparent viscosity as a function of applied shear stress in Fig. 2. The degree of shear-thinning decreased with increasing PEI concentration until nearly Newtonian flow behavior was observed at 0.2 mg PEI/m^2 mullite.

The apparent viscosity is plotted as a function of applied shear stress in Fig. 3 for CB2 suspensions (a) of varying PAA-PEO concentration and (b) of varying solids loading. Strong shear-thinning flow behavior was observed in the absence of PAA-PEO dispersant; however, the degree of shear-thinning was reduced with the addition of PAA-PEO until a stable suspension, as indicated by Newtonian flow behavior, was observed at 0.1 mg PAA-PEO/g CB2 powder. Nearly Newtonian flow behavior was observed for suspensions with solids loading as high as 57.5 vol% in the presence of 1 mg PAA-PEO per g. CB2 powder. Similar flow behavior was observed for the other chromia-based systems at the high solids loading of 57.5 vol%, as shown in Fig. 4. High solids loading suspensions are required for the formation of dense, thick coatings on the refractory brick.

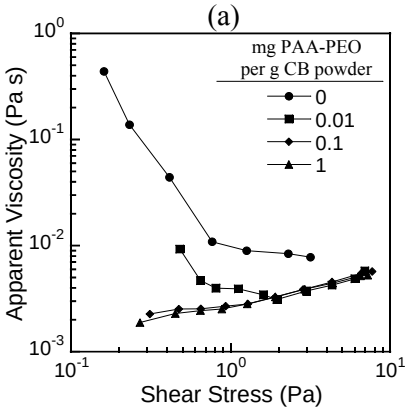

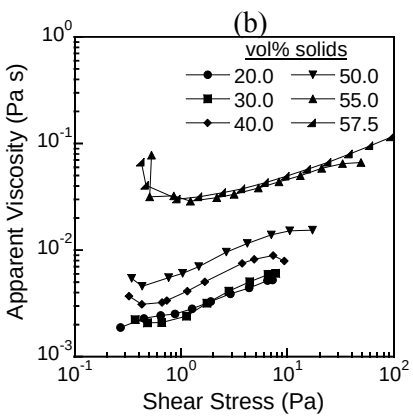

Fig. 3. Apparent viscosity as a function of shear stress for CB2 suspensions of (a) varying PAA-PEO addition (45 vol% solids) and (b) vary solids loading (1 mg PAA-PEO per g. CB1 powder).

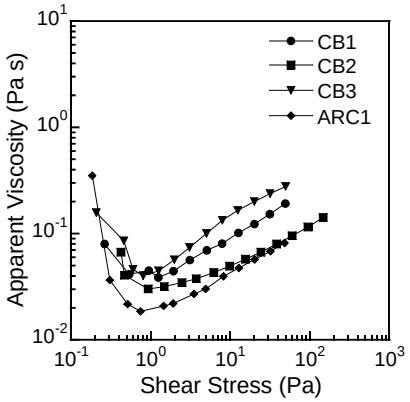

Fig. 4. Apparent viscosity as a function of shear stress for CB1, CB2, CB3, and ARC1 suspensions (57.5 vol% solids, 1 mg PAA-PEO per g. powder).

COATING FORMATION

Silicon carbide substrates were dipped into mullite suspensions (45 vol% solids) of varying rheological behavior and the resulting coatings are displayed in Fig. 5. Excellent coatings were obtained from mullite suspensions with slightly shear-thinning flow behavior obtained with the addition of 0.1625 - 0.175 mg PEI/m^2 mullite surface. Below this range, the coatings were thick and uneven, and cracks formed after drying. Above this range, uneven coatings were obtained because the slurry formed beads away from the corners and edges and flowed off of the substrate under the influence of gravity. By reducing the solids loading to 25 vol% and utilizing colloidal processing techniques to mimic the shear-thinning rheology of the more concentrated mullite suspensions discussed above (45 vol%), uniform layers of lesser thickness were formed by the dip-coating process.

Fig. 5. Resultant coatings from dipping SiC substrates into concentrated mullite suspensions (45 vol%) of varying PEI concentration ranging between 0.15-0.20 mg PEI/m^2 mullite.

The chromia-based refractory brick "cubes" were inserted into Newtonian, chromia-based suspensions (57.5 vol%, 1 mg PAA-PEO per g. powder) with ceramic powder composition identical to the cubes. The resultant coatings deposited onto the brick are shown in Fig. 6. Our results confirm that chromia-based slurries with Newtonian flow behavior are sufficient to uniformly coat the porous brick.

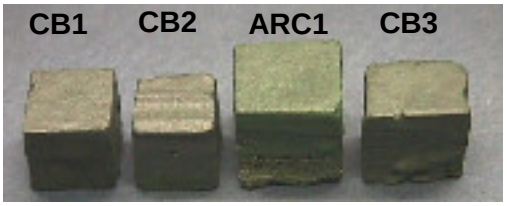

Fig. 6. Resultant coatings formed from dipping chromia-based brick into suspensions (57.5 vol% solids, 1 mg PAA-PEO per g. powder) of like composition. Note, the coating conformed uniformly to the CB2 brick, whose surface was rough compared to the other bricks shown here.

SINTERING BEHAVIOR

After sintering at 1400°C for 2 h in air (1 atm), a uniform, adherent mullite layer of ~ 20 μm thickness was obtained, as shown in Fig. 7. The presence of the mullite layer did not reduce the mechanical strength of the substrate, as determined by four-point bend tests of coated and uncoated bend bars. These early results are encouraging since the application of plasma sprayed coatings can significantly reduce the high temperature mechanical strength.[14] Although it is not apparent that there is interconnected porosity in the coatings, some silica was detected at the mullite/SiC interface after exposure to 1200°C steam for 500 h. Presumably, this reaction is a result of oxygen diffusion through pores in the coating; however, further iteration is necessary to qualify the density of the coatings required to protect the underlying substrate from fossil environments.

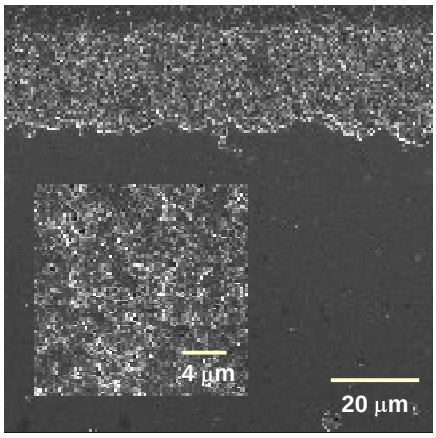

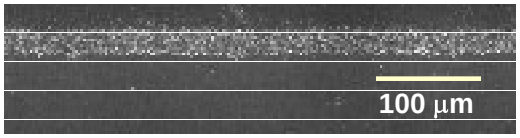

Fig. 7. SEM micrographs of a mullite layer on a SiC substrate. The layer was formed by dipping the substrate into a mullite suspension of 0.25 volume fraction solids, drying, and sintering at 1400°C for 2 h.

Micrographs of the chromia-based coatings are shown in Fig. 8 after sintering at 1600°C for 2 h in air (1 atm). Uniform layers, approximately 50-100 μm in thickness were obtained (note, the final, desired coating thickness will not be determined until corrosion testing can be completed). Furthermore, some of the slurry penetrated into the brick through the larger pores (~ 100 μm diameter). The coating density varied for the different systems, where the ARC composition was the densest of all the systems, and CB2 was the densest of the commercial brick systems. The coating density did not improve after sintering for longer times (12 h).

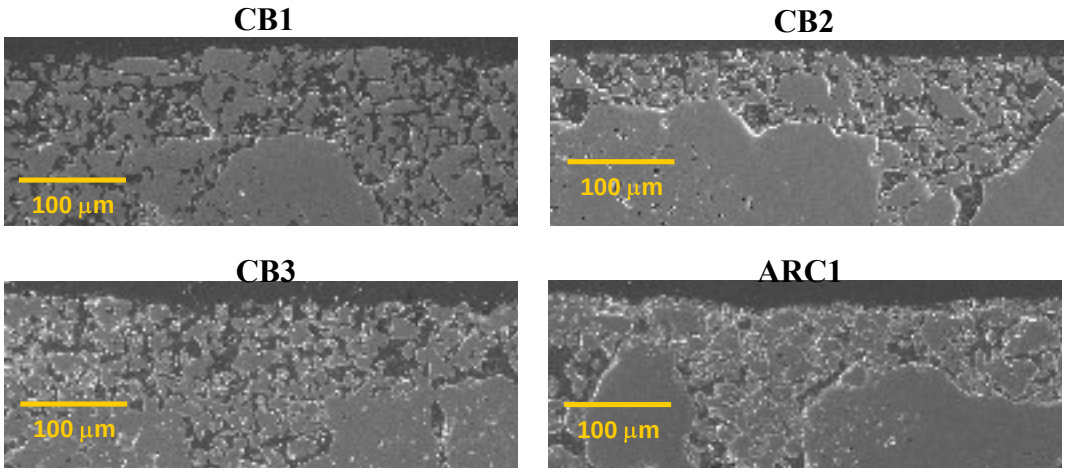

Fig. 8. SEM micrographs of chromia-based layers on refractory brick. The layers were formed by dipping the bricks into suspensions (57.5 vol%, 1 mg PAA-PEO per g. powder) of like composition to each respective brick. The coated bricks were dried and sintered at 1600°C in air.

The CB2 system was sintered in Ar (1 atm) for 2 h, and exhibited marked improvement in coating density as shown in Fig. 9. Furthermore, the coating density was improved after air sintering with the addition of a sintering aid (see

Fig. 10). Initial coating studies are promising, thus the internal surface of chromia-based refractory cups will be coated for molten slag penetration tests to be performed at Albany Research Center.

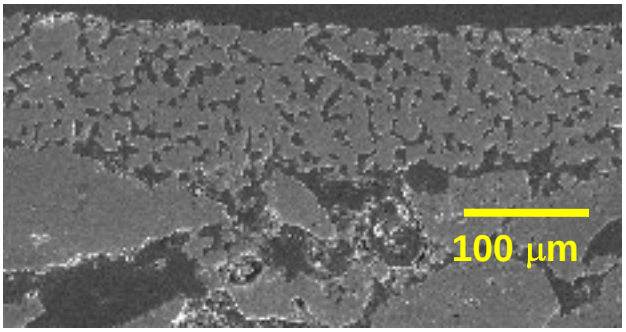

Fig. 9. A SEM micrograph of a CB2 coating on CB2 refractory brick. The layer was formed by dipping a CB2 brick into a suspension (57.5 vol%, 1 mg PAA-PEO per g. powder) of like composition. The coated brick was dried and sintered at 1600°C in Ar.

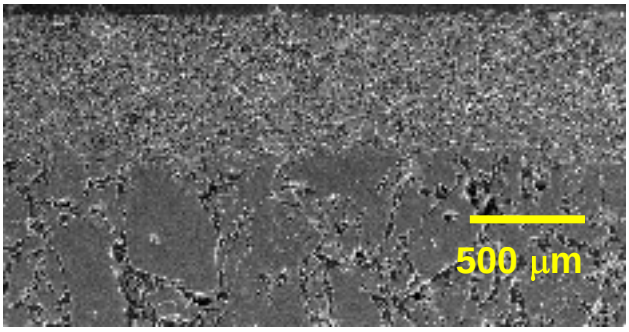

Fig. 10. A SEM micrograph of a CB2 coating on CB2 refractory brick. The layer was formed by dipping the brick into a suspension (57.5 vol%, 1 mg PAA-PEO per g. powder) of like composition to the brick, with the exception of a sintering aide. This addition also promoted slightly shear-thinning flow behavior, resulting in increased coating thickness. The coated brick was dried and sintered at 1600°C in air.

The focus of previous project funding was the evaluation of slurry coatings for ceramic material systems. The project demonstrated the feasibility of utilizing an inexpensive, non-line of sight process for a variety of coating material systems through developing a basic colloidal understanding of material surfaces and how to control them. The work is not complete; the key issues that are still being addressed are the stability of the interface between the coating and the substrate. Instability will result in detrimental interactions and/or loss of adhesion of the coating to the substrate after long term thermal cycling. These are issues that will have to be addressed by industrial collaborators.

In metallic systems, one advantage of a coating is that the substrate alloy can be optimized for properties other than corrosion resistance (i.e. ductility, formability, creep strength, etc) (15-16). The technical challenge, as in the ceramic system, is that the physical, chemical, and mechanical differences between the substrate and the coating can lead to detrimental interactions, which can limit lifetime. Again, the interdiffusion between coating and substrate can result in the formation of brittle intermetallic phases or the loss of protective scale-forming elements. For example, in thermal barrier coating (TBC)/superalloy systems, a major problem is the loss of Al from the bond coat to the substrate superalloy over time at temperature, which ultimately contributes to an inability to maintain Al_2O_3 growth and subsequent coating failure (17-18). Thus, the design of the protective coatings in consideration of the substrate, has thus received increased attention in recent years. For example, recent work by Gleeson et al has identified Ni-Al-Pt bond coat compositions for which Al diffuses from the substrate superalloy into the coating, helping to maintain a reservoir of Al for Al_2O_3 formation by the coating, rather than loss of Al from the coating alloy to the substrate. Typically, these Al coatings are applied after annealing of the metal and require further post heat treatment processing to convert the Al to Al_2O_3. This step can degrade physical properties of the metal while added additional processing time and thus expense to the process. A slurry coating process may allow changes to current processing steps by either limiting the processing temperatures that the coating/metal interface sees (slurry coating is a room temperature process) and/or by combining the coating and metal annealing process into one. If a less expensive, non-line of sight process can be utilized to apply a metallic coating or a film that will react to form the appropriate metal or ceramic phase directly, potentially control of the metal's physical properties can be maintained while minimizing processing time and/or expense. This has been demonstrated recently by Agüero who has used aluminide slurries to coat ferritic martensitic steels (19).

Key performance indicators will be whether or not a slurry coating system can be developed to coat metallic

substrates while developing an understanding of how the interfacial properties of the coating material system and the surface of the metallic support affect the structure of the metal and its physical properties. Key decision points will be whether or not the correct protective phase can be achieved, if the protective phase can be achieved at low enough processing temperatures as to prevent physical property degradation of the metal, if the protective phase can be added earlier in the processing regime, can a systematic understanding be developed to correlate coating parameters to material properties and lifetime predictions.

CONCLUSIONS

The ORNL slurry coating approach is a low-cost method to deposit protective layers on SiC ceramics and chromia-based refractory brick for use in fossil energy applications. The surface of chromia particles in aqueous suspension was characterized using zeta potential measurements. Polyelectrolyte dispersants were identified to modify the rheological behavior of concentrated mullite and chromia-based suspensions. Slightly shear thinning and nearly Newtonian flow behavior was identified as the optimal slurry rheology needed to coat nonporous SiC and porous, chromia-based refractory brick, respectively. Sintering conditions have been explored to densify the coatings. and ongoing, iterative efforts are underway to maximize the properties of the systems in their respective environments.

ACKNOWLEDGMENTS

The ceramic coating research was jointly sponsored by the U.S. Department of Energy, Office of Fossil Energy Advanced Research Materials Program under Work Breakdown Structure Element ORNL-1(B) and by the Albany Research Center under work breakdown element 3FEAA075. The Oak Ridge National Laboratory is operated by UT–Battelle LLC for the U.S. Department of Energy under contract DE-AC05-00OR22725.

REFERENCES

1. Fox, D., Cuy, M., and Strangman, T., *J. Am. Ceram. Soc.*, **80** (11) 2798-804 (1997).
2. Opila, E., *J. Am. Ceram. Soc.*, **82** (3) 625-36 (1999).
3. More, K., Tortorelli, P., Ferber, M., and Keiser, J., *J. Am. Ceram. Soc.*, **83** (1) 211-13 (2000).
4. Bonar, J.A., Kennedy, C.R., and Swaroop, R.B., *Am. Ceram. Soc. Bull.* **59** 473-478 (1980).
5. Bakker, W.T., *Key Engineering Materials* **88** 41-70 (1993).
6. Fahrion, M.E., *Materials at High Temperatures* **1**1 107-112 (1993).
7. Bakker, W.T., EPRI Report TR-110507, Palo Alto, CA. (1999).
8. Guo, Z-Q and Zhang, H., *J. European Ceramic Soc.*, **19** 113-117 (1999).
9. Kwong, K-S., etal., DOE Invention Disclosure S-97-969 (2001).
10. Cesarano, J. and Aksay, I., *J. Am. Ceram. Soc.*, **71** (4) 250-55 (1988).
11. Cesarano, J. and Aksay, I., *J. Am. Ceram. Soc.*, **71** (12) 1062-67 (1988).
12. Kirby, G. H., Harris, D., Li, Q., and Lewis, J., *J. Am. Ceram. Soc.,* **87** [2] 181-186 (2004).
13. Kirby, G., Cooley, K., and Armstrong, B., *Proceedings of GT2005 ASME Turbo Expo 2005: Power for Land, Sea, and Air*, Reno-Tahoe, NV.
14. Data presented at the 2004 Environmental Barrier Coating Workshop in Nashville, TN.
15. Brady, M.P., Tortorelli, P.F., More, K.L., Payzant, E.A., Armstrong, B.L., Lin, H-T., Lance, M.J., Huang, F., and Weaver, M.L., 2005, submitted to *Materials and Corrosion*.
16. Brady, M.P., Armstrong, B.L., Lin, H-T., et al., 2005, *Scripta Materialia*, **52** (5): 393-397.
17. Gleeson, B., Wang, W., Hayashi, S., Sordelet, D., Materials Science Forum (in press).
18. Opila, E., 2003, *J. Am. Ceram. Soc.*, **86** [8], 1238.
19. Agüero, A., Muelas, et al, 2005, *Surface & Coatings Technology 200*, 1219-1224.

DEVELOPMENT OF NONDESTRUCTIVE EVALUATION METHODS FOR CERAMIC COATINGS

W. A. Ellingson, S. Naday, R. Visher,* R. Lipanovich,[+] L. Gast and C. Deemer
Argonne National Laboratory, Energy Technology Division
9700 S. Cass Ave., Argonne, IL 60439
* Graduate Student, Illinois Institute of Technology, Chicago, IL 60616
[+]Undergraduate Student, Illinois Institute of Technology, Chicago, IL 60616

E-mail: ellingson@anl.gov; Telephone (630)252-5068; FAX (630)252-4798

ABSTRACT

Nondestructive evaluation (NDE) methods are being developed for use with ceramic coatings for components in the hot-gas path of advanced gas-fired turbine engines with low emissions. The main coatings studied are thermal barrier coatings (TBCs) for vanes, blades, and combustor liners to allow hotter gas-path temperatures. The NDE methods will be used to: (a) provide data to assess the reliability of new coating processes, (b) identify defective components that could cause unscheduled outages, (c) track growth rates of delaminations and defects during use in engines, and (d) provide data for reaching rational decisions for replace/repair/re-use of components.

THERMAL BARRIER COATINGS

Advances in thermal barrier coatings (TBCs), applied by two deposition methods, electron beam–physical vapor deposition (EB-PVD) and air plasma spraying (APS), are allowing higher temperatures in the hot-gas path of gas turbines, including syn-gas fired turbines.[1-3] However, as TBCs become "prime reliant," it becomes important to know their condition at scheduled or unscheduled outages.

Work at Argonne National Laboratory (ANL) is underway to develop NDE methods to assess the condition of the TBC primarily from the point of view of detecting pre-spall conditions.[4] Prior to spallation of EB-PVD coatings, it has been suggested that the interface topography between the thermally grown oxide layer (TGO) and the substrate changes as a function of the number of thermal cycles.[5] The growth and change in topography for APS coatings are less clear. However, if an NDE method could be developed that would allow interrogation of this interface for either EB-PVD or APS coatings, it would seem possible to begin to develop a method for pre-spall prediction. One such NDE method under development utilizes polarized laser light in a back-scattering is based on a modification of the reflectometry method[6] and was described previously.[7] Laser scatter data for an entire test sample are acquired by raster scanning the sample under computer control.

Last year[8] we reported on the use of a new finite element model for predicting the back scatter characteristics from the laser system. A separate issue reported on last year was the fact that raster scanning would be necessary to cover an entire airfoil. This would mean that the time to scan an entire airfoil section, while not prohibitively long, would be longer than might be desired. This year, in cooperation with a collaborative project funded by the Air Force, we began to explore the use of polarization maintaining optical fibers placed in an array such that data from an entire surface could be obtained in one scan. Figure 1 shows a photograph and other details of one of the first fiber array fabricated for use on silicon nitride bearing balls. In this first fiber array, the fibers used were 250 μm in diameter and the light was transmitted to the surface with one fiber and reflected light was detected by an adjacent fiber. This allowed initial test data to be acquired and software to be developed for automation. Initial test data

obtained from an automated scan of a bearing ball is shown in Fig. 2. In this case, on the surface of the ball were written a set of numerals. Note that the detected reflected light faithfully reproduces these numerals. In addition this year, we initiated work on use of a new nondestructive evaluation technology, optical coherence tomography, (OCT).[9] This technology was explored because images from this technique will provide a direct measurement of thickness of optically translucent coatings such as most environmental barrier coatings or thermal barrier coatings. A schematic diagram of the OCT system under development at Argonne is shown in Fig. 3. Initial OCT test data taken from environmental barrier coatings (EBCs) deposited on a glass substrate is shown in Fig. 4. In this case the slurry-dipped EBC coating was applied with an estimated thickness of 40 μm. Indeed as noted in Fig.4, the OCT thickness measurement estimates the thickness to be approximately 40 μm. The limits of use for the OCT are the fact that the material must be optically translucent at the wavelength of the diode laser and that the optical scattering within the material not be so severe that the signal is lost.

Fig 1. Photograph of first fiber optic array used for laser back scatter experiments. Each fiber is 250 μm in diameter. Shown here is an application for a 25 mm diameter silicon nitride bearing ball. Currently a system is being fabricated with 50 μm diameter fibers.

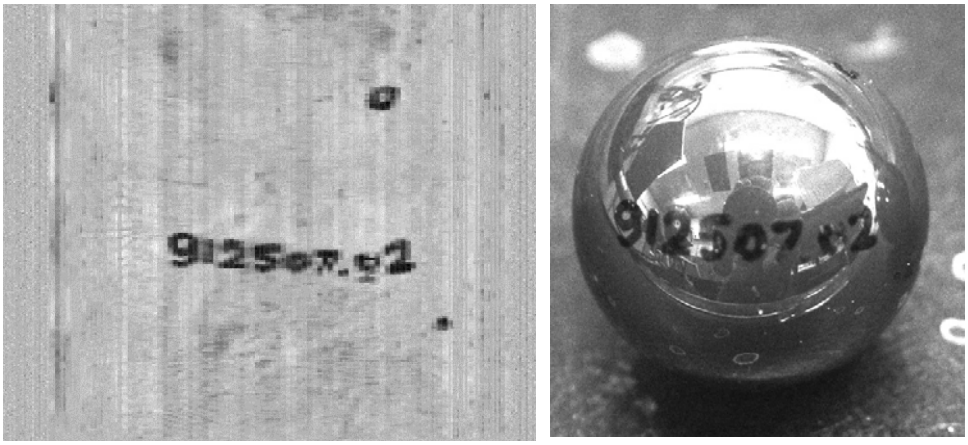

(a) (b)

Fig 2. Initial laser back scatter data from a 25 mm diameter ceramic bearing ball using the optical fiber array shown in Fig. 1. (a) Back scatter data obtained from rotation of the ball, (b) photograph of the ball showing the numerals on the ball surface.

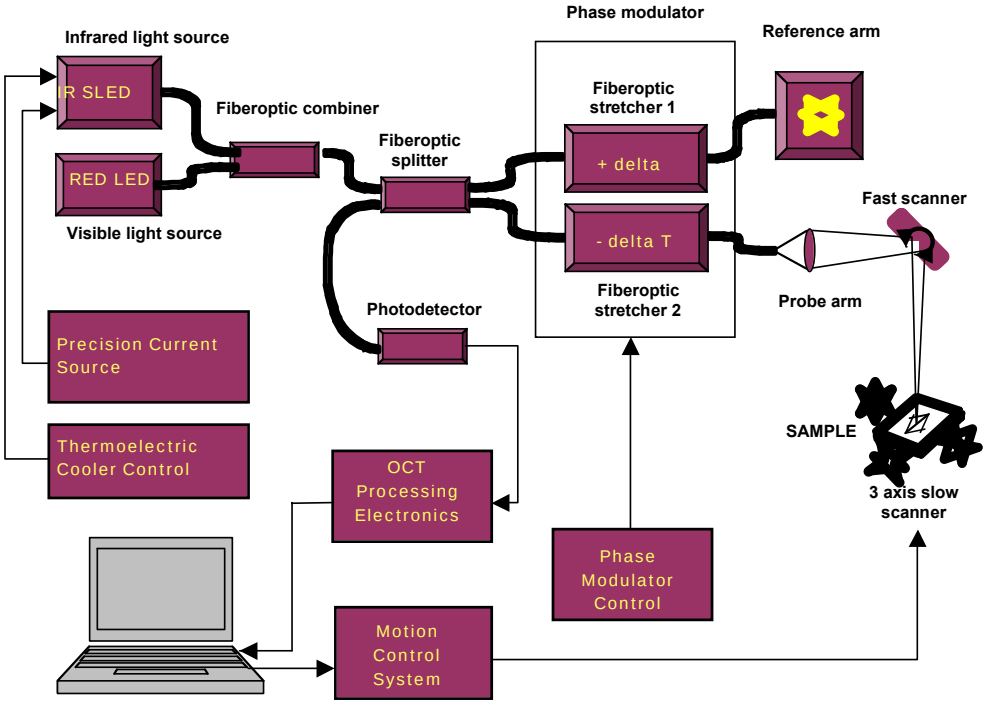

Fig. 3. Block diagram of basic elements in OCT system.

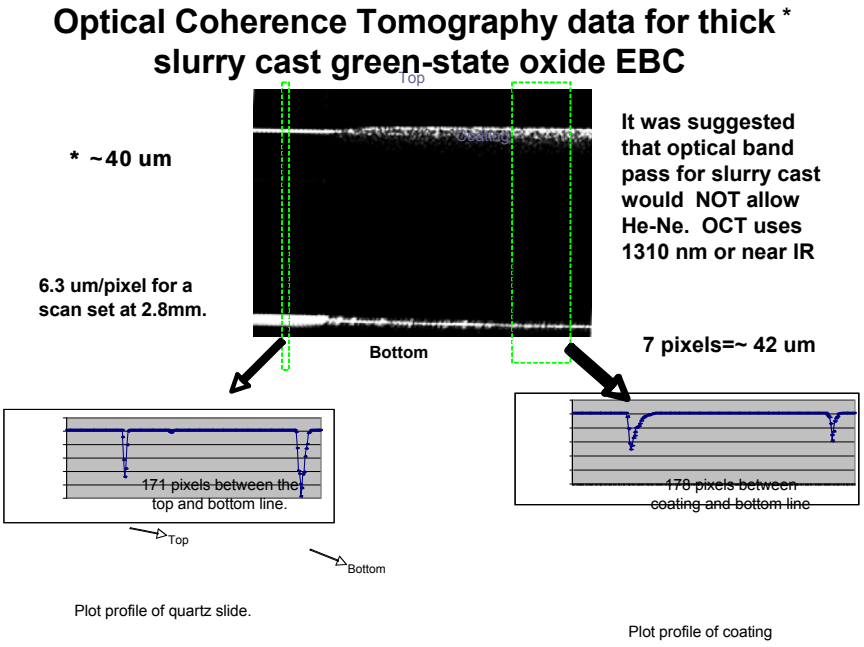

Fig. 4 Examples of direct thickness measurements of thickness of slurry dipped coatings through use of the optical coherence tomography system shown in Figure 3.

REFERENCES

1. North Atlantic Treaty Organization. "Thermal Barrier Coatings," Advisory Group for Aerospace Research and Development report, AGARD-R-823, Neuilly-Sur-Seine, France, April 1998.
2. US National Research Council, National Materials Advisory Board, "Coatings for High Temperature Structural Materials," National Academy Press, Washington, DC, 1996.
3. US National Aeronautics and Space Administration, "Thermal Barrier Coating Workshop," NASA Conference Publication 3312, 1995.
4. Ellingson, W. A., Visher, R. J., Shields, M. D. and Deemer, C. M. "Development of Nondestructive Evaluation Methods for Ceramic Coatings," in Proc. 18th DOE-Fossil Energy Materials meeting, June 2-4, 2004
5. Evans, A. G., Wang, J. S., and Mum, D., "Mechanism-Based Life Prediction Issues for Thermal Barrier Coatings," in Proc. of the TBC Workshop, US National Aeronautics and Space Administration, pp. 45-52, 1997.
6. Tompkins, H. G., and McGahan, W. A., "Spectroscopic Ellipsometery and Reflectometry," J. Wiley and Sons, Inc., New York, 1999.
7. Visher, R. J., Ellingson, W. A., Gast, L. and Feuerstein, A., " Health Monitoring and Life Prediction of Thermal Barrier Coatings using a Laser-Based Method." ASME paper, GT2005-68252, 2005
8. Ellingson, W. A., Naday, S. D., Visher, R.J., and Deemer, C. M. "Development of Nondestructive Evaluation Technology for High Temperature Ceramic Coatings," Proc. 19th Annual Conference on Fossil Energy Materials, Knoxville, TN, May 11-13, 2005.
9. Ellingson, W. A., Visher, R. J., Lipanovich, R. S. and Deemer, C. M. , "Optical NDT Methods for Ceramic Thermal Barrier Coatings," Materials Evaluation Vol. 64, No. 1, pgs 45-51, 2006.

SESSION 4

FUNCTIONAL MATERIALS

LOW CHROME/CHROME FREE REFRACTORIES FOR SLAGGING GASIFIERS

James P. Bennett
National Energy Technology Laboratory, 1450 Queen Ave., SW, Albany, OR 97321
E-mail: james.bennett@netl.doe.gov; Telephone: (541) 967-5983; Fax: (541) 967-5845

Kyei-Sing Kwong, Cindy Powell, Rick Krabbe, Hugh Thomas, and Art Petty
National Energy Technology Laboratory, 1450 Queen Ave., SW, Albany, OR 97321

ABSTRACT

Gasifiers are containment vessels used to react carbon-containing materials with oxygen and water, producing syngas (CO and H_2) that is used in chemical and power production. It is also a potential source of H_2 in a future hydrogen economy. Air cooled slagging gasifiers are one type of gasifier, operating at temperatures from 1275-1575º C and at pressures of 400 psi or higher. They typically use coal or petroleum coke as the carbon source, materials which contain ash impurities that liquefy at the gasification temperatures, producing liquid slag in quantities of 100 or more tons/day, depending on the carbon fed rate and the percent ash present in the feedstock. The molten slag is corrosive to refractory linings, causing chemical dissolution and spalling. The refractory lining is composed of chrome oxide, alumina, and zirconia; and is replaced every 3-24 months. Gasifier users would like greater on-line availability and reliability of gasifier liners, something that has impacted gasifier acceptance by industry. Research is underway at NETL to improve refractory service life and to develop a no-chrome or low-chrome oxide alternative refractory liner. Over 250 samples of no or low chrome oxide compositions have been evaluated for slag interactions by cup testing; with potential candidates for further studies including those with ZrO_2, Al_2O_3, and MgO materials. The development of improved liner materials is necessary if technologies such as IGCC and DOE's Near Zero Emissions Advanced Fossil Fuel Power Plant are to be successful and move forward in the marketplace.

INTRODUCTION

Gasifiers are the high temperature containment vessels used to react carbon-containing materials with oxygen and water using fluidized-bed, moving-bed, or entrained-flow system designs to produce syngas (CO and H_2) and/or other gases [1]. Sulfur compounds and ash in a powder or a molten slag form are the primary solid by-products of the gasification process, and are associated with impurities in the carbon feedstock. In air cooled slagging gasification systems, coal or petroleum coke is the typical carbon feedstock. Examples of two types of air cooled slagging gasifiers are shown in figure 1. Gasification in these processes is conducted at temperatures between 1275º and 1575º C, and with pressures of 400 psi or higher. The slagging gasifier shell is lined using refractory materials capable of withstanding the severe environment; protecting the outer steel shell from erosion, corrosion, and temperature (gasifier cross section is shown in figure 2). The refractory liner materials used in today's slagging gasifiers are typically fused or dense firebrick containing Cr_2O_3 (60 to 90 wt pct) with a second refractory oxide (typically Al_2O_3, ZrO_2, or MgO).

Early slagging gasification research concentrated on developing sound gasifier designs and on determining appropriate refractory liners for different systems under development. Refractory practices in industries thought to be similar to gasification; including petrochemical processing, blast furnaces for steel production, coke ovens, glass furnaces, and coal fired boilers; were evaluated for applicability to gasification. The high chrome oxide content of refractories used in today's slagging gasifier evolved through industrial efforts to develop an improved performance material, through plant trials conducted by industry, and through DOE and Electric Power Research Institute funded efforts traceable back to the 70's and 80's [2-10]. Materials that were evaluated included alumina-silicate, high alumina, chromia-alumina-magnesia spinels, alumina and magnesia, alumina and chrome, and SiC materials – both sintered and fused cast shapes of many refractory compositions. Liner materials for high wear areas in today's gasifiers evolved from these materials to those utilizing high chrome oxide content, with a minimum of 75 pct chromia thought to be necessary for satisfactory performance [11]. Wear mechanisms considered in early gasifier research included gaseous corrosion, corrosion/erosion by molten slags, erosion/abrasion by particulates, thermal/mechanical failures, and condensation of acids or steam entrapment at the shell.

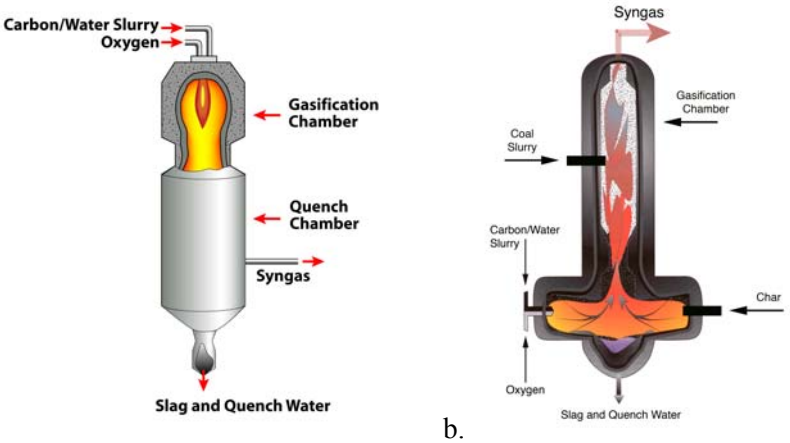

Figure 1 - Two types of air cooled slagging gasifiers; a) single injector GE type, and b) opposing flow dual injector ConocoPhillips type.

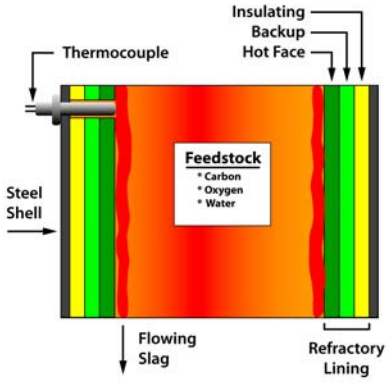

Figure 2 – General cross-section of an air cooled slagging gasifier.

Failure of today's refractory lining in a slagging gasifier is expensive, both in terms of refractory replacement costs (as high as $1,000,000 depending on shell size and the extent of rebuild necessary) and in terms of lost production. Re-lining a gasifier requires that the system be

completely shut down, and under the best of circumstances takes 7 days for a partial rebuild. A rebuild involves cool-down (4-6 days), refractory tearout, and refractory installation (3 days for a partial reline, 7-10 days for a full reline). Some gasification facilities maintain a second gasifier for use while repairs are made to reduce downtime or off line availability. Even then, the time to switch gasifiers can vary from hours to days, depending on the spare gasifier availability and if it is pre-heated. Because of the long down time required for repair, gasifier operators would like to install refractory linings with a reliable service life of at least three years. The current generation high chrome oxide refractory liners installed in gasifier systems have yet to meet this requirement, failing in as little as 3 months in high wear areas. Because of short refractory service life, gasifier manufacturers and operators have identified it as the most important barrier to reliable and efficient gasification [12]. Users desire a gasifier availability of 85-95% for utility applications and more than 95% in applications such as chemicals, creating a roadblock if technology such as IGCC is to move forward in the marketplace [13]. Gasifiers are also a key component of new energy systems being developed as part of the Department of Energy's Near Zero Emissions Advanced Fossil Fuel Power Plant.

Several issues exist with Cr_2O_3 refractory materials used in air cooled slagging gasifiers, which include: a) current high Cr_2O_3 containing refractories do not meet the performance requirements of gasifier users, b) perceived/real long term safety concerns associated with the use of Cr_2O_3 refractory materials and their interaction with slags, c) the high cost associated with refractory materials containing high Cr_2O_3 content, and d) possible long-term domestic supply issues. To address these and other concerns, this research project will investigate and develop low-chrome/no-chrome oxide liner materials for use in slagging gasifiers. These goals will be achieved by:

1) investigating the role chrome oxide plays in gasifier refractories,
2) evaluating wear mechanisms that play a role in gasifier failure,
3) evaluating non-chrome or low-chrome high temperature refractory oxides with potential for use in combating known wear mechanisms in gasifier refractories,
4) developing and evaluating engineered refractory shapes containing low or no chrome oxide, and
5) conducting field tests of these engineered refractory materials.

Past refractory research conducted on spent high chrome oxide liners at NETL-Albany has indicated two major wear mechanisms, corrosion and spalling (see figure 3). The causes of gasifier refractory spalling are complicated, but are thought to include: time, gasifier feedstock, slag penetration and differential thermal expansion between slag penetrated/non-penetrated layers in the refractory, high temperature creep [14], reactions between Cr_2O_3 and FeO that cause different expansion between components in the refractory [15], and thermal cycling of the gasifier [16]. A refractory material with phosphate additions was developed, patented (US Patent # 6,815,386) by NETL, and is commercially produced by a refractory company. It is currently undergoing evaluation in plant trials at several gasification facilities. Preliminary results indicate this newly developed refractory material produces an incremental improvement in service life, but may not achieve that desired by industry.

This research focuses on non-chrome oxide refractory research efforts for slagging gasifier applications and outlines initial efforts to add low levels of Cr_2O_3 into the fine grain refractory microstructure of what would otherwise be a non-chrome oxide composition.

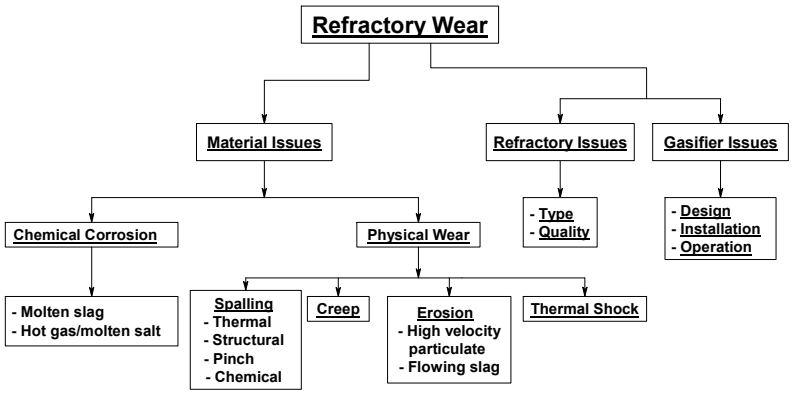

Figure 3 – Causes of refractory wear in air cooled slagging gasifier liner materials

NO/LOW CHROME OXIDE RESEARCH

The focus of no/low chrome oxide refractory research is on improving the resistance to chemical corrosion and spalling, identified as primary wear mechanisms in earlier research. The long range research goal is to develop no/low chrome oxide refractories for use in gasifiers with a service life of at least 3 years, or with a service life that matches the plant maintenance schedule for the gasification facility. All aspects of this research are being performed in close collaboration with commercial manufacturers and operators to ensure that refractories are developed that can be produced commercially and used in slagging gasifiers. Refractory material selection is based on thermodynamic considerations, phase diagram compatibility, laboratory research, and literature reviews.

In the past, non-chrome oxide refractory compositions did not show comparable performance to high chrome oxide refractory materials. Chrome oxide materials have low chemical solubility in gasifier slags and formed high melting spinels/solid solutions with iron oxides. It is important to remember that most coal slags are "acidic", being high in Al_2O_3 and SiO_2; and that petroleum coke slags contain other impurities, such as vanadium and nickel. Because only a few materials, including ZrO_2, have the potential to resist slag corrosion as well as chrome oxide, a refractory material must be designed with an engineered microstructure that helps to resist dissolution into the slag and slag penetration.

Compositions selected for testing were first evaluated in small scale lab cup tests (sample size less than 2.5 cm cube; test conditions of 1600^{o}C for 1 hour in an Ar atmosphere) using a coal gasifier slag. An example of small cup test samples is shown in figure 4. Those samples identified for further testing based on slag penetration and corrosion resistance were evaluated as both single and multiple component mixtures in large sample cups (5.1 mm cube) under similar conditions. Both coarse and fine grain raw materials were used to make large cup samples and were blended to achieve an engineered microstructure of controlled porosity. An indication of the effect of controlling both the sample composition and microstructure in large sample cups is shown in figure 5. Over 250 slag cup tests have been evaluated using a variety of different raw materials. Those with the greatest potential are listed in table 1.

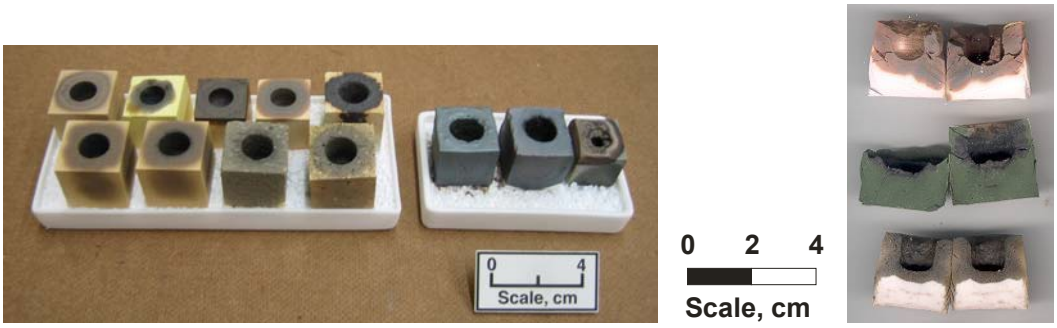

Figure 4 – Small 2.5 cm "cup" tests used to evaluate refractory/slag interactions at 1600°C in an Ar atmosphere. Once exposed, samples are cut in half to determine slag penetration.

Figure 5 - Large 5 cm "cup" tests samples used to evaluate refractory/slag interactions at 1600°C in an Ar atmosphere. Once exposed, samples are cut in half to show slag penetration. a) slag penetrated refractory microstructure with typical microstructure, and b) improved refractory microstructure.

Table 1 – General composition being evaluated in non-chrome refractory research
(note that minor additions of Cr_2O_3 are being made to specific compositions)

Refractory compositions
- NETL focused compositional areas
  - Major component - Al_2O_3
  - Secondary component - ZrO_2, MgO, Cr_2O_3
  - Minor additives - CaO, MgO, rare earths, TiO_2, SiO_2, Cr_2O_3
- Commercial submitted compositions
  - Major component - Al_2O_3, ZrO_2
  - Secondary additives - MgO, SiC
  - Minor additives - CaO, MgO, others (unknown)

Target Properties/considerations
- Porosity - 15 pct
- Mechanical strength (CCS) - 45 N/mm2 (or higher)
- Corrosion resistance - approaching high Cr_2O_3 (probably not equal)
- Slag penetration - equal or better to high Cr_2O_3
- Thermal shock resistance - expect better than high Cr_2O_3
- Cost - targeting lower than chrome oxide

Samples of commercially produced refractories have been submitted for gasification slag evaluation by several companies, with negotiations underway with one company for evaluating

specific zirconium oxide based materials. A general listing of refractory materials with potential for use as a substitute for high chrome oxide gasifier refractories that were developed at NETL or that are commercially produced are listed in table 1. Specific information on compositions is not given because of patent potential and because of the proprietary nature of the commercial compositions. Besides focusing on refractory compositions with minimal interaction with gasifier slag; research is also focused on grain sizing/particle packing, on the correct use of coarse and fine grained materials to limit slag penetration, and on the use of minor additives to impact slag penetration into the refractory matrix. Promising materials identified in cup testing are being targeted for rotary slag testing, which simulates the slagging gasifier environment better than the isothermal environment of a cup test. Rotary slag testing exposes samples to a thermal gradient, has a constant replenishment of slag preventing slag saturation, and has a constant slag flow over the surface of a sample that can release refractory grains into the slag.

CONCLUSIONS

NETL is researching no/low chrome oxide refractory materials for use in slagging gasifiers to increase their performance and reliability. These materials are being researched because high chrome oxide refractories currently used by industry do not meet its needs. Two wear mechanism identified in high chrome oxide materials will play a critical role in the wear of no/low chrome oxide materials; chemical corrosion and spalling. No/low chrome oxide research has focused on refractory compositions containing ZrO_2, Al_2O_3, MgO, and Cr_2O_3; although other minor additives are being considered, with encouraging results obtained in both NETL developed and commercially produced materials. Research has focused on 2.5 cm and 5 cm cube cup tests using commercial coal slag, with over 250 samples being evaluated. Slag penetration into the refractory structure appears to be a critical factor in controlling refractory wear. Larger scale testing using the rotary slag test is underway to evaluate encouraging compositions in a flowing slag environment.

REFERENCES

1. Mahgagaokar, U. and A.B. Krewinghaus, “Coal Conversion Processes (Gasification),” Ch. in Kirk-Othmer Encyclopedia of Chemical Technology, ed by J. I. Kroschwitz and M. Howe-Grant, John Wiley & Sons, V. 6, 1992, pp 541-568.
2. Dial, R.E., "Refractories for Coal Gasification and Liquefaction," Cer. Bul., Vo. 54, No. 7 (1975), pp 640-43.
3. Crowley, M.S., "Refractory Problems in Coal Gasification Reactors," Cer. Bul., Vol. 54, No. 12 (1975), pp 1072-74.
4. Kennedy, C.R., R. Swaroop, et al, "Evaluation of Ceramic Refractories for Slagging Gasifiers: Summary of Progress to Date," research sponsored by USDOE, ANL report 78-61, Sept., 1978, 56 pp.
5. Kennedy, C.R. and R.B. Poppel, "Corrosion Resistance of Refractories Exposed to Molten Acidic Coal-Ash Slags," Interceram, Vol. 27, No. 3 (1978), pp. 221-26.
6. Bakker, W.T., S. Greenberg, M. Trondt, and U. Gerhardus, “Refractory Practice in Slagging Gasifiers,” Amer. Ceram. Soc. Bulletin, Vol. 63, No. 7, 1984, pp 870-876.
7. Bonar, J.A., C.R. Kennedy, and R.B. Swaroop, “Coal-Ash Slag Attack and Corrosion of Refractories,” Amer. Ceram. Soc. Bulletin, Vol. 59, No. 4, (1980), pp 473-478.
8. Greenberg, S. and R.B. Poeppel, "The Corrosion of Ceramic Refractories Exposed to a

Synthetic Coal Slag by Means of the Rotating-Drum Technique," Research Report ANL/FE--85-9, research sponsored by USDOE/FE, 15pp.
9. Greenberg, S. and R.B. Poeppel, "The Corrosion of Ceramic Refractories Exposed to Synthetic Coal Slags by Means of the Rotation-Cylinder Technique: Final Report," research sponsored under USDOE/FE AA 15-10, April 1986, 66 pp.
10. Sorell, G., M.J. Humphries, E. Bullock, and M. Van de Voorde, "Material Technology Constraints and Needs in Fossil Fuel Conversion and Upgrading Processes," Int. Metals Reviews, Vol. 31, No. 5, 1986, pp 216-242.
11. Bakker, W.T., "Refractories for Present and Future Electric Power Plants," Key Eng. Mat, Vol. 88 (1993), pp 41-70.
12. Gasification Markets and Technologies – Present and Future – An Industry Perspective, US DOE/FE Report 0447, US DOE, (July, 2002), pp. 1-53.
13. G.Stiegel, and S. Clayton, ″DOE Gasification Industry R& D Survey: A Perspective of Long Term Market Trends and R&D needs″ in Proceedings from the Gasification Technologies 2001 Annual Meeting, San Francisco, CA.
14. C.P. Dogan, et al, Proceedings of Unified International Technical Conference on Refractories, Hosted by ALAFAR (2001), Vol. 1, pp 270-275.
15. Rigby, G.R., "The Mechanism of Bursting Expansion in Chrome-Magnesite Bricks," Trans. of the Brit. Ceram. Soc., Vol. 55 (1956), pp. 22-35.
16. Fahrion, M.E., "Materials Testing at Cool Water Coal Gasification Plant," Mat. At High Temp., Vol. 11, No. 1-4 (1993), pp. 107-12.

ACKNOWLEDGEMENTS

Support for this research was given by USDOE – FE/NETL (Advanced Research/Materials) and NETL/Albany (Advanced Metallurgical Processes).

PILOT FACILITY FOR THE PRODUCTION OF SILICON CARBIDE FIBRILS

Richard D. Nixdorf
ReMaxCo Technologies, Inc., 1010 Commerce Park Drive, Suite I,
Oak Ridge, Tennessee, 37830
E-mail: nixdorfr@indceramicsolns.com ; Telephone: (865) 423 7552; Fax: (865) 482-7505

ABSTRACT

Silicon Carbide Fibrils offer a super-strength material, resistant to high temperature oxidation and corrosion, for use in the combustion chamber materials, heat-exchanger tubes and hot gas filtration components of advanced coal-fired and coal gasification plants. Investigators have attempted to produce the Fibrils for 25 years for U.S. DOD and DOE applications. Progress was inhibited by low-efficiency use of expensive raw materials, high energy consumption and slow Fibrils growth rates. The current project discovered a unique microwave energy growth process that eliminated most of these issues to potentially lower the production cost of Fibrils from $2,000/ pound to less than $500/pound. The Generation #1 Reactor demonstrated that the microwave process was feasible. The Generation #2 Reactor verified a 4.4X improvement in Fibrils growth rates and a significant reduction in energy and raw material consumption. A Generation #3 reactor was designed and fabricated to produce sample volume quantities of Fibrils in June 2005. Unfortunately, this reactor was dropped from a loading dock by the shipper, causing significant damage. Nine months were consumed in reaching a settlement with the shipper to repair the damages. Repairs are in progress to be complete by August 2006. The paper presents Fibrils properties, potential advantages for high temperature coal fired plants, advances in the commercialization process, and the advantages offered by the Generation #3 Reactor. The pilot facility, pilot equipment experimental plan, and criteria for evaluating results to continue the project will be discussed.

INTRODUCTION

The higher combustion temperatures required for the Advanced Coal-Fired and Coal Gasification systems create a number of potential materials failures with existing combustion chamber and gas transfer components. Primary heat exchanger tubes exhibit corrosion and thermal stress failures. Combustion chamber wall tiles can be made of chrome oxide or aluminum oxide. The chrome oxide is a hazardous material presenting health problems in manufacturing and disposal. The potential safer replacement, aluminum oxide, suffers fatigue failure and sagging at the higher combustion temperatures. Hot gas filters required for the combustion gases made of sintered ceramics or ceramic fibers, suffer significant cracking and breaking. Silicon carbide is normally a good high temperature material in an oxidizing atmosphere. However, at temperatures over 1,000^{o}C, existing silicon carbide materials rapidly oxidize and convert to glass. The subject Silicon Carbide Fibrils, being perfect single crystals, do not begin to oxidize below 1,600^{o}C. The increased temperature stability, creep resistance and strength of the Fibrils offer relief to the technical issues that concern the industry, as defined above. The application of Fibrils in heat exchanger tubes, combustion wall tiles, and hot gas filters will be discussed under “Technical Challenges”.

Background Work - Work has been conducted on the VLS (vapor-liquid-solid) process to grow silicon carbide Fibrils for over 25 years. DARPA-sponsored work at Los Alamos National Laboratory was conducted throughout the 1980's with some industrial partners to improve ceramic composites. The work was transferred to Carborundum under the DOE Fossil Energy AR&TDM Program in the 1990's, for a possible scale-up to a commercial product. Both parties were passing methyltrichlorosilane gas over iron seed crystals in an 1,800^{o}C furnace. Most of the reaction gas and heat energy was wasted and the high temperature furnace components were coated with silicon carbide and destroyed. Carborundum dropped the project in 1998, when they were purchased by St. Gobain. Their last projected price for Fibrils was $2,000/pound. The current contractor, ReMaxCo Technologies, agreed to continue the Fibrils development work, using microwave energy to grow the Fibrils, thus, conserving reaction gas, energy and furnace components. The projected price of Fibrils based on the microwave process dropped to $300/pound.

Two previous Fibrils growth equipment designs have shown that the microwave process grows the Fibrils at three times the rate of the previous process with a minimal use of raw materials and energy. The process has been demonstrated to work. The 3rd generation reactor is an improved design of the previous two and was built to test the efficiency of the process. Raw material consumption and energy use will be measured as a function of volume of Fibrils produced to determine the actual projected unit cost of volume production. Key decision points will be based on the unit cost factors. Can the equipment or processing parameters be improved to lower cost? Is the process scalable to ton quantities per year at reasonable capital equipment costs? If these changes offer a high probability of success, funds will be spent on improving the 3rd generation reactor or building a 4th generation reactor. If scaling to volume production is cost prohibitive or if the volume unit cost is shown to be above $500/pound, the project will be terminated at the conclusion of the testing of the current reactor performance.

TECHNOLOGY APPROACH

The 3rd generation reactor microwave system was designed and built by RF Technologies and Ferrite Corporation, a major industrial microwave systems company that supplies large industrial processing systems to the food, laminated wood processing, military radar, and digital TV antenna markets. Ferrite will build any future volume production equipment for ReMaxCo. A major component of the Fibrils growth process is the chemical vapor reaction gas feed and distribution. This work has been contracted to MS&E Resources and Starfire Industries, both recognized experts in CVD (chemical vapor deposition) processes and unique CVD reaction gas products. Evaluation of the Fibril product will be conducted by the "High Temperature Materials Laboratory" at Oak Ridge National Laboratory. ReMaxCo has access to ceramic composite and fiber components testing and manufacturing through Honeywell Aerospace, General Electric Global Research and Industrial Ceramic Solutions.

Outstanding Research Questions:

1 Will the design improvements to the Generation 3 Reactor translate to performance improvements?

2 Will the Fibrils product demonstrate a consistent 5 to 10 micron diameter?
3 Will the production cost vs Fibrils volume yield a unit product cost of less than $500/pound?
4 Is the process scalable to tons per year?

Industry Benefits from the Fibrils Product – In the area of primary heat exchanger tubes, the Fibrils can be formed into a non-woven paper. This paper can be rolled into tubes and bent into any shape desired for heat exchanger tubes. The non-woven paper tubes can then be infiltrated with chemical vapor silicon carbide to form a solid, liquid-impermeable, pipe for the primary heat-exchanger liquid medium. Fibrils reinforced aluminum oxide combustion chamber tiles will increase the fatigue strength of standard aluminum oxide by a factor of three. This will allow aluminum oxide to replace the hazardous chrome oxide tiles. ReMaxCo is skilled in the art of hot gas filters, due to its work in ceramic fiber diesel exhaust filters. This technology can be applied to a Fibrils filter media to yield filters that are tough enough to withstand high pressures at temperatures up to 1,600^{o}C. Other application areas may be discovered as ReMaxCo begins to work with fabricators of coal-fired processing equipment.

Cost is always the major concern. Fibrils must exhibit performance characteristics that support high product costs. This will require fabrication of optimized components – heat exchange tubes, combustion wall tiles, or hot gas filters, for durability testing in the customer's pilot plants. Reliable component suppliers with experience in servicing the energy industry must be licensed to use the Fibrils in manufacturing volume, high quality parts for the fossil fuel industry.

The major objection of the power plant fabricators to the Fibrils work is the ability to form ceramics into complicated shapes and create reliable joints. ReMaxCo has concentrated efforts over the last year to solve that issue. Near–net completed shapes are formed with pliable "green" paper forms, then, rigidified upon establishing the final tube configuration.

2006/2007 PLANS TO COMMERCIALIZE FIBRILS

A detailed project plan is in place to verify the performance of the Generation 3 Fibrils Reactor. A decision point is scheduled for the end of 2006 to determine whether to continue the project or terminate it. This effort is certainly cost-effective for DOE since ReMaxCo is funded at a level that is approximately 30% of the project costs through the end of 2006.

ReMaxCo has signed a joint development agreement with XYLON Ceramics, Inc of Alfred, NY to install the Generation 3 Reactor in their facility and conduct the required statement-of-work experiments. XYLON manufactures ceramic joint implants for orthopedic surgery and fuel cell components. XYLON has an interest in using the Fibrils to produce smaller unbreakable ceramic joint implants. Alfred University is a recognized ceramic materials school. Much benefit will come to the program through exposure and materials development by Alfred scientists. Fibrils samples will be shared with the materials research groups at General Electric Global Research and Honeywell Aerospace to generate composite materials properties.

The silicon carbide Fibrils are a new material system that has outstanding properties. These properties have never been considered by industrial users because no previous effort has

produced a cost-effective product. If ReMaxCo is able to bring this Fibrils product to a volume production level at a reasonable price, many of the problems in future fossil energy technologies can be resolved and the efficiencies possible through higher temperature combustion can become a reality.

FUTURE PLANS

Completion of the first phase of 2006/2007 Fibril production experiments will yield enough Fibrils to make test components. At this point ReMaxCo will form joint development agreements with an electric utility, a coal-gasification plant developer, a ceramic components manufacture and a ceramic filter manufacture. These JDA will conclude with commercialization of the Fibrils in various components

ACTIVATED CARBON COMPOSITES FOR AIR SEPARATION

Frederick S. Baker
Oak Ridge National Laboratory, Bethel Valley Road, P. O. Box 2008, Oak Ridge, TN 37831-6087
E-mail: bakerfs@ornl.gov; Telephone: (865) 241-1127; Fax: (865) 576-8424

Cristian I. Contescu
Oak Ridge National Laboratory, Bethel Valley Road, P. O. Box 2008, Oak Ridge, TN 37831-6087
E-mail: contescuci@ornl.gov; Telephone: (865) 241-3318; Fax: (865) 576-8424

Costas Tsouris
Oak Ridge National Laboratory, Bethel Valley Road, P. O. Box 2008, Oak Ridge, TN 37831-6087
E-mail: tsourisc@ornl.gov; Telephone: (865) 241-3246; Fax: (865) 241-4289

Timothy D. Burchell
Oak Ridge National Laboratory, Bethel Valley Road, P. O. Box 2008, Oak Ridge, TN 37831-6087
E-mail: burchelltd@ornl.gov; Telephone: (865) 576-8595; Fax: (865) 576-8424

ABSTRACT

With increased emphasis being placed on the development of fuel cells, coal-derived synthesis gas is a potential major source of hydrogen. Oxygen-blown coal gasification is the most effective and efficient approach to achieving the foal of producing hydrogen from coal, but a cost-effective means of enriching O_2 concentration in air is required. A key objective of this project is to assess the utility of a system that exploits a porous carbon material and electrical swing adsorption (ESA) to produce an O_2-enriched air stream suitable for coal gasification. Technical performance indicators include development of an adsorbent with pronounced molecular sieving properties to obtain effective separation of O_2 and N_2 from air via a fast-cycling process, and with the desired characteristics to exploit the ESA techniques to obtain a seamless production of an O_2-enriched air stream.

To better tailor the porosity of the carbon composite material to enhance molecular sieving properties, emphasis was placed on deriving a fundamental understanding of how precursor properties and activation conditions can be manipulated to obtain the desired pore size characteristics in the composite material. As a complement to O_2 and N_2 adsorption measurements, CO_2 was introduced as a more sensitive probe molecule for the characterization of molecular sieving effects. To further enhance the potential of activated carbon composite materials for air separation, work was implemented on incorporating a novel twist into the system; namely the addition of a magnetic field. On theoretical grounds, it has been postulated that magnetic fields should influence gas adsorption which is accompanied by a transition between the paramagnetic and diamagnetic states of the adsorbate, as possible for the O_2 molecule. Indeed, Judkins and Burchell have been granted a United States patent on the separation of gases via magnetically-enhanced adsorption. The preliminary findings in this respect are discussed. Future directions for the project include in-house production of carbon fibers for more suitable precursor materials, evaluation of composite adsorbents comprising carbon and zeolite, and production of lower pressure drop honeycomb monoliths.

INTRODUCTION

A novel adsorbent material, carbon fiber composite molecular sieve (CFCMS), has been developed by the Oak Ridge National Laboratory (ORNL).[1-3] Upon thermal activation, usually in CO_2 or steam, the carbon fiber-based material develops a large micropore volume (0.5-1.0 cm^3/g) and high BET surface area (1000-2200 m^2/g). As shown in the scanning electron microscopy (SEM) image in Figure 1, the structure of CFCMS comprises carbon fibers (about 10 μm in diameter) bonded at their contact points to

provide a continuous carbon skeleton that is electrically conductive. The structure is open and permeable, which allows fluids to readily flow through the material with minimal pressure drop. The unique combination of the open structure, microporosity, and electrical conductivity allows the material to be used in a regenerative, electrical swing adsorption (ESA) system. [4-6]

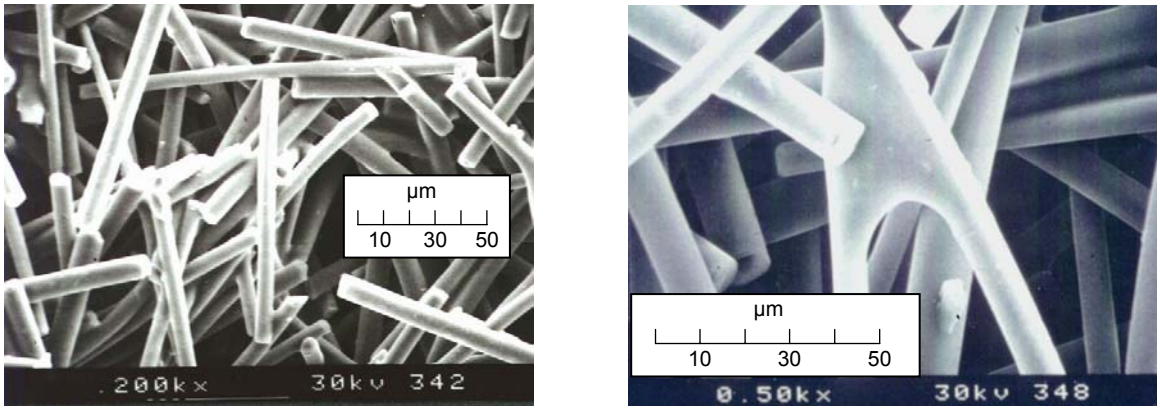

Figure 1 - SEM images showing the structure of CFCMS material

In essence, ESA is an electrical analog of pressure swing adsorption (PSA), whereby desorption of the adsorbate is facilitated by the passage of an electric current through the adsorbent to obtain resistive heating. [5,6] In this context, CFCMS represents an enabling technology for an ESA process in which efficient desorption could be achieved in the absence of pressure swings. The bottom line is that significant energy savings could be realized because the adsorption beds do not, in principle, require repressurization after each desorption step.

Preliminary work demonstrated that CFCMS material has the potential for separating O_2 and N_2 in air. [7] However, the findings also indicated that a more efficient separation could be obtained if the micropore size distribution of the activated carbon fiber component could be better tailored for this purpose. Therefore, to provide the foundation for developing a suitable CFCMS material, a series of isotropic pitch-based activated carbon fiber monoliths was prepared in which the degree of activation of the fiber was varied in the range of 5-30% (carbon burn-off). The pore size distributions of these products were characterized, and correlated with the kinetics of adsorption of O_2 and N_2, respectively, on the activated carbon fibers. The results revealed that O_2 was more rapidly adsorbed on the carbon fiber than N_2, and with higher equilibrium uptakes, provided the fiber contained a high proportion of very narrow micropores. Thus, it was concluded that CFCMS activated under certain conditions is able to separate O_2 and N_2 from air based on kinetic effects, i.e. the difference in diffusion rates of the two molecules in the narrow micropore network of the activated carbon fibers.

To further enhance the potential of CFCMS material for $O_2 - N_2$ separation, a magnetic field was added to the adsorption system. Based on theoretical grounds, magnetic fields should affect phase change equilibria (such as adsorption and desorption) if the phase changes are accompanied by a significant variation of magnetic properties. The literature on magnetic fields effects on adsorption and desorption (MAD) is scarce. For several microporous materials a correlation was reported between MAD effects and certain properties of the adsorbate-adsorbent system, such as molecular magnetic properties, nature and concentration of adsorption sites, and porosity of solids. For example, nitrous oxide (NO) is paramagnetic in the gas phase, but $(NO)_2$ dimmers condensed on solids are diamagnetic, and because of that the capillary condensation on microporous solids is greatly enhanced by magnetic fields. [8] Gaseous oxygen is paramagnetic, but oxygen dimers $(O_2)_2$ adsorbed in micropores of zeolites at temperatures lower than 100 K are diamagnetic. [9] Generally speaking, magnetic energies are insignificant in comparison with

thermal energy. Therefore, while one would expect MAD effects in ferromagnetic systems (such as H_2 on $LaCo_5H_x$ hydrides [10]), it is less likely that such effects would be detected in paramagnetic systems, much less for a diamagnetic system such as water. [11] However, magnetic fields effects on adsorption have been demonstrated even for water [12] and some organic molecules. [13] This may be an indication that the magnetic properties of such molecules change upon interaction with the adsorbent, but it also highlights the fact that more experimental studies on magnetic field effects on gas adsorption are needed in order to shed light on this poorly understood phenomenon. [11]

In microporous materials such as activated carbon, MAD effects depend strongly on the nature of solids and gases, temperature, and the intensity of magnetic fields. An appropriate combination of these factors could lead to a separation process based on selective adsorption from a mixture of gases. In this context it has been reported that separation of O_2 and N_2 in high magnetic fields is in principle plausible in a steady magnetic field through adsorption of paramagnetic O_2 molecules into micropores of porous ferromagnetic solids. [11] A series of tests have been carried out in order to check this assumption.

DISCUSSION OF CURRENT ACTIVITIES

AIR SEPARATION BY MOLECULAR SIEVING EFFECTS

Materials Preparation and Characterization

On a Hiden Analytical gravimetric analyzer (IGA-1), 140 mg samples of isotropic pitch-based carbon fibers (Anshan East Asia Carbon Co.) were activated to the desired level of carbon burn-off, as measured by weight loss, at a temperature of 835°C in an atmosphere of pure CO_2 (at ambient pressure). The surface area and pore size distribution of representative samples of activated carbon fibers were characterized by N_2 adsorption at 77 K and CO_2 adsorption at 273 K using a Quantachrome Autosorb-1 instrument. The apparent surface areas were derived from the N_2 and CO_2 adsorption isotherms using the BET method. [14,15] Pore size distributions were calculated using the density functional (DFT) approach,[16,17] and micropore volumes were estimated using Dubinin-Astakhov (DA) equation,[15] applied to adsorption data. The results are shown in Table 1.

Table I - Surface area and micropore volume data for activated carbon fiber products

Burn-off level (%)	5	10	15	20	30
N_2 BET area (m^2/g)	15	415	(790)	730	960
CO_2 BET area (m^2/g)	550	635	795	955	1170
Micropore volume (< 2 nm, DFT)	0.00	0.16	(0.32)	0.29	0.38
Micropore volume (< 2 nm, DA)	0.00	0.19	(0.33)	0.34	0.44

Except for the values shown in parentheses, the N_2 and CO_2 adsorption data show the expected trend in the development of surface area and micropore volume with the progress of activation (as measured by the burn-off level). However, at the lowest burn-off level of 5 % a very pronounced molecular sieving effect between N_2 and CO_2 was observed. The micropores of the sample with 5 % burn-off were so narrow, that the N_2 molecules could not penetrate the ultra fine structure, resulting in an apparently very low BET surface area (15 m^2/g) and no measurable pore volume. In contrast, the flat CO_2 molecules were able to enter the fine pores at 273 K, revealing a significant surface area (550 m^2/g) and details of the smallest micropores. [18]

Dynamic O_2 and N_2 Adsorption Studies

The rates O_2 and N_2 adsorption, respectively, on the activated carbon fibers were measured at 294 K. Each gas was dosed to the sample at two linear rates of pressure increase of 0.015 and 0.025 MPa/minute, respectively, over the pressure range of 0.001-0.1 MPa. The rates of O_2 and N_2 adsorption are summarized in Figure 2. More experimental details and an analysis of results were presented elsewhere.[19]

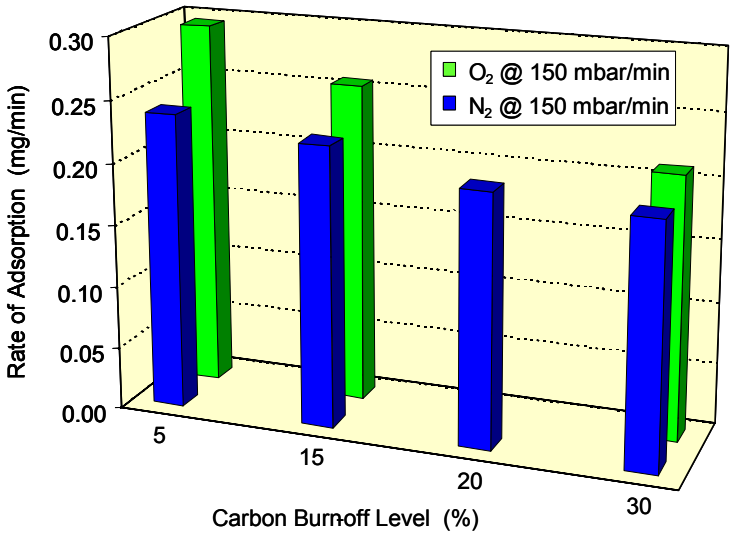

Figure 2 - Rates of O_2 and N_2 adsorption at 294 K as a function of carbon burn-off level

The rate of O_2 adsorption was markedly higher than that of N_2, notably on the carbon fibers of the lowest burn-off of 5 % which exhibited a 25 % higher rate of O_2 adsorption (on a mass basis). The rate of adsorption of both O_2 and N_2 fell with progressive increase in the degree of activation of the carbon fibers. The amount of N_2 adsorbed at equilibrium at 0.1 MPa increased at the highest burn-off level of 30 %, indicative of the larger pore volume in this material. A sharp discontinuity was observed in the rate of N_2 adsorption, at a pressure of about 0.045 MPa, and only on the 5 and 15 % burn-off carbon fiber products, This effect, which could be associated with a very pronounced molecular sieving effect of these materials, is significant for the separation of O_2 and N_2 relying on differences in the diffusion rates of these molecules in narrow pore networks. The closer the pore width is to the molecular dimensions of the gasses the more significant the kinetic effects will be. Lower carbon burn-off level appears to be advantageous in this respect; higher levels (> 15%) increased micropore width to the point where molecular sieving effects were eliminated, which is counter-productive for air separation.

In addition to activation parameters, the adsorptive characteristics of activated carbon fibers are dependent on the nature of the precursor. In this context, lignin is a precursor known to produce highly microporous activated carbon products. In a very preliminary work, an activated carbon fiber was produced from a kraft hardwood, melt-spun lignin fiber. Characterization of adsorption properties indicated that its microporous structure is more developed compared to the pitch-based fibers at comparable burn-off.

INFLUENCE OF MAGNETIC FIELDS ON OXYGEN ADSORPTION

Materials Preparation and Characterization

For the study of magnetic fields effects on O_2 adsorption commercially available activated carbon fibers made from an isotropic pitch precursor (AP-400 fibers furnished by Anshan East-Asia Carbon Co.) were used. In order to mimic a ferromagnetic microporous adsorbent, the fibers were modified by depositing nanosized magnetite (Fe_3O_4) onto activated carbon fibers, using a cold precipitation method.[20] In contrast with the ceramic method for synthesis of magnetite, which involves high temperature processes and results in a highly sintered product, the cold synthesis method (< 120ºC) preserves the nanosized colloidal particles of magnetite. Several runs were made to obtain different loadings of magnetite in the activated carbon fibers. The presence of the magnetite phase in the activated carbon fibers was confirmed through X-ray diffraction (XRD) measurements (Figure 3). For the highest loading of 10 wt % Fe_3O_4, the BET surface area of the activated carbon fibers was reduced from 1530 to 1170 m^2/g, and the average pore size increased from 1.4 nm to 1.7 nm due to obliteration of the smallest pores. The magnetite particles were well dispersed on the activated carbon fibers, with an average particle size of 16 nm, calculated from broadening of XRD lines.

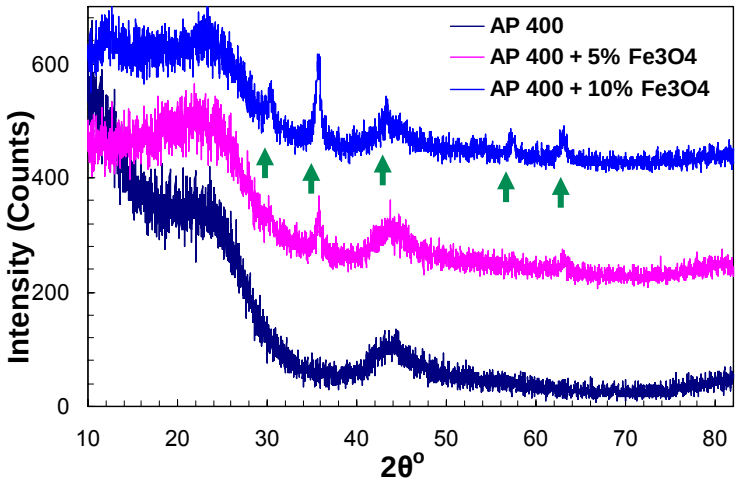

Figure 3: X-ray diffraction patterns of pure AP-400 fibers and fibers with magnetite loading

Magnetic susceptibility at room temperature of carbon fiber materials with and without magnetite loading was measured using a MSB auto magnetic susceptibility balance (Sherwood Scientific, U.K.). Although pure carbon is diamagnetic ($\chi = -2 \times 10^{-5}$ for diamond, $\chi = -2 \times 10^{-5}$ for graphite), the activated carbon fibers AP-400 were slightly paramagnetic ($\chi = +1.8 \times 10^{-6}$). The paramagnetism of activated carbons is caused by the existence of impaired electrons and dangling bonds at carbon atoms exposed at the extended surface of these materials. [21] On the other hand, in contrast with the notorious ferromagnetic character of magnetite, susceptibility measurements for magnetite loaded carbon fibers indicated a paramagnetic character ($\chi = +1.2 \times 10^{-4}$ for 5 wt % Fe_3O_4 and $\chi = +3.6 \times 10^{-4}$ for 10 wt % Fe_3O_4). The phenomenon by which magnetic materials exhibit a behavior similar to paramagnetism even at temperatures below the Neel or the Curie temperatures is known as superparamagnetism. It is observed in very fine particles, each behaving as an individual magnetic domain, for which the energy required to align the direction of magnetic moments is comparable to thermal energy. [22] The superparamagnetism of Fe_3O_4 supported on AP-400 carbon fibers, corroborated with the information from XRD analysis, indicates that each Fe_3O_4 nanoparticle (average size of 16 nm) is an individual magnetic domain.

Oxygen adsorption measurements on the activated carbon fibers, with and without magnetite, were made at room temperature over the pressure range of 5-800 Torr (0.66-105 KPa), using a volumetric adsorption instrument (Autosorb-1, Quantachrome Instruments). The sample (~ 200 mg) was outgassed in high vacuum at 300ºC overnight immediately before the adsorption measurements. For the adsorption

measurements in the presence of a magnetic field, a pair of rare earth permanent magnets (NdFeB 36, Edmunds Industrial Optics) was placed around the glass tube containing the sample and in the immediate vicinity of the sample. The separation between the magnets was in the range of 1.0-1.2 cm. The intensity of the magnetic field was enhanced by adding a second pair of permanent magnets. The magnetic field intensities measured in the immediate vicinity of the sample were 0.45 and 0.82 Tesla (T) for one and two pairs, respectively, of magnets. The setup is extremely accurate for gas volumetric measurements, as shown by the perfect overlap of data point in a series of repeated baseline tests with pure carbon materials in absence of magnetic fields.

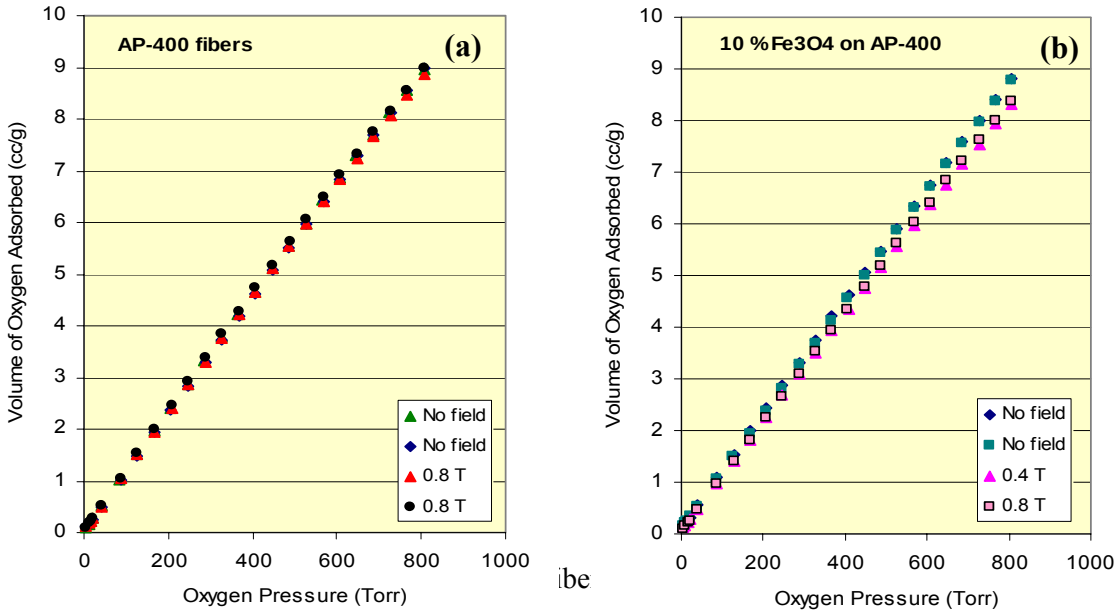

Figure 4 - O_2 adsorption on activated carbon fibers in presence of a magnetic field (at room temperature)

The results revealed that magnetic fields of intensity of up to 0.8 Tesla (T) had almost no effect on O_2 adsorption on pure carbon fibers (Fig. 4 a). However, when magnetite was incorporated into the carbon fiber to amplify the magnetic field, the amount of O_2 adsorbed in presence of magnetic fields (up to 0.8 T) were slightly lower than the amounts measured at equal pressures but without applied magnetic field. With 10 wt % magnetite, the amount of O_2 adsorbed at near atmospheric pressure (800 Torr) decreased from 8.8 to 8.3 cc/g (STP basis) when the magnetic field was applied; i.e. a decrease of about 6%. This was an unexpected result, whereby a magnetodesorption, not magnetoadsorption effect was observed. Nevertheless, the existence of a magentodesorption effect at room temperature for O_2 on magnetite supported on activated carbon has not been previously reported in the literature.

A brief explanation of this effect is provided below on the thermodynamic grounds developed by Ozeki and Sato.[11] When the equilibrium pressure of a gas-solid adsorption system changes by Δp on application of a magnetic field H at constant temperature T, the total variation of the free energy of the system, ΔG, has a pressure component, $\Delta G_p = RT\,[\ln(p+\Delta p) - \ln p]$, and a magnetization component, $\Delta G_m = \Delta MH$, where ΔM is the magnetization change of the system per mol of gas adsorbed. The equilibrium condition is $\Delta G = \Delta G_p + \Delta G_m = 0$, which gives $\Delta p/p = -\Delta MH/RT$ (assuming $p >> \Delta p$). This relationship demonstrates that, whenever the magnetization of the adsorption system changes during adsorption, the equilibrium pressure in the system should change; for example, a negative ΔM can cause an increase in equilibrium pressure, i.e. magnetoadesorption (as observed with O_2 on Fe_3O_4 supported on activated carbon).[11]

In the system investigated here, oxygen is adsorbed on carbon at room temperature, in absence of external magnetic fields (Fig. 4, a). The state of O_2 molecules confined in the narrow micropores of activated carbon is not entirely clear. Depending on oxygen pressure, pore size, and temperature, O_2 molecules may form random clusters containing spin-interacting molecules, with the result that the paramagnetism of isolated O_2 molecules is replaced by the random magnetism of these clusters. [23] On zeolites, oxygen forms diamagnetic clusters. [9] On activated carbon fibers, chemisorbed oxygen is stabilized in a non-magnetic state through spin interactions with dangling bonds of graphene layers. [24] Because adsorption and clustering of O_2 molecules confined in narrow micropores leads always to a *decrease* in magnetization of the system (compared to the state of a non-adsorbing system), i.e. $\Delta M < 0$, a magnetodesorption effect should be measured ($\Delta p > 0$), as predicted above on thermodynamic grounds. The effect is however too weak to be observed (at room temperature and with the magnetic fields available in this study) on a weakly paramagnetic adsorbent, such as the virgin AP-400 fiber (Fig. 4, a). However, if the adsorbent has a paramagnetic susceptibility larger by two orders of magnitude (as is the case with 10 wt % Fe_3O_4 on AP-400 fiber), the influence of external magnetic fields in carbon micropores is amplified, and the magnetodesorption effect becomes measurable even at room temperature and in relatively weak magnetic fields (fig. 4, b).

The observation of magnetodesorption of O_2 from a microporous carbon fiber loaded with a superparamagnetic Fe_3O_4 phase, made in this study, confirms predictions in the literature according to which magnetic separation of O_2 and N_2 in steady magnetic fields is plausible. [11] To exploit the magnetodesorption effect and to achieve air separation it might be useful to optimize the system for adsorption at equilibrium of N_2 (not O_2) by the activated carbon fibers in a steady magnetic field. It might be also useful to modify the adsorbent by incorporation of zeolites (where oxygen is adsorbed in a diamagnetic state[9]), to use much higher intensity magnetic fields, and possibly to design a "magnetic swing adsorption" system with the adsorbent in a column configuration.

CONCLUSIONS

The findings reported here confirm that CFCMS materials have the potential for separating O_2 and N_2 from air on the basis of the different diffusion rates of the two molecules in the composite. O_2 was more rapidly adsorbed on the activated carbon fiber than N_2, and with higher uptake under equilibrium conditions, providing the fiber contained a high proportion of very narrow micropores. This depends on identifying and demonstrating alternative techniques of activation, and using new carbon precursors (such as lignine) that are known to produce extensive networks of uniformly narrow micropores. The oxygen adsorption measurement made in the presence of a magnetic field demonstrated an effect of the field when the adsorbent was magnetite supported on activated carbon fibers. These data require more sophisticated measurements, using much higher intensity magnetic fields, to verify the preliminary results and determine whether magnetic fields can be exploited for separation of O_2 and N_2 from air.

ACKNOWLEDGEMENTS

Research sponsored by Office of Fossil Energy, U.S. Department of Energy, National Energy Technology Laboratory, under the Fossil Energy Advanced Research Materials Program, contract number DE-AC05-00OR22725 with UT-Battelle, LLC.

REFERENCES

1. Burchell, T. D., Judkins, R. R., Rogers, M. R., and Williams, A. M., A Novel Process for the Separation of Carbon Dioxide and Hydrogen Sulfide for Gas Mixtures, *CARBON*, **35** (1997) 1279-1294.
2. Burchell, T. D., Weaver, C. E., Chilcoat, B. R., Derbyshire, F., and Jagtoyen, M., Activated Carbon Fiber Composite Material and Method of Making, U.S. Patent 6,030,698 (February 29, 2000) Assigned to Lockheed Martin Energy Research Corporation.
3. Burchell, T. D., Weaver, C. E., Chilcoat, B. R., Derbyshire, F., and Jagtoyen, M., Activated Carbon Fiber Composite Material and Method of Making, U.S. Patent 6,258,300 (July 10, 2001) Assigned to UT-Battelle, LLC.
4. Burchell, T. D., and Judkins, R. R., A Novel Carbon Fiber Based Material and Separation Technology, *Energy Conservation and Managemen*t, **38** Supplement, S99-S10 (1997).
5. Wilson, K. A., Burchell, T. D., and Judkins, R. R., Carbon Fiber Composite Molecular Sieve Electrically Regenerable Air Filter Media, U. S. Patent 5,827,355, (October 27, 1998), Assigned to Lockheed Martin Energy Research Corporation.
6. Judkins, R. R., and Burchell, T. D., Gas Separation Device Based on Electrical Swing Adsorption, U. S. Patent 5,972,077 (October 26, 1999) Assigned to Lockheed Martin Energy Research Corporation.
7. Burchell, T. D., Omatete, O., Gallego, N. C., and Baker, F. S., Novel Activated Carbon Composites for Air Separation, *Proceedings of the 18th Annual Conference on Fossil Energy Materials*, Knoxville, TN, June 2-4, 2004.
8. Kaneko, K., Fukuzaki, N., and Ozeki, S., The Concentrated NO Dimer in Micropores Above Room Temperature, *J. Chem. Phys*., **87** (1987) 776-777.
9. Takaishi, Y., Dimers of Oxygen Molecules in the Pores of Ca_6A Zeolite, *J. Chem. Soc. Faraday Trans*., **93** (1997) 1257-1260.
10. Yamamoto, I., Yamaguchi, M., Goto, T., and Miura, S., Chemical Equilibrium of the Ferromagnetic LaCo-H_5 System in Strong Magnetic Fields, *J. Alloys Compounds*, **231** (1995) 205-207.
11. Ozeki, S., and Sato, H., Magnetic Interactions in Adsorption at Solid Surfaces, in *Encyclopedia of Surface and Colloid Science*, Marcel Dekker, New York, pp. 3120-3131 (2002).
12. Ozeki, S., Wakai, C., and Ono, S., Is Magnetic Effect on Water Possible?, *J. Phys. Chem*., **95** (1991) 10557-10559.
13. Miyamoto, J., Matsubara, Y., Kurashima, H, Tazaki, T., and Ozeki, S., Magnetic Field Effects on Physical Adsorption Equilibrium Between Solids and Gases of Organic Molecules and Oxygen, *Nippon Kinzoku Gakkaishi*, **61** (1997) 1300-1305.
14. Brunauer, S., Emmett, P. H., and Teller, E., Adsorption of Gases in Multimolecular Layers, *J. Am. Chem. Soc*., **60** (1938) 309-319.
15. Gregg, S. J., and Sing, K. S. W., "*Adsorption, Surface Area and Porosity*", 2nd Edition, Academic Press, London (1982).
16. Lastoskie, C., Gubbins, K. E., and Quirke, N., Pore Size Distribution Analysis of Microporous Carbons: A Density Functional Theory Approach, *J. Phys. Chem*., **97** (1993) 4786-479.
17. Jagiello, J., and Thommes, M., Comparison of DFT Characterization Methods Based on N_2, Ar, CO_2, and H_2 Adsorption Applied to Carbons with Various Pore Size Distributions, *CARBON*, **42** (2004) 1227-1232.
18. Rodriquez-Reinoso, F. and Linares-Solano, A., Microporous Structure of Activated Carbons as Revealed by Adsorption Methods, in "*Chemistry and Physics of Carbon"*, Edited by P. A. Thrower, Volume 21, pp. 1-146, Marcel Dekker, New York (1988).
19. Baker, F. S., Contescu, C. I., Tsouris, C., Gallego, N. C., and Burchell, T. D., Carbon Fiber Composite Molecular Sieve for Air Separation, *Extended Abstracts, Carbon 2006 International Conference,* Aberdeen, Scotland, July 16-21, 2006.
20. Spacu, P., Brezeanu, M., Patron. L., Contescu, A., and Crisan, D., Coordination Compounds as Raw Materials for Mixed Oxides, *Thermochimica Acta*, **178** (1991) 231-239.

21. Ishii, C., Shindo, N., and Kaneko, K., Random Magnetism of Superhigh Surface Area Carbon Having Minute Graphitic Structures, *Chem. Phys. Letters,* **242** (1995) 196-201.
22. Selwood, P. W., "*Chemisorption and Magnetization*," Academic Press, New York (1975).
23. Kaneko, K., Nanodimensional Magnetic Assembly of Confined O_2, in *"Surfaces of Nanoparticles and Porous Materials"*, Eds. J. A. Schwarz and C. I. Contescu, *Surfactant Science Series* vol 78, M. Dekker, New York, (1999).
24. Kobayashi, N., Enoki, T., Ishii, C., Kaneko, K., and Endo, M., Gas Adsorption Effects on Structural and Electrical Properties of Activated Carbon Fibers, *J. Chem. Phys*., **109** (1998) 1983-1990.

Gas Sensors for Fossil Energy Applications

Timothy R. Armstrong
Oak Ridge National Laboratory
1 Bethel Valley Road, P. O. Box 2008, Oak Ridge, Tennessee 37831-6186
Phone: (865) 574-7996, E-mail: armstrongt@ornl.gov

David L. West,
Oak Ridge National Laboratory
1 Bethel Valley Road, P. O. Box 2008, Oak Ridge, Tennessee 37831-6063
Phone: (865) 576-2264, E-mail westdl@ornl.gov

Fred C. Montgomery
Oak Ridge National Laboratory
1 Bethel Valley Road, P. O. Box 2008, Oak Ridge, Tennessee 37831-6063
Phone: (865) 576-8808, E-mail: montgomeryfc@ornl.gov

ABSTRACT

The main pollutants (neglecting carbon dioxide (CO_2)) from combustion of low-sulfur fossil fuel are carbon monoxide (CO), hydrocarbons (HC), and oxides of nitrogen ("NO_x", a mixture of NO and NO_2), oxides of sulfur ("SO_x", a mixture of SO_2 and SO_3) and mercury. Measurement of sulfur dioxide is a serious global problem in relation to environment pollution, occupational and public health, and industrial emissions control. SO_2 is a major atmospheric pollutant resulting from the combustion of fossil fuels. It produces acidity in rainwater and is a major source of corrosion in buildings. The major health concerns associated with exposure to high concentrations of SO_2 are respiratory illness, alteration of the lungs defenses, and aggravation of existing cardiovascular disease. One of the first steps towards solving these environmental and health problems is measuring the concentration of these gases in many locations. Thus, there is an increasing interest in the development of simple, inexpensive and reliable methods for the analysis and monitoring of SO_2 for control of advanced combustion and gasification system.

To date, none of the approaches described in the literature have resulted in a viable SO_2, SO_3, or "total" SO_x (i.e., total refers to the ability of the sensor to measure the total SO_x (SO_2 + SO_3) in a gas stream). An interesting point in the literature is the lack of reference to the development of a pure electrochemical sensor that takes advantage of the inherent redox conditions and thermal equilibrium in SO_2, SO_3, and O_2 containing exhaust gas. This equilibrium is nearly identical to that of the NO-NO_2 system where advances in electrochemical sensors are showing the ability to measure NO, NO_2 and "total" NO_x (NO + NO_2).

Recent advances in NOx sensor development at The Oak Ridge National Laboratory (ORNL)have demonstrated that a simple, single material, mixed-potential sensor using a current bias can measure "total" NO_x and NO. The ORNL work takes advantage of the natural redox conditions between NO, NO_2 and O_2, and the thermal equilibrium at temperature. In a mixed potential sensor, the difference in catalytic response between two different electrode materials provides a "differential electrode equilibria" (mixed potential sensor) that could be used to selectively measure SO_X. The advantages of mixed potential sensors include: simple design, simple electronics, large signal, and the elimination of an air reference. The development of mixed-potential sensors offers tremendous potential to reduce the overall

cost of the sensor through simplified design and low-cost electronics. ***The ORNL NOx sensor is considered state-of-the-art and one of only two in development in the world today. The operating principles from this sensor will be used as the basis for the SOx sensor to be developed.***

The objective of this project is to develop a low-cost electrochemical sensor based on mixed potential phenomena that will detect SO_2, SO_3 and/or total SO_x at temperatures from 500-600°C. The goals of this program are to develop a sensor with the following properties:

Operate at temperatures up to 1000°C
Time to temperature < 10 seconds
Measure SO_x in the range 1 ppmV $\leq [SO_x] \leq$ 500 ppm
Exhibit minimal or no cross sensitivity to H_2O, O_2, hydrocarbons, NO_x, and ammonia
Response time ≈1 second

The research will follow a logical progression from: the catalytic evaluation of mixed conducting oxide powders; the evaluation of the kinetics at the surfaces of these materials under the influence of applied electric potentials; the development of sensors based on the materials; and finally, testing of the sensors developed. Recent results of this redirected project will be presented.

INTRODUCTION

Measurement of sulfur dioxide is a serious global problem in relation to environment pollution, occupational and public heath, and industrial emissions control. SO_2 is a major atmospheric pollutant resulting from the combustion of fossil fuels. It produces acidity in rainwater and is a major source of corrosion in buildings. The major health concerns associated with exposure to high concentrations of SO_2 are respiratory illness, alteration of the lungs defenses, and aggravation of existing cardiovascular disease. One of the first steps towards solving these environmental and health problems is measuring the concentration of these gases in many locations. Thus, there is an increasing interest in the development of simple, inexpensive and reliable methods for the analysis and monitoring of SO_2 Conventional methods employed for the determination of SO_2 have limitations due to the expensive and bulky instrumentation techniques and time-consuming procedures [1]. Hence attention has been focused on electrochemical sensors owing to their ease of fabrication, high sensitivity, rapid response, online monitoring and the feasibility for miniaturization [2,3].

In the last 5 years numerous approaches [4-20] to measure SO_2 concentrations in gas streams have been investigated. These approaches are varied as indicated by the large number of electrolytes evaluated: 1) solid sulfates[19,20], 2) polymers [15], 3) tin oxide [9, 18], 4) Nasicon [13], 5) phosphates [4,16], 6) perovskite oxides with p-type conduction [5] 7) yttria-stabilized zirconia combined with a sulfite ion conductor [8], and 8) doped titania (TiO2) [12], to name a few. Most of these approaches have issues limiting their development and deployment as functional SO_x sensors and none have resulted in a viable sensor.

For example, research has been carried out to develop SO_2 sensors using solid sulfate (K_2SO_4, Ag_2SO_4 + Li_2SO_4) electrolytes [19,20]. These electrolytes, however, cannot operate above 463K, are difficult to densify, and undergo phase transitions with associated large volumetric changes which lead to microcracking and failure. Another approach utilizes a functional bilayer of yttria stabilized zirconia and Nasicon. In this sensor the zirconia is a protective layer

preventing the reaction between SO_3 and Na β-alumina to form $NasSO_4$. As such, it becomes the rate limiting material for diffusion of oxygen and limits the sensitivity of this sensor type.

Adsorption based sensors using SnO_2, WO_3, and perovskite oxides have been successfully tested. These sensors operate by measuring a resistivity change when a gas adsorbs on the surface of the electrode or electrolyte. However, these sensors are almost always sensitive to other oxidic gases (e.g., CO and NO_x) and in the case of the perovskites are additionally sensitive to changes in the oxygen concentration. The sensitivity to oxygen is important as the oxygen level can vary from 3-20% during normal plant operation. Due to all of these sensitivities, these type of sensing elements almost always need to operate in an array and are limited to applications with a defined temperature and gas composition range as they require calibration to operate properly.

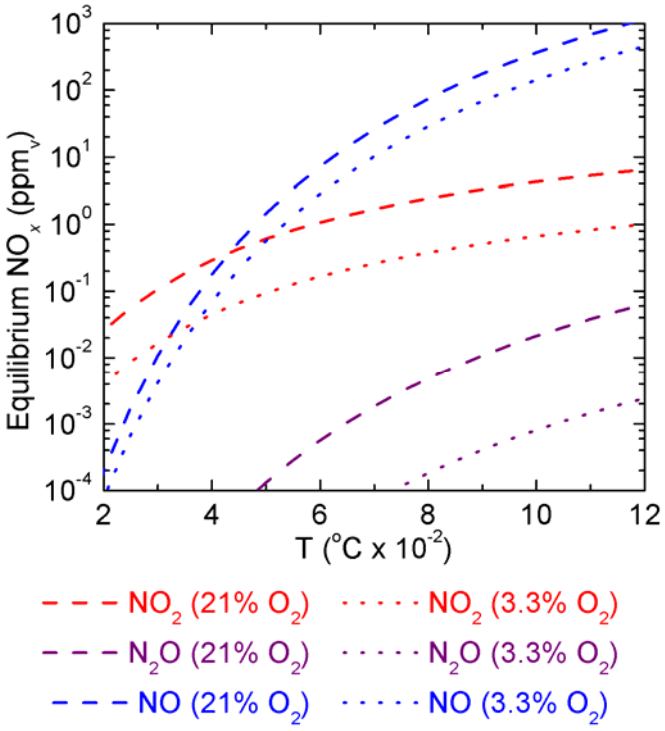

Figure 1. Equilibrium NO_x concentration as a function of temperature and oxygen content.

To date, none of the approaches described in the literature have resulted in a viable SO_2, SO_3, or "total" SO_x (i.e., total refers to the ability of the sensor to measure the total SO_x (SO_2 + SO_3) in a gas stream). sensor that can operate in a fossil fueled power plant. An interesting point in the lituerature is the lack of reference to the development of a pure electrochemical sensor that takes advantage of the inherent redox conditions and thermal equilibrium in SO_2, SO_3, and O_2 containing exhaust gas. This equilibrium is nearly identical to that of the NO-NO_2 system where advances in electrochemical sensors are showing the ability to measure NO, NO_2 and "total" NO_x (NO + NO_2).

In a mixed potential sensor the difference in catalytic response between two different electrode materials provides a "differential electrode equilibria" (mixed potential sensor) that could be used to selectively measure SO_x. The advantages of mixed potential sensors include: simple design, simple electronics, large signal, and the elimination of an air reference. The development of mixed-potential sensors offers tremendous potential to reduce the overall cost of the sensor through simplified design and low-cost electronics.

Recent advances in NOx sensor development at The Oak Ridge National Laboratory have demonstrated that a simple, single material, mixed-potential sensor using a current bias can measure "total" NO_x and NO. The ORNL work takes advantage of the natural redox conditions between NO, NO_2 and O_2, and the thermal equilibrium at temperature (Figure 1). In the case of

$_{NOx}$, at low temperature the NO_2 concentration dwarfs that of NO and this relationship switches upon heating, depending on the equilibrium oxygen concentration.

The test coupon (Figure 2) is set up with a current bias between 2 electrodes and operates between 550 to 700°C. The sensor operates such that one electrode is an anode and the other the cathode. Thus, during operation an EMF is generated between the two electrodes, whose magnitude is proportional to the "total" NO_x in the gas stream. The reactions that take place at the electrodes are:

Anodic Reaction:

$$NO + O^{2-} \rightarrow NO_2 + 2e^- \quad (1)$$

Cathodic Reaction

$$NO_2 + 2e^- \rightarrow NO + O^{2-} \quad (2)$$

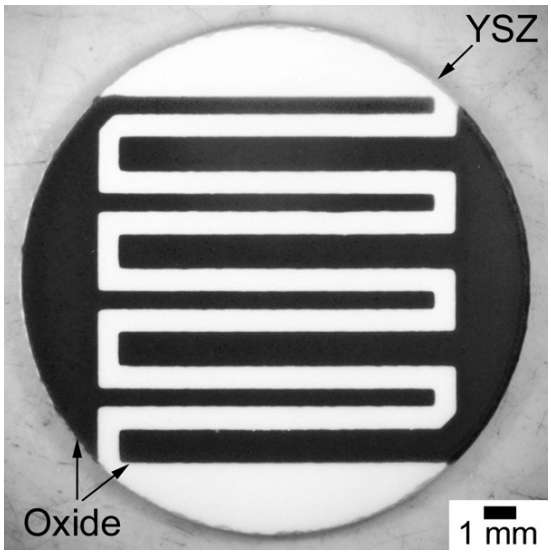

Figure 2. ORNL test coupon configuration.

The output of these sensors is a logarithmic response to NOx from 1 ppm to several thousand ppm.

The current biasing (μA levels) allows for a variety of sensor design and measurement schemes. ORNL has been able to couple current biasing with novel materials selection that have demonstrated regimes where the sensor output for NO_2 is 0 volts. Therefore, fixing the bias current the sensor can be selectivity tuned to measure only NO (i.e., the response to NO_2 is essentially turned off). These findings can be applied to SO_x sensing, albeit new materials will have to be developed and tested to determine their catalytic activity to SO_2 and SO_3.

SO_3 and SO_2 have a similar thermal equilibrium to NOx (Figure 3). As shown in Figure 3 at low temperatures thermal equilibrium favors SO_3 formation and at high temperature SO_2. Further, like NO_x, there is an inherent influence of oxygen on the SO_x levels and cross over point(i.e. point where the concentration of SO_2=SO_3). This data also indicates that there is a potential at low temperature to eliminate or minimize the effect of oxygen on the gas concentration. The dynamic equilibrium in the $SO_2/SO_3/O_2$ system clearly indicates that a electrochemical sensor emulating the NO_x sensor could be developed.

Anode Reaction:

$$SO_2 + O^{2-} \rightarrow SO_3 + 2e^- \quad (3)$$

Cathode Reaction

$$SO_3 + 2e^- \rightarrow SO_2 + O^{2-}$$

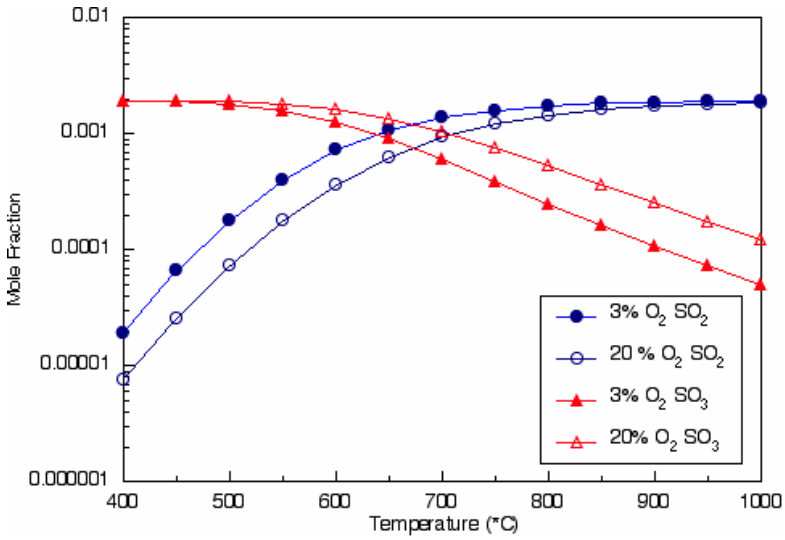

Figure 3. Equilibrium concentration of SO_2 and SO_3 as a function of temperature and oxygen concentration.

DISCUSSION OF CURRENT ACTIVITIES

A sensing element fabricated for the present investigation is shown in Fig 2. The element is comprised of interdigitated oxide electrodes on a yttria-stabilized zirconia (YSZ) substrate ~1.6 cm in diameter and ~0.1 cm thick. The YSZ substrates were fabricated from Tosoh TZ8YS zirconia by tape casting, lamination, and sintering (in air) at 1400 ^oC for 2 hr. Electrodes were patterned onto one side of the YSZ substrate by screen-printing dispersions at a wet print thickness of ~75 μm, drying at 130 ^oC, then firing (in air) at 1200 ^oC for 0.5 hr. Since the two electrodes in Fig. 2 are identical in composition, only a single screen print and firing step was required. Non-contact profilometry (Rodenstock RM600) was used to measure the thickness of the fired electrodes.

To evaluate sensing performance, the elements were mounted in a fixture with provisions for pressure contacts (Pt wire) to each of the oxide electrodes. This fixture was then placed in a resistively heated furnace. A computerized gas mixing unit (Environics 4000) was used to produce mixtures of N_2, O_2, and either NO or NO_2 and these mixtures were presented to the electroded face of the sensing element at a flow rate of 0.75 l/min. During testing, the element temperature (T_{meas}) was monitored by a type K thermocouple placed about 1 cm from the sensing element.

The signals applied to or extracted from the sensing element varied. If it was desired to only measure the DC voltage developed between the two electrodes electrometer (Keithley 617) was used to measure this voltage. In cases where a “current bias” (maintenance of a fixed DC current

(I_{bias})) was desired a Keithley 2400 source meter was placed in parallel with the electrometer. If "voltage bias" (maintenance of a fixed potential (V_{bias}) across the electrodes) was desired then a Keithley 6517 electrometer was used to both maintain V_{bias} and measure the DC current through the electrodes.

Primarily results from the tests are reported here. Finally, electrode surfaces were examined post-test with scanning electron microscopy. The surfaces were carbon-coated before examination in the SEM (Hitachi S-800) with an accelerating voltage of 5 kV. The signal selected for imaging was the secondary electron signal.

A profilometer trace across the electroded side of a fired sensing element indicated the electrode thickness is about 25 µm. Examination of polished cross-sections in the optical microscope led to similar conclusions regarding the fired electrode thickness. The microstructure is porous, consisting primarily of non-faceted, sub-micron size primary particles in the initial sintering stage. This porous microstructure should be well-suited for the intended gas sensing application.

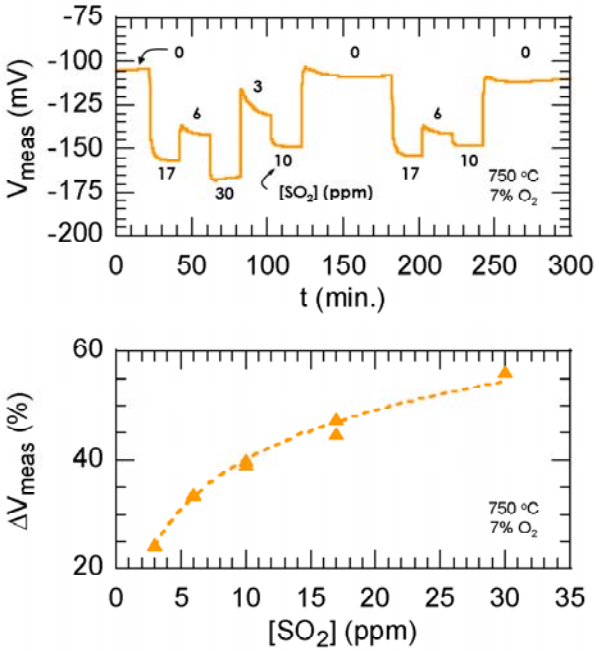

Figure 4. Change in DC resistance (mV) between 2 oxide electrodes at 750°C in a dry environment containing varying amounts (3-30 ppm) of SO_2, 7% O_2 and the balance N_2.

Proof of principal experiments were carried out using the standard ORNL electrode configuration shown in Figure 2 where 2 oxide electrodes are placed on a dense 8YSZ electrolyte and tested at temperatures >400°C in a variety of gas environments. Initial experiments at 7%0°C indicated that small amounts of SO_2 results in large reversible decreases in DC resistance of the sensor (Figure 4). The high operating temperature indicates that this sensor may be used for both flue gas and combustion applications. Similar results were achieved when operating a sensor with two noble metal electrodes and thus it appears that there may be several options for electrodes materials for a SO_2 sensor.

All flue gases contain typically contain hydrocarbon, NO_x, steam, ammonia and other chemical species. Initial analysis of contaminant effects on sensor performance was carried out evaluating ammonia, NO, NO_2, propylene as a surrogate for hydrocarbons, and oxygen. The results of this study are shown in Figure 5, and clearly indicate that NO, NO_2 and ammonia have essentially no impact on the performance of the initial sensor materials. Oxygen and hydrocarbons have a slightly larger impact, however, when compared to the change in DC output from SO_2, their impact is minor and will not affect the sensor performance. Studies are planned to determine the effects of steam on the sensor in the future. Thermodynamic analysis clearly indicated that steam could shift SO_2 to H_2SO_4, which will have to be evaluated.

CONCLUSIONS

Proof of principal studies have demonstrated that a solid state electrochemical sensor can adequately detect SO2 to 3 ppm at temperatures in excess of 700°C. In addition, analysis have indicated that few of the trace species found in fossil energy flue gases will impact the sensor performance. However, steam effects have not be studied and they have been shown to impact NOx sensor performance. Future work will focus on developing a combinatorial approach to rapidly screening catalyst materials for sensor, evaluating the affects of steam on sensor performance and continued long term testing.

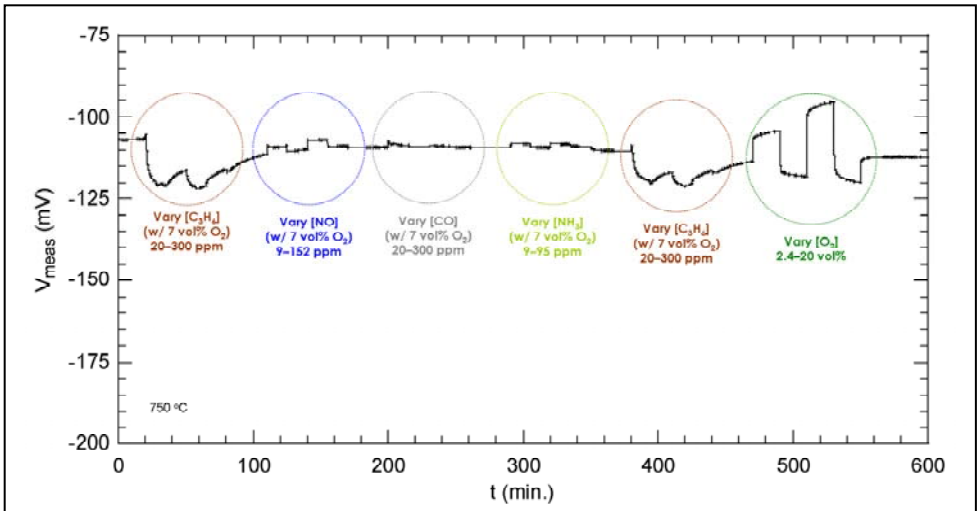

Figure 5. Effects of trace contaminants such as ammonia, NO, NO2, and propylene on SO_2 sensor performance at 750°C.

REFERENCES

1. J. Svitel, M. Stredansky, A. Pizzariello, S. Miertus, Electroanalysis 10 591-596 (1998).
2. U. Bilitewski and A. P. F. Turner Biosensors for environmental monitoring Harwood Academic Publishers, the Netherlands 2000.
3. K. S. Alber, J. A. Cox, P. J. Kulesza Electroanalysis 9 97-102 (1997).
4. L. Wang and R. V. Kumar, J. Electroanalytical Chemistry, **543** 190-114) (2003).
5. R. Moos, F. Rettig, A. Hurland, and C. Plog, Sensors and Actuators B, **93** 43-50 (2003).
6. C. Imawan, H. Steffes, F. Solzbacher, and E. Obermeier, Sensors and Actuators B, **78** 119-125 (2001).
7. R. Angelucci, A. Poggi, L. Dori, G. C. Cardinali, A. Parisini, A. tagliani, M. Mariasaldi, F. Cavani, Sensors and Actuators B, **74** 95-99 (1999).
8. 5. S. Suganuma, M. Watanabe, T. Kobayashi, S. Wakabayashi, Solid State Ionics, **126** 175-179 (1999).
9. J. L. Solis, V. Latto, Sensors and Actuators B, **48** 322-327 (1998).
10. D. R. Shankaran, and N. Uehera, and T. Kato, Sensors and Actuators B, **87** 442-447 (2002).

11. Sasaki, H. Tsuchiya,, M. Nishioka, M. Sadakata, and T. Okubu, Sensors and Actuators B, **86** 26-33 (2002).
12. D. Morris and R. G. Egdell, J. Mat. Chem., 11 3207-3210 (2001).
13. B. Min and S. Choi, Sensors and Actuators B, 93 209-213 (2003).
14. H. Li, and Q. Wang, J. Xu, W. Zhang, and L. Jin, Sensors and Actuators B, **87** 18-24 (2002).
15. R. Knake, P. Jacquinot, and P. C. Hauser, Analyst, **127** 114-118 (2002).
16. G. M. Kale, L. Wang, and Y. R. Hong, Solid State Ionics, **161** 15-163 (2003).
17. W. E. Hodgson, D. Pletcher, and S. Sotiropoulos, Sensors and Actuators B, **50** 181-185 (1998).
18. F. Berger, M. Fromm, A. Chambaudet, and R. Planade, Sensors and Actuators B, **45** 175-181 (1997).
1. M. Gautheir, A. Chamberland, A. Belanger, and M. Poirier, J. Electrochem. Soc. **124** 1584 (1977).
19. W. L. Worrell, and Q. Liu, J. Electrochem. Soc., **168** 355 (1984).
20. L.G. Tejuca, A.T. Bell, J.L.G. Fierro, and M.A. Peña, *Appl. Surf. Sci.*, 31, 301-316 (1988).
21. G. Kremenic, J.M.L. Nieto, J.M.D. Tascon, and L.G. Tejuca, *J. Chem. Soc*. *Faraday Trans.*, 81, 939-949 (1985).
22. T. Nakamura, M. Misono, and Y. Yoneda, *J. Catal*., 83, 151-159 (1983).
23. J.G. McCarty and H. Wise, *Catalysis Today*, 8, 231-248 (1990).
24. C. G. Vayenas, S. Bebelis. I. V. Yentekakis, and H. G. Linz, *Catal. Today* 11(3), 303-442 (1992).
25. E. D. Wachsman, P. Jayaweera, G. Krishnan, and A. Sanjurjo, accepted for publication *Solid State Ionics*

DEVELOPMENT OF INORGANIC MEMBRANES FOR HYDROGEN SEPARATION

Brian. L. Bischoff
Oak Ridge National Laboratory, P.O. Box 2008, Oak Ridge, TN 37831-6044
E-mail: bischoffbl@ornl.gov; Telephone: (865) 241-3172; Fax: (865) 576-3502

K. Dale Adcock
Oak Ridge National Laboratory, P.O. Box 2008, Oak Ridge, TN 37831-6044
E-mail: adcockkd@ornl.gov; Telephone: (865) 574-239; Fax: (865) 576-3502

Lawrence E. Powell
Oak Ridge National Laboratory, P.O. Box 2008, Oak Ridge, TN 37831-6044
E-mail: powellle@ornl.gov; Telephone: (865) 574-9415; Fax: (865) 576-3502

T. Gordon Sutton
Oak Ridge National Laboratory, P.O. Box 2008, Oak Ridge, TN 37831-6044
E-mail: suttontg1@ornl.gov; Telephone: (865) 574-8758; Fax: (865) 576-3502

Curtis J. Miller
Oak Ridge National Laboratory, P.O. Box 2008, Oak Ridge, TN 37831-6044
E-mail: millercj@ornl.gov; Telephone: (865) 574-3781; Fax: (865) 576-3502

ABSTRACT

The purpose of this work is to improve the method of fabricating tubular metal supported microporous inorganic membranes. Earlier work focused on the original development of inorganic membranes for the purification of hydrogen. These membranes are now being scaled up for demonstration in a coal gasification plant for the separation of hydrogen from coal-derived synthesis gas for a project funded by the Office of Fossil Energy's Gasification and Coal Fuels programs [1]. This project is part of FutureGen, an initiative to build the world's first integrated sequestration and hydrogen production research power plant. Although previous work in the Advanced Research Materials Program project lead to development of a tubular metal supported microporous membrane which was approved by the Department of Energy for testing, the membranes generally have lower than desired selectivities for hydrogen over other gases common in synthesis gas including carbon dioxide. The work on this project over the next three years will lead to general improvements in fabrication techniques that will result in membranes having higher separation factors and higher fluxes. Scanning electron microscopy and profilometry data will be presented to show qualitatively and quantitatively the surface roughness of the support tubes. We will discuss how the roughness affects membrane quality and methods to improve the quality of the support tube surface.

INTRODUCTION

The purpose of this work is to improve the method of fabricating tubular metal supported microporous inorganic membranes. Earlier work focused on the original development of these membranes which are now being scaled up for demonstration in a coal gasification plant for the separation of hydrogen from coal-derived synthesis gas for a project funded by the Office of Fossil Energy's Gasification and Coal Fuels programs. Although previous work lead to development of a tubular metal supported microporous membrane based on ORNL technology which was approved by the Department of Energy for testing, the membranes generally have lower than desired selectivities for hydrogen over other gases including carbon dioxide. The work on this project over the next three years will lead to general improvements in fabrication techniques that will lead to membranes having higher separation factors and higher fluxes.

EXPERIMENTAL

Previous work (see Figure 1) has shown that high selectivities for He over CO_2 can be achieved and that the permeance of He and H_2 increases with increasing temperature. At 250°C the ideal separation factor for the data shown was 48.3. Based on the permeance measurements of He and H_2 for many membranes, the permeance for H_2 is consistently higher than for He. Data has also shown that membranes produced using supports made from water atomized metal powers had a higher rate of imperfections than membranes produced using supports made from gas atomized powder. Scanning electron micrographs (SEM) of supports made from water atomized stainless steel powder are shown in Figures 2 and 3. Figure 2 was taken perpendicular to the inside surface and Figure 3 was taken by tilting the sample to 60°. While Figure 2 shows the irregularity of the particles, Figure 3, shows the roughness of the surface that results from these irregularly shaped particles. SEMs of supports made from gas atomized stainless steel powder are shown in Figures 4 and 5. Figure 4 was taken perpendicular to the inside surface and Figure 5 was taken by tilting the sample to 60°. While Figure 4 shows the nice spherical shape of the particles, Figure 5, shows that even with the more spherical particle shape, there is still some surface irregularities due to the larger particles protruding from the surface. However, the surface of the support made from the gas atomized powders appears much smoother than the surface of the support made from water atomized particles.

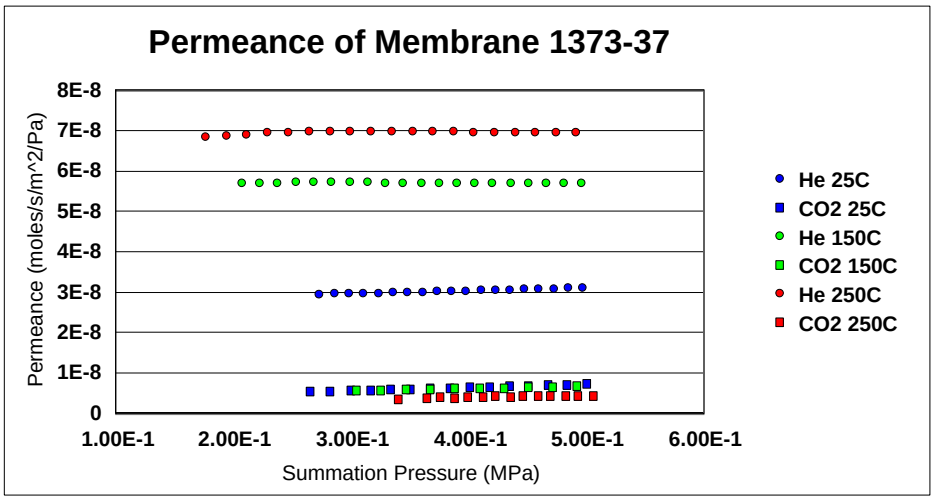

Figure 1 Permeance of Membrane 1373-37.

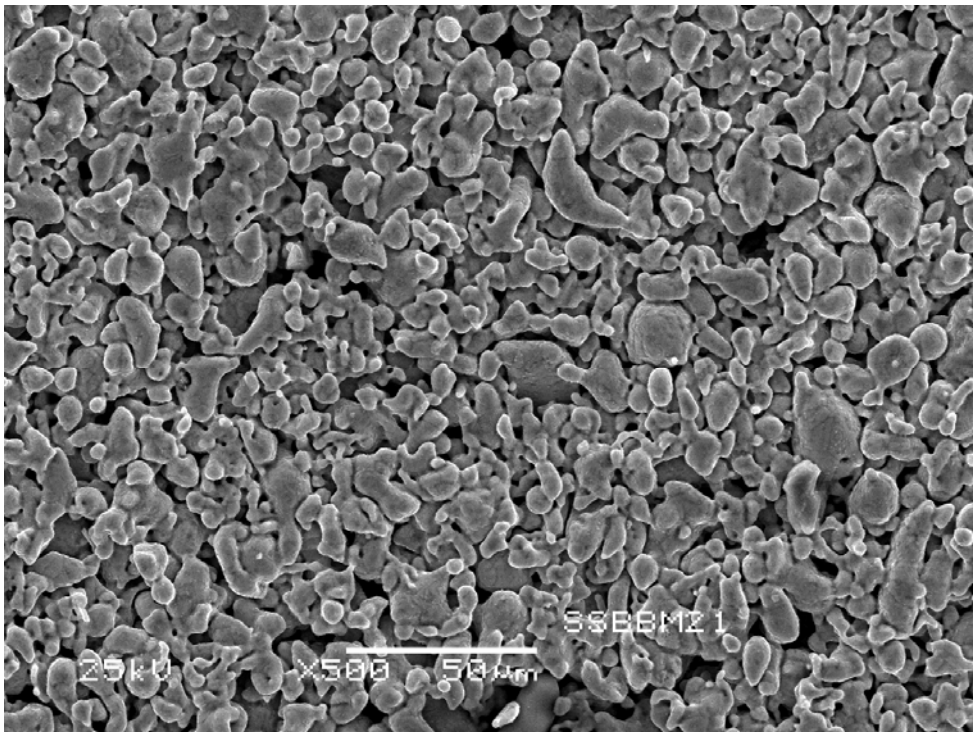

Figure 2 SEM of inside surface of support tube made from water atomized powder.

Profiliometry of the surface of the support tubes has been initiated using a software product called MeX from Alicona Imaging (Figure 6). This software works with SEM images taken at various tilt angles to evaluate the roughness of the surface along an axis. This analysis will be used to correlate measured surface roughness with membrane properties and powder properties used to make the supports. Figure 6 shows the surface non-uniformity of the support in Figures 2 and 3 made from water atomized powder. It shows that in the field of view analyzed, the magnitude of the difference between the peaks and valleys can be as high as approximately 14 micrometers. Since the intermediate layer is only approximately 2 micrometers thick (see Figure 7), the intermediate layer would have a difficult time

smoothing out the surface of a support tube made from water atomized powder. Without a smooth layer to apply the nanoporous separative layer on top of, it would be difficult to fabricate membranes having no leaks in the separative layer. Profilometry will be completed on the supports made from gas atomized powder shown in Figures 4 and 5 and the results will be compared the analysis of the supports made from water atomized powder.

Samples of gas atomized powder in varying particle size have been procured. Also, a sample of a gas atomized stainless steel powder having a narrower particle size distribution than our earlier as-received powders has been procured. This powder is essentially the same as the powder used to fabricate the tubes shown in Figures 4 and 5 with the largest particles removed leaving particles mostly less than 10 micrometers in diameter. When these tubes are formed, we will evaluate the supports for surface roughness, apply membrane layers and measure for the quality of membrane layer, mainly leak rate.

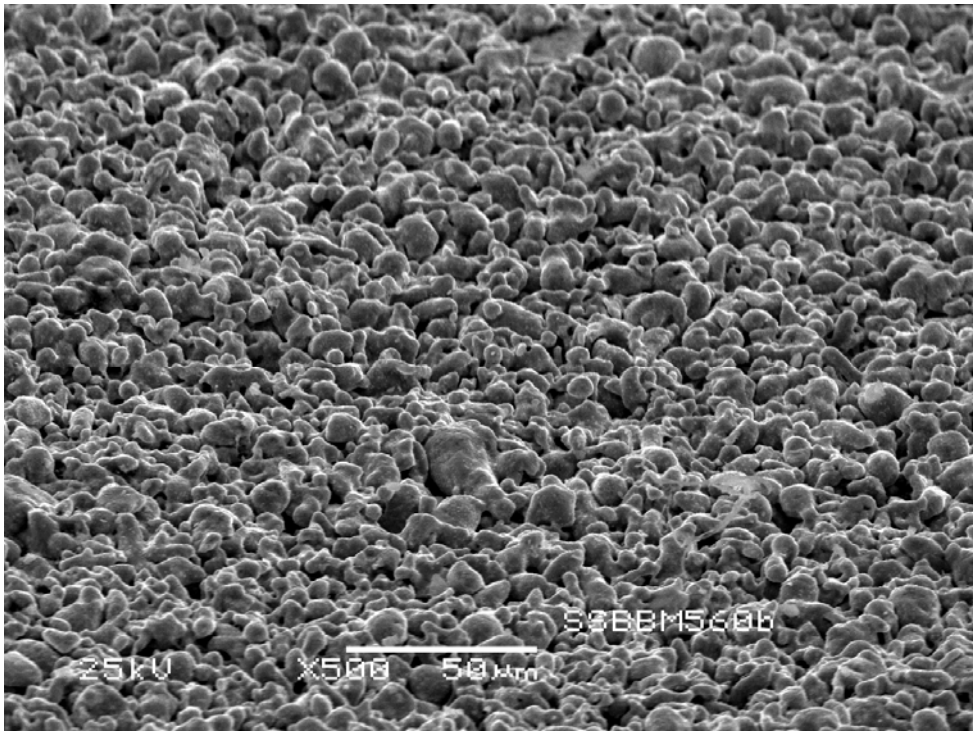

Figure 3 SEM of inside surface of support tube made from water atomized powder taken at 60°.

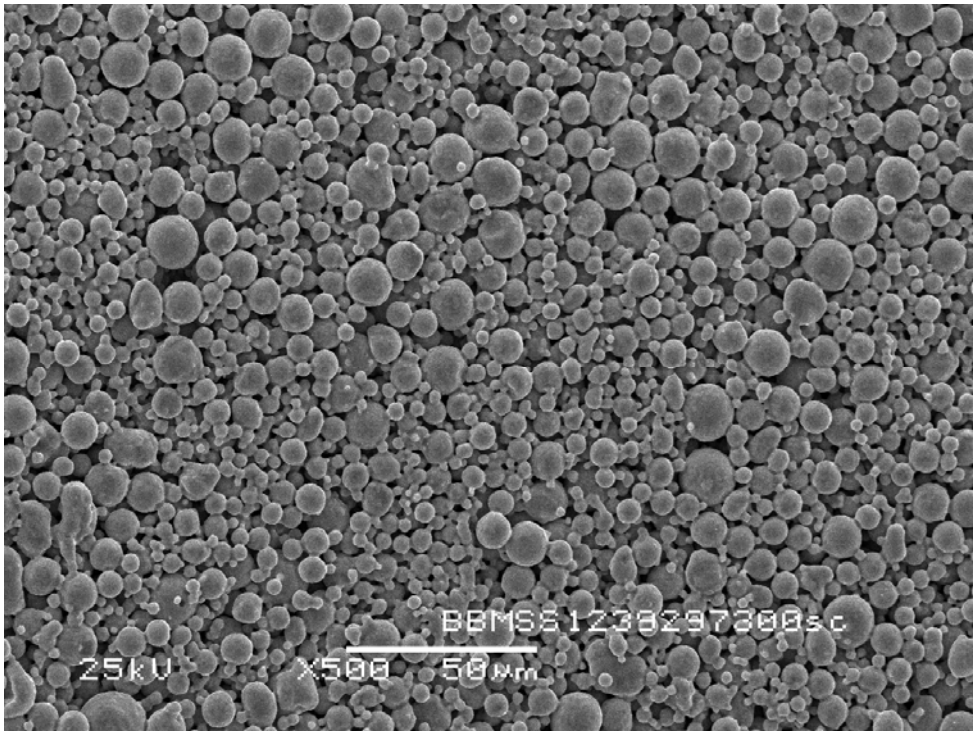

Figure 4 SEM of inside surface of support tube made from gas atomized powder.

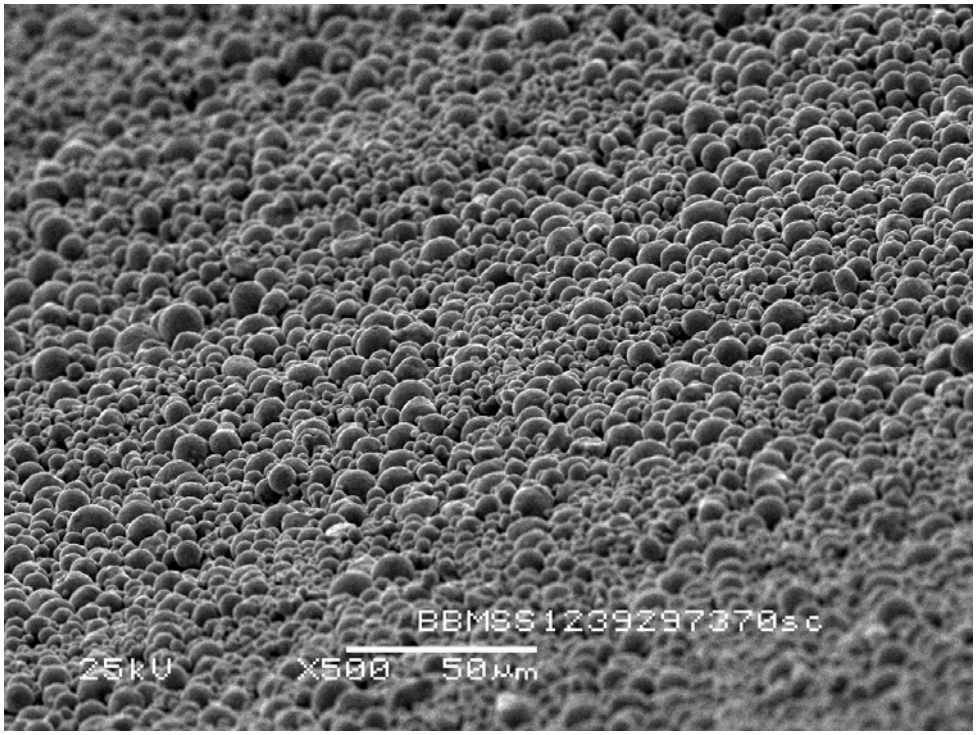

Figure 5 SEM of inside surface of support tube made from gas atomized powder taken at 60°.

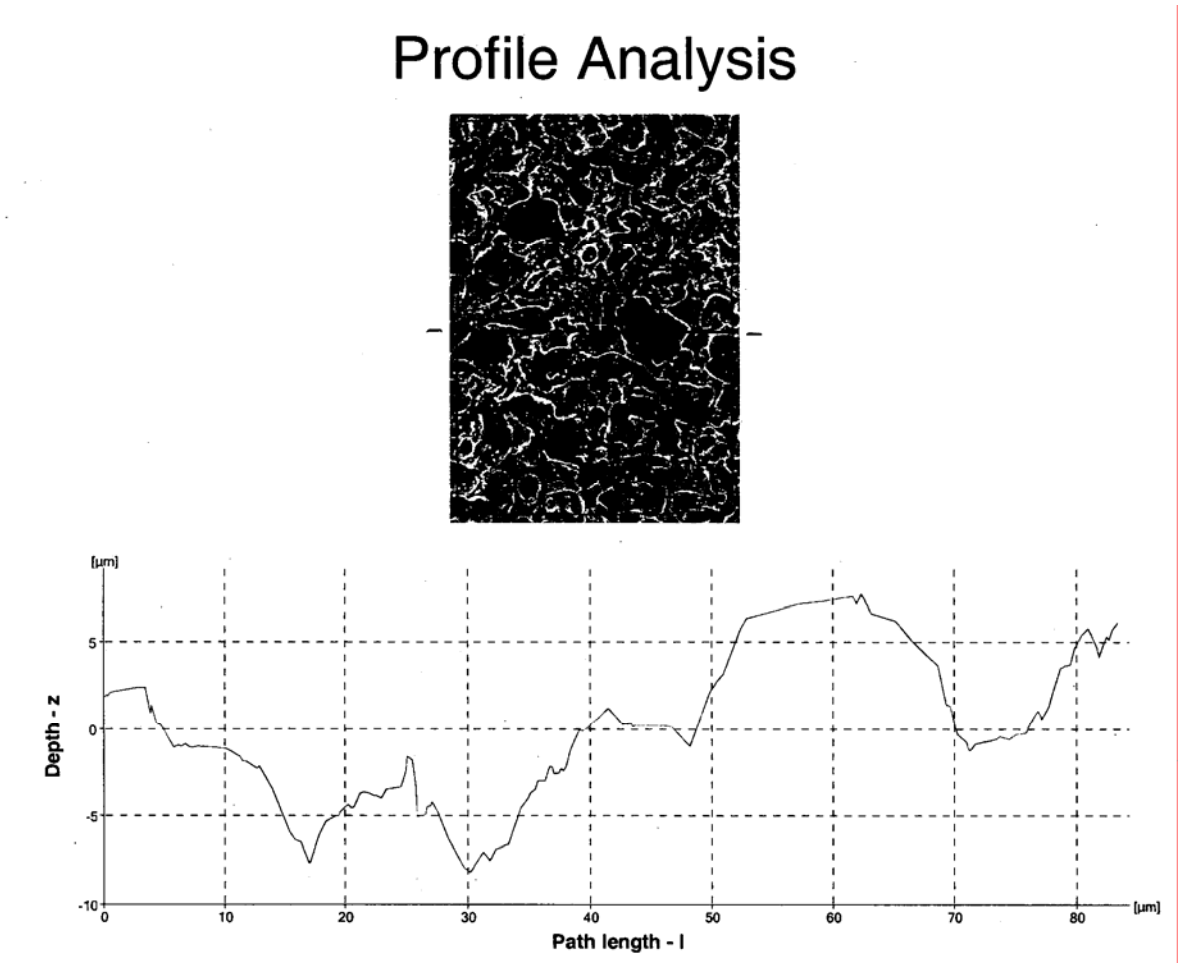

Figure 6 Depth Profile of Surface of Support Tube Made from Water Atomized Particles

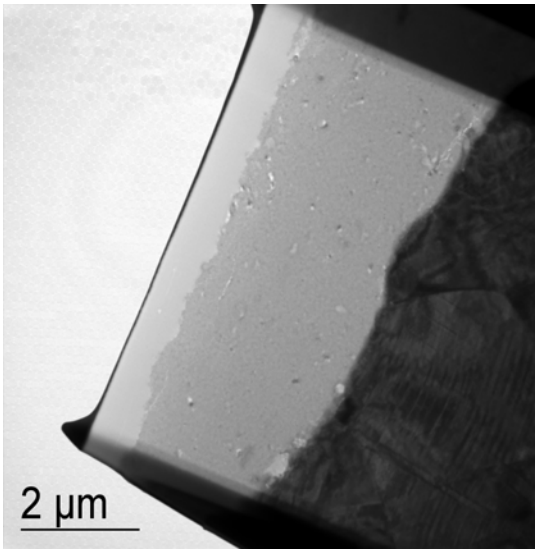

Figure 7 Transmission micrograph showing the support tube (dark), intermediate aluminum oxide layer (gray), nanoporous separative layer (almost white), and sputtered metal layer added to aid in sectioning.

PROJECT PLAN

The separation of gases including hydrogen from gas streams can be vitally important to the success of many applications including coal gasification. The separation of hydrogen from CO_2 requires a membrane having a very small pore size with very few oversized pores. Although earlier work has led to the development of a membrane having an average pore size less than 1 nm, these membranes will benefit from improvements in the processing to improve the quality of the membranes throughout the complete fabrication process. These improvements will reduce the quantity of over-sized pores which could eliminate the need for any further processing to repair these defects.

The microporous membrane task is designed to improve the fabrication process for metal supported microporous membranes to improve both the permeance and selectivity. This task will include a number of subtasks intended to improve the processing at each step of the fabrication process. The tasks over the next three years will include:

Task B1. Investigate surface roughness of support tube and its relationship to membrane properties. We would utilize profilometry (and other yet to be determined techniques) to analyze the surface of the support tube and intermediate layers and compare leak rates etc., of membrane layers. During earlier work, it was learned that supports produced from gas atomized powder produced membranes having fewer leaks. This task will be used to gain a better understanding of how changes in support tube properties affect membrane properties. Surface roughness is a possible cause of defects in the applied membrane. Support tube samples made from both types of powders, and powders with a narrower size distribution, will be characterized using profilometry

Task B2. Forming Study – Evaluate powder properties such as size, size distribution, and morphology, using various methods including light scattering, SEM, and tap density. Use this data to be able to better predict forming parameters for good forming run. Tubes made during this study will also be evaluated in Task B1. Powders will be procured for future support tube forming runs in order to correlate powder properties with support tube properties including surface roughness. The support tube quality dictates the quality of the separative layers applied. Improvements will improve membrane performance and reduce or eliminate the need for reparation processing.

Task B3. Improvement of pore-size uniformity – Reduce quantity of oversized pores in membranes without reducing quantity of desire pores. The number of oversized pores may be reduced greatly from improvements in Tasks B1 and B2. Techniques to eliminate oversized pores will improve separation properties of membranes which could eliminate or reduce the need for multiple membrane stages or additional cleanup steps such as PSA.

Task B4. End-member Joining Improvement (ferrules) – Recent developments in laser welding have resulting in improvements in the quality of attachment of nonporous end-members onto support tubes. However, there are still some problems with splattering and the transition between porous and non-porous for membrane application. We will investigate the variables in the welding process such as end-member thickness and laser power to create an improved means of attaching end-members in order to minimize leaks at the point of

attachment. In order to fit the ends of support tubes to the non-porous end members they must be rounded and sized to mate with the endmember stock. It is important that this operation not introduce defects in the support tubes that result in membranes with high leak rates. Support tubes will be rounded using a swaging machine and the diameter of the support tubes will be reduced in varying amounts in order to determine whether and to what extent swaging may create defects in the ends of the support tubes.

Task B5. Thermal stability of microporous membrane layer – Evaluate membrane properties before and after exposure to high temperatures. Investigate how the membrane stability is affected by changes is amounts of Al, Zr, etc. in the membrane layer. Membranes must operate for years without need for replacement. Many of these membranes operate at temperatures ranging from 250-800°C in the presence of steam or potentially corrosive gases.

REFERENCES

1. Judkins, R.R.; Bischoff, B.L., "Scale-Up of Microporous Inorganic Hydrogen-Separation Membranes," *Proceedings 22nd Annual International Pittsburgh Coal Conference, Sept. 12-15, 2005*.

METAL MEMBRANES FOR HYDROGEN SEPARATION

Stephen N. Paglieri
Los Alamos National Laboratory; P.O. Box 1663, MS-C927; Los Alamos, NM 87545
E-mail: steve.paglieri@lanl.gov; Telephone: (505) 667-0652; Fax: (505) 665-1226

Iver E. Anderson
Ames Laboratory, 222 Metals Development Building, Ames, IA 50011-3020
E-mail: andersoni@ameslab.gov, Telephone: (515) 294-9791; Fax: (515) 294-8727

Robert L. Terpstra
Ames Laboratory, 222 Metals Development Building, Rm. 109, Ames, IA 50011
E-mail: terpstra@ameslab.gov; Telephone: (515) 294-5747; Fax: (515) 294-8727

Thomas J. Venhaus
Los Alamos National Laboratory; P.O. Box 1663, MS-C927; Los Alamos, NM 87545
E-mail: steve.paglieri@lanl.gov; Telephone: (505) 665-4829; Fax: (505) 665-1226

Yongqiang Wang
Los Alamos National Laboratory; P.O. Box 1663, MS- K765; Los Alamos, NM 87545
E-mail: yqwang@lanl.gov; Telephone: (505) 665-1596; Fax: (505) 665-2992

Robert E. Buxbaum
REB Research & Consulting, 3259 Hilton Rd., Ferndale, MI 48220
E-mail: buxbaum@rebresearch.com; Telephone: (248) 545-0155; Fax: (248) 545-5430

Kurt S. Rothenberger
National Energy Technology Laboratory, P.O. Box 10940, Pittsburgh, PA 15236-0940
E-mail: Kurt.Rothenberger@netl.doe.gov; Telephone: (412) 386-6082; Fax: (412) 386-5920

Bret H. Howard
National Energy Technology Laboratory, P.O. Box 10940, Pittsburgh, PA 15236-0940
E-mail: Bret.Howard@ netl.doe.gov; Telephone: 412-386-5908; Fax: (412) 386-5920

ABSTRACT

Porous membranes were fabricated from Fe-16Al-2Cr (wt.%) particles of 3-μm average diameter. A slurry of 3-μm particles was applied onto porous Inconel supports. At temperatures up to 600°C, the membrane had high hydrogen and argon permeability, but the gas permselectivities were indicative of Knudsen diffusion. The porous Fe-16Al-2Cr membrane was covered with a layer of alumina that should serve as an effective barrier to metallic interdiffusion for the thin palladium film deposited onto the surface. To reduce the amount of palladium used in a composite membrane, V-6Ni-5Co (at.%) alloy foils were ion-milled, and 100-nm-thick palladium coatings were applied to both sides *in situ* via electron-beam-evaporation physical vapor deposition (EB-PVD). The membranes were completely permselective for hydrogen. The hydrogen permeance of a 0.37-mm-thick Pd/V-6Ni-5Co/Pd composite membrane was 1.5E-4 mol m^{-2} s^{-1} $Pa^{-0.5}$ at 400°C (greater than that expected for pure palladium at the same conditions). The addition of cobalt to the V-Ni system was expected to lower the diffusivity of vanadium. Indeed, the Pd/V-6Ni-5Co/Pd membrane had excellent stability compared with palladium-coated pure vanadium membranes, with constant hydrogen flux measured for over 500 h at 400°C. However, at 500°C, the hydrogen flux through the composite membrane steadily decreased, reaching half of its initial value in less than 41 h. Interdiffusion between the palladium surface coating and the V-6Ni-5Co foil was characterized with Rutherford backscattering spectrometry (RBS) and Auger electron spectroscopy (AES) depth profiles. After testing a membrane at 400°C for 500 h, a substantial quantity of vanadium had diffused to the surface (40 at.%), whereas essentially no palladium had diffused into the bulk V-6Ni-5Co foil according to an AES depth profile. At 500°C, the extent of metallic interdiffusion was much greater and the surface region was heavily oxidized.

INTRODUCTION

Ultra-pure hydrogen can be conveniently produced using metal membranes. Palladium alloy membranes are frequently used to purify hydrogen for compound semiconductor manufacturing, and in laboratories. It is also advantageous to use membranes reactors to perform chemical reactions more efficiently[1]. Unfortunately, the high cost of palladium prevents metal membrane technology from replacing large-scale hydrogen purification methods such as pressure swing adsorption. Filters for hot gas cleanup have been fabricated using iron-aluminide particles that resist oxidation and degradation by gaseous impurities commonly present in coal gas[2]. Extruding the molten metal through a nozzle and shearing the stream with high-velocity gas such as helium produces microparticles with a narrow size distribution[2]. Alloys with extra aluminum such as Fe-16Al-2Cr can form a thermally grown aluminum oxide layer on the surface that protects the metal from further degradation. An advantage of thermally grown layers compared to coatings is more uniform surface coverage with fewer defects. For example, chrome-containing alloys have been shown to form a continuous nitride layer at 1373 K that resists leaching in the acidic environment of a proton exchange membrane fuel cell (PEMFC)[3].

Porous metal as a palladium membrane support has the advantages of similar coefficient of thermal expansion to palladium, increased strength compared to porous ceramic or glass, and the potential to more easily seal into a module[4]. Porous metal tubes and sheet are commercially available in poresizes as small as 0.1 μm particle retention. However, the as-received surface roughness and poresize is too great to successfully deposit a thin (< 10 μm), pinhole-free palladium or palladium alloy film[5]. The deposition of a palladium film without defects depends on the ability to span all of the pores in the support membrane[6]. Therefore, the critical qualities of a palladium membrane support are low surface roughness and small poresize[7]. Metallic atoms from stainless steel such as chromium are also known to diffuse through into palladium and cause a decrease in membrane permeability. Metallic interdiffusion that occurs between palladium and porous stainless steel at temperatures ≥ 450°C has been reduced by thin layers of oxide, nitride, or refractory metal[5; 8-12]. Of course, membrane stability then depends on the stability of the intermediate layer.

Metals with bcc structure such as vanadium, niobium, tantalum, and titanium have higher hydrogen permeabilities than palladium but suffer from surface contamination and hydrogen embrittlement. However, alloys of these metals may possess some of the properties desired in a metal membrane including high hydrogen permeability, low cost, and ductility under hydrogen over a large temperature range. Generally, these metals require a thin film of palladium on their surfaces to catalyze the dissociation of molecular hydrogen and enable absorption into the metal (and recombination on the downstream side). The palladium film thickness required is generally much less than a freestanding or supported foil membrane. Palladium-coated vanadium, niobium, and tantalum membranes have been studied, although they embrittle due to the formation of hydride phases, especially at lower temperatures[13-16]. Vanadium alloys that have been investigated for hydrogen membranes include V-Ni, V-Al, V-Ni-Al, and V-Cr-Ti[17-21]. Promising ternary alloys based on the V-Ti-Ni or Ta-Ti-Ni systems exhibit hydrogen permeabilities comparable to palladium and they resist embrittlement[22]. Besides embrittlement, another problem experienced by metal composite membranes is metallic interdiffusion between the substrate foil and the palladium overcoat[13]. For example, palladium-coated tantalum membranes have experienced a slow decline in hydrogen flux at temperatures ≥ 400˚C[15; 23].

RBS and AES have been used previously in membrane characterization studies[15; 24]. RBS is excellent for quick, nondestructive analysis of the composition of surface coatings as a function of depth (up to a couple of microns). AES is a surface technique that determines the elemental composition of the first few monolayers. When combined with ion-milling, compositional depth profiles can be obtained. Both RBS and AES were used to determine the changes that occur in the surface region of palladium-coated vanadium-alloy membranes as a result of hydrogen permeation tests. The results of the long-term hydrogen permeability tests and membrane characterization study presented here will show that the V-6Ni-5Co alloy has increased resistance to metallic interdiffusion with palladium coatings during permeation testing at temperatures of 400°C and higher. The ability to operate at higher temperatures will improve efficiency and enable more flexibility in membrane applications.

EXPERIMENTAL

The iron-aluminide microparticles were prepared by a high-velocity gas jet extrusion method described in detail elsewhere[2]. The Fe-16Al-2Cr particles had a size distribution centered around 3 μm. A slurry of particles was prepared and applied to a porous Inconel frit (nominal 0.1 μm particle retention). Porous Inconel (Mott Metallurgical) frits were press fit into the ends of 0.95 cm ID tubes that had been drilled out to form a lip inside. A 1 mm gap was left between the porous frit and the end of the tube for the microparticle slurry. The top of the particle film was smoothed off evenly with a razor blade and the membrane was fired in a vacuum furnace. A picture of the

Figure 1: Iron-aluminide microparticle membrane sintered onto a porous Inconel frit press-fit into the end of a 0.95-cm diam. tube

sintered membrane is shown in Figure 1. Single gas hydrogen and argon permeation tests were performed using a flow-through system. Retentate pressure was controlled using a back-pressure regulator and permeate flowrate was measured using a calibrated flowmeter. Overall system control and datalogging was carried out using National Instruments Labview software and Fieldpoint modules.

Before deposition of the palladium film, the Inconel tube was milled down on a lathe using a carbide-tipped tool so that it was flush with the surface of the porous microparticle membrane (which had contracted slightly during firing). A 2-μm-thick palladium film was deposited onto the membrane by EB-PVD in a vacuum chamber at < 10^{-6} Pa.

To prepare the V-6Ni-5Co membrane, high purity (>99.9%) metals were mixed and electron beam (*e*-beam) melted into buttons in a vacuum furnace. The buttons were flipped and re-melted to ensure compositional uniformity. A button was sliced and cold rolled into a sheet with a nominal thickness of 0.37 mm. The foil was washed with warm water and soap, rinsed with methanol, blown dry with nitrogen, mounted by clamping the ends of the foil strip, and loaded into the physical vapor deposition (PVD) chamber. After evacuation, argon was bled into the chamber to a pressure of $1.5 \cdot 10^{-4}$ torr and the ion-gun was set to a power of 1 keV and 20-25 mA to ion-mill each side of the foil for 60-90 min. The foil was visually inspected through a window during ion-milling to ensure removal of all remaining macroscopic contaminants. After ion-milling, the chamber was evacuated again to $1 \cdot 10^{-7}$ torr and palladium was *e*-beam evaporated onto each side of the foil to the desired thickness at 3-5 Å/s. A quartz crystal was used to monitor the thickness of metal deposited.

Discs (19 mm diameter) were laser cut from the foil. The membrane foil was sandwiched between two nickel VCR gaskets (12.7 mm OD) and positioned in the fixture, a stainless steel VCR fitting adapted with an impinging flow design. The membrane surface area was ~1 cm^2. The mated fixture was tightened roughly one-quarter turn. A final helium pressurization test was performed to confirm the absence of leaks. The membrane module was placed in a furnace and connected to a gas plumbing and measurement system. Mass flow controllers metered the gas flows while 0-10,000 or 0-100 torr pressure transducers measured upstream and downstream pressures, respectively. The feed pressure was set at 760 torr and the permeate pressure was typically 10 torr. Sweep gas was not used during the permeation experiments. Gases were 99.99995% pure and used without further purification. The membrane module was heated in the absence of hydrogen (argon purge at the feed and vacuum on the permeate side).

Membranes were examined using an Aspex PSEM 2000 equipped with EDS prior to and following flux testing to determine micro-scale morphological changes such as those in the palladium coating and alloy grains. EDS was used to determine the elemental constituents of observed features. A PANalytical X'Pert Pro MPD powder diffractometer having a theta-theta configuration, a copper X-ray source operated at 45 kV and 40 mA and an X'Celerator detector with a monochromator was used to determine crystalline phases present in the membranes and changes resulting from flux testing. Patterns were typically recorded over a 2θ range of 10 to 100°. RBS measurements were done on a NEC 9SDH-2 Pelletron Tandem Accelerator with a 2 MeV $^4He^+$ ion beam. The ion beam perpendicularly impinged on the sample surface, whereas the backscattered helium particles were energy-analyzed by a silicon detector located at 167° in relative to the beam direction. The energy resolution of the RBS system was ~14 keV, corresponding to a depth resolution of ~115 Å at the palladium surface. AES depth profiles were performed in a Kratos Axis-Ultra surface analysis system. A 5 kV argon ion gun was used to sputter a 2×2 mm crater. AES was performed with an electron gun at a primary beam energy of 5 kV. Relative species concentrations were determined using the peak-to-peak height of the differentiated signal for each component, and applying published Auger sensitivity factors[25].

RESULTS AND DISCUSSION

MEMBRANE PERFORMANCE

Permeation measurements were conducted on the porous Inconel (0.1 μm poresize) coated with a layer of the 3-μm particles. The flowrate versus pressure drop through the composite membrane is shown in Figure 2. The ideal gas permselectivities ($\alpha_{H2/Ar}$ = H_2-flowrate/Ar-flowrate) calculated from the data in Figure 2 were around 3.0 to 3.3. For Knudsen flow, where the interaction of gaseous atoms or molecules with the pore wall becomes more prevalent

because of the small poresize, the separation factor is determined by the inverse ratio of square root of molecular weights of the gases [26]:

$$\alpha_{Knudsen} = \sqrt{\frac{MW_{Ar}}{MW_{H_2}}} = 4.45$$

The ideal gas permselectivities ($\alpha_{H2/Ar}$) calculated from the data in Figure 2 were between 3.0 and 3.3. Therefore, the gas permeation mechanism through the porous membrane had contributions from both Knudsen and viscous flow.

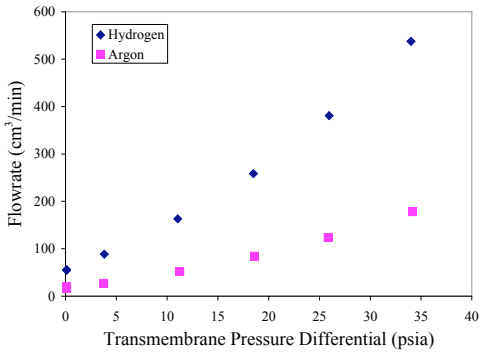

Figure 2: H_2 and Ar flowrates through Fe-16Al-2Cr (3-μm particle) membrane at 350°C and ΔP = 0-35 psig (0-241 kPa)

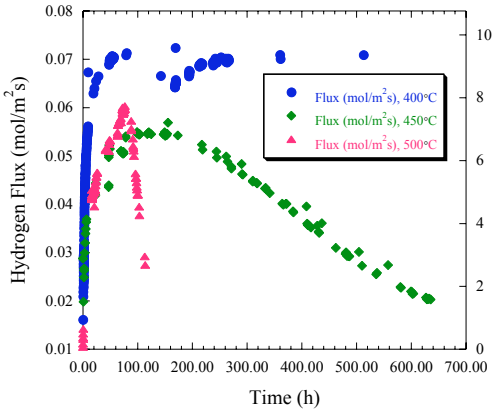

Figure 3: Hydrogen flux at 400, 450, and 500°C through a 0.37-mm thick V-6Ni-5Co foil coated with 100 nm of palladium

Long-term tests were performed on individual Pd/V-6Ni-5Co/Pd membranes at 400, 450, and 500°C. The hydrogen flux through each membrane over time is shown in Figure 3. All of the membranes experienced a gradual increase in hydrogen flux over the first 24-48 hrs of testing. At 400°C, the flux was essentially constant for more than 500 hrs. Some variations in flux were due to interruptions in the hydrogen supply. After testing the membrane for 500 hrs at 400°C, it was taken to 200°C and then back to 400°C (under hydrogen). At that point, the membrane fractured, probably from hydrogen embrittlement. Hydrogen permeance was determined by plotting hydrogen flux data vs. the square root of pressure. A value of 1.5E-4 mol m^{-2} s^{-1} $Pa^{-0.5}$ was obtained.

For the hydrogen flux test at 450°C, a membrane was held at 400°C for a period of 75 hrs until the hydrogen flux stabilized. Once the temperature was increased to 450°C, the hydrogen flux was fairly constant with no apparent flux decrease for about 100 hrs, followed by a slow, steady decrease over the next ~500 hrs of testing. The membrane tested at 500°C was first tested over a period of 64 hrs at 400°C, and then the temperature was increased to 500°C. During only 41 hrs of exposure to hydrogen at 500°C, the flux decreased rapidly to less than half of its highest value, 0.054 mol m^{-2} s^{-1}, measured at 400°C. The flux decreased more quickly than at 450°C, presumably due to an increase in the rate of metallic interdiffusion.

MEMBRANE CHARACTERIZATION

After sintering, the surface of the Fe-16Al-2Cr membrane was analyzed using AES (Figure 4). AES was used to probe small areas of the surface. As shown in Figure 4, aluminum, oxygen, some iron, and traces of carbon, sulfur, and boron are detected. The boron and sulfur appeared to be localized on the surface of the blisters shown in the accompanying SEM image. The surface was also analyzed by XPS to confirm the chemical state of the iron and aluminum. The location and structure of the photoelectron peaks for both elements show a mixture of oxidized and non-oxidized components, although the iron chemical state observed from the smooth areas is mostly elemental with only a very small oxide component. Carbon is a commonly seen contaminant, and some of the carbon present is undoubtedly a result of air exposure. The sulfur and boron may be artifacts of the particle manufacturing process. The composite microparticle membrane tested for gas permeability (see Figure 2) was coated with 2 μm of palladium using EB-PVD. The palladium-coated membrane was annealed at 500°C for 100 h under vacuum to test membrane durability. As displayed in Figure 5, much of the palladium film exfoliated off of the porous Fe-16Al-2Cr membrane. The membrane was analyzed using XPS (Table 1). Interestingly, the surface was almost entirely iron oxide and no aluminum oxide was observed. Further study will be required to understand why the palladium film delaminated and why no aluminum was detected on the surface of the porous Fe-16Al-2Cr after heat treatment.

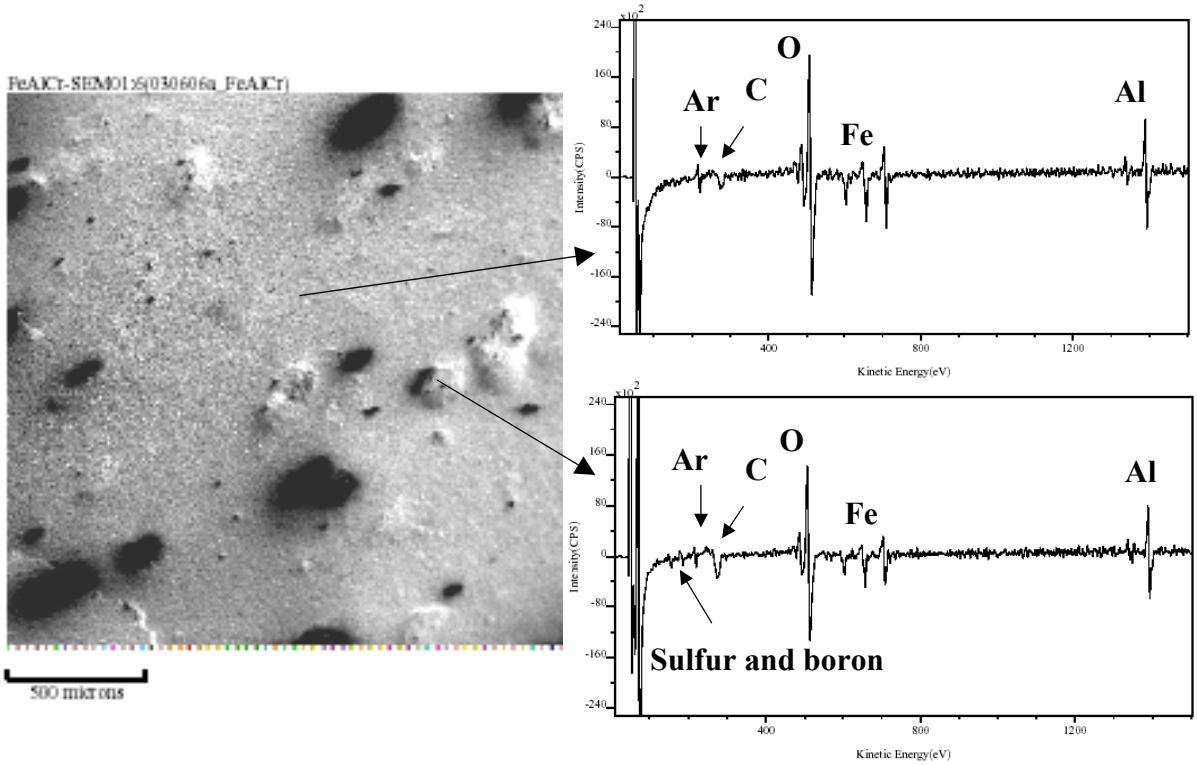

Figure 4: SEM image of the surface of a sintered membrane composed of 3-μm Fe-16Al-2Cr microparticles and AES results showing surface composition at two different locations

Table 1: Results of XPS analysis of Pd/Fe-16Al-2Cr surface, heat-treated at 500°C for 100 h under vacuum

Bare region		Palladium	
Element	Atomic %	Element	Atomic %
oxygen	51	oxygen	56
carbon	21	carbon	23
sodium	1	sodium	0.5
iron	26	iron	6
palladium	1	palladium	14

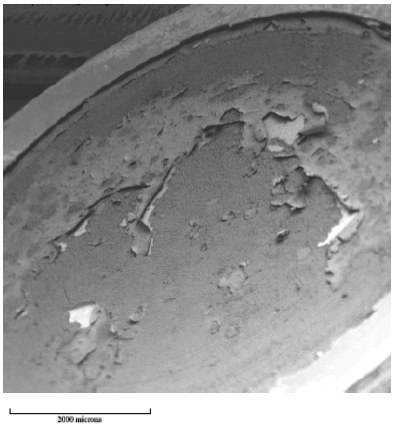

Figure 5: SEM image of Fe-16Al-2Cr microparticle membrane coated with 2 μm of palladium and heat treated at 500°C for 100 h

V-6Ni-5Co membrane samples were examined by SEM/EDS before and after flux testing to identify gross changes in morphology. SEM results (Figure 6) on the pre-test V-6Ni-5Co samples showed a uniform palladium coating with occasional defects (patches, scratches), usually extending for many microns across the sample. These areas had higher measured vanadium composition, consistent with having lost (or never received) the palladium coating. However, these areas represented a very small proportion (less than 3% as estimated by eye) of the membrane surface. The palladium coating on the membrane tested at 400°C was very similar. The only differences of note were that the tested sample appeared to have slightly roughened morphology and also contained smaller, submicron defects. Because of the small size of these defects, it was difficult to get an accurate composition, but they did show enhanced vanadium content. These defects again represented a very small portion of the total membrane surface.

XRD results on both untested and tested V-6Ni-5Co samples showed strong peaks corresponding to the palladium coating. The only other observable peaks were located at positions slightly shifted from that expected for elemental

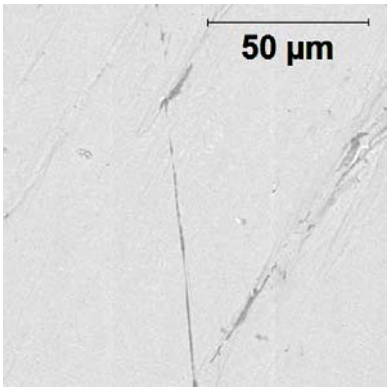

Figure 6: SEM image of fresh membrane surface (backscattered mode). Dark areas are the Pd-6Ni-5Co substrate visible through defects in the palladium coating

vanadium. No peaks assignable to elemental nickel or cobalt were observed, consistent with alloying. Comparison of tested and untested samples showed no assignable differences in terms of phase or composition changes. No differences in peak position between tested and untested samples were observed. Although differences in peak intensity were observed, these were within the range expected for differences in sample positioning and other effects unrelated to testing.

The basic concept behind RBS is the measurement of the energy spectrum of backscattered helium nuclei (He^{++}). The collision of helium nuclei with atoms at the surface results in backscattered helium energies that vary depending on the atomic mass. For the same atomic mass, the helium backscattering energy decreases with increasing depth. RBS spectra were measured on the uncoated and coated V-6Ni-5Co foils as well as a membrane tested at 500°C (Figure 7). RBS results indicated significant metallic interdiffusion at the Pd/V interface on both sides of the membrane after hydrogen permeation testing at 500°C, while such diffusion was much less pronounced after testing at 450°C (not shown). At both temperatures, more vanadium had diffused to the surface on the upstream side of the membrane, perhaps because it was exposed to higher hydrogen pressure. Also, a noticeable amount of oxygen (near channel number 260) was detected only on the surface of the upstream side of the membrane after testing at 500°C.

AES depth profiling was conducted to refine understanding of the elemental concentration throughout the surface region of the tested membranes. The relative concentrations of palladium and vanadium as a function of sputter time were measured on the membrane tested at 400°C for 500 hrs. In Figure 8a, it is apparent that vanadium diffused to the surface of the membrane. Interestingly, this did not affect the hydrogen flux (see Figure 3). Furthermore, palladium did not seem to diffuse into the V-6Ni-5Co foil.

On the membrane tested at 500°C for 41 hrs, an attempt was made to also measure the oxygen concentration, as well as the concentrations of cobalt and nickel, during the depth profile (Figure 8b). The rate of metallic interdiffusion is clearly faster at 500°C. The oxygen measurement is complicated by the vanadium L_3VV Auger peak at ~511 eV, which overlaps the primary oxygen KLL peak. To determine an approximate oxygen concentration, the oxygen KLL peak was adjusted by taking into account the small vanadium peak, using the main vanadium LMM peak as a reference[27]. Oxygen was observed at a concentration of 80% at the surface (Figure 8b), linearly decreasing in concentration to a depth of ~150 nm. Apparently, the vanadium gettered oxygen from the ultra-high purity hydrogen feed stream during testing. Additionally, palladium diffused at least 100 nm into the V-6Ni-5Co foil at 500°C, whereas nickel and cobalt did not seem to migrate towards the surface.

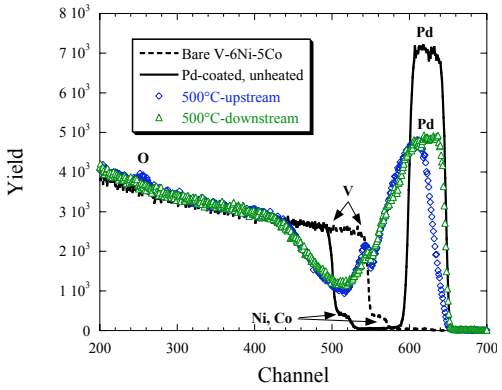

Figure 7: RBS spectra of V-6Ni-5Co membranes: bare foil (unheated), foil coated with 100 nm of palladium (unheated), and both sides of a foil coated with 100 nm of palladium and tested at 500°C for 41 h

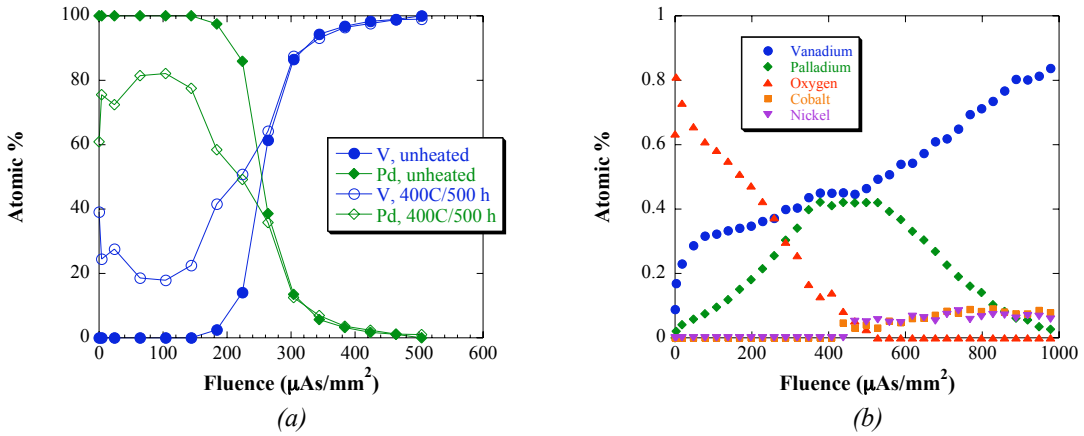

Figure 8: AES depth profile of V-6Ni-5Co foils coated with 100 nm of palladium and (a) comparison of unheated membrane and membrane tested at 400°C for 500 hrs (b) membrane tested at 500°C for 41 h

CONCLUSIONS

Porous membranes fabricated from Fe-16Al-2Cr (wt.%) particles of 3-μm average diameter were characterized. At temperatures up to 600°C, the membrane had high hydrogen and argon permeability, but the gas permselectivities were indicative of Knudsen diffusion. The membrane was covered with a thin layer of alumina that could serve as an effective barrier to metallic interdiffusion for the thin palladium film deposited onto the surface. However, a 2-μm-thick palladium film deposited on the surface did not fully adhere after treating at 500°C for 100 h under vacuum. Some iron had diffused to the surface of the intact portion of the palladium film, suggesting that the alumina layer that had existed before the heat treatment was not sufficiently thick to prevent metallic interdiffusion.

Alloying vanadium with nickel and cobalt seems to retard metallic interdiffusion of a 100-nm Pd overcoat into the V-6Ni-5Co foil. This may be due to stabilization of the vanadium through formation of a structured alloy. With the rough approximation that an order of magnitude more palladium (1 μm) on the surface would provide two orders of magnitude increase in the duration of stable hydrogen flux through the membrane, the membrane performance approaches the U.S. Dept of Energy 2010 durability target of 7 years. However, at temperatures above 400°C, vanadium diffused faster through the palladium overcoat to the surface of the membrane where it oxidized and caused the hydrogen flux to decrease. A palladium alloy surface coating could help reduce the diffusion rate of vanadium to the surface. Although the V-6Ni-5Co alloy was easily embrittled by hydrogen, it could serve as a starting point for the development of other alloys with improved properties. RBS and AES depth profile analysis were both very helpful for studying metallic interdiffusion.

ACKNOWLEDGEMENTS

This work was funded by the U.S. DoE, Office of Fossil Energy (Advanced Research Materials program). The authors are grateful for alloy foil preparation by Ames Laboratory. Collaboration with REB Research took place under contract DE-FC26-05NT42400. Thanks to Ronny C. Snow for PVD, and Hain Oona and Blake P. Nolen for experimental assistance.

REFERENCES

1. V.M. Gryaznov, "Metal containing membranes for the production of ultrapure hydrogen and the recovery of hydrogen isotopes," *Sep. Purif. Meth.*, 29(2) (2000), 171-187.

2. I.E. Anderson, and R.L. Terpstra, "Progress toward gas atomization processing with increased uniformity and control," *Mater. Sci. and Eng. A*, 326 (2002), 101-109.
3. M.P. Brady, K. Weisbrod, I. Paulauskas, R.A. Buchanan, K.L. More, H. Wang, M. Wilson, F. Garzon, and L.R. Walker, "Preferential thermal nitridation to form pin-hole free Cr-nitrides to protect proton exchange membrane fuel cell metallic bipolar plates," *Scr. Metall.*, 50(7) (2004), 1017-1022.
4. J. Shu, B.P.A. Grandjean, E. Ghali, and S. Kaliaguine, "Simultaneous deposition of Pd and Ag on porous stainless steel by electroless plating," *J. Membr. Sci.*, 77 (1993), 181-195.
5. P.P. Mardilovich, Y. She, Y.H. Ma, and M.-H. Rei, "Defect-Free Palladium Membranes on Porous Stainless-Steel Support," *AIChE J.*, 44(2) (1998), 310-322.
6. Z. Shi, S. Wu, and J.A. Szpunar, "Bridge Model of Nanoparticles Deposited on Pores Area of the Substrate During a Membrane Fabrication," *Appl. Phys. Lett.*, 87 (2005).
7. F. Roa, J.D. Way, R.L. McCormick, and S.N. Paglieri, "Preparation and characterization of Pd-Cu composite membranes for hydrogen separation," *Chem. Eng. J.*, 93(1) (2003), 11-22.
8. K.S. Rothenberger, A.V. Cugini, B.H. Howard, R.P. Killmeyer, M.V. Ciocco, B.D. Morreale, R.M. Enick, F. Bustamante, I.P. Mardilovich, and Y.H. Ma, "High pressure hydrogen permeance of porous stainless steel coated with a thin palladium film via electroless plating," *J. Membr. Sci.*, 244 (2004), 55-68.
9. C. Su, T. Jin, K. Kuraoka, Y. Matsumura, and T. Yazawa, " Thin Palladium Film Supported on SiO_2- Modified Porous Stainless Steel for a High-Hydrogen-Flux Membrane," *Ind. Eng. Chem. Res.*, 44 (2005), 3053-3058.
10. J. Shu, A. Adnot, B.P.A. Grandjean, and S. Kaliaguine, "Structurally Stable Composite Pd-Ag Alloy Membranes: Introduction of a Diffusion Barrier," *Thin Solid Films*, 286(1-2) (1996), 72-79.
11. S.E. Nam, and K.H. Lee, "Preparation and Characterization of Palladium Alloy Composite Membranes with a Diffusion Barrier for Hydrogen Separation," *Ind. Eng. Chem. Res.*, 44 (2005), 100-105.
12. G. Gao, Y. Li, J.Y.S. Lin, and B. Zhang, "Characterization of zirconia modified porous stainless steel supports for Pd membranes," *J. Porous Mater.*, 13 (2006), 419-426.
13. D.J. Edlund, and J. McCarthy, "The relationship between intermetallic diffusion and flux decline in composite-metal membranes: implications for achieving long membrane lifetime," *J. Membr. Sci.*, 107 (1995), 147-153.
14. R.E. Buxbaum, and A.B. Kinney, "Hydrogen Transport through Tubular Membranes of Palladium-Coated Tantalum and Niobium," *Ind. Eng. Chem. Res.*, 35 (1996), 530-537.
15. N.M. Peachey, R.C. Snow, and R.C. Dye, "Composite Pd/Ta metal membranes for hydrogen separation," *J. Membr. Sci.*, 111 (1996), 123-133.
16. T.S. Moss, N.M. Peachey, R.C. Snow, and R.C. Dye, "Multilayer metal membranes for hydrogen separation," *Int. J. Hydrogen Energy*, 23(2) (1998), 99-106.
17. C. Nishimura, M. Komaki, S. Hwang, and M. Amano, "V--Ni alloy membranes for hydrogen purification," *J. Alloys Compd.*, 330-332 (2002), 902-906.
18. M. Amano, M. Komaki, and C. Nishimura, "Hydrogen permeation characteristic of palladium-plated V-Ni alloy membranes," *J. Less-Common Met.*, 172-174 (1991), 727-731.
19. Y. Zhang, T. Ozaki, M. Komaki, and C. Nishimura, "Hydrogen permeation of Pd-Ag alloy coated V-15Ni composite membrane: effects of overlayer composition," *J. Membr. Sci.*, 224 (2003), 81-91.
20. T. Ozaki, Y. Zhang, M. Komaki, and C. Nishimura, "Hydrogen permeation characteristics of V--Ni--Al alloys," *Int. J. Hydrogen Energy*, 28 (2003), 1229-1225.
21. R.E. Buxbaum, R. Subramanian, J.H. Park, and D.L. Smith, "Hydrogen transport and embrittlement for palladium coated vanadium--chromium--titanium alloys," *J. Nucl. Mater.*, 233-237 (1996), 510-512.
22. K. Hashi, K. Ishikawa, T. Matsuda, and K. Aoki, "Hydrogen permeation characteristics of (V, Ta)-Ti-Ni alloys," *J. Alloys Compd.*, 404 (2005), 273-278.
23. K.S. Rothenberger, B.H. Howard, R.P. Killmeyer, A.V. Cugini, R.M. Enick, F. Bustamante, M.V. Ciocco, B.D. Morreale, and R.E. Buxbaum, "Evaluation of tantalum-based materials for hydrogen separation at elevated temperatures and pressures," *J. Membr. Sci.*, 218 (2003), 19-37.
24. L.C. Witjens, J.H. Bitter, A.J. Van Dillen, W.M. Arnoldbik, F.H.P.M. Habraken, and K.P. de Jong, "Improving the control of the electroless plating synthesis of Pd/Ag membranes for hydrogen separation using Rutherford backscattering," *J. Membr. Sci*, 254 (2005), 241-248.
25. C.L. Hedberg, (1995). "Handbook of Auger electron spectroscopy, 3rd ed." Physical Electronics, Inc., Eden Prairie, Minnesota, U.S.A.
26. M. Mulder. (1991). *Basic Principles of Membrane Technology*, Kluwer Academic Publishers, Dordrecht, The Netherlands.
27. A.Z. Moshfegh, and A. Ignatiev, "Formation and characterization of thin film vanadium oxides. Auger electron spectroscopy, X-ray photoelectron spectroscopy, X-ray diffraction, scanning electron microscopy, and optical reflectance studies," *Thin Solid Films*, 20 (1991), 251.

Advances in Air Brazing:
Braze Sealing Technology for Gas Separation Membranes

K. Scott Weil,[*] Jens T. Darsell,[**] and Jin Yong Kim[*]

[*]Pacific Northwest National Laboratory, 902 Battelle Blvd, P.O. Box 999, Richland, WA 99352
[**]Washington State University, P.O. Box 642920, Pullman, WA 99164-2920

ABSTRACT

Coal is potentially an inexpensive source of clean hydrogen fuel for use in fuel cells, turbines, and various process applications. To realize its potential however, efficient, low-cost gas separation systems are needed to provide high purity oxygen that will enhance the coal gasification reaction and to extract hydrogen from the resulting gas product stream. Several types of inorganic membranes are being developed for hydrogen or oxygen separation, including porous alumina, transition metal oxide perovskites, and zirconia. One of the key challenges in developing solid-state membrane based gas separation systems is in hermetically joining the membrane to the metallic gas manifold system. To address this issue a new metal-ceramic joining concept referred to as air brazing has been developed. This paper reviews recent progress in understanding the underlying mechanisms responsible for wettting between these novel filler metals and ceramic substrates.

INTRODUCTION

As described in the Office of Fossil Energy's FutureGen and Vision 21 Technical Roadmaps, coal is a potential source of clean hydrogen fuel for use in fuel cells, turbines, and various process applications. However to realize this goal, efficient low-cost gas separation systems are needed to provide high purity oxygen to enhance the coal gasification reaction and to extract hydrogen from the resulting gas product stream. Membrane-based separation is also a promising means of removing carbon dioxide from gasified coal, thereby enabling sequestration. Composed primarily of hydrogen, water, carbon monoxide, carbon dioxide, methane, and hydrogen sulfide, high temperature coal gas presents an aggressive chemical environment for the membranes, seals, and support structures that will be used in potential separation devices. The exact composition of the coal gas depends on a number of factors, including how the gas is produced (i.e. through an oxygen or a steam blown process), the oxygen- or steam-to-carbon ratio, the temperature of reaction, and the original composition of the coal itself. Once the gasification reaction is initiated, hydrogen separation can take place. Continuous removal of hydrogen from the high temperature gas stream alters the equilibrium of the gasification reaction via the water-gas shift. The resulting imbalance of hydrogen in the product gas causes water and carbon monoxide to react, forming additional hydrogen and carbon dioxide. Once the removal of hydrogen is complete, the remaining carbon dioxide-rich gas stream is ready for sequestration. Several types of inorganic membranes are being developed for hydrogen separation. Research approaches that are currently being supported by the Office of Fossil Energy include microporous, solid MIEC, and palladium-based separation membranes.

One of the critical issues in designing and fabricating high temperature electrochemical devices such as gas separation equipment is the ability to hermetically seal adjacent metal and ceramic components and ensure that the seal retains its hermeticity, mechanical ruggedness, and chemical stability over the lifetime of the device; typically on the order of several thousand hours. Not only must the sealing materials be stable in gasified coal, they should also provide either a good thermal expansion match or thermomechanical compliance with the membrane and support structures to permit thermal cycling without a loss in hermeticity. Other issues of concern include:

- Retention of hermeticity under prototypical operating conditions
- Acceptable bonding strength
- Long-term chemical compatibility with respect to the adjacent sealing surface materials
- Resistance to hydrogen embrittlement
- Low cost

- Facile processing and high reliability with respect to forming a hermetic seal
- Sealing conditions that do not adversely affect the properties of the components or the performance of the separation membrane

We have recently developed a method of ceramic-to-metal brazing specifically for high temperature membrane materials. Referred to as air brazing, the technique differs from traditional active metal brazing in two important ways: (1) it utilizes a liquid-phase oxide-noble metal melt as the basis for joining and therefore exhibits high-temperature oxidation resistance and (2) the process is conducted directly in air without the use of fluxes and/or inert cover gases. In fact, the strength of the bond formed during air brazing relies on the formation of a thin, adherent oxide scale on the metal substrate. The technique employs a molten oxide that is at least partially soluble in a noble metal solvent to pre-wet the oxide faying surfaces, forming a new surface that the remaining molten filler material easily wets. To date, we have focused our efforts on proof-of-principle development and testing of the Ag-CuO system, for example demonstrating the use of air brazing in joining a variety of ceramic membranes and heat resistant alloys of interest to the FE program, as well as examining the resulting strengths and microstructures of these joints in the as-joined condition; after long-term, high-temperature exposure testing; and upon thermal cycling. Until recently however, little emphasis has been placed on fundamentally understanding the wetting and adhesion characteristics of the braze as a function of composition. Specifically, we want to consider what effect ternary phases may have on the thermodynamic and joining properties of the Ag-CuO system and whether can we use this knowledge to engineer the braze and enhance its performance properties, such as resistance to corrosion in the coal-gas environment. With this in mind, we have continued development of the air brazing technique along two distinct paths, as shown in Figure 1: (1) a series of scientific studies to explore how the base Ag-CuO filler metal can be modified to alter the metallurgical and brazing properties such as lqiuidus/solidus temperature, wettability, joint strength, and maximum exposure temperature of the joint for future fossil energy joining applications and (2) technology development, including an engineering investigation of air brazed joint properties, specifically hermeticity as a function of coal gas exposure. Reported here are results from a recent study to investigate the wetting behavior between various air braze filler metal compositions and a non-reactive ceramic substrate.

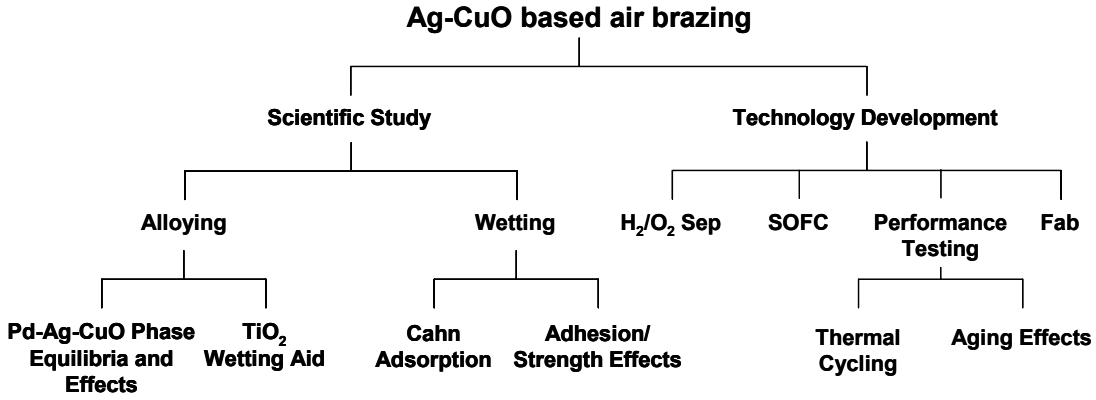

Figure 1 A schematic of the research activities being conducted on air braze technology.

It is well known that immiscible liquids undergo a wetting transition, from partial to complete wetting, at a temperature below the critical point. This was originally predicted in 1977 by Cahn[1] and by Ebner and Saam.[2] Since that time, the phenomenon has gained a significant amount of theoretical attention, which has been surveyed in several excellent review papers.[3-5] Essentially, when two fluid phases coexist near their mutual critical point, one of the fluid phases will form a layer which intrudes between the other fluid phase and any third phase that happens to be present. In the case of a solid substrate adjacent two liquids present under near critical point conditions, one liquid will perfectly wet the solid and thereby encapsulate the second liquid phase excluding it from contact with the solid. As the two liquid system is moved away from its thermodynamic critical point, T_c, to a lower temperature, T_w, a phase transition will occur such that the intruding layer vanishes.

Over the past two decades, substantial progress has been made in the experimental study of this phenomenon with significant attention paid to the transitions observable in room-temperature binary liquids such as methanol-

cyclohexane.[6,7] More recently, work by Freyland and Nattland[8] and by Chatain and Wynblatt and co-workers[9,10] provide experimental evidence of a similar phenomenon in liquid metal systems, namely Ga-Tl and Ga-Pb. Unlike the organic binary liquids, in which bonding is typically characterized by long-range van der Waals interactions, the wetting behavior observed in the metallic systems appeared to be indicative of short ranged interactions. For example in the Ga-Pb system, the wetting transition temperature was found to lie in the metastable region of the liquid miscibility gap (i.e. below the monotectic temperature), far from the critical temperature for the system at approximately $0.3T_c$.[10] In contrast, T_w in the methanol-cyclohexane lies above $0.5T_c$.[6]

In our recent development of braze filler metals based on the Ag-CuO system, we observed evidence of a first-order wetting transition. Like the previously studied liquid metal systems, the Ag-CuO phase diagram displays a wide region of liquid-liquid immiscibility, in this case between a silver-rich liquid L_2 and a copper oxide-rich liquid L_1, that lies above the 969°C monotectic reaction temperature[11] as shown in Figure 2. Rule of mixtures estimates of the densities of the two liquids in the miscibility gap indicate that the density of silver-rich L_2 should be greater than that of L_1 by nearly 40%. However as will be shown, due to its lower surface energy with the yttria-stabilized zirconia (YSZ) substrate the copper oxide-rich liquid maintains a condition of complete wetting despite being the lighter of the two fluids.

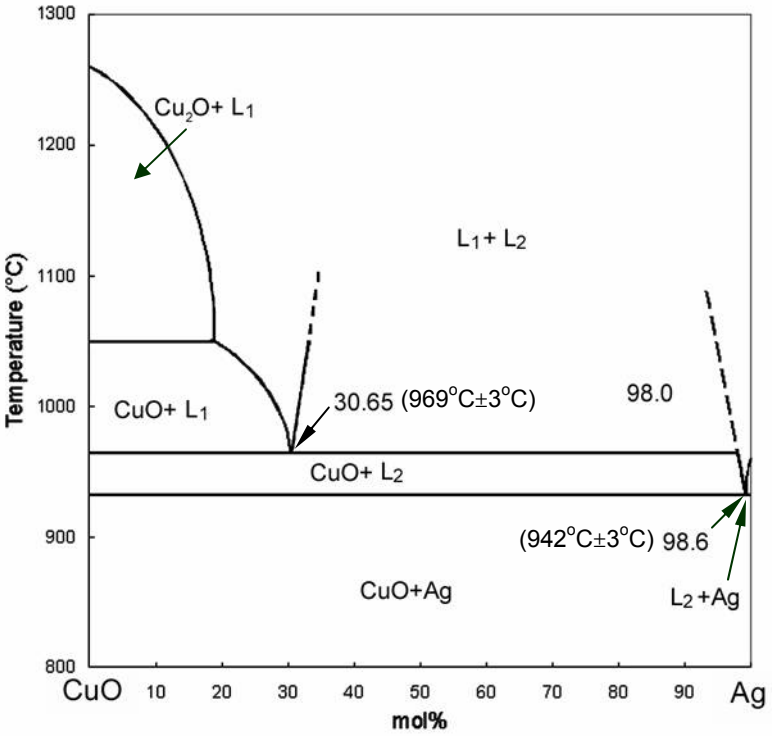

Figure 2 Ag-CuO phase diagram, from Ref [11] with updated invariant reaction temperatures based on Ref [12].

EXPERIMENTAL

Materials: YSZ discs measuring ~3 cm in diameter and ~0.5 cm in thickness were used in the wetting experiments. These were prepared by isostatically cold-pressing 8 mol% yttria-stabilized zirconia powder (YSZ, Tosoh) into pellets under a pressure of 150 MPa. These pellets were subjected to sintering in static air at 1450°C for 1 h. The sintered discs were then polished along one face to a 10 μm finish, ultrasonically cleaned in methanol, and dried at 300°C for 1hr prior to use. Polycrystalline YSZ cups containing 8 mol% yttria (Netzsch) and measuring 7 mm tall x 7 mm in diameter x 0.7mm wall thickness were used in the quenching experiments.

The Ag-CuO compositions employed in both the wetting and quenching experiments were prepared by mixing copper powder (99% purity; 1 – 1.5 μm average particle size; Alfa Aesar) and silver powder (99.9% purity; 0.5 – 1 μm average particle size; Alfa Aesar) in the appropriate ratios to yield the compositions given in Table I. It has been previously shown that the copper readily oxidizes to become CuO under the air brazing conditions.[12] The braze compositions given in Table 1 take this into account. The powder mixtures were then pressed into pellets measuring ~ 0.6 mm in diameter by 0.6 mm thick.

Testing and Characterization: Wetting experiments were conducted by the classical sessile drop technique.[13] Each Ag-CuO pellet was placed on a polished YSZ substrate and heated through a series of temperatures above which the pellet becomes molten. Changes in the braze droplet's base diameter, height, and angle of contact with the substrate were monitored by high speed video camera. The specimens were heated at 30°C/min to a sub-liquidus temperature of 900°C, at which point the heating rate was reduced to10°C/min for the rest of the cycle. Once stable at 900°C, the furnace temperature was raised to 950°C, where it remained for fifteen minutes. It was then increased again to a second isothermal hold at 1000°C for fifteen minutes, followed by a fifteen minute soak at 1050°C, and again at 1100°C. In this way, the shape of the sessile drop was allowed to stabilize for measurement at each temperature. Once the wetting experiment concluded, each sample was quenched at 10°C/min to 550°C, then furnace cooled to room temperature. Conversion of the analog video data to digital form for image analysis was performed using VideoStudio6™ (Ulead Systems, Inc.) frame capturing and video editing software. The digitalized images were subsequently imported into Canvas™ graphic software (version 8.0.5, Deneba Systems, Inc.) for droplet shape measurement. The outline of the droplet was circumscribed with a circle of best fit, which was used to determine the droplet's radius. The contact angle was then calculated from the radius and the diameter of contact between the droplet and the substrate.

Table 1. Target compositions of the Ag-CuO filler materials investigated in this study

Braze ID	Ag content (mol%)	CuO content (mol%)
CA0	100	0
CA01	99	1
CA01.4	98.6	1.4
CA01.8	98.2	1.8
CA02	98	2
CA03	97	3
CA04	96	4
CA05	95	5
CA07	93	7
CA08	92	8
CA10	90	10
CA16	84	16
CA34	66	34
CA69	30.7	69.3

A series of quenching experiments were conducted in an effort to capture the original molten state of the wetting specimens. In each experiment a silver-copper oxide pellet was set into a YSZ crucible that was then placed onto a fecralloy harness as shown in Figure 3. The harness was tied to a fecralloy wire such that the specimen could be suspended in the hot zone of a vertical tube furnace. The specimen was heated at 3°C/min to the temperature of interest and held for 30 min to reach equilibrium. The insulation plug at the bottom of the furnace was then removed and the wire cut, allowing the specimen to drop into a room temperature water bath. Subsequent to quenching, the samples were sectioned and mounted for examination. Microstructural analysis was conducted on polished cross-sectioned samples by scanning electron microscopy (SEM; JEOL, JSM-5900LV) and energy dispersive X-ray analysis (EDX; Oxford Systems). The SEM is equipped with a windowless detector, allowing detection and quantitative measurement of both light and heavy elements. To avoid electrical charging of the samples in the SEM,

they were carbon coated and grounded. Elemental profiles were recorded across joint interfaces in the line-scan mode.

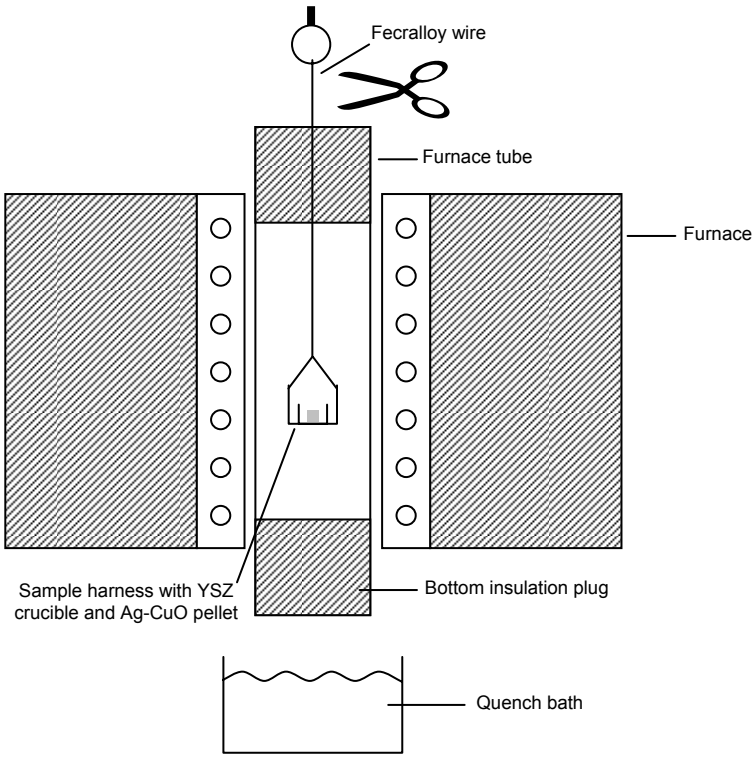

Figure 3 A schematic of the equipment used in the quenching experiments.

RESULTS AND DISCUSSION

Wetting Experiments: Shown in Figures 4(a) and (b) are the contact angles measured between molten Ag-CuO and YSZ as a function of copper oxide content and temperature. During the initial stage of heating each composition, liquefaction was observed to begin approximately at the temperature predicted by the Ag-CuO phase diagram,[5] implying that neither diffusion nor solid-state reaction kinetics significantly impeded the CuO and Ag from reaching equilibrium. In addition, the fifteen minute isothermal dwell times employed in the heating cycle appeared to be sufficiently long for the contact angles to reach their equilibrium values. As seen in Figure 4(a), the addition of CuO causes a significant decrease in the contact angle between the molten drop and YSZ, from the non-wetting condition displayed by pure silver to an apparent minimum value reached at ~35mol% CuO. Much of the drop occurs in a narrow compositional band bounded at an upper limit of $X_{CuO} \approx$ 4mol%. In fact, each curve appears to consist of three distinct regions, as defined by obvious changes in slope: (1) $0 < X_{CuO} \lesssim$ 4mol%, where the greatest decrease in contact angle occurs; (2) 4mol% $\lesssim X_{CuO} \lesssim$ 35mol%, denoted by a more gradual decrease in contact angle as a function of composition; and (3) 35mol% $\lesssim X_{CuO} \lesssim$ 69mol%, in which a small, but reproducible increase in contact angle is observed at the end point composition. In Figure 4(b), a second compositional effect on wetting behavior is observed. Below 4mol% CuO content (specimens CA0 – CA02), the contact angle appears to be nearly invariant of temperature. However at this threshold and above, the contact angle displays a small but measurable decrease with increasing temperature.

When the first derivative of the contact angle with respect to composition is plotted as a function of composition, as in Figure 5, a “near step” change can be observed in each isothermal curve [which appear to lie upon each other, but as shown in Figure 6(a) do not]. Note that changes in the slope of the isothermal curves in Figure 4(a) are not

completely abrupt, leading to some ambiguity in identifying the exact composition at which each break takes place. In an effort to provide some clarity, a tangent line was drawn from the initial point on the derivative curve to the abscissa or compositional axis, by focusing on the narrow low-CuO concentration portion of the diagram as in Figure 6(a). Direct comparison with the Ag-CuO phase diagram of Nishiura et al.,[14] Figure 6(b), indicates that the discontinuities occur approximately at the corresponding silver-rich miscibility gap boundary compositions for each temperature. That is, the first order change in equilibrium contact angle appears to be due to the formation of a second liquid phase.

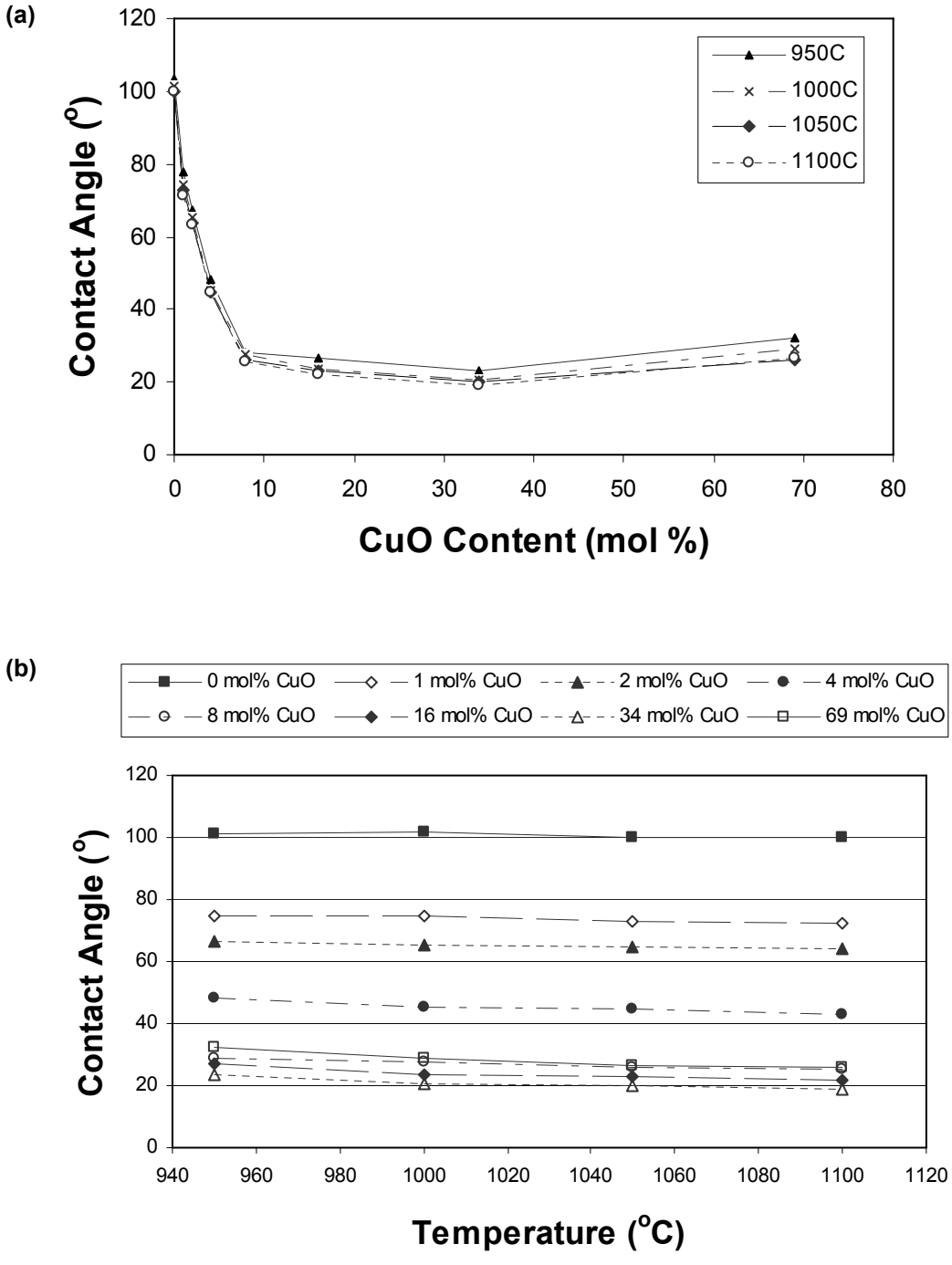

Figure 4 A plot of the contact angle formed between Ag-CuO and YSZ as a function of: (a) CuO content and (b) temperature.

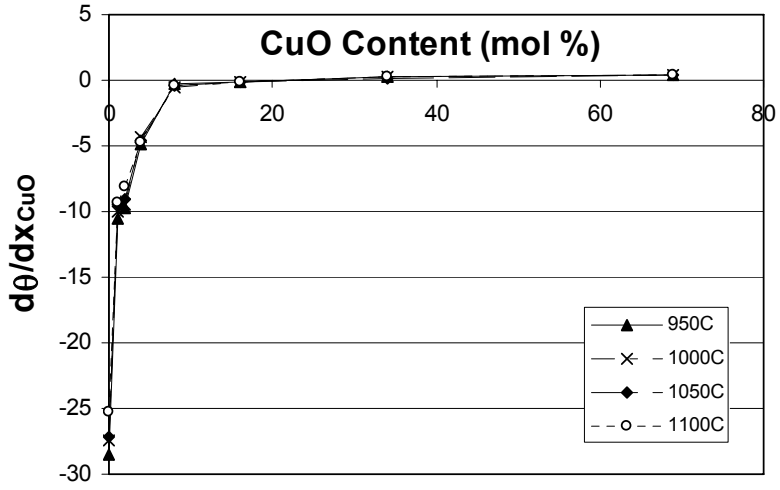

Figure 5 A plot of the derivative of contact angle as a function of composition for each hold temperature.

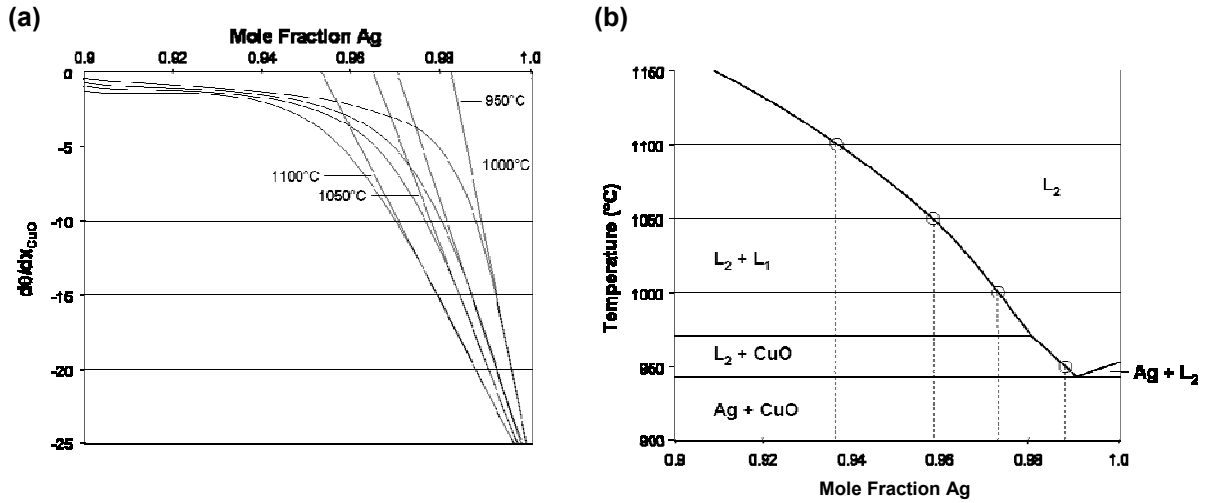

Figure 6 Plots of the silver-rich portions of (a) Figure 5 and (b) Figure 2. A comparison between the two indicates the correspondence between the discontinuities in the isothermal contact angle curves and the miscibility gap boundary compositions at each temperature.

Quenching Experiments: Subsequent to the wetting experiments, two series of quenching experiments were conducted at 1000°C and 1100°C in an effort to capture direct evidence of the nature of the wetting transition observed in Figures 4 and 5. Specifically, pellets were prepared with the following compositions in order to bracket the silver-rich miscibility gap boundary compositions at each of the two temperatures: (a) 1000°C; 1mol% CuO, 1.4 mol% CuO, 1.8 mol% CuO, 3mol% CuO, 5 mol% CuO, 7 mol% CuO, and 10 mol% CuO and (b) 1100°C; 3 mol% CuO, 5 mol% CuO, 7 mol% CuO, and 10 mol% CuO, with the balance silver in each case. Shown in Figures 7 and 8 are back-scattered electron images of typical as-quenched monophasic and diphasic Ag-CuO liquids in contact with a YSZ crucible after allowing each sample to equilibrate at 1000°C and 1100°C, respectively.

In the specimen wetted by 1mol% CuO in Ag (CA01) and quenched from an equilibrium temperature of 1000°C, shown in Figure 7(a), the copper oxide is observed both in the solidified silver matrix that made up the bulk of the liquid sessile drop and along the interface with the YSZ as fine-scale precipitates measuring approximately 1 – 2μm in size. Along the interface with the YSZ, both silver and copper oxide are observed. Reference to the Ag-CuO phase diagram suggests that this microstructure results from a single phase liquid, L_2. Results obtained upon quenching from a two-phase liquid region are found in Figure 7(b), which displays the interface within a CA03 specimen that was equilibrated at 1000°C. A higher magnification image is shown in Figure 7(d). Note the very fine-scale, interwoven monotectic structure in contact with the YSZ interface. Since it is the copper oxide-rich L_1 liquid that undergoes monotectic decomposition, these two micrographs provide evidence that this liquid preferentially wets the YSZ substrate, even though it is the lighter of the two liquids (i.e. of much higher oxide content) present at 1000°C. With a composition that lies further in the diphasic liquid region, the CA05 specimen as quenched from 1000°C is shown in Figure 7(c). Again the oxide-rich L_1 liquid appears to have segregated to the YSZ interface forming an even thicker intruding layer when molten, over six times that observed in the CA03 specimen.

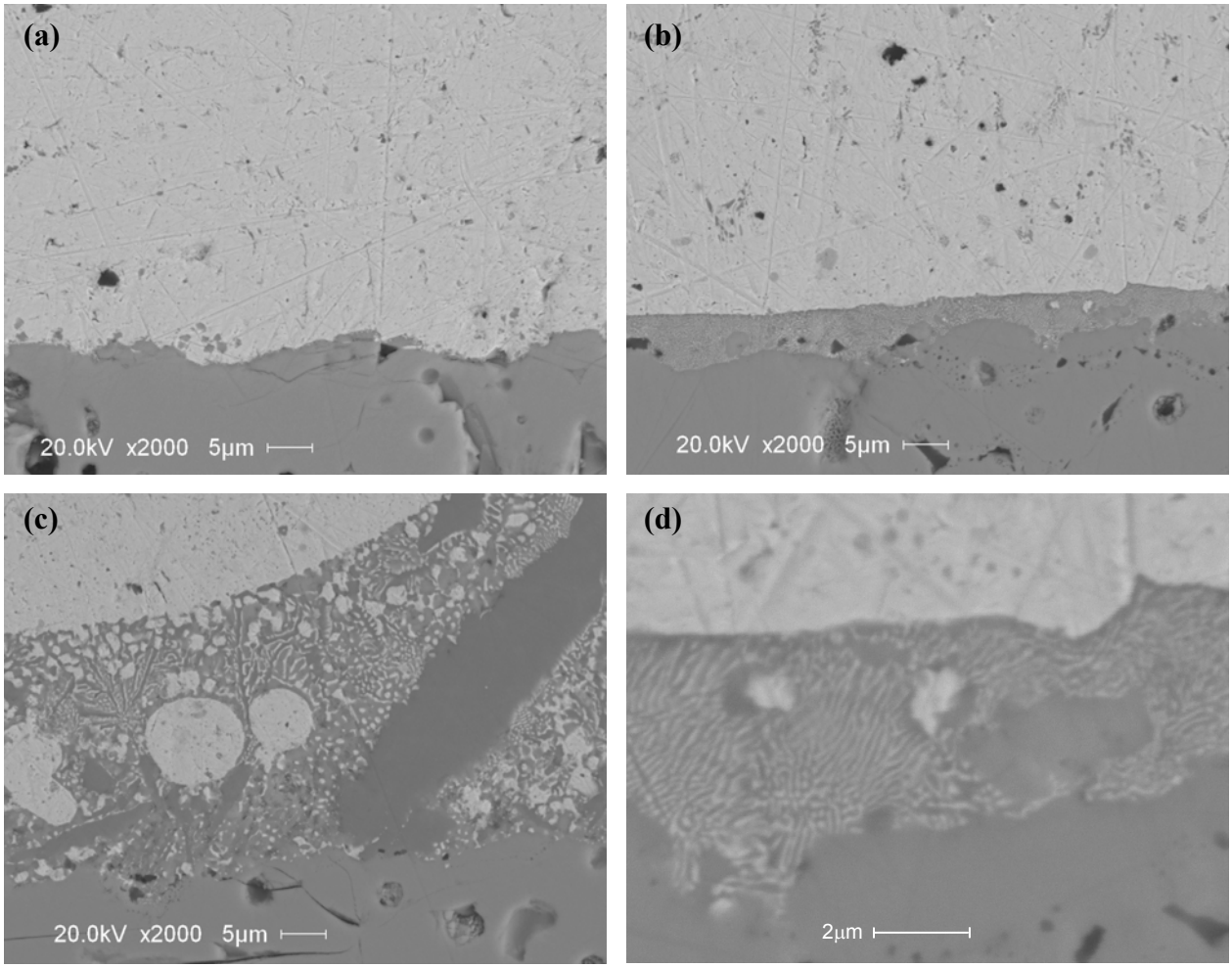

Figure 7 Cross-sectional SEM micrographs of the Ag-CuO/YSZ interface in the following specimens quenched from 1000°C: (a) CA01, (b) CA03, (c) CA05. A higher magnification micrograph of the interfacial region in the CA03 specimen is shown in (d). The YSZ appears as the darker gray, homogeneous material in the lower half of each picture, while silver has a lighter gray contrast. The copper oxide appears as the darker gray phase in the solidified material. The black regions are voids.

The second series of micrographs (Figure 8), taken of specimens that were quenched from 1100°C, display characteristics with respect to interfacial microstructure that are similar to the first set except that the corresponding compositions have shifted to higher CuO content. For example, the sample that displays the microstructure of a quenched monophasic liquid is CA03, Figure 8(a), whereas at lower temperature this same composition yielded a diphasic structure. Similarly, in Figure 8(b) the remnant of the intruding oxide-rich liquid layer in the CA05 specimen equilibrated at 1100°C is much thinner than that equilibrated at 1000°C. Even the intruding liquid of the CA07 specimen in Figure 8(c) is thinner, up to the leading edge of the sessile drop which is dominated by the copper oxide rich L_1 liquid. Note that this liquid encapsulates the silver-rich liquid, keeping it from wetting the solid substrate.

When compared with the contact angle data given in Figures 4 – 6, two major conclusions can be drawn from the microstructural data obtained on the quenched specimens: (1) the continuous and sharp decrease in contact angle observed between 0 and 8 mol% CuO in silver in Figure 4(a) is due to CuO adsorption at the silver-YSZ interface that leads to a decrease in interfacial energy and (2) the approximate first order change in contact angle with composition observed in Figure 6(a) is due to the formation of a diphasic liquid state as the miscibility gap

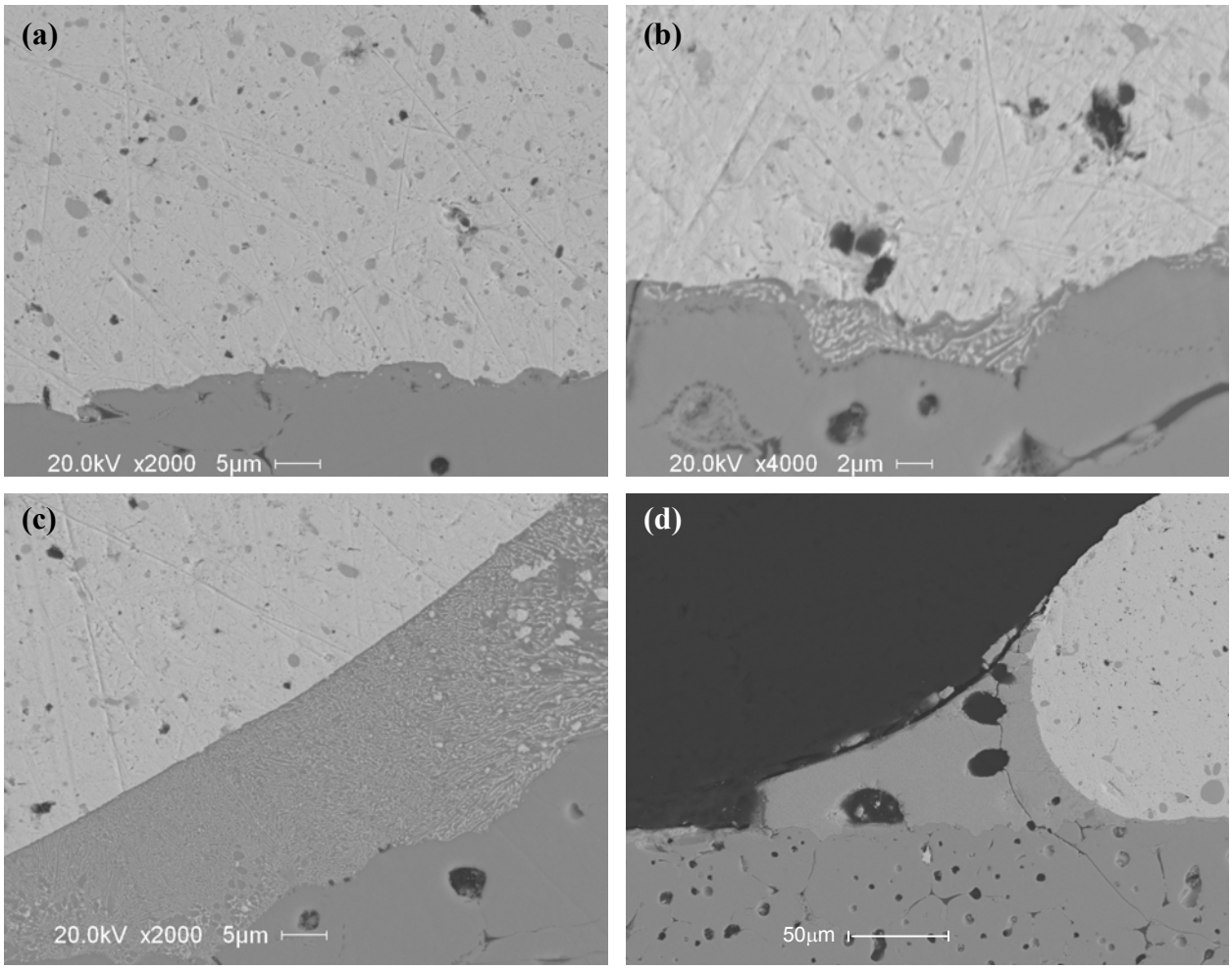

Figure 8 Cross-sectional SEM micrographs of the Ag-CuO/YSZ interface in the following specimens quenched from 1100°C: (a) CA03, (b) CA05, (c) CA07. A micrograph of the leading edge of the as-quenched CA07 sessile drop is shown in (d). The YSZ appears as the darker gray, homogeneous material in the lower half of each picture, while silver has a lighter gray contrast. The copper oxide appears as the darker gray phase in the solidified material. The black regions are voids.

boundary is isothermally crossed. Even though it is greater in density, the silver-rich liquid does not displace the copper oxide-rich liquid and is hindered from wetting the YSZ substrate by an intruding L_1 liquid film. A similar observation was made by Wang et al. of the wetting of graphite by Pb-Ni alloys.[15] In addition, evidence of encapsulation of the silver-rich liquid by the copper-rich liquid is a signature of complete wetting of L_2 by L_1. From the contact angle data in Figures 4(a) and 6(a), this phenomenon appears to occur at the monotectic temperature, i.e. the lowest temperature at which the two liquids can coexist in equilibrium, suggesting that if a critical wetting transition of the type predicted by Cahn exists, it must occur in the metastable region of liquid-liquid coexistence and therefore would only be observed upon careful super-cooling below the monotectic temperature. As has been previously noted by Chatain et al.[10] in their work on wetting transitions in liquid Ga-Pb alloys, this corresponds to the "wet-not-wet" scenario discussed by Pandit and Fisher.[16]

CONCLUSIONS

The addition of copper oxide to silver enhances wetting on YSZ substrates via CuO adsorption at the interface. As the miscibility gap is entered isothermally from the monophasic L_2 liquid region, the wetting mechanism changes abruptly. Two immiscible liquids form within the sessile drop and the one containing the higher copper oxide content intrudes between the second liquid and the substrate forming a thin liquid film. In addition, evidence of complete wetting of the two liquids down to the monotectic temperature for the Ag-CuO system implies that a critical wetting transition, if it exists, likely takes place in the metastable liquid-liquid domain.

ACKNOWLEDGEMENTS

This work was supported by the U.S. Department of Energy, Office of Fossil Energy, Advanced Research and Technology Development Program. The Pacific Northwest National Laboratory is operated by Battelle Memorial Institute for the United States Department of Energy (U.S. DOE) under Contract DE-AC06-76RLO 1830.

REFERENCES

[1] J. W. Cahn, J. Chem. Phys., **66**, 3667 (1977).
[2] C. Ebner and W. F. Saam, *Phys. Rev. Lett*., **38**, 1486 (1977).
[3] D. Bonn and D. Ross, *Rep. Prog. Phys.*,**64**, 1085 (2001).
[4] P. G. de Gennes, *Rev. Mod. Phys*., **57**, 827 (1985).
[5] M. Schick, "Liquids at Interfaces," *Les Houches Sessions***,** ed. J. Charvolin, 1990, Amsterdam: Elsevier, p. 415.
[6] M. R. Moldover and J. W. Cahn, *Science*, **207,** 1073 (1980).
[7] H. Kellay, D. Bonn, and J. Meunier, *Phys. Rev. Lett*., **71**, 2607 (1993).
[8] W. Freyland and D. Nattland, *Ber. Bunsenges. Phys. Chem*., **102**, 1 (1998).
[9] H. Shim, P. Wynblatt, D. Chatain, *Surf. Sci.*, **476**, L273 April (2001).
[10] D. Chatain and P. Wynblatt, Surf. Sci., **345**, 85 (1996).
[11] Z.B. Shao, K.R. Liu, L.Q. Liu, H.K. Liu, S. Dou, *J. Amer. Cer. Soc*., **76**, 2663 (1993).
[12] J. T. Darsell and K. S. Weil, *J. Ph. Equil. Diff*., in press.
[13]D.A. Mortimer and M.G. Nicholas, *J. Mater. Sci*., **8**, 640 (1973).
[14]H. Nishiura, R. O. Suzuki, K. Ono, and L. J. Gauckler, *J. Amer. Cer. Soc*., **81**, 2181 (1998).
[15]Z. Wang, P. Wynblatt, and D. Chatain, Interf. Sci., **7**, 173 (1999).
[16]R. Pandit and M. E. Fisher, *Phys. Rev. Lett*., **51**, 1772 (1983).

APPENDIX 1

FINAL PROGRAM

PROGRAM FOR THE

20TH ANNUAL CONFERENCE ON FOSSIL ENERGY MATERIALS
HILTON-KNOXVILLE; 501 W CHURCH AVENUE (DOWNTOWN)
KNOXVILLE, TENNESSEE
JUNE 12-14, 2006

Monday, June 12th, 2006

12.00 noon Registration

1.00 pm Welcome and Introductory Remarks
Roddie Judkins, Oak Ridge National Laboratory

1.10 pm Brief Update on DOE's Advanced Research Materials Program
Robert Romanosky, U.S. Department of Energy, National Energy Technology Laboratory

Session 1 – NEW ALLOYS

1.25 pm Introduction/Chair
Roddie Judkins, Oak Ridge National Laboratory

1a. High-Temperature 'Conventional' Wrought Alloys

1.30 pm Advanced Pressure Boundary Materials
Mike Santella, Oak Ridge National Laboratory

2.05 pm Fireside and Steamside Corrosion of Alloys for USC Plants
Ken Natesan, Argonne National Laboratory

2.40 pm Multiphase HT Alloys: Exploration of Laves-Strengthened Steels
Mike Brady, Oak Ridge National Laboratory

3.15 pm Break

1b. Oxide Dispersion-Strengthened Alloys

3.45 pm Enabling the Practical Application of Oxide Dispersion-Strengthened Ferritic Steels
Ian Wright, ORNL

4.20 pm Control of Defects and Microstructure in ODS Alloys
Andy Jones, University of Liverpool

4.55 pm Optimization of ODS –FE_3AL and MA956 Alloy Heat Exchanger Tubes
Bimal Kad, University of California at San Diego

5.30 pm Adjourn

Monday, June 12th, 2006

6.00-7.30 p.m. Networking and Poster Session

BREAKTHROUGH CONCEPTS

Session 2 – POSTERS

1. Development of Ultra-High Temperature Molybdenum Borosilicides
   Joachim Schneibel, Oak Ridge National Laboratory, and Rob Ritchie, UC Berkeley

2. Optimizing Processing of Mo-Si-B Intermetallics Through Thermodynamic Assessment of the Mo-Si-B and Related Systems
   Matt Kramer, Ames Laboratory

3. Effects of Tungsten on the Microstructures of TiAl-Based Intermetallics
   Peter Liaw, University of Tennessee

4. Influence of Impurities on Ductility of Cr-Based Alloys and In-situ Mechanical Property Measurement
   Bruce Kang, West Virginia University

5. Microstructure and Properties of HVOF-Sprayed Ni-50Cr Coatings
   Richard Wright, Idaho National Engineering and Environmental Laboratory

6. New Processing Developments in Metallic Powders for Fossil Energy Applications
   Iver Anderson, Robert Terpstra, Ames Laboratory

7. Steam Turbine Materials and Corrosion
   Gordon Holcomb, U.S. Department of Energy, National Energy Technology Laboratory

8. Fireside Corrosion Probes: How Well Do They Work?
   Bernie Covino, U.S. Department of Energy, National Energy Technology Laboratory

9. In-Plant Corrosion Probe Tests
   Gregg Stanko, Foster Wheeler Development Corporation

10. Corrosion and Joining of ODS FeCrAl Alloys for Very High Temperature Heat Exchangers
    John Hurley, University of North Dakota, Energy and Environmental Research Center

Tuesday, June 13th, 2006

7.30 am Continental Breakfast

Session 3 – COATINGS & PROTECTION OF MATERIALS

8.30 am Introduction/Chair
Udaya Rao, U.S. Department of Energy, National Energy Technology Laboratory

3a. Metallic Coatings for Structural Alloys

8.40 am Aluminide Coatings for Power Generation Applications
Ying Zhang, Tennessee Technology University

9.15 am High-Temperature Corrosion Resistance of Candidate FeAlCr Coatings in Low NO_x Environments
Joe Murphy, Lehigh University

9.50 am Concepts for Smart, Protective High-Temperature Coatings
Peter Tortorelli, Oak Ridge National Laboratory

10.25 am Break

3b. Ceramic/Composite Coatings

10.55 am YSZ Thermal Barrier Coatings by MOCVD
Ted Besmann, Oak Ridge National Laboratory

11.30 am Protection Systems: Corrosion-Resistant Coatings
Beth Armstrong, Oak Ridge National Laboratory

12.05 pm Development of Nondestructive Evaluation Methods for Ceramic Coatings
Bill Ellingson, Argonne National Laboratory

Working Lunch

12:40 pm Presentation by Roddie R. Judkins, Director, ORNL Fossil Energy Program

Session 4 – Functional Materials

2.00 pm Introduction/Chair, Cindy Powell
U.S. Department of Energy, National Energy Technology Laboratory

4a. Ceramics & Refractories

2.10 pm Low-Chrome/Chrome Free Refractories for Slagging Gasifiers
James Bennett, Albany Research Center

2.45 pm Pilot Facility for the Production of Silicon Carbide Fibrils
Richard Nixdorf, ReMaxCo Technologies, Inc.

3.20 pm Break

4b. Activated Carbon Structures

3.50 pm Activated Carbon Composites for Air Separation
Fred Baker, Oak Ridge National Laboratory

4c. Inorganic Membranes & Structures

4.25 pm Gas Sensors for Fossil Energy Applications
Tim Armstrong, Oak Ridge National Laboratory

5.00 pm Adjourn

Wednesday, June 14th, 2006

7.30 am Continental Breakfast

8.30 am Introduction/Chair
Tim Armstrong, Oak Ridge National Laboratory

3extra. Metallic Coatings for Structural Alloys

8.40 am Extended Alloy Lifetimes Through Improved Coating Performance and Composition Optimization
Bruce Pint, Oak Ridge National Laboratory

Session 4 – FUNCTIONAL MATERIALS (CONTINUED)

4c. Inorganic Membranes & Structures (continued)

9.15 am Development of Inorganic Membranes for Hydrogen Separation
Brian Bischoff, Oak Ridge National Laboratory

9.50 am Metal Membranes for Hydrogen Separation
Steve Paglieri, Los Alamos National Laboratory

10.25 am Break

11.00 am Brazing Technology for Gas Separation Membranes: Advances in Air Brazing
Scott Weil, Pacific Northwest National Laboratory

11.35 am Closing Remarks
Robert Romanosky
U.S. Department of Energy, National Energy Technology Laboratory
Roddie Judkins
Oak Ridge National Laboratory

12.00 pm. Adjourn

APPENDIX 2

LIST OF ATTENDEES

EVENT PARTICIPANT LIST

20th Annual Conference on Fossil Energy Materials
June 12, 2006 - June 14, 2006

1. Derek Allen
   ALSTOM Power
   Cambridge Road
   Whetstone
   Leicester, UK LE8 6LH
   Phone: 44/11-6284-5624
   Fax: 44/11-6284-5456
   E-mail: derek.allen@power.alstom.com

2. Mary Anne Alvin
   U.S. Department of Energy
   National Energy Technology Laboratory
   P.O. Box 10940, MS 58-202A
   Pittsburgh, PA 15236-0940
   Phone: 412/386-5498
   Fax: 412/386-4806
   E-mail: maryanne.alvin@netl.doe.gov

3. Beth Armstrong
   Oak Ridge National Laboratory
   One Bethel Valley Road
   MS 6063
   Oak Ridge, TN 37716
   Phone: 865/241-5862
   Fax: 865/574-6918
   E-mail: armstrongbl@ornl.gov

4. Tim Armstrong
   Oak Ridge National Laboratory
   One Bethel Valley Road
   MS 6186
   Oak Ridge, TN 37831
   Phone: 865/574-7996
   Fax: 865/241-0112
   E-mail: armstrongt@ornl.gov

5. Fred Baker
   Oak Ridge National Laboratory
   One Bethel Valley Road
   MS 6087
   Oak Ridge, TN 37831
   Phone: 865/241-1127
   Fax: 865/576-8424
   E-mail: bakerfs@ornl.gov

6. James Bennett
   U.S. Department of Energy
   National Energy Technology Laboratory
   1450 Queen Avenue, SW
   Albany, OR 97321
   Phone: 541/967-5983
   Fax: 541/967-5845
   E-mail: bennett@netl.doe.gov

7. Theodore M. Besmann
   Oak Ridge National Laboratory
   P.O. Box 2008
   MS 6063
   Oak Ridge, TN 37830
   Phone: 865/574-6852
   Fax: 865/574-6918
   E-mail: besmanntm@ornl.gov

8. Ron Bhada
   New Mexico State University
   WERC, Eng. Complex 3
   P.O. Box 30001, MSC WERC
   Las Cruces, NM 88003
   Phone: 770/389-4836
   Fax: 770/474-7869
   E-mail: ronbhada@aol.com

EVENT PARTICIPANT LIST

20th Annual Conference on Fossil Energy Materials
June 12, 2006 - June 14, 2006

9. Brian Bischoff
Oak Ridge National Laboratory
P.O. Box 2008
MS 6044
Oak Ridge, TN 37831-6205
Phone: 865/241-3172
Fax: 865/576-3502
E-mail: bischoffbl@ornl.gov

10. Charles Boohaker
Southern Company Services
600 North 18th Street
Mail Stop 14N-8195
Birmingham, AL 35203
Phone: 205/257-7537
Fax: 205/257-5367
E-mail: cgboohak@southernco.com

11. Mike Brady
Oak Ridge National Laboratory
One Bethel Valley Road
MS 6115
Oak Ridge, TN 37831-6115
Phone: 865/574-5153
Fax: 865/241-0215
E-mail: bradymp@ornl.gov

12. Leslie Buchanan
Mitsui Babcock Energy Limited
Porterfield Road
Suite 1200
Atlanta, GA 30338
Phone: 44 (0) 1418853969
Fax: 44 (0) 1418853668
E-mail: lbuchanan@mitsuibabcock.com

13. Domenic Andrew Canonico
Consultant
35 Old Riding Way
Signal Mountain, TN 37377
Phone: 423/886-7730
Fax: 423/886-7730
E-mail: canonicod@bellsouth.net

14. Ashok Choudhury
Oak Ridge National Laboratory
One Bethel Valley Road
MS 6196
Oak Ridge, TN 37831
Phone: 865/574-0393
Fax: 865/574-9241
E-mail: choudhurya@ornl.gov

15. Bob G. Coleman
Engineered Fiber Solutions, Inc.
3619 Burning Tree Ct.
Augusta, GA 30907
Phone: 706/860-5047
Fax: 706/860-6611
E-mail: bobcoleman137@comcast.net

16. Cristian Contescu
Oak Ridge National Laboratory
One Bethel Valley Road
P.O. Box 2008, MS 6087
Oak Ridge, TN 37831
Phone: 865/241-3318
Fax: 865/576-8424
E-mail: contescuci@ornl.gov

EVENT PARTICIPANT LIST

20th Annual Conference on Fossil Energy Materials
June 12, 2006 - June 14, 2006

17. Kevin Cooley
Oak Ridge National Laboratory
One Bethel Valley Road
MS 6063
Oak Ridge, TN 37831
Phone: 865/938-3044
Fax: 865/574-6918
E-mail: cooleykm@ornl.gov

18. Bernard Covino
U.S. Department of Energy
National Energy Technology Laboratory
1450 Queen Avenue, SW
Albany, OR 97321
Phone: 541/967-5828
Fax: 541/967-5914
E-mail: bernard.covino@netl.doe.gov

19. Sebastien Dryepondt
Oak Ridge National Laboratory
One Bethel Valley Road
MS 6156
Oak Ridge, TN 37831
Phone: 865/241-5158
Fax: 865/241-0215
E-mail: dryepondtsn@ornl.gov

20. Richard Dunst
U.S. Department of Energy
National Energy Technology Laboratory
P.O. Box 10940, MS 922-273C
Pittsburgh, PA 15236-0940
Phone: 412/386-6694
Fax: N/A
E-mail: dunst@netl.doe.gov

21. William A. Ellingson
Argonne National Laboratory
9700 South Cass Avenue
Bldg. 212
Argonne, IL 60439
Phone: 630/252-5068
Fax: 630/252-4798
E-mail: ellingson@anl.gov

22. Carl Evenson
Eltron Research Inc.
4600 Nautilus Court South
Boulder, CO 80301
Phone: 303/530-0263
Fax: 303/530-0264
E-mail: folson@eltronresearch.com

23. Fred Glaser
U.S. Department of Energy
19901 Germantown Road
MS FE-22
Germantown, MD 20874
Phone: 301/903-2676
Fax: N/A
E-mail: fred.glaser@hq.doe.gov

24. Stephen Goodstine
ALSTOM Power Inc.
2000 Day Hill Road
Windsor, CT 06095
Phone: 860/285-5686
Fax: 860/285-4033
E-mail: stephen.l.goodstine@power.alstom.com

EVENT PARTICIPANT LIST

20th Annual Conference on Fossil Energy Materials
June 12, 2006 - June 14, 2006

25. Robert Gottschall
6421 Hollins Drive
Bethesda, MD 20817-2347
Phone: 301/530-8875
Fax: N/A
E-mail: bobyukiko@yahoo.com

26. Steve Halcomb
Tennessee Valley Authority
1101 Market Street
Chattanooga, TN 37402
Phone: 423/751-4522
Fax: N/A
E-mail: smhalcomb@tva.gov

27. Gordon Holcomb
U.S. Department of Energy
NETL Albany
1450 Queen Ave., SW
Albany, OR 97321
Phone: 541/967-5874
Fax: 541/967-5914
E-mail: Gordon.Holcomb@netl.doe.gov

28. John P. Hurley
Energy & Environmental Research Center
15 N. 23rd Street
Mail Stop 9018
Grand Forks, ND 28503
Phone: 701/777-5000
Fax: 701/777-5181
E-mail: jhurley@undeerc.org

29. Andrew P. Jones
SAIC
P.O. Box 10940
MS 922-273C
Pittsburgh, PA 15236
Phone: 412/386-5531
Fax: 412/386-4516
E-mail: andrew.jones@netl.doe.gov

30. Roddie Judkins
Oak Ridge National Laboratory
One Bethel Valley Road
MS 6084
Oak Ridge, TN 37831
Phone: 865/574-4572
Fax: 865/574-4357
E-mail: judkinsrr@ornl.gov

31. Bimal Kad
University of California-San Diego
409 University Center
La Jolla, CA 92093
Phone: 858/534-7059
Fax: 858/534-6373
E-mail: bkad@ucsd.edu

32. Bruce S. Kang
West Virginia University
Mechanical and Aerospace Engineering
Morgantown, WV 26506
Phone: 304/293-3111 x 2316
Fax: 304/293-6689
E-mail: bruce.kang@mail.wvu.edu

EVENT PARTICIPANT LIST

20th Annual Conference on Fossil Energy Materials
June 12, 2006 - June 14, 2006

33. Bohumil Kazimierzak
Via-Cesty, s.r.o.
Oscadnica 1180
Oscadnica, Slovak Republic 023 01
Phone: 421905461562
Fax: 421414332623
E-mail: viacesty@viacesty.sk

34. James Keiser
Oak Ridge National Laboratory
P.O. Box 2008
MS 6156
Oak Ridge, TN 37831-6156
Phone: 865/574-4453
Fax: 865/241-0215
E-mail: keiserjr@ornl.gov

35. Matthew Kramer
Ames Laboratory
225 Wilhelm Hall, ISU
Ames, IA 50011
Phone: 515/294-0276
Fax: 515/294-4281
E-mail: mjkramer@ameslab.gov

36. Peter K. Liaw
University of Tennessee
Materials Science Engineering
434 Dougherty Hall
Knoxville, TN 37996
Phone: 865/974-5304
Fax: 865/974-4115
E-mail: pliaw@utk.edu

37. Zhao-Ping Lu
Oak Ridge National Laboratory
One Bethel Valley Road
MS 6115
Oak Ridge, TN 37831
Phone: 865/576-7196
Fax: 865/574-7659
E-mail: luzp@ornl.gov

38. Mani Manivannan
U.S. Department of Energy
National Energy Technology Laboratory
P.O. Box 880, MS E06
Morgantown, WV 26507-0880
Phone: 304/285-2078
Fax: 304/285-4638
E-mail: manivana@netl.doe.gov

39. Ravi Menon
Thermadyne Stoody
5557 Nashville Road
Bowling Green, KY 42101
Phone: 270/781-9777 x2009
Fax: 270/782-9237
E-mail: rmenon@thermadyne.com

40. Joseph Murphy
Lehigh University
5 East Packer Avenue
Whitaker Lab
Bethlehem, PA 18015
Phone: 610/758-4270
Fax: 610/758-6407
E-mail: jtm4@lehigh.edu

EVENT PARTICIPANT LIST

20th Annual Conference on Fossil Energy Materials
June 12, 2006 - June 14, 2006

41. Ken Natesan
Argonne National Laboratory
9700 South Cass Avenue
Argonne, IL 60439
Phone: 630/252-5103
Fax: 630/252-8681
E-mail: natesan@anl.gov

42. Richard Nixdorf
ReMaxCo Technologies, Inc.
1010 Commerce Park Drive
Suite I
Oak Ridge, TN 37830
Phone: 865/482-7552
Fax: 865/482-7505
E-mail: nixdorfr@indceramicsolns.com

43. Stephen Paglieri
Los Alamos National Laboratory
P.O. Box 1663
MS C927
Los Alamos, NM 87545
Phone: 505/667-0652
Fax: 505/665-1226
E-mail: steve.paglieri@lanl.gov

44. Bruce A. Pint
Oak Ridge National Laboratory
P.O. Box 2008
MS 6156
Oak Ridge, TN 37831-6156
Phone: 865/576-2897
Fax: 865/241-0215
E-mail: pintba@ornl.gov

45. Cynthia Powell
U.S. Department of Energy
National Energy Technology Laboratory
1450 Queen Avenue, SW
Albany, OR 97321
Phone: 541/967-5803
Fax: 541/967-5845
E-mail: cindy.powell@netl.doe.gov

46. Ravi Prasad
Praxair, Inc.
175 East Park Drive
Tonawanda, NY 14150
Phone: 716/879-2614
Fax: 716/879-7091
E-mail: ravi_prasad@praxair.com

47. Udaya Rao
U.S. Department of Energy
National Energy Technology Laboratory
P.O. Box 10940, MS 922-273C
Pittsburgh, PA 15236-0940
Phone: 412/386-4743
Fax: 412/386-5917
E-mail: rao@netl.doe.gov

48. Mary Rawlins
Oak Ridge National Laboratory
One Bethel Valley Road
Building 4500, MS 6269
Oak Ridge, TN 37831
Phone: 865/576-4507
Fax: 865/241-1290
E-mail: rawlinsmh@ornl.gov

EVENT PARTICIPANT LIST

20th Annual Conference on Fossil Energy Materials
June 12, 2006 - June 14, 2006

49. Richard Read
U.S. Department of Energy
National Energy Technology Laboratory
P.O. Box 10940, MS 922-273C
Pittsburgh, PA 15236-0940
Phone: 412/386-5721
Fax: 412/386-5917
E-mail: read@netl.doe.gov

50. Robert Romanosky
U.S. Department of Energy
National Energy Technology Laboratory
P.O. Box 880, MS E02
Morgantown, WV 26507-0880
Phone: 304/285-4721
Fax: 304/285-4777
E-mail: rroman@netl.doe.gov

51. Mike Santella
Oak Ridge National Laboratory
1 Bethel Valley Road
Mail Stop 6096
Oak Ridge, TN 37831
Phone: 865/574-4805
Fax: N/A
E-mail: santellaml@ornl.gov

52. Joachim H. Schneibel
Oak Ridge National Laboratory
P.O. Box 2008
MS 6115
Oak Ridge, TN 37831-6115
Phone: 865/576-4644
Fax: 865/574-7659
E-mail: schneibeljh@ornl.gov

53. John Shen
U.S. Department of Energy
MS FE-24
Germantown, MD 20874
Phone: 301/903-4344
Fax: 301/903-2238
E-mail: john.shen@hq.doe.gov

54. John Shingledecker
Oak Ridge National Laboratory
One Bethel Valley Road
MS 6155
Oak Ridge, TN 37831-6155
Phone: 865/574-5108
Fax: 865/574-0641
E-mail: shingledecjp@ornl.gov

55. Nigel Simms
Cranfield University
Building 43A
Bedford, Bedfordshire MK43 0AL
Phone: 44 1234 754754
Fax: 44 1234 754755
E-mail: n.j.simms@cranfield.ac.uk

56. Joel Simpson
Idaho National Laboratory
P.O. Box 1625
MS 2218
Idaho Falls, ID 83401
Phone: 208/526-9797
Fax: 208/526-4822
E-m joel.simpson@inl.gov

EVENT PARTICIPANT LIST

20th Annual Conference on Fossil Energy Materials
June 12, 2006 - June 14, 2006

57. Greg Stanko
Foster Wheeler North America
12 Peach Tree Hill Road
Livingston, NJ 07039
Phone: 973/535-2256
Fax: N/A
E-mail: greg_stanko@fwc.com

58. David P. Stinton
Oak Ridge National Laboratory
P.O. Box 2008
MS 6065
Oak Ridge, TN 37831
Phone: 865/574-4556
Fax: 865/241-0411
E-mail: stintondp@ornl.gov

59. John Stringer
Consultant
221 Hudson Street
Redwood City, CA 94062-1921
Phone: 650/365-2434
Fax: 650/365-2471
E-mail: johnstringer@comcast.net

60. Robert Terpstra
Ames Laboratory
109 Metals Development Building
Ames, IA 50011-3020
Phone: 515/294-5747
Fax: 515/294-8727
E-mail: terpstra@ameslab.gov

61. Paul Torgerson
World Wide Energy
15 South Excelsior Avenue
Butte, MT 59701
Phone: 406/723-8110
Fax: 406/723-8105
E-mail: paul.torgerson@wesofc.com

62. Peter Tortorelli
Oak Ridge National Laboratory
P.O. Box 2008
Oak Ridge, TN 37831-6156
Phone: 865/574-5119
Fax: 865/241-0215
E-mail: tortorellipf@ornl.gov

63. Terry C. Totemeier
Idaho National Laboratroy
P.O. Box 1625
Mail Stop 2218
Idaho Falls, ID 83401
Phone: 208/526-3074
Fax: 208/526-4822
E-mail: terry.totemeier@inl.gov

64. K. Scott Weil
Pacific Northwest National Laboratory
902 Battelle Boulevard
Mail Stop K2-44
Richland, WA 99352
Phone: 509/375-6796
Fax: 509/375-2186
E-mail: scott.weil@pnl.gov

EVENT PARTICIPANT LIST

20th Annual Conference on Fossil Energy Materials
June 12, 2006 - June 14, 2006

65. Mark Williams
World Wide Energy
15 South Excelsior Avenue
Butte, MT 59701
Phone: 304/904-3977
Fax: 304/292-2040
E-mail: mark.williams@wesofc.com

66. Ian Wright
UT-Battelle, LLC
One Bethel Valley Road
Oak Ridge, TN 37830
Phone: 865/574-4451
Fax: 865/241-0215
E-mail: wrightig@ornl.gov

67. Richard Wright
INEEL
P.O. Box 1625
MS 2218
Idaho Falls, ID 83415
Phone: 208/526-6127
Fax: 208/526-4822
E-mail: RNW2@inel.gov

68. Yukinori Yamamoto
Oak Ridge National Laboratory
P.O. Box 2008
MS 6115
Oak Ridge, TN 37831
Phone: 865/576-7095
Fax: 865/576-6298
E-mail: yamamotoy@ornl.gov

69. Ying Zhang
Tennessee Technological University
115 West 10th Street
P.O. Box 5014
Cookeville, TN 38505-0001
Phone: 931/372-3265
Fax: 931/372-6340
E-mail: yzhang@tntech.edu

70. William Zielke
Tennessee Valley Authority
1101 Market Street
Mail Stop LP-2L
Chattanooga, TN 37402
Phone: 423/751-2762
Fax: 423/751-3860
E-mail: whzielke@tva.gov

71. Jeff Zollar
Oak Ridge National Laboratory
P.O. Box 2008
MS 6084
Oak Ridge, TN 37831
Phone: 865/574-5135
Fax: 865/574-4357
E-mail: zollarja@ornl.gov

Participant Count: 71